Author:
Hossain, Sayeed

Title:
Residual stresses under conditions of high triaxiality

RESIDUAL STRESSES UNDER CONDITIONS OF HIGH TRIAXIALITY

BY

Sayeed Hossain

MEng, MSc, ACGI, DIC

A thesis submitted to the University of Bristol in accordance with the requirements of the Degree of Doctor of Philosophy in the Department of Mechanical Engineering in the Faculty of Engineering

July 2005

Solid Mechanics Group

Department of Mechanical Engineering

University of Bristol

Bristol BS8 1TR

United Kingdom

Abstract

The present study was motivated by a need to model and understand creep in an ageing power plant particularly when residual stresses are present. A number of methods of generating residual stress in laboratory specimens are presented. Both numerical and experimental studies were conducted. The finite element (FE) analysis used in the numerical study was validated with an extensive experimental study of residual stress field characterisation in the test specimens. Two novel means of generating highly triaxial residual stress field in the laboratory specimens were identified and were followed up with design and manufacture. The specimens with internal residual tensile stresses of high triaxiality were used in the subsequent creep study. Using specimens containing residual tensile stress field with variable triaxiality and plastic strain the influence of prior straining in the creep cavitation initiation was also highlighted.

A mechanical strain relief deep-hole (DH) drilling residual stress measurement technique used in residual stress measurement of specimens with high triaxiality highlighted a potential difficulty in using a simple elastic approach to data reduction in the DH measurement method. A comprehensive FE study modelling the DH using an elasto-plastic analysis and an incremental trepanning process in contrast to a previous elastic analysis with a single-step trepanning process [George 2000] was carried out to study further the influence of DH process on the residual stress field.

The reconstructed residual stress distribution obtained in the DH FE analysis considering the influence of the electro-discharge machining (EDM) trepanning showed a good correlation with the DH measured residual stress distribution in the components with residual stress field with high triaxiality. A further DH FE study of the repair welded pipe three material models were considered and the result was found to be highly sensitive to the material model selected. The DH FE study of repair weld revealed that the original residual stress distribution was generated even considering the cutting process of the DH method.

Consequently the deep hole drilling technique was used to characterise the residual stress field in a number of selected locations in practical components including thick-section steel welds consisting of a welded nozzle component which was thermally aged at 550°C for 19,644 hours and a pipe with repair weld.

Acknowledgements

The list of people who assisted me during the course of this research is endless and selected personalities are only mentioned here. First of all I acknowledge the sincere and professional supervision of my advisors Prof. David J Smith and Dr. Christopher E Truman. Truly their continuous encouragement and guidance throughout this research were invaluable.

For this work, I am grateful for financial and scientific support of British Energy Generations Ltd (BEGL) and BNFL-Magnox and beamtime allocated by the ISIS, PSI and NFL facilities. Professional and practical advice during the course of this study by external personnel is also acknowledged, e.g., Mr David Gladwin, Mr Dennis Clutterbuck and Mr Keith Abbott for their assistance with using external laboratory facilities. Special thanks are due to Mr John Bouchard and Dr Mike Smith for their continuous advice throughout the project.

The people at the workshop particularly Ian Milnes, Guy Pearnes, John Byles and Ivan Lavers have all been very helpful in dealing with my last-minute job requests. My sincere gratitude goes to all the dynamic and friendly members of Structural Integrity Research Team. Additional thanks are due to Hassan Alizadeh for his continuous administrative support with aspects related to computing and IT and to Dr M Y Kassim of LUSAS for his time with initial proof reading of this thesis.

Finally but not least I wish to thank all members of my family especially my parents for their continuous moral and additional financial support and my wife for being very understanding and encouraging as well as my loving son for providing a joyful atmosphere at home.

Declaration

The accompanying dissertation entitled "Residual stresses under conditions of high triaxiality" is submitted in support of an application for the degree of Doctor of Philosophy in Engineering at the University of Bristol. The candidate bases the dissertation on independent work unless otherwise acknowledged or referenced in the text. This work has not been submitted for any other degree or diploma at the University or any other institution. The views expressed in the dissertation are those of the author and not of the University.

I declare that the above statements are true.

Sayeed Hossain

July 2005

Original features and publications

The experimental data and analyses of this thesis are directed towards modelling and predicting thermal creep damage in the presence of residual stress and especially thermal creep crack growth in stainless steels. The study includes methods of generating residual stress with high triaxiality and its characterisation. The following features are believed to be original:

Novelties:

- In generating residual stress field with high triaxiality in laboratory small-scale specimens, a novel high-pressure water-jet quenching rig was designed where residual stress was induced in a controlled manner.
- In generating residual stress field with both high triaxiality and high plastic strain for subsequent creep study, a novel "figure-of-eight" shaped punching tool was designed and manufactured.

New findings:

- A full characterisation of residual stress field by reliable neutron diffraction (ND) measurement was achieved in the quenched specimens.
- The use of deep-hole (DH) drilling method in measuring residual stress field in the quenched specimen posed potential problems in using the elastic approach.
- An elasto-plastic DH finite element (FE) simulation with incremental material removal to represent the electro-discharge-machining (EDM) trepanning process in the DH measurement in contrast to the previous elastic analysis by George [2000] modelled the DH process more accurately.
- The elasto-plastic DH FE study demonstrated the influence of the triaxiality, the plasticity and the presence of the residual normal component on the DH measurement process.
- The presence of prior-plasticity in the creep formation subroutine was found important.

Published papers based on the research study:

- S. Hossain, M.R. Daymond, C.E. Truman, D.J. Smith, " Prediction and measurement of residual stresses in quenched stainless-steel spheres", Materials Science and Engineering A Vol. 373, pp. 339–349, 2004.
- S. Hossain, C.E. Truman, D.J. Smith and M.R. Daymond, " Creating Highly Triaxial Residual Stresses and Relaxation of the Stress Field due to Thermal Ageing", Journal of Neutron Research, Vol. 12, No. 1-3, pp. 111-115, 2004.
- S. Hossain, C.E. Truman, D.J. Smith, P.J. Bouchard, "Measurement of residual stresses in a type 316H stainless steel offset repair in a pipe girth weld", ASME – J. Press. Ves. Tech., in press, 2005.
- S. Hossain, C. E. Truman, D. J. Smith, M. R. Daymond, "Creating highly triaxial residual stresses in a type 316H stainless steel", submitted to International Journal of Mechanical Sciences, 2004.

Conference proceedings

- S. Hossain, C.E. Truman, D.J. Smith, M.R. Daymond, "Creating highly triaxial stresses in stainless steel", In proceedings of *International Conference on Advanced Technology in Experimental Mechanics* 2003, ATEM'03, JSME-MMD, Nagoya, Japan, 2003.
- S. Hossain, C.E. Truman, D.J. Smith, M.R. Daymond, "Creating Highly Triaxial Residual Stresses and Relaxation of the Stress Field due to Thermal Ageing", Meca Sens, 2003.
- S. Hossain, C.E. Truman, D.J. Smith and M.R. Daymond, "Measurement of residual stresses in quenched components using neutron diffraction", Materials Congress, London, Institute of Materials, IOM, 2004.
- S. Hossain, C.E. Truman, D.J. Smith and M.R. Daymond, "Prediction and measurement of residual stresses arising from quenching of stainless steels", ASME PVP Conference, 479, San Diego, 2004.
- S. Hossain, P.J. Bouchard, C.E. Truman and D.J. Smith, "Measurement of residual stresses in a type 316H stainless steel offset repair in a pipe girth weld", ASME PVP Conference, 479, San Diego, 2004.
- S. Hossain, A.H. Mahmoudi, C.E. Truman, D.J. Smith, "Generation of Residual Stresses in Compact Tension Specimens for a Study of Creep Damage", Abaqus UK User Group Conference, 2004.

List of Contents

Abstract ii
Acknowledgements iii
Declaration iv
Original features and publications v
List of Contents vii
List of Tables xi
List of Figures xii
Nomenclature xxv

Chapter 1: Introduction 1

Chapter 2: Literature Review 5
2.1 Stainless steel 5
2.2 Creep 6
2.2.1 The creep curve 7
2.2.2 Temperature dependency 9
2.2.3 Stress dependency 9
2.2.4 Creep mechanism 10
2.3 Creep damage models 12
2.4 Definitions and origin of residual stress 14
2.4.1 Origin and nature of residual stresses 15
2.5 Methods of generating residual stress 18
2.5.1 Quenching 18
2.5.2 In-plane loading 21
2.5.3 Side punching 22
2.6 Measurement of residual stress 23
2.6.1 Neutron diffraction 24
2.6.2 Incremental centre-hole drilling 26
2.6.3 Deep hole drilling technique 27
2.6.4 Triaxial residual stresses in metal parts 29

Chapter 3: Creating residual stresses in laboratory specimens 32
3.1 Finite element studies of quenching 32
3.1.1 Theory and FE models 34

3.1.2 FE results....35
3.2 Quenching and post quenching experiments....38
3.2.1 Summary of process conditions....38
3.2.2 Experimental set-up....39
3.2.3 Quenching and post quenching tests....40
3.2.4 Pre-trepanned cylinders....42
3.3 FE studies of side punching....42
3.3.1 FE models....43
3.3.2 FE results....44
3.4 Side punching experiments....46
3.4.1 Experimental rig....46
3.4.2 Side punch tests....46

Chapter 4: Measurement of residual stresses using neutron diffraction....48
4.1 Neutron diffraction time of flight at ISIS....49
4.1.1 Basic principles....49
4.1.2 Instruments....50
4.1.3 Experiments and results for quenched samples....51
4.1.4 Experiments and results for pre-trepanned quenched samples....55
4.1.5 Experiments and results for C(T) specimens....56
4.2 Neutron diffraction time of flight at PSI....57
4.2.1 Instrument and basic principles....57
4.2.2 Experiments and results....58
4.3 Neutron diffraction at NFL....59
4.3.1 Basic principles....60
4.3.2 Instrument....60
4.3.3 Experiments and results for as-quenched sample....62
4.3.4 Experiments and results for pre-trepanned quenched cylinders....62

Chapter 5: Mechanical strain relaxation measurement of residual stress...66
5.1 Incremental Centre Hole Drilling....66
5.1.1 Basic principles....66
5.1.2 Experiments and results for quenched samples....67
5.2 Deep hole drilling....68
5.2.1 Basic principles....69
5.2.2 Application to quenched cylinders....71

Chapter 6: Deep hole drilling developments....74
6.1 Elasto-plastic simulations for simple load cases....75
6.1.1 Validity zone of deep-hole technique under high triaxiality....75
6.1.2 Stress triaxiality....76
6.1.3 Effect of deep-hole simulation....77

6.1.4 Summary and discussion 78
6.2 Simulation for quenched specimens 78
6.2.1 Deep hole drilling simulation 79
6.2.2 Result and discussion 80
6.3 Simulation of the deep hole drilling process on repair weld 82
6.3.1 Validation of 35mm repair weld pipe 83
6.3.2 Effect of deep hole simulation on 35mm repair weld 87
6.3.3 Result and discussion 89
6.4 Application to practical components 90
6.4.1 Residual stress measurement in a nozzle 91
6.4.2 Residual stress measurement in a pipe with repair weld 93
6.5 Concluding remarks 97

Chapter 7: Comparison of residual stress measurement and analysis 99
7.1 Quenched spheres 99
7.2 Quenched cylinders 101
7.3 Side punched C(T) specimens 107

Chapter 8: Analysis of creep damage formation 108
8.1 Damage prediction model 108
8.1.1 Creep model 109
8.1.2 Finite element implementation 111
8.2 Initial predictions of creep damage 112
8.2.1 Damage prediction following quenching 112
8.2.2 Damage prediction following side punching 114
8.3 Measurement of creep damage 115
8.3.1 Damage measurement in quenched samples 115
8.3.2 Damage measurement in side punched specimens 116
8.4 Concluding remarks 118

Chapter 9: General Discussion 120
9.1 Residual stresses prior to thermal ageing 120
9.1.1 Finite element modelling 120
9.1.2 Quenching residual stress 121
9.1.3 Heat transfer coefficient 122
9.1.4 Measured quenched residual stress field 123
9.2 Thermally relaxed residual stresses 125
9.3 Simulation of deep-hole drilling method 126
9.3.1 Validation of deep-hole simulation 126

9.3.2 Other approach to data reduction 129
9.4 Welded components 130
9.4.1 Welded nozzle component 130
9.4.2 Welded pipe component with repair 131
9.5 Quantification of creep damage 132
9.5.1 Metallography 132
9.5.2 Influence of prior strain 132
Mismatch of loading 134
Chapter 10: Conclusions and Recommended Further Studies 136
10.1 Summary 136
10.2 Conclusions 136
10.3 Recommended Further Study 138
References 140
Tables 194
Figures 203
Appendix A: Mapping Methodology 324
Appendix B: Tensile test of 35mm mock up 327

List of Tables

Tables in Chapter 3

Table 3.1 Material properties of types 316H, 316L and 321 stainless steel.

Table 3.2(a) Effect of heat transfer coefficient h (W/m2 K) on residual stress (MPa); initial temperature Ti = 850°C. See Figure 3.8 for illustration of the position in the table.

Table 3.2(b) Effect of initial temperature Ti (°C) on residual stress (MPa); heat transfer coefficient h = 16742 W/m2 K. See Figure 3.8 for illustration of the position in the table.

Table 3.3 Catalogue of quenched specimens.

Table 3.4 Effect of dimensions and applied loading on the triaxiality factor and the plastic strain.

Table 3.5 Dimension of C(T) specimens. SP denotes single-punch, DP denotes double-punch and FOE refers to Figure-of-eight punching configuration.

Table 3.6 Measured and predicted indentations. Samples P215, P241, P242 single punch; Samples P211, P251, P252 double punch; Samples 224, P261, P262 figure-of-eight punch.

Tables in Chapter 4

Table 4.1 Catalogue of quenched specimens in the residual stress measurement programme using neutron diffraction technique. See also Table 3.3 for additional details.

Tables in Chapter 6

Table 6.1 Summary of applied loading cases.

Table 6.2 Summary of deep-hole validation zone result.

List of Figures

Figures in Chapter 2

Figure 2.1 Creep curve

Figure 2.2 Categorisation of residual stresses according to length scales (after Kandil et al, 2001].

Figure 2.3 Schematic of material behaviour on loading unloading (after Noyan and Cohen, 1987).

Figure 2.4 Schematic distortion of a butt-welded plate due to shrinkage of hot weld metal (after Parlane, 1981).

Figure 2.5 Model for solid cylindrical body and FE mesh illustrating the mechanical boundary condition in the FE analysis (after Sen et al, 2000).

Figure 2.6 Inplane comression loading of C(T) specimen (after Turski et al, 2004).

Figure 2.7 Local compression process (after Meith and Hill, 2002).

Figure 2.8 Schematic diagram of a neutron diffractometer (after Pintschovius, 2003).

Figure 2.9 Typical hole-drilling apparatus and residual stress strain gauge rosette design (http://www.measurementsgroup.com).

Figure 2.10 Schematic illustration of the DH method.

Figure 2.11 Measured and predicted through-thickness residual stress distribution in an aluminium alloy plate (after Yazdi et al, 1998).

Figure 2.12 Measured and predicted residual stress in a cylindrical test piece, diameter 20mm, length 60mm (after Mukai et al, 2003).

Figure 2.13 Measured and predicted residual stress in a cylindrical test piece, diameter 30mm, length 10mm (after Mukai et al, 2003).

Figure 2.14 Comparison of crack opening, HEXRD mid thickness measurements (ID15A, ESRF, France) of residual elastic strains and 3D FE predictions for CT5 along the ligament of the pre-strained, notched CT specimen. (after Turski 2004].

Figure 2.15 Comparison between the predicted and measured residual stresses (three measurement methods) through the thickness of the aluminium alloy plate following side punching. (after Mahmoudi et al 2005].

Figures in Chapter 3

Figure 3.1 Finite element mesh of one quarter of the specimens. Axes of symmetry along Or and Oy.

Figure 3.2 Stainless steel mechanical and physical properties.

Figure 3.3 Residual stresses across radial line of quenched cylindrical bars and sphere.

Figure 3.4 Hydrostatic stresses across radial line of quenched cylindrical bars and sphere.

Figure 3.5 Effect of geometry on hydrostatic and principal stress.

Figure 3.6 Residual stress distributions along the longitudinal axis of a quenched cylinder, diameter 60mm, length 60mm (a) of type 321 and (b) 316L stainless steel.

Figure 3.7 Comparison between the FE predicted and analytical distribution of residual stresses across the radial plane from the centre of a solid stainless steel sphere, diameter 30mm. Heat transfer coefficient, h = 7000 W/m^2 K, initial temperature 850°C and kinematic hardening model.

Figure 3.8 Section through a cylinder showing the locations used in Table 3.2.

Figure 3.9 Effect of heat transfer coefficient h (W/m^2 K) on the predicted residual stress distribution.

Figure 3.10 Effect of initial temperature on the predicted residual stress distribution.

Figure 3.11 Schematic layout of the quenching rig.

Figure 3.12 Schematic of generic quenched specimens, cylinder, diameter *D*, length *L* and sphere, diameter *D*.

Figure 3.13 Plan view of a solid sphere, diameter 30mm illustrating the positions of thermocouples for temperature measurements during heating and subsequent quenching. Also shown is a vertical section of a generic cylindrical body, diameter *D*, length *L* to illustrate the locations of thermocouples during quenching test.

Figure 3.14 Temperature distributions in a quenched cylinder (s2) during preheating.

Figure 3.15 Typical temperature-time curve measured during cooling at the centre and surface of a quenched sphere, 30 mm diameter (s22).

Figure 3.16 Typical temperature-time curve measured during cooling at the centre and surface of a quenched sphere (s22), 30 mm diameter, compared with finite element results. Heat transfer coefficient, h = 7000 W/m^2 K.

Figure 3.17 Typical temperature-time curve measured during quenching at the centre and surface of a quenched cylinder (s26), diameter 60mm, length 160mm. Comparison is made with finite element simulation. Heat transfer coefficient, h = 7000 W/m^2 K.

Figure 3.18 FE predicted temperature-time curve with heat transfer coefficient, h = 200 W/m^2 K compared with measured temperature fields for sample s26.

Figure 3.19 Schematic of the preparation of trepanned cylinders. For (a) large cylinders the edm depths d were 0, 15.5, 30.0, 45.5, 60.0 corresponding to samples s44, s40, s41, s42, s43, respectively listed in Table 3.3. For (b) small cylinders the edm depths *d* were 0, 8.5, 15.5, 21.5, 28.0 corresponding to samples s38, s34, s35, s36, s37, respectively

(see Table 3.3). All dimensions in mm. As shown the drilling diameter was 1.5mm, the edm trepan diameter was 5.0mm and the thickness of copper electrode was 1.0mm.

Figure 3.20 Side punch C(T) specimen (dimensions in mm).

Figure 3.21 Schematic of the side-punching process on C(T) specimen. A quarter of the specimen is shown.

Figure 3.22 Residual stress distribution across the ligament from the notch tip of the C(T) specimen under various loading conditions for single punch. For clarity distribution in the first 2.5mm from the notch tip is also shown.

Figure 3.23 Residual stress distribution across the ligament from the notch tip of the C(T) specimen under various loading conditions for double punch. For clarity distribution in the first 2.5mm from the notch tip is also shown.

Figure 3.24 Residual stress distribution across the ligament from the notch tip of the C(T) specimen under various loading conditions for figure-of-eight punch. For clarity distribution in the first 2.5mm from the notch tip is also shown.

Figure 3.25 Distributions of triaxiality factor (TF) and equivalent plastic strain (PS) across the ligament from the notch tip of the side punch C(T) specimen under various loading conditions for (a) single and (b) double punch. Only the distribution in the first 2.5mm from the notch tip is shown for clarity.

Figure 3.26 Effect of positions of punch on distributions of triaxiality factor and equivalent plastic strain across the ligament from the notch tip of the side punch C(T) specimen. Figure-of-eight punch: x/R=1, y/R=0.5. See Figure 3.27 for illustration of x/R and y/R ratios.

Figure 3.27 Illustration of variation of X and Y on double punch. X is the distance between the crack tip and the punch centre; Y is the distance between the crack plane and the punch centre.

Figure 3.28 Schematic of (a) single and (b) double punching tools.

Figure 3.29 "Figure of eight" shape punching tool. Dimensions in "mm".

Figures in Chapter 4

Figure 4.1 Schematic layout of the ENGIN neutron diffractometer on the PEARL beam line at the ISIS facilities.

Figure 4.2 Schematic diagrams showing types 316H and 316L stainless steel solid sphere, diameter 30mm, the solid cylinder, diameter D, length L and the reference comb sample used for the ND measurements. Note different cylinder sizes were used. The *D*, *L* pair consisted of 60, 60; 60, 160; 30, 30 and 29, 29. All dimensions in mm.

Figure 4.3 Schematic of quenched 316H stainless steel cylinders s19, s27 and s26 respectively.

Figure 4.4 Summary of the measured stress-free lattice parameter d_0 across the seven fingers on the comb s9 used to determine residual elastic strain on quenched sample s8.

Figure 4.5 Summary of ND measured residual strains in quenched sphere s8.

Figure 4.6 Measured residual stress distributions across radial plane in quenched sphere s8.

Figure 4.7 Summary of ND measured residual strains in a quenched sphere s22.

Figure 4.8 Measured residual stress distributions across radial plane in quenched sphere s22.

Figure 4.9 Comparison of residual stress distribution across equatorial plane between quenched spheres s8 (type 316L) and s22 (type 316H).

Figure 4.10 Summary of ND measured strains in quenched cylinder s19 across OS (see Figure 4.3a).

Figure 4.11 Measured residual stress distribution across OS (see Figure 4.3a) in a quenched stainless steel solid cylinder s19.

Figure 4.12 Summary of ND measured residual strains in a quenched cylinder s27 at 18mm offset from the flat of the cylinder across NA (see Figure 4.3b).

Figure 4.13 Summary of ND measured residual strains in a quenched cylinder s27 across OB (see Figure 4.3b).

Figure 4.14 Summary of ND measured residual strains in a quenched cylinder s26 along the longitudinal axis at positions A, B and C (see Figure 4.3c).

Figure 4.15 Comparison of measured residual stress distributions in cylinder s27 across OB and NA (see Figure 4.3b) and cylinder s19 across OS (see Figure 4.3a).

Figure 4.16 Summary of ND measured residual strains in a quenched and aged 316H solid SS sphere s24.

Figure 4.17 Measured residual stress distribution across the radial plane in a quenched and aged 316H SS solid sphere s24.

Figure 4.18 Comparison of residual stress distributions between as-quenched 316H SS solid sphere s22 and quenched and aged 316H SS solid sphere s24 across OS.

Figure 4.19 Distribution of residual (a) strain and (b) stress across a radial plane 18.5mm below the top surface in a quenched cylinder bar s40 with 1.5mm diameter drill and 5mm diameter trepanned up to 15.5mm depth.

Figure 4.20 Distribution of residual (a) strain and (b) stress along an axial line 8mm away from the centreline in a quenched cylinder bar s40 with 1.5mm diameter drill and 5mm diameter trepanned up to 15.5mm depth.

Figure 4.21 Distribution of residual (a) strain and (b) stress across a radial plane 48.5mm below the top surface in a quenched cylinder bar s42 with 1.5mm diameter drill and 5mm diameter trepanned up to 45.5mm depth.

Figure 4.22 Distribution of residual (a) strain and (b) stress along an axial line 8mm away from the centreline in a quenched cylinder bar s42 with 1.5mm diameter drill and 5mm diameter trepanned up to 45.5mm depth.

Figure 4.23 Measured residual strain distribution along the ligament ahead of crack tip in the mid-plane of an as-punched C(T) specimen.

Figure 4.24 Measured residual stress distribution along the ligament ahead of crack tip in the mid-plane of an as-punched C(T) specimen.

Figure 4.25 Measured residual strain distribution along the ligament ahead of crack tip in the mid-plane of a punched and thermally aged C(T) specimen.

Figure 4.26 Measured residual stress distribution along the ligament ahead of crack tip in the mid-plane of a punched and thermally aged C(T) specimen.

Figure 4.27 Comparison of measured residual stress distribution along the ligament ahead of crack tip in the mid-plane between the as-punched and punched and thermally aged C(T) specimens.

Figure 4.28 Schematic layout of the POLDI neutron diffractometer at the PSI facility.

Figure 4.29 Summary of measured stress-free lattice parameter d_0 across comb s30 used to determine the residual elastic strain distribution across sample s29.

Figure 4.30 Summary of measured stress-free lattice parameter d_0 across comb s31 used to determine the residual elastic strain distribution across sample s28.

Figure 4.31 Measured and predicted residual stress distribution across the equatorial plane of a quenched and short-term (1.25 hours) thermally aged cylinder s29.

Figure 4.32 Measured and predicted residual stress distribution across the equatorial plane of a quenched and long-term (1800 hours) thermally aged cylinder s28.

Figure 4.33 Description of residual stress instrument REST at NFL, Sweden (http://www.studsvik.uu.se/)

Figure 4.34 Summary of the measured Bragg angles across the seven fingers on the comb s25 used to determine the stress free parameter.

Figure 4.35 Summary of ND measured residual strains for a quenched stainless steel solid cylindrical bar s39, diameter 29mm, length 29mm, across the equatorial plane from the centre to the surface of the bar.

Figure 4.36 Measured residual stress distribution across the equatorial plane of a quenched cylinder s39, diameter 29mm, length 29mm, measured from the centre to the surface of the bar.

Figure 4.37 Distribution of residual (a) strain and (b) stress across a radial plane 12mm below the top surface in a quenched cylinder bar s34 with 1.5mm diameter drill and 5mm diameter trepanned up to 8.5mm depth.

Figure 4.38 Distribution of residual (a) strain and (b) stress along an axial line 6mm away from the centreline in a quenched cylinder bar s34 with 1.5mm diameter drill and 5mm diameter trepanned up to 8.5mm depth.

Figure 4.39 Distribution of residual (a) strain and (b) stress across a radial plane 18mm below the top surface in a quenched cylinder bar s35 with 1.5mm diameter drill and 5mm diameter trepanned up to 15.5mm depth.

Figure 4.40 Distribution of residual (a) strain and (b) stress along an axial line 6mm away from the centreline in a quenched cylinder bar s35 with 1.5mm diameter drill and 5mm diameter trepanned up to 15.5mm depth.

Figure 4.41 Distribution of residual (a) strain and (b) stress across a radial plane 24mm below the top surface in a quenched cylinder bar s36 with 1.5mm diameter drill and 5mm diameter trepanned up to 21.5mm depth.

Figure 4.42 Distribution of residual (a) strain and (b) stress along an axial line 6mm away from the centreline in a quenched cylinder bar s36 with 1.5mm diameter drill and 5mm diameter trepanned up to 21.5mm depth.

Figure 4.43 Distribution of residual (a) strain and (b) stress along an axial line 6mm away from the centreline in a quenched cylinder bar s37 with 1.5mm diameter drill and 5mm diameter trepanned up to 28mm depth.

Figure 4.44 Effect of edm depth on the measured residual stress distribution across a radial plane ahead of the edm front.

Figure 4.45 Effect of edm depth on the measured residual stress distribution along an axial line 6-8mm away from the centreline.

Figures in Chapter 5

Figure 5.1 Incremental centre hole measured residual strains of a 30mm diameter sphere s8.

Figure 5.2 Centre hole surface residual stress result for a 30mm diameter sphere s8.

Figure 5.3 Incremental centre hole measured residual strains of a quenched cylinder, diameter 60mm, length 60mm s12.

Figure 5.4 Surface residual stress result for a 60mm diameter cylinder s12.

Figure 5.5 Incremental centre hole measured residual strains of a quenched cylinder, diameter 30mm, length 100mm s1.

Figure 5.6 Surface residual stress result for a quenched cylinder, diameter 30mm, length 100mm (sample s1).

Figure 5.7 Schematic illustration of the deep hole drilling (DHD) method.

Figure 5.8 Residual stress distributions measured from the font through the quenched cylinders fabricated from stainless steel of type (a) 321 (s12) and (b) 316L (s2).

Figures in Chapter 6

Figure 6.1 Three dimensional, prismatic block of material in the deep hole technique zone of validity study.

Figure 6.2 Finite element model of the 3D block used in the deep hole validity zone study.

Figure 6.3 Through-thickness applied and reconstructed deep hole stress distribution for uniaxial loading case with triaxiality factor of 0.333.

Figure 6.4 Through-thickness applied and reconstructed deep hole stress distribution for biaxial loading case with triaxiality factor of 0.6.

Figure 6.5 Through-thickness applied and reconstructed deep hole stress distribution for triaxial loading case with triaxiality factor of 1.

Figure 6.6 Through-thickness applied and reconstructed deep hole stress distribution for triaxial loading case with triaxiality factor of 0.5.

Figure 6.7 Summary of "measured" principal stress versus applied equivalent stress normalised by yield stress.

Figure 6.8 Summary of "measured" versus applied principal stress normalised by yield stress.

Figure 6.9 Summary of "measured" principal stress normalised by equivalent stress versus applied stress normalised by yield stress.

Figure 6.10 Axi-symmetric model of the quenched cylinder illustrating the drilling and trepanning steps of deep hole drilling measurement technique. The edge A'B' represents the inner surface of the gun-drilled reference hole used to measure the diametral distortions.

Figure 6.11 Deep hole measured residual stresses compared with the finite element predicted residual stresses due to simulation of deep hole method. The predicted initial quenched residual stresses (Figure 3.6) are also shown. (a) type 321, (b) type 316L.

Figure 6.12 FE predicted distribution of equivalent plastic strain along the edge of drilled region A'B' (see Figure 6.10) before drilling, before trepanning and after trepanning.

Figure 6.13 Initial FE predicted and deep hole simulated residual stress distributions along the longitudinal axis of type 316L stainless steel cylinder, with heat transfer coefficient, h = 400 W/m^2 K and kinematic hardening.

Figure 6.14 FE predicted distribution of equivalent plastic strain along the edge of drilled region A'B' (see Figure 6.10) before drilling, before trepanning and after trepanning. Comparison is made between the distributions for heat transfer coefficients, h = 7000 W/m2 K and h = 400 W/m^2 K.

Figure 6.15 Welded pipe geometry, ¼ model of the full pipe, inner diameter = 362mm, outer diameter = 432mm, wall thickness = 35mm.

Figure 6.16 Stress distributions through the pipe with no weld cap from the inner surface. The theoretical result assuming an elastic case compares very well with the finite element predicted stress distribution.

Figure 6.17 Calculated and finite element predicted autofrettage residual stress distribution through the pipe thickness.

Figure 6.18 Illustration of the outer and inner surface of the welded pipe model.

Figure 6.19 Illustration of the three regions – Parent, Repair and Girth, highlighted. Also shown is the original unmodified weld profile on the top right hand corner.

Figure 6.20 Boundary conditions consist of a) 1-Symmetry BC, b) 3-Symmetry BC and c) Fixed displacement BC in 2-direction.

Figure 6.21 3D mesh showing the drilling and trepanning regions.

Figure 6.22 Figure showing detailed mesh of the welded region.

Figure 6.23 Illustration of drill and trepan parts.

Figure 6.24 Core illustrating the additional boundary conditions on two nodes required in the deep hole simulation in the pipe axial (2-direction) shown by the arrows on the outer and inner surface.

Figure 6.25 Back bush fixed in the normal (3-direction) during the deep hole simulation.

Figure 6.26 Illustration of single-step drilling and 6-step trepanning process.

Figure 6.27 Stress distributions through the specimen from the outer surface (along thick line in Figure 6.21). An initial internal pressure of 50 MPa was applied, with tensile load of 157.24 MPa at either free end to simulate the end cap conditions.

Figure 6.28 Residual stress distributions through the specimen from the outer surface. The residual stresses result in the specimen after loading unloading sequence.

Figure 6.29 Initial applied residual stress distributions through the specimen.

Figure 6.30 Comparison of the initial applied residual stresses with the deep hole reconstructed residual stresses.

Figure 6.31 Initial weld residual stress and mapped residual stress distribution through the thickness of the welded pipe. Note that due to differences in coordinate systems of the pipe specimen in the two models, the coordinates in the mapped stresses are different from the initial weld stress directions, e.g., "zz" in original becomes "xx" in mapped, etc.

Figure 6.32 Parent and girth weld material properties at room temperature. Also shown is the fictitious weld material property with an identical linear hardening (LH) as the parent material.

Figure 6.33 Non-linear kinematic hardening model based on VORSAC data.

Figure 6.34 Comparison of mapped equilibrium residual stress distribution through the thickness of the pipe specimen along a line, based on two material properties, elastic-perfect plastic and non-linear kinematic hardening models.

Figure 6.35 Reconstructed deep hole simulated residual stresses.

Figure 6.36 Comparison of initial FE residual stresses with reconstructed deep hole simulated residual stresses for elastic perfect plastic (PP) material model.

Figure 6.37 Comparison of initial FE residual stresses with reconstructed deep hole simulated residual stresses for linear hardening (LH) material model.

Figure 6.38 Comparison of initial FE residual stresses with reconstructed deep hole simulated residual stresses for non-linear kinematic hardening (NKH) material model.

Figure 6.39 Initial FE predicted residual stresses through the thickness of the pipe from outer surface along a line compared with a hole-average.

Figure 6.40 Nozzle Arrangement, Mock-up specimen S4.

Figure 6.41 Location of deep hole measurements on mock-up S4 specimen.

Figure 6.42 Measured residual stresses after thermal soak test at 550°C for 19,644 h.

Figure 6.43 Comparison of measured residual stresses at the nozzle after the thermal soak test (19,644 h at 550°C) with the as-welded state and measured stresses from a service-aged (55,000 h at 525°C) component.

Figure 6.44 Arrangement of stainless steel pipe girth weld (dimensions in mm).

Figure 6.45 Set-up of butt-weld and offset repair weld (all dimensions in mm).

Figure 6.46 Bead run sequence.

Figure 6.47 Locations of Deep Hole Measurements.

Figure 6.48 Measured residual stresses near the intersection of the girth centreline with the mid-length of the repair weld (Hole 1).

Figure 6.49 Measured residual stresses along the girth weld centreline at the stop end of the repair weld (Hole 2).

Figure 6.50 Measured residual stresses in a 218mm long, offset, 316 Stainless Steel repair weld compared with 3D FE predictions for a similar Esshete Repair.

Figure 6.51 Measured residual stresses at mid-length of repair weld (Hole 1) compared with predicted residual stresses mapped from BEGL-FNC model (see Figure 6.38).

Figure 6.52 Comparison of measured residual stresses at mid-length of the repair weld (Hole 1) with the DH FE reconstructed residual stresses (see Figure 6.38).

Figures in Chapter 7

Figure 7.1 Summary of the measured strains and FE strains with heat transfer coefficient h = 7000 W/m^2 K and kinematic hardening model in quenched sphere s8.

Figure 7.2 Measured residual stresses compared with FE predictions with heat transfer coefficient h = 7000 W/m^2 K in quenched sphere s8.

Figure 7.3 Summary of ND measured and FE predicted strains for a 30 mm diameter quenched stainless steel solid sphere s22.

Figure 7.4 ND measured and FE predicted residual stresses in a 30 mm diameter quenched stainless steel solid sphere s22.

Figure 7.5 ND measured residual stress results in a 30 mm diameter stainless steel solid sphere s22, compared with an analytical distribution [McKenzie and Moakler 1973].

Figure 7.6 Summary of ND measured and FE predicted residual strain distributions across the equatorial plane of a thermally aged quenched SS solid sphere s24, diameter 30mm measured from the centre to the surface of the sphere.

Figure 7.7 Measured and predicted residual stress distribution across the equatorial plane of a quenched sphere, diameter 30mm followed by thermal ageing at 550°C for 3200 hours, s24, measured from the centre to the surface of the sphere. The heat transfer coefficient, h = 7000 W/m2 K, initial temperature = 850°C, kinematic hardening model

Figure 7.8 Summary of ND measured and FE predicted strains for a quenched stainless steel solid cylindrical bar s19, diameter 60mm, length 60mm across OS (see Figure 4.3a). The heat transfer coefficient, h = 7000 W/m2 K, initial temperature = 850°C, kinematic hardening model.

Figure 7.9 ND measured and FE predicted residual stresses in a quenched stainless steel solid cylinder s19, diameter 60mm, length 60mm across OS (see Figure 4.3a). The heat transfer coefficient, h = 7000 W/m^2 K, initial temperature = 850°C, with kinematic hardening model. Also shown is the ICHD measured of a similar quenched cylinder sample s12.

Figure 7.10 Summary of ND measured and FE predicted strains for a quenched stainless steel solid cylindrical bar s27, diameter 60mm, length 160mm, at 18mm offset from the end, across NA (see Figure 4.3(b)). The heat transfer coefficient, h = 7000 W/m^2 K, initial temperature = 850°C, kinematic hardening model.

Figure 7.11 Summary of ND measured and FE predicted strains for a quenched stainless steel solid cylindrical bar s27, diameter 60mm, length 160mm, across OB (see Figure 4.3(b)). The heat transfer coefficient, h = 7000 W/m^2 K, initial temperature = 850°C, kinematic hardening model.

Figure 7.12 Summary of ND measured and FE predicted strains for a quenched stainless steel solid cylindrical bar, diameter 60mm, length 160mm, along the longitudinal axis. The measurements are at positions A, B and C on specimen s26 (see Figure 4.3(c)). The heat transfer coefficient, h = 7000 W/m^2 K, initial temperature = 850°C, kinematic hardening model.

Figure 7.13 Summary of ND measured and FE predicted strains for a quenched stainless steel solid cylindrical bar s39, diameter 29mm, length 29mm, across the equatorial plane from the centre to the surface of the bar.

Figure 7.14 Measured and predicted residual stress distribution across the equatorial plane of a quenched cylinder s39, diameter 29mm, length 29mm, measured from the centre to the surface of the bar. The heat transfer coefficient, h = 7000 W/m^2 K, initial temperature = 850°C, kinematic hardening model.

Figure 7.15 Comparison of residual stress distribution in s19 and s39.

Figure 7.16 Measured and predicted residual stress distribution across the equatorial plane of a quenched and short-term (1.25 hours) thermally aged cylinder s29.

Figure 7.17 Measured and predicted residual stress distribution across the equatorial plane of a quenched and long-term (1800 hours) thermally aged cylinder s28.

Figure 7.18 Comparison of residual stress distribution between cylinders s29, s28 and s39.

Figure 7.19 Distribution of residual (a) strain and (b) stress across a radial plane 12mm below the top surface in a quenched cylinder bar s34 with 1.5mm diameter drill and 5mm diameter trepanned up to 8.5mm depth.

Figure 7.20 Distribution of residual (a) strain and (b) stress along an axial line 6mm away from the centreline in a quenched cylinder bar s34 with 1.5mm diameter drill and 5mm diameter trepanned up to 8.5mm depth.

Figure 7.21 Distribution of residual (a) strain and (b) stress across a radial plane 18mm below the top surface in a quenched cylinder bar s35 with 1.5mm diameter drill and 5mm diameter trepanned up to 15.5mm depth.

Figure 7.22 Distribution of residual (a) strain and (b) stress along an axial line 6mm away from the centreline in a quenched cylinder bar s35 with 1.5mm diameter drill and 5mm diameter trepanned up to 15.5mm depth.

Figure 7.23 Distribution of residual (a) strain and (b) stress across a radial plane 24mm below the top surface in a quenched cylinder bar s36 with 1.5mm diameter drill and 5mm diameter trepanned up to 21.5mm depth.

Figure 7.24 Distribution of residual (a) strain and (b) stress along an axial line 6mm away from the centreline in a quenched cylinder bar s36 with 1.5mm diameter drill and 5mm diameter trepanned up to 21.5mm depth.

Figure 7.25 Distribution of residual (a) strain and (b) stress along an axial line 6mm away from the centreline in a quenched cylinder bar s37 with 1.5mm diameter drill and 5mm diameter trepanned up to 28mm depth.

Figure 7.26 Distribution of residual (a) strain and (b) stress across a radial plane 18.5mm below the top surface in a quenched cylinder bar s40 with 1.5mm diameter drill and 5mm diameter trepanned up to 15.5mm depth.

Figure 7.27 Distribution of residual (a) strain and (b) stress along an axial line 8mm away from the centreline in a quenched cylinder bar s40 with 1.5mm diameter drill and 5mm diameter trepanned up to 15.5mm depth.

Figure 7.28 Distribution of residual (a) strain and (b) stress across a radial plane 48.5mm below the top surface in a quenched cylinder bar s42 with 1.5mm diameter drill and 5mm diameter trepanned up to 45.5mm depth.

Figure 7.29 Distribution of residual (a) strain and (b) stress along an axial line 8mm away from the centreline in a quenched cylinder bar s42 with 1.5mm diameter drill and 5mm diameter trepanned up to 45.5mm depth.

Figure 7.30 Measured and FE predicted residual strain distribution along the ligament ahead of the crack tip in the mid-plane of an as-punched C(T) specimen.

Figure 7.31 Measured and FE predicted residual stress distribution along the ligament ahead of the crack tip in the mid-plane of an as-punched C(T) specimen.

Figure 7.32 Measured and FE predicted residual strain distribution along the ligament ahead of the crack tip in the mid-plane of a punched and aged C(T) specimen.

Figure 7.33 Measured and FE predicted residual stress distribution along the ligament ahead of the crack tip in the mid-plane of a punched and aged C(T) specimen.

Figure 7.34 Comparison of residual stress distribution along the ligament ahead of crack tip in the mid-plane between as-punched and punched and thermally aged (at 550°C for 3900hours) C(T) specimens.

Figures in Chapter 8

Figure 8.1 Measured and FE predicted von Mises equivalent residual stress distribution across the radial plane in a quenched cylinder during thermal exposure.

Figure 8.2 Predicted damage in a selected region of a quenched cylinder, diameter 60mm, length 60mm subjected to thermal exposure at 550°C.

Figure 8.3 Region of creep damage accumulation predicted in a quenched cylinder bar followed by thermal ageing at 550°C for 2880hours and 4320hours under empirical functions set 1 and set 2 respectively.

Figure 8.4 Measured and FE predicted von Mises equivalent residual stress distribution along the ligament ahead of crack tip in the mid-plane of a figure-of-eight punched C(T) specimen during thermal ageing.

Figure 8.5 Contour plots illustrating the development of predicted damage parameter in thermally exposed single punch C(T) specimens with time.

Figure 8.6 Contour plots illustrating the development of predicted damage parameter in thermally exposed double punch C(T) specimens with time.

Figure 8.7 Contour plots illustrating the development of predicted damage parameter in thermally exposed figure-of-eight punch C(T) specimens with time.

Figure 8.8 Predicted damage in a selected region of punched C(T) specimen subjected to thermal exposure at 550°C. See Figure 8.9 for illustration of the selected positions "a", "b" and "c".

Figure 8.9 Illustration of the selected location in the punched specimen where the creep damage parameter is shown in Figure 8.8.

Figure 8.10 Micrographs of quenched and thermally aged cylinder s17.

Figure 8.11 Side punched and thermally aged C(T) specimens including (a) figure-of-eight, (b) double and (c) single punch cases left to right. The top fractured samples are used for fractography and the bottom samples for metallography study.

Figure 8.12 Scanning electron micrograph showing creep cavities in figure-of-eight side punched C(T) fracture surface. See Figure 8.15 for illustration of X and Z.

Figure 8.13 Scanning electron micrograph showing creep cavities in double punched C(T) fracture surface. See Figure 8.15 for illustration of X and Z.

Figure 8.814 Scanning electron micrograph showing formation of creep cavities in single punched C(T) specimen fracture surface.

Figure 8.15 Section trough the fracture surface of C(T) specimen illustrating the positions X and Z used in Figures 8.12 to 8.14 to measure the extent and location of creep cavitation.

Figure 8.16 Optical micrograph taken from the mid-thickness plane of figure-of-eight side punched and thermally aged (at 550°C for 3900 hours) showing creep cavities along grain boundaries.

Figure 8.17 FE predicted and SEM observed damage regions on the fracture surface of punched C(T) specimens.

Figures in Chapter 9

Figure 9.1 FE predicted (a) radial, (b) axial and (c) hoop residual stress distribution across a radial plane from the centreline towards the outer surface in a pre-trepanned quenched cylinder with variable edm depths along the trepan edge.

Figure 9.2 FE predicted (a) radial, (b) axial and (c) hoop residual stress distribution along an axial line in a pre-trepanned quenched cylinder with variable edm depths along the trepan edge.

Figure 9.3 FE predicted residual stress distribution (a) radial, (b) axial and (c) hoop components in the deep hole core for different edm trepan depths.

Nomenclature

The following lists the symbols used in the main text.

$A(z)$, $B(z)$	Functions that account for the variations in reference hole strain with respect to z
B	Thickness of C(T) specimen
D	Diameter of solid sphere and cylinder; nominal outer diameter of the trepanned core
D_c	Creep damage parameter
E	Young's modulus
L	Length of solid cylinder
$[M(z_i)]$	Matrix relating hole strains to residual stress components
Q	Activation energy for creep,
R	Universal gas constant; radius of punching tool
T	Temperature
TF	Triaxiality factor = σ_h/σ_e
a	Internal radius of a pipe
b	External radius of the pipe
$d(\theta, z)$	Measured diameter of reference hole before core removal
$d'(\theta, z)$	Measured diameter of reference hole after core removal
d_{hkl}	Lattice spacing of a monochromator
d_o	Stress-free interplanar spacing
$f(\theta, z)$, $g(\theta, z)$, $h(\theta, z)$	Functions used in the data reduction scheme
h	Heat transfer coefficient
k	Secondary creep constant
p, q	Empirical material constants
p_i	Internal applied pressure
r	Distance from the centre of the pipe; distance from the centre of the sphere
r_o	Radius of outer surface of sphere
t	Time of flight
t_{fp}	Time of transition from primary to secondary behaviour
t_g, t_p, t_r	Thickness of girth weld, pipe and repair weld respectively
w	Estimated width of the girth weld
z_i	Depths where reference hole strains are measured

β	Primary creep constant
δ	Applied displacement load on C(T) specimen
δd_{err}	Deformation error in the reference hole
$\Delta d(\theta, z)$	Change in reference hole diameter
$\dot{\varepsilon}_c$	Creep strain rate
$\dot{\bar{\varepsilon}}_c$	Instantaneous von Mises equivalent creep strain rate
$\dot{\bar{\varepsilon}}_{ct}$	Equivalent creep strain rate including the tertiary behaviour
$\varepsilon_{f,uni}$	Uniaxial ductility
$\bar{\varepsilon}_f$	von Mises strain at failure
$\bar{\varepsilon}_{fp}$	Equivalent creep strain at the end of the primary creep stage
$\bar{\varepsilon}_p$	Equivalent creep strain in the primary creep range
$\bar{\varepsilon}_s$	Equivalent creep strain in the secondary creep stage
$\tilde{\varepsilon}(\theta, z)$	Reference hole strain for a given unknown applied remote stress
$\{\tilde{\varepsilon}(z_i)\}$	Vector of reference hole strains at depth z_i
ε_x, ε_y	Relaxed strain on surface along x and y direction
λ_m	Wavelength of neutron beam
θ	Number of angles around the reference hole axis
θ_m	Scattering angle at the monochromator; angles where reference hole strains are measured
$\bar{\sigma}$, σ_e	von Mises (equivalent) stress
σ_1	Maximum principal stress component
σ_h	Hydrostatic (mean) stress
σ_r, σ_θ, σ_z	Radial, hoop, axial stress component
σ_Y	Yield stress
$\sigma_x(H)$	Stress distributions along the generic orthogonal x direction
$\sigma_y(H)$	Stress distributions along the generic orthogonal y direction
$\sigma(z_i)$	Unknown stress components
$\{\sigma(z_i)\}$	Vector of residual stress components at depth z_i
σ_{xx}, σ_{yy}, σ_{xy}	Residual stress components in the plane normal to the axis of the reference hole
ν	Poisson's ratio of the component material

Chapter 1

Introduction

The principal deterioration mechanisms in engineering components operating at high temperature are creep damage, microstructural degradation, high temperature fatigue, creep-fatigue, embrittlement, carburisation, thermal shock, erosion, and high temperature corrosion of various types [Furtado and Le May 2004]. Of these, creep is one of the most serious high-temperature damage mechanisms. Calculations of creep damage under conditions of strain control are often carried out using either time fraction or ductility exhaustion approaches. The presence of multiaxial stress states further complicates the calculation of creep damage. In the case of time fraction methods there are a number of models that predict the effect of state of stress on creep rupture strength: e.g. Huddleston [1985] developed a model from data based on stainless steels. The R5 procedure [R5 2001] uses a ductility-exhaustion approach to calculate creep damage and includes a model that takes account of the effect of triaxial states of stress. Spindler [2004] developed this model by considering cavity nucleation and growth and multiaxial creep data on Type 304 and 316 stainless steels. An underlying feature of the ductility-exhaustion approach is that it relies on accurate predictions of creep strains arising during thermal relaxation of weld residual stresses and the local multi-axial creep ductility.

The primary purpose of the present study was to gain an understanding of whether the presence of multiaxial residual stresses could act as a driving force for the creation of creep damage. The present study was motivated by a need to model and understand creep in an aged power plant. This was done by attempting to induce creep damage in small sized stainless steel specimens under laboratory conditions in a controlled manner. Numerical studies were carried out in the initial stage of the work using the commercial ABAQUS finite element code to simulate the desired residual stresses. Two methods of introducing residual stresses into samples were studied: (a) rapid spray water quenching of spherical and cylindrical bodies, (b) side punching of compact tension C(T) specimens. Description of these methods and numerical studies of these process conditions are detailed in Chapter 3. Experimental studies were conducted to create residual stresses using the quenching and side punching processes. The relatively simple

specimen shapes used in the experiments allowed the residual stress field to be measured with ease using neutron diffraction techniques as well as reducing the complexity of the supporting finite element study. Other methods of residual stress measurement, such as the mechanical strain relief methods, were also included in the measurement programme. Details of the methods and descriptions of specimens and the measured results are provided in Chapters 4 and 5. Measured residual stresses created by quenching and side punching and then relaxed due to post thermal heat treatment were used to validate finite element simulations which predicted the residual stresses due to quenching and side punching, the stress relaxation and the creep damage due to thermal ageing. This comparison between the measurement and prediction to validate the finite element simulation is made in Chapter 7. The description of the damage model and the assumptions made along with the predicted and experimentally measured results are discussed in Chapter 8.

One reason why residual stresses occur in engineering components is because they are created by repair welds. Repair welds are usually introduced into structures either to remedy initial fabrication defects found in castings or welds by routine inspection, or to rectify in-service degradation of components and thereby extend the life and economic operation of ageing engineering plant. The type of repair can range from filling a much localised shallow excavation using standard weld procedures to welding deep excavations that can extend around a significant proportion of a structure. The need to rectify lack of sidewall fusion defects (when the weld metal fails to fuse completely with the sidewall of the joint) or degraded heat affected zone material typically leads to repairs that are offset from the weld centreline. A survey of weld repair technologies currently used by EPRI member utilities [Gandy et al 2001] has found that 40 percent of all repairs to steam chests, piping and headers resulted in subsequent cracking. It further reports that over 70 percent of the repairs were performed without implementing post weld heat treatment. It is therefore reasonable to infer that high residual stresses associated with the repair process probably played an important role in many of these subsequent failures.

Accurate structural integrity assessments of engineering plant require a good description of the through-wall residual stress field in the component. A number of deep-hole residual stress measurements [George et al 2002] were carried out on a number of type 316H stainless steel mock-up components provided by British Energy Generation Ltd, together with information about the fabrication history. Deep-hole

drilling residual stress measurement technique is a practical means of measuring residual stresses deep into metal parts, e.g., 500mm deep into steels, whereas the non-destructive diffraction types of measurements suffer from limitations in penetrative depths and costs and availability involved. However the present research programme highlighted that the measurement of highly triaxial residual stresses using mechanical strain relaxation methods such as the deep-hole drilling technique, is problematic because of the redistribution of the stresses during the mechanical strain relaxation. The secondary branch of the research undertook a numerical study of the deep-hole drilling process to examine how stress triaxiality and redistribution influenced the deep-hole measurement technique. These are briefly discussed in Chapter 6.

An overall discussion of the research is presented in Chapter 9 where residual stresses prior to thermal ageing of crept specimens and following thermal relaxation are characterised; the quantification of creep damage is also assessed after a brief discussion on the simulation of residual stress measurement. The thesis is concluded in Chapter 10 together with a summary of recommended further studies.

Chapter 2

Literature Review

This chapter reviews previous work on residual stress in engineering components and on the residual-stress driven creep failure. The emphasis is given to the subjects related to residual stress and the ways to generate tensile residual stresses with substantial triaxiality in laboratory specimens in order to study creep formation in stainless steels.

A concise background on the metallurgy of stainless steel is provided in Section 2.1 since stainless steel is the material studied exclusively in this thesis. A theoretical definition of creep and its dependency on temperature and stress is provided in Section 2.2. This is followed by a discussion on the various mechanisms of creep formation. A model that predicts creep damage initiation and its formation under the influence of multi-axial stress field is given in Section 2.3.

Aspects related to the definition, origin, nature of residual stresses and different techniques to measure these stresses have already been detailed in [Bonner 1996, George 2000]. A summary of the existing literature on these topics and new published literature since then has been added to expand the topic and are provided in Sections 2.4 and 2.6. Methods of generating specimens with high residual tensile stress field are described in Section 2.5.

2.1 Stainless steel

Stainless steels are iron-base alloys containing chromium (Cr) [ASM 1980]. Stainless steels usually contain less than 30% Cr and more than 50% iron (Fe). It is the formation of an adherent chromium-rich oxide surface film which gives rise to their stainless characteristics. A few other alloying elements added to enhance specific characteristics include nickel, molybdenum, copper, titanium, aluminium, silicon, niobium and nitrogen. Carbon is usually present in amounts ranging from less than 0.03% to over 1.0% in certain martensitic grades. When selecting a grade of stainless

steel for a given application it is usually the corrosion resistance and the mechanical properties which are the main factors. Stainless steels are commonly divided into five groups: martensitic, ferritic, austenitic, duplex (ferritic-austenitic) and precipitation-hardening stainless steels [Marshall 1984]. Furthermore these grades, designated according to the American Iron and Steel Institute (AISI), can also be classified into further three numbers: 200, 300 and 400 to cover the ferritic, austenitic and martensitic stainless steel grades respectively. The austenitic stainless steel grades including types 316H, 316L and 321 have been extensively used in the current study and a brief background on austenitic stainless steels is therefore provided next.

Austenitic stainless steels

Austenitic stainless steels have an austenitic, face centred cubic (fcc) austenite phase crystal structure. Austenite is formed through the generous use of austenitising elements such as nickel, manganese and nitrogen. Austenitic stainless steels are effectively nonmagnetic in the annealed condition and can be hardened only by cold working. Some ferromagnetism may be introduced due to cold working or welding. Austenitic stainless steels typically have reasonable cryogenic and high temperature strength properties. Chromium content typically is in the range of 16 to 26%; nickel content is normally less than 35%.

Microstructures

Most of the stainless and high-temperature alloys contain iron as their major component and structurally show the familiar phases, ferrite, austenite and carbide. Austenitic structures in the annealed state offer considerable difficulty in metallography. Surface flow occurs during ordinary polishing, and localised transformation along scratches or other sites of more severe flow greatly alter the appearance of the structure. Electrolytic polishing of these steels is particularly desirable since the electrolytic polishing minimises these effects [Brick et al 1977].

2.2 Creep

At elevated temperatures, the life of a properly designed component may severely be limited even for loads less than the design load; a sustained load may produce inelastic strain in the material that increases with time. Under such circumstances the material is said to creep where creep is defined as the time-dependent inelastic strain created under sustained load and at elevated temperature. If the load is maintained for a

sufficiently long time either excessive deflection or creep-fracture can occur. The combination of temperature, load and time that produces creep and possibly creep-failure or creep-fracture of a component depends on the material and the environment. Consequently, creep and creep-fracture of a component may occur over a wide range of temperatures and loads [Boresi et al 1993].

At a temperature slightly above the recrystallisation temperature of a metal the atoms become quite mobile. Accordingly the time-dependent alterations of the metal's structure occur [Boresi et al 1993]. The temperature at which a component's function is limited by creep is not directly related to the melting temperature T_m. In practice the meaning of elevated temperature must be determined individually for each material on the basis of its behaviour. For example in the American Society for Metals handbook (ASM, 1976) elevated temperature behaviour for various metals occurs over a wide range of temperatures: 370°C for low-alloy steels, 540°C for austenitic, iron-based high-temperature alloys, 980°C to 1540°C for nickel-based and cobalt-based high-temperature alloys, etc [Boresi et al 1993].

Although the subject of creep was studied by the French engineer L.J. Vicat [1834], by looking into the creep of wires of hardened iron at room temperature, as long ago as 1834 it was not until the beginning of the twentieth century that the entire creep curve was developed for iron wire as well as several other materials [Phillips 1905, Andrade 1910]. In the late 1950s and 60s, a great increase in studies of creep occurred partly due to the interest in nuclear reactor power generation and the high temperatures used in such systems [Boresi et al 1993].

2.2.1 The creep curve

A description of the creep behaviour of materials is often based on results created from a uniaxial tensile test by applying a constant load or stress at constant temperature. Various standards for creep testing specify the geometric design of test specimens [ASTM 1983, BSI 1987, ISO 1987]. Careful control of machined dimensions was specified by Loveday [1988]. During the test, the tension specimen is subjected to sufficiently high stress σ and temperature T to produce time-dependent inelastic strain (creep). In the creep test, the strain in the specimen varies with time. For an appropriate constant stress and elevated temperature, a strain-time plot shown in Figure 2.1 is called a creep curve. There are three dominant creep regimes. However, the extent to which

these stages are distinguishable depends strongly on the applied stress and temperature [Dieter 1986].

(a) *Primary or transient Creep* (Stage I in Figure 2.1). Beginning at time t = 0, the strain ε_o is due to the initial loading. The strain ε_o may partly be elastic and partly plastic, depending on the level of load and temperature. Following a rapid initial accumulation the primary creep regime is characterised by decreasing strain rate until reaching a minimum rate. The creep rate decreases with time due to work hardening of the material. In metals the dislocations also tend to form low-energy networks of sub-boundaries which tend to drain mobile dislocations out of the structure. However, sub-boundary formation is often retarded for long times in austenitic stainless steel due to their low stacking fault energy [Marshall 1984].

(b) *Secondary or Steady State Creep* (Stage II in Figure 2.1). Strain is almost linear with time in the secondary creep regime. The minimum strain rate at the end of primary creep regime is maintained in the secondary creep regime until a time at which the strain rate begins to increase. The secondary stage is often the longest section of the creep curve. It is known as steady state creep since it is a period of constant creep rate where there is a balance between work hardening and thermally activated recovery (softening) processes.

Primary and secondary creep can be represented by the following relation [Andrade 1910]:

$$\varepsilon = \varepsilon_0\left(1+\beta t^{1/3}\right)e^{(kt)} \tag{2.1}$$

where β and k are constants representing primary and secondary creep respectively.

(c) *Tertiary or Accelerated Creep* (Stage III in Figure 2.1). In the tertiary range the strain rate continues to increase under the sustained stress and temperature until a time t_R where the specimen ruptures. This is usually due to localised necking leading to an increase in the local stress in the constant load test. The difference between a constant load test and a constant stress test becomes significant at larger strains (about 5%) [Webster and Ainsworth 1994]. With a constant stress test the creep life is longer than the constant load test, because there is no increase in local stress due to necking. This means that steady state creep will continue for longer period. However, tertiary creep will eventually occur due to the formation of voids and or cracking. In both types of test

tertiary creep can also occur due to over-ageing of the alloy [Webster and Ainsworth 1994].

2.2.2 Temperature dependency

The temperature dependency of creep is often related to thermodynamics and rate processes of solid-state physics [Dorn 1962, Cadek 1988]. Consequently the temperature dependence is often of an exponential form. A well-known creep deformation equation is given by the Arrhenius equation:

$$\dot{\varepsilon}_c = \alpha e^{(-Q/RT)} \tag{2.2}$$

where $\dot{\varepsilon}_c$ is the creep rate, Q is the activation energy for creep, T is the temperature and R is the universal gas constant and α is a material constant. Therefore increasing the temperature will increase the creep rate exponentially.

Generally all creep parameters are affected by temperature. Experimental evidence indicates that the creep rate in the secondary stage of creep increases more rapidly with temperature increases than does the creep rate in the primary stage of creep. The crystallographic and metallurgical structure also has a great influence on the temperature at which creep becomes significant. For example body-centred cubic (bcc) ferritic and face-centred cubic (fcc) austenitic steels both have a similar melting temperature, but creep becomes significant above 300°C for ferritic steel and above 500°C for austenitic steel [Greenfield 1972]. The superior creep properties of austenitic compared to ferritic steels may be attributed to the large difference in diffusion rate when iron transforms from ferritic to austenite at 910°C. The ratio of diffusivities between the two phases is 1:350 and the creep rates drop by a similar factor as the material transforms on heating [Greenfield 1972].

2.2.3 Stress dependency

Creep rates are dependent on stress. In most cases for isothermal conditions, a common form of creep rate is the power function of stress [Nabarro and de Villiers 1995]:

$$\dot{\varepsilon}_c = K\sigma^n \tag{2.3}$$

where K and n are constants. In the power-law creep equation n is usually in the range 3-5 for pure metals and higher for stainless steels [Marshall 1984]. Nevertheless since n

is affected by temperature, there are variations to this rule. At higher temperatures where diffusional flow dominates metals behave in a viscous manner and n has a value of 1, i.e., the creep rate varies linearly with stress. Work hardening results in piling up of dislocations and recovery occurs by dislocation climb. During secondary creep the two processes are equal and so the creep rate is controlled by climb. Recovery involves the reduction in dislocation density and the rearrangement of dislocations into lower energy arrays or sub-grain boundaries. In order for this to happen, dislocations have to climb as well as slip, and this in turn requires atomic movement or self-diffusion within the lattice provided the atoms have enough energy to jump into a neighbouring site that has a vacancy. The creep rate in this case can be expressed as [Weertman, 1957]:

$$\dot{\varepsilon}_c = \frac{C\sigma^{4.5}D}{N^{1/2}GkT} \tag{2.4}$$

where C is a constant, D is the coefficient for self diffusion, N is the density of dislocations taking part in climb, G is the shear modulus, k is Boltzmann's constant and T is the absolute temperature.

With higher stresses the power law breaks down and an exponential law is found more appropriate [Garofalo 1965]:

$$\dot{\varepsilon}_c = A' e^{(\beta\sigma)} \tag{2.5}$$

where A' and β are values independent of stress but temperature-dependent. This acceleration of creep at high stresses has been explained by Sherby and Burke [1968] as being due to the generation of excess vacancies which in turn enhance dislocation climb. This interpretation derives support from Weertman's dislocation climb model [Weertman 1957] and the dislocation jog model by Barret and Nix [1965] which can both predict the breakdown of the power law at high stress, associating high stress creep with a high vacancy concentration. This behaviour has been observed for 316 stainless steel by Garofalo et al [1963].

2.2.4 Creep mechanism

Anderson et al [1990] presents an overview of the mechanisms of creep. The primary creep is solely due to the dislocation movement in crystalline materials. In the secondary creep regime the steady-state creep deformation occurs by grain boundary sliding. At high temperatures creep can take place by vacancy migration without any dislocation motion. In the tertiary creep regime the formation of voids or micro-cracks

at the grain boundaries drives the creep rate. The voids are formed by vacancy coalescence at the boundaries producing rounded voids, or by grain boundary sliding. At high temperatures, the voids grow and link up and the material fails in an intercrystalline manner at the grain boundaries.

Creep cavitation is the most common form of creep damage during plant operating conditions which includes the formation and joining of micro-cavities on grain boundaries. The mechanism of creep fracture depends on the stress and temperature the material is subjected to and the material parameter such as the grain size [Ashby et al 1979]. Tabuchi et al [1990] have divided the creep fracture modes for 316 stainless steel into three categories: intergranular fracture due to wedge-type cracks, transgranular fracture and intergranular fracture due to formation and coalescence of cavities (creep cavitation).

McLean [1966] discussed in detail the theory of the main creep range, i.e., 0.3-0.9T_m range and compared some of the theories to experimental data. McLean [1966] provides an understanding of the mechanism of the nucleation of holes and their subsequent progress in light of thermodynamics. Most of the current theories of creep are based on the close correlation between creep and atomic diffusion processes as pointed out in [Weertman 1957, Barret and Nix, 1965, McLean 1966, Lagneborg 1969]. Materials deform by crystal planes slipping over each other by movement of dislocations. Below 0.4T_m in most metals these dislocations can move freely by the action of self-diffusion through the lattice until they pile up (work hardening) at some internal obstacle, i.e., precipitates, particles, grain boundaries or the stress fields of other dislocations. The back stresses generated by the pile-up of dislocations will eventually balance the external stress, so deformation will stop, i.e., the end of primary creep. However for temperature range of 0.4T_m to 0.5T_m dislocations have a considerably higher thermal activity giving them increased mobility. The mobility is confined to the screw component of the dislocation. The dislocations can therefore pass obstacles by moving out of their original planes by a mechanism known as cross slip. At higher temperatures up to 0.6T_m dislocations can climb over the obstacle by diffusion. It is through these mechanisms that recovery can occur, removing the effects of earlier work hardening. This is the beginning of secondary creep, where work hardening and recovery are balanced. The creep rate now becomes proportional to the climbing rate, which in turn is controlled by the rate of atomic diffusion. At even higher temperatures,

$0.8T_m$, and above it is possible for creep to occur by pure diffusion. However, this temperature is usually outside any engineering interest.

2.3 Creep damage models

Creep damage occurs in materials when the rate of deformation changes from a constant value to a gradually increasing value, i.e., from secondary to tertiary creep shown in Figure 2.1 until fracture. Relations between the creep and the loading conditions such as applied stress, temperature, strain rate are usually carried out under uniaxial tensile tests. The relationships were discussed in Sections 2.2.2 and 2.2.3. However practical components creep under multi-axial states of stress. Calculations of creep damage under conditions of strain control are often carried out using either a time fraction approach [Huddleston 1985, Hayhurst 1972] or a ductility exhaustion approach [Hales 1983] in which the ductility is a function of creep strain rate and temperature [R5 2001].

Creep rupture life can be predicted using a continuum damage mechanics approach incorporated within a finite element formulation. The rate of change of a damage parameter, D, ranging from D=0 (no damage) to D=1 (100% damage), is computed within each element, until failure occurs in the material cross-section. Continuum damage mechanics approaches, first devised by Kachanov [1958], is used to predict the creep rupture time during the tertiary stage of creep by modelling the kinetics of damage accumulation in the continuum [Chaboche 1988].

Creep damage constitutive equations used in the damage codes including typical Kachanov–Robotnov continuum damage constitutive equations can be expressed in multi-axial form as follows [Leckie and Hayhurst 1974, Hyde et al 1999]:

$$\frac{d\varepsilon_{ij}^{c}}{dt} = \frac{3}{2} A \frac{(\sigma_{eq})^{n-1} S_{ij}}{(1-D)^{n}} t^{m} \tag{2.7}$$

where A, m and n are material constants, σ_{eq} is the equivalent (von Mises) stress and S_{ij} is the deviatoric stress. The damage parameter, D is a scalar quantity varying from D=0 (no damage) to D=1 (i.e. 100% failure) and its rate of change can be expressed in terms of a "rupture stress", σ_r, as follows [Leckie and Hayhurst 1974, Hyde et al 1999]:

$$\frac{dD}{dt} = M \frac{(\sigma_r)^{\chi}}{(1+\phi)(1-D)^{\phi}} t^{m} \tag{2.8}$$

where M, ϕ and χ are continuum damage material constants. The rupture stress σ_r is a function of the maximum principal stress, σ_1 and the equivalent stress, σ_{eq}, as follows:

$$\sigma_r = \alpha\sigma_1 + (1-\alpha)\sigma_{eq} \tag{2.9}$$

which is suitable for materials obeying mixed stress criteria [Becker et al 2002], where $\alpha = 1$ (maximum principal stress dominant) and $\alpha = 0$ (equivalent stress dominant). The accurate determination of α plays an important role in the application of the multi-axial stress continuum damage model.

In the present study a ductility exhaustion approach was utilised to predict the creep damage. This approach calculates the creep damage per cycle, D_c arising from a creep dwell by the following equation [Spindler 2004, Yatomi et al 2004]:

$$D_c = \int_0^t \frac{\dot{\bar{\varepsilon}}_c}{\bar{\varepsilon}_f\left(\dot{\bar{\varepsilon}}_c\right)} dt \tag{2.10}$$

where $\dot{\bar{\varepsilon}}_c$ is the instantaneous von Mises equivalent creep strain rate at time t, and $\bar{\varepsilon}_f$ is the corresponding multi-axial creep ductility, expressed as the von Mises equivalent strain at failure, which is a function of the strain rate and stress state. The von Mises creep strain at failure has been expressed by Spindler [2004] as the uniaxial creep strain at failure (as a function of creep strain rate) multiplied by a multiaxial ductility factor, *MDF*:

$$\bar{\varepsilon}_f\left(\dot{\bar{\varepsilon}}_c\right) = \varepsilon_{fu}\left(\dot{\bar{\varepsilon}}_c\right) MDF \tag{2.11}$$

where ε_{fu} is uniaxial creep strain at failure and can be determined from a creep test by subtracting the loading strains from the total strain at failure [Spindler 2004]. The *MDF* effectively allows uniaxial creep data to be applied to a component in a multiaxial state of stress. Based on observation of microstructural failure mechanisms Spindler [2004] derived the *MDF* term by modelling the response of the material to multiaxial stresses. A number of models exist describing mechanisms for the growth of cavities. For example Manjoine [1975] proposed that for type 304 steel at 593°C the effect of stress on the von Mises strain at failure, $\bar{\varepsilon}_f$ is given by

$$\bar{\varepsilon}_f = \varepsilon_{fu}\frac{\bar{\sigma}}{3\sigma_h} \tag{2.12}$$

where ε_{fu} is the uniaxial failure strain. Rice and Tracey [1969] developed a model for hole growth by the rigid plastic deformation of the surrounding matrix:

$$\bar{\varepsilon}_f = \varepsilon_{fu} \exp\left(\frac{1}{2} - \frac{3}{2}\frac{\sigma_h}{\bar{\sigma}}\right) \tag{2.13}$$

Based on a number of existing models considering cavity nucleation and growth mechanisms which related the von Mises creep strain at failure with the uniaxial creep strain at failure Spindler [2004a] developed a model for use under triaxial states of stress. Spindler [2004a] obtained the model from biaxial creep data on type 304 and 316 steels and found it suitable for use with triaxial stress states. The model based on cavity growth by rigid plastic deformation of surrounding matrix and developed by Rice and Tracey [1969] was closest with the 316 creep data [Spindler 2004]. Spindler showed that in addition to cavity growth the inclusion of a cavity nucleation term gave a good agreement with the observed effect of stress on the creep strain at failure. Using Equation 2.13 and a cavity nucleation term Spindler derived an empirical equation describing the effects of stress state on ductility [Spindler 2004]. This approach includes two material constants, p and q, which describe the decreasing ductility with increasing stress triaxiality according to:

$$\frac{\bar{\varepsilon}_f}{\varepsilon_{f,uni}} = \exp\left[p\left(1 - \frac{\sigma_1}{\bar{\sigma}}\right)\right]\exp\left[q\left(\frac{1}{2} - \frac{3\sigma_h}{2\bar{\sigma}}\right)\right] \tag{2.14}$$

where $\varepsilon_{f,uni}$ is the uniaxial ductility, $\bar{\sigma}$ is the von Mises equivalent stress, σ_1 is the maximum principal stress and σ_h is the hydrostatic stress. The first term in Equation 2.14 represents the cavity nucleation. The second term represents cavity growth by creep deformation. Creep initiation is conceded when damage $D_c \geq 1$ (Equation 2.10).

2.4 Definitions and origin of residual stress

Residual stress may be defined as the self-equilibrating internal stress existing in a free body under uniform temperature conditions and in the absence of external loads or thermal gradients. It is most commonly termed as the "residual stress" as it may be "left over" by a previous manufacturing process. At equilibrium in the absence of any external load both the resultant force and the resultant moment of the body are zero. It is thought that reheat cracking in plant structures is solely driven by the presence of residual stress field [Baikie et al, 1997, Dhooge 1998, Skelton et al 2003].

Macherauch and Kloos [1986] suggested a classification of residual stress into three groups using the term "homogeneous" to mean "constant in magnitude and direction".

(a) Type I - Macro residual stresses which are homogeneous across several grains of the material and are equilibrated over the body.

(b) Type II - Nearly homogeneous micro residual stress which are homogeneous only on a part of a grain or one grain and equilibrated over several grains. Such stresses may be expected to exist in single-phase materials because of anisotropy in the behaviour of each grain. They may also develop in multi-phase materials because of the different properties of the different phases.

(c) Type III - Inhomogeneous micro residual stresses which are inhomogeneous even over sub-microscopic distances inside the body but in equilibrium on small parts of a grain essentially as a result of the presence of dislocations and other crystalline defects.

The different types of residual stress are shown schematically in Figure 2.2. One or a superposition of these three categories defines all the residual stress states. However from an engineering perspective the first category has more importance than the other two since any modification to equilibrium may also modify the external dimensions of the body.

2.4.1 Origin and nature of residual stresses

Residual stresses develop mostly during manufacturing processes involving material deformation, heat treatment, machining or processing operations which transform the shape or change the properties of a material. The residual stresses arise from a number of sources and can be present in the unprocessed raw material, introduced during manufacturing or can also arise from in-service loading [Withers and Bhadeshia 2000]. The origins of residual stresses in a component may be categorised by: (a) mechanical, (b) thermal and (c) chemical process.

Mechanical

Machining (grinding, turning, drilling, milling)

Most engineering components of metallic material require some form of machining such as turning, drilling, milling, shaping or grinding. The cutting tool, more specifically the abrasive particles of the grinding wheel parts the chip from the work-

piece by a process of plastic shear. The machining process used on the metallic material usually generates compressive residual stress in the working direction of the cutting zone [Bainbridge 1969]. The intensity of the residual stress field generated due to the cutting process varies according to the cutting speed, cutting depth, geometry and material properties.

Forming (rolling, shot-peening, drawing, extrusion)

Shot-peening process generates compressive residual stresses in a component. A high-speed shot causes local plastic yielding on the surface. The surface is therefore extended relative to the interior. The interior acts to constrict the surface, causing high local compressive residual stresses in the surface balanced by tensile residual stresses within the interior [Noyan and Cohen 1981].

In the rolling operation, the surface can be extended more than the interior due to friction at the rolls, resulting in compression on the surface. In this operation, the magnitude of stress is a function of the thickness of the test piece, the roll diameter and the degree of reduction [Baldwin 1949].

Elasto-plastic loading (bending, torsion, tension, compression)

The removal of an external load in a tensile extension of a specimen into the plastic zone can produce residual stresses [Noyan and Cohen 1987]. Figure 2.3 shows a schematic of material behaviour during a loading-unloading cycle. If the surface is harder than the interior due to defect pile-up occurring during plastic extension, then on the release of the load at point 'A' in Figure 2.3, the elastic recovery tries to leave the surface shorter than the interior. But since both must contract by equal amounts, tensile stress remains at the surface balanced by compressive stress in the interior. The reverse occurs when the surface is softer than the interior.

Thermal

Heat-treatment

Heat-treatment can result in thermal residual stresses even without change in the crystalline structure [Noyan and Cohen 1987]. When a material is cooled down sufficiently fast from its heat-treatment temperature, the microstructural transformation change does not occur. Due to a temperature gradient in the material, during cooling, the surface and the interior contract at different rates. At some point this difference coupled with the low material yield strength at high temperature induces plastic flow or

permanent yielding. Due to the temperature gradient the surface regions want to contract on cooling more than the interior. The surface regions are consequently extended by the interior and the interior restrained by the surface regions. Once at room temperature, the surface regions extend relative to the interior resulting in residual compression.

Heat-treatment does not always produce surface compressive stresses provided the cooling is not rapid enough. Therefore there is the possibility of the formation of transformational stresses in addition to thermal stresses due to crystalline structural change [Ericsson and Hildenwall 1981, Mayr 1987]. During cooling of the component, if a non-uniform phase transformation of the material occurs, non-uniform crystalline packing densities may develop. This can cause the core to be in residual compression and the surface in residual tension.

Joining (welding, soldering, brazing, adhering)

Many of the processes used to join one metal to another are based on casting where the materials are welded together by casting in a mould. The most extensively used welding process is the arc welding where an electric arc is struck between an electrode of filler metal and the workpieces. This process provides the heat required to melt the filler and fuse it to the parent plates. The temperature distributions about the weld seam are continuously changing during the welding process. This results in thermal residual stresses. The principal source of welding residual stresses is the localised shrinkage of cooling weld metal which is restrained by surrounding colder section of the fabrication as illustrated in Figure 2.4. Other less important factors, such as residual stresses remaining in the parent metal due to cutting processes, preheating or the welding process employed, can also influence the final residual stress distribution.

Chemical

Chemically generated residual stresses

The chemically generated stresses can develop due to volume changes associated with chemical reactions, precipitation, or phase transformation. Chemical surface treatments and coatings can lead to the generation of substantial residual stress gradients in the surface layers of the component. Nitriding produces compressive stress in the diffusion region because of expansion of the lattice and precipitation of nitrides, and carburising causes a similar effect [Littmann 1964]. The magnitude of residual stresses

generated in coatings can be very high. Compressive stresses of the order of 6-8GPa or even higher have been measured at the interface of some thermal barrier coatings (TBC).

2.5 Methods of generating residual stress

Several techniques of generating residual stresses in small-scale laboratory specimens exist in literature. The techniques employed to generate residual stresses within samples in a controlled manner can be divided into mechanical and thermo-mechanical methods. The methods studied in the literature review in generating residual stresses with sufficient high triaxiality for the present study include quenching of spherical and cylindrical bodies, in-plane compression of beam specimen and side-punching of C(T) specimen.

2.5.1 Quenching

Quenching is one of the most common heat-treatment processes used to impart the desired mechanical properties to metal parts [Aksel 1990, Sedeghi and McMahon 2000]. In the quenching process components are heated to a high uniform temperature and then allowed to cool using a quenching medium such as air, water or polymer solution. A component may be immersed in a cooling liquid or be subjected to surface spray. A rapid cooling rate may impart beneficial mechanical properties such as hardening but can also introduce high levels of residual stress and distortion. For a slow cooling rate on the other hand the levels of residual stress and distortion are lower but the mechanical properties obtained may not be so desirable. Severe temperature gradient induces thermal stresses resulting in plastic strain. The residual stress arises from complex interaction of thermal stresses and phase transformation [Sedeghi and McMahon 2000]. Residual stresses in a component are partially compressive and partially tensile in the absence of any external load satisfying equilibrium. Tensile residual stresses may combine with in-service loading and may have detrimental effects on the integrity of the component. The prediction of residual stresses generated due to quenching process has been the subject of interest for a long time [Landau and Weiner 1958]. The characterisation of residual stresses due to quenching can be categorised as numerical, analytical and experimental.

There are extensive works in literature regarding the use of numerical methods in predicting residual stress due to quenching. Mackerle [2003] has published a

bibliographical review of the application of finite element analysis in the simulation of quenching for the period of 1997 to 2001. In order to undertake quenching simulations it is important to have knowledge of the quenching heat transfer coefficient. An encyclopaedia of heat transfer [Kutateladze and Borishanskii 1966] provides solutions for cooling temperatures at radial positions and theoretical heat transfer coefficient variations with coolant temperature.

Weiner [1956] determined the thermal stresses in a free plate of elasto-plastic material subjected to a varying heat input over one face of the plate. The elasto-plastic theory is based on the Prandtl-Reuss stress-strain relations with von Mises yield condition. All mechanical and thermal properties were assumed to be temperature-independent. Weiner considered a free plate subjected to a heat input uniformly distributed over one face, which increased monotonically from zero to a maximum value before decaying monotonically back to zero. The other face and edges of the plate were insulated. The temperature distribution was expressed in a simple form by restricting the analysis to heat inputs, which did not vary too rapidly.

Landau et al [1960] provided equations for determination of transient and residual stresses in plates subject to transient temperature distributions. The equations were derived assuming that the material was viscoelastic, and was perfectly plastic obeying a von Mises temperature-dependent yield condition. The viscous effects were expressed by a Maxwell type relation, and residual stress calculations were made with a viscosity coefficient, which was a function of temperature. They found that for steel, viscoelasticity had little effect on the residual stress distribution, but the temperature-dependence of the yield stress is important.

Heming et al [1999] calculated, using the finite element technique, residual stress in a 45 steel cylinder with the surface heat-transfer coefficients. These coefficients were non-linear functions of temperature and the volume fraction of the phase constituents. They considered the thermal physical and mechanical properties to vary as functions of the temperature and the volume fraction of the phase constituents.

Sen et al [2000] also used finite element techniques to predict residual and thermal stresses which occur during water quenching of solid cylindrical rods and ring cross-sectioned steel tubes. They investigated the effect of internal diameter of tubes on residual stress. Due to symmetry the FE method was conducted for only one quarter of the axi-symmetric model as shown in Figure 2.5. The analysis consisted of thermal

analysis where temperatures obtained in thermal elements were used to calculate stresses in thermal-stress analysis In the thermal analysis, Sen et al [2000] used a convective heat transfer coefficient independent of temperature to model the convective heat transfer from the outer surface of the specimen, and an adiabatic condition along the symmetry lines to represent symmetry.

Analytical solutions for prediction of residual stress in solid sphere following quenching have been addressed by McKenzie and Moakler [1973]. In their study MacKenzie and Moakler demonstrated that high levels of tensile residual stresses are generated in quenched spheres. They presented simple distributions of the residual stress across the equatorial plane of the sphere. More on this subject is included in Section 3.1.4.

The internal stresses during quenching of a plate were calculated using a mathematical model by Fletcher and Price [1998].

Experimental, analytical or numerical tool cannot be recommended solely as a general approach to predict the residual stresses in all quenching problems. Usually they complement each other. In some cases, the complexity of geometry and material characteristics limit experimental and analytical approach. Moreover the numerical tool is a less costly and effective approach which enables us to simulate the quenching conditions and predict the residual stresses in geometries of various complexity. However, experimental and analytical approaches are required to validate the numerical results since there is a variety of influencing factors, which contribute, in quenching process such as thermal boundary condition and thermo-physical properties. These factors cannot easily be simulated in numerical codes, especially when there is material transformation during quenching. Aksel et al [1992] investigated a quenching process of a long thin rectangular aluminium bar. The work was a good example of utilising all three approaches to predict residual stress fields during quenching. His numerical simulation was validated by an analytical approach. Moreover, distortion of bar during quenching was compared with numerical study as an experimental tool. Following him, Becker et al [1996] compared a numerical approach with residual stress measurement using layer removal technique for a similar problem. In general the significant role of residual stresses in structural integrity assessment motivates many researches to be carried out experimentally, numerically or analytically in order to characterise residual stresses following quenching process.

2.5.2 In-plane loading

Cotton [1997] worked on finding a suitable test piece with sufficiently deep tensile residual stress field for creep crack studies in the presence of residual stress fields. He considered single edge notch beam SEN(B) specimen in his study. Cotton [1997] showed that the extent of tensile stress field was dependent on the geometry of the specimen and the types of notch. He found that an a/W ratio of 0.38, where a is the total notch length and W is the maximum ligament size with no notch present, would result in a maximum tensile region ahead of the notch root. This effectively produces a shortened notch.

Turski [2004] continued the work of Cotton by initially considering a C(T) specimen of similar notch and later modifying the a/W ratio with the gap ahead of the notch increased to accommodate compressive deformation. In addition, Turski used a thinner than usual C(T) specimen to allow high energy X-ray and neutron diffraction through-thickness residual stress measurements to be made. Residual stresses were generated as a result of the in-plane compression of the C(T) specimen followed by unloading. Turski used specially designed spheres for the compressive loading instead of drilling holes and using loading fixtures. Turski [2004] compared the residual elastic strains measured along the ligament using the high energy X-ray at the European Synchrotron Radiation Facility (ESRF) and the neutron diffraction at the Institute Laue-Langevin (ILL) in Grenoble, France with predicted FE strains and found the comparisons to be good in general, especially away from the notch root.

Turski [2004] used finite element analysis to simulate the in-plane compression loading of a C(T) specimen. Turski used a rigid circular body to represent a ball bearing used for the loading purpose. During loading a frictionless contact between the rigid circular body and the C(T) model was allowed. Due to two symmetry planes along the ligament and mid-thickness plane (see Figure 2.6), Turski modelled one-quarter geometry 3D mesh of the in-plane compression loading of the C(T) specimen. From a series of finite element analyses with various applied deformation, Turski [2004] determined the amount of preloading required to generate sufficient residual stresses within the sample for creep study.

Mirzaee-Sisan et al [2005] used a similar procedure developed by Cotton [1997] to generate residual tensile stress field in a ferritic steel SEN(B) specimen to investigate its fracture behaviour at low temperature. They preloaded a SEN(B) specimen with a

shallow notch of 12.5mm radius at mid-length by applying a compressive load of 73kN at either ends of the specimen followed by unloading.

2.5.3 Side punching

Local compression technique is mentioned in standards as a method to relax residual stresses [ASTM 2001, British Standard 1997, Towers et al 1982]. Other applications of the technique includes hardness tests on materials [Shield 1955]. Local compression also known as the side punching can also be used to generate residual stress field into test specimens.

For example Mahmoudi et al [2003] studied using the finite element analysis (FEA) the application of side punching to introduce a residual stress field into fracture specimens. Mahmoudi et al [2004] carried out a parametric study using the FEA and found that the size and the position of the punching tools relative to the fracture specimen to have a strong influence on the magnitude and direction of the residual stress field generated in the specimen. Measurement of the residual stresses in similar fracture specimens using the Synchrotron X-rays compared very well with the predicted FE results [Hossain et al 2004a].

Meith and Hill [2002] studied the effect of local compression in generating residual stress fields ahead of crack tips in a single edge notched bend (SENB) fracture specimen. The local compression (LC) process is illustrated in Figure 2.7 [Meith and Hill 2002]. They simulated the LC by modelling the compression platen (the punching tool) shown in Figure 2.7 as a rigid body, in frictionless contact with a notched SEN(B) model, and applying a through-thickness displacement to the platen sufficient to reduce the thickness by 1% (after removal of the compression load). After the compression load was removed the residual stress state remained in the model.

Compression platens (also termed the punching tools in the present study) are used to apply displacement to the faces of an SEN(B) in the vicinity of the notch tip. In the compression-loading cycle the displacement δ is increased until there is enough plastic deformation and the specimen thickness is reduced by 1%. Because plastic deformation occurs during local compression the process always leaves behind an altered state of residual stress. Studies using other shapes of the platens or the punching tool are also available in literature.

For example, Lim et al [2003] induced residual stresses in aluminium SEN(B) specimens by indenting the surface of the specimen with a rigid circular ring punch. Lim et al [2003] showed that the position of the indentation, i.e., the location of the punch relative to the notch root and the size of applied compressive load influenced both the residual stress distribution along the ligament from the notch root and its extent along the ligament. They obtained a maximum increase in compressive residual stress at the crack tip by moving the punch closest to the notch root.

2.6 Measurement of residual stress

Residual stress measurement techniques invariably measure strains rather than stresses, and the residual stresses are then deduced from the measured strains through the simple elastic relation using the appropriate material parameters such as Young's modulus and Poisson's ratio. Often only a single value of the stress is quoted and the stresses within the measurement volume are assumed to be constant, both in the surface plane and through the depth. When comparing the measured results from different techniques, consideration should be given to the sampling volume and the resolution of each measurement method in relation to the type of residual stress being measured (see Figure 2.2), particularly when the Type II and III micro residual stresses are of interest [Kandil et al 2001]. It is important to also consider the concept of the characteristic volume, which can be used to describe the volume over which a given type of residual stress averages to zero. Most material removal techniques (e.g. hole drilling, layer removal) remove large volumes of material over which Type II and III stresses average to zero so that only the macro residual stresses can be measured. Furthermore from an engineering standpoint Type I macro residual stresses category has more importance than the other two since any modification to equilibrium may also modify the external dimensions of the body.

Residual stress measurement methods range from non-destructive technique via semi-destructive means to the destructive technique. Non-destructive technique includes the diffraction, magnetic and ultrasonic. Semi-destructive techniques where the component is partially damaged and does not compromise its integrity include the incremental centre-hole drilling technique and the deep-hole drilling technique. In the destructive technique the component is destroyed completely and includes the Sachs method and the Curvature and the layer removal method.

Here a description of the neutron diffraction and the mechanical strain relief incremental centre-hole drilling and the deep-hole drilling methods are reviewed since these methods were employed in the residual stress measurement programme of the research and are therefore relevant to the present study.

2.6.1 Neutron diffraction

Neutrons are the fundamental subatomic neutral particles with the mass of the proton. These particles are usually produced at nuclear reactors during the fission process, after which they are allowed to scatter from the light atoms in a moderator of heavy water or graphite. During these scattering collisions the neutrons lose energy, coming to thermal equilibrium with the moderator. The kinetic energy of the majority of neutrons is given by [Noyan and Cohen 1987]

$$\tfrac{1}{2}mv^2 = \tfrac{3}{2}kT_m \qquad (2.1)$$

where T_m is the moderator temperature. For $T_m \cong 600K$, the moderated neutron energies are in the millielectronvolt (meV) range. The wavelength of a neutron beam can thus be determined from the equation of wave-particle duality:

$$\lambda_m = \frac{h^2}{(3mkT_m)^{1/2}} \qquad (2.2)$$

As the mass of the neutron is approximately 10^{-27} kg [Noyan and Cohen 1987], the wavelength of the moderated neutron is around 1Å, which is appropriate for diffraction from crystals. For wavelengths comparable to the atomic spacing the advantage of neutron over *X*-rays in the residual stress measurement includes its penetration into engineering materials to be much higher [Withers and Bhadeshia 2001].

Essentially there are two forms of neutron diffraction namely the monochromatic wavelength measurements [Pintschovius 2003] and the time-of-flight spectrometry measurements [Johnson and Daymond 2003]. The two types of sources producing these beams of thermal neutrons are nuclear fission reactors (continuous flux sources) and neutron spallation (pulsed) sources respectively [de Novion 2003].

Monochromatic wavelength measurement

The outline of a neutron diffractometer for strain measurements in the monochromatic wavelength measurement method is shown in Figure 2.8 [Pintschovius 2003]. A beam of polychromatic neutrons originating from the neutron source impinges

on the monochromator which reflects a monochromatic beam according to Bragg's law [Holden and Roy 1996]:

$$2d_{hkl}\sin\theta_m = n\lambda_m \qquad (2.6.3)$$

where d_{hkl} denotes the lattice spacing of the monochromator, θ_m the scattering angle at the monochromator, λ_m the neutron wavelength and n is a small integer number. A small fraction of beam hitting the sample is diffracted. Since the incident beam is monochromatic the diffracted beam is confined to a well-defined direction, again according to Bragg's law. A neutron detector records the diffracted beam. By using collimators at various positions the angular spreads of the neutron beam in the horizontal and vertical planes are defined. A slit of a few mm width placed before the sample narrows down the relatively wide beam (few cm) generated by a typical neutron monochromator. A second slit placed after the sample confines the diffracted beam. These two slits therefore define the gauge volume (also known as the sampling volume) which is much smaller than the sample. Stress mapping over the entire sample is made by moving the sample stepwise with respect to the gauge volume.

Time-of-flight spectrometry measurement

The time-of-flight (tof) method differs from the monochromatic wavelength measurement in one simple respect: the time-of-flight, t of each neutron from the moderator to the detector is measured and is used to determine its wavelength. An entire spectrum $I(\lambda)$ can be recorded by a single stationary detector placed at a fixed scattering angle 2θ. When the Bragg condition $\lambda=2d\sin\theta$ is satisfied the peaks in the scattering intensity can be determined [Johnson and Daymond 2003]. Several detectors are normally used to increase the count rate of the instrument. The individual spectra are then added together to provide an effective spectrum of $I(\lambda/2\sin\theta)$. In this method the normal distance $d(hkl)$ between the $\{hkl\}$ lattice planes within a small gauge volume is measured. The strain at this point is then calculated by comparing this measurement with the corresponding $d(hkl)$ within an un-strained part of the material termed as $d_0(hkl)$. Thus, the strain $\varepsilon = (d - d_0)/d_0$. The measured strain is therefore an average value over the gauge volume and its precision depends on the size of the gauge volume.

By using a wide range of wavelengths (0.5-5Å) in the tof instrument a large number of diffraction peaks are simultaneously recorded. The information from these diffraction peaks can either be analysed separately as in the continuous flux sources, or

used to establish an average unit cell parameters *a*, *b* and *c* using the Rietveld refinement technique [Rietveld 1969].

It is also possible to carry out tof measurements at continuous flux reactors making use of choppers, as at the GKSS source at Geesthacht in Germany and the SINQ source at Villigen in Switzerland.

Near-surface residual stress measurement by neutron diffraction

Conventionally neutron diffraction has been used to characterise residual stresses deep into metal components. The measurement of near-surface residual stresses has historically been undertaken by X-ray diffraction. However with a number of adjustments it is also possible to measure accurately the near-surface residual stresses using the neutron diffraction. For example in [Edwards 2003] three basic requirements for the precise near surface strain measurement by the neutron diffraction are described. First, the position of the surface with respect to neutron beam must be accurately determined. Based on the study of Wang and Edwards [1998] Edwards [2003] achieved an alignment better than 0.05mm. Second, the centroid of a near-surface gauge volume must be calculated as the centroid of the diffracting material clearly differs from the centre of the volume defined by the collimator neutron beam as soon as the latter volume leaves the specimen surface. Third, a correction required allowing for any pseudo-strain effects caused when the gauge volume leaves the surface.

2.6.2 Incremental centre-hole drilling

The incremental centre-hole drilling (ICHD) technique first proposed by Mather [1934] is based on the partial relief of residual strain near the surface of a specimen through the drilling of a shallow and blind hole. The radial component of the initial residual stress is reduced to zero at the edge of the drilled hole and is modified to different values further away from the edge of the hole. The strain relief corresponding to the change in the stress can be detected by attaching a radially aligned resistance strain gauge rosette concentrically about the hole-axis. From a set of experimental and numerical studies Schajer [1998 and 1998a] proposed a set of coefficients which can be used to convert the measured strains into the residual stress distribution. Based on solutions of FE calculations the Integral Method [Schajer 1998a] is best suited for highly non-uniform stress fields where the individual contribution to the measured strain is identified at each depth increment. However, the main limitation is that the

residual stresses are assumed constant with each depth increment. More on the method is discussed in Section 4.2.1.

In the ICHD technique it is important to produce high quality flat-bottomed holes and ensure that the drilling method itself does not induce additional stresses. Several techniques of drilling reported by Keller et al [1989] includes hand drilling, high speed drilling with an air turbine, use of an air-abrasive jet, electrically powered drilling, spark erosion drilling and drilling with laser beams. The air-abrasion normally induces the least stress and high-speed drilling produces the best hole shape.

Figure 2.9 shows a typical commercially available hole drilling rig and gauge geometry. An example of special strain rosette type 031RE attached to a sample is shown. In practical terms there is no point making measurements beyond a depth roughly equivalent to the drill diameter, since no additional strain can be measured. However Yazdi et al [1998] by drilling with a large hole of diameter 10mm measured the through-thickness residual stress distribution in a 24mm thick water quenched aluminium plate and compared with residual stress distribution measured by neutron diffraction technique. The comparison between the two methods was found to be very good.

The basic hole-drilling analysis assumes that the material is isotropic and linear-elastic. The accuracy of the calculated stress depends on the quality of drilling including eccentricity, profile and depth of the hole, surface roughness, flatness and specimen preparation. Despite the several drawbacks, the ICHD method remains one of the most widely used techniques for measuring residual stress and main advantages of the method include it being relatively straightforward, economical, quick and versatile. The equipment can be laboratory-based or portable, and the technique can be applied to a wide range of materials and components.

2.6.3 Deep hole drilling technique

Deep Hole Drilling is a variation of the technique which has been developed for measuring residual stresses in thick-section components. A schematic illustration of the method is shown in Figure 2.10. The basic procedure involves drilling a small reference hole through the component and subsequent removal of a cylindrical column (core) of material from the component, where the core is larger and concentric with the reference hole, using a trepanning technique. The diameter $d(\theta, z)$ of the reference hole is measured accurately along its length before the column is machined out. When the

column is removed the stresses relax and the reference hole diameter and column dimensions change, the dimensions of the column and reference hole $d'(\theta, z)$ are then re-measured and the residual stresses calculated from the dimensional changes caused by removing the material from the bulk of the specimen.

The method was originally developed in the 1970s by Zhdanov and Gonchar [1978] and Beany [1978]. Zhdanov and Gonchar [1978] measured residual stress in steel welds by drilling 8mm diameter hole followed by an incremental cutting of a concentric column of metal of 40mm diameter from the specimen using a hollow drill. By using changes in the axial length during incremental trepanning and measuring the diameter changes in two mutually perpendicular directions at a number of fixed distances along the reference hole Zhdanov and Gonchar [1978] measured the residual stresses in the component.

Beany's [1978] approach to the measurement procedure was to gun-drill a very smooth and straight hole of diameter 3.175mm along the direction of a principal stress component and to measure its diameter at three in-plane angles of 0, 45 and 90° at every 2mm depth along the reference hole. Beany [1978] measured the hole diameter using strain gauges fixed onto two parallel beams fixed together and drawn along the sidewalls of the hole. By using the strain gauges Beany [1978] determined the changes in diameter due to the trepanning of the core by electro-chemical machining (ECM) process by measuring the changes in the beam deflection.

A substantial development of the technique has undergone over the past decade mainly at University of Bristol [Bonner and Smith 1994, Smith and Bonner 1996, George et al 2000, Smith et al 2000] both in the improvement of the method and its accuracy. George et al [2002] used small holes to determine stresses in calibration of aluminium and steel samples arising from external applied loading.

The most recent improvement of the technique includes the use of an even smaller hole and core which generally improves the precision of the stresses measured. Furthermore measurements of diametral distortions at more angles (the current practice includes 18 angular measurements) reduced substantially the error associated with the air-probe measurements. Further advancement includes the design of a small-scale portable deep-hole drilling rig [Kingston, 2004] capable of measuring residual stresses in metal parts of depths in the range of 5-500mm.

Deep-hole drilling simulation

George [2000] used finite element to model a pipe under autofrettage and compared the predicted FE residual stress distribution with the stress distribution measured using deep-hole drilling and Sachs methods. By considering removal of elements which defined drilled reference hole and edm thickness, George [2000] further modelled the deep-hole (DH) drilling of the autofrettaged tube. George [2000] found that the predicted FE residual stresses following DH simulation compared better with the stresses measured by DH method. In his DH FE analysis, George [2000] removed the set of elements defining the edm thickness in a single step. However, in practice the trepanning process takes place incrementally so that the removal of elements defining the edm thickness carried out incrementally models the trepanning process more realistically.

2.6.4 Triaxial residual stresses in metal parts

Residual stress measurement techniques [Withers and Bhadeshia, 2001] are the experimental tools to evaluate residual stresses in engineering components. Accurate characterisation of residual stress distributions in components is essential in the structural integrity assessment as well as in the validation of the finite element-predicting models. In this subsection residual stresses studied and measured by various authors are described. The residual stress generated by the three processes described in section 2.5 relevant to the present study namely the quenching, the in-plane loading and the side punching are considered here.

Quenching residual stresses

Centre-hole drilling [Hossain et al 2004], X-ray [Sedeghi and McMahon 2000] and Neutron diffraction [Yazdi et al 1998, Hossain et al 2004, Mukai et al 2003] have been used to measure the residual stresses in quenched specimens. The centre-hole drilling and X-ray can only measure the near surface residual stresses. The neutron diffraction can give a good depiction of residual stress field through thickness of components but the size (of component) limitation and expensive procedure are main drawbacks of the this method in industry application.

Yazdi et al [1998] studied the quenching process to induce residual stresses in aluminium alloys. They studied the influence of different quenching parameters on the level of residual stress induced in an aluminium alloy plate shown in Figure 2.11(a).

They modelled the quenching process using finite element analysis and validated the finite element predicted residual stresses by measured residual stresses using both neutron diffraction and incremental centre hole drilling. The measured and predicted residual stress distribution in the plate is shown in Figure 2.11(b). They used the diffractometer of residual stress and texture measurement (REST) of Studsvik Neutron Research Laboratory (NFL) in Sweden to measure the residual stresses. By drilling a large hole (diameter 10mm) Yazdi et al [1998] also measured the residual stress distribution 5mm from each surface of the 24mm thick plate using the incremental centre hole drilling technique. These results compared very well with the neutron diffraction measured residual stresses shown in Figure 2.11(c).

Mukai et al [2003] studied the quenching of S45C carbon steel cylindrical test pieces of diameters 20mm, 30mm and lengths 60mm, 10mm, respectively. They measured residual stress in the quenched material with phase transformation using the neutron diffraction method. From metallo-thermo-mechanical theory, Mukai et al [2003] carried out the simulation using the coupled analysis by finite element method and predicted the residual stresses in the test pieces. Figure 2.12 (a) and (b) shows respectively the measured and finite element predicted residual stress distribution in the mid-section across the radial plane from the centre of a cylindrical test piece, diameter 20mm, length 60mm. The measured and predicted residual stress results in the cylindrical test piece, diameter 30mm, length 10mm are shown in Figure 2.13 (a) and (b).

In-plane compression residual stresses

The measured residual elastic strains along the ligament of a compact tension specimen [Turski 2004] can be seen in Figure 2.14 (a) compared to residual elastic strains predicted before and after creep simulation of the 3D FE pre-strained model. Turski [2004] observed a good agreement between the predicted and measured residual elastic strains. Figure 2.14 (b) displays a subset of data from Figure 2.14 (a) showing the comparison between measurements and predictions of residual elastic strain after thermal exposure more clearly, indicating that the only discrepancies that exist are those close to the notch root, with up to 500με higher residual elastic strains being predicted by the FE model. Turski [2004] attributed the lower residual elastic strains close to the notch root of the CT specimen to the extent of creep damage found in CT5.

Side punching residual stresses

Mahmoudi et al [2005] introduced residual stress in C(T) specimens by side punching in order to study the influence of residual stress on fracture behaviour in Aluminium alloy. Mahmoudi et al used incremental centre hole drilling, synchrotron X-ray and deep hole drilling techniques to measure the residual stress distribution in the punched specimen. Figure 2.15 shows a direct comparison between all three sets of measurements and finite element predictions, obtained using the combined hardening model, of the residual stresses along a line joining the two punch centre points. They observed an excellent agreement between the three sets of measurements. The FE results were in general agreement with the measurements, however they over predicted compressive residual stresses by approximately 10% higher than measured. Mahmoudi et al [2005] attributed this discrepancy to the material modelling in their FE and the mismatch between plane stress assumption in measurement and a three-dimensional FE model.

Chapter 3

Creating residual stresses in laboratory specimens

High triaxial residual stresses exist in practical components e.g., welded nozzle to cylinder intersections. However these components are large and are difficult to test, e.g., measuring residual stresses present in the components and subsequent creep tests. Therefore it was decided to attempt to introduce residual stresses into laboratory size samples in a controlled fashion in sufficiently large sample volumes to be measured.

In this chapter, the method of introducing residual stresses into stainless steel specimens under laboratory conditions is described. The aim was to obtain a highly triaxial residual stress field for subsequent creep study. Two methods as described below were used to introduce a highly triaxial residual stress state into small sized laboratory specimens. Firstly, a rapid spray water quenching method was used to introduce residual stress field with high triaxiality into samples. A parametric study was carried out in order to obtain a high triaxiality condition by changing the geometry of the specimens and the cooling conditions. These initial studies were carried out using the commercial finite element code ABAQUS 6.3 [HKS 1998]. Experimental measurements of these residual stress fields were followed using various techniques in order to validate the appropriate boundary conditions and assumptions used in the finite element analyses. These measurements are described in Chapter 4.

Secondly, novel side punching of compact tension C(T) specimens was considered in the residual stress generation programme. By utilising the results from the finite element analyses, an optimum C(T) specimen with appropriate geometry and boundary condition was achieved. In this process, three types of punching methods were considered, each with different levels of triaxiality and plasticity. The finite element and experimental studies are described in Sections 3.3 and 3.4 respectively.

3.1 Finite element studies of quenching

Earlier work performed by McKenzie and Moakler [1973] has demonstrated that high levels of tensile triaxiality are generated in quenched spheres. In their study, it was

assumed that the residual stresses in a solid sphere were given by the following functions of distance, r, from the centre of the sphere,

$$\sigma_r = \sigma_o\left[1-\left(\frac{r}{r_o}\right)^2\right] \tag{3.1}$$

$$\sigma_\theta = \sigma_o\left[1-2\left(\frac{r}{r_o}\right)^2\right] \tag{3.2}$$

$$\sigma_e = \sigma_o\left(\frac{r}{r_o}\right)^2. \tag{3.3}$$

The suffixes r and θ refer to radial and circumferential directions respectively; σ_e is the effective stress; r_o is the radius of the outer surface of the sphere; σ_o, is the normalising stress assumed to be less than or equal to the initial yield stress σ_{yi} of the material. Other stress distributions were also considered, such as those based on an initial temperature distribution given by

$$t = t_c - t_d\left(\frac{r}{r_o}\right)^\gamma, \tag{3.4}$$

where t_c is the temperature at the centre of the sphere, t_d is the difference in temperature between the centre and the outer surface, r is the radial distance from the centre, r_o is the radius of the sphere and γ is a radius exponent in stress and temperature distributions. McKenzie and Moakler [1973] assumed the minimum temperature to be high enough for the material to offer little or no resistance to creep and creep strains occur to satisfy conditions for compatibility without significant stresses arising. The mean temperature was lowered but the distribution (Eq. 3.4) was maintained until the maximum temperature was below that at which creep occurs. The temperature was then allowed to become uniform. The centre of the sphere cooled through a greater temperature range than the outer surface.

Assuming linear elastic conditions and independent of plastic/creep properties, MacKenzie and Moakler showed the resulting radial, hoop and von Mises stresses were given by

$$\sigma_r = \frac{2E\alpha t_d}{(1-\nu)}\left(\frac{1}{3+\gamma}\right)\left[1-\left(\frac{r}{r_o}\right)^\gamma\right] \tag{3.5}$$

$$\sigma_\theta = \frac{2E\alpha t_d}{(1-\nu)}\left(\frac{1}{3+\gamma}\right)\left[1-\left(1+\frac{\gamma}{2}\right)\left(\frac{r}{r_o}\right)^\gamma\right] \tag{3.6}$$

$$\sigma_e = \frac{2E\alpha t_d}{(1-\nu)}\left(\frac{1}{3+\gamma}\right)\frac{\gamma}{2}\left(\frac{r}{r_o}\right)^{\gamma}, \tag{3.7}$$

where α is the thermal coefficient of expansion of the material, ν is the Poisson ratio, E is the Young's modulus and γ is a radius exponent in stress and temperature distributions. Typical material properties for type 316H stainless steel [R66, Nuclear Electric] are $E = 196$ GPa, $\alpha = 15 \times 10^{-6}$ /K, $\nu = 0.294$.

The work of Mackenzie and Moakler has been extended here using the finite element method to estimate the residual stress field generated in quenched spheres and cylinders. A number of specimen geometries were explored so that a defined residual stress field could be introduced into specimens of sufficient magnitude and triaxiality in a controlled manner.

3.1.1 Theory and FE models

The finite element analysis was carried out using the ABAQUS finite element commercial code [HKS 1998] to simulate quenching of both cylinders and spheres of type 316H stainless steel. Cylinders were used in the present study in addition to the spheres as the cylinders were easy to manufacture and more importantly easier for residual stress measurement. Two-dimensional axi-symmetric models were employed in the simulations with temperature gradients in both the radial and axial directions. Using symmetry conditions, only a quarter of the model was modelled. Figure 3.1 shows the mesh and the boundary conditions for the quarter model of a cylinder, diameter D, length L and a sphere, diameter D, respectively. To represent the symmetry, the points on the y-axis were restricted to displace only vertically and the displacement along the r-direction was set to be zero. Similarly, the points on the r-axis were restricted to displace only horizontally and the displacement along the y-direction was set at zero.

For the thermal analysis, the boundary conditions included convective heat transfer on the outer surfaces and an adiabatic condition imposed on both the axial and radial axes of symmetry. The quenching water temperature was 20°C. The water temperature was maintained at 20°C in the model, a good representation of the spray water quench used in practice. Initially, a heat transfer coefficient, h, of 16700 W/m^2 K was used in the analysis, similar to that used by [Sen et al 2000]. Subsequently, different values of h were examined. It was assumed that the heat transfer coefficient was independent of temperature [Gür et al 1996]. The use of spray water quenching in the experimental process minimised the effects of film boiling in the analysis.

The numerical analysis consisted of an uncoupled heat transfer analysis solving an energy balance equation with a subsequent thermal stress analysis i.e. the temperatures predicted by the heat transfer analysis were used as input for the thermal stress analysis. The analysis predicted the residual stress fields generated by rapid spray water quenching of cylinders and spheres of various sizes fabricated from stainless steel of types 316H, 316L and 321. These grades of stainless steel are extensively used in the power generation sector. The materials were assumed elastic with strain hardening plasticity and with a yield stress that decreases with temperature. The specimens were initially at a uniform temperature of 850°C and were assumed to be stress-free in this condition. Creep was not taken into account in the analysis. The surface was then quenched in water at room temperature (20°C). Cooling was allowed to continue until the entire specimen reached the water temperature. During the heat transfer analysis the temperature distributions were recorded on the ABAQUS results file. This temperature-time history was then used as input to the thermal stress analysis. The transient stresses were sufficiently large to cause significant plastic flow. Residual stresses therefore remained after the specimens had reached the coolant temperature.

The mechanical and physical properties of stainless steel types 316H, 316L and 321 are shown in Figure 3.2 [R66, Nuclear Electric]. These are also included in Table 3.1. The temperature dependent material properties were defined in the ABAQUS input deck by tabulating the material data as a function of temperature [HKS 1998]. ABAQUS assumes a linear function between data points for stress-strain curves. For stainless steel, phase transformations were assumed to have negligible contribution in the resulting residual stress field and the distortion was assumed unimportant. On completion of the thermal analysis the temperature-time history was input into the thermal stress analysis. Two material hardening models, isotropic and kinematic were used for the stress analysis. The resulting residual stress states in specimens of various dimensions were examined using FE analysis. The results from the FE simulations are summarised in the following section.

3.1.2 FE results

The initial FE study included quenching specimens of grade 316H stainless steel. Figure 3.3 shows the resulting residual stress fields (radial, axial and hoop) after water quenching of type 316H stainless steel specimens of various geometries. All of the results shown in Figure 3.3 assumed a heat transfer coefficient, h = 16700 W/m^2 K, and an initial temperature of 850°C. Various dimensions were considered so that the length-

to-diameter (*L/D*) ratio of the cylinders varied from 0.3 to 3.4, with *L/D* = 0.3 corresponding to a short, flat cylinder and *L/D* = 3.4 corresponding to a long, slender cylinder.

The radial residual stresses in both the cylinders and the sphere were tensile close to the centre and decreased to zero as the surface was approached along a radial line. The axial and hoop stresses were compressive (about -400 MPa) close to the surface and changed to tensile towards the centre, except for the short, flat cylinder (Figure 3.3a) where the axial residual stress decreased to zero at the centre. The shear stresses, $\tau_{r\theta}$ were essentially zero for all cases. The magnitude of the residual stresses increased with an increasing *L/D* ratio as the greater length provided greater constraint. Figure 3.3(d) shows the residual stresses for a quenched sphere of 30mm diameter. The residual stresses are equi-triaxial tensile near the centre. The magnitude of the hydrostatic (mean) stress, defined by $\sigma_h = \frac{1}{3}(\sigma_{11} + \sigma_{22} + \sigma_{33})$, where 1, 2 and 3 correspond to the radial, axial and hoop directions respectively, in the centre of the sphere was high. The level of triaxiality in the sphere was higher than in the cylinders as the residual stresses near the centre of the sphere shown in Figure 3.3(d) are equi-triaxial. Figure 3.4 shows that the hydrostatic stress predicted in the cylinders increased as the *L/D* ratio increased from 0.3 to 1.0, but subsequently decreased for an *L/D* ratio of 3.4. The triaxiality factor, defined by σ_h/σ_e, where σ_e is the effective stress and defined by $\sigma_e = \sqrt{\frac{1}{2}\{(\sigma_{11} - \sigma_{22})^2 + (\sigma_{22} - \sigma_{33})^2 + (\sigma_{33} - \sigma_{11})^2\}}$, is therefore dependent on the specimen geometry. The optimum triaxiality was found to occur with an *L/D* ratio of unity.

The effect of geometry on triaxiality is also illustrated in Figure 3.5, where the triaxiality factor is plotted as a function of normalised principal stress (σ_p/σ_e) averaged over central regions of four cylindrical bars of various dimensions, where σ_p is the principal stress. Residual stresses increase with increasing *L/D* ratio since the length provides a greater constraint. However, the hydrostatic stresses vary differently, as previously explained. Therefore the degree of triaxiality depends on the shape of the quenched specimen. For the sphere in Figure 3.3(d), $\sigma_e \rightarrow 0$ in the centre and therefore the triaxiality factor $\sigma_h/\sigma_e \rightarrow \infty$. The cylinder with highest triaxiality most suitable for the study of creep damage is one with *L/D* = 1.0. This is equivalent to a cylinder of diameter 60mm, length 60mm. The predicted residual stress distribution along the longitudinal axis of a quenched cylinder is shown in Figure 3.6. Stainless steel types of

both 321 and 316L are shown. Only a small difference is present due to the differences in the yield data shown in Figure 3.2.

The theoretical distribution of residual stresses in a quenched solid sphere provided by McKenzie and Moakler [1973] (Equations 3.1 and 3.2) are compared with the FE predicted residual stress distribution in Figure 3.7. The distributions are very similar particularly in trend. However differences occur close to the centre of the sphere. This may be attributed to the choice of heat transfer coefficient and assumption made in the material modelling in the FE simulation. Secondly, whereas the theoretical distribution of residual stresses decreases parabolically in general, the FE predicted residual stresses remain uniform up to about 35% of the radial distance from the centre of the sphere before decreasing towards the outer surface. For the finite element analysis, a heat transfer coefficient of 7000 $W/m^2 K$ and an initial temperature of 850°C was used in the heat transfer analysis with a kinematic hardening model in the thermal stress analysis.

The effects of different heat transfer coefficients and initial temperatures on residual stress distributions are summarised in Table 3.2. For this investigation a cylinder of diameter 60mm and length 60mm was considered. The positions of interest in a section through the cylinder are illustrated in Figure 3.8. A number of different initial temperatures and thermal heat transfer coefficients were separately considered in the heat transfer analysis to study the effect of initial temperature and heat transfer coefficient on residual stresses predicted in the subsequent thermal stress analysis. The magnitudes of the tensile residual stress in the central region of the cylinder were not sensitive to initial temperatures in the range 850°-1000°C. However, large changes in heat transfer coefficient had a major influence on the internal stress levels that are not always evident from the surface stresses. A high compressive stress at the surface did not guarantee a high tensile internal stress. High tensile triaxial stresses were predicted in the central volume of the cylinders when the heat transfer coefficient was greater than 1000 $W/m^2 K$. The relative magnitude of the principal components of stress and degree of triaxiality depended on the cylinder length. The maximum principal stress was in the order of 540 MPa in a 60mm diameter, 60mm long cylinder. These effects are also illustrated in Figures 3.9 and 3.10 which show respectively the effects of heat transfer coefficient and the initial temperature on the residual stress distribution across the radial plane from the centre of the cylinder, diameter 60mm, length 60mm.

Residual stress measurements were made in order to validate the FE simulations of residual stresses in quenched specimens. Near surface measurements were made using the incremental centre hole drilling (ICHD) technique, which provided a quick comparison with the FE simulations. The neutron diffraction (ND) technique was used to measure the internal residual stresses in the quenched specimens. Description of residual stress measurement by the neutron diffraction technique and the main result is provided in Chapter 4. Chapter 5 describes the mechanical strain relief residual stress measurement methods including the incremental centre hole and the deep hole drilling techniques and the measured results. The FE results of the present chapter are compared with the experimental measurements and are discussed in Chapter 7.

3.2 Quenching and post quenching experiments

The first method of introducing a highly triaxial tensile residual stress involved rapid spray water quenching. In this method the test specimens were heated and held at a high temperature of about 850°C for a known time. The heated specimens were then cooled rapidly by high-pressure water spray. The temperatures of the quenching specimens were recorded in a data-logger using K-type thermocouples. The process conditions are summarised in the following section.

3.2.1 Summary of process conditions

The earlier numerical studies using ABAQUS to model quenching process revealed that the following process conditions to be suitable for introducing high levels of triaxial residual stresses in solid cylindrical bars and spheres of type 316H stainless steel.

Geometry of Specimens:

Cylindrical bars of length 60mm and diameter 60mm

Spheres of diameter 60mm

Preheating:

All samples to be preheated to 850°C from room temperature (20°C). Preheating to occur over a period of about 2½ hours sufficient to achieve a uniform temperature throughout the specimen. This was achieved during initial trials.

Quenching:

All specimens to be subjected to quenching by spraying pressurised water directly onto the specimen. The water remaining at ambient temperature. Water quenching to take place until the specimen has achieved ambient temperature.

In the next section a summary of the experimental conditions for achieving these process conditions is described.

3.2.2 Experimental set-up

The experimental rig consists of three sections: a stainless steel rod quick release mechanism, an electrical three-zone heating cylindrical furnace and a cooling chamber. The schematic diagram is shown in Figure 3.11. The furnace was isolated from the cooling chamber by using a removable heat resistant plate.

The cooling chamber consisted of two concentric hollow cylinders of stainless steel sheet of material sealed at each end so that water could be pumped between the two cylinders. The inner cylinder wall had a series of regularly spaced holes positioned on the inner wall. Using a Multiline pumping system water was pumped into the cooling chamber. A high-pressurised jet of water was thereby released on to the surface of the specimens which cooled the surface of the quenching sample. Excess water from the cooling chamber was collected in a bucket placed below the experimental rig.

Each specimen was heated in the furnace at the required temperature controlled by a Eurotherm furnace controller. The furnace controller ensured that the sample did not overheat by maintaining a steady temperature using a R-type thermocouple. When the specimen reached the required temperature, it was released via the quick release mechanism. The quick release mechanism consisted of a long rod with two concentric cylindrical bars held to the rod by screw thread mechanism and a spring inserted between these two bars in such as way that the sample is held in position in the furnace during heating process. When the centre of the sample reached the required temperature the bottom cylindrical bar is unscrewed and let loose so that the sample is then lowered into the cooling chamber as shown in Figure 3.11. The function of the spring is to avoid any jerky landing of the sample into the cooling chamber at temperatures as high as 850°C. The specimen was held in position in the middle of the cooling chamber where it was quenched by rapid-spray water under high pressure. The rapid water spray was used to quench the specimen in order to avoid film boiling and consequently to avoid complications in numerical simulations.

By attaching K-type shielded thermocouples on to the specimens it was possible to register the temperatures both during heating and quenching. An InstruNet Model 100B Analog/Digital Input/Output datalogger system was used to log the temperatures during the quenching tests. Because the temperatures changed rapidly during quenching

it was necessary to increase the frequency of the data acquisition. On the other hand a low frequency data acquisition was necessary during heating.

3.2.3 Quenching and post quenching tests

A total of 46 specimens consisting of cylindrical bars and spheres, of sizes in addition to those described above (Section 3.2.1), were manufactured for rapid-spray water quench study. Details of the specimens and dimensions and positions of thermocouples are provided in Table 3.3. Also shown in the table are the various residual stress measurement methods used on the specimens. These are discussed later in Chapters 4 and 5. Table 3.3 has been divided into four major groups according to different process conditions including (a) as-quenched, (b) thermally exposed, (c) pre-trepanned and (d) annealed. As-quenched specimens include *s1*, *s2*, *s7-s9*, *s12*, *s19*, *s22*, *s25-s27*, *s39* and *s45*. Thermally exposed samples include quenched specimens followed by thermal heat treatment at 550°C for a known period and include 14 specimens, *s3-s6*, *s16-s18*, *s20*, *s23*, *s24*, *s28*, *s31*, *s29* and *s30*. Pre-trepanned specimens were quenched followed by drilling by 1.5mm diameter drill bit and trepanning by electro-discharge machining (EDM) to variable depths as described in Table 3.3 and include 10 specimens, *s34-s38* and *s40-s44*. Sample *s46* is an unquenched specimen which was annealed at 370°C for 2½ hours. The remaining unquenched test specimens *s10*, *s11*, *s13-s15*, *s21*, *s32* and *s33* were supplementary specimens of which specimens *s32* and *s33* were used as trial at a neutron facility described in Section 4.3. The samples are also grouped in a way that the table discriminates between the non-destructive residual stress measurements carried out on the specimens at various neutron facilities and these are relevant to Chapter 4.

A schematic of a generic section of a quenched solid cylinder, diameter D, length L and sphere, diameter D is shown in Figure 3.12. Initially, a selected number of quenched specimens (samples *s1-s3*, *s5*, *s7*, *s12*, *s16*, *s22* and *s26*) had thermocouples attached to measure temperatures during both preheating and cooling. The thermocouples were attached to the specimens by drilling holes and inserting the thermocouples into the specimens. The thermocouples were then secured in position by modifying the ends of the holes. Figure 3.13 shows the arrangement of thermocouple positions in a quenched solid spherical specimen *s8* of diameter 30mm. Also shown in the figure is a vertical section of a generic cylindrical body, diameter D, length L to illustrate the locations of thermocouples during quenching test. Later, preheating and cooling were conducted in an identical manner to obtain similar residual stress

distributions. For example, Figure 3.14 shows the temperatures at the centre, side and top (see Figure 3.13 for illustration) of a quenched cylinder (*s2*), diameter 60mm, length 60mm during preheating. Clearly the figure shows a uniform temperature distribution of 850°C after 2½ hours heat soak. The centre, side and top surface of the specimen and the furnace all have a uniform temperature of 850°C by this time. Figure 3.15 shows the temperature distributions during cooling of a quenched sphere (*s22*), 30mm diameter. As expected the surface cools faster than the centre.

The temperature fields obtained in the heat transfer analysis during quenching process for initial temperature of 850°C and heat transfer coefficient of 7000 W/m^{2}K [Gür and Tekkaya 1998] compare very well with the thermocouple measured temperature-time cooling curves. Results are shown in Figures 3.16 and 3.17 for a water quenched sphere (*s22*), diameter 30mm and a water quenched cylinder (*s26*) diameter 60mm, length 160mm respectively. The close correlation between the measured and predicted temperature-time cooling curves validates the boundary conditions and assumptions made in the heat transfer analysis. Conversely, using a different heat transfer coefficient, e.g., h = 200 W/m^2 K in the heat transfer analysis of the FE study the predicted temperature-time cooling curve was much different from that measured as illustrated in Figure 3.18.

Aged specimens

Eight test specimens, viz. two quenched spheres, diameter 60mm (*s6* and *s20*), four quenched cylinders, diameter 60mm, length 60mm (*s3*, *s5*, *s16* and *s17*) and two unquenched cylinders, diameter 60mm, length 60mm (*s4* and *s18*) were subjected to an initial ultrasonic inspection [Bouchard 2001]. An automated process with 4 MHz single and twin crystal compression probes was used to inspect the cylinders from the curved surface and a manual procedure with a single crystal probe was used for the spheres. The 'ultrasonic fingerprints' for each component were recorded electronically for later reference comparisons. Following inspection, the specimens were placed in a Muffle furnace at Berkeley Laboratory [Bouchard 2001]. The furnace was being maintained at a constant temperature of 550°C. The temperature was being continuously monitored using a type K thermocouple and the signal recorded using a data logger. These specimens were allowed to age at 550°C for about 4320 hours.

Other aged specimens include *s23*, *s24*, *s28* and *s31*; specimens *s29* and *s30* include short time thermal heat treatment at 550°C. These were all used in the residual stress measurement programme to validate the FE study and are discussed in Chapter 4.

3.2.4 Pre-trepanned cylinders

This set of specimens consists of rapid spray water quenched cylindrical bars followed by drilling (using 1.5mm diameter drill bit) and EDM trepanning (using 5mm diameter copper electrode) to variable depths as detailed in Table 3.3. This study was carried out in order to understand the influence of EDM trepanning on the redistribution of residual stress. Two different dimensions of cylinders were used in the study. Figure 3.19 shows the schematic of the cylinders illustrating drilling and the subsequent trepanning processes to variable depths as tabulated in Table 3.3. These depths were generally 25%, 50%, 75% and 100% of the total length of the cylinder.

In order to prepare these specimens quickly they were drilled by using a 1.5mm diameter drill bit rather than the conventional gun drill used in the deep hole measurement technique as described in Chapter 2 after they were water quenched in an identical manner as described in Section 3.2. Consequently a blind hole as shown in Figure 3.19 was produced in each of these specimens rather than a through hole. In the study of the influence of trepanning on the redistribution of residual stress a blind hole was sufficient. After the specimens were centrally drilled they were aligned carefully on to the EDM machine and then trepanned to the respective depths as detailed in Table 3.3.

3.3 FE studies of side punching

Side punching as a local compression technique is mentioned in standards [ASTM 2001, British Standard 1997, Towers et al 1982] as a method to relax residual stresses. Other applications include hardness tests on materials [Shield 1955]. Meith et al [2002] have studied side punching as a means of generating residual stress fields ahead of a notch tip in single-edge-notched-bend (SENB) fracture specimens. Side punching was used to introduce a residual stress field into fracture specimens and the resulting residual stress field studied using finite element analysis by Mahmoudi et al [2003]. The parametric study by Mahmoudi et al [2004] using FEA revealed that the size and the position of the punching tools has a strong influence on the magnitude and direction of the residual stress field. The work of Mahmoudi et al has been used as a general guideline for selecting the size of the specimens, the punching tool and the amount of indentation. The objective of the test here is to generate residual stresses of sufficient triaxiality in order to study creep formation. In order for creep initiation to occur, it is hypothesised that the presence of both triaxiality and plasticity are prerequisites.

The dimensions of the C(T) specimen are shown in Figure 3.20. Side punching as shown in Figure 3.21 consisted of a cycle of punching along the depth of the C(T) specimen followed by unloading. Three categories of punched specimens are considered here:

(a) A single punch where the specimen is compressed using one punch on either side of the C(T) specimen. Details of the method and the result of the parametric studies may be found in [Mahmoudi et al 2003a]. A brief description of the method is provided in Section 3.4.

(b) A double punch where the specimen is compressively loaded using two punches on each side of the C(T) specimen. The punching tools and the method used are briefly described in Section 3.4. Further details of the method and the result of the parametric studies are provided in [Mahmoudi et al 2004].

(c) A figure-of-eight punch where the specimen is compressed using one punch on either side of the C(T) specimen as in the case of single punch. But the shape of the punching tool is an eight shape rather than circular as in the case of single punch.

The purpose of the double punch was to remove the punch imprint from the vicinity of the notch. By punching away from the notch tip, no plastic strain is accumulated at the notch tip. The intention of this test was to discriminate between the influence of prior plastic strain in the creep cavitation initiation sites and the absence of prior plasticity. Figure 3.21 shows a schematic diagram of side punching, illustrating the arrangement of the single, double and figure-of-eight punch. The finite element study is described in the next section followed by a brief summary of the main result.

3.3.1 FE models

As previously, the numerical modelling work was carried out using the commercial finite element code ABAQUS [HKS 2002]. The aim of the study was primarily to obtain a C(T) geometry with a residual stress field of high triaxiality by varying the size of the punching tool and the indentation following a previous general guideline [Mahmoudi et al 2003a, 2004]. This information was used for subsequent experimental tests. The second objective of the FE study was to model the effects of prolonged high temperature exposure.

Due to the two symmetry planes along the ligament and the mid-thickness plane, one-quarter geometry of the C(T) specimen was modelled using 6,048 linear 3D quadrilateral elements with 7,190 nodes.

Figure 3.21 shows the schematic of the side punching process on a C(T) specimen. The relative positions of the punch and the specimen are characterised by a dimensionless parameter (X/R), where X represents the distance between the centre of the punching tool and the notch tip; and R is the radius of the punch. Previous FEA work, [Mahmoudi et al 2003a, 2004], examining the effect of size and position of the punch on the development of residual stresses, has shown that the position where X/R = 1 provides the maximum tensile region ahead of the notch tip. In the present study a series of finite element studies was carried out keeping X/R = 1 initially, varying the thickness (B) of the C(T) specimen, the size of the punching tool (R) and the applied displacement loading (δ) in order to find an optimum geometric and loading condition for the subsequent study of creep formation.

An analytic rigid body [HKS 2002] was considered for applying the displacement controlled loading in the finite element model. The rigid body plays the role of side-punching the experimental rig. A uniform displacement was incrementally applied at the surface of the C(T) specimen in the through-thickness axis to simulate the out-of-plane side punching. The rigid body was constrained in all directions except the through-thickness axis of the C(T). A frictionless contact [HKS 2002] was assumed between the rigid body and the C(T) model.

3.3.2 FE results

The method of introducing a highly triaxial tensile residual stress includes pre-straining a C(T) specimen, by incrementally applying a known displacement via a rigid body located on the outer surface of the C(T) specimen, shown in Figure 3.21; this is then followed by an unloading cycle. As a result of local compression, a permanent deformation occurs at the vicinity of the notch tip. This introduces a highly triaxial residual stress field ahead of the notch tip.

The compression loading in the finite element study was applied via a rigid body using prescribed displacement as described above. The displacement δ was used in the finite element simulation, which in turn provided the applied load P from the reaction force. This applied load was then used in the experimental study. By changing the thickness, B, of the C(T) specimen, the size (or radius) of the punch, R, and the applied

displacement, δ, an optimum geometry for the C(T) specimen with an appropriate level of applied compression load was determined for which a highly tensile triaxial residual stress field was obtained.

Figures 3.22 - 3.24 show the residual stress distribution across the ligament from the notch tip of the C(T) specimens under various loading conditions for single, double and figure-of-eight punching cases. For clarity distribution of the stresses in the first 2.5mm from the notch tip is also shown. Table 3.4 shows a preliminary result of the parametric study in terms of triaxiality factor and the plastic strain. The triaxiality factor is defined as the ratio of the hydrostatic mean stress to the von Mises equivalent stress. The dimensions used in the table are all illustrated in Figure 3.21.

Figure 3.25(a) shows the distributions of triaxiality factor and the equivalent plastic strain across the ligament from the notch tip of the single punch local compression C(T) specimen under various applied displacements. For the single punch case, a 25mm diameter punch was considered in the FE analysis, whereas both 20mm and 25mm diameter punch sizes were considered for the double punch case in the FE analysis. The double punch results with both these punch sizes are shown in Figure 3.25(b). For both punching cases, the triaxiality factor decreases and the plastic strain increases with increasing applied displacement. For the double punching case, the effect of the size of the punch is illustrated by the case of increasing punch diameter from 20mm to 25mm: though the triaxiality factor increases close to the notch tip with greater punch diameter, the extent of triaxiality is much lower. Furthermore, the plastic strain is also lower with greater punch size.

An earlier study [Mahmoudi et al 2003a, 2004] which considered the effect of the punching position (X/R) showed the maximum tensile stress region to exist ahead of the notch tip for a position of the punch at $X/R = 1$. In the present study, both the triaxiality factor and the plastic strains were important. Figure 3.26 illustrates the effect of punch positions on the stress triaxiality and plasticity. Variations in both the X and Y positions (see Figure 3.21) were considered. Figure 3.26 consists of results for double punch only and therefore consists of a sufficiently high triaxiality factor. It may be noted that the parameter X/R has little effect on the plasticity compared to the Y/R position. Thus decreasing the Y/R ratio increases the plasticity. Although reducing Y/R further to zero would increase the plastic strain even further, this would however be equivalent to the single punch case, where the triaxiality factor is significantly reduced. Therefore, from the present analyses, an optimum configuration for the creep damage study included the

case where X/R = 1.0 and Y/R = 0.5. This configuration was essentially a modified double punch with a shape similar to "eight", and therefore was known as a "figure of eight" configuration. Figure 3.27 illustrates this concept.

3.4 Side punching experiments

3.4.1 Experimental rig

In this second method of introducing a highly triaxial tensile residual stress a C(T) specimen of dimension 62.5×60.0×25 mm^3 (Figure 3.20) was side-punched by applying a measured compressive load to the specimen. Side punching was carried out by using punching tools. The tools were manufactured from ferritic steel EN24. These were then hardened by heat treatment at 850°C for one hour followed by annealing to room temperature. Note that for the single and double punch cases, the same punching tools were used as those used by Mahmoudi [2005]. The schematic of these punching tools is shown in Figure 3.28. For the "figure of eight" punch case, a new tool was manufactured following the same manufacturing and heat treatment procedures described above. A detailed drawing of this punching tool is shown in Figure 3.29. The measured compressive loading was then followed by an unloading cycle. For accuracy of loading, a displacement controlled loading was used with a pre-calibrated linear voltage displacement transducer (LVDT). Loading and un-loading was maintained quasi-static with loading at 0.2mm per minute. As a result of side punching the component, yielding occurred. This introduced significant plasticity in the component and a residual stress state with high triaxiality.

3.4.2 Side punch tests

From the parametric study using finite element analysis, optimum geometries of the C(T) specimens with appropriate levels of loading under all the punching configurations were obtained and these were side punched by applying a measured compressive load using the punching tool as described above. A total of nine C(T) specimens manufactured from type 316H stainless steel were used in the local punch tests. Details of the specimen dimensions are provided in Table 3.5. Three specimens were side-punched using each punch configuration. The permanent indentations on each specimen as a result of local punching was measured and are provided in Table 3.6 and are comparable to those predicted by FE. Some difference between the measured indentation and that predicted by FE may however be noticed. The reason may be as

follows. While in the FE study an analytic rigid body was considered for the punching tool material, in practice the punching tool, manufactured from a deformable material and despite its heat-treatment in order to harden, underwent deformation during the compressive loading. Consequently under the same applied load the deformation in the punched specimen was reduced.

Of the three specimens side-punched under each configuration, two specimens have been put into a furnace to age at 550°C for a set period to study creep damage formation. The remaining specimen has been kept for the residual stress measurement programme to obtain the initial residual stress field in the as-punched case prior to thermal ageing.

Chapter 4

Measurement of residual stresses using neutron diffraction

In the preceding chapter, design of laboratory specimens with residual stresses of high triaxiality has numerically been studied using the commercial FE code ABAQUS. The two main processes involved quenching of cylinders and spheres and a side punching of C(T) specimens. The finite element analyses predicted residual stresses of various magnitudes for each case with different degree of triaxiality. Experimental test programmes were implemented based on the initial finite element analyses and in order to verify and validate the finite element findings, measurements of residual stress distributions were performed.

Three main measurement techniques involved in the residual stress measurement programme were: (a) the neutron diffraction (ND) method, (b) the incremental centre hole drilling (ICHD) method and (c) the deep hole drilling (DHD) method. This chapter describes the measurements of residual stresses made in selected specimens using neutron diffraction. Residual stress measurements using the ICHD and DHD methods are reported in Chapter 5.

Both diffraction and time-of-flight techniques were used in the internal residual stress measurement programme by neutron diffraction. Neutron diffraction using the time-of-flight (tof) technique was used to determine the residual stress fields in specimens labelled *s8*, *s9*, *s19*, *s22-s27*, *s40*, *s42* and *s46* at ISIS, Rutherford Appleton Laboratory (RAL), UK and specimens *s28-s31* at Paul Scherer Institute (PSI), Switzerland. The diffraction method at Studsvik Neutron Research Laboratory (NFL) in Sweden with the residual stress and texture measurement diffractometer REST was used to measure the internal residual strain distribution in specimens *s34-s39*. These are also summarised in Table 4.1. The main characteristics of the neutron diffraction method at each facility are described followed by experimental results.

4.1 Neutron diffraction time of flight at ISIS

The neutron diffraction technique is now widely used to measure internal stresses in crystalline materials [Webster and Webster 1985]. The samples used for residual stress measurement using the time of flight technique at ISIS include *s8*, *s9*, *s19*, *s22-s27*, *s40*, *s42* and *s46* shown in Table 3.3 and repeated in Table 4.1 for convenience. The ND technique used for the specimens uses a time-of-flight method developed at the ISIS facility at the Rutherford Appleton laboratory. Only the salient features of the method are described in the next section and further details can be found in [Noyan and Cohen 1987, Ezeilo and Webster 2000].

4.1.1 Basic principles

The technique relies on the precise measurement of the separation of similarly oriented planes of atoms in a polycrystal. This is achieved by the interaction of scattered waves, which produce localised maxima and a diffraction peak. The position of this peak is given by Bragg's law [Holden and Roy 1996]

$$n\lambda = 2d_{hkl}\sin\theta_{hkl} \tag{4.1}$$

where λ is the wavelength of the neutrons, n is an integer, d is the distance between sets of parallel (hkl) crystal planes and 2θ is the scattered angle. For a change in lattice separation Δd, the residual strain ε becomes

$$\varepsilon_{hkl} = \frac{\Delta d_{hkl}}{d_{hkl}} \tag{4.2}$$

This change in separation can be obtained by recording the time of flight of neutrons from a moderator to a detector when a pulsed polychromatic beam is used. The time t that it takes neutrons to travel the distance L from the moderator to the detector, after scattering from the sample, is obtained from de Broglie's wave-particle duality by

$$t = \frac{\lambda m L}{h} \tag{4.3}$$

where m is the mass of the neutron and h is Planck's constant. In a spallation source, thermalised neutrons with a higher energy will take the shortest time to reach the detectors; the detectors are positioned at a fixed scattering angle 2θ [Noyan and Cohen 1987]. Substitution of Eq. (4.3) into Eq. (4.1), for a change in time Δt and change in wavelength $\Delta\lambda$ at constant θ, gives

$$\frac{\Delta t}{t} = \frac{\Delta \lambda}{\lambda} = \frac{\Delta d_{hkl}}{d_{hkl}} = \varepsilon_{hkl} \tag{4.4}$$

Thus changes in the time of flight can be used to measure strain.

A pulse of neutrons consists of a range of wavelengths covering a full spectrum. Strain can therefore be measured by analysing the whole diffraction pattern using profile refinement techniques to produce an overall average [Daymond et al 1997]. Refinement of the neutron intensity spectrum involves the prediction of a lattice parameter by performing a least-squares minimisation procedure on selected peaks from the measured spectrum. The predicted lattice parameter for strained material is then compared with the lattice parameter for unstrained material. In order to obtain the complete strain and stress tensors at a point, six independent strain measurements are necessary. However, when the principal directions are known, three orientations are sufficient and the strain components measured by ND are converted to stress by the generalised Hooke's law:

$$\sigma_1 = \frac{E}{(1+\nu)}\varepsilon_1 + \frac{E\nu}{(1+\nu)(1-2\nu)}(\varepsilon_1 + \varepsilon_2 + \varepsilon_3) \tag{4.5}$$

where 1, 2 and 3 are the principal directions, E is the elastic modulus and ν the Poisson's ratio. Similar expressions hold for the σ_2 and σ_3 components of stress. When these directions coincide with the coordinate axes x, y and z the corresponding stresses can be obtained

$$\sigma_x = \frac{(1-\nu)\varepsilon_x + \nu(\varepsilon_y + \varepsilon_z)}{(1+\nu)(1-2\nu)}E \tag{4.6}$$

with similar expressions for the y and z directions.

4.1.2 Instruments

ENGIN and ENGIN-X are purpose-built neutron scattering instruments for engineering residual stress measurements. The main features are shown in Figure 4.1 and include a sample-positioning device, focusing collimator slits, two position sensitive detectors at 90° from the incident neutron beam and a masking slit for the incident beam. The incident and diffracted beams define the sampling or gauge volume within the specimen.

4.1.3 Experiments and results for quenched samples

Rapid spray water quenching of stainless steel cylinders and spheres meets the objective of acquiring the residual stress field with high triaxiality in a well-controlled manner [Hossain et al 2004, 2004d]. The quenching test is considered as a small-scale experimental model of welded components with highly triaxial residual stress fields operating at high temperatures with probable creep damage failure. Finite element (FE) analyses carried out demonstrated that high levels of tensile triaxiality could be generated in both cylinders and spheres (see Section 3.1). Optimum dimensions of experimental specimens were selected based on the anticipated levels of residual stresses predicted by the FE analyses. Experiments were performed on both spheres and cylindrical bars. The samples were water quenched to room temperature by high-pressure rapid spray water after preheating to a high temperature of 850°C.

In order to validate the assumptions and the boundary conditions used in the numerical analyses in Section 3.1, a programme of residual stress measurements was conducted. This section describes the quenched specimens, the implementation of neutron diffraction non-destructive residual stress measurement technique and the results obtained. The neutron diffraction measurements may be categorised under two main sections: internal residual stress measurement in quenched specimens prior to thermal heat treatment and residual stress measurement following heat treatment.

As-quenched specimens

Initially, two quenched specimens including *s8* and *s9* were studied on the stress diffractometer ENGIN on the PEARL beam line at the ISIS facility at the Rutherford Appleton Laboratory. These measurements were carried out on the 4th - 6th October 2001 [Hossain et al 2001]. Further residual stress measurements were made in additional quenched specimens including *s19*, *s22*, *and s25* - *s27* (see Table 4.1) on the stress diffractometer ENGN-X on ENGIN-X beam line at ISIS on the 8th - 12th May 2003 [Hossain et al 2003].

The samples used in the ND measurements (shown in Figure 4.2) were: 316L and 316H stainless steel (SS) spheres, with diameter 30mm, *s8* and *s22* previously subjected to rapid-spray water quenching and "combs", *s9* and *s25* extracted from identically quenched SS spheres of diameter 30mm, and three other SS quenched cylindrical bars each of diameter 60mm with length 60mm for one (*s19*) and 160mm for the remaining two (*s26*, *s27*). The cylinders are shown in Figure 4.3. The specimens included a small

rod to aid heating and quenching of the specimens. The rod also helped to locate the samples in the neutron beam. The comb samples *s9* and *s25* (shown in Figure 4.2) started as quenched spheres of diameter 30mm. They were then electro-discharge machined to produce combs with 7 fingers at the end of the rod. The fingers of the comb measured 2 mm by 2 mm in cross-section. The comb was treated as a reference sample to provide a stress-free diffraction spacing d_0 as a function of the distance across the measurement plane in the sphere, accounting for microstructure and micro-stresses. These spacings were then used together with the measurements from the sphere to obtain the strain components. In Equation 4.2 $\Delta d=d-d_0$. Gauge volumes in the ND measurements consisted of $2\times2\times2mm^3$ for 30mm diameter spheres for all three strain directions, and $4\times4\times4mm^3$ for the 60mm diameter cylinders in the radial and hoop orientations and $4\times4\times6mm^3$ in the axial orientation.

Figure 4.4 presents a summary of the measured stress-free lattice parameter d_0 across the seven fingers on the comb *s9* used to determine residual elastic strain distribution in the quenched sphere *s8*. It is desirable to have each of the finger measurement corresponding to the same spatial positions as the sphere stress measurements. However, as expected of the stress-free comb sample the variation in the measured stress-free lattice parameter shown in Figure 4.4 for both detectors PSD1 and PSD2 was insignificant and did not vary much across the comb. Therefore for simplicity an average lattice parameter was used to determine the residual elastic strain distribution in the quenched sphere *s8* using Equation 4.4.

Figure 4.5 shows a summary of the measured strain distribution across the mid-section of the quenched sphere *s8*. Using Equation 4.6 these strains were converted into the respective residual stress components. The elastic constants E (Young's modulus) and v (Poission ration) were 196 GPa and 0.294 respectively (see Table 3.1). Figure 4.6 summarises these residual stresses measured by the neutron diffraction time of flight (tof) method.

The strain distribution measured across the equatorial plane of a quenched SS solid sphere *s22* is shown in Figure 4.7. The corresponding residual stress components, calculated using Equation 4.6 and the elastic constants provided in Table 3.1, are shown in Figure 4.8. The measurements revealed the presence of essentially an equi-triaxial tensile residual stress field in a central core of diameter about 10mm. Figure 4.9 compares the residual stress distributions between quenched spheres *s8* and *s22*. Yield stress of 316H is greater than that of 316L stainless steel (see Table 3.1). Therefore the

measured residual stresses were in general higher in the solid 316H SS quenched sphere *s22* compared to those in the solid 316L SS quenched sphere *s8*. It can also be noticed in Figure 4.9 that more measurement points were present in sample *s22*. This is because the stress instrument ENGIN-X used for sample *s22* is much more powerful than the instrument ENGIN used for sample *s8*.

The strain distribution measured in a 316H SS solid quenched cylinder *s19* across OS (see Figure 4.3a) is shown in Figure 4.10. As before using Equation 4.6 and the elastic constants provided in Table 3.1 the corresponding residual stress components are calculated and are provided in Figure 4.11. Note that the measurement of the axial component of the residual strain required a total flight path length greater than 60mm which resulted in noisy and inadequate data. The effect of this can be seen in Figure 4.10. At the centre the axial strain component became highly unreliable. Furthermore in calculating the corresponding residual stresses all the three measured residual strain components are needed. The discrepancy in the measured axial strain component near the centre therefore contributes to all the three components of the calculated residual stresses near the centre. This is shown in Figure 4.11; at the centre the axial stress component is compressive and the hoop and radial stress components much lower. Nevertheless the measurements revealed the presence of an essentially triaxial residual stress field in a central region of diameter about 25mm. A second point to notice is that the number of measurements of the axial strain components shown in Figure 4.10 was much lower than the hoop and radial strain components. This is because the counting time required for the axial strain components was much higher.

Measured strain distributions in larger solid cylinders, diameter 60mm, length 160mm are shown in Figures 4.12-4.14. Figure 4.12 summarises the ND measured residual strains in cylindrical bar *s27*, 18mm offset from the end of the bar, across NA (see Figure 4.3b). Here only one measurement data point for the axial strain component was taken at point N; the counting time was high for the axial components.

Figure 4.13 shows the residual strains measured across the mid-section OB (see Figure 4.3b) of the cylinder *s27*. For the same reason, ie, longer counting time in the axial orientation only the hoop and radial strain components were measured across OB in the cylinder *s27*.

The residual strains measured along the longitudinal axis of the cylinder *s26* at positions A, B and C (Figure 4.3c) is shown in Figure 4.14. The holes drilled into the

quenched cylinder *s26* (Figure 4.3 c) shortened only the incoming path length during the ND measurement; the outgoing path consisted of the diverged beam. So the constant diameter hole drilled "for the outgoing beam" did not facilitate in reducing the total path length. Nevertheless, the counting time was essentially reduced during measurement of the radial and hoop residual strains at positions A, B and C of cylinder *s26* (Figure 4.14). Diverging hole for the outgoing beam may be considered in future measurements to considerably reduce the total counting time.

Figure 4.15 shows a comparison of residual strains measured in cylinder *s27* across OB and NA (see Figure 4.3b) and in cylinder *s19* across OS (see Figure 4.3a). The strain distributions in general are similar. It is interesting to note that near the inner core of the cylinders the residual strains across OS in cylinder *s19* compare better with cylinder *s27* across NA. On the other hand away from the centre the residual strains across OS in cylinder *s19* compare better with cylinder *s27* across OB.

Post thermal heat-treated quenched specimens

The quenched specimen *s24* which had been subjected to thermal heat treatment after quenching was measured at the ISIS facility at the RAL. The measurement took place using the stress instrument ENGIN-X. In the preceding section, the residual stress fields in rapid spray water quenched specimens have been characterised. Figures 4.5-4.8 showed the residual strain and stress distributions in quenched SS solid spheres of diameter 30mm including samples *s8* and *s22*. The effect of thermal ageing on the relaxation of residual strains and stresses in the 30mm diameter sphere are shown in Figures 4.16 and 4.17, respectively. These are the residual strain and stress distributions across the equatorial plane from the centre towards the outer surface of a quenched and aged 316H SS solid sphere *s24*.

A comparison is made between the residual stress distributions in as-quenched 316H SS solid sphere *s22* and quenched and thermally aged 316H SS solid sphere *s24* across the equatorial plane from centre towards the outer surface across OS in Figure 4.18. The internal residual stresses relax from about 300MPa in the quenched sample (*s22*) to just under 200MPa in the thermally aged sample (*s24*). Also shown in the figures are the von Mises equivalent stresses. As expected, the equivalent stresses are very low near the centres of both quenched and thermally aged spheres due to the high triaxiality near the centre of the spheres.

4.1.4 Experiments and results for pre-trepanned quenched samples

The set of pre-trepanned quenched specimens, where the internal residual stresses were measured by neutron diffraction at the ISIS facility in order to validate the FE simulation of the stress redistribution in deep hole drilling measurement technique (further detail in Chapter 6), consisted of cylinders, diameter 60mm, length 60mm. These included pre-trepanned quenched cylinders *s40* and *s42* (see Table 4.1). The measurements were conducted on stress diffractometers ENGIN-X on ENGIN-X beam line at the ISIS facility at RAL. The configurations of these specimens are described in Section 3.2.4. Here, a short summary of the measured results is provided. The objective of these measurements is to validate the FE model used to simulate the DHD measurement process (see Chapters 5 and 6).

The time of flight method developed at ISIS facility at the Rutherford Appleton Laboratory with stress instrument ENGIN-X was used to measure the internal residual strain distribution in the pre-trepanned quenched cylinder specimens *s40* and *s42*. Strain scans were made in all radial, axial and hoop directions across the radial plane of the cylinder as well as along the axial line. A sampling volume of $4\times4\times6mm^3$ was used in these measurements. The stress-free interplanar spacing d_o was obtained by studying a comb specimen (*s25*), as shown in Figure 4.2, extracted from a quenched sphere of diameter 30mm. The stress-free diffraction spacings were then used together with the measurements from the cylinder to obtain strain distribution. The basic principle of the method is provided in Section 4.1.1. The specimens in the present study included two rapid spray water quenched cylindrical bars, diameter 60mm, length 60mm each with a drilled hole of diameter 1.5mm. These were then edm pre-trepanned to depths of 15.5mm and 45.5mm corresponding to specimens *s40* and *s42* respectively by using copper electrode of diameter 5mm with thickness 1mm.

s40 edm depth 26%

Figure 4.19 shows the distribution of residual strain and residual stress across a radial plane in a rapid spray water quenched cylinder with 1.5mm diameter drilled hole and edm pre-trepanned up to depth of 15.5mm (*s40*). A clearance of 3mm ahead of the edm trepan front was maintained during the ND measurement. Although the measurements started from the origin inside the drilled hole, not all the strain components were zero. This is because the sampling volume used in the measurement was $4\times4\times6mm^3$ so that part of the neutron beam was always inside the material away

from the drilled gap. Also the large sampling volume resulted in averaging over a larger volume. In particular the axial component was the most affected. This is clearly shown in the figure. The distributions of residual strain and residual stress along the axial line shown in Figure 4.20 were obtained 8mm away from the centreline. The sampling volume was therefore well clear of the trepanned edge (about 4.5mm clear). The outer edge of the trepan was 3.5mm away from the central axial line; this is half of the trepan diameter plus 1mm thickness of the EDM electrode.

s42 edm depth 76%

Figure 4.21 shows the distributions of residual strain and stress in a through-hole drilled rapid spray water quenched cylinder with 45.5mm depth edm trepan (*s42*) across a radial line 3mm ahead of the edm front from the centreline. The results measured along the axial line 8mm away from the centreline are shown in Figure 4.22.

4.1.5 Experiments and results for C(T) specimens

As mentioned in Section 3.4 a total of nine C(T) specimens were studied. Three of each were side punched using a single, double and figure-of-eight punching tools. Previous studies with single and double punch in Aluminium C(T) specimens by Mahmoudi [2005] revealed the presence of high residual stresses near the vicinity of the crack tip. Mahmoudi [2005] used a Synchrotron to measure these stresses [Hossain et al 2004a]. In the present study only the specimens side punched by figure-of-eight punching tool were studied for the neutron diffraction residual stress measurement. Due to the time constraint of the available neutron beam time the single and double side punched C(T)s were not measured. Two figure-of-eight side punched C(T) specimens, the first as-punch only and the second punched and aged at 550°C for 3900 hours, were considered in the neutron diffraction residual stress measurement study. The results are presented here.

As-punched C(T) specimen

Figure 4.23 shows the measured residual strain distribution along the ligament ahead of crack tip in the mid-plane of an as-punched C(T) specimen. Using Hooke's law (Equation 4.6) and the elastic constants for 316H stainless steel material listed in Table 3.1 the corresponding residual stress components were calculated and these are presented in Figure 4.24 along the same path ahead of the crack tip as for the measured strains. The region near the vicinity of the crack tip is important for the damage study. It may be seen from Figure 4.24 that the measured residual stresses are quite large here.

Secondly moving in closer to the crack tip the residual stresses rise. Since the sampling gauge volume used in the neutron diffraction was $2\times2\times2mm^3$ measurement was restricted to start about 1.4mm away from the crack tip. This was so that the gauge volume was entirely in the material of the specimen in order to prevent wasting beam counting time with part of gauge volume lying outside the material.

Post thermal aged C(T) specimens

The same gauge volume was used for the residual stress measurement of the punched and thermally aged (550°C for 3900 hours) C(T) specimen. The measured strain distribution along the ligament ahead of crack tip in the mid-plane of the C(T) specimen is shown in Figure 4.25. The calculated corresponding residual stress distribution is shown in Figure 4.26. In order to see the effect of thermal ageing on the initial residual stresses same scale in Figures 4.23-4.26 were used. Both strains and stresses were relaxed as a result of thermal ageing. This is clearer in Figure 4.27 which presents a comparison of the measured residual stress distribution along the ligament ahead of crack tip in the mid-plane between the as-punched and punched and thermally aged C(T) specimens.

4.2 Neutron diffraction time of flight at PSI

Internal residual stresses were measured using time-of-flight at PSI in thermally heat treated and thermally aged quenched cylinders, diameter 30mm, length 30mm including samples *s28* and *s29*. This measurement provided the effect of both short time heat treatment and thermal ageing on the initial residual stresses in quenched specimens. The next section describes briefly the instrument and basic principles of the neutron facility at PSI followed by experimental measurements and results.

4.2.1 Instrument and basic principles

An elastic neutron scattering experiment on the thermally aged specimens *s29* and *s28* was performed on the SINQ high intensity, high resolution multiple Pulse Over Lap time-of-flight Diffractometer, POLDI to measure the internal strains. The main features of the stress instrument is similar to that of ENGIN and ENGIN-X shown in Figure 4.1 but with a difference that there is only one detector in the case of POLDI as shown in Figure 4.28 and include a sample-position device, focussing collimator slits, a position sensitive detector at 90° from the incident neutron beam and a masking slit for the incident beam.

Internal strains measurement with neutrons requires the following: high resolution, a scattering angle 2Θ near 90° (necessary to define a small gauge volume within a larger sample) and high intensity. The conflicting conditions of high intensity and high resolution have been partially decoupled in the POLDI concept by allowing multiple frame overlap which means that the condition that the fastest neutrons of one pulse may not catch up the slowest one of the previous pulse has been dropped [http://poldi.web.psi.ch/]. The intensity, which is mainly given by the duty cycle of the chopper and the time resolution (determined by the ratio of pulse width and length of flight path s_{tot}), can be optimised independently. The angular information, usually not used by tof-diffractometers, allows the reconstruction of the diffraction pattern from the multiple pulse-spectrum. Two comb specimens *s30* and *s31*, extracted from two further spheres which had undergone identical process conditions as specimens *s29* and *s28* respectively, were used as the stress-free reference samples for obtaining the lattice spacing d_o.

For an unambiguous determination of the diffraction pattern the dependence of the time-of-flight t on the scattering angle is measured. This angle dependence is given by

$$\frac{dt}{d\theta} = t_{flight}\left(\cot\theta + \frac{1}{s_{tot}}\frac{ds_{tot}}{d\theta}\right) \tag{4.7}$$

which defines the slope of a Bragg-line in a time versus scattering-angle plot [http://poldi.web.psi.ch/]. From this slope the time of flight of the neutron can be calculated with sufficient accuracy so that the slit where the neutrons came from can be accurately determined. Finally, the position of the Bragg-line gives the exact value of the time of flight, and therefore, the lattice spacing. The analysis of the measured data was carried out using an in-house "StressCalc" program which determined via a direct comparison of the lattice spacing between the stressed components and their corresponding stress-free combs for a selected reflection planes, the residual stress distributions in the specimens.

4.2.2 Experiments and results

The quenched specimens following thermal heat treatment measured at PSI facility consisted of cylinders *s28* and *s29* with the corresponding stress-free comb specimens *s31* and *s30*, (see Table 4.1). The measurements took place at PSI facility in Switzerland using the stress instrument POLDI. Details of the specimens and process

conditions are provided in Section 3.2. A brief discussion of the measured results is provided here.

Figure 4.29 shows the measured lattice parameter d_0 across the seven fingers on the short-term heat treated comb *s30*. Figure 4.30 shows the measured stress free lattice parameter d_0 across the seven fingers on the long-term thermally aged comb *s31*. Reflection planes 111, 220 and 311 are shown. The average d_0 across the thermally heat-treated comb specimens are very similar: 3.5979Å for comb *s30* and 3.5981Å for comb *s31*. In contrast the average d_0 across the as-quenched comb specimen s9 (Figure 4.4) measured at ISIS is 3.5955Å.

Figure 4.31 shows the residual stress distribution across the equatorial plane of a quenched and short-term (heat treated at 550°C for 1.25 hours) thermally aged cylinder, diameter 30mm, length 30mm (sample *s29*). Figure 4.32 shows the residual stress distribution across the equatorial plane of a quenched and long-term (heat treated at 550°C for 1800 hours) thermally aged cylinder, diameter 30mm, length 30mm (sample *s28*). Note that as mentioned in the preceding section by using the host "StressCalc" data analysis software the stress components were determined directly from the measured raw data. Therefore the strains are not shown here.

These measured residual stresses will be compared with as quenched measured residual stresses in other cylinders and the effects of both short-term and long-term (creep) thermal ageing on the initial quenched residual stresses will be discussed later in Chapter 7.

4.3 Neutron diffraction at NFL

The diffraction method at Studsvik Neutron Research Laboratory (NFL) in Sweden with the residual stress and texture measurement diffractometer REST was used to measure the internal residual strain distribution in the quenched cylinder specimens *s34-s39* during the period 23rd - 27th November 2004 [Hossain et al 2004c]. These were quenched cylinders, diameter 29mm, length 29mm followed by drilling at the central longitudinal axis by using a 1.5mm diameter drill bit and edm pre-trepanned to various depths using a copper electrode of diameter 5mm and thickness 1mm. As shown in Table 4.1 sample *s39* is as-quenched cylinder, *s38* is quenched and drilled cylinder, samples *s34-s37* are quenched cylinders with a 1.5mm hole drilled at the central axis and edm pre-trepanned to various depths ranging from 8.5mm to 28mm, i.e., pre-

trepanned to depths approximately 25%, 50%, 75% and 100% of the total cylinder length. A brief description of the instrument and basic principle of the method is described in the following section followed by description of the experimental measurements and results.

4.3.1 Basic principles

Strain scans were made in the radial, axial and hoop directions across the radial plane of the cylinder. The (*311*) reflection of 316H stainless steel, with a $2\times2\times2mm^3$ gauge volume, was used for the measurements. The stress-free interplanar spacing, d_o, was obtained by studying a comb sample (*s25*) extracted from a quenched sphere of diameter 30mm. The stress-free diffraction spacings were then used together with measurements from the cylinder to obtain the strain distribution.

The principle of the diffraction method is very similar to the well-known X-ray diffraction technique [Yazdi et al 1998] which is widely used to determine the surface residual stress. When a monochromatic neutron beam interacts with a crystalline material, incident neutrons are subject to diffraction at planes of atoms and produce strongly diffracted beams leaving in directions defined by Bragg's law [Holden 1996] through:

$$\lambda = 2d\sin\theta \tag{4.8}$$

where λ, d and θ are defined in Equ. 4.1.

Assuming that λ is constant, the differentiation of Bragg's law (4.8) gives the following relationship:

$$\varepsilon_i = \frac{d_i - d_0}{d_0} = \frac{\sin\theta_0}{\sin\theta_i} - 1 \tag{4.9}$$

These measured strain distributions across the cylinder were used to calculate the corresponding stress distributions using the generalised Hooke's law in Equ. 4.5 and Equ. 4.6.

4.3.2 Instrument

The stress instrument REST at the NFL facility in Sweden is a neutron diffractometer designed and constructed for residual stress and texture analysis in polycrystalline materials. Attributed to a double focusing monochromator of Si 331 and a high resolution position sensitive detector, REST has a high instrument resolution for

2θ ranging from 60° to 110°. The nominal wavelength of neutrons is 1.7 Å which is suitable for strain measurements in many engineering materials. Figure 4.33 shows the set-up for strain scans.

The incident and diffracted beam slit units are mounted on compound guides. This makes repositioning of the slits readily and precisely. Two sets of slits are available: one with adjustable width from 0.1 to 2 mm and another between 0.5 and 3.5 mm. The width is changed via a pre-calibrated micrometer. The beam height can be selected from 0.5 to 40 mm by inserting Cd mask into the slit holder. Neutron beams as large as $50\times50mm^2$ can be obtained by using simple slit units made of Cd masks.

The position sensitive detector is an ODELA 1150N having a $100\times50mm^2$ detection window. It can be positioned 50 to 100 cm from the goniometer centre. The goniometer consists of two Huber tables, one carrying the detector and the other rotating the sample stage which contains a XY and a Z table. Both tables are equipped with rotary optical encoders. The uncertainty in positioning is 0.001°. Three dimensional strain scans can be carried out by moving the sample in the scattering plane via the XY table and out of the scattering plane via the Z table. The sample stage is equipped with VAMAS standard mounting plates. Linear optical encoders on the tables ensure a position accuracy of 10mm for the X and Y axes and 20mm for the Z axis. A small Huber table can be mounted on the sample stage to provide an additional rotation axis for the sample. Using a lifting crane and a cantilever system, samples up to 250kg can be supported on the sample table for strain measurement. The vast space above the sample stage provides possibility for measurement on large components. For example, measurements on a ring of $\phi700\times200mm^2$ and on a pipe of $\phi432\times830mm^2$ had been successfully carried out. For texture pole figure or strain pole figure measurement, two-circle Eulerian cradle will be mounted on XY table to rotate the sample in Euler space.

The instrument is controlled from a PC using a control file or inputs from keyboard. Parameters that can be specified in the control file for measurement are: detector positions, sample directions, sample positions (X, Y, and Z), and beam monitor factor which determine the sampling time at each point. If necessary, an additional movement, such as rotation around a particular sample direction using the spare rotary table, can be made available.

4.3.3 Experiments and results for as-quenched sample

The quenched specimen where the internal residual stresses were measured using the stress instrument REST at the NFL facility consisted of a cylinder, diameter 29mm, length 29mm (sample *s39*).

Strain scans were made in the radial, axial and hoop directions across the radial plane (see Figure 4.2) of the as-quenched cylinder *s39*. The (*311*) reflection of 316H stainless steel, with a $2\times2\times2mm^3$ gauge volume was used for the measurements. The stress-free interplanar spacing d_o was obtained by studying a comb (*s25*) extracted from an as-quenched sphere of diameter 30mm. The Bragg angles measured across the seven fingers on comb *s25* in both radial and hoop orientations shown in Figure 4.34 do not vary substantially. Therefore, an average value of these measured angles was used to determine the strain components. The strain components were calculated from the measured Bragg angles by using Equation 4.9. Strain distributions measured in the quenched cylinder *s39* are shown in Figure 4.35. The distributions are measured across the equatorial plane from the centre of the cylinder bar towards the outer surface. Using Hooke's law (Equation 4.6) and the elastic constants tabulated in Table 3.1 the respective residual stresses were calculated. Figure 4.36 shows the residual stress distribution across the radial plane from centre towards the outer surface of the as-quenched cylinder *s39*.

4.3.4 Experiments and results for pre-trepanned quenched cylinders

The residual strains in the pre-trepanned quenched samples (*s34-s37*) were obtained from the measured Bragg angles in the samples and the average Bragg angle from the stress free comb sample (*s25*) measurement using Equation 4.9 in the same way as described above. Similarly using Hooke's law (Equation 4.6) and the elastic constants listed in Table 3.1 the corresponding stress components were determined. The strain and stress distributions along a number of selected paths in the pre-trepanned quenched cylinders are described here.

Figures 4.37-4.43 show the residual strain and stress distributions in quenched cylinders with variable trepanned depths. The measurement paths in the samples are shown clearly on the figures. The aim of this study is the influence of the edm trepanning on the redistribution of residual stresses.

s34 edm pre-trepan depth 29%

Figure 4.37 shows the distribution of residual strain and stress across a radial plane 12mm below the top surface in a quenched cylinder bar *s34* with 1.5mm diameter drill and 5mm diameter trepanned up to 8.5mm depth. Although the specimen was trepanned up to 8.5mm from the top flat surface, it was not possible to measure the strain and stress along the radial line at the edge of the edm front. This was to prevent part of the sampling volume from falling into the discontinued material space created as a result of the edm trepanning process. Since the sampling volume consisted of $2\times2\times2mm^3$ throughout the measurement programme, a clearance of 2.5 to 3.5mm from the edm front was maintained in general. The distribution of strain and stress along the axial line 6mm away from the centreline is shown in Figure 4.38. By measuring along the path 6mm away from the centreline a clearance of 2.5mm was maintained from the outer edm trepan edge; the edm electrode diameter was 5mm with 1mm thickness.

s35 edm pre-trepan depth 53%

Figure 4.39 shows the measured residual strain and stress distribution in a 15.5mm depth pre-trepanned quenched cylinder *s35* across the radial line 18mm below the top surface. Thus a clearance of 2.5mm from the edm front was maintained during the measurement. Note that in both samples *s34* and *s35* the measurements were made across the radial line by starting from the centre of the specimen. The samples had holes drilled through the centre with a diameter of 1.5mm. Since the sampling volume of the neutron beam was $2\times2\times2mm^3$ part of the gauge volume was therefore present in the material adjacent to the hole edge. This is why the measured strains and stresses at the drilled hole were non-zero as seen in Figures 4.37 and 4.39. The subsequent measurements in the other pre-trepanned samples across the radial line were made at 1.5mm away from the centreline. The measurements along the axial line are shown in Figure 4.40. As may be noticed in the figures measurements were only made near the vicinity of the edm front. The specimen was not scanned along the axial line completely in order to effectively utilise the available beam time on the measurements. By concentrating the measurements near the vicinity of the edm front the influence of trepanning on the initial residual stresses was obtained.

s36 edm pre-trepan depth 74%

Figure 4.41 shows the measured residual strain and stress distribution in the 21.5mm depth pre-trepanned quenched cylinder *s36* across the radial line 24mm below

the top surface (and 2.5mm clear of the edm front). The distributions of measured residual strains and stresses along the axial line 6mm away from the centreline are shown in Figure 4.42. Although the quenched cylinder is an axi-symmetric problem, both the measured strains and measured stresses shown in Figures 4.38 and 4.42 (29% and 74% edm pre-trepan depth respectively) are not a mirror image of one another. That is, the problem is not symmetric about the radial plane across the centre. This is because the drilling and trepanning are both carried out in a single direction and is not symmetric about the radial plane and hence the redistribution of stresses is also not symmetric.

s37 edm pre-trepan depth 97%

Figure 4.43 shows the measured distributions of residual strains and stresses in the 28mm depth pre-trepanned quenched cylinder *s37*. Here only the distribution along the axial line is measured for obvious reason.

Effect of trepanning on stress redistribution

A comparison is made of the measured residual stresses between the samples with various pre-trepan depths to show the influence of edm trepanning on the redistribution of the residual stress distribution. Both sets of pre-trepanned quenched cylinders, i.e., cylinder of diameter 60mm, length 60mm manufactured from 316L SS including samples *s40* and *s42* and cylinder of diameter 29mm, length 29mm manufactured from 316H SS including samples *s34*, *s35*, *s36* and *s37*, are compared. Because of different size and material normalised results were used in the comparison. The measured residual stresses were normalised by the respective yield stress (0.2% proof stress) provided in Table 3.1.

Figure 4.44 shows the comparison of measured residual stress distribution as a radial variation across the radial plane ahead of the edm front. For convenience the radial (Figure 4.44a), axial (Figure 4.44b) and hoop (Figure 4.44c) components of the residual stress are shown separately. Generally the residual stresses were relaxed as a result of edm trepanning. This was particularly true for the radial component. Note that for sample *s36*, i.e., 74% pre-trepan depth, the residual stresses were measured 24mm below the top surface (in other words only 5mm above the bottom surface). Close to the (bottom) surface the residual stress distribution in the as-quenched sample prior to trepanning/drilling is lower than that close to the mid-plane. Therefore a comparison with the 74% pre-trepan depth (sample *s36*) introduces an uncertainty. Similarly sample

s42 (76% pre-trepan depth) also introduces an uncertainty; the measurement line in this case was 11.5mm above the bottom surface as illustrated by Figure 4.21. A comparison between the 26% (sample *s40*), 29% (sample *s34*) and the 53% (sample *s35*) pre-trepan depth revealed that all radial, axial and hoop components of the residual stress were relaxed as a result of the edm trepanning. The level of relaxation was however higher for the radial component.

Figure 4.45 shows the comparison of measured residual stress distribution as an axial variation along the longitudinal path 6mm away from the centreline i.e., 2.5mm clear of the outer edm trepan edge for the smaller cylinders and 8mm away from the centreline for the larger cylinders. Again the radial, axial and hoop components are shown separately. The result showed that the radial component (Figure 4.45a) of the residual stress relaxed considerably due to the edm trepanning. The hoop component (Figure 4.45c) on the other hand generally increased. A slight change was observed in the axial component (Figure 4.45b) as a result of the edm trepanning. Moving down from the top surface along the axial line the axial component first decreased, then increased and finally decreased closer to the bottom surface.

Chapter 5

Mechanical strain relaxation measurement of residual stress

In the preceding chapter residual stress measurement in laboratory specimens containing highly triaxial stress consisting of rapid spray water quench and side punch C(T) specimens using the non destructive neutron diffraction technique at different neutron facilities was described. This chapter describes the residual stress measurement in the specimens using semi-destructive mechanical strain relief methods including the incremental centre hole drilling and the deep-hole drilling techniques.

5.1 Incremental Centre Hole Drilling

The incremental centre hole drilling (ICHD) technique relies on measurement of surface strains when a hole is drilled through the centre of a strain gauge rosette. In the ICHD technique, the hole is drilled incrementally and the relaxed strains measured at each increment. The measured strains are converted to residual stresses using compliance functions that are determined from FE analysis. Further details of the method are explained in [Tech Note TN-503-5 1993] and only the salient features of the method is summarised in the next section.

5.1.1 Basic principles

The introduction of a hole into a residually stressed body relaxes the stresses at that location. This occurs because every perpendicular to a free surface (the hole surface in this case) is necessarily a principal axis on which the shear and normal stresses are zero. The elimination of these stresses on the hole surface changes the stress in the immediate surrounding region causing the local strains on the surface of the test object to change consequently. This principle is the foundation for the hole-drilling method of residual stress measurement, first proposed by [Mather, 1934].

With strain sensors sensibly placed before drilling a hole into the part, the sensors respond to the deformation produced by relaxation of the stress owing to material removal. The initial residual stress can then be inferred from the measured strains by elasticity considerations. The measurement procedure involves six basic steps:

(a) Installing a special three-element strain gauge rosette, e.g., type EA-06-031RE-120, supplied by the Measurements Group on the test part at the point where residual stresses are determined.

(b) Wiring and connecting the three gauge grids to a static strain indicator through a switch-and-balance unit.

(c) Attaching a precision milling guide of the RS-200 model to the test part and accurately centring it over a drilling target on the rosette.

(d) Drilling a small, shallow hole through the centre of the rosette in increments of small depths, e.g., 0.05mm, after zero-balancing the gauge circuits.

(e) Taking readings of the relaxed strains at the end of each increment, corresponding to the initial residual stress.

(f) Using special data-reduction relationships to calculate the principal residual stresses and their angular orientations from the measured strains.

From the relaxed strains the residual stresses were calculated using the integral method [Schajer 1998]. In this method, the relaxed strain on the surface along the generic x-direction, at a hole of depth h, is related to the residual stresses by the following,

$$\varepsilon_x(h)=\frac{1}{2E}\int\{(1+\nu)\hat{A}(h,H)[\sigma_x(H)+\sigma_y(H)]+\hat{B}(h,H)[\sigma_x(H)-\sigma_y(H)]\}dH \qquad (5.1)$$

where $\sigma_x(H)$ and $\sigma_y(H)$ are the residual stress distributions along the generic orthogonal x and y directions, and $\hat{A}$ and $\hat{B}$ are the influence functions determined by numerical methods [Schajer 1998]. Similar expression holds along the y-direction. This leads to an inverse problem in which the unknown stress distributions $\sigma_x(H)$ and $\sigma_y(H)$ are determined numerically by dividing the maximum hole depth into N intervals and approximating the stresses in each interval with appropriate stress distributions. The cumulative influence function values were derived numerically by Schajer [1998] for the calculation of the required influence coefficients. An 8^{th} degree polynomial was fitted to the cumulative influence functions following a procedure proposed by Zuccarello [1999].

5.1.2 Experiments and results for quenched samples

The incremental centre hole drilling (ICHD) method was used to measure the near surface residual stresses in a number of selected quenched samples, including a sphere, diameter 30mm (*s8*), and cylinders, diameter 60mm, length 60mm (*s12*), and diameter

30mm, length 100mm (*s1*). Table 3.3 summarises the quenched specimens with a brief note on the method used on the specimens for the residual stress measurement.

In order to use the ICHD technique on the sphere *s8*, strain gauge rosettes with an external diameter 2.56 mm, corresponding to Type EA-06-031RE-120, were used. A strain gauge rosette was installed on the equatorial plane of the sphere. Incremental hole drilling was carried out using a type RS-200 precision milling guide. The hole was drilled in increments of 0.05 mm as described above, and the relaxed strain of each gauge of the rosette measured. The measured, relaxed strains are shown in Figure 5.1. The corresponding calculated residual stresses are shown in Figure 5.2. As expected, the residual stresses were compressive along the outer surface of the quenched sphere. The average axial surface residual stress was approximately -350 MPa and the average hoop stress approximately -400 MPa. The shear stress was essentially zero.

Note that the application of the ICHD method on a sphere with double curvature without any further modification to the method is likely to give rise to error in the results as pointed out by Cherouat et al [2002]. Cherouat et al showed the error to lie in the range 7 to 20% for the case with double curvature.

A similar procedure was followed in the surface residual stress measurement of the remaining specimens. The only difference was that a larger strain rosette was used since the cylinders had only a single curvature and a bigger rosette could be mounted quite easily on to the surface of the cylinder samples. Thus, strain gauge rosettes with an external diameter of 5.13 mm, corresponding to type CEA-06-062UL-120, were used on the quenched cylinders. The measured surface residual strain distributions are shown in Figures 5.3 and 5.5 for quenched cylinders *s12* and *s1*, respectively. The corresponding surface residual stress fields are shown in Figures 5.4 and 5.6. The in plane axial, the hoop and the shear components of the stress are shown in the figures. As expected, the axial and hoop stresses in general were of similar magnitude corresponding to equi-biaxial compression on the outer surface of the quenched parts. The shear stress was practically zero.

5.2 Deep hole drilling

Two rapid spray water quenched cylinders, diameter 60mm, length 60mm manufactured from type 316L SS (sample *s2*) and type 321 SS (sample *s12*) were studied in the deep hole drilling measurement programme. The basic principle of the

measurement method is described below followed by the experimental measurement and result for the quenched cylinders.

5.2.1 Basic principles

The deep hole (DH) method determines the through-thickness residual stress distribution in a component by measuring the change in diameter of a reference hole that occurs when a core of material is removed from the component by trepanning. A schematic illustration of the DH method is shown in Figure 5.7. The steps (i-iv) in the DH method are as follows [Smith et al 2000]:

i. A reference through hole is gun-drilled through the component.
ii. Accurate measurements of the initial reference hole diameter are taken at a number of angles around the reference hole axis θ and at several increments of depth z, giving $d(\theta, z)$.
iii. A core of material containing the reference hole is trepanned free of the rest of the component using a plunge electric discharge machine. The trepanned cylindrical core is macroscopically "stress-free".
iv. After core removal, the reference hole diameter is re-measured in the same manner as before, giving $d'(\theta, z)$.

The changes in diameter of the reference hole are used to calculate the through-thickness distribution of residual stress in the component. Changes in the axial dimension of the column may also be measured during the trepanning to obtain the axial strains. Details of the method may be found in [Bonner 1996, George et al 2002] and only the main features are described here. The experimentally measured changes in reference hole diameter are converted into strains by normalising them with the reference hole diameter measured before core removal. The change in the reference hole diameter is calculated according to

$$\Delta d(\theta,z) = d'(\theta,z) - d(\theta,z) \tag{5.2}$$

where d and d' are the reference hole diameters before and after trepanning respectively, and are each functions of the angular orientation around the hole, θ, and the depth through the core thickness, z. The changes in reference hole diameter are then converted to strain using

$$\tilde{\varepsilon}(\theta,z) = \frac{\Delta d(\theta,z)}{d(\theta,z)} \tag{5.3}$$

The reference hole strains are related to the residual stress components, $\sigma_{xx}(z)$, $\sigma_{yy}(z)$ and $\sigma_{xy}(z)$ in the plane normal to the reference hole axis, through simple elastic considerations. The analysis is based on deformations occurring at a hole in a finite-thickness planar-infinite plate subjected to remote planar stress components assumed constant through the plate thickness [Bonner 1996]. The reference hole strain that would occur for the given applied remote stress is given by

$$\tilde{\varepsilon}(\theta,z)=\frac{f(\theta,z)\sigma_{xx}+g(\theta,z)\sigma_{yy}+h(\theta,z)\sigma_{xy}}{E} \tag{5.4}$$

where the functions f, g and h were given by Garcia Granada et al [1998] as

$$f(\theta,z)=A(z)[1+B(z)2\cos(2\theta)] \tag{5.5}$$

$$g(\theta,z)=A(z)[1-B(z)2\cos(2\theta)] \tag{5.6}$$

$$h(\theta,z)=4A(z)B(z)\sin(2\theta) \tag{5.7}$$

$A(z)$ represents a measure of the uniform expansion of the reference hole and $B(z)$ the eccentricity of the reference hole.

To find residual stresses that vary with depth, it is assumed that the trepanned core is composed of a stack of annular slices, which act independently of one another behaving in a manner predicted by the constant remote stress analysis [Bonner 1996].

A through-thickness residual stress distribution is calculated from measured reference hole strains through the use of a compliance matrix. Since the trepanned core is assumed to be composed of a stack of independent annular slices, stresses at a given depth are found independently from those at other depths. Reference hole strain is measured at a set of n depths $z=\{z_1, z_2, \ldots, z_n\}$ and a set of m angles $\theta=\{\theta_1, \theta_2, \ldots, \theta_m\}$, where $m \geq 3$. At each depth z_i, the measured strains are assembled into a vector of m components

$$\{\tilde{\varepsilon}(z_i)\}=[\tilde{\varepsilon}(\theta_1,z_i),\tilde{\varepsilon}(\theta_2,z_i),\ldots,\tilde{\varepsilon}(\theta_m,z_i)]^T \tag{5.8}$$

The strain vector is then related to a vector of unknown stress components

$$\{\sigma(z_i)\}=[\sigma_{xx}(z_i),\sigma_{yy}(z_i),\sigma_{xy}(z_i)]^T \tag{5.9}$$

through

$$\{\tilde{\varepsilon}(z_i)\}=-[M(z_i)]\{\sigma(z_i)\} \tag{5.10}$$

where the elements of the matrix $[M(z_i)]$ are derived from equations (Eq. 5.4) to (Eq. 5.7) and are given by

$$[M(z_i)] = \frac{1}{E}\begin{bmatrix} f(\theta_1, z_i) & g(\theta_1, z_i) & h(\theta_1, z_i) \\ \vdots & \vdots & \vdots \\ f(\theta_m, z_i) & g(\theta_m, z_i) & h(\theta_m, z_i) \end{bmatrix} \tag{5.11}$$

Finally, the unknown stress components $\{\sigma(z_i)\}$ are calculated from the measured reference hole strains using least squares:

$$\{\sigma(z_i)\} = -\left\{[M(z_i)]^T [M(z_i)]\right\}^{-1} [M(z_i)]^T \{\tilde{\varepsilon}(z_i)\} \tag{5.12}$$

5.2.2 Application to quenched cylinders

Rapid spray water quenching of stainless steel cylinders and spheres meets the objective of acquiring the residual stress field with high triaxiality in a well-controlled manner [Hossain et al 2004]. Finite element (FE) analyses carried out in Section 3.1 demonstrated that high levels of tensile triaxiality could be generated in both cylinders and spheres. For reasons explained in Section 3.1, mainly von Mises equivalent stress near the centre of sphere being zero, only cylinders were considered in the creep study. The optimum cylinder, diameter 60mm, length 60mm was then selected.

A programme of residual stress measurements similar to the previous cases was conducted in order to verify the numerically predicted residual stress distributions in the quenched specimens. This will be discussed in Chapter 7. This section describes the quenched cylinders, implementing the deep hole drilling residual stress measurement technique and the results obtained.

Residual stresses were measured using the deep hole technique in two quenched stainless steel cylinders of diameter 60mm and length 60mm (*s2*, *s12*). The samples were rapid-spray water-quenched from a preheated temperature of 850°C to an ambient room temperature about 20°C. Measurements were made along the longitudinal axes of the quenched cylinders to determine the thorough-thickness residual stresses along the axis of the cylindrical bars. The measured residual stress distributions are shown in Figure 5.8. Only the radial, hoop and shear components of the residual stresses were measured. The error due to air probe measurements shown by Kingston [2004] is:

$$\delta\sigma_{xx} = -\tfrac{1}{2} E \delta d_{err} / d_0 \tag{5.13}$$

where $\delta\sigma_{xx}$ is the calculated error in residual stress, δd_{err} is the deformation error, d_0 is the original reference hole diameter (3.18mm) and E is the Young's modulus. From

previous calibration experiments George [2000] found the deformation of the reference hole to be accurate within ±0.5μm.

Therefore for E=195.6 GPa, δd_{err}=±1μm (due to the compounded error in the diameter measurements from both before and after EDM trepanning) and d_0=3.18mm, the error in the measured stresses $\delta\sigma_{xx}$=±30MPa.

As expected both ends (outer surfaces) of the cylinder are in compression. Moving inwards into the specimen away from the outer (front) surface, the stresses change to tensile at about 8mm and peak at about 15mm. Thereafter, the measured stresses begin to decrease, falling to zero about 32mm into the specimen, becoming compressive (about -75MPa) at 40mm before rising to zero at 47mm and then decreasing again to compressive close to the other end of the cylinders. Shear stresses were essentially zero.

From our previous FE simulations on quenched cylinders (Section 3.1), we know that there is a tensile triaxial region about 50% of the length in the middle section of the quenched cylinder bar specimen. Note that in the current research study, an extensive residual stress measurement programme has been conducted using the well-established non-destructive neutron diffraction (ND) techniques at various neutron sites using rapid spray water quenched stainless steel specimens of a variety of sizes and shapes in order to verify and validate the use of the selected heat transfer boundary conditions, material definitions and assumptions made in our finite element studies to predict the residual stresses. This is discussed in Chapter 7.

The agreement between the DHD measured and the expected residual stress distribution in a quenched cylinder, a component with high triaxiality is very poor. The DHD method used in the residual stress measurement only obtains quenched residual stresses in a limited region close to the outer surfaces of the specimens. Both cylinders showed a very similar stress distribution. Only a slight difference was present due to the differences in the yield data (see Figure 3.2).

A FE predicted residual stress distribution along the longitudinal axis of the cylinders is shown in Figure 3.6. The deep hole measured residual stresses shown in Figure 5.8 clearly demonstrate that a simple elastic approach in the deep hole drilling method should be used with care when analysing residual stresses of a highly triaxial nature and also close to yield. In the case when the residual stresses are close to yield and are highly triaxial, there is an effect of the deep hole drilling process on the initial residual stress distribution as shown from discrepancies between Figures 3.6 and 5.8. In

order to observe the effect of the deep hole drilling process on initial residual stress state in a quenched cylinder, a finite element model was used to simulate the deep hole drilling process. This is discussed in Chapter 6.

An accurate characterisation of residual stress fields in safety related component is vital in the structural integrity assessment. A recently modified and developed deep hole drilling method [Smith et al 2000] has been used frequently in the residual stress measurement of safety critical components particularly for thick components. Therefore, the influences of plasticity and residual stress redistribution during residual stress measurement using the deep hole drilling method are significant. Chapter 6 attempts to address this issue by considering simple and elementary test cases.

Chapter 6

Deep hole drilling developments

The previous two chapters presented the measured results of residual stress distributions in specimens with high triaxiality. Both quenched and side-punched specimens were studied. Chapter 4 presents results of measurements by using neutron diffraction method at various neutron facilities. Chapter 5 presents results of measurements using the mechanical strain relief including the incremental centre hole drilling and the deep hole drilling techniques. It was noticed that the neutron diffraction measured results were in line with those predicted by the finite element simulation discussed in Chapter 3. A more detailed comparison made between the measurement and prediction is discussed in Chapter 7.

The distribution of residual stress measured in the quenched cylinders by using the deep hole drilling technique however did not match with those predicted by the FE. This is noticed upon comparing the deep hole measured residual stress distribution shown in Figure 5.8 with the FE predicted shown in Figure 3.6. The deep hole measured result failed to pick up the FE predicted peak residual stresses towards the central core of the quenched cylinders. The elastic assumption used in the deep hole drilling method of residual stress measurement therefore needs to be used with particular care for high triaxiality cases such as the quenched samples. Practical components with high triaxiality include welded pipes with repair welds where the deep hole drilling method is often used to measure the internal residual stress distribution.

This chapter focuses on the finite element simulation study of the deep hole drilling technique with elasto-plastic material response. The effect of the measurement technique on the existing initial residual stress field is highlighted. At first a rectangular block under simple loading cases was considered in the elasto-plastic deep hole drilling simulation study. Later two example specimens were used in the study including two quenched cylinders and a welded pipe with a repair weld. These are described in the subsequent sections with a description of the preliminary results. The complexity of the problem associated with elasto-plastic redistribution of the residual stresses is

highlighted. A detailed finite element study was undertaken to investigate the influence of stress triaxiality on the deep hole measurement.

6.1 Elasto-plastic simulations for simple load cases

The focus of this section is on a finite element (FE) study to simulate the deep-hole drilling (DHD) measurement process. The primary aim of the deep-hole simulation was to determine a validity zone in the application of deep-hole technique under conditions of variable triaxiality. This was carried out by subjecting a three-dimensional prismatic block of material of varying dimensions to a triaxial stress state whose magnitude can be adjusted. The deep-hole drilling was simulated on the block and a systematic variation of the dimensions of the block and the magnitude of the applied stress permitted a "zone of validity" of the deep-hole technique to be established in terms of the applied stress normalised by the effective stress, σ/σ_e, and the triaxiality factor, σ_h/σ_e.

6.1.1 Validity zone of deep-hole technique under high triaxiality

George et al [2002] demonstrated that stresses arising from external applied loading could be measured. In their paper, George et al presented a series of calibration studies using aluminium and steel samples, with thickness varying from 5 to 50 mm. The samples were subjected to tension, bending and torsion. They showed that the deep-hole method could measure linear and non-linear stress distributions. In the present section a three-dimensional block of material was subjected to a combination of varying stress state as shown in Figure 6.1. By changing the applied stresses, four cases of triaxiality factors were investigated.

a) Uniaxial case with triaxiality factor, $(TF) = 0.333$

b) Biaxial case with $TF = 0.6$

c) Triaxial case with $TF = 1.0$

d) Triaxial case with $TF = 0.5$

The applied stresses were adjusted in a way such that the x-component stress, σ_x (see Figure 6.1) was always the maximum principal stress, σ_1. Initially, a block of width 60mm, height 60mm and thickness 15mm was considered for the study. Due to symmetry, a ¼ model was considered in the finite element simulation of the block.

Figure 6.2 shows the FE model used with 5400 quadratic elements in the FE mesh. Also highlighted in the figure are the drilling and trepanning regions for the deep-hole drilling simulation.

6.1.2 Stress triaxiality

The triaxiality factor is defined by the ratio of the hydrostatic stress, σ_h to the von Mises equivalent stress, σ_e. The maximum principal stress in terms of the applied stress and stress triaxiality factor is defined by the following relation by re-arranging the definitions of *TF*.

$$\frac{\sigma_1}{\sigma_e} = \frac{3\sigma_x}{\sigma_x + \sigma_y + \sigma_z}.TF \tag{6.1}$$

The triaxiality factor for the uniaxial case is ⅓ whilst for biaxial and triaxial cases, the magnitude of applied stresses σ_x, σ_y and σ_z were selected in a way such that σ_x was always the principal stress component and a triaxiality factor (*TF*) of 0.6 for the biaxial case and *TF* of 1.0 and 0.5 for the triaxial case was used. Thus, the corresponding maximum principal stresses are given as follows:

Uniaxial: $$\frac{\sigma_1}{\sigma_e} = \frac{3\sigma_x}{\sigma_x}.\frac{1}{3} = 1 \tag{6.2}$$

Biaxial: $$\frac{\sigma_1}{\sigma_e} = \frac{3\sigma_x}{\sigma_x + \sigma_y}.0.6 = \frac{1.8\sigma_x}{\sigma_x + \sigma_y} = 1.15 \tag{6.3}$$

Triaxial: $$\frac{\sigma_1}{\sigma_e} = \frac{3\sigma_x}{\sigma_x + \sigma_y + \sigma_z}TF\ ,\ (TF = 1.0 \text{ and } 0.5) \tag{6.4}$$

For the biaxial case, the ratio $\sigma_x/(\sigma_x + \sigma_y)$ is constant at a value of 0.64 for a triaxiality factor (*TF*) of 0.6, giving a principal stress ratio σ_1/σ_e of 1.15. Therefore, under uniaxial and biaxial loading cases the principal stress ratios are constant for the triaxiality factors given above. In contrast, under the triaxial loading cases variable principal stress ratios are obtained (Equation 6.4). In the next section results are presented for a 3D block under different loading conditions and the effect of deep-hole simulation on the applied load is discussed.

6.1.3 Effect of deep-hole simulation

A total of 25 different loading cases were considered in the deep-hole validity zone study. The aim of this study was to find a zone defined in terms of applied load and triaxiality where the deep-hole drilling was valid. The loads were applied under a constant triaxiality factor for all uniaxial, biaxial and triaxial cases, with the *x*-component of the applied stress being the principal or one of the maximum principal stresses. Table 6.1 summarises the applied loading conditions. For this analysis 316H stainless steel material properties shown in Figure 3.2(a) were used. Figures 6.3 to 6.6 show the through-thickness applied and deep-hole reconstructed stresses (termed "measured" stresses) for the uniaxial, biaxial and triaxial loading cases. Under each loading case, only one pair of results is shown corresponding to the following: the loading case that reconstructs the deep-hole simulated result with the initial applied loads and the case that deviates from the original applied load, respectively. It can be seen that under each class of loading, i.e., the uniaxial with TF=0.33, biaxial with TF=0.6, and triaxial with TF=1.0 and 0.5, the deep-hole "measured" stress diverge from the initial applied loads with an increase in the principal applied stress. The "measured" stress provided in Table 6.1 is obtained by taking an average of the stress distributed over the entire deep hole through thickness.

From the applied and the "measured" results the triaxiality factor and the principal stress are obtained for both applied and "measured" stresses. These results are summarised in Table 6.2. By comparing "measured" principal stress with the applied in both Tables 6.1 and 6.2 show the loading cases where the deep-hole method breaks down corresponding to major deviation of the "measured" from the applied stress. Figure 6.7 shows the "measured" principal stress component normalised by the yield stress plotted against the applied equivalent stress component normalised by the yield stress. Under each loading class it is the linear part of the graph where the deep hole reconstructed stress closely matches with the applied stress. Moving away from linearity the deep hole drilling breaks down. Figure 6.8 summarises the "measured" principal stress normalised by yield stress plotted against the applied principal stress normalised by yield stress. The "measured" residual stress under each loading class compare very well with the applied stress for lower applied stress. Generally for the applied normalised stress, σ_1/σ_Y less than about 0.6 the deep hole drilling works well.

Figure 6.9 compares the "measured" principal stress normalised by the equivalent stress with the applied equivalent stress normalised by the yield stress. From Equations 6.2 and 6.3 the maximum principal stress normalised by the equivalent stress for the uniaxial and the biaxial loading case are 1.0 and 1.15 respectively. Figure 6.9 shows the effect of increasing the applied load on the "measured" principal stress: the "measured" principal stress component diverges from the maximum applied principal stress component. This is clear for the uniaxial and biaxial cases where the maximum applied principal stress components are also shown by horizontal lines.

6.1.4 Summary and discussion

This is an ongoing finite element simulation work to establish a "zone of validity" of the deep-hole technique in terms of the applied stress and triaxiality factor (*TF*). The results obtained to date cannot be used to draw any conclusion. More work is needed before establishing a relation between the triaxiality factor and the zone of validity. The effect of the size of the block will be considered by carrying out the same finite element analyses on the 3D block with the same order of applied loadings but of various dimensions as future consideration. Nevertheless it was shown that generally the deep hole reconstructed stress started to diverge from the applied stress on increasing the applied load. Secondly it was noticed that the reduction of the "measured" principal stress was highest under the uniaxial loading case than the biaxial case. Under triaxiality factor of 1.0 the reduction was minimum. This observation may be attributed to the stress concentration. Note that in the present study a primary stress was applied. That is, applied rather than residual stress was used for the initial loading condition. When the hole is drilled in the FE simulation the cutting process induces and increases the stress concentration closer to the hole edge. This effect is highest for the uniaxial case. This is why the reconstructed stress seemed to diverge from the applied stress.

6.2 Simulation for quenched specimens

The quenched samples where deep hole drilling technique was used to measure the residual stress distribution consisted of two stainless steel types 321 and 316L rapid-spray water-quenched cylinders of diameter 60mm and length 60mm corresponding to samples *s12* and *s2*, respectively. The specimens and the measured stress distributions were described in Section 5.2. It was realised that the deep hole measured residual stress distribution did not follow the FE predicted residual stress distribution.

Therefore, the focus in this section is on the simulation of the deep-hole drilling technique and the subsequent effects on the initial quenched residual stress field. The sub-section below describes the finite element procedure of the deep-hole drilling simulation followed by initial results and discussion.

6.2.1 Deep hole drilling simulation

Figure 6.10 shows the axi-symmetric model used to simulate the deep hole (DH) drilling process in a quenched cylinder. The drilling steps in the DH method were modelled by removing a set of elements defining the drilling region. Likewise, the electro-discharge machining (EDM) trepanning steps were modelled by removing a set of elements defining the trepanned region. This is physically equivalent to removal of material from the specimen of the same thickness as the electrode used to electro-discharge the specimen during trepanning. The trepanning process was carried out in twenty steps in the DH FE analysis. The multi-step trepanning simulates the physical EDM process. In contrast, no difference exists in the results between drilling in single and multiple steps. Hence, the drilling step was carried out in a single step to save computation time.

From the nodal displacements along the edge of the drilling section A'B' (Figure 6.10) distortions of the hole diameters are obtained after drilling (before trepanning) and after trepanning. The difference in measured diameters before and after trepanning provides the radial strains using Equation 5.3:

$$\varepsilon_x^i = \frac{x_2^i - x_1^i}{x_1^i}, \tag{6.5}$$

where, i is the node number

x_1 is the radius of the reference hole before trepanning

x_2 is the radius of the reference hole after trepanning

The reference hole radius before and after trepanning, x_1 and x_2, respectively are calculated from the initial positions and the displacements of the nodes at the end of the run of the EDM model.

The in-plane residual stresses are then calculated from these strains by using (Equation 5.12).

6.2.2 Result and discussion

The radial strains in Equation 6.5 are then converted into stresses by using a pseudo-inverse matrix as shown by Equation 5.12.

$$\sigma = M^* \varepsilon^T \tag{6.6}$$

where the pseudo-inverse matrix is given by

$$M^* = (M^T M)^{-1} M^T \tag{6.7}$$

where

$$[M] = [1+2\cos 2\theta \qquad 1-2\cos 2\theta \qquad -4\sin 2\theta] \tag{6.8}$$

and for eighteen-angle formulation (m=18 in Equation 5.11) θ is 10°, 20°, 30°, ... 180°.

Due to the axi-symmetric nature of the present problem, the coefficients of the pseudo-inverse matrix in Equation 6.7 are added together and the sum, rather than 18 coefficients for each angle, used to determine the residual stresses from the strains using Equation 6.6. The effect of DH simulation on the initial quenched residual stress state in two stainless steel cylinders of type 321 and 316L, respectively, is shown in Figures 6.11 (a) and (b). Also shown are the deep hole drilling (DHD) measured residual stresses and the FE predicted initial quenched residual stresses. A good correlation, particularly in trend, exists between the DHD measured residual stresses and the predicted DH FE residual stresses (i.e., the application of deep-hole simulation on the initial quenched residual stress distributions). Both the measured and the predicted residual stresses highlighted the potential problem taking an essentially elastic approach. This is particularly relevant in cases with a highly triaxial residual stress field and the principal stress component close to yield value. The initial FE predicted residual stress component in the quenched cylinder was about 300-350 MPa. The 0.2% proof stress at room temperature was about 205MPa and 245.5MPa for stainless steel of types 321 and 316L, respectively. It was shown in the FE analysis of simple block in Section 6.1.3 that for a loading case where the normalised applied stress σ_1/σ_Y exceeded about 0.6 the deep hole method breaks down (see Figure 6.8).

DHD measurements were used to measure the through-thickness residual stress distribution of two rapid-spray water-quenched stainless steel cylindrical bars (see Section 5.2.2). The purpose of the experiments was to assess the capability of measuring highly triaxial stresses using the DHD method. From the measurements of highly triaxial quenched specimens, it was seen that the DHD method only obtained the residual stresses in a limited region close to the outer surfaces of the specimen (see

Figure 6.11). In these regions the mechanical relaxation of the residual stress occurred within the 3D yield surface. However, when the DHD method penetrated into a region where there is redistribution, i.e., elasto-plastic redistribution of the residual stresses due to the creation of free surface the DHD method with simple elastic approach breaks down. The DHD method measures the redistributed stress instead of the initial residual stress. Also the "measured" peak residual stress is close to the room temperature yield stress. The problem lies with the effective residual stress being greater than the yield stress, $\sigma_e > \sigma_y$.

The purpose of the present FE simulation of the DHD method was to verify this effect. These results highlight a fundamental problem: under certain conditions namely high triaxiality and effective stress greater than yield stress, the deep hole method does not measure the initial residual stress field. In the cases considered here, plastic redistribution because of the presence of the trepan leads to residual stress relaxation. Figure 6.12 shows the equivalent plastic strain distribution along the edge of the drilled region A'B' (see Figure 6.10 for illustration of the path A'B') under three situations: before drilling, after drilling and after trepanning. The equivalent plastic strain distribution increases after drilling. But more importantly the equivalent plastic strain distribution further increases as a result of trepanning. The simple elastic analysis approach of the present method therefore does not account for any further plastic strain and hence the deviation from the initial quenched residual stresses as shown in Figure 6.11. It can clearly be seen that the regions where the deep-hole breaks down (i.e. 18mm and 52mm from the front surface into the specimen) are where these plastic effects are present. For the length of the quenched cylinder between 18mm and 52mm from the outer (front) surface the equivalent plastic strain distribution after trepanning shown in Figure 6.12 deviates and increases further from that after drilling. For the same length the DH FE residual stress distribution also deviates from the initial FE predicted residual stress distribution as shown in Figure 6.11. In order to validate the above arguments a further FE study was conducted using a very low level of initial residual stress state compared to the one here and in Section 5.2.

By controlling cooling conditions and changing the dimensions of quenching components, differing levels of triaxial residual stress states can be achieved in a controlled manner [Hossain et al 2003a, 2004]. Thus, by lowering the heat transfer coefficient, h substantially (h=400 W/m^2 K) in the heat transfer analysis a relatively low triaxial stress state was simulated in the thermal stress analysis. This heat transfer

coefficient corresponds to a very slow quenching process such as air-cooling. Figure 6.13 shows the initial predicted residual stress distribution for this heat transfer coefficient value with kinematic hardening model and material properties for 316L stainless steel. Also shown are the reconstructed deep hole simulated residual stresses. A very good correlation exists between the two. Figure 6.14 shows the plastic strain distributions before drilling, before trepanning and after trepanning along A'B' for different heat transfer coefficients, corresponding to high and low initial residual stress levels. Clearly for the case with low *h*, the equivalent plastic strains were essentially zero (the initial residual stresses shown in Figure 6.13 were well below yield), particularly the equivalent plastic strain distribution after drilling and after trepanning were not any different from each other and hence a good correlation between the initial and DH FE predicted residual stress distributions as shown in Figure 6.13, i.e., least effect of deep hole drilling on the initial residual stresses.

A simple loading case was considered in Section 6.1 in order to understand from first principles what happens for a simple loading case before attempting a more complex 3D quench residual stress state. Furthermore, Sections 4.1.4 and 4.3.4 provided useful residual stress measurements using the neutron diffraction (ND) technique in quenched specimens consisting of a series of similar cylindrical bars which were pre-drilled and pre-trepanned in order to provide a full understanding of the redistribution of residual stresses caused by the EDM process. These results are also used to verify and validate the predicted redistribution of the residual stresses in the DH FE models in Section 7.2.

The deep hole drilling technique has been commonly used in the recent years to measure the through thickness residual stress distribution in practical components [Smith and Bonner 1996, Smith et al 2000, George et al 2000, George et al 2002]. A welded component particularly with repair weld is practical example of specimen with potentially high triaxial residual stresses. In the present study a finite element simulation was carried out to investigate the influence of the deep hole drilling process on the initial residual stress in a repair weld mock up specimen. The welded component and the simulation are described in Section 6.3.

6.3 Simulation of the deep hole drilling process on repair weld

A 3D block-dumped [Elcoate et al 2004] finite element analysis was undertaken by British Energy Generation Limited (BEGL) and Frazer Nash Consultancy (FNC) to

model both girth and repair weld in the welded pipe with repair weld. The arrangement of the stainless steel pipe girth weld and the set-up of butt-weld and offset repair weld with bead sequence and the positions of deep-hole measurements made are shown in Figures 6.44-6.47. Further details are discussed in Section 6.4.2. The residual stress field from the block-dumped model was mapped onto a further model developed at the University of Bristol by the author which incorporated the deep-hole (DH) drilling steps to investigate the effect of the DH drilling on the mock-up initial residual stress field predicted by FE. Before mapping the residual stresses from the block-dumped model onto the mock-up model with the DH simulation, a benchmark exercise was carried out using the mock-up model under autofrettage loading to verify and validate the 35mm repair welded pipe model in the finite element study. The autofrettage loading consisted of applying an internal pressure of sufficient intensity to in-elastically deform the pipe to some distance into the wall from the inner surface followed by the removal of the applied pressure upon which residual stress distribution remained in the pipe. These are summarised below.

6.3.1 Validation of 35mm repair weld pipe

A finite element study was carried out to model a pipe containing an initial residual stress field. The initial residual stress was introduced into the entire specimen by autofrettage method [Boresi et al 1993]. By simulating the DH process, the effect of DH process on the initial residual stress state in the component was shown. The reconstructed residual stresses were found to be close to the initial applied autofrettage residual stresses. This illustrated the DH simulation to be working.

FE model of 35mm offset repair weld

A 3D FE model was constructed to simulate the DH measurements and illustrate its effect on the initial residual stress distribution in a 316H stainless steel girth weld cylinder containing an offset repair weld [Smith and Hossain 2003]. Due to two symmetry planes (*X-Y* and *Y-Z*) only one quarter of the specimen was modelled as shown in Figure 6.15.

Initially a simple pipe without any welding was modelled (Figure 6.15) with appropriate boundary conditions (as in Figure 6.20). The pipe was elasto-plastically loaded with an internal pressure of 50 MPa, and 117.9 MPa on the free ends to simulate the closed pipe condition. By elastically releasing these applied loads, the pipe was

autofrettaged. Figure 6.16 shows the through-thickness stress distributions predicted by FE through the pipe from the inner surface. The elastic stresses were obtained from an elastic analysis. Also shown, are the analytical results for both plastic and elastic cases. These distributions were obtained from the following relations [Boresi et al 1993].

Plastic:

$$\sigma_r = -\frac{2\sigma_Y}{\sqrt{3}} \ln \frac{b}{r} \tag{6.9}$$

$$\sigma_\theta = \frac{2\sigma_Y}{\sqrt{3}} \left(1 - \ln \frac{b}{r}\right) \tag{6.10}$$

$$\sigma_z = \frac{\sigma_r + \sigma_\theta}{2} \tag{6.11}$$

Elastic:

$$\sigma_r = \frac{a^2 p_i}{b^2 - a^2} \left(1 - \frac{b^2}{r^2}\right) \tag{6.12}$$

$$\sigma_\theta = \frac{a^2 p_i}{b^2 - a^2} \left(1 + \frac{b^2}{r^2}\right) \tag{6.13}$$

$$\sigma_z = \frac{a^2 p_i}{b^2 - a^2} \tag{6.14}$$

where σ_r, σ_θ, σ_z are the radial, hoop and axial component of residual stress; a is the internal radius, b is the external radius and r is the distance from the centre of the pipe, and p_i is the internal applied pressure.

An excellent agreement exists between the finite element simulation and the theoretical results shown in Figure 6.16. Figure 6.17 shows the predicted FE and analytical distribution of residual stresses for the autofrettage process. The analytical result was obtained by the superposition of the plastic distribution onto the elastic one. The good correlation between the FE and the analytical results shown in Figures 6.16 and 6.17 validates the use of appropriate boundary conditions in the FE model of the pipe.

Figure 6.18 shows the outer and inner surface of the pipe model with welding. Figure 6.19 illustrates the three regions with three different material properties – parent material, repair weld and girth weld. Note that these welded regions are simplified in the

model from the original geometry (shown on top right corner of Figure 6.19). Boundary conditions (BC) consist of two symmetry planes and a "prescribed displacement" BC (Figure 6.20).

A structured 3-D mesh with 14330 quadratic brick elements was used to model ¼ of the pipe. The mesh is shown in Figure 6.21, illustrating the fine mesh of the welded region near the centre of the pipe and coarse mesh away from the welded region. Also shown are the detailed through-thickness mesh for the welded part and the close-up of the mesh illustrating the deep hole simulation parts. Figure 6.22 shows a detailed mesh of the welded region 90° away from the deep hole simulation parts. The drilling and trepanning regions are shown in Figure 6.23. Figure 6.24 illustrates the additional nodal boundary conditions required during the deep hole simulation in the pipe axial (2-direction). Note that directions 1, 2 and 3 are the same as x, y and z which are respectively the hoop, axial and normal with reference to the pipe and the longitudinal, transverse and normal with reference to the weld (Figures 6.15 and 6.18). The two nodes shown by the arrows in Figure 6.24 are fixed in the 2-direction on the outer and inner surfaces. This boundary condition prevents the core from rotation. The second additional boundary condition required during the deep-hole simulation is the inner surface of the core being fixed in the normal (3-direction) as shown in Figure 6.25. This boundary condition represents the back bush in practice [Bonner 1996, George et al 2002]. The inner surface of the core is restricted from any relative movement in practice by gluing this surface with the back bush. The deep hole simulation was carried out by the subsequent removal of elements representing the drill region and the trepan region. While drilling was carried out in a single step the trepanning process was carried out in 6 steps. This is illustrated in Figure 6.26 which shows the drill part and alternate trepan parts. Due to the complexity of the welded mesh illustrated by Figures 6.21 and 6.22, the width of trepan parts are not uniform and span from about 5 to 6mm.

Pipe under autofrettage

The pipe was loaded with an initial internal pressure of 50 MPa. The axial loads at the two free ends to simulate the end cap conditions were calculated to be 117.9 MPa. For the present analysis material properties of type 316H stainless steel were used.

Figure 6.27 shows the stress distribution through the specimen for these initial applied loads. As expected the hoop stress was maximum. Both the hoop and the axial components were tensile. The through-thickness component was zero at the outer (front)

surface and compressive towards the inner surface. The applied loads were then unloaded in the next step. This resulted in residual stresses being generated in the specimen. Figure 6.28 shows the residual stress distribution across the through-thickness section of the pipe from the outer surface.

Since the residual stress generated in the specimen by the autofrettage process shown in Figure 6.28 were of low magnitude the residual stresses in the entire model from the analysis were multiplied by 7.5 times so that residual stresses close to the material yield strength was achieved. These new residual stresses were then used as initial applied residual stresses for the subsequent deep-hole finite element simulation test. The residual stress distribution across the through-thickness section of the pipe is shown in Figure 6.29.

The DH FE simulation was carried out with drilling in 1 step followed by trepanning in 6 steps. Nodal displacements along the edge of the drilled hole at 18 angles before and after trepanning were used to determine the in-plane residual strains and the residual stresses using the compliance matrix in Equation 5.12 [George et al 2002].

The displacements, u_1 and u_2 at each of the eighteen angles were resolved into the corresponding angular directions to determine the diametrical displacements before and after trepanning. For convenience, equal intervals were assumed for the eighteen angles. The equal intervals were obtained by meshing the drill parts with equally spaced nodes using constraints in the Abaqus CAE pre-processor [HKS 2002]. This is also illustrated in Figure 6.23 where the outer edge of the drill and trepan parts both have equally spaced eighteen elements. Strain at each of these 18 angles was calculated using the following relation:

$$\varepsilon = (u_{\text{after trepan}} - u_{\text{before trepan}})/(u_{\text{before trepan}} + \text{radius of drilled hole}) \quad (6.15)$$

A pseudo-inverse matrix (Equation 6.7) was then used to convert these strains into stresses using Equation 6.6.

Figure 6.30 shows a comparison of the initial applied residual stresses with the deep-hole reconstructed measured residual stresses. With the exception of near the outer and inner surfaces the reconstructed residual stresses generally compare very well with the initial applied residual stresses which confirms and validates the assumptions made and that appropriate boundary conditions were chosen in the deep-hole simulation study. Section 6.3.2 below describes the FE simulation and the results of the effect of

deep-hole drilling measurement on the initial residual stresses present in the 35mm repair welded pipe.

6.3.2 Effect of deep hole simulation on 35mm repair weld

This section contains results from a finite element study carried out on a 35mm repair weld to illustrate the effect of deep-hole drilling on the initial stress fields contained in the pipe. Detail of the pipe and the philosophy of the deep-hole simulation were concisely described above. A verification study was also conducted to illustrate the DH FE simulation modelling the DH measurement process. In the present problem, appropriate material properties were used for the parent, girth and repair welded regions as shown in Figure 6.19. The material properties used in the analysis were the same as for type 316H stainless steel provided in Table 3.1. Additional material information was based on tensile tests carried out partly at University of Bristol (see Appendix B) and partly obtained from British Energy Generation Ltd (BEGL) [Smith 2004].

A 3D FE analysis was previously undertaken by BEGL and Frazer Nash Consultancy (FNC) to model weld simulation and to predict the residual stress field in the 35mm welded pipe with an offset repair weld. The arrangement of the stainless steel pipe girth weld, the set-up of the butt-weld, the offset repair weld with bead sequence and the positions of the deep-hole measurements made are shown in Figures 6.44 to 6.47. The weld simulation methodology carried out by BEGL-FNC is very similar to that described in [Elcoate et al 2004] which presents a series of results simulating the deposition of a multi-bead, single manual metal arc (MMA) weld pass on a stainless steel flat plate. The simulations adopted a "hybrid" methodology that uses finite element codes FEAT [2002] and ABAQUS [HKS 2001] in series to carry out the thermal and mechanical parts of the analysis, respectively. This approach made use of the powerful thermal modelling capabilities and the flexibility provided by the command language to facilitate the "coupling" between codes in FEAT, and the robust and efficient elasto-plastic solver in ABAQUS.

Deep-hole simulation

The residual stress fields from the combined heat source simulation were mapped onto a further model developed at the University of Bristol (BU) by the author. This model incorporated the deep-hole simulation steps to investigate the effect of DH drilling on the mock-up predicted FE initial residual stress fields. An outline of the

mapping methodology is provided in the next section followed by a brief description of the model for the offset repair weld geometry. Finally, results are presented to illustrate the deep-hole simulation effect on the initial residual stress fields and assumptions made in the model discussed, in particular with reference to the weld material properties.

Mapping Methodology

The mapping procedure using the FE interpolation process is described in Appendix-A, [Tipping 2004] and maps the residual stress fields and plastic strains from the BEGL-FNC combined heat source multi-pass weld model onto the BU model at each gauss point at all points in the model. Figure 6.31 shows the residual stress distribution through the 35mm welded specimen from the outer surface into the inner surface of the pipe. Both the original residual stresses in the BEGL-FNC model and the mapped stresses in the BU model are shown. Note that due to differences in coordinate systems of the pipe specimen in the two models, the coordinates in the mapped stresses are different from the initial weld stress directions, e.g., "zz" in original becomes "xx" in mapped, etc. An excellent correlation illustrates successful mapping. More details of the mapping methodology are provided in Appendix A. An outline of the FE model of the welded pipe with material definitions and boundary conditions is described next.

Finite element model

A 3D FE model of the welded pipe with repair weld was constructed with drilling and trepanning parts incorporated into the model for subsequent deep-hole simulation. The same FE model as the one described in Section 6.3.1 is used here. Due to symmetry planes, only one quarter of the specimen was modelled as shown in Figure 6.18. A close-up of the mesh illustrating the deep-hole simulation parts is shown in Figure 6.21. The drilling and trepanning regions are shown in Figure 6.23. Figures 6.24 and 6.25 illustrate additional boundary conditions required during the deep-hole simulation as described earlier in Section 6.3.1. The global boundary conditions used for this model is identical to that used in the BEGL-FNC model, with two (x-y, y-z) symmetry planes and a node on the free end of the pipe fixed in y-direction (Figure 6.20c) to prevent any rigid body motion. Results are presented in the next section to illustrate the effect of deep-hole drilling on the initial residual stress fields predicted by FE in the welded pipe with the offset repair weld.

6.3.3 Result and discussion

The deep-hole simulation was carried out by removing the elements defining the drilling region followed by removal of the trepanning regions. Trepanning was carried out in six steps (see Figure 6.26 for illustration), the depth of each trepan step varying from 5 to 6mm; the drilling process was carried out in a single step since carrying out the drilling process in multiple steps made no difference to the results obtained. The nodal displacements along the eighteen paths (representing the eighteen angles) after drilling and at the end of the trepanning process were used to determine the in-plane radial strains. Note that the nodal displacements were in x and y directions and needed to be transformed into the respective radial components before determining the radial strains. A pseudo-inverse matrix as defined in Equation 6.7 was used to convert these strains into stresses.

For both the original BEGL-FNC weld simulation model and the BU DH FE model, a number of material models with various hardening were considered in the finite element study. The material models are illustrated in Figures 6.32 and 6.33. These include: (a) elasto-plastic with linear hardening for parent material and elastic perfect plastic (PP) for girth and repair welds, (b) elasto-plastic with linear hardening for parent and an identical linear hardening (LH) for girth and repair welds and (c) non-linear kinematic hardening (NKH) for parent and weld materials (see Figure 6.33) based on VORSAC data [Smith 2004]. Note that the LH model in (b) was not used in the BEGL-FNC model and was only used for the BU DH FE model. The effect of different hardening models on the initial residual stresses is shown in Figure 6.34. The stresses are plotted across a line from the outer surface into the inner surface of the pipe (illustrated by a bold line in Figure 6.21). In Figure 6.34 almost a difference of 100MPa exist in the residual stress distributions due to the influence of different hardening models consisting of elastic-perfect plastic (*PP*) and non-linear kinematic (*NKH*).

Figure 6.35 shows the reconstructed deep-hole simulated residual stresses. Also shown, is the effect of hardening models assumed in the analyses on the DH FE residual stresses. The comparison of the initial residual stresses predicted by FE with the reconstructed DH simulated residual stresses are shown in Figures 6.36, 6.37 and 6.38 for elastic perfect plastic (*PP*), linear hardening (*LH*) and non-linear kinematic hardening (*NKH*) material models respectively. In general the trends in the stress distributions are similar. However, with the exception of Figure 6.37 for the *LH* material

model case, a marked difference exists in the longitudinal stress component. In particular, the peaks in the original stresses are not reconstructed as a result of the deep-hole process. Furthermore, in both the transverse and longitudinal components towards the inner surface, a difference of about 200 to 300MPa in the *PP* case and 130 to 230MPa in the *NKH* case exist. The shear stress is essentially zero. Note that in Figure 6.37, a *PP* material model was used for the BEGL-FNC FE residual stress prediction, whereas the DH FE assumed a *LH* model.

Figure 6.39 compares the initial FE predicted residual stresses through the specimen thickness from the outer surface along a line plot with a hole-average. The hole-average consisted of stress distribution averaged over the reference hole. The good correlation between the graphs illustrating a good agreement between the line-plot data and the hole-average data points out the fact that the stress field did not vary over the reference hole.

From the summary of the results, it may be concluded that the hardening behaviour of the weld zone can substantially affect the finite element analysis. Slight variations in the stresses between the initial and deep-hole reconstructed residual stresses could be resolved with mesh refinements as future consideration. The initial FE residual stresses along the line-plot and a hole-average showed no difference illustrating the stress field over the reference hole did not vary, i.e., the stress gradient in the axial direction with respect to the pipe was negligible. The present deep hole finite element simulation study revealed that the effect of the deep hole drilling on the initial residual stress in the repair welded pipe component was substantially lower compared with the case of the quenched cylinders. The reconstructed residual stress distribution through the repair welded pipe component generally compared well with the initial residual stress distribution.

6.4 Application to practical components

A finite element study of the deep hole drilling process carried out in the preceding section on the repair weld revealed that the reconstructed residual stress distribution was generally similar to the initial residual stress distribution and the influence of the deep hole drilling process was much lower than that compared to the quenched cylinder case. The implication of the finite element study in the preceding section was then to apply the deep hole drilling method to characterise the residual stress distribution in practical components in the present study.

Two practical components supplied by British Energy Generations Ltd were used in the deep hole drilling residual stress measurement study at University of Bristol. The components included a nozzle-to-cylinder weld mock-up and a cylindrical pipe containing a girth weld with a 218mm long offset repair weld. Both components were fabricated from type 316H stainless steel material. The description of the components and the measurements are provided in the following sub-sections.

6.4.1 Residual stress measurement in a nozzle

At the request of British Energy, two sets of Deep Hole residual stress measurements were carried out on a type 316H stainless steel nozzle-to-cylinder weld mock-up component that had been thermally aged in a furnace for 19,644 hours at 550°C. This section describes the mock-up component, the locations of the measurements and the results obtained. Note that residual stress measurements were previously made on the mock-up component in the as-welded condition, prior to the thermal soak test. These earlier measurements, reported already by George [2000] and Smith et al. [2000], are compared with the recent stress measurements after the furnace heat soak treatment, and with measurements on a similar ex-service nozzle component aged for 55,000 hours at about 525°C.

Welded nozzle component

The component consisted of a nozzle-to-cylinder weld mock-up, fabricated to represent the design of a super-heater header for a steam power generation system. The nozzle was welded onto the side of a cylinder containing a hole, with most of the weld preparation made on the nozzle, and only a small amount of machining of the cylinder. The cylinder and outlet nozzle were both about 63.5mm thick. The basic arrangement of the nozzle is shown in Figure 6.40 and details of the welding conditions can be found in [Mitsui Babcock Report 2002]. After welding the component was thermally aged in a furnace at 550°C for a total of 19,644 hours.

The locations of the deep hole measurements at the nozzle-to-cylinder intersection are shown in Figure 6.41. Hole 1 is the measurement location at the flank for the as-welded condition. Hole 2 is the measurement location after thermal ageing, positioned on the flank at 180° around the circumference of the nozzle from Hole 1. Hole 3 is the measurement location near the crown for the thermally aged condition, positioned at about 70° around the circumference from Hole 1.

Experimental procedure for nozzle

The experimental procedure for measuring the residual stresses for each location shown in Figure 6.41 was essentially the same as that in the earlier measurements [George 2000, Smith et al 2000]. The standard experimental procedure [George et al 2000] was employed for both sets of measurements except that a 10mm diameter trepanned core containing the reference hole was used instead of the 20mm diameter core used in earlier work [George 2000, Smith et al 2000]. At each measurement location a reference bush of similar material characteristics to the mock-up was adhered to the outside surface of the component. This reference bush provided sacrificial material to encompass any bell mouthing from gun drilling giving a reference between repeated measurements of the hole diameter and also minimising hole entrance effects that can influence near-surface hole diameter measurements. Measurements of the reference hole diameter at eighteen regularly spaced angles of 10° were taken at axial increments of 0.2mm in each reference front bush and through the thickness of the component. Changes in the axial dimension of the column during the trepanning operation were not measured. The standard analysis technique [George et al 2000] was used to interpret the displacement measurements and derive the in-plane stresses. A Young's Modulus value of 195.6 GPa and Poisson's ratio of 0.294 obtained from [R66 1999] was assumed in the analysis. Residual stress results are described in the next section.

Results and discussion for nozzle

In the following discussion, the hoop direction corresponds to the direction of the main longitudinal axis of the weld (i.e. the welding direction) and the transverse residual stresses are those transverse to the main weld axis.

Figure 6.42(a) shows the through-thickness residual stress distribution at the flank position (Hole 2) after thermal ageing. A mainly equi-biaxial stress distribution is apparent with a maximum tensile stress of 230MPa near the outer surface and decreasing gradually to 0MPa at about 25mm into the thickness. The stress decreases exponentially until a plateau of about -50MPa is reached. The hoop stress then increases to 0MPa at the inner surface of the sample (67mm) whereas the transverse stress remains at the plateau magnitude of about -50MPa.

The through-thickness residual stresses at the crown position (Hole 3) are shown in Figure 6.42(b). The maximum hoop stress of 230MPa near the outer surface

decreases to 0MPa at a depth of 30mm. The stress continues to decrease reaching -50MPa at 43mm depth and increases to 0MPa near the inner surface. The maximum transverse stress magnitude of about 225MPa near the outer surface decreases to 25MPa at about 20mm depth and then decreases slowly until it becomes compressive at 29mm. The stress continues to decrease reaching -25MPa at 43mm and finally increases to +25MPa at the inner surface. The shear stress is practically zero for both holes. This indicates that the hoop and transverse stresses correspond to the maximum principal directions.

The transverse residual stress profiles after thermal ageing at the flank position (Hole 2) and the crown position (Hole 3) have an identical shape but the stress magnitude is higher at the saddle (crown) position. This is consistent with higher geometrical constraint at the crown and observations of reheat cracking damage (not shown here).

Residual stress measurements at the flank of the mock-up (Hole 1) in the as-welded condition [George 2000] are shown in Figure 6.43, together with similar measurements on an ex-service steam header, aged for about 55,000 hours at approximately 525°C [Smith et al 2000]. Also shown on the figure for comparison are the residual stress measurements (Holes 2 and 3) after the thermal ageing test. It is seen that the thermal treatment at 550°C has significantly relaxed the weld residual stresses; the hoop stress profile is almost identical to the service aged condition, whereas the transverse stress distribution has been only partially relaxed.

6.4.2 Residual stress measurement in a pipe with repair weld

Accurate structural integrity assessments of engineering plant require good description of the through-wall residual stress field in the component. Therefore, two sets of deep-hole residual stress measurements were carried out on a type 316H stainless steel cylindrical pipe containing a girth weld with a 218mm long offset repair weld. British Energy Generation Ltd provided the mock-up component together with information about the fabrication history. This section describes the mock-up component, the locations of the measurements, the measurement method and the results obtained.

Welded pipe component with repair

Full details of the fabrication history of the supplied mock-up can be found in [Mitsui Babcock Report 2002]. The global dimensions of the cylindrical component are shown in Figure 6.44 and are: overall length 1022mm, outer diameter 432mm and wall thickness varying from 32 to 39mm around the pipe. Each end of the mock-up contained a nozzle (not shown in the figure) from which excess material had been machined. A girth butt weld, at approximately mid-length, was made using a 2.4mm diameter wire TIG root followed by 16 manual metal arc (MMA) passes with an average girth weld heat input of 2.2 kJ/mm using 2.5, 3.2, 4 and 5mm diameter electrodes. Figures 6.45(a) and 6.46(a) show the weld groove geometry and schematic bead lay-up. A repair cavity was excavated by grinding at a location 180° remote from the remaining header nozzles. The cavity was 218mm long at the outer surface of the cylinder, 26mm deep with an offset of 7mm from the girth weld centreline with sidewall and end run-out angles of 15° and 45°, respectively (see Figure 6.45). The locations of the end of the cavity (at the surface and deepest point) were carefully marked on the outer surface of the component (see Figure 6.47). The repair excavation was filled with 14 MMA passes having an average heat input of 2.1 kJ/mm using a combination of 3.2 and 5mm diameter electrodes. All welding was deliberately carried out in one direction only to maximize superposition of weld torch start and stop effects. After welding, the repair cap was ground flush. Note that the supplied mock-up component was made by removing a repaired ring of weld metal and 15mm of adjacent heat affected zone (HAZ) from a previous test component, containing a girth weld with fully contained repairs [Wilby 1999], on which deep hole residual stress measurements were also performed [George 2000].

The original header stainless steel material specification was ASME II: 1968 SA-182F-316H. During manufacture of the previous mock-up, the headers were solution heat treated (for 1 hour at 1050°C followed by air cooling) to remove any remnant residual stresses from start of life fabrication and to eliminate the material strain hardening history [Wilby 1999]. The MMA welding consumables used for the present mock-up girth weld and repair were Babcock S type electrodes to EN 1600-E19 12 3 LB 42. Welding was in a flat downhand position with the pipe rotated. The welding conditions and a photographic record of the fabrication history are recorded in [Mitsui Babcock Report 2002]. The locations of the deep hole residual stress measurements in the offset repair are shown in Figure 6.47. Measurement Hole 1 was located at the

intersection of the centreline of the girth weld and the line defining the mid-length of the repair. Hole 2 was located at the intersection of the girth weld centreline with the line defining the stop end of the repair, the latter being identified by "pockmark b" aligned with the deepest point of the excavation (see Figure 6.47).

Experimental procedure for repair weld

Residual stress measurements were made at the two locations shown in Figure 6.47 (denoted as Holes 1 and 2). The procedure described in [George and Smith 2000] was employed for both sets of measurements except that a 10mm diameter trepanned core was used instead of a 20mm diameter core containing the reference hole to increase measurement accuracy. An identical step-by-step procedure was followed, similar to the residual stress measurement in the nozzle component (Section 6.4.1) to measure the diametral distortions at eighteen regularly spaced angles with increment 10° at every 0.2mm through the component. The standard analysis technique [George and Smith 2000] was used to interpret the displacement measurements and derive the in-plane stresses. A Young's Modulus value of 171 GPa and Poisson's ratio of 0.294 were assumed in the analysis. These properties are relevant to austenitic stainless steel weld metal [R66 1999] at room temperature. Note that it was deemed more appropriate to use weld metal elastic properties in the analysis instead of parent properties because the trepanned cores were entirely contained within the repair weld or original girth weld metal. The residual stress results are described in the next section.

Results and discussion for repair weld

In the following, the longitudinal direction corresponds to the direction of welding (i.e. the pipe hoop direction) and the transverse direction refers to that normal to the welding direction (pipe axial) as shown in Figure 6.44.

Figure 6.48 shows the through-thickness residual stress distributions measured at mid-length of the repair weld (Hole 1). The stresses are tensile and almost equi-biaxial near the outer surface. The longitudinal residual stress plateau at about 280MPa tension 11mm below the outer surface; it then decreases and oscillates to a minimum level of around 110MPa before increasing again to a tensile peak of about 250MPa towards the inner surface. The transverse stresses are generally lower in magnitude than the longitudinal stresses. The transverse stress profile decreases from a plateau of about 250MPa to approximately -50MPa at about 19mm below the outer surface and then

increases gradually to a maximum tensile residual stress of about 350MPa close to the inner surface.

The through-thickness profiles of residual stress at the repair weld stop-end (Hole 2) are shown in Figure 6.49. The longitudinal residual stress profile plateau is at around 250MPa for depths up to 13mm below the outer surface before falling gradually to a compressive peak of about -100MPa at 30mm depth and then rising to about 25MPa tension near the inner surface. The transverse stress profile increases to a peak value of 225MPa at a depth of 5mm from the outer surface then falls to about 20MPa and remains at this level for depths roughly between 16mm and 26mm. Towards the inner surface the stress profile increases again to a peak of 150MPa. The shear residual stresses measured were practically zero in both locations, thus, indicating that the stresses in the weld longitudinal and transverse directions corresponded closely with the maximum principal directions.

On comparing the measured longitudinal residual stresses at mid-length of the repair weld (Hole 1) with the stop-end results (Hole 2) it may be seen that the residual stress profiles have an almost identical distribution over depths up to 20mm from the outer surface. However, over the inner half of the wall the stress magnitude at mid-length is much greater than at the stop-end. Similar comparison of the measured transverse residual stresses shows the stress profiles to be essentially identical over depths of up to 25mm from the outer surface; towards the inner surface, though, the stresses at mid-length (Hole 1) are significantly more tensile than at the end position.

Figure 6.50 shows the through-thickness variation (from the inner surface) of the measured residual stresses in the weld longitudinal and transverse directions. The stresses have been normalised with respect to the weld 1% proof stress (380MPa). Also shown are three-dimensional finite element predictions for a similar stainless steel (Esshete 1250) repair [Bouchard 2003], performed using a modelling approach identical to that described in [Elcoate et al 2003]. The general correlation between the measured and predicted profiles is excellent for the transverse stresses (Figure 6.50b). For the longitudinal stresses (Figure 6.50a), the FE predictions are generally higher in magnitude compared to the measurements. Nevertheless, the through-thickness distribution of the longitudinal residual stresses predicted by FE follow a similar trend to the DH measurements. Note that the results shown in Figures 6.48 to 6.50 are as measured. Using Equation 5.13 the error in the measured residual stress was ±27MPa (see Section 5.2.2).

Figure 6.51 compares the measured residual stress distribution in the repair weld with the present finite element prediction for the same repair weld model. The predicted distribution shown in the figure is the mapped stress distribution shown earlier in Figure 6.38 and was mapped from the BEGL-FNC weld simulation (see Section 6.3.2). Note only the residual stresses measured at the mid-length of the repair weld (Hole 1) are compared with FE. This is because in the present FE study (Section 6.3) the repair weld was modelled circumferentially as shown in Figure 6.19. The start and stop ends of the repair weld length (Figure 6.47) were not considered in the FE model for simplicity; the objective of the FE simulation described in Section 6.3 was to study the influence of deep hole drilling process on the initial residual stresses present in the repair weld. Thus comparing the residual stresses measured at the stop end of the repair weld (Hole 2) with FE will lead to error due to the end effect. Overall a good correlation exists between the measured and predicted residual stress distribution shown in Figure 6.51, particularly with the transverse component of the residual stress. The FE however over predicts the longitudinal component of the residual stress.

Figure 6.38 showed the influence of deep hole drilling on the initial residual stress distribution. These DH FE residual stresses are compared with the present DHD measured residual stresses in Figure 6.52. Again generally a good correlation is seen between the measurement and the prediction. However, a better agreement between measurement and prediction is obtained in the longitudinal component of the residual stress compared to that in Figure 6.51, particularly near the inner surface of the repair weld pipe.

6.5 Concluding remarks

The study in the present chapter revealed that the present method of the deep hole analysis must be carried out with care for high triaxial cases. The simple elastic approach to the DHD method does not work on a quenched cylinder which has highly triaxial residual stress. Finite element studies with simple loading cases however showed that under load cases with higher triaxiality the deep hole works. Distinction is made here between the applied load for simple loading cases and residual stress in the case of quenched cylinder. Plastic redistribution effects in the deep hole simulation for the quenched cylinder revealed why the method breaks down. The deep hole simulation agrees well with the measurement carried out by the deep hole method. Different

analysis method of the deep hole analysis to the existing simple elastic approach is suggested for the highly triaxial case and discussed in Sections 9.3.2 and 10.3.

Further finite element analysis of the deep hole simulation on the repair welded component revealed that the deep hole method works well for the practical component. Measurements were made in practical components using the deep hole drilling method and were compared with both previous and present finite element predicted residual stress distributions. An overall good correlation was seen.

Chapter 7

Comparison of residual stress measurement and analysis

Previous chapters described the exploratory designs of the laboratory specimens, the process conditions and various measurements of the residual stresses. In Chapter 3 an extensive finite element study was undertaken to obtain an optimum laboratory specimen design, the process and loading condition. Chapter 4 provides a detailed description of the measurement of internal through thickness residual stress distribution in quenched and side punched samples both before and after thermal heat treatment. A summary of measurement of both the surface and through-thickness residual stress distribution using the incremental centre hole drilling (ICHD) and the deep hole drilling (DHD) techniques is provided in Chapter 5.

In this chapter the measurements are compared with the respective finite element predicted distributions and briefly discussed. The purpose of the present chapter is to rationalise the large number of the experimental measurements made on numerous specimens. This chapter is divided into three sections presenting results from quenched spheres, quenched cylinders and side punched C(T)s.

7.1 Quenched spheres

The quenched spheres studied in the residual stress measurement programme include *s8*, *s22* and *s24* all of diameter 30mm. As shown in Table 3.3 sample *s8* was manufactured from type 316L SS and samples *s22* and *s24* from 316H SS. Samples *s8* and *s22* are as-quenched and sample *s24* quenched and thermally aged at 550°C for 3200 hours.

As-quenched spheres s8, s22

Figure 7.1 shows a summary of the measured residual strain distribution across the mid-section of the quenched sphere *s8* as well as a comparison with numerical simulations [Hossain et al 2004]. The residual strains were converted to the corresponding residual stress components by using Hooke's law (Equation 4.6) and the elastic constants listed in Table 3.1. Figure 7.2 (a) and (b) summarise the residual stresses measured by the neutron diffraction time of flight (tof) method at ISIS and a

comparison with the results predicted using both isotropic and kinematic hardening models in the thermal stress analysis step of the finite element (FE) analysis. Also shown in the figures are the ICHD measured surface residual stresses. Only an average value of the residual stress at a point close to the outer surface of the quenched sphere, *s8* is shown. Detailed distribution of the ICHD measured surface residual stress is shown in Figure 5.2.

The measurements were generally in good agreement with the FE predicted results. In particular correlation between the measured and the FE predicted results is better with the kinematic hardening model. The heat transfer coefficient h = 7000 W/m^2 K was used in the heat transfer analysis step of the FE analysis.

The strain distribution measured across the as-quenched 316H SS solid sphere *s22* is shown in Figure 7.3. Also shown, is the strain distribution predicted from the FE analysis using a constant value of heat transfer coefficient of 7000 W/m^2 K in the heat transfer analysis step. This value of h is the same as that used by Gür et al [1996, 1998]. With this value of h, the predicted and measured temperatures in the quenched sphere *s22* were in excellent agreement (see Figure 3.16). Kinematic hardening material model was assumed in the thermal stress analysis step. As mentioned above the measurement in sample *s8* compared better with FE prediction under kinematic hardening material model as shown in Figure 7.2. Material properties for the 316H SS were taken from [R66 Nuclear Electric].

The corresponding residual stress components, calculated using Equation 4.6 and the elastic constants provided in Table 3.1, are shown in Figure 7.4. The FE simulations predicted higher tensile residual stresses about the centre of the sphere than measured by the ND. Nevertheless, the measurements revealed the presence of essentially an equi-triaxial tensile residual stress field in a central core of diameter about 10mm. Figure 7.5 compares these measured residual stresses with an analytical distribution [McKenzie and Moakler 1973] satisfying conditions for equilibrium (Equations 3.1 to 3.3). A good correlation exists between the experimental and the analytical distribution.

Post thermal heat-treated quenched sphere s24

The quenched specimens following thermal heat treatment measured at the ISIS facility consisted of sphere sample *s24*. The measurement took place at the ISIS facility at the RAL using the stress instrument ENGIN-X on ENGIN-X beam line. The measurements in the as-quenched spheres compared very well with the corresponding

FE predictions as shown in Figures 7.1 to 7.4. The effect of thermal ageing on the relaxation of residual strains and stresses in the 30mm diameter quenched and aged sphere *s24* are shown in Figures 7.6 and 7.7, respectively. The FE predicted strain and stress distribution in the thermally aged sphere is also in excellent agreement with the neutron diffraction measured residual strain and stress distribution. Comparing Figure 7.7 with Figure 7.4 it may be noted that the internal residual stresses relax from about 300MPa in the as-quenched sample to just under 200MPa in the thermally aged sample (see also Figure 4.18 for a direct comparison). Also shown in the figures are the von Mises equivalent stresses and FE predictions. As expected, the equivalent stresses are very low near the centres of the spheres due to the high triaxiality. Overall, an excellent correlation exists between the measurement and the predicted FE results. The measured residual stresses on the outer surface however do not relax as predicted by FE.

7.2 Quenched cylinders

A total of 15 quenched cylinders were studied in the residual stress measurement programme by neutron diffraction at various neutron facilities and the incremental centre hole drilling and the deep hole drilling method. Samples *s19*, *s26-s29*, *s34-s37*, *s39*, *s40* and *s42* were used in the neutron diffraction residual stress measurement study. The ICHD was used to measure the surface residual stress distribution in samples *s1* and *s12*. Samples *s2* and *s12* were used in the deep hole measurement study. More detail of the samples is provided in Table 3.3. A comparison between DHD measured and FE predicted residual stresses in samples *s2* and *s12* was made in Section 6.2. Here comparisons are made between the ND and ICHD measured results and FE predictions and measurements used to validate the FE simulations.

As-quenched cylinders s19, s26, s27, s39

The strain distribution measured across the as-quenched cylinder, diameter 60mm, length 60mm (sample *s19*) is shown in Figure 7.8. Also shown, is the strain distribution predicted from the FE analysis. For the FE analysis, a constant value of heat transfer coefficient of 7000W/m^2 K was used in the heat transfer analysis step for which the measured and predicted temperatures during quenching were in good agreement (see Figure 3.17). A kinematic hardening model was assumed for the thermal stress analysis. The corresponding residual stress components, calculated from the strains by using Equation 4.6 and the elastic constants in Table 3.1, are compared with the FE predictions in Figure 7.9. An excellent correlation exists between the two. Note that the

measurement of strain in the axial direction near the centre required a flight path length greater than 60mm which resulted in noisy and inadequate data. This effect was shown in Figures 4.10 and 4.11. Close to the centre, the measured axial strain component was unreliable. In calculating the corresponding residual stress components all three residual strain components are used and therefore the unreliable axial strain component near the centre gives rise to unreliability in all three calculated stress components close to the centre (see Figure 4.11). In Figure 7.9 the measured stress components at the centre are not included. The measurements in conclusion revealed the presence of an essentially triaxial residual stress field in a central region of diameter about 25mm. Also shown in the figure are the ICHD measured surface residual stresses in a similar quenched cylinder *s12*. Only an average value at a point close to the outer surface is shown. Detailed distribution of the ICHD measured residual stresses is shown in Figure 5.4.

Measured strain distributions in larger solid cylinders, diameter 60mm, length 160mm are shown in Figures 7.10-7.12. Figure 7.10 summarises the ND measured strains in cylindrical bar *s27*, 18mm offset from the end of the bar, across NA (see Figure 4.3b). Figure 7.11 shows the strains measured across the mid-section OB of the bar *s27* (see Figure 4.3b). The strains measured along the longitudinal axis of the bar *s26* at positions A, B and C (Figure 4.3c) are shown in Figure 7.12. Also shown in Figures 7.10-7.12 are the corresponding FE predicted strains. For the FE analysis, a heat transfer coefficient, h, of 7000 W/m^2 K and an initial temperature of 850°C were used in the heat transfer analysis and a kinematic hardening model in the thermal stress analysis. Overall a good correlation is seen in each case. The holes drilled into the quenched cylinder *s26* (Figure 4.3c) shortened only the incoming path length during the ND measurement; the outgoing path consisted of the diverged beam. So the constant diameter hole drilled "for the outgoing beam" did not facilitate in reducing the total path length. Nevertheless, the counting time was essentially reduced during measurement of the radial and hoop residual strains at positions A, B and C of cylinder *s26* (Figure 7.12). Diverging hole for the outgoing beam may be considered in future measurements to considerably reduce the total counting time.

The measured and FE predicted residual strain distributions across the equatorial plane of the as-quenched cylinder, diameter 29mm, length 29mm (sample *s39*) are shown in Figure 7.13. The respective residual stress components, calculated using Equation 4.6 and the elastic constants in Table 3.1, are shown in Figure 7.14. Both measured and the FE predicted stresses are shown. For the FE analysis, a heat transfer

coefficient, h of 7000 W/m^2 K and an initial temperature of 850°C were used in the heat transfer analysis step and a kinematic hardening model in the thermal stress analysis step. Generally an excellent correlation exists between the measured and predicted FE results.

A comparison is made of the residual stress distribution between as-quenched cylinders *s19* and *s39* across the radial plane from the centre towards the outer surface in Figure 7.15. Because of different diameters the stresses are plotted as a function of normalised radial distance. Residual stresses in sample *s19* were measured using stress instrument ENGIN-X at ISIS and residual stresses in sample *s39* were measured using instrument REST at NFL. Both the effect of different neutron facility and the size effect are shown in the figure. Generally the distributions of the stresses are of similar pattern. The magnitude of the stresses in the larger sample *s19* is slightly greater than sample *s39* as expected. This is true for both measured and FE predicted.

Quenched and aged cylinders s29, s28

The short-term thermal ageing specimen (sample *s29*) consisted of heat treatment of a quenched cylinder, diameter 30mm, length 30mm at 550°C for 1.25 hours. The long-term thermal ageing specimen (*s28*) included heat treatment of a quenched cylinder, diameter 30mm, length 30mm at 550°C for 1800 hours. Figure 7.16 shows the residual stress distribution in the short-term thermally aged cylinder *s29*. Both measured and FE predicted residual stress distributions are shown in the figure. The modelling of ageing is discussed in Section 8.1. Figure 7.17 shows the measured and FE predicted residual stress distribution in the long-term thermally aged cylinder *s28*. Only the stresses are shown for these cylinders as they were obtained by using the host "StressCalc" data analysis software at the SINQ facility. In both cases the FE predicted stress distribution was in line with the measurement.

Figure 7.18 compares the residual stresses in the thermally heat treated cylinders *s28* and *s29* measured using POLDI at SINQ facility in Switzerland with the as-quenched cylinder *s39* measured using REST at NFL facility in Sweden. The effect of both the short-term thermal ageing and long-term thermal ageing are shown clearly in the figure. The residual stresses relax to about 75% in the short-term thermally aged sample and to about 50% in the long-term thermally aged cylinder. In general, a good correlation exists between the predicted FE and the measured results. However, the

surface residual stresses did not relax as predicted by FE during the long-term thermal ageing as compared with the internal stress relaxation (shown in Figure 7.18).

Pre-trepanned cylinders at NFL (s34, s35, s36, s37) and at ISIS (s40, s42)

Figures 7.19 to 7.25 show the residual stress measurements in specimens with variable trepanned depths measured using stress instrument REST at NFL in Sweden. Figures 7.26 to 7.29 present the residual stress measurements in pre-trepanned quenched specimens using stress instrument ENGIN-X at ISIS. The influence of edm trepanning on the redistribution of residual stress fields is illustrated. Also shown in the figures are the corresponding FE predicted residual stresses for quenched specimens with drill and trepan. More details on the quenching simulation can be found in Section 3.1 and the simulation of drilling and trepanning is similar to the deep hole drilling simulation provided in Section 6.2.

s34 edm pre-trepan depth 29%

Figure 7.19 shows the distribution of residual strain and stress across a radial plane 12mm below the top surface in a quenched cylinder bar *s34* with 1.5mm diameter drill and 5mm diameter trepanned up to 8.5mm depth. Although the specimen was trepanned up to 8.5mm below the top flat surface, it was not possible to measure the strain and stress along the radial line from the edge of the edm front in order to prevent part of the sampling volume from coming into the discontinued material space due to the edm process. Since the sampling volume consisted of $2\times2\times2mm^3$ throughout the measurement programme, a clearance of 2.5-3.5mm from the edm front was maintained in general. The FE predicted residual strains and stresses show a similar trend to the measured values. The predictions are highly dependent on the material model assumed in the FE analysis. For the present study a linear kinematic hardening model was assumed. The ND measured results were averaged over a gauge volume of $2\times2\times2mm^3$ whereas the FE predicted results are plotted as line plots. It is interesting to note however that the order of measured strain and stress components correspond precisely with the FE predictions. The distribution of strain and stress along the axial line were measured 6mm away from the centreline shown in Figure 7.20. A clearance of 2.5mm was thus maintained from the outer edm trepan edge; the edm electrode diameter was 5mm with 1mm thickness. The FE predicted results show a good correlation with the measurements. In particular predicted peaks and troughs were also obtained by the measurements as well as the order of the components. Of course with more measured

points and with smaller sampling gauge volume, an even better correlation would be obtained. But both would contribute to an increase in the counting time.

s35 edm pre-trepan depth 53%

Figure 7.21 shows the measured and predicted results for 15.5mm depth pre-trepanned quenched cylinder *s35* along the radial line with a 2.5mm clearance from the edm front. An excellent correlation is observed between the measurements and predictions. In both specimens *s34* and *s35* the measurements along the radial line were started from the centre of the specimen. This included the drilled through hole in the measurements. Note that the hole diameter was 1.5mm and since the sampling volume was $2\times2\times2mm^3$, part of the gauge volume was therefore in the material adjacent to the hole edge. This explains why the measured strains and stresses at the drilled hole were non-zero in Figures 7.19 and 7.21. After this point became apparent, measurements across the radial line were started 1.5mm away from the centreline. The measurements along the axial line shown in Figure 7.22 compared very well with the FE predicted. The peaks and troughs in the strains and stresses predicted by FE simulation were picked up by the measurements. In order for an efficient usage of available beam time, it was decided not to scan through the specimen completely during measurement along the axial line. Instead the measurements were concentrated about the edm front, i.e., along the axial line few "mm" behind and ahead of the edm front.

s36 edm pre-trepan depth 74%

Figure 7.23 shows the measured and predicted results for 21.5mm depth pre-trepanned quenched cylinder *s36* along the radial line 2.5mm clear of the edm front. The order of the measured components matches very well with predicted, as well a good agreement in the general trend. However it may be noted that the predicted peak hoop component is not obtained by the measurement. The predicted peak strain and stress obtained can be attributed to the numerical uncertainty. The edm process was modelled by material removal. During material removal in Abaqus finite element code the stiffness of the elements suddenly fall to zero. This may increase the stresses in neighbouring elements quite substantially. This issue has been observed by Mirzaee-Sisan [2004]. The distributions of strains and stresses along the axial line are shown in Figure 7.24. With the exception of the peak axial component an excellent correlation exists overall between the measured and predicted results. Although the quenched cylinder is an axi-symmetric problem, both the measured and predicted strains and

stresses shown in Figures 7.20 and 7.24 (29% and 74% edm depths respectively) do not represent a mirror image. That is the problem is not symmetric about the radial plane across the centre. This is because the drilling and trepanning are both carried out in a single direction and not symmetrically about the radial plane.

s37 edm pre-trepan depth 97%

Figure 7.25 shows the measured and predicted distributions of strains and stresses for 28mm depth pre-trepanned quenched cylinder *s37*. Distributions along the axial line are only measured. A very good correlation between the measured and predicted results is observed including the order of components as well as obtaining the FE predicted peaks and troughs.

s40 edm pre-trepan depth 26%

Figure 7.26 shows the distribution of residual strain and stress across a radial plane in a rapid spray water quenched cylinder with 1.5mm diameter through hole and edm pre-trepanned up to depth of 15.5mm (*s40*). A clearance of 3mm was maintained during the ND measurement. Although the measurements started from the origin inside the drilled hole, not all the strain components were zero. This is because the sampling volume was 4×4×6mm, which contributed part of neutron beam to be inside the material. Also the large sampling volume resulted in averaging over a larger volume. In particular the axial component was the most affected. This is clearly shown in the figure. The measurements closer to the drilled hole, particularly the axial component do not match as closely to the FE predicted as towards the outer surface of the cylinder. The distributions along the axial line shown in Figure 7.27 were obtained 8mm away from the centreline. The sampling volume was therefore clear of the trepanned edge. The measured strains and stresses compared very well with the predictions.

s42 edm pre-trepan depth 76%

Figure 7.28 shows the distributions of residual strain and stress in a through-hole drilled rapid spray water quenched cylinder with 45.5mm depth edm trepan (*s42*) across a radial line 3mm ahead of the edm front from the centreline. For the reasons as already mentioned in the preceding paragraph the measured results nearer the centreline did not match closely with the FE predictions. A more refined sampling volume would be required to represent a more realistic result, especially nearer the drilled and trepanned edges. In contrast the results measured along the axial line 8mm away from the

centreline shown in Figure 7.29 were in excellent agreement with the respective FE simulations.

Summary of pre-trepanned quenched cylinders

In general the measured residual strains and stresses across the radial and axial lines in quenched cylinders pre-trepanned to variable depths were in good agreement with the finite element predicted results. The close correlations thus verified and validated the various assumptions made in the material model and boundary conditions in the deep hole drilling measurement simulations. The FE model of the deep hole drilling process was described in Chapter 6. The implications of the validated DH FE simulations of the present section are discussed later in Section 9.3. The ND measured residual stresses revealed only a limited effect of trepanning on the redistribution of residual stresses as the ND measurements were made some distance away from the edge of edm trepan. The redistribution of residual stresses was sensitive to the position from the trepan edge and the effect of trepanning on the redistribution is shown better close to the trepan edge. This is carried out by utilising the validated DH FE simulation and is discussed further in Section 9.3.

7.3 Side punched C(T) specimens

Figure 7.30 shows the measured and FE predicted residual strain distribution along the ligament ahead of the notch tip in the mid-plane of an as-punched C(T) specimen. The corresponding residual stress components calculated using Equation 4.6 and the elastic constants in Table 3.1 are shown in Figure 7.31. Only the figure-of-eight punched specimens were considered in the neutron diffraction measurement study and the residual stress results presented here belong to figure-of-eight punched cases only. The measurements were performed on ENGIN-X at ISIS facility. The correlations between the measured and the FE predicted in general are excellent.

Figures 7.32 and 7.33 show respectively the residual strain and stress distributions along the ligament ahead of crack tip in the mid-plane of a punched and thermally aged C(T) specimen. The aged specimen was thermally aged at 550°C for 3900 hours. The thermal ageing of the specimens have relaxed the residual strain and stress considerably. It is clearer in Figure 7.34 which shows a comparison of the residual stress distributions between the as-punched and the punched and aged C(T) specimens. Both measurement and FE prediction show a considerable relaxation of the initial punched residual stresses.

Chapter 8

Analysis of creep damage formation

In preceding chapters results have been presented on various processes to obtain suitable candidate specimens with residual stresses of sufficient triaxiality for subsequent creep studies. Both numerical and experimental studies were performed. These studies were presented in Chapters 3, 4 and 5 where the quenching of cylinders and spheres and the side punching of C(T) specimens were considered. Verification and validation of the numerical studies were made in lieu of residual stress measurements in Chapter 7. This chapter is dedicated to the creep study following the abovementioned residual stress generation procedures on the respective specimens. Detail of the finite element study is presented to describe the damage prediction model. The study of the relaxation of residual stresses, both experimental and numerical, due to thermal ageing is then provided. This study was also considered as a verification of the damage prediction model. Later results from both the predicted and the experimentally measured damage are presented followed by a brief discussion.

8.1 Damage prediction model

Creep is one of the most serious high temperature damage mechanisms. Calculations of creep damage under conditions of strain control are often carried out using either a time fraction approach or a ductility exhaustion approach. The presence of multiaxial stress states induced in practice by welding arcs further complicates the calculations of creep damage. In the case of the time fraction approach, there are a number of models that predict the effect of the state of stress on the creep rupture strength, e.g., Huddleston developed a model from data based on stainless steels. The R5 procedure [2001] uses a ductility exhaustion approach to calculate creep damage and includes a model for use under triaxial states of stress. Spindler [2004] developed this model considering the cavity nucleation and growth and multiaxial creep data on Type 304 and 316 stainless steels. The ductility exhaustion approach relies on accurate predictions of creep strains arising during thermal relaxation of weld residual stresses and the local multi-axial creep ductility.

8.1.1 Creep model

Thermal exposure of quenched samples and side-punched C(T) specimens was simulated using the finite element models developed in Chapter 3. The two methods of generating residual stresses in the samples were studied using finite element analysis in Chapter 3. Measurements of residual stresses in the samples provided in Chapters 4 and 5 were used to validate the finite element predictions in Chapter 7. Chapter 7 also presents a comparison of the measured with the finite element predicted internal residual stress distribution in specimens following thermal exposure in the creep study. The simulation of the creep study was carried out by adding a number of further steps to the FE analysis described in Chapter 3, including (i) raising the temperature of the quenched and side-punched specimens to operating temperature of 550°C and (ii) thermal exposure at 550°C for selected number of hours as described earlier. The temperature was raised within the FE analysis by instantaneously raising the temperature field within the whole model. The temperature-dependent material properties used in the analysis are provided in Table 3.1. Creep deformation was modelled by the RCC-MR empirical law [RCC-MR 1985] for primary and secondary creep of AISI 316.

Primary creep

A subroutine written to describe the 316 stainless steel material [Bradford 1998] was used for the finite element analysis to examine the effect of thermal exposure. This subroutine was based on the RCC-MR creep law [RCC-MR 1985] which was known to be representative for type 316H stainless steel [Holt and Spindler 1996]. In this model during the primary stage of creep the creep strain was calculated by the following formula for temperatures in the range 425°C to 725°C:

$$\bar{\varepsilon}_p = \frac{C_1}{100} t^{C_2} \bar{\sigma}^{n_1} \tag{8.1}$$

where $\bar{\varepsilon}_p$ is the equivalent creep strain in the primary creep range, $\bar{\sigma}$ is the equivalent stress (MPa) and t is the time (hours). The dimensionless constants C_1, C_2 and n_1 are temperature dependent coefficients and are 2.9618×10^{-12}, 0.42131 and 4.18 respectively at 550°C [R66 1999].

Secondary creep

The creep strain in the secondary creep stage for temperatures in the range 425°C to 725°C is given by [RCC-MR 1985]:

$$\bar{\varepsilon}_s = \bar{\varepsilon}_{fp} + C\bar{\sigma}^n\left(t - t_{fp}\right) \tag{8.2}$$

where $\bar{\varepsilon}_{fp}$ is the equivalent creep strain at the end of the primary creep stage, t_{fp} is the time of transition from primary to secondary behaviour (where the primary and secondary strain rates are equal). The temperature dependent coefficients C and n at 550°C are 5.2900×10^{-26} and 8.20 respectively. In the finite element analysis of the creep study the creep strain for both primary and secondary stage is calculated for each increment and the larger increment of the strain is subsequently selected. This means that the changeover from the primary to secondary creep occurs when the primary and secondary rates become equal. The primary law applies when the predicted primary creep rate is higher than the secondary creep rate and vice-versa.

Creep damage and tertiary creep

The subroutine used in the creep step of the simulation combines calculations for both creep strain and the creep damage for each analysis increment and predicts the onset of reheat cracking within the thermally exposed crept specimen. The finite element damage analysis is based on the ductility exhaustion approach which considers the relaxation of residual stresses during creep exhausting the available ductility within the material. The creep damage D_c at any point is calculated from:

$$D_c = \int_0^t \frac{\dot{\bar{\varepsilon}}_c}{\bar{\varepsilon}_f\left(\dot{\bar{\varepsilon}}_c\right)} dt \tag{8.3}$$

where $\dot{\bar{\varepsilon}}_c$ is the instantaneous von Mises equivalent creep strain rate at time t, and $\bar{\varepsilon}_f$ is the corresponding multi-axial creep ductility, expressed as the von Mises equivalent strain at failure, which is a function of the strain rate and stress state. Within this model an empirical approach has been adopted for describing the effects of stress state on ductility [Spindler 2004]. This approach includes two material constants, p and q, which describe the decreasing ductility with increasing stress triaxiality according to:

$$\frac{\bar{\varepsilon}_f}{\varepsilon_{f,uni}} = \exp\left[p\left(1 - \frac{\sigma_1}{\bar{\sigma}}\right)\right]\exp\left[q\left(\frac{1}{2} - \frac{3\sigma_h}{2\bar{\sigma}}\right)\right] \tag{8.4}$$

where $\varepsilon_{f,uni}$ is the uniaxial ductility, $\bar{\sigma}$ is the von Mises equivalent stress, σ_1 is the maximum principal stress and σ_h is the hydrostatic stress. The first term in Equation 8.4 represents the cavity nucleation. The second term represents cavity growth by creep deformation. Creep initiation is conceded when damage $D_c \geq 1$. The constants p and q are empirically derived from multiaxial tests on a particular material, and two sets of values have been proposed by Spindler [2004] for AISI 316 stainless steel, set 1: p = 2.38, q = 1.04; set 2: p = 0.15, q = 1.25.

Tertiary creep is predicted by incorporating the damage function throughout the analysis with adjustment made to the RCC-MR [1985] law:

$$\dot{\bar{\varepsilon}}_{ct} = \frac{\dot{\bar{\varepsilon}}_c}{1 - D_c^3} \tag{8.5}$$

where $\dot{\bar{\varepsilon}}_c$ is the equivalent creep strain rate from the RCC-MR [1985] equations and $\dot{\bar{\varepsilon}}_{ct}$ is the equivalent creep strain rate including the tertiary behaviour. Equation 8.5 shows that the tertiary creep strain rate progressively becomes larger as the creep damage D_c increases until the strain rate theoretically becomes infinite at rupture.

8.1.2 Finite element implementation

Two user subroutines (CREEP and UVARM) and a BLOCK DATA subprogram are used to encode the continuum damage mechanics (CDM) equations. Both subroutines are called by ABAQUS at each integration point of each element in the model for each time increment. As long as an element is of a type that employs integration points these routines may be used to calculate its creep and creep damage behaviour [Holt 1996].

In the case of the creep strain, the CREEP user subroutine uses the modified RCC-MR law [Holt 1996] to calculate the equivalent creep strain increment given the current equivalent creep strain, von Mises stress, temperature, damage and time increment. The damage increment is similarly calculated using the UVARM subroutine, given the current stresses (von Mises, hydrostatic and maximum principal) and the equivalent creep strain increment. This subroutine also finds the current damage at each element integration point by maintaining a sum of all previous increments.

$$D^{t+\Delta t} = D^t + \frac{\Delta D}{\Delta t} \tag{8.6}$$

The rate dependent uniaxial creep ductility model is incorporated by evaluating the current equivalent strain rate and Spindler function in an increment and thus calculating the current ductility factor [Holt 1996]. The damage is then calculated using this current ductility factor rather than a fixed ductility factor.

Care should be taken with the units in the creep analysis. The stresses must be in MPa, temperature in °C and time in hour. Length units could be in mm or m, as long as force units are in N or 10^6N (MN) respectively. The restriction on the time units only applies to steps involving creep.

8.2 Initial predictions of creep damage

The above creep model was implemented in the ABAQUS code to predict the extent of creep damage formation and the initiation time under both residual stress generation processes: quenching and side punching. Residual stress relaxation due to thermal ageing, both short and long term in quenched specimens were measured by neutron diffraction. This compared very well with the respective finite element predictions, thereby validating the creep model (see Section 7.2). The present section provides results from the damage predictions for both processes. Experimental study of creep damage formation is included in Section 8.3.

8.2.1 Damage prediction following quenching

Figures 7.16-7.18 showed the effect of thermal exposure at 550°C on the residual stress distribution in a quenched specimen for 1.25 and 1800 hours. From the measured residual stress distributions the von Mises equivalent residual stress distribution across the radial plane of the quenched cylinder is calculated and compared with the FE predicted equivalent residual stress distribution in Figure 8.1 with exposure times. Although the comparison between the measured and FE predicted in Figure 7.18 was generally good a marked difference may however be noticed in the von Mises equivalent residual stress components in Figure 8.1. For example the measured equivalent residual stress close to the core of as-quenched cylinder (sample *s39*) was much lower than the prediction. This is also noticed for the long-term exposure *s28*. A reason for the poor correlation in the equivalent residual stress distribution between the measurement and prediction may be due to uncertainty in the measurement of the axial residual elastic strain component in the neutron diffraction measurement owing to the longer path length. In calculating residual stress and equivalent residual stress the error

associated with the uncertainty may be compounded. Secondly the relaxation of surface residual stress may be over predicted as compared with the measurement shown in Figure 8.1.

For initial creep damage analysis, a 316H stainless steel cylindrical bar, diameter 60mm, length 60mm was considered. Figure 8.2 shows the development of the predicted damage parameter D_c over time at selected regions in the quenched cylinder. Figure 8.2(a) shows the accumulation of predicted damage under set 1 of empirical coefficients with $p = 2.38$ and $q = 1.04$. Figure 8.2(b) shows the accumulation of predicted damage under set 2 of the empirical coefficients with $p = 0.15$ and $q = 1.25$. Also shown in the figures are quarter sections of the quenched cylinder where the selected locations are illustrated.

Under set 1 of empirical coefficients damage was predicted as an annulus about the vertical axis of the cylinder (Figure 8.2a). Moderate damage was predicted to accumulate within 2880 hours of heat soak at 550°C. The maximum predicted damage was found at a location 13mm from the centre on the radial plane corresponding to the point "b" in Figure 8.2(a).

Under set 2 of empirical coefficients the region of damage forms two cylindrical regions within the cylindrical bar, offset from the radial plane by about 12mm as illustrated by the quarter model of the cylinder in Figure 8.2(b). Compared to set 1 predicted accumulation of creep damage takes much longer for set 2 of the empirical coefficients. After 4320 hours heat soaking at 550°C only a fractional damage occurs in the cylinder compared to that under set 1. For complete damage, longer that 17200 hours (~2years) of heat soak is required. The maximum damage is predicted on the axial plane 10 mm from the centre corresponding to the point "c" in Figure 8.2(b). The region of damage in this assumption is also different from the results of set 1. Under set 1 of the Spindler's function, where $p > q > 1.0$, the damage is driven by the maximum principal stress, whereas with Set 2, where $p < 1$ and $q > 1.0$, hydrostatic stresses are the main driving force for damage [Spindler 2004].

These results are summarised in Figure 8.3 which shows a section through the cylinder and also illustrates the location of the predicted creep damage accumulation under set 1 (Figure 8.3a) and set 2 (Figure 8.3b) of the empirical constants.

8.2.2 Damage prediction following side punching

By using side punched C(T) specimens described in Section 3.3 it was possible to generate residual tensile stress in the specimen with variable triaxiality and plasticity in a controlled manner. The objective of the side punching method in residual stress generation was to discriminate between the influence of prior plastic strain and the presence of triaxiality on the creep cavitation initiation site. The FE study related to the side punch is described in Section 3.3. The effect of thermal exposure at 550°C for 3900 hours on the residual stress distribution in an as-punched figure-of-eight C(T) specimen was shown in Figures 4.27 and 7.34. The residual stresses relaxed due to thermal exposure and the relaxation compared very well with the FE predicted relaxed residual stress distribution shown in Figure 7.34. From the residual stress components the von Mises equivalent residual stress was calculated. Figure 8.4 shows measured and FE predicted von Mises equivalent residual stress distribution along the ligament ahead of crack tip in the mid-plane of a figure-of-eight punched C(T) specimen. Results for both as-punched and punched and aged (at 550°C for 3900 hours) C(T) specimens are shown. Relaxation of equivalent residual stress distribution due to thermal exposure is shown and the correlation between the measurement and FE prediction is excellent.

Figures 8.5, 8.6 and 8.7 present contour plots showing the zone of predicted damage using the creep subroutine [Holt 1996, Spindler 2004] for single punch, double punch and figure-of-eight punch C(T) specimens respectively. Contour plots at different exposure times are shown to illustrate the development of damage accumulation. Figures 8.5 (a), (b) and (c) show the onset of predicted damage parameter at exposure times of 200, 2100 and 3900 hours respectively at 550°C for single punch C(T) specimen. A very limited region of damage is predicted shown by red colour in the contour plots. The position of the contour plot relative to the C(T) specimen is illustrated by the half model of the C(T) specimen on the top right corner in each figure. Figure 8.6(a) presents contour plot of predicted damage for double punch C(T) specimen at exposure time of 1.5 hours illustrating a significant development of damage compared to the single punch case within short exposure time. Figures 8.6 (b) and (c) show the onset of damage parameter at exposure times of 2100 and 3900 hours respectively in double punch C(T) specimen. Figure 8.7(a) also illustrates the onset of damage parameter in figure-of-eight punch C(T) specimen within short exposure time compared to the single punch case. However the zone of the predicted damage parameter was small compared to the double punch case (Figure 8.6a). Moderate size of

damage was predicted in the figure-of-eight punch C(T) specimen at thermal exposure times of 2100 and 3900 hours as shown in Figures 8.7 (b) and (c) respectively. The creep model predicted the size of damage in the C(T) specimen shown in Figures 8.6(b) and 8.7(b) was $1.2\times1.8\times22$ mm^3 in the double punched case and $0.8\times0.6\times22$ mm^3 in the figure-of-eight after 2100 hours thermal ageing at 550°C. Much limited damage zone was predicted in the single punch case (Figure 8.5b) compared to double and figure-of-eight punch cases. Overall the amount of predicted damage in the double punch C(T) specimen was highest followed by the figure-of-eight punch C(T) specimen. Triaxiality factor near the vicinity of crack tip in the double punch C(T) specimen was highest followed by the figure-of-eight C(T) specimen. The triaxiality factor in the single punch C(T) specimen was very low.

Figure 8.8 shows the development of the predicted damage parameter D_c over time at selected regions close to the crack tip near the mid-section of the side punched C(T) specimens (see Figure 8.9 for illustration of the locations) for single, double and figure-of-eight punched cases. The predicted damage accumulation shown in Figure 8.8 used set 1 of the empirical coefficients (p = 2.38 and q = 1.04). In the single punch specimen a much longer exposure time (~20 years) is required for the initiation of creep damage. Based on the level of triaxiality the predicted damage was highest for the double punch and the initiation time was lowest.

8.3 Measurement of creep damage

The extent, location and the initiation time of creep damage formation were predicted by the creep model in the previous section. Here, an experimental study undertaken for quenched cylindrical bars and side punched C(T) specimens is provided. As discussed in Section 3.3, the use of different available punching tools, residual stresses of variable triaxiality and plasticity were introduced into C(T) specimens in a controlled manner. The assumption made in the creep formation with plastic strains as a pre-requisite, will be addressed in the present section where the side punching of C(T) specimens are analysed for creep formation under various punching impressions. First, the quenched cylinder bars are analysed followed by the side punched specimens.

8.3.1 Damage measurement in quenched samples

Four test specimens, viz. one quenched sphere of diameter 60mm (*s20*), two quenched cylinders of diameter 60mm and length 60mm (*s16* and *s17*) and one

unquenched cylinder of diameter 60mm and length 60mm (*s18*) were subjected to an initial ultrasonic inspection in September 2001 [Bouchard 2001]. An automated process with 4 MHz single and twin crystal compression probes was used to inspect the cylinders from the curved surface and a manual procedure with a single crystal probe was used for the sphere. The 'ultrasonic fingerprints' for each component were recorded electronically for later reference comparisons. Following inspection, the specimens were placed in a Muffle furnace at mid-day on the 4th October 2001, at Berkeley Laboratory [Bouchard 2001]. The furnace was being maintained at a constant temperature of 550°C. The temperature was being continuously monitored using a type K thermocouple and the signal recorded using a data logger. The specimens were removed from the furnace after 4320 hours initial heat treatment for NDT ultrasonic inspections. The inspection results were compared with the initial ultrasonic inspection fingerprints to assess whether any measurable creep damage can be identified. Following no significant change, the specimens were returned to the furnace for a further heat soak period of about 4000 hours. However, due to practical considerations NDT ultrasonic inspections were not repeated.

The specimens were later sectioned and polished to detect any micro-cracks using optical microscopy. No visible cavitation damage was noticed optically. Figure 8.10 shows the micrographs of a sectioned quenched and aged cylinder (*s17*) after etching. The locations in Figures 8.10 (a) and (b) correspond to the locations of predicted damage accumulation under empirical functions set 1 and set 2 shown in Figures 8.3 (a) and (b) respectively. The dark shaded rounded regions shown in Figure 8.10 running through the grain boundaries are possibly manganese sulphides and not micro-cracks [Spindler 2005]. To observe any possible cavitation of less than ½ μm scale, either an electron microscope or small angle neutron scattering (SANS) technique may be used.

8.3.2 Damage measurement in side punched specimens

Section 3.3 detailed the finite element procedure for residual stress prediction in side punched C(T) specimens. A parametric study was carried out in order to achieve a suitable specimen geometry and size for the subsequent creep study. From the finite element analysis, a total number of nine C(T) specimens were manufactured from type 316H stainless steel to use in the side punch tests. Details of the specimen dimensions are provided in Table 3.5. All three different punching tools (single, double and figure-of-eight) were used on the nine specimens to generate residual stresses of variable

triaxiality and plasticity so that three specimens were side punched using each punch configuration. Of the three specimens side punched under each configuration, two specimens were put into a furnace to age at 550°C for a set period to study creep damage formation. This sub-section describes these specimens and the effect of the thermal treatment on the punched specimens.

Figure 8.11 shows the side punched and thermally aged (at 550°C for 2112 hours) C(T) specimens edm sectioned along the mid-thickness for (a) figure-of-eight, (b) double and (c) single punch cases. The top row in the figure consists of fractured samples for fractography study whereas the bottom row consists of samples for the metallography study. For the fractography study the samples were fractured by a combination of fatigue and saw cutting [Gladwin 2005].

Fractography study

Figures 8.12 to 8.14 present scanning electron micrographs of the figure-of-eight, double and single punch case consisting of the transgranular fracture surface with intergranular facets showing creep cavitation. The location of the creep cavities is also shown in the figures denoted by *Z*, distance through thickness of the specimen from the midplane and *X*, distance from the crack tip along crack. These locations are also illustrated in Figure 8.15. Figure 8.12(a) illustrates the grain boundary with cracks having creep cavities. In Figure 8.12(c) the cavities are attached to carbides. A much larger cavities is shown in the double punch C(T) specimen in Figure 8.13(b) compared to Figure 8.12(c). However in the latter case the cavities are further (~11.7mm) from the midplane. Figure 8.13(c) shows the linkage of cavities. The formation of creep cavities in the single punch C(T) specimen is shown in Figure 8.14. The cavities in the single punch C(T) specimen were very scarce and confined to a very small location close to the outer surface of the specimen about 9mm away from the midplane, i.e., $Z = 9$mm in Figure 8.15.

The scanning electron micrographs in the present fractography study was used to quantify the extent of creep cavitation in the punched specimens which were thermally exposed at 550°C for 2112 hours. In the present study only the cross section of the creep cavitation represented by X and Z in Figure 8.15 was possible. In order to quantify the creep cavitation normal to the crack tip into the specimen a detailed metallography study (see below) is required. The fractography study revealed that the extent of creep cavitation was highest in the figure-of-eight punched C(T) specimen followed by the

double punched C(T) specimen. It was not possible to quantify the extent of cavitation in the single punch C(T) specimen which showed a very limited region of creep cavitation close to the outer surface. Thus, for the figure-of-eight punched C(T) specimen, X = 0.38mm, Z = 11.7mm; and for the double punched C(T) specimen, X = 0.37mm, Z = 9.0mm (see Figure 8.15 for illustration of X and Z).

Metallography study

Metallographic samples were obtained from the remaining half of each C(T) specimen shown in the bottom row of Figure 8.11 that had not been broken open. The metallographic samples were prepared by grinding and polishing followed by a repeat polish and etch procedure. This procedure involved polishing the surface to a 1μm finish followed by etching with Marbles Reagent (10g $CuSO_4$ 50ml HCl and 50ml H_2O) for less than 5 seconds. The surface was then re-polished using a 1μm polishing cloth and then etched as before. This procedure was repeated four times as this is necessary in order to show up the creep damage in the form of small intergranular cavities and cracks in the microstructure in isolation to any artefacts. That is, to limit removal of carbides from the microstructure which could be mistaken for creep cavitation.

C(T) specimens including single, double and figure-of-eight punch thermally exposed at 550°C for 2112 hours were all used in the metallography study. These results are however not included here as it was not possible to see any evidence of creep cavitation. It may be possible that the cavities are visible along a plane different to the midplane. The figure-of-eight punch specimen which was thermally exposed for 3900 hours was used in the residual stress measurement programme as detailed in Section 4.1.5. Therefore only the figure-of-eight specimen was edm sectioned for the metallography study. Figure 8.16 shows an optical micrograph taken from the mid-thickness plane of figure-of-eight side punched and thermally aged (at 550°C for 3900 hours) C(T) specimen showing creep cavities along grain boundaries (pointed by an arrow).

8.4 Concluding remarks

The creep damage model predicted significant damage in both quenched and side-punched specimens. Using the creep model the size of predicted damage in the C(T) specimen shown in Figures 8.6(b) and 8.7(b) was 1.2×1.8×22 mm^3 in the double punched case (X=1.2mm, Y=0.9mm, Z=11mm in Figure 8.15) and 0.8×0.6×22 mm^3 in

the figure-of-eight (X=0.8mm, Y=0.3mm, Z=11mm in Figure 8.15) respectively after 2100 hours thermal ageing at 550°C. A very limited damage zone was predicted in the single punch case (Figure 8.5b).

The metallography study (Figure 8.10) did not reveal the presence of any creep cavitation in the quenched sample. In contrast the fractography study revealed evidence of creep cavitation in all the punched C(T) specimens. The table below compares the measured and FE predicted extent of creep. This is also illustrated in Figure 8.17. It was not possible to quantify the extent of cavitation in the single punch C(T) specimen which showed a very limited region of creep cavitation close to the outer surface. Using the co-ordinate system shown in Figure 8.15 the maximum extent of damage measured was X = 0.37mm, Z = 9.0mm for the double punched C(T) specimen and X = 0.38mm, Z = 11.7mm for the figure-of-eight punched specimen. The extent of creep cavitation measured in the figure-of-eight punched specimen was found to be larger than that in the double punched specimen. In contrast the extent of FE predicted damage was larger in the double punched specimen. The FE simulation overall gave a conservative prediction for the extent of the damage. This was also observed by Turski [2004].

	X (mm)		Y (mm)		Z (mm)	
	Measured	FE	Measured	FE	Measured	FE
SP	-	-	-	-	-	-
DP	0.37	1.2	-	0.9	9.0	11.0
FOE	0.38	0.8	-	0.3	11.7	11.0

Chapter 9

General Discussion

Throughout the thesis care has been taken in order to describe the work performed by the author exhaustively and where necessary any peculiarity found in the results has been addressed and complemented with a detailed discussion. A summary already discussed in the preceding chapters and additional comments are discussed here. The aim of the present chapter on the general discussion is to pull together and integrate the various aspects of the research studied.

This chapter is conveniently divided into four parts. Firstly aspects of results of the residual stress prior to thermal ageing including experimental and numerical study of stress generation and their characterisation are discussed. Secondly the measured thermally relaxed residual stress following thermal heat treatment is compared with predicted FE results. Thirdly, a brief summary of the quantification of the creep damage is included. A comparison is made between the predicted FE damage and the experimental observation. The section provides a useful discussion on the possible modification to the damage model used in the creep FE study by accounting for the effect of prior straining in the crept component. Fourthly, a short discussion on the influences of stress redistribution on the deep-hole drilling measurement is provided. A further possible approach to the existing elastic approach is discussed. Finally results on the residual stress measurements in the welded components are discussed.

9.1 Residual stresses prior to thermal ageing

9.1.1 Finite element modelling

The methodology utilised in the selection of test specimens with residual tensile stress of high triaxiality for subsequent creep testing in essence included a parametric study using finite element modelling. Both the dimension of specimens and the process condition were obtained following an initial FE study. Based on the predicted result the specimens were designed and manufactured and the process condition defined. It is known that an accurate definition of material model is pre-requisite for reliable predictions including for example, stress, strain and distortion. Ordinarily the best code

of practice is to carry out material testing in-situ in order to obtain reliable material properties. However in the present study no material testing was performed. A very limited material test programme, which was carried out towards the end of the research study, included for an industrial repair-welded pipe specimen for a limited FE study detailed in Appendix B.

Although type 316H stainless steel material data were provided from [R66 1999], it should be noted that the material data depicted by Figure 3.2 (b) and (c) for grades 316L and 321 stainless steels respectively are based on a master curve of type 316H [Bouchard 2002]. It has been suggested by Bouchard [2002] that the austenitic 300 series stainless steels follow a similar trend of curves. Therefore based on a single room temperature material value, data at higher temperatures for both grades 316L and 321 were fitted to a master curve. The reliability of such assumption therefore needs further verification.

9.1.2 Quenching residual stress

In the process of quenching of the austenitic stainless steel specimens in this study there is no phase transformation of material. Therefore, thermal gradient is the only cause of residual stress formation. In the present study the specimens were rapid-spray water-quenched and were therefore fully immersed in water at all time during quenching. This suggests that the residual stress field thus obtained resulted from the interaction of heat transfer from both the curved outer surface as well as from the flat surface at either end of the cylindrical specimens. This is why a variation of the axial component of the predicted residual stress was noticed with the variation of cylinder dimension, i.e., the length-to-diameter (L/D) ratio as can be seen in Figure 3.3 (a) to (c). The distribution here is across a radial line from the centre of the cylindrical bar to its outer surface. When the length of the bar is one-third of its diameter (L/D = 0.3) the specimen resembles a flat disc. In such a case, firstly, the problem becomes a plane stress one and secondly, the effect of heat flow from the flat surface supersedes the effect of heat flow from the curved outer surface. Consequently the residual stress due to heat transfer results in lower axial component of residual stress compared to the hoop and the radial components. Moreover from the geometrical standpoint the axial component is negligible.

On the other hand due to the same reason as above on increasing the length of the cylindrical bar the effect of heat flow from the outer surface supersedes that from its

ends and the plane stress case is lost. The axial component of the residual stress therefore becomes the principal stress component. This effect can be seen Figure 3.3 (b) and (c). This is where the *L/D* ratio is greater than 1.0. Therefore as mentioned in Section 3.1 earlier greater length provides a greater constraint.

9.1.3 Heat transfer coefficient

The residual stresses obtained are particularly sensitive to the heat transfer coefficient, which enables the boundary conditions in the thermal problem to be defined. This result is presented in Table 3.2 and is discussed in Section 3.1. It is observed that large changes in heat transfer coefficient had a major influence on the internal stress levels that are not always evident from the surface stresses. A high compressive stress at the surface did not guarantee a high tensile internal stress. High tensile triaxial stresses were predicted in the central volume of the cylinders when the heat transfer coefficient was greater than 1000 W/m^2 K. In general the magnitude of residual tensile stress near the core of the specimen increased with higher heat transfer coefficient. Therefore, a quench rig where a maximum heat flow from the specimen during the quenching process could be achieved needed to be designed in order to obtain specimens with high residual stress field. This was achieved in practice by using high-pressure water jets in the cooling chamber of the quench rig (shown in Figure 3.11). Hence the term rapid-spray water-quench.

Although secondary an equally significant advantage of the use of rapid-spray water-quench was to minimise the effect of film boiling during quenching. Film boiling results in a parabolic distribution of heat transfer coefficient with temperature: the heat transfer is poor at high and low temperatures, with a peak value of the heat transfer coefficient in the mid-range of the temperature [Sedighi and McMahon 2000]. However, the use of rapid-spray water-quench justifies the assumption of a constant heat transfer. The verification of the assumption may be provided by the result shown in Figures 3.16 and 3.17. Each figure compares the measured temperature-time profile with the predicted FE profile based on a constant heat transfer coefficient. Moreover, in the study by Yazdi et al [1998], where both the heat transfer coefficient calculated from the measured temperature-time profile and the measured temperature-time profiles were used for the boundary condition in the thermal analysis, a same temperature field is obtained. Thus, the temperature measured exactly at the part surface can be used as the boundary condition in the thermal problem and conversely a heat transfer coefficient

can be assumed in the thermal model for which the predicted temperature field correlates well with the measured temperatures, e.g., as in Figures 3.16 and 3.17. Moreover good correlation between the measured and FE predicted residual stress distributions further confirmed the choice of heat transfer coefficient.

9.1.4 Measured quenched residual stress field

The characterisation of residual stress field in the quenched specimens was carried out by mainly neutron diffraction (ND) and incremental centre-hole drilling (ICHD) residual stress measurement techniques. A limited number of measurements using the deep-hole drilling technique were also employed; the results from these were not used for reasons discussed in Section 9.4 below. Here a general discussion on the ND measurement is provided initially followed by discussion on the ICHD measurement.

Neutron diffraction

Results of residual strains and stresses measured by the ND method using both time-of-flight and diffraction techniques are presented in Figures 4.5 to 4.15 and 4.35 and 4.36. Detail of the specimen and the measurement path in each specimen are provided in each figure. The ND measurements are sensitive to the sampling (gauge) volume. The sampling volume should be small enough to obtain a suitable resolution of the residual stresses but at the same time large enough to be statistically representative of grains. A square section is desirable in order that same volume of material is examined when measurement is carried out in different coordinate directions. [Ezeilo and Webster 2000].

Measured residual results were compared with the predicted FE results and discussed in Chapter 7. The FE simulations generally predicted higher residual tensile stresses in the centre of the specimens than were measured. This is mainly because of choice of heat transfer coefficient h in the heat transfer step of the FE analysis. Both isotropic and kinematic hardening models were considered in the thermal stress analyses. The magnitude of the peak predicted residual stress was found to be lower for the kinematic hardening model than for the isotropic hardening model and was found to be closer to the measured residual stress field. Nevertheless, the experimental measurements revealed the presence of an essentially triaxial residual stress field in a central core of about $1/3^{rd}$ of the specimen diameter. Furthermore the level of triaxiality

was found to be of sufficient intensity for the study of creep damage but as discussed in Section 8.3.1 no visible creep damage was formed.

The effect of path-length can be seen in Figure 7.8. Here the measurement of residual strain across a radial line from the centre of quenched cylinder bar (*s19*) to its outer surface is shown. In the central core of the specimen, the comparison of the measured radial and hoop components of residual strain are excellent with the predicted FE strains. However, for the axial component of the strain the comparison between the measurement and prediction near the central core was poor. The measurement of strain in the axial direction required a flight path-length greater than 60mm which resulted in noisy and inadequate data. The measured axial strain component was unreliable close to the centre.

Results shown in Figures 7.13 and 7.14 correspond to the measured residual strain and residual stress distribution in quenched cylinder bar *s39*. The correlation between the measurement and the prediction was generally good. However the measured axial component of both the strain and stress was lower than the corresponding predicted FE. The ND measurement of sample *s39* was conducted using the diffraction technique at NFL with the diffractometer REST. Note that a gauge volume of $2\times2\times2mm^3$ was used during this measurement for all the strain components. This may have contributed to a poorer measurement in the axial component where the path-length was larger. A larger gauge volume would therefore possibly improve the quality of the axial strain component.

Incremental centre-hole drilling

The measured surface compressive residual stresses in the quenched sphere *s8* appeared to be larger than predicted. The ICHD methods shown in Figure 5.2 revealed high compressive residual stresses compared to the FE results. Note the surface residual stresses measured by the ND method shown in Figure 7.2 was also higher in magnitude than predicted. There are two possible reasons for these higher than predicted near surface residual stresses. First, during quenching the surface experienced rapid cooling for a time less than about 10 s (see Figure 3.16 for temperature-time curve for a similar size quenched sphere). This suggests that the material exhibited relatively high strain rates. However, in the FE analysis conventional quasi-static yield data are used. At high strain rates the yield stresses in stainless steel are higher than under quasi-static conditions, which would lead to higher compressive residual stresses on the surface.

Secondly, the effects of elasto-plastic strain relaxation during drilling may have played a role. Elasto-plastic relaxation leads to higher relaxed strains and consequently higher measured stresses. The second reason is thought less likely as the ICHD results and the ND results were in close agreement.

9.2 Thermally relaxed residual stresses

Results for the thermally relaxed residual stresses are shown in Figures 4.16-4.18, 4.31 and 4.32 in samples *s24*, *s28* and *s29*. Sample *s24* is a quenched sphere of diameter 30mm which has been thermally aged for 3200 hours in a furnace at 550°C. Sample *s28* is a quenched cylinder of diameter 30mm and length 30mm and was thermally aged at 550°C for 1800 hours. Sample *s29* is a quenched cylinder of diameter 30mm and length 30mm and was thermal heat-treated at 550°C for 1.25 hours.

A comparison is made between the measurement and predicted FE result in Figures 7.6, 7.7, 7.16-7.18 and discussed in Chapter 7. Generally a good comparison exists. This is in particular near the central core of the specimens. However towards the outer surface the relaxation of residual strain and stress in the thermally aged specimens was not as predicted. The finite element over-predicted the thermal relaxation near the outer surface. Two potential reasons for this discrepancy in the comparison between the measurement and the prediction near the outer surface could be identified. Firstly, as discussed in Section 9.1.4 the effect of the high strain rate material data in the thermal stress analysis model may be too significant to ignore. The material near the surfaces exhibited relatively high strain rates due to greater cooling rates. At high strain rates the yield stresses are higher than under quasi-static conditions. Since quasi-static yield data are used in the FE analysis the predicted compressive residual stresses are lower near the surface. Secondly, the thermal heat-soaked specimens *s24*, *s28* and *s29* after the completion of thermal heat-treatment at 550°C in the furnace were each made to stand in the furnace (after switching off the furnace) for about 24 hours to cool to room temperature (20°C). This ensured a quasi-static cooling of the specimens to room temperature. The effect of the subsequent cooling of the thermal heat-treated specimens to room temperature was not considered in the predicted FE modelling. A good correlation between the measurements and predictions near the centre and a poor correlation towards the outer surface highlights the effect of subsequent cooling of the specimens from 550°C to room temperature to be significant near the surface in contrast to that near the centre.

Furthermore these two reasons may also be interrelated. The effect of high strain rate material data in the thermal stress analysis was not considered in the thermal stress analysis so that the predicted FE residual stress components were not as compressive as measured. This effect was imparted on to the subsequent creep analysis where the stresses relaxed proportionally. In the creep analysis the initial stress field in the FE model was that due to the quenching process with the compressive component of residual stress of lower magnitude.

9.3 Simulation of deep-hole drilling method

The close agreement between the ND measured and the predicted FE residual stress distribution in the quenched cylindrical bar validated the boundary condition and assumed material model in the FE study. In addition a large number of measurements in the residual stress measurement programme provided sufficient confidence in the characterisation of residual stress field due to quenching. Thus, the disagreement between the predicted FE residual stress distribution shown in Figure 3.6 and the distribution measured by deep-hole (DH) drilling method shown in Figure 5.8 only suggests that the use of DH technique under certain condition should be made with care. This is in particular the case with a high triaxiality such as in the quenched cylindrical bar.

9.3.1 Validation of deep-hole simulation

The work carried out in Section 6.1 on the zone-of-validity under the influence of stress triaxiality in deep-hole process was overall an important and a beneficial study and in addition was an engineering approach to provide a useful and practical solution. This study was still at an early stage and before progressing any further with the study a need to verify and validate the DH simulation was required.

Figures 7.19 to 7.29 provide comparison between the ND measured and the predicted FE residual stress distribution in quenched cylindrical bars of various sizes which were EDM pre-trepanned up to different depths. The choice of these quenched specimens was due to their well characterisation of the residual stress field via extensive previous ND measurements (see Chapter 4). The good comparison between the measurement and the prediction validated and verified the DH FE simulation. It should be noted that in the ND measurement the path along which the measurement took place was separated from the EDM trepanned gaps by quite a large margin in order to ensure

that the sampling gauge volume did not interfere with the trepan gap. During trepanning there is a zone of influence which reduces away from the trepanned edge. Therefore in order to capture the influence of trepanning on the redistribution of the initial residual stress field more precisely the sampling volume should be brought as close as possible to the trepan edge.

Implications of the validated finite element simulation

The main purpose of the neutron diffraction residual strain and stress measurements of the pre-trepanned quenched cylinders was to validate the finite element simulation of the deep hole drilling measurement process. The deep-hole finite element model was indeed validated by the close correlation between the measurement and the predicted results shown in Section 7.2. Two points may be implied from the finite element study of the deep-hole model: (a) the effect of trepanning on the stress redistribution and (b) the relaxation of residual stress in the core. The stress redistribution was sensitive to the position relative to the trepan edge so that in order to study the effect of trepanning on the stress redistribution the proximity close to the trepan edge should be done. The residual stress measurements made in pre-trepanned quenched cylinders did not reveal clearly the influence of trepanning on the stress redistribution since the measurements were made over a large volume in the specimens. Therefore in the present study the validated finite element simulation is comprehensively used to study the effect of trepanning on stress redistribution and on relaxation of residual stresses in the core.

Effect of trepanning on the stress redistribution

In order to address on the influence of stress redistribution on the deep hole measurement, it is instructive to observe the effect of trepanning process in the deep hole drilling measurement technique on the stress redistribution. The finite element model has shown to be a useful tool in such study. In Section 7.2 both measured and predicted results were discussed for quenched specimens with 25%, 50%, 75% and 100% edm depths. Measurements were made such that the centroids of the sampling volumes were at least 2.5-3.5mm clear of the drill and trepan edges. Consequently the predicted results compared with the measurements were along lines 2.5-3.5mm clear of the drill and trepan edges. However the effect of edm trepanning on the redistribution of the residual stresses is best shown along the EDM edges. This is possible by using the validated DH FE analysis.

Figure 9.1 shows the FE predicted residual stress distribution across a radial plane from the centreline towards the outer surface in a pre-trepanned quenched cylinder with variable edm depths ahead of the edm front along the trepan edge. The radial, axial and hoop components are plotted separately for clarity. The distributions in the as-quenched condition, after drilling and following edm trepan depths of 25%, 50% and 75% of the cylinder lengths are presented. The effect of drilling on the initial stress field is shown by the dotted lines (AQD). Both radial and axial stresses are relaxed due to drilling process. In contrast the hoop components rise sharply above the initial value. This sharp increase in the hoop component may however be attributed to the numerical effect observed by Mirzaee-Sisan [2004]. The effect of trepanning on the relaxed residual stresses due to drilling is shown by the dashed lines (AQDT). In general the stresses are relaxed. As expected the axial components fall to zero up to radial distance of 3.5mm from the centreline (the outer edge of the edm trepan from the centreline, see also Figure 3.19); in the edm process the material defining the thickness of the edm copper electrode is removed so that the axial stress which is normal to the removed material is zero too. The relaxation of the hoop component is interesting. Whereas the radial component rises from zero to a peak about 4mm away from the centreline and the axial component is almost zero up to 3.5mm and rises to a peak about 4mm from the centreline, the hoop component in contrast rises from zero at 0.75mm to a first peak at 1.5mm before falling to a trough at 3mm followed by a gradual rise to second peak at 4mm from the centreline.

The distributions of the redistributed residual stresses along the axial line about the EDM trepan edge are shown in Figure 9.2. The black solid line represents the stress distributions in the as-quenched cylinder. The effect of drilling on the initial residual stresses is shown by the grey line (AQD). The magnitude of the radial stress decreases due to the drilling process (Figure 9.2a). The stresses in the tensile and compressive region decrease. The hoop stress in contrast increases in magnitude (Figure 9.2c) in both tensile and compressive regions. The axial component however shows no difference (Figure 9.2b). The dashed, dashed-dotted and dotted lines represent the effect of trepanning on the stress redistribution. Edm depths of 25%, 50% and 75% of the cylinder length are represented by grey dashed, black dashed-dotted and black dotted lines respectively. As expected the radial components are zero along the trepan edges (Figure 9.2a). The axial stress initially becomes compressive of about -50MPa before increasing gradually to about 70MPa (Figure 9.2b) along the trepan edges. The hoop

stress decreases in magnitude both in the compressive and tensile regions and remain about 160MPa along the trepan edges (Figure 9.2c).

So far the redistribution of residual stresses have been studied about the EDM front and along the trepan edges. Both experimental and numerical studies have been considered. It would be interesting to see the influence of trepanning on the relaxation of residual stresses in the deep-hole core. No measurements have been performed in this study due to the requirement of fine resolution in the ND measurements. Only FE study is reviewed in the following.

Relaxation of residual stresses in the core

The hypothesis in the deep hole drilling technique demands that the stresses in the core left as a result of edm trepanning process are completely relaxed. George [2000] has shown that the smaller the core is, better the resolution is. Moreover the relaxation of stresses assumed in the theory is more representative. The residual stress distribution in the core is shown in Figure 9.3. An average stress is considered. The residual stresses are plotted for different EDM trepan depths. The influence of the trepanning on the residual stresses is illustrated. The residual stresses in the core are effectively zero up to the edm depths. Also shown are the residual stresses for complete trepan process. The stresses are all practically zero in the deep hole core.

9.3.2 Other approach to data reduction

DeWald and Hill [2003] describe an improved data reduction scheme for the deep-hole method of residual stress measurement. The new data reduction seeks to determine the unknown eigenstrain distribution that gives rise to the residual stress state and to the reference hole deformations in the deep-hole method; once the eigenstrain distribution is found, it is input to an elastic finite element analysis to provide the residual stress distribution in the original component. The new data reduction relies on expressing the unknown eigenstrain field in a polynomial basis, and finding the unknown basis function amplitudes from the measured reference hole diameter changes. DeWald and Hill compared the new data reduction with the current technique, and showed that the proposed scheme offered several advantages to the current method of data reduction.

DeWald and Hill [2003] however mainly considered the accuracy in their improved data reduction scheme for the deep-hole method of residual stress

measurement. In the elastic approach to the data reduction in the DH method a plane stress is assumed during the relaxation of strain in each blocklength during the EDM process [Bonner 1996, George 2000]. The influence of the normal component of stress during the strain relaxation is not taken into account. A method is provided by George [2000] to calculate the normal component of residual stress by considering the normal distortion measured by a capacitance gauge system from which the thermal effect of deformation is subtracted. However in this method the normal component of the stress is evaluated as an uncoupled analysis. Therefore the effect of the stress gradient in the normal direction of the component is not accounted for. The axial component of the FE predicted residual stress in the quenched cylindrical bar shown in Figure 3.6 is the principal stress component. The effect of this component in the subsequent data reduction is too significant to ignore. Therefore a general approach rather than a plane stress assumption to the deep-hole data reduction should give an appropriate solution. Furthermore, by using the CEGB FE approach described by Walker [1987], where the third (normal) component of the residual stress is evaluated as a coupled problem rather than the typical uncoupled one and takes into account the influence of normal stress component during strain relief, the evaluated three-dimensional residual stress field would be more representative.

9.4 Welded components

9.4.1 Welded nozzle component

Residual stress distribution in the welded nozzle component measured by the deep-hole drilling method are presented and discussed in Section 6.4.1. The nozzle component in the current study was thermal heat-treated at 550°C for 19,644 hours. A comparison is made between the measurement in the present study and previous measurements in the as-welded condition [George 2000] and an ex-service steam header which was aged at 525°C [Smith et al 2000] for about 55,000 hours in Figure 6.43. Compared with the as-welded case it can be seen that the thermal heat-treatment of the welded nozzle component significantly relaxed the weld residual stresses. Both the longitudinal and transverse stresses were significantly relaxed. Compared with the service-aged condition although the longitudinal stress distribution relaxed completely the transverse stress distribution only partly relaxed. However the residual stress distribution measured in both locations (Hole 1 and Hole 2) and shown in Figure 6.42 suggests that the stresses were almost equibiaxial. Moreover the residual stress

distribution in the as-welded state measured at the flank location (Hole 1) is also shown to be equibiaxial particularly near the outer surface as shown in Figure 9.4. Therefore both the longitudinal and the transverse residual stress distributions relaxed proportionally as a result of thermal heat soak at 550°C for 19,644 hours.

Based on these two observations it may be argued that the ex-service steam header with the same geometry and shape as the welded nozzle component in the present study must also have equibiaxial residual stress distribution. Therefore for the service-aged condition the transverse residual stress distribution might have over-relaxed or the longitudinal stress distribution under-relaxed. In any case a comparison between the service-aged and the as-welded condition for the same ex-service header would be helpful.

9.4.2 Welded pipe component with repair

Results of the residual stress distribution in the welded pipe component with repair are presented and discussed in Section 6.4.2. A comparison is made with residual stress distribution in a similar stainless steel (Esshete 1250) repair [Bouchard 2003] predicted by a previous 3D FE [Elcoate et al 2003] in Figure 6.50. The comparisons between the measurement and the prediction were generally good. However towards the outer surface of the welded pipe component the deep-hole measurement did not reveal the peak tensile residual stress predicted by the FE.

Prior to the measurement an extensive FE study was carried out to model the DH process in the welded pipe component with repair. This study is discussed in detail in Section 6.3. The study illustrated the influence of the DH process on the residual stress distribution initially present in the component. Similar to the measurement the reconstructed residual stress distribution also did not reveal the initial peak tensile residual stress towards the outer surface of the welded pipe component as shown in Figures 6.36 and 6.38. The study also illustrated the effect of the material hardening models. Both the initial and the reconstructed residual stress distributions were sensitive to the material hardening behaviour.

Firstly, it can be seen that based on the non-linear kinematic hardening model the level of the initial residual stress distribution was lower than that with elasto-plastic and linear hardening models as illustrated in Figures 6.36 to 6.38. The measured residual stress distribution was much lower than that predicted by FE. It is anticipated that using a combined hardening model in the FE study will be more representative of the initial

residual stress field in the welded pipe model. Secondly, the reconstructed residual stress distribution shown in Figure 6.37 was very similar to the initial distribution when assuming a hardening model for the repair and girth weld material identical to the parent material. However an elasto-plastic model was assumed for the repair and girth weld material in the BEGL-FNC model to simulate the initial as-welded residual stress field. Therefore using a linear hardening model for the weld material as in Figure 6.37 would result in an inconsistent plastic strain when the initial residual stress and plastic strain fields in BEGL-FNC model are mapped on to the BU model.

The measured residual stresses compared very well with the FE predicted residual stresses mapped from the BEGL-FNC model shown in Figure 6.51. The FE however over predicted the longitudinal component of the residual stress. Furthermore the measured longitudinal component compared better with FE to some extent after considering the effect of deep hole drilling on the initial residual stresses (Figure 6.52).

9.5 Quantification of creep damage

A number of specimens with internal residual tensile stress of high triaxiality were generated by rapid-spray water-quenching process. A selected number of the quenched specimens were thermal heat-treated for a set period of time in a furnace at 550°C to study creep formation. Other set of specimens used in the creep study included the side-punched C(T) specimens with a triaxial residual stress field of variable triaxiality and plasticity generated by single, double and figure-of-eight punch deformations.

9.5.1 Metallography

Most of the stainless and high-temperature alloys contain iron as their major component and structurally show the familiar phases, ferrite, austenite and carbide. Austenitic structures in the annealed state offer considerable difficulty in metallography. Surface flow occurs during ordinary polishing and localised transformation along scratches or other sites of more severe flow greatly alter the appearance of the structure. Electrolytic polishing of these steels is particularly desirable since these minimise these effects.

9.5.2 Influence of prior strain

In the thermally aged quenched cylinder, sample *s17* shown in Figure 8.10 no optical evidence of cavitation damage was present as might be expected. Figure 8.10

shows the micrographs of a sectioned quenched and aged cylinder, *s17* after etching. The dark shaded rounded regions running through the grain boundaries are possibly manganese sulphides and not micro-cracks. To observe any possible cavitation of less than ½ μm scale, either an electron microscope or small angle neutron scattering (SANS) technique needs to be used. However the creep model based on two empirical constants in the creep subroutine predicts the initiation of creep in the time-scale of 2880 and 4330 hours for each empirical constant. The creep subroutine does not consider the plasticity and uses only the triaxiality in calculating creep initiation.

It was hypothesised that the driving force for the initiation of creep damage formation is not only the triaxiality but also prior plasticity is a prerequisite. By using punched C(T) specimens described in Section 3.3 it was possible to generate residual tensile stresses in the specimen with variable triaxiality and strain in a controlled way. Both single [Mahmoudi et al 2003a] and double [Mahmoudi et al 2004] punch was considered. The purpose of the double punch was to remove the imprint from the vicinity of the notch. By punching away from the notch tip, no plastic strain is accumulated at the notch tip. This test therefore discriminated between the influence of prior plastic strain in the creep cavity initiation sites and the absence of prior plasticity. The creep model predicted a large zone of damage as shown in Figure 8.6 for the double punch case with a short time of initiation shown in Figure 8.6(a). In contrast for the single punch case where the level of triaxiality was lower the zone of predicted creep was much lower as shown in Figure 8.5. Moreover Figure 8.8 (a) shows that much longer exposure time (~20 years) is needed for initiation of creep damage in single punch specimens. Based on the initial work of Mahmoudi et al [2003a, 2004] on the effect of size and position of the punch on the development of residual stresses, where the position x/R=1 (see Figures 3.21 and 3.27) was shown to provide the maximum tensile region ahead of the crack tip, a third type of punching tool was designed and manufactured in the present study known as "figure-of-eight" punch shown in Figure 3.29. For this punching case a large plasticity was present without compromising the triaxiality. It was anticipated that the presence of both the plasticity and the triaxiality would result in creep formation in practice as was predicted by FE shown in Figure 8.7. The experimental study of the side punch test (Section 3.4) was carried out by side punching a selected number of C(T) specimens using single (Figure 3.28a), double (Figure 3.28b) and figure-of-eight (Figure 3.29) punch tools with applied displacement of 0.5mm on each surface of the specimen. For this loading condition, predicted

triaxiality factor and predicted equivalent plastic strain near the vicinity of crack tip (averaged over a region of 0.12mm from the crack tip) in each specimen provided in Table 3.4 may be summarised as follows.

	TF	PEEQ
SP	0.57	0.18
DP	1.85	0.06
FOE	0.92	0.19

The level of triaxiality was highest in the double punch specimen followed by figure-of-eight and then single punch. Based on the level of triaxiality the predicted damage shown for the case of double punch was highest (Figure 8.6b compared to Figure 8.7b) and the damage initiation time was lowest in double punch as shown in Figure 8.8(b) compared to Figure 8.8(c). Since the level of triaxiality was low for the case of single punch very limited damage zone was predicted (Figure 8.5). In contrast in the figure-of-eight punch the level of triaxiality was not as low as in the case of single punch and hence a sufficiently large zone of predicted damage shown in Figure 8.7 though the extent of predicted damage in figure-of-eight punch was lower than double punch as discussed in Section 8.2.2.

From the fractography study discussed in Section 8.3.2 it was concluded that the extent of creep cavitation was greater in figure-of-eight punch specimen than that in double punch specimen. The trend of this findings therefore point towards the hypothesis of the importance of prior plasticity in addition to the presence of triaxiality as prerequisite for creep cavitation. Although the level of plasticity in the double punch specimen was lower compared to the single and figure-of-eight punch specimens but was still sufficient to create cavitation as observed in the fractography study. Moreover in the case of quenched cylinder where the level of triaxiality was very high (about 4.25 shown in Figure 3.5) the level of plasticity shown in Figure 6.12 was very low (zero). This finding further reinforce the above hypothesis on the importance of prior plasticity.

Mismatch of loading

Generally the load predicted by FE required to side-punch the C(T) specimens was similar to that in practice. A slight difference in the loads however existed since in the FE simulation it was assumed that the punching tool was analytic rigid body whereas in reality the punching tool was deformable to some degree. Nevertheless because the punching tool was heat-treated and hardened significantly the rigid-body assumption in the FE study was still valid. Moreover the indentation measured

compared very well with that predicted by FE. This was true for both the single and figure-of-eight punch shapes. For the double-punch case however the indentation measured was much lower than that predicted by FE. One possible and likely reason is as follows. The load required to imprint the specimen with double-punch tool was predicted to be about 430kN. The specimens were side-punched using the Meyes test rig with a 500kN maximum load capacity. Therefore there was a possibility that during loading the grips were slipping as the applied load was very close to the maximum. This is evident from the comparison between the indentation in the double-punch specimen measured and that predicted by FE as shown in Table 3.6.

Chapter 10

Conclusions and Recommended Further Studies

10.1 Summary

In this thesis the numerical and experimental study of method of generating residual stress in laboratory specimens were presented. The finite element (FE) analysis used in the numerical study was validated with experimental characterisation of residual stress field in the specimens. Two novel means of generating highly triaxial residual stress fields in laboratory specimens, consisting of rapid spray water quenching of solid cylinders and spheres and side punching of C(T) specimens, were identified and followed by design and manufacture. A comprehensive FE study modelling the deep hole (DH) drilling process was carried out to understand further the influence of DH process on the residual stress field.

10.2 Conclusions

Two approaches consisting of quenching and side punching to generating residual stress of high triaxiality were studied using the finite element (FE) analysis. An extensive FE study provided with an optimum design of specimens and process conditions generating a residual stress field with sufficiently high triaxiality. Novel quenching and side punching stress generation techniques were experimentally studied. The specimens with the residual stress field were thermally aged at 550°C for a selected period to study creep formation.

An extensive study of residual stress measurement in the quenched and side punched specimens before and after thermal heat treatment was carried out. The residual stress distribution measured by neutron diffraction (ND) and incremental centre-hole drilling (ICHD) methods well characterised the specimens and a comparison with the finite element study further validated the FE analyses.

The evidence of creep cavitation in the thermally aged quenched specimens was not present as its location and size were predicted by the creep model. A hypothesis was proposed where creep formation would be initiated in the presence of both the triaxiality and the prior plastic strain. By varying the position of punching relative to the notch in

the C(T) specimens the test specimen with variable levels of triaxiality and plasticity was obtained in a controlled manner. Three types of side punching was studied both numerically and experimentally: single punch with low triaxiality and high plastic strain, double punch with high triaxiality and low plastic strain, and "figure-of-eight" punch with high triaxiality and high plasticity. From a fractography study the scanning electron micrographs of the crept C(T) specimens revealed the presence of creep cavitation. The FE simulation however over predicted the size of creep damage.

The mechanical strain relief deep-hole (DH) drilling method used to measure residual stress distribution in quenched specimens highlighted a potential problem in using the simple elastic approach to data reduction in the DH measurement method. A comprehensive FE study modelling the DH process was carried out in order to further study the influence of DH process on the residual stress field using a simple geometric model under a simple loading case

A detailed FE study on modelling the DH process using elasto-plastic analysis and an incremental trepanning process in contrast to an elastic analysis with a single-step trepanning by George [2000] illustrated the effect of DH process on the initial residual stress field. The reconstructed residual stress distribution following the DH FE analysis also compared well with the DH measured residual stress distribution in the quenched cylinder. The DH simulation of the repair weld revealed the effect of cutting in the DH process on the initial residual stress distribution to be not as significant compared to the quenched cylinder case. In the DH FE study of the repair welded pipe three material models were considered and the result was found to be highly influenced by the material model selected. The DH technique was consequently utilised in characterising the residual stress distribution in practical components consisting of a welded nozzle component that was thermally aged at 550°C for 19,644 hours and a pipe with repair weld.

The thermal heat treatment of the nozzle component significantly reduced the weld residual stresses as measured by George [2000]. The measured through-thickness residual stress distribution in the repair welded pipe generally compared well with the predicted FE with the exception of losing the peak stress predicted by FE for the longitudinal component and some degree of discrepancy between the measurement and prediction towards the inner surface of the pipe for both longitudinal and transverse components.

10.3 Recommended Further Study

3D general approach to data reduction in DH process

In light of the arguments presented in Section 9.3.2 with regards to the approach to the data reduction in deep-hole (DH) process a more general approach such as the CEGB FE approach described by Walker [1987], where the third (normal) component of residual stress is evaluated as a coupled problem and takes into account the effect of normal stress component during strain relief, would be expected to provide a better solution for the case where the normal component of the residual stress is sufficiently high. This approach may also be suitable for a case with high triaxiality.

Plane strain assumption

Before using a more complex general CEGB FE approach [Walker 1987] the data reduction of the deep-hole process can proceed with a plane strain assumption and evaluate the effect on the residual stress distribution in the quenched cylindrical bar shown in Figure 6.11.

Study of validity zone

The results obtained to date cannot be used to draw any conclusion. More work is needed before establishing a relation between the triaxiality factor and the zone of validity. The effect of the size of the block needs to be considered by carrying out the same finite element analyses on the 3D block with the same order of applied loadings but of various dimensions as future consideration.

Deep-hole simulation of welded pipe with repair

Comparing the residual stress distribution in the welded pipe component with repair measured by the deep-hole drilling technique with that predicted by FE shows that the FE over-predicts the stresses. Moreover it was found that the deep-hole reconstructed residual stress distributions were very sensitive to the material hardening model. Therefore the use of a combined hardening model to represent the measured residual stress fields more closely for further studies is recommended.

Generic deep-hole simulation for practical components

An exhaustive finite element (FE) analysis modelling the influence of cutting process in the deep hole drilling technique on the redistribution of original residual

stress present in a repair welded component was carried out as described in Section 6.3. Using a 3D model the deep hole simulation was carried out specifically on the repair welded pipe component. The deep hole measured residual stress results in a practical component are important in the structural integrity assessment. Equally important therefore is the FE result of the influence of trepanning process on the original FE predicted residual stress state present in the component. Therefore a more generic and versatile approach to the present deep hole simulation model would be a useful and effective tool to assess any influence of deep hole drilling on future measurements. For example the drilling, the core and the trepanning parts may only be modelled. By using appropriate loads and boundary conditions on this model the effect of original residual stress present in the whole practical component can then be modelled. Finally the deep hole can be simulated on the new model.

References

Aksel, B., "Analysis of stress and displacement fields generated during quenching and casting", PhD Thesis, Cornell University,USA. 1990

Aksel, B., Arthur, W.R., Mukherjee, S., "A study of Quenching: Experiment and modelling", Journal of Engineering for Industry, 114, pp. 309-316, 1992.

American Society for Testing and Materials ASTM, E1820, 2001.

American Society for Testing and Materials ASTM, E139, 1983.

American Society of Metals ASM, Metals handbook, vol. 3: "Properties and selection", 9th edition, 1980.

Anderson, J.C., Leaver, K.D., Rawlings, R.D. and Alexander, J.M., "Materials Science", Fourth Edition, Chapman and Hall, 1990.

Andrade, E.N. da C., "The viscous flow in metals and allied phenomena", Proc. Roy. Soc. Ser. A, 84: 1, 1910.

Ashby, M.F., Gandhi, C., Taplin, D.M.R., "Fracture-mechanism maps and their construction for F.C.C. metals and alloys", Acta Metallurgica, 27, pp. 699-729, 1979.

Baikie, B.L., Bradford, R.A., Hales, R., Miller, D.A., Spindler, M.W. and Stevens, R.A., "Reheat cracking in austenitic stainless steels - current status of understanding", Technical Report EPD/AGR/REP/0346/97, British Energy Generations Ltd, Gloucester, UK, 1997.

Bainbridge, A.T., "Residual stresses arising from machining and fabrication", AGARD Conf. Proc. No. 53, Symposium on Eng. Practice to Avoid SCC, Istanbul, Turkey, pp. 8-21, 1969.

Baldwin, W.M. Jr., "Residual Stresses in Metals", Proc. ASTM, 4a: 539, 1949.

Barret, C.R. and Nix, W.D., "A model for steady state creep based on the motion of jogged screw dislocations", Acta Metallurgica, 13, pp. 1247-1258, 1965.

Beaney E. M., "Measurement of sub-surface stress", Central Electricity Generating Board (CEGB) Report No. RB/B/N4325, July 1978.

Becker, A.A., Hyde, T.H., Sun, W., Andersson, P., "Benchmarks for finite element analysis of creep continuum damage mechanics", Computational Materials Science 25, pp. 34–41, 2002.

Becker, R., Karabin, M.E., Liu,J.C.,Smelser,R.E., "Distortion and residual stress in quenched Aluminum bars", Journal of applied mechanics,63, pp. 699-705,1996.

Bonner N.W. and Smith D.J., "Measurement of residual stresses in a thick section steel weld", Proc Int. Conf. on Engineering Integrity Assessment, Engineering Materials Advisory Services Ltd., pp. 259-274, 1994.

Bonner N.W., "Measurement of residual stresses in thick section steel welds", PhD Thesis, University of Bristol, 1996.

Boresi A.P., Schmidt R.J., Sidebottom O.M., "Advanced mechanics of materials", 5th Edition, New York; Chichester: Wiley & Sons, inc., 1993.

Bouchard P.J., British Energy Generations Ltd, Private Communications, 2004.

Bouchard, P.J., British Energy Generations Ltd, Private communication, 2003.

Bouchard, P.J., British Energy Generations Ltd, Private communication, 2001.

Bradford, R.I., "Finite element modelling of reheat cracking initiation in austenitic weldaments. In Assuring It's Safe", I. Mech. E. Conference Transactions, pp. 287-295, London, 1998.

Brick R.M., Pense A.W., Gordon R.B., "Structure and properties of engineering materials", McGraw-Hill Publishing Company, 1977.

British Standard, Annex D, BS7448: Part 2: 1997.

British Standard Institute BSI, BS3500: Part 6: 1987.

Cadek, J., "Creep in Metallic Materials", New York: Elsevier, 1988.

Chaboche, J.L., Continuum damage mechanics: Part 1, General concepts, J. Appl. Mech. 55, pp.59–64, 1988.

Cherouat A., Montay G., Lu J., "Study of residual stresses in complex parts by experimental and numerical methods", Mater. Sci. Forum 404-407, pp. 251-256, 2002.

Cotton, Christopher C., "A Candidate Test-Piece To Investigate Creep Crack Growth In A Residual Stress Field", MSc Thesis, Structural Integrity, Department of Mechanical and Process Engineering, University of Sheffield, 1997.

Davis, J.R., (Ed.), Metals Handbook, (American Society for Metals, Metals Park, Ohio), 1984.

Daymond M.R., Bourke M.A.M., Von Dreele R.B., Clausen B., Lorentzen T., "Use of Rietveld refinement for elastic macrostrain determination and for evaluation of plastic strain history from diffraction spectra", J. Appl. Phys. 82 (4), pp. 1554-1562, 1997.

de Novion C.H., "The use of neutrons for materials characterisation", *Analysis of Residual Stress by Diffraction using Neutron and Synchrotron Radiation*, Chapter 1, pp. 3-27, Taylor and Francis, London, 2003.

DeWald A T and Hill M R, "Improved data reduction for the deep-hole method of residual stress measurement", J. Strain Analysis Vol. 38 No. 1, pp. 65-78, 2003.

Dhooge, A., "Survey on reheat cracking in austenitic stainless steels and Ni base alloys", Welding in the World, 41, pp. 206-219, 1998.

Dieter, G.E., "Mechanical Metallurgy". McGraw-Hill series in Materials Science and Engineering. McGraw Hill, 3rd edition, 1986.

Dorn, J.E., "Progress in understanding high-temperature creep", H.W. Gillet Mem. Lecture. Philadelphia, Pa.: ASTM, 1962.

Edwards L., "Near-surface stress measurement using neutron diffraction", *Analysis of Residual Stress by Diffraction using Neutron and Synchrotron Radiation*, Chapter 14, pp. 233-248, Taylor and Francis, London, 2003.

Elcoate C.D., Dennis R.J., Bouchard P.J., Smith M.C., "3 Dimensional repair weld simulations-bead sequencing studies", PVP-Vol. 479, San Diego, PVP2004-2643, 2004.

Elcoate, C.D., Dennis, R.J., Bouchard, P.J., Smith, M.C., "3-Dimensional repair weld simulations", Proc. 2nd Int. Conf. on Integrity of High Temperature Welds, IoM Communications, London, pp. 207-215, 2003.

Ericsson T. and Hildenwall B., "Thermal and Transformational Stresses", 28th Sagamore Army Materials Research Conf., pp 19-38, 1981.

Ezeilo A. N. and Webster G. A., "Neutron diffraction analysis of the residual stress distribution in a bent bar", J. Strain Analysis, 35-4, pp. 235-246, 2000.

FEAT, Version 3.4.0, Finite Element Analysis Toolbox User Guide, Serco Assurance, Harwell UK, 2002.

Fletcher A.J. and Price R.F., "Generation of thermal stress and strain during quenching of low-alloy steel plate", Metals technology, pp. 427-446, 1998.

Furtado H.C. and Le May I., "High temperature degradation in power plants and refineries", Materials Research, 7 (1), pp. 103-110, 2004.

Gandy D.W., Findlan S.J. and Viswanathan R., "Weld repair of steam turbine casings and piping – an industry survey", ASME J. Pres. Ves. Techn. 123, pp. 157-160, 2001.

Garcia Granada, A.A., George, D. and Smith, D.J., "Assessment of distortions in the deep hole technique for measuring residual stress". In Proceedings of the 11th Conference on Experimental Mechanics, Oxford, pp.1301-1306, 1998.

Garofalo, F., "Fundamental of creep and creep rupture in metals", New York: MacMillan, 1965.

Garofalo, F., Richmond, O., Domis, F.W. and von Gemmingen, F., "Strain-time, rate-stress, and rate-temperature relations during large deformations in creep", In Joint International Conference On Creep, Institute of Mechanical Engineering, London, pp. 1-31, 1963.

George D., Kingston E., Smith D.J., "Measurement of through-thickness stresses using small holes", J. Strain Analysis, 37(2), pp. 125-139, 2002.

George D., Kingston E., Smith D.J., "Residual Stress Measurement in Thick Section Components", PVP Vol. 410-1, pp. 275- 282, 2000.

George, D.B.F and Smith D.J., "Determination of Residual Stresses in Large Section Weldments", IMC Contract PC/GNSR/5051, Final Report, 2000.

George, D.B.F. "Determination of Residual Stresses in Large Section Stainless Steel Welds", PhD Thesis, University of Bristol, 2000.

Gladwin, D, BNFL Magnox, Private Communications, 2005.

Greenfield, P., "Creep of metals at high temperatures", Mills and Boon Limited, London, 1972.

Gür, C.H., Tekkaya, A.E., Schuler, W., Steel Res. 67 (11), pp. 501-506, 1996.

Gür C.H., Tekkaya A.E., J. Mech. Behav. Mater. 9 (4), pp. 237-256, 1998.

Hales, R., "A method of creep damage summation based on the accumulated strain for the assessment of creep fatigue endurance", Fatigue and Fracture of Engineering Materials and Structures, 6, pp. 121-135, 1983.

Hayhurst, D.R., "Creep rupture under multi-axial states of stress", Journal of the Mechanics and Physics of Solids, 20, pp. 381-390, 1972.

Heming Cheng, Xieqing Huang, Honggang Wang, "Calculation of the residual stress of a 45 steel cylinder with a non-linear surface heat-transfer coefficient including phase transformation during quenching", Journal of Materials Processing Technology 89-90, pp. 339-343, 1999.

Hibbit, Karlsson and Sorenson HKS Inc., 1080 Main Street, Pawtucket, RI 02680-4847, USA, ABAQUS v. 6.3, 2002.

Hibbit, Karlsson and Sorenson HKS Inc., 1080 Main Street, Pawtucket, RI 02680-4847, USA, ABAQUS v. 6.2, 2001.

Hibbit, Karlsson and Sorenson HKS Inc., 1080 Main Street, Pawtucket, RI 02680-4847, USA, ABAQUS v. 5.8, 1998.

Holden T.M., Roy G., "The application of neutron diffraction to the measurement of residual stress and strain". In Handbook of Measurement of Residual Stresses, (1996) pp. 133-148 (Society for Experimental Mechanics, New York) (Fairmont Press and Prentice-Hall, Englewood, Cliffs, New Jersey).

Holt, P.J., "Prediction of Reheat Crack Initiation by Continuum Damage Mechanics incorporated in Finite Element Creep Analysis", Nuclear Electric Report EPD/AGR/REP/0005/96, 1996.

Holt, P.J., and Spindler, M.W., "A practical application of continuum damage mechanics to plant integrity assessment", In Inelasticity and damage in solids subject to microstructural change, Canada, 1996.

Hossain, S., Daymond, M.R., Truman, C.E., Smith, D.J., "Prediction and measurement of residual stresses in quenched stainless-steel spheres", Materials Science and Engineering A 373, pp. 339-349, 2004.

Hossain S., Mahmoudi A.H., Smith D.J., Stefanouscu D., Truman C.E. and Withers P.J., "European Synchrotron Radiation Facility, ESRF Report", ME622, 2004a.

Hossain S., Smith D.J. and Truman C.E., "IMC Progress Review", PC/GNSR/5051, Contract Reference BWD 40033000, 2004b.

Hossain S., Truman C.E., Smith D.J., "Measurement of stress redistribution caused by plasticity", NMI3 Experimental Report at NFL, 2004c.

Hossain S., Truman C.E., Smith D.J., "Triaxial Residual Stress Measurement in Quenched Steel Spheres", ISIS Experimental Report at Rutherford Appleton Laboratory, RB12398, 2001.

Hossain S., Truman C.E., Smith D.J., "Triaxial Residual Stress Measurement in Quenched and Thermally Aged Stainless Steels", ISIS Experimental Report at Rutherford Appleton Laboratory, RB 13472, 2003.

Hossain S., Truman C.E., Smith D.J., Daymond M.R., "Creating highly triaxial stresses in stainless steel", OS12W0072, ATEM'03, JSME-MMD, Nagoya, Japan, 2003.

Hossain S., Truman C.E., Smith D.J., Daymond M.R., "Creating highly triaxial residual stresses in a type 316H stainless steel", submitted to International Journal of Mechanical Sciences, 2004d.

Hossain, S., Truman, C.E., Smith, D.J., Daymond, M.R., "Creating Highly Triaxial Residual Stresses and Relaxation of the Stress Field due to Thermal Ageing", Journal of Neutron Research, Vol. 12 (1-3), pp. 111–115, 2004e.

Huddleston, R.L., "An improved multiaxial creep-rupture strength criterion". ASME Journal of Pressure Vessel Technology, 107, pp. 421-429, 1985.

Hyde, T.H., Sun, W., Becker, A.A., "Creep modelling of welds using continuum damage mechanics analysis", in: W.J. Evans, R.W. Evans, M.R. Bache (Eds.), Proceedings of the First International Conference on Component Optimisation, Component Optimisation from Materials Properties and Simulation software, EMAS Ltd, West Midlands, pp. 219-226, 1999.

International Standards Organisation ISO, DIS9513: 1987.

Johnson M.W. and Daymond M.R., "Neutron pulsed source instrumentation", *Analysis of Residual Stress by Diffraction using Neutron and Synchrotron Radiation*, Chapter 9, pp. 146-169, Taylor and Francis, London, 2003.

Kachanov, L.M., "On creep rupture time", Proc. Acad. Sci., USSR Div. Engng. Sci. 8, pp. 26-31, 1958.

Kandil F.A., Lord J.D., Fry A.T. and Grant P.V., "A Review of Residual Stress Measurement Methods - A Guide to Technique Selection", NPL Report MATC(A)04, 2001.

Keller, H.P., Kerkoff, H., Giffeler, R. and Meinhardt, J., "Residual Stresses and Their Influence on the Integrity of Pressure Vessels", TUV Rheinland Institute for Material Testing, Report No. SB 203/89, Dec. 1989.

Kingston, E.J., "Advances in the deep-hole drilling technique for residual stress measurement", PhD Thesis, University of Bristol, 2004.

Kutateladze S.S. and Borishanskii V.M., "A Concise Encyclopaedia of Heat Transfer", Pergamon Press, 1966.

Lagneborg, R., "Development and refinement of the recovery creep theory", Metal Science Journal, 3, pp. 161-168, 1969.

Landau H.G., Weiner J.H., Zwicky JR. E.E., "Thermal Stress in a Viscoelastic-Plastic Plate with Temperature-Dependent Yield Stress", Journal of Applied Mechanics, pp. 297-302, June 1960.

Landau, H.G., and Weiner, J.H., "Transient and residual stresses in heat-treated plates", Journal of Applied Mechanics, 25, pp. 459-465, 1958.

Leckie, F.A. and Hayhurst, D.R., "Creep rupture of structures", Proc. R. Soc. London A 340, pp. 323-347, 1974.

Lim, W.K., Song, J.H. and Sankar, B.V., "Effect of ring indentation on fatigue crack growth in an aluminium plate", International Journal of Fatigue, 25, pp. 1271-1277, 2003.

Littmann W E, "Measurement and significance of residual macrostress in steel", SAE 793A, Proc. of the Automatic Eng. Cong., Detroit, MI, pp. 13-17, January 1964.

Loveday, M.S., "Creep Testing. In Mechanical Testing", (I. Curbishley, ed.). London: Inst. of Metals, Chapter 2, 1988.

Macherauch, E. and Kloos, K.H., "Origin, Measurement and Evaluation of Residual Stresses", Residual Stresses in Science and Technology, Vol. 1, ISBN 3-88355-099-X, pp. 3-26, 1986.

Mackerle,J., "Finite element analysis and simulation of quenching and other heat treatment processes-A bibliography (1976-2001)", Computational Material Science,27, pp 313-332, 2003.

Mahmoudi, A.H., "Influence of residual stresses on fracture", PhD Thesis, University of Bristol, 2005.

Mahmoudi, A.H., Stefanescu, D., Hossain, S., Truman, C.E., Smith, D.J., Withers, P.J., "Measurement and prediction of the residual stress generated by side-punching", submitted to Materials Science and Engineering A, 2005.

Mahmoudi, A.H., Hadidi-Moud, S., Truman, C.E., Smith, D.J., "A Numerical and experimental investigation into the generation of residual stress in fracture specimens using local compression", The 15th European Conference of Fracture, ECF15, Sweden, 2004.

Mahmoudi, A.H., Hadidi-Moud, S., Truman, C.E., Smith, D.J., "Influence of residual stress on the fracture behaviour of aluminium alloy", Int. Conf. Mech. Eng., ISME, Iran, 2003.

Mahmoudi, A.H., Hadidi-Moud, S., Truman, C.E., Smith, D.J., "Measurement and prediction of residual stress generated by local compression", 5th European Solid Mechanics Conference, edited by E.C. Aifantis, Giapoulis Publishers, Thessaloniki, 2003a.

Manjoine, M.J., "Ductility indices at elevated temperature", ASME J. Engng Mater Technol. April, pp. 156-161, 1975.

Marshall, P., "Austenitic stainless steels: Microstructure and mechanical properties". Elsevier applied science publishers, London 1984.

Mather J., "Determination of Initial Stresses by Measuring Deformation around Drilled Holes", Trans. ASME, Vol. 56 (No. 4), pp. 249-254, 1934.

Mayr P., "Dimensional Alteration of Parts Due to Heat Treatment", Residual Stresses in Science and Technology, Vol. 1, pp 57-77, 1987.

Mckenzie,A. C., Moakler,M., "On the relaxation of residual stress fields by thermal relief", Proceeding of 2nd International conference of pressure vessel technology, San Antonio, pp. 1167-1178, 1973.

McLean D., "The physics of high temperature creep in metals", *Reports on progress in Physics*, Metallurgy Division, National Physical Laboratory, Teddington, Middlesex, pp.1-33, 1966.

Meith, W.A. and Hill, M.R., "Domain-independent values of the J-integral for cracks in three-dimensional residual stress bearing bodies", Engineering Fracture Mechanics 69, pp. 1301-1314, 2002.

Meith, W.A., Panontin, T.L., Hill, M.R., "Analytical and experimental study of fracture in bend specimens subjected to local compression", Fatigue and Fracture Mechanics, 33, ASTM STP 1417, 2002.

Mirzaee-Sisan A., Mahmoudi A.H., Truman C.E. and Smith D.J., "Application of the Local Approach to Predict Load History Effects in Ferritic Steels", In Proceedings of PVP, Denver, Colorado, 2005.

Mirzaee-Sisan, "Effect of tensile residual stresses on brittle fracture", Abaqus UK User Conference, Warrington, UK, 2004.

Mitsui Babcock Report, 316 Girth Weld with offset Repair for British Energy Generation Ltd, TR022/2002, 2002.

Mukai, R., Ju, D.Y., Minakawa,N., Morii,Y.,Moriai, A. and Hanabusa, T., "Residual stress measurement of the quenching material by neutron diffraction", ATEM'03, JSME-MMD, Sep.10-12, 2003.

Nabarro, F.R.N. and de Villiers, H.L., "The physics of creep". Taylor and Francis, London, 1995.

Noyan I.C. and Cohen J.B., "Residual Stress, Measurement by Diffraction and Interpretation", Springer-Verlag, New York, 1987.

Noyan, I.C. and Cohen, J.B., "The nature of residual stress and its measurement", Residual Stress and Stress Relaxation, ISBN 0-306-41102-4, pp. 1-17, 1981.

Parlane A.J.A., "Origin and nature of residual stresses in welded joints", TWI Report, Residual stresses and their effect, ISBN 0-85300141-3, pp 1-4, 1981.

Phillips, F., "The slow stretch in India rubber, glass and metal wire when subjected to a constant pull", Phil. Mag., 9: 513, 1905.

Pintschovius L., "Neutron diffraction using a constant wavelength", *Analysis of Residual Stress by Diffraction using Neutron and Synchrotron Radiation*, Chapter 8, pp. 133-145, Taylor and Francis, London, 2003.

R5, "Assessment Procedure for the High Temperature Response of Structures", Issue 3, British Energy, Gloucester, UK, 2001.

R66, "AGR Materials Data Handbook", Issue 5, British Energy Maintained Document, 1999.

R66, "AGR Materials Handbook", Issue 3, Nuclear Electric.

RCC-MR, "Design and Construction Rules for Mechanical Components of FBR Nuclear Islands", Section 1, Sub-Section Z, Technical Appendix A3, AFCEN, Paris, 1985.

Rice, J.R. and Tracey, D.M., "On ductile enlargement of voids in triaxial stress fields", J. Mech. Phys. Solids, **17**, pp. 201-217, 1969.

Rietveld H.M., *J. Appl. Crystallogr.*, **2**, 65-71, 1969.

Schajer G.S., "Measurement of Non-Uniform Residual Stresses Using The Hole Drilling Method, Part I – Stress Calculation Procedures", Journal of Engineering Materials and Technology, Vol. 110, pp. 338-343, 1998.

Schajer G.S., "Measurement of Non-Uniform Residual Stresses Using The Hole Drilling Method, Part II –Practical Application Of The Integral Method", Journal of Engineering Materials and Technology, Vol. 110, pp. 344-349, 1998a.

Sedighi, M. and McMahon, C.A., "The influence of quenchant agitation on the heat transfer coefficient and residual stress development in the quenching of steels", In Proc. Instn Mech Engrs Vol 214 Part B, pp. 555-567, 2000.

Sen S., Aksakal B., Ozel A., "Transient and residual thermal stresses in quenched cylindrical bodies", International Journal of Mechanical Sciences 42, pp. 2013-2029, 2000.

Sherby, O.D. and Burke, P.M., "Progress in Materials Science", 13:325, 1968.

Shield, R.T., "On the plastic flow of metals under conditions of axial symmetry", Proceedings Royal Society of London, Series A Maths & Phys, A233, 267, 1955.

Skelton, R.P., Goodall, I.W., Webster, G.A. and Spindler, M.W., "Factors affecting reheat cracking in the HAZ of austenitic steel weldaments", International Journal of Pressure Vessels and Piping, 80, pp. 441-451, 2003.

Smith D.J. and Bonner N.W., "Measurement of residual stresses using the deep hole method", PVP Vol. 327, pp. 53- 65, 1996.

Smith D.J., Bouchard P.J., and George D., "Measurement and prediction of residual stresses in thick section steel welds", J. Strain Analysis, Vol. 35, No.4, pp. 287-305, 2000.

Smith D.J., Hossain S., "Measurement of residual stresses in a type 316H stainless steel offset repair in a pipe girth weld", BWD 40033000, British Energy External Report, 2003.

Smith, M., British Energy Generations Ltd, Private Communication, 2004.

Spindler, M. W., British Energy Generations Ltd, Private Communication, 2005.

Spindler, M.W., "The multiaxial creep ductility of austenitic stainless steels", Fatigue Fract Engng Mater Struct 27, pp. 273-281, 2004.

Spindler M. W., "The multiaxial and uniaxial creep ductility of Type 304 steel as a function of stress and strain rate", Materials at High Temperatures, Vol.21 No.1, pp.47–52, 2004a.

Tabuchi, M., Yagi, K. and Ohba, T., "Characterisation of creep crack growth behaviour of 316 stainless steel in terms of microscopical fracture mechanism", ISIJ International, 30 (10), pp. 847-853, 1990.

Tech Note TN-503-5, "Measurement of Residual Stresses by the Hole-Drilling Strain Gage Method", Measurements Group, Inc., Hampshire, RG24 8FW, UK, 1993.

Tipping D., British Energy Generation Limited, Personal Communications, 2004.

Towers, O.L., Robinson, P., The Welding Institute Research Bulletin, 23(4), 1982.

Turski, M., "High temperature creep cavitation cracking under the action of residual stress in 316H stainless steel", PhD Thesis, University of Manchester, UK, 2004.

Turski, M., Sherry, A.H., Bouchard, P.J. and Withers, P.J., "Residual Stress Driven Creep Cracking in Type 316 Stainless Steel", Journal of Neutron Research, Vol. 12 (1–3), pp. 45–49, 2004.

Vicat, L.J., Note sur l'allongemont progressif du fil de fer soumis à diverses tensions, Ann. ponts et chausées, Mem. et Doc. 7(1):40, 1834.

Walker, J., "Development of the Elasticity Matrix Used in Deep Hole Residual Stress Measurement", CEGB Report No. TPRD/B/0895/R87, Unrestricted, March 1987.

Wang, D. and Edwards, L., "Precise determination of specimen surface position during near-surface strain scanning by neutron diffraction", Proceedings of the 4th European Conference on Residual Stresses, eds., Denis, S et al., Société Française de Métallurgie et de Matériaux, 1, pp. 135-144, 1998.

Webster, G.A., "Role of residual stress in engineering applications", Mater. Sci. Forum, 347, pp. 1-9, 2000.

Webster, G.A. and Ainsworth, R.A., "High temperature component life assessment", Chapman and Hall, London, 1994.

Webster, G.A. and Webster, P.J., "Measurement of Residual Stress Using High Resolution Neutron Diffraction", TWI Seminar, Newcastle: Residual Stresses in Welded Construction, 1985.

Weertman, J., "Steady state creep through dislocation climb", Journal of Applied Physics, 28, pp. 362-364, 1957.

Weiner J.H., "An Elastoplastic Thermal-Stress Analysis of a Free Plate", Journal of Applied Mechanics, Vol. 23, Trans. ASME, Vol. 78, pp. 397 – 401, 1956.

Wilby A.J., "The Manufacture of Austenitic Stainless Steel Welded Specimens for the IMC/TRAINSS Project", British Energy Generation Report EPD/AGR/REP/0666/99 Issue 2, 1999.

Withers P.J. and Bhadeshia H.K.D.H., "Residual Stress – II: Nature and Origins", Mat. Sci. Tech., 2000.

Withers, P.J. and Bhadeshia H.K.D.H, "Residual Stress: Part 1 - Measurement Techniques", Material Science and technology, 17, pp. 355-365, 2001.

Yatomi M., Bettinson A.D., O'Dowd N.P. and Nikbin K.M., "Modelling of damage development and failure in notched-bar multiaxial creep tests", Fatigue Fract Engng Mater Struct 27, pp. 283-295, 2004.

Yazdi S.R., Retraint D., Lu J., "Study of through-thickness residual stress by numerical and experimental techniques", J. Strain Anal. 33 (6), 449-458, 1998.

Zhdanov I. M. and Gonchar A. K., "Determining the residual welding stresses at a depth in metal", Automatic Welding, Vol.31, No.9, 22-24, 1978.

Zuccarello B., "Optimal calculation steps for the evaluation of residual stress by the incremental hole-drilling method", Exp. Mech. 39 (2), pp. 117-124, 1999.

316H	Proof stress (MPa)			Young Modulus (GPa)	Conductivity (W/m K)	Specific Heat (kJ/kg K)
	ε = 0.2%	ε = 2.0%	ε =10.0%			
20	286.8	363.5	512.6	195.6	14.12	0.492
100	261.1	335.6	476.6	191.2	15.26	0.502
200	233.0	309.1	445.3	185	16.69	0.514
300	199.2	265.5	408.9	179.6	18.11	0.526
400	188.9	252.3	399.6	172.6	19.54	0.538
900	96.9	105.7	106.6	116.8	26.66	0.599

316L	Proof stress (MPa)			Young Modulus (GPa)	Conductivity (W/m K)	Specific Heat (kJ/kg K)
	ε = 0.2%	ε = 1.0%	ε =10.0%			
20	245.5	282.8	437.4	195.6	14.12	0.492
300	153.3	188.9	307.4	179.6	18.11	0.526
400	145.3	177.8	299.5	172.6	19.54	0.538
500	135.3	167.7	293.5	164.5	20.96	0.550
600	126.3	157.6	262.0	155.0	22.38	0.562
700	110.2	138.4	215.4	144.1	23.81	0.575
850	82.0	108.0	150.0	124.1	25.95	0.593

321	Proof stress (MPa)			Young Modulus (GPa)	Conductivity (W/m K)	Specific Heat (kJ/kg K)
	ε = 0.2%	ε = 2.0%	ε =10.0%			
20	205.0	236.0	364.9	193.0	14.12	0.500
250	148.9	178.0	285.1	180.2	17.40	0.528
500	121.2	149.4	261.5	162.3	20.96	0.559
750	94.9	118.0	176.4	135.9	24.52	0.590
900	62.3	69.1	82.9	115.2	26.66	0.609

Table 3.1 Material properties of types 316H, 316L and 321 stainless steel.

Position	$h = 16742$			$h = 2000$			$h = 200$		
	radial	axial	hoop	radial	axial	hoop	radial	axial	hoop
O	411	541	411	290	410	290	13	2	13
M	411	434	412	322	186	323	4	5	4
A	-396	-1	-395	-341	1	-342	-45	0	-45
B	0	-7	-363	0	-7	-329	2	0	-80
N	9	-396	-371	7	-345	-322	0	-38	-30
C	7	-421	-348	6	-375	-301	2	-106	-98

Table 3.2(a) Effect of heat transfer coefficient h (W/m^2 K) on residual stress (MPa); initial temperature $T_i = 850$°C. See Figure 3.8 for illustration of the position in the table.

Position	$T_i = 1000$°C			$T_i = 850$°C			$T_i = 500$°C		
	radial	axial	hoop	radial	axial	hoop	radial	axial	hoop
O	464	602	464	411	541	411	261	357	261
M	427	480	428	411	434	412	345	201	345
A	-403	-1	-403	-396	-1	-395	-361	0	-361
B	3	-4	-366	0	-7	-363	-11	-17	-341
N	9	-407	-389	9	-396	-371	7	-357	-332
C	7	-436	-358	7	-421	-348	6	-385	-311

Table 3.2(b) Effect of initial temperature T_i (°C) on residual stress (MPa); heat transfer coefficient $h = 16742$ W/m^2 K. See Figure 3.8 for illustration of the position in the table.

Process condition	Sample ID	Shape	Dimension	More detail	Measurement	Material
As-quenched	S1	Cylinder	D30×L100	S+T	ICHD	NM
	S2	Cylinder	D60×L60	S+T+C	ICHD, DHD	316L
	S7	Sphere	D30	S+C		NM
	S12	Cylinder	D60×L60	C+MC+S	ICHD, DHD	321
	S8	Sphere	D30		ICHD ND ENGIN ENGIN-X	316L
	S9	Comb/sphere	D30			316L
	S19	Cylinder	D60×L60			316H
	S22	Sphere	D30	C+S		316H
	S25	Comb/sphere	D30			316H
	S26	Cylinder with holes	D60×L160	S+C		316H
	S27	Cylinder	D60×L160			316H
	S45	Cylinder	D60×L60	Quenched only		316L
	S39	Cylinder	D29×L29	Quenched only	ND REST	316H
Thermal exposure at 550°C	S3	Cylinder	D60×L60	S+T+C 4320 hours		
	S4	Cylinder	D60×L60	4320 hours		
	S5	Cylinder	D60×L60	S+T 4320 hours		
	S6	Sphere	D60	4320 hours		
	S16	Cylinder	D60×L60	S+T+C 4320 hours		316H
	S17	Cylinder	D60×L60	4320 hours		316H
	S18	Cylinder	D60×L60	4320 hours		316H
	S20	Sphere	D60	4320 hours		316H
	S23	Comb/sphere	D30	3200 hours	ND ENGIN-X	316H
	S24	Sphere	D30	3200 hours		316H
	S28	Cylinder	D30×L30	1800 hours	ND POLDI	316H
	S31	Comb/sphere	D30	1800 hours		316H
	S29	Cylinder	D30×L30	1.25 hours		316H
	S30	Comb/sphere	D30	1.25 hours		316H

Pre-trepanned	S34	Cylinder	D29×L29	EDM 8.5	ND REST	316H
	S35	Cylinder	D29×L29	EDM 15.5		316H
	S36	Cylinder	D29×L29	EDM 21.5		316H
	S37	Cylinder	D29×L29	EDM 28		316H
	S38	Cylinder	D29×L29	drill 1.5mm		316H
	S40	Cylinder	D60×L60	EDM 15.5	ND ENGIN-X	316L
	S41	Cylinder	D60×L60	EDM 30		316L
	S42	Cylinder	D60×L60	EDM 45.5		316L
	S43	Cylinder	D60×L60	EDM 60.0		316L
	S44	Cylinder	D60×L60	drill 1.5		316L
Annealed	S46	Cylinder	D60×L60	Annealed, 370°C, 2½ hrs		316L
Unquenched test specimens	S10	Sphere	D60			NM
	S11	Sphere	D60			NM
	S13	Cylinder	D60×L60			NM
	S14	Sphere	D30			NM
	S15	Sphere	D30			NM
	S21	Sphere	D60			316H
	S32	Cylinder	D30×L30		ND REST	316H
	S33	Cylinder	D40×L40			316H

Table 3.3 Catalogue of quenched specimens.

Dimension: D (diameter), L (length). Thermocouple positions: S (side), T (top), C (centre), MC (mid centre). Measurement type: ICHD (incremental centre hole drilling), DHD (deep hole drilling), ND (neutron diffraction). Process condition: EDM8.5 (quenched, 1.5mm diameter drilled and 5mm diameter trepanned up to 8.5mm edm depth etc), drill1.5 (quenched and drilled with 1.5mm diameter drill etc).

B (mm)	R (mm)	x (mm)	δ (mm)	P (kN)	TF	PE
Single punch results						
25	12.5	12.5	0.2	236	0.77	0.07
25	12.5	12.5	0.3	256	0.74	0.11
25	12.5	12.5	0.5	290	0.57	0.18
25	12.5	12.5	0.8	330	0.45	0.28
Double punch results						
25	10	10	0.3	386	1.90	0.03
25	10	10	0.5	432	1.85	0.06
25	12.5	12.5	0.3	494	1.92	0.01
25	10	7.5	0.5	436	1.64	0.11
Figure-of-eight punch results (y/R=0.5)						
25	10	10	0.5	322	0.92	0.19

Table 3.4 Effect of dimensions and applied loading on the triaxiality factor and the plastic strain.

Punch type	Sample ID	Thickness B (mm)	Width W (mm)	Length L (mm	Punch diameter (mm)
SP	P215	25	60	62.5	25
	P241	25	60	62.5	25
	P242	25	60	62.5	25
DP	P211	25	60	62.5	20
	P251	25	60	62.5	20
	P252	25	60	62.5	20
FOE	P224	25	60	62.5	"20"
	P261	25	60	62.5	"20"
	P262	25	60	62.5	"20"

Table 3.5 Dimension of C(T) specimens. SP denotes single-punch, DP denotes double-punch and FOE refers to Figure-of-eight punching configuration.

Sample ID	Measured indentation (mm)	FE Predicted indentation (mm)
P215	0.7	0.94
P241	0.96	0.94
P242	0.94	0.94
P211	0.67	0.93
P251	0.66	0.93
P252	0.77	0.93
P224	0.90	0.94
P261	0.88	0.94
P262	0.90	0.94

Table 3.6 Measured and predicted indentations. Samples P215, P241, P242 single punch; Samples P211, P251, P252 double punch; Samples 224, P261, P262 figure-of-eight punch.

ID	Shape	Dimension	Thermocouple position	Measurement type	Process condition	Material
8	Sphere	D30		ICHD	AQ	NM
9	Comb/sphere	D30				316L
19	Cylinder	D60×L60				316H
22	Sphere	D30	C+S			316H
23	Comb/sphere	D30		ND ENGIN	QA	316H
24	Sphere	D30				316H
25	Comb/sphere	D30		ENGIN-X	AQ	316H
26	Cylinder *with holes*	D60×L160	S+C			316H
27	Cylinder	D60×L160				316H
40	Cylinder	D60×L60	EDM 15.5		QDT15.5	316L
42	Cylinder	D60×L60	EDM 45.5		QDT45.5	316L
46	Cylinder	D60×L60	Annealed, 370°C, 2½ hrs		Annealed, 370°C 2½hrs	316L
28	Cylinder	D30×L30		ND POLDI	1800h	316H
29	Cylinder	D30×L30			1.25h	316H
30	Comb/sphere	D30			1.25h	316H
31	Comb/sphere	D30			1800h	316H
34	Cylinder	D29×L29	EDM 8.5	ND REST	QDT8.5	316H
35	Cylinder	D29×L29	EDM 15.5		QDT15.5	316H
36	Cylinder	D29×L29	EDM 21.5		QDT21.5	316H
37	Cylinder	D29×L29	EDM 28		QDT28	316H
38	Cylinder	D29×L29			QD1.5	316H
39	Cylinder	D29×L29	Quenched only		AQ	316H

Table 4.1 Catalogue of quenched specimens in the residual stress measurement programme using neutron diffraction technique. See also Table 3.3 for additional details.

Loading case	σ_x		σ_y		σ_z	
	Applied	Measured	Applied	Measured	Applied	Measured
Uniaxial Loading Case a-e; TF = 0.333						
Case a	50	*48.54*	0	*1.54*	0	
Case b	100	*97.02*	0	*3.07*	0	
Case c	150	*141.18*	0	*2.24*	0	
Case d	200	*146.98*	0	*1.42*	0	
Case e	250	*4.58*	0	*-34.97*	0	
Biaxial Loading Case f-j; TF = 0.6						
Case f	50	*49.45*	28.2	*28.94*	0	
Case g	100	*98.84*	56.4	*57.86*	0	
Case h	150	*147.30*	84.6	*86.32*	0	
Case i	200	*178.36*	112.9	*107.88*	0	
Case j	250	*170.87*	140.7	*104.68*	0	
Triaxial Loading Case k-r; TF = 1						
Case k	50	*49.42*	27.3	*28.03*	15	
Case l	100	*98.49*	45	*46.78*	35.7	
Case m	130	*127.19*	32.0	*35.05*	125	
Case n	130	*130.05*	125	*125.24*	32.0	
Case o	180	*173.43*	175	*168.60*	44.4	
Case p	180	*173.57*	44.4	*47.04*	175	
Case q	200	*183.80*	80	*77.48*	80	
Case r	200	*184.53*	100	*96.98*	64.7	
Triaxial Loading Case t-z; TF = 0.5						
Case t	50	*48.57*	0	*1.56*	16.3	
Case u	100	*98.48*	45	*46.77*	-6.6	
Case v	150	*144.33*	21.4	*24.39*	21.4	
Case w	180	*162.80*	25.7	*24.76*	25.7	
Case x	180	*157.71*	175	*153.50*	-35.5	
Case y	180	*148.29*	-35.5	*-17.65*	175	
Case z	180	*162.01*	15	*14.37*	37.5	

Table 6.1 Summary of applied loading cases.

Loading case	Applied TF	Applied σ_1/σ_e	Measured TF	Measured σ_1/σ_e
Uniaxial Loading Case a-e; TF = 0.333				
Case a	0.333	1	0.333	0.971
Case b	0.333	1	0.333	0.970
Case c	0.333	1	0.333	0.941
Case d	0.333	1	0.333	0.735
Case e	0.333	1	0.333	0.018
Biaxial Loading Case f-j; TF = 0.6				
Case f	0.600	1.151531	0.600	1.139
Case g	0.600	1.151531	0.600	1.138
Case h	0.600	1.151531	0.600	1.131
Case i	0.600	1.151531	0.600	1.027
Case j	0.600	1.151662	0.600	0.787
Triaxial Loading Case k-r; TF = 1				
Case k	1.000	1.625592	1.000	1.607
Case l	1.000	1.660654	1.000	1.636
Case m	1.000	1.359225	1.000	1.330
Case n	1.000	1.359179	1.000	1.360
Case o	1.000	1.351933	1.000	1.303
Case p	1.000	1.351935	1.000	1.304
Case q	1.000	1.666667	1.000	1.532
Case r	1.000	1.645226	1.000	1.518
Triaxial Loading Case t-z; TF = 0.5				
Case t	0.4999	1.1318	0.500	1.099
Case u	0.5000	1.0835	0.500	1.067
Case v	0.5000	1.1667	0.500	1.123
Case w	0.5000	1.1667	0.500	1.055
Case x	0.5000	0.8450	0.500	0.740
Case y	0.5000	0.8450	0.500	0.696
Case z	0.5000	1.1614	0.500	1.045

Table 6.2 Summary of deep-hole validation zone result.

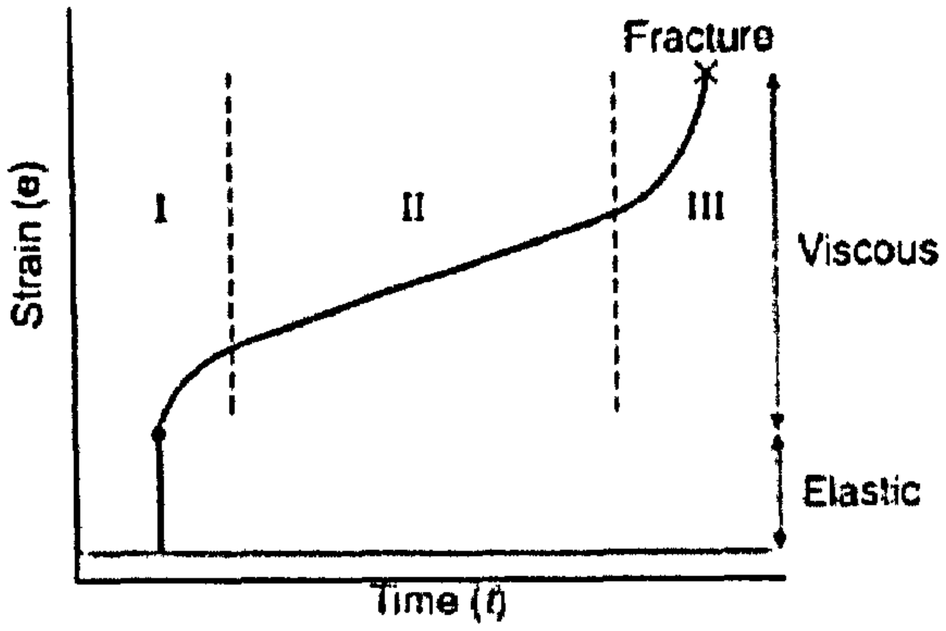

Figure 2.1 Creep curve

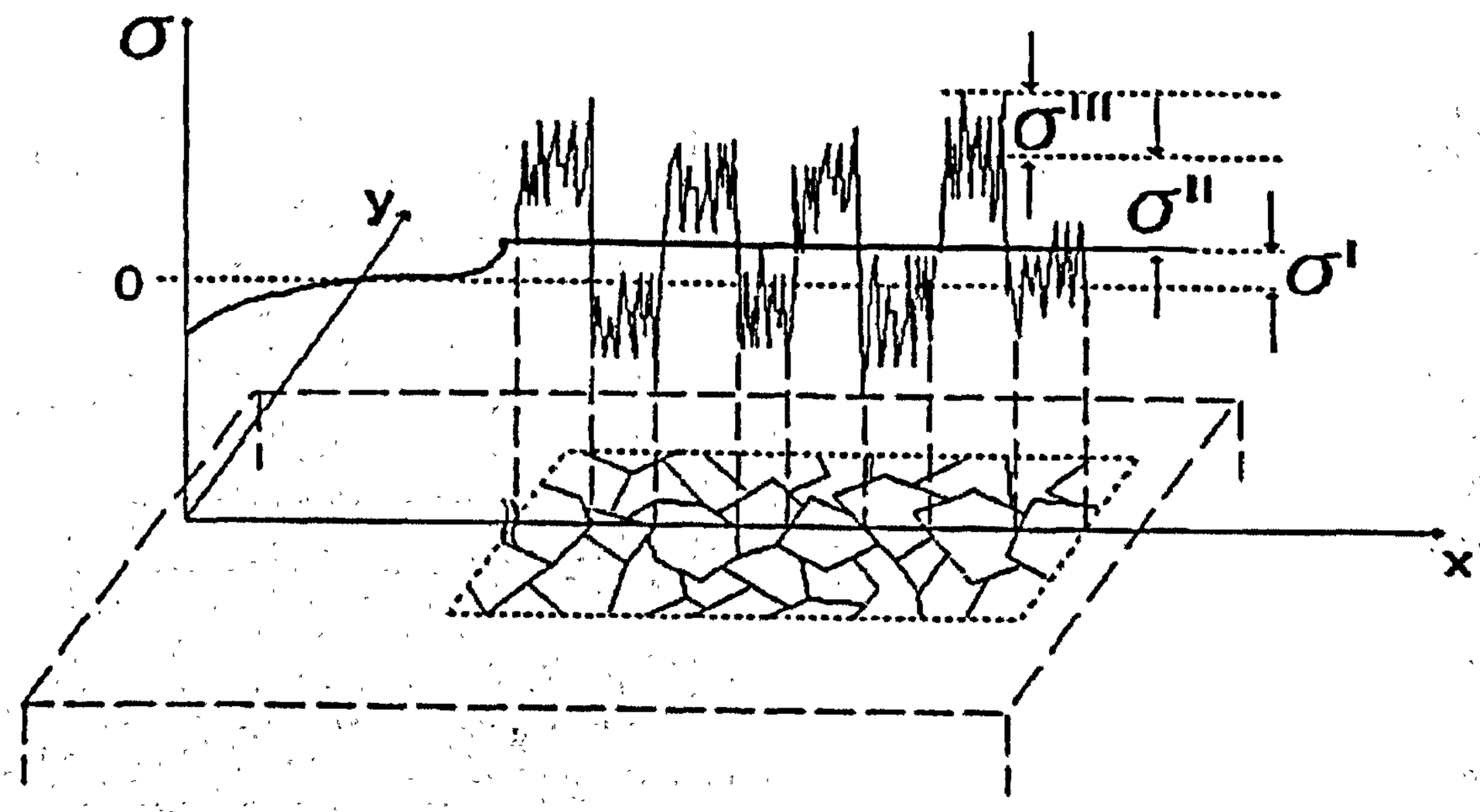

Figure 2.2 Categorisation of residual stresses according to length scales (after Kandil et al, 2001].

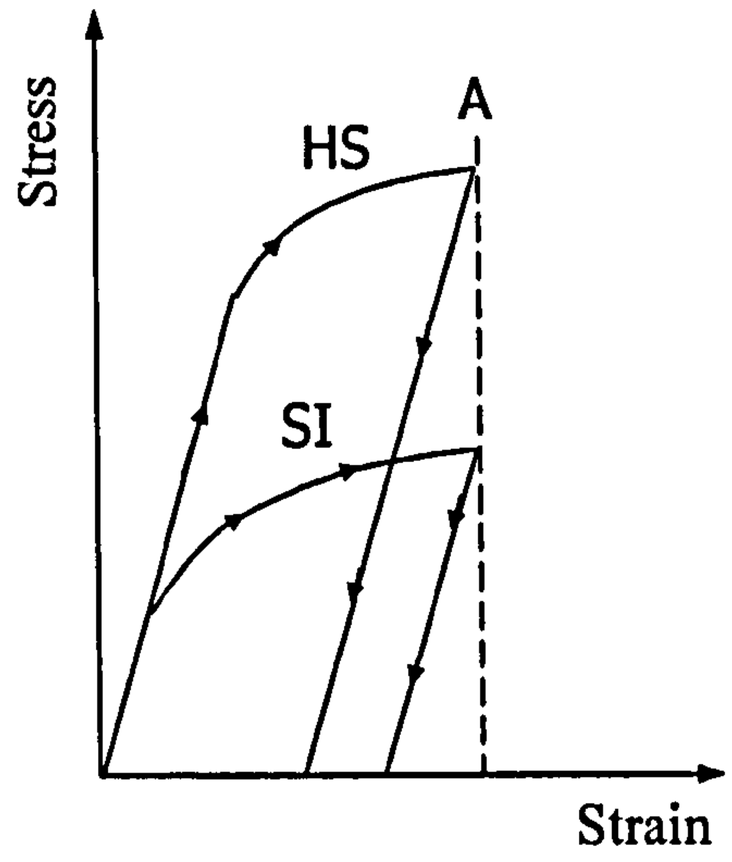

Figure 2.3 Schematic of material behaviour on loading unloading (after Noyan and Cohen, 1987).

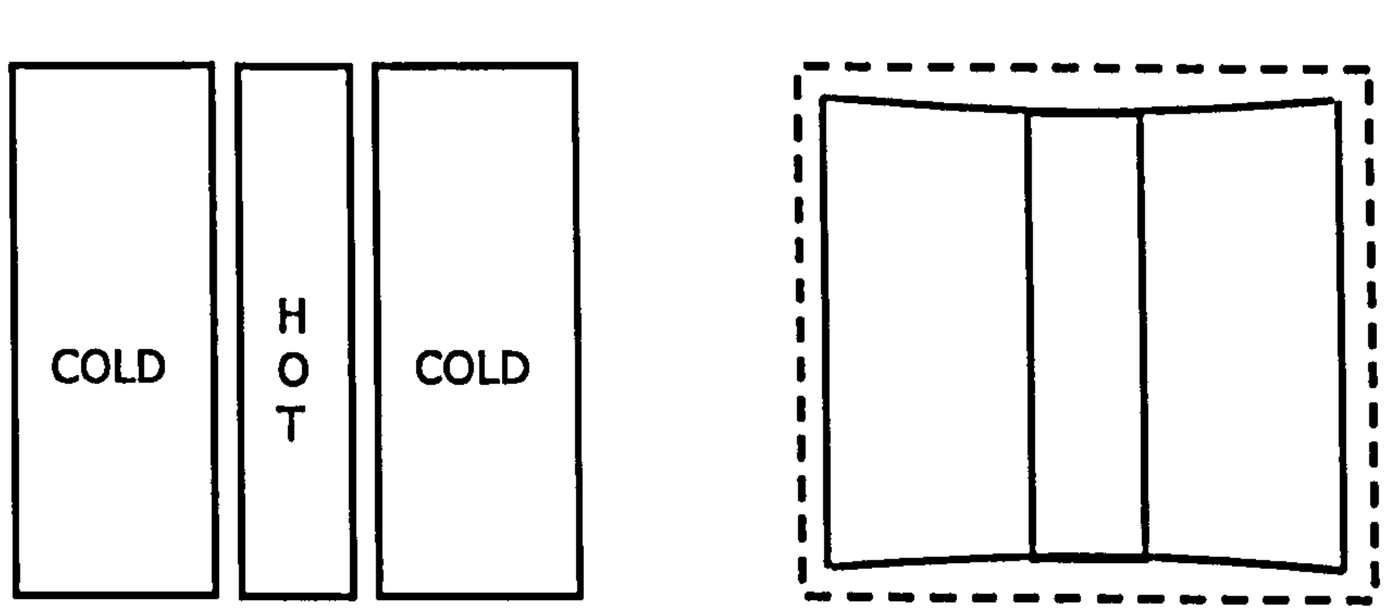

Figure 2.4 Schematic distortion of a butt-welded plate due to shrinkage of hot weld metal (after Parlane, 1981).

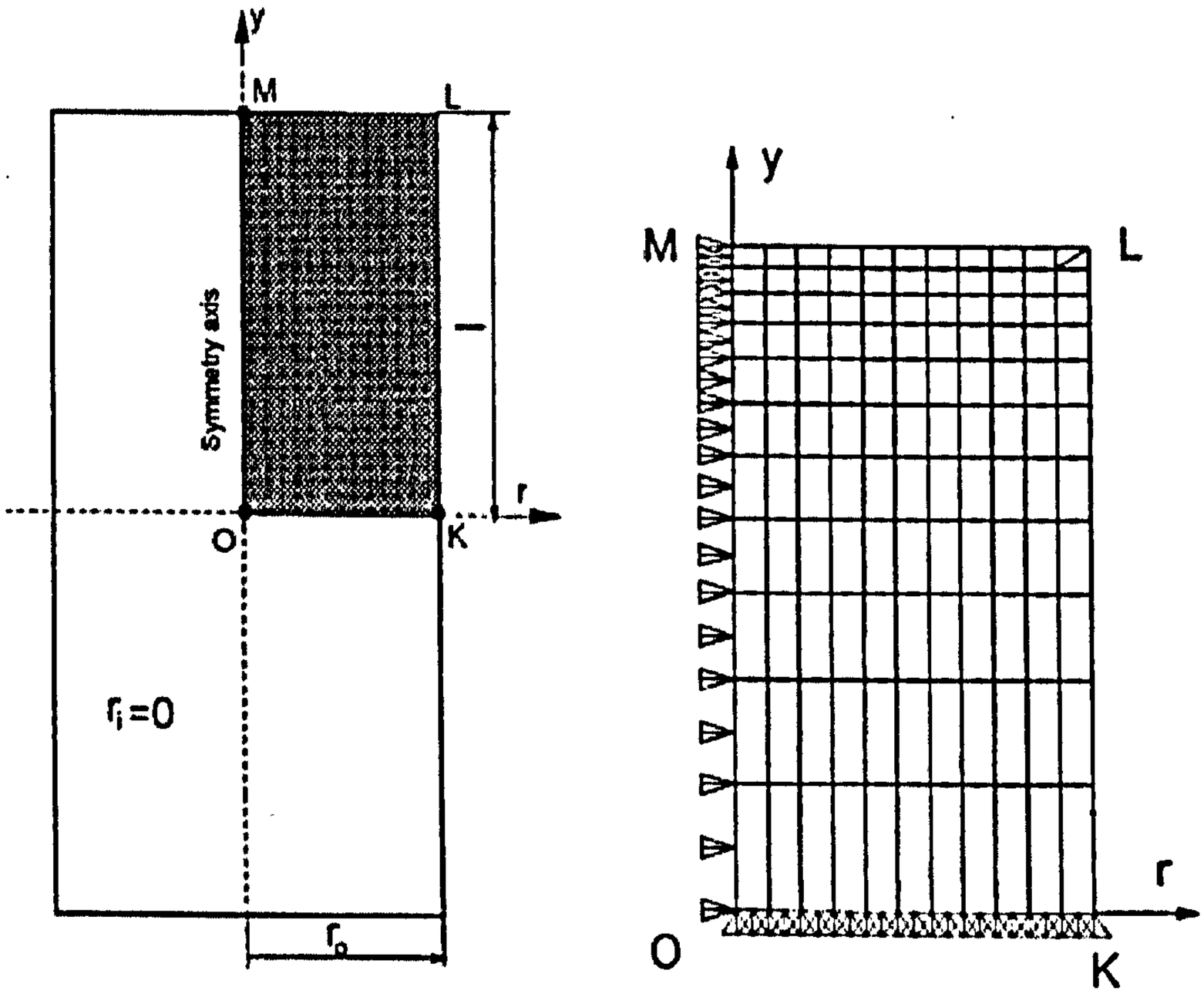

Figure 2.5 Model for solid cylindrical body and FE mesh illustrating the mechanical boundary condition in the FE analysis (after Sen et al, 2000).

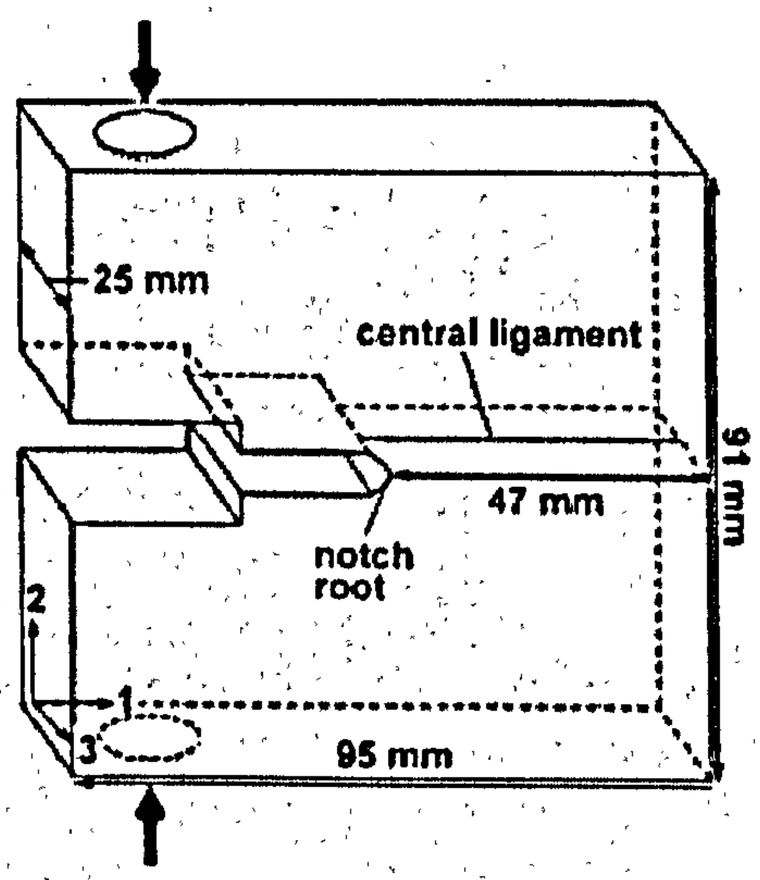

Figure 2.6 Inplane comression loading of C(T) specimen (after Turski et al, 2004).

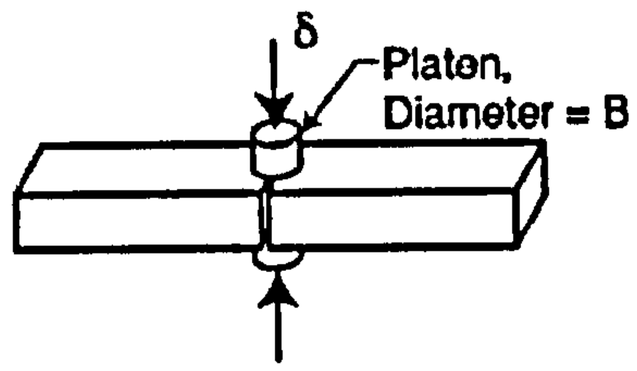

Local Compression
(apply δ to achieve compression)

Figure 2.7 Local compression process (after Meith and Hill, 2002).

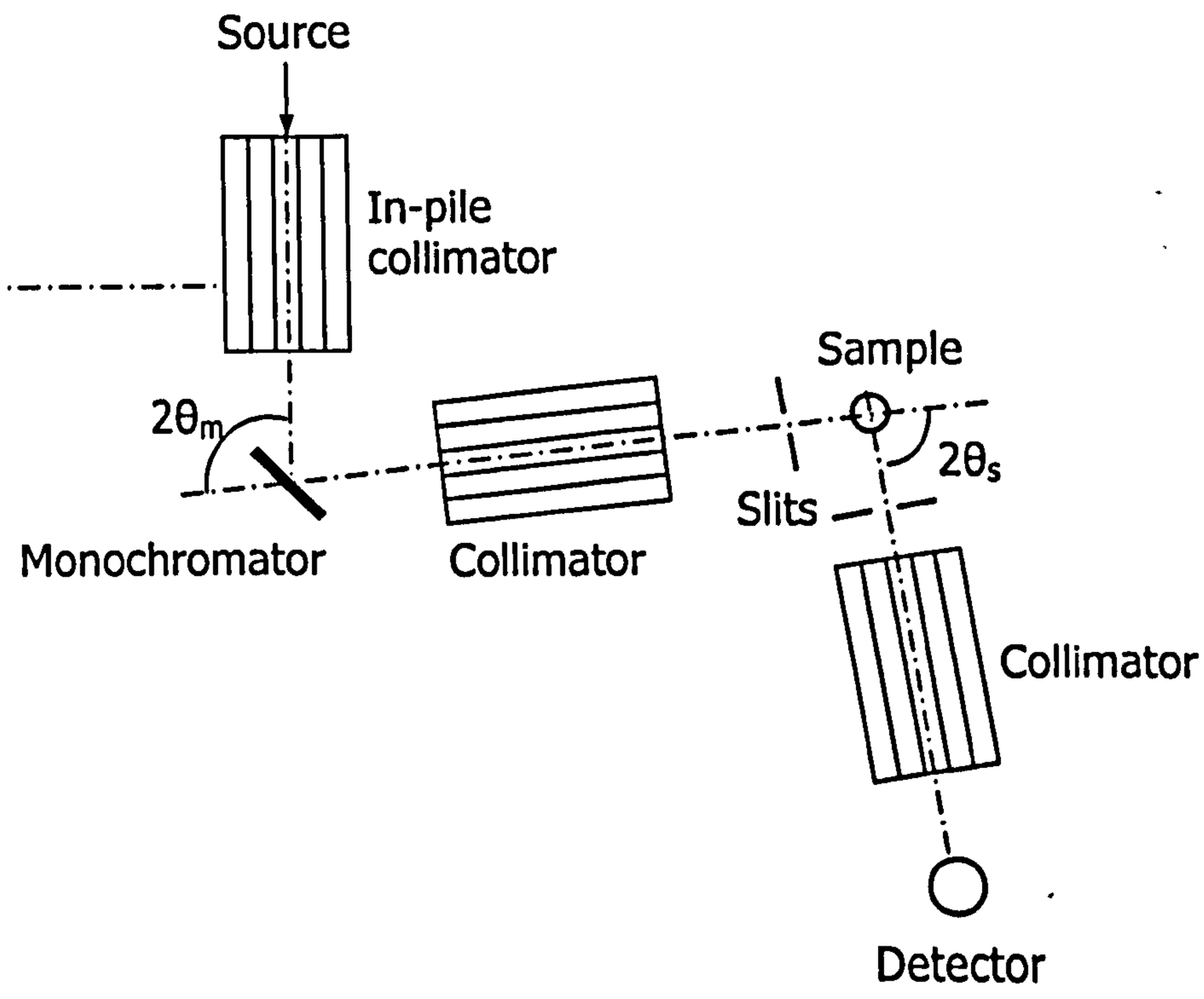

Figure 2.8 Schematic diagram of a neutron diffractometer (after Pintschovius, 2003).

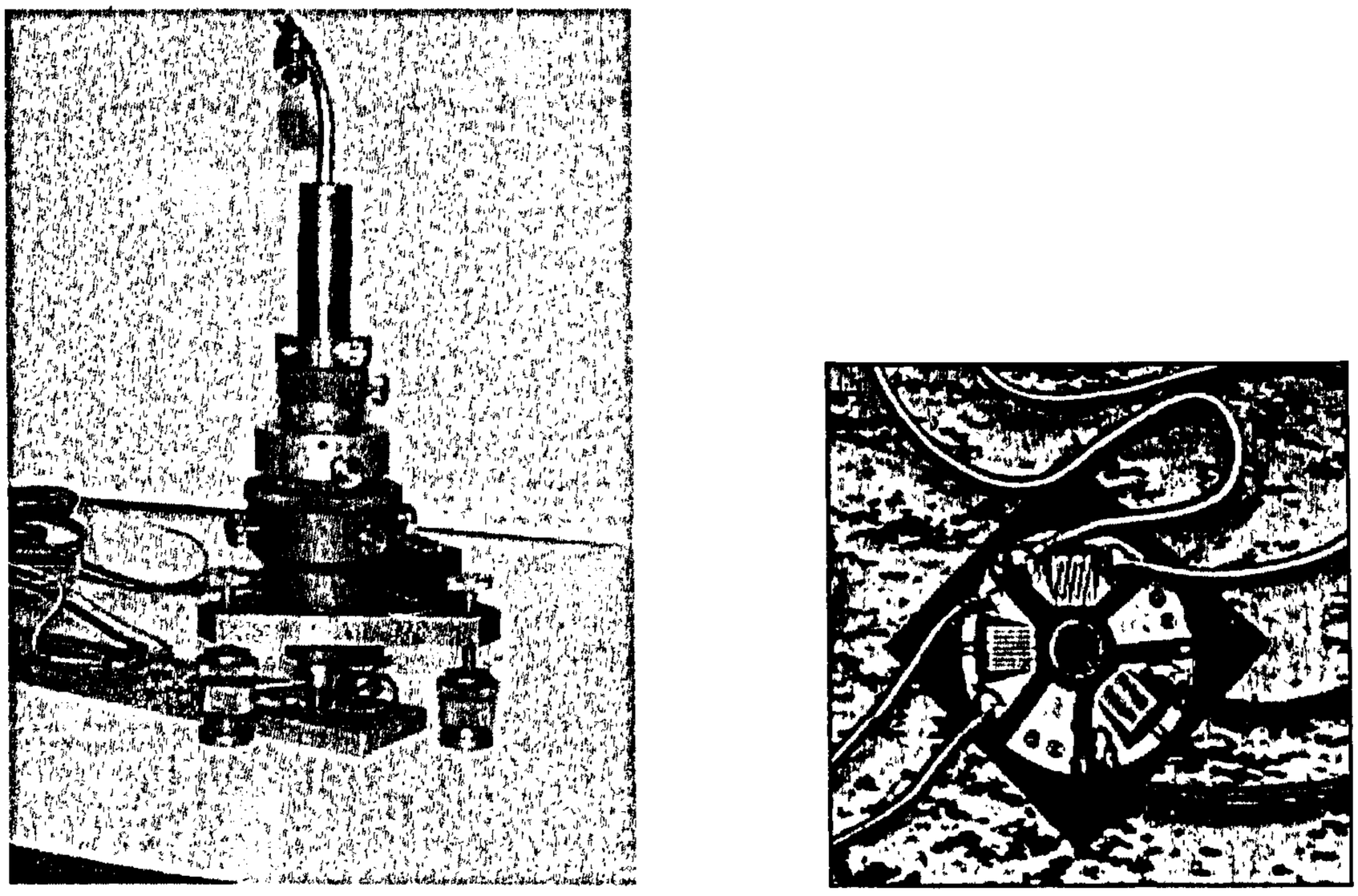

Figure 2.9 Typical hole-drilling apparatus and residual stress strain gauge rosette design (http://www.measurementsgroup.com).

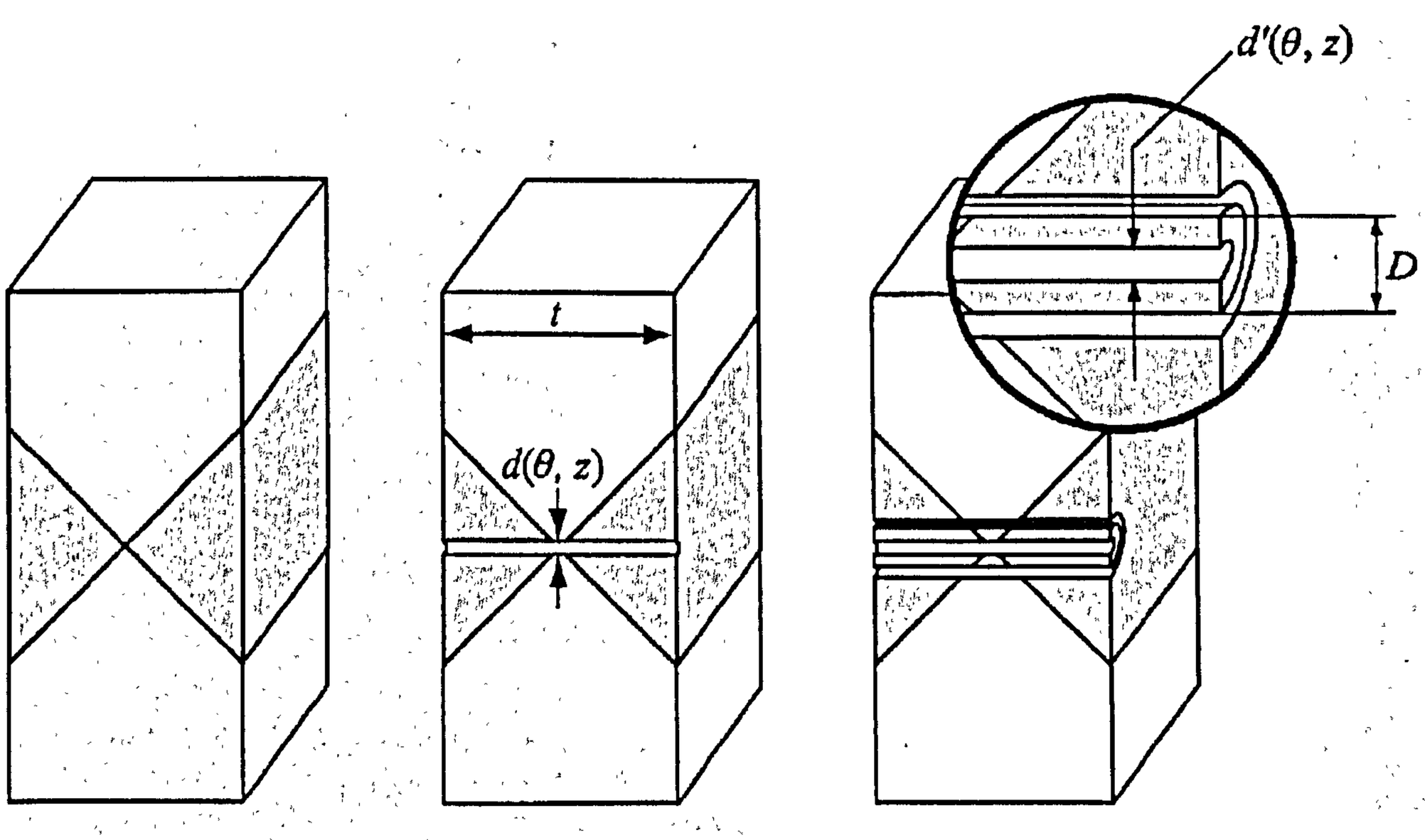

Figure 2.10 Schematic illustration of the DH method.

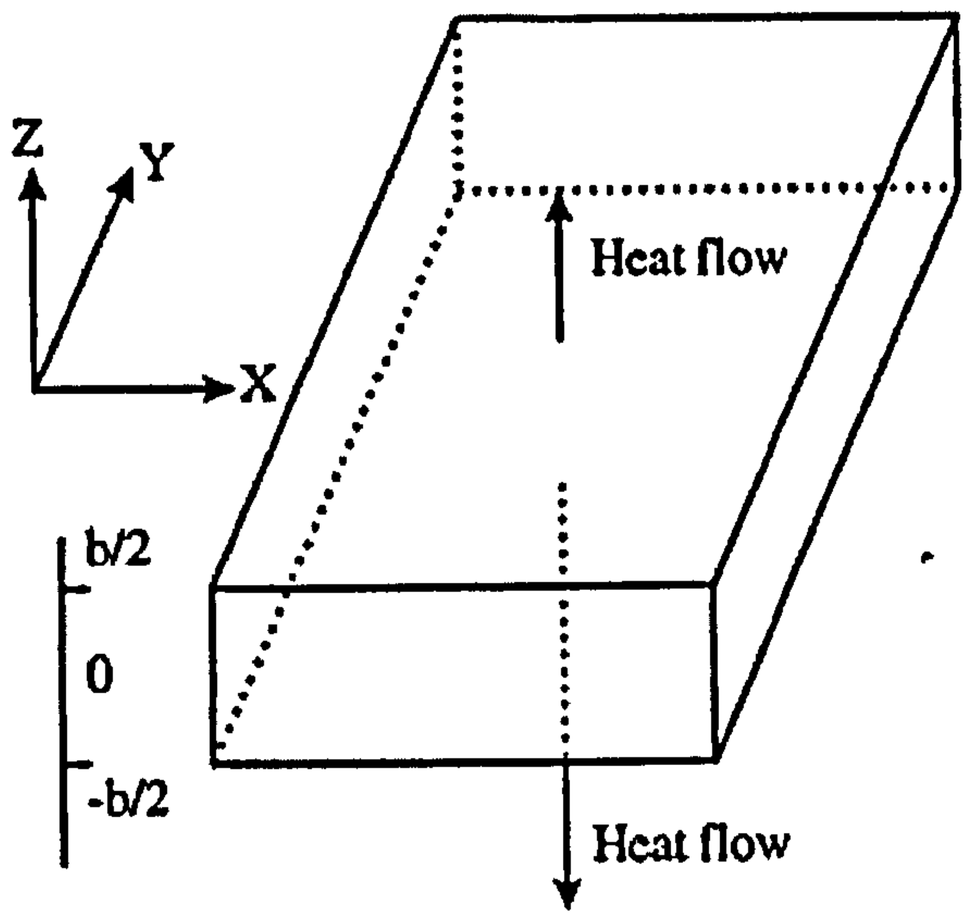

(a) Geometry and measurement directions (after Yazdi et al, 1998).

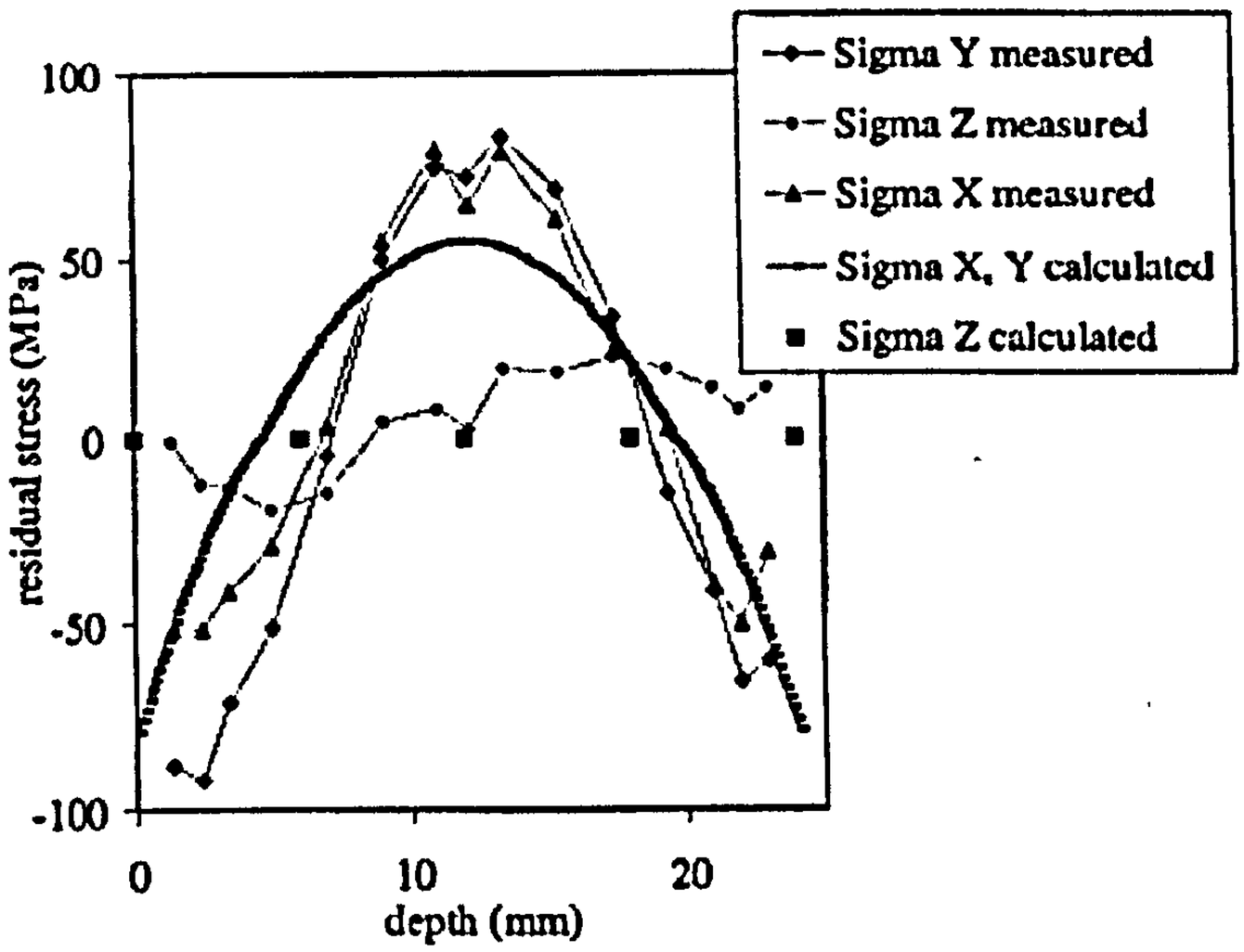

(b) Residual stress in the quenched plate (thickness, 24 mm) obtained by the neutron diffraction method and the numerical method (after Yazdi et al, 1998).

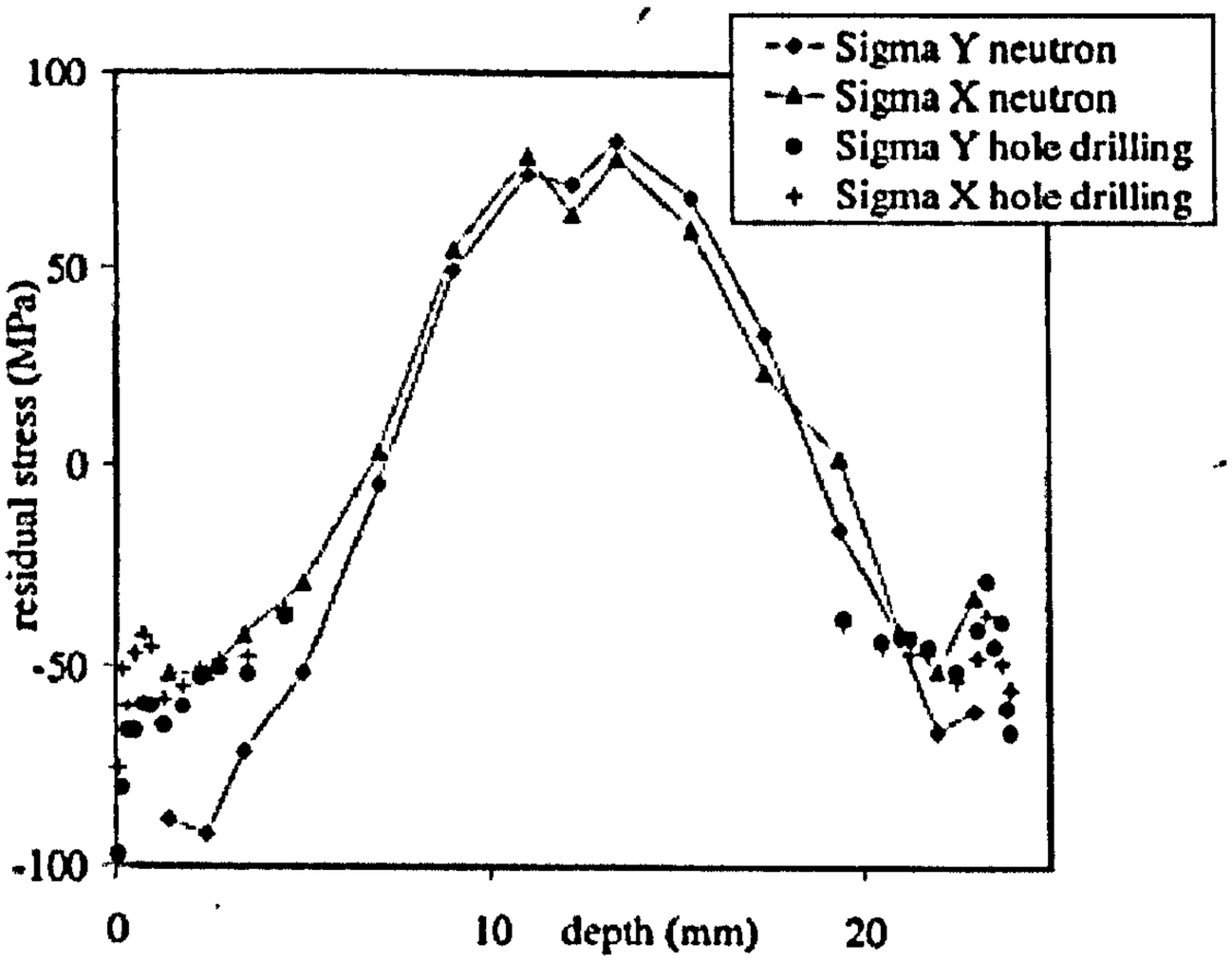

(c) Residual stress in the quenched plate (thickness, 24 mm) obtained by the neutron diffraction method and the incremental large hole drilling method (after Yazdi et al, 1998).

Figure 2.11 Measured and predicted through-thickness residual stress distribution in an aluminium alloy plate (after Yazdi et al, 1998).

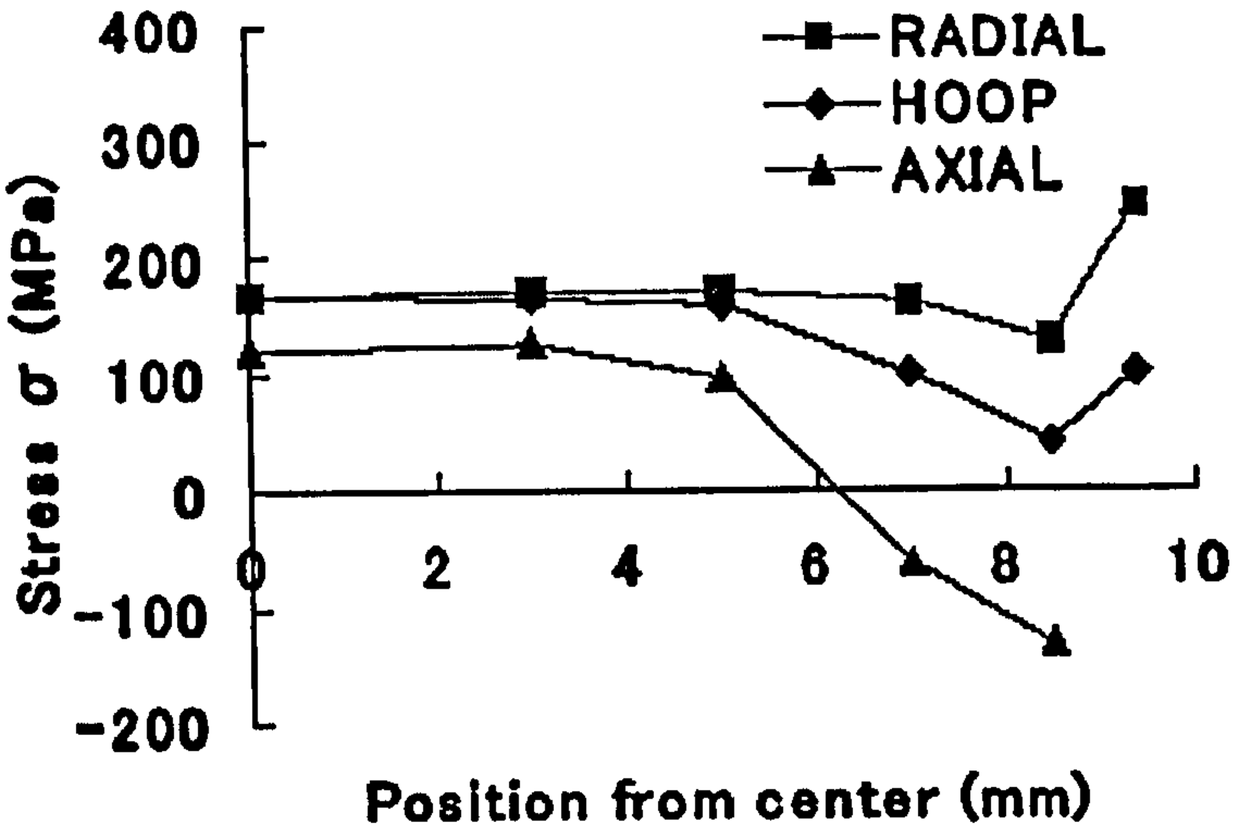

(a) Measurement result

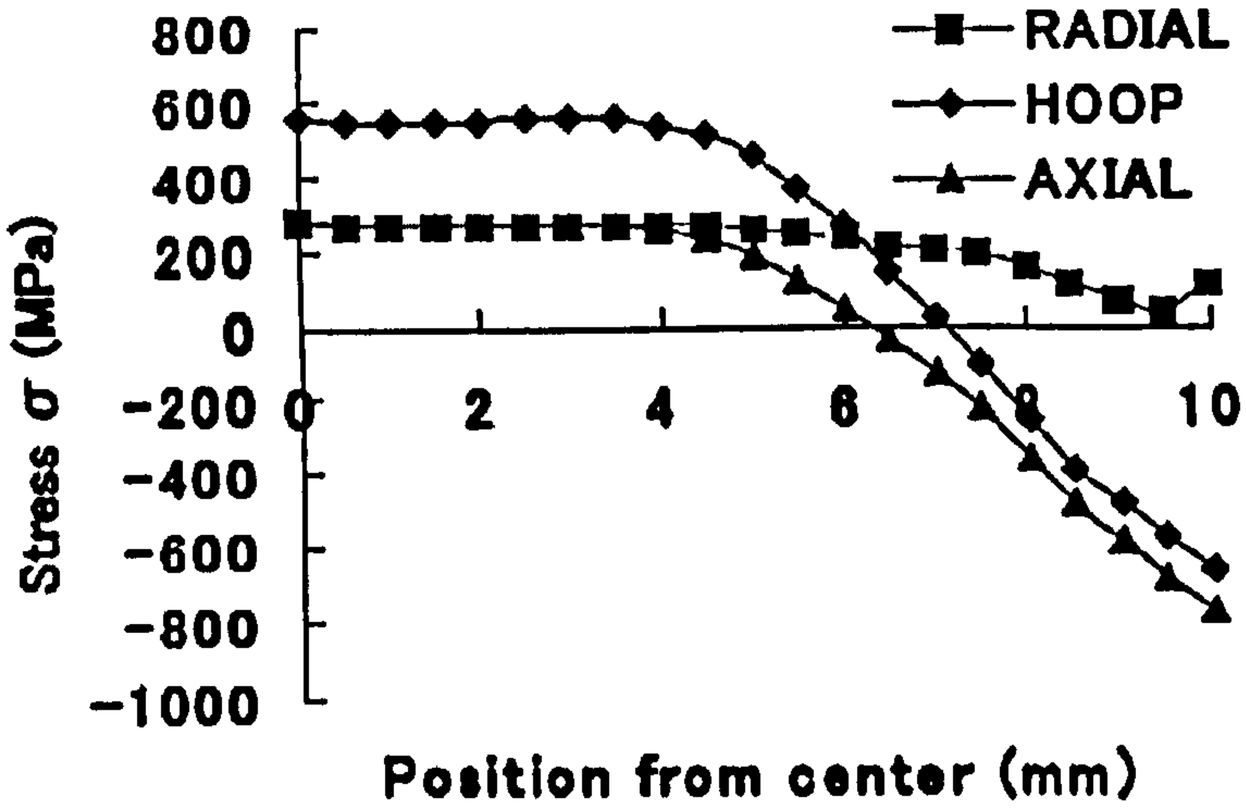

(b) Analysis result

Figure 2.12 Measured and predicted residual stress in a cylindrical test picce, diameter 20mm, length 60mm (after Mukai et al, 2003).

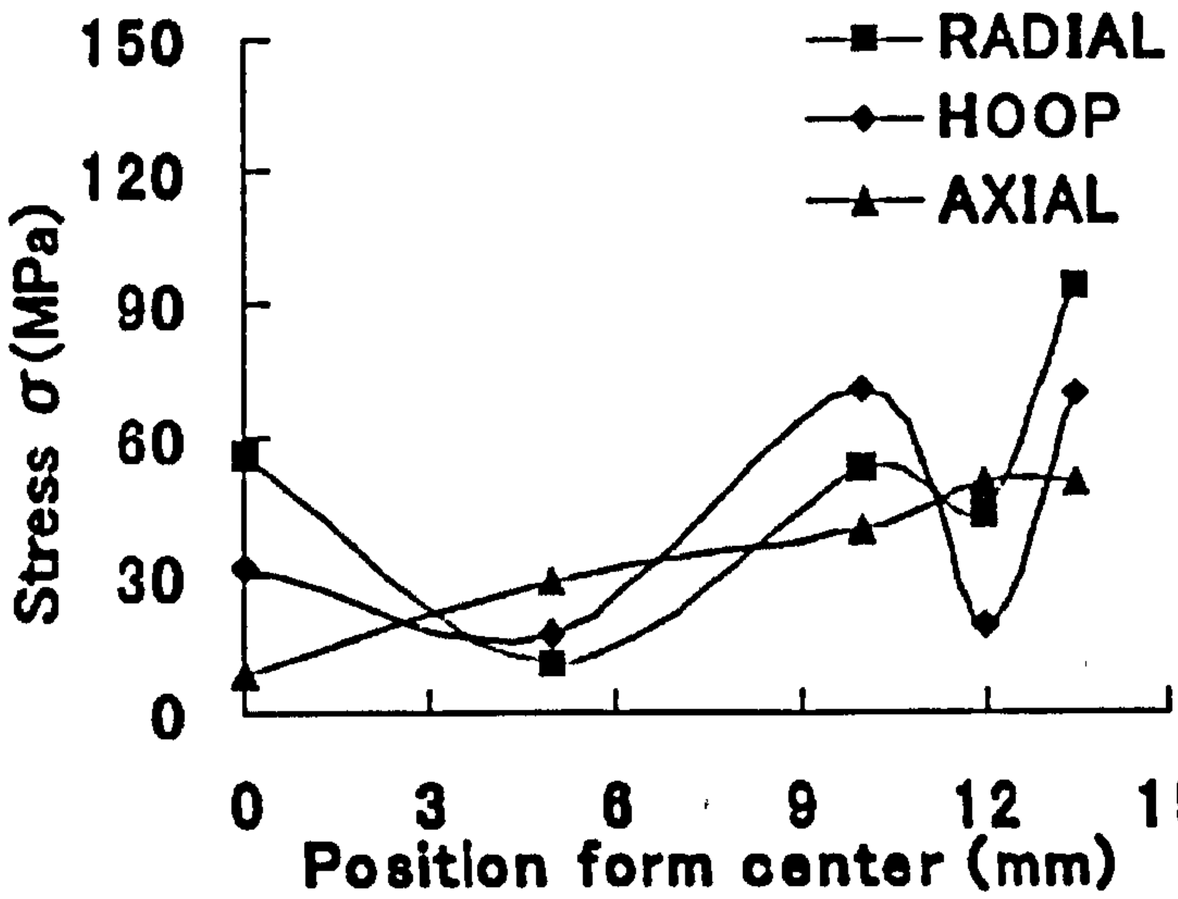

(a) Measurement result

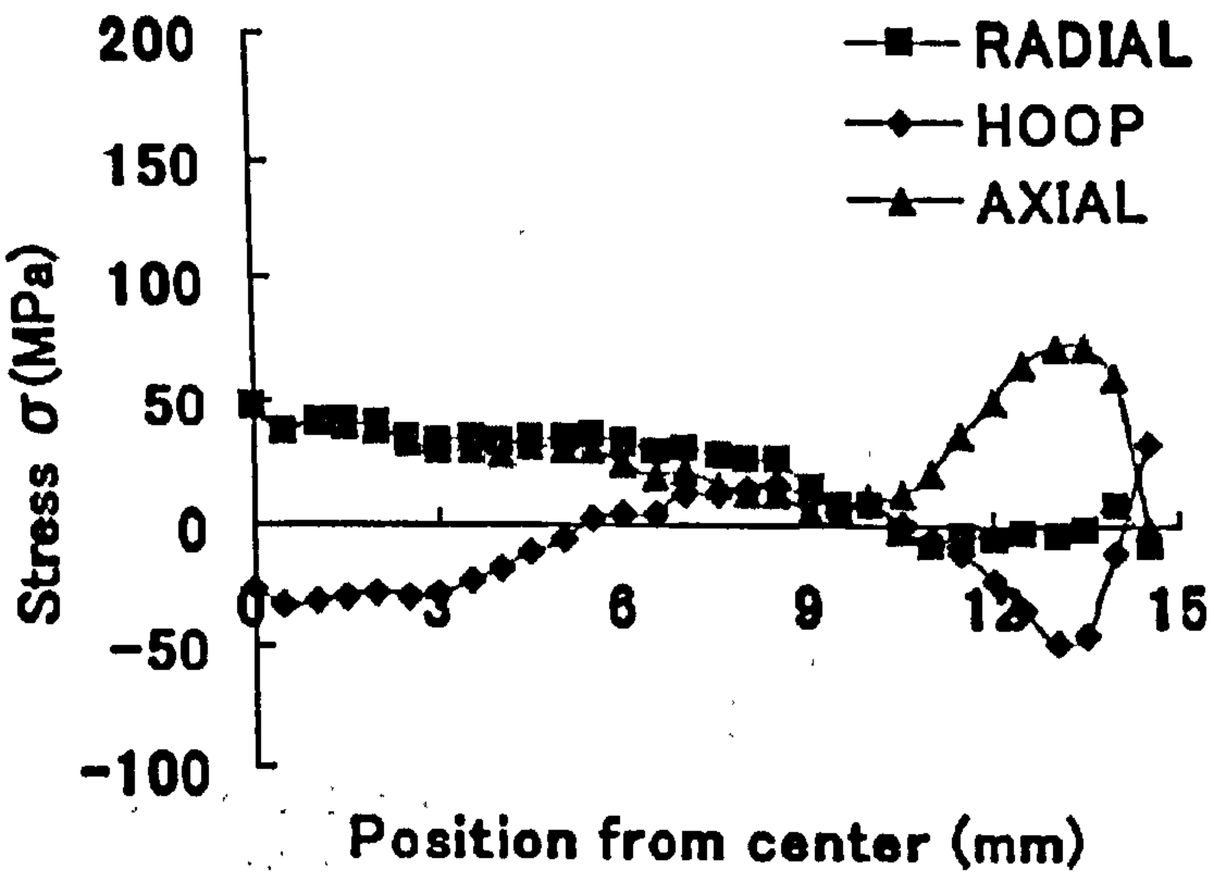

(b) Analysis results.

(b) Analysis result

Figure 2.13 Measured and predicted residual stress in a cylindrical test piece, diameter 30mm, length 10mm (after Mukai et al, 2003).

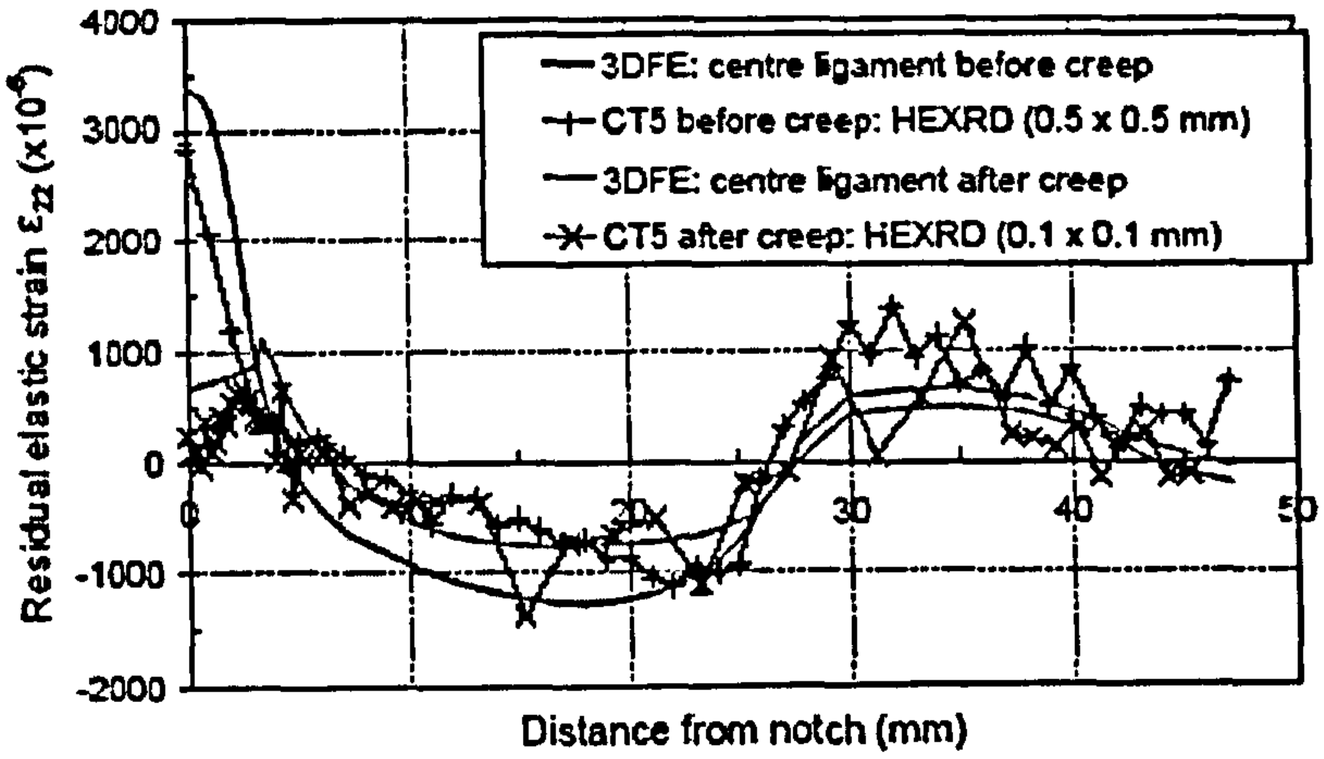

(a) Comparisons of measurements and predictions before and after thermal exposure

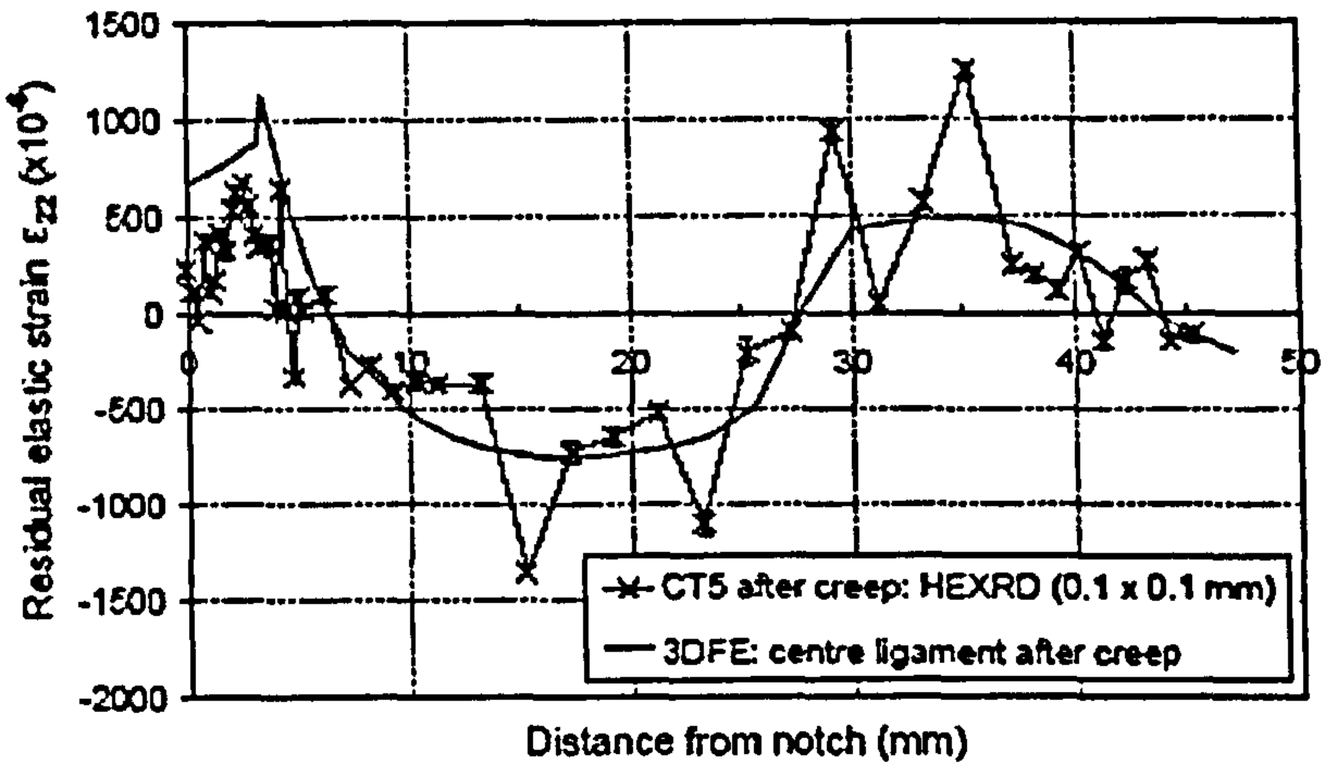

(b) A subset of data from (a) on a different scale

Figure 2.14 Comparison of crack opening, HEXRD mid thickness measurements (ID15A, ESRF, France) of residual elastic strains and 3D FE predictions for CT5 along the ligament of the pre-strained, notched CT specimen. (after Turski 2004].

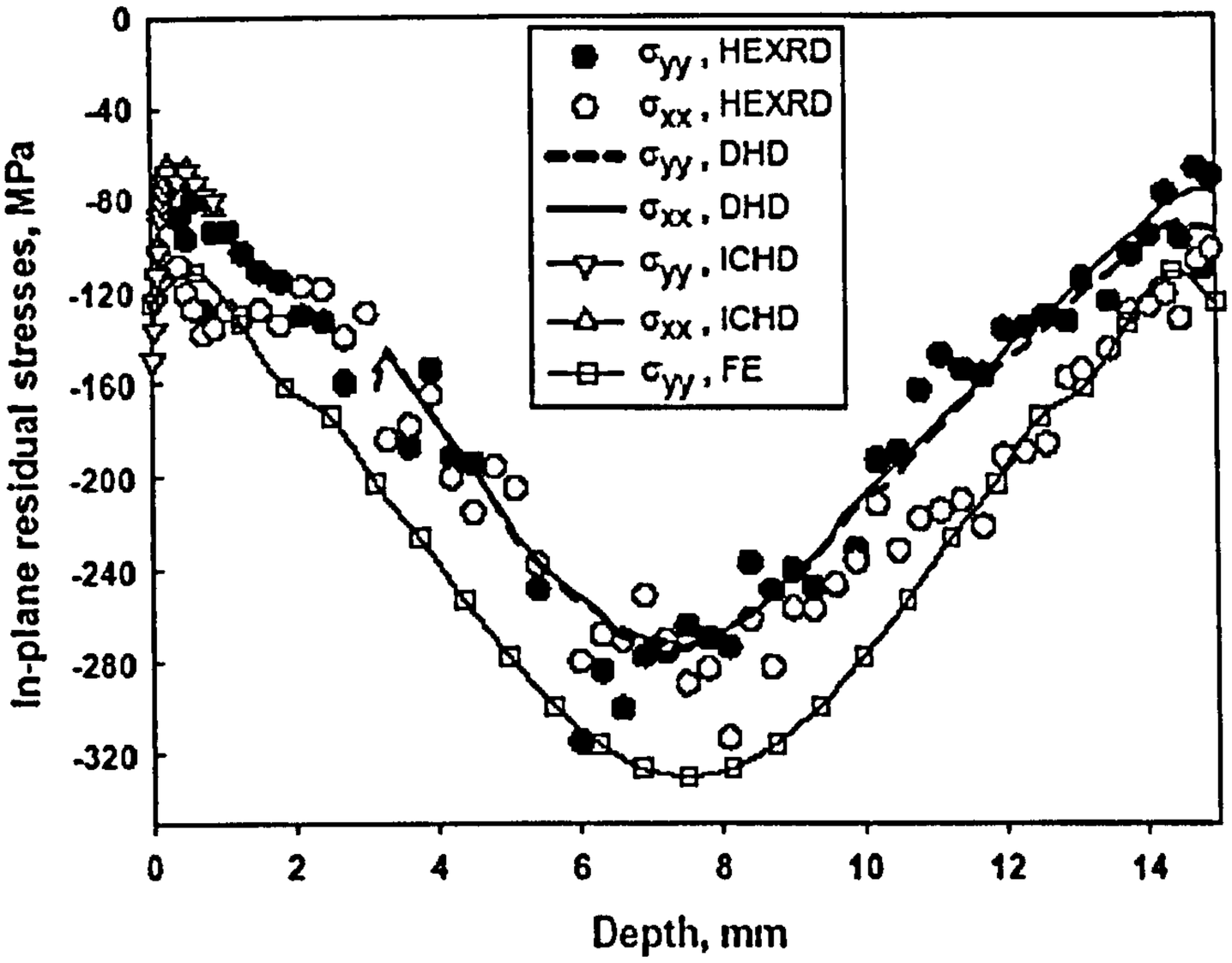

Figure 2.15 Comparison between the predicted and measured residual stresses (three measurement methods) through the thickness of the aluminium alloy plate following side punching. (after Mahmoudi et al 2005].

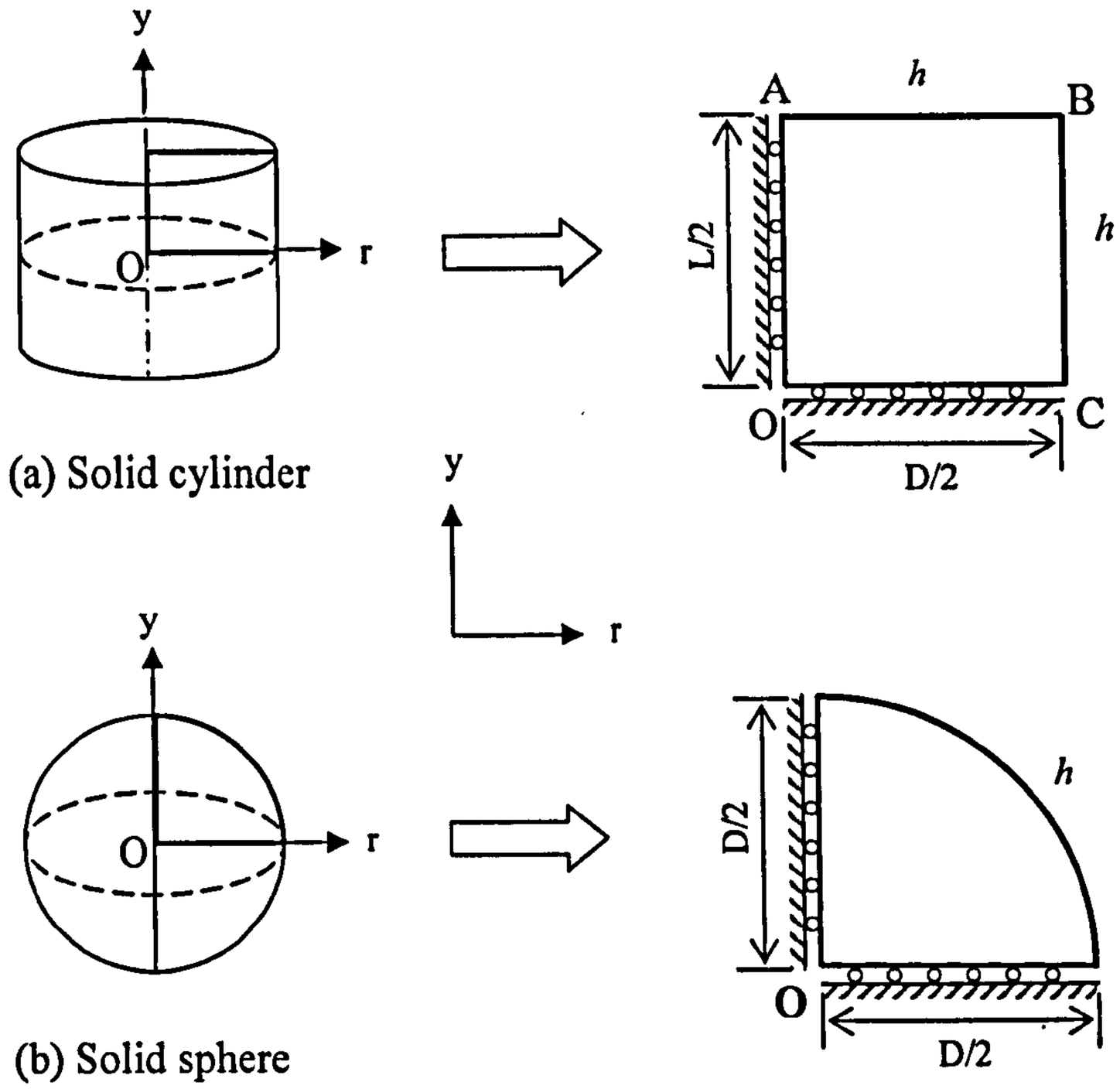

(a) Solid cylinder

(b) Solid sphere

Figure 3.1 Finite element mesh of one quarter of the specimens. Axes of symmetry along Or and Oy.

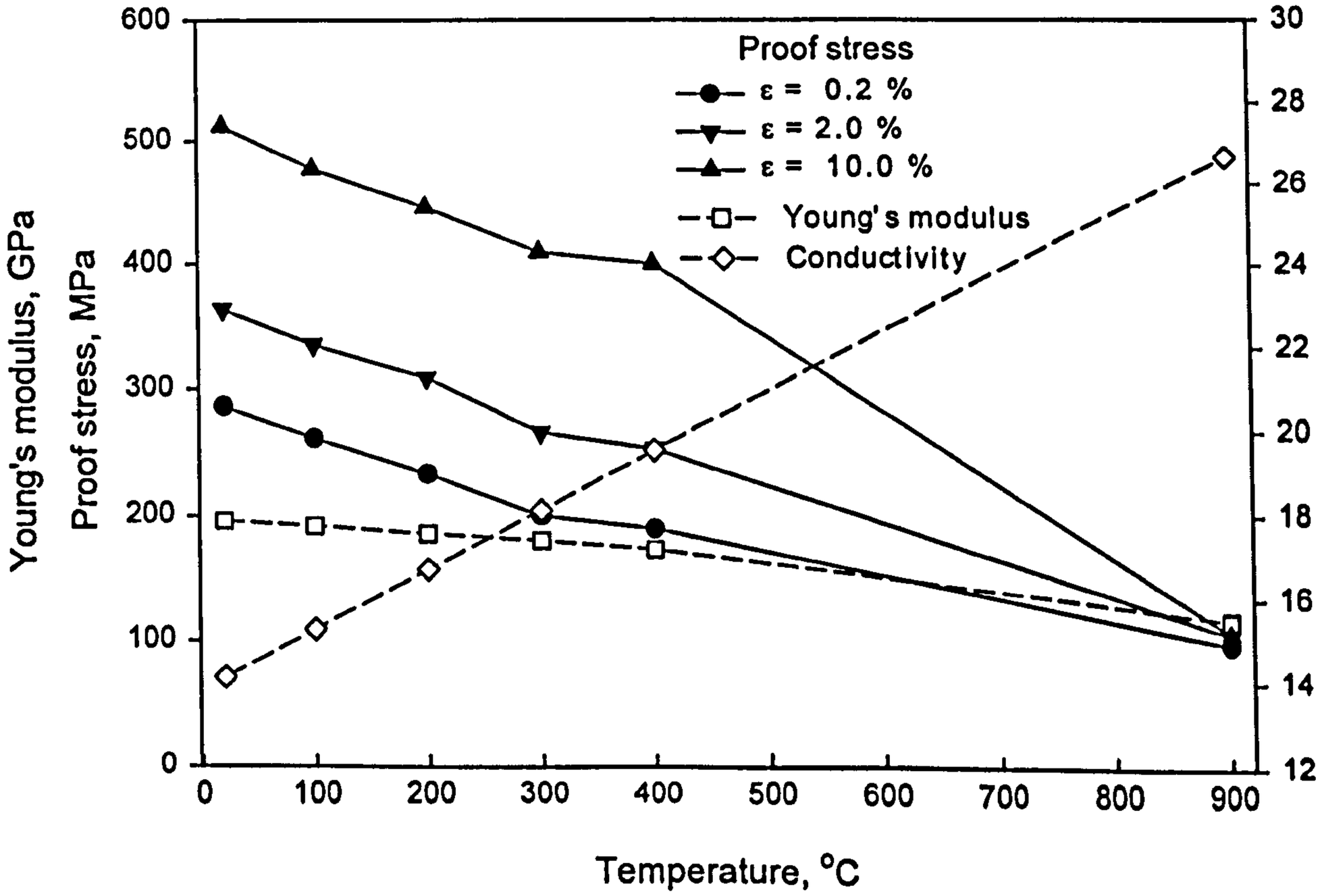

(a) Type 316H

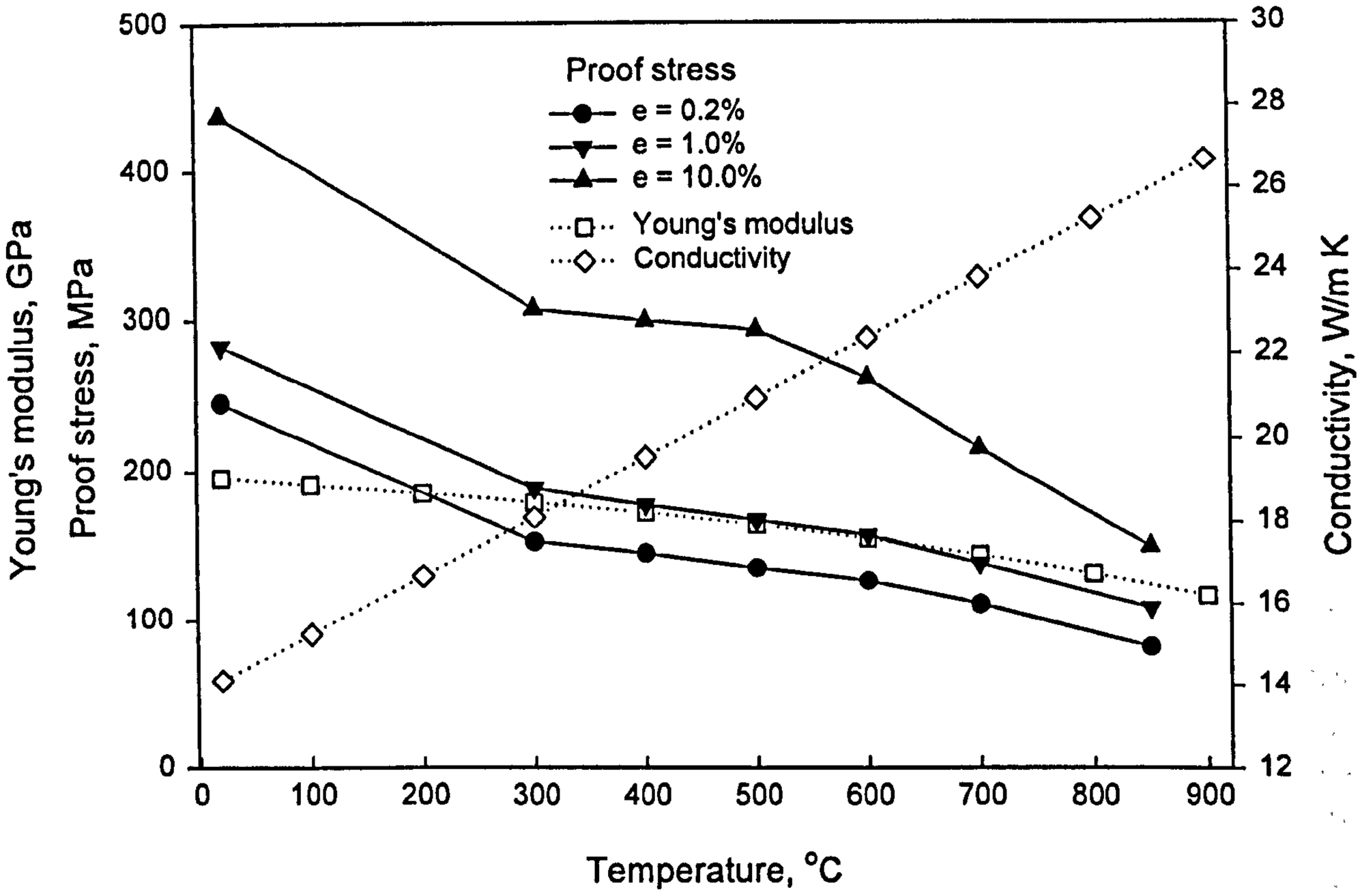

(b) Type 316L

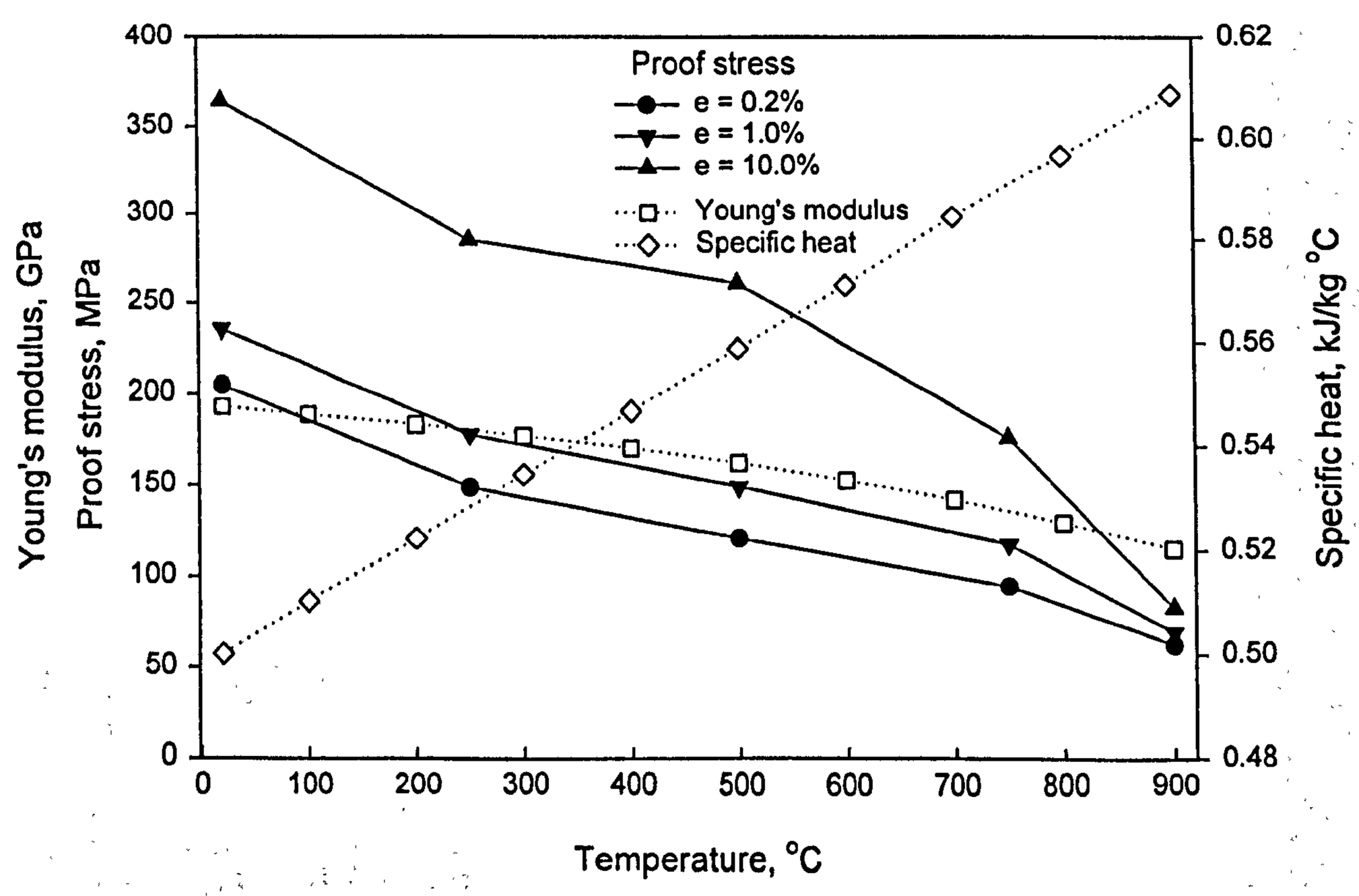

(c) Type 321

Figure 3.2 Stainless steel mechanical and physical properties.

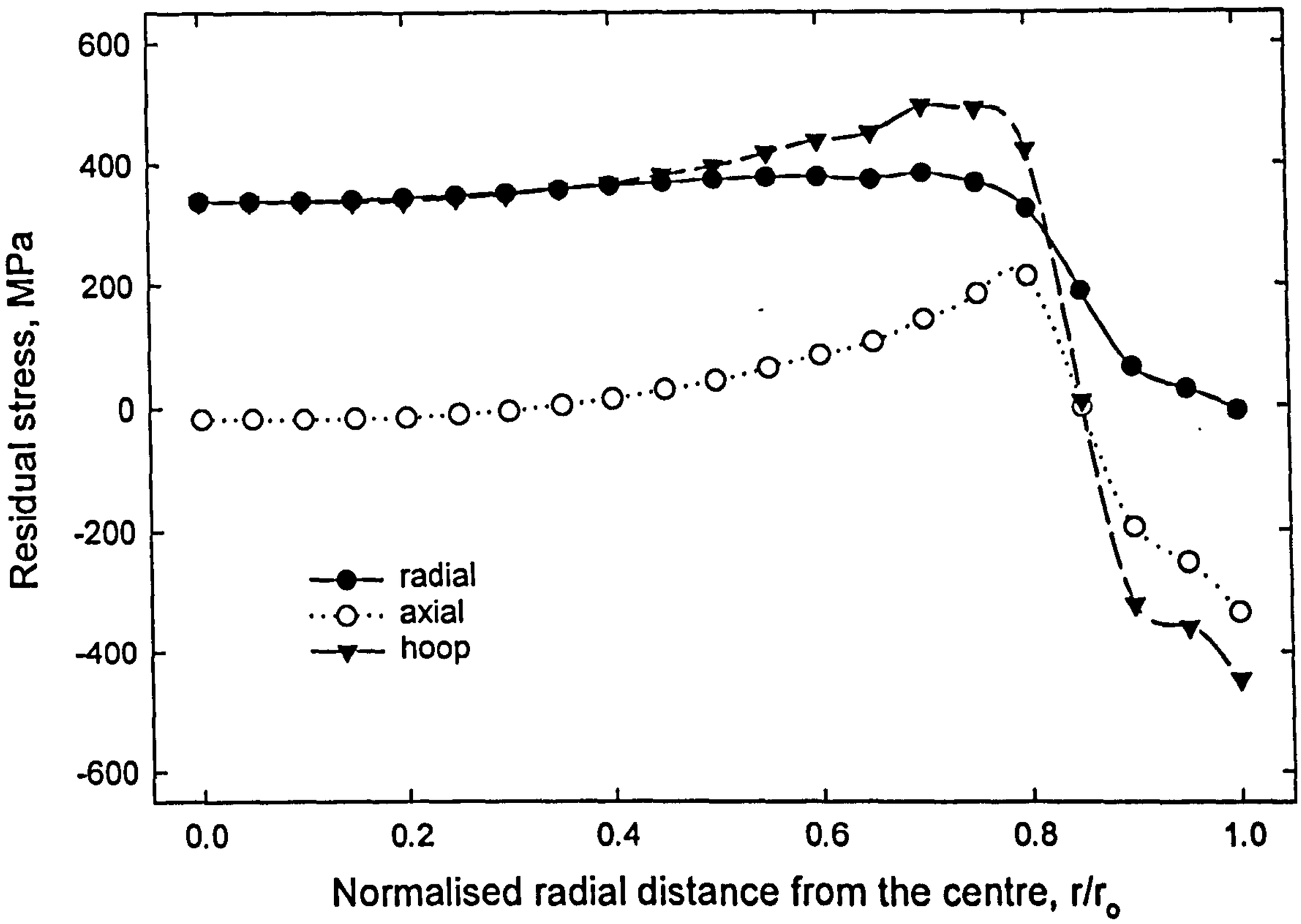

(a) L/D = 0.3, L=27mm, D=90mm

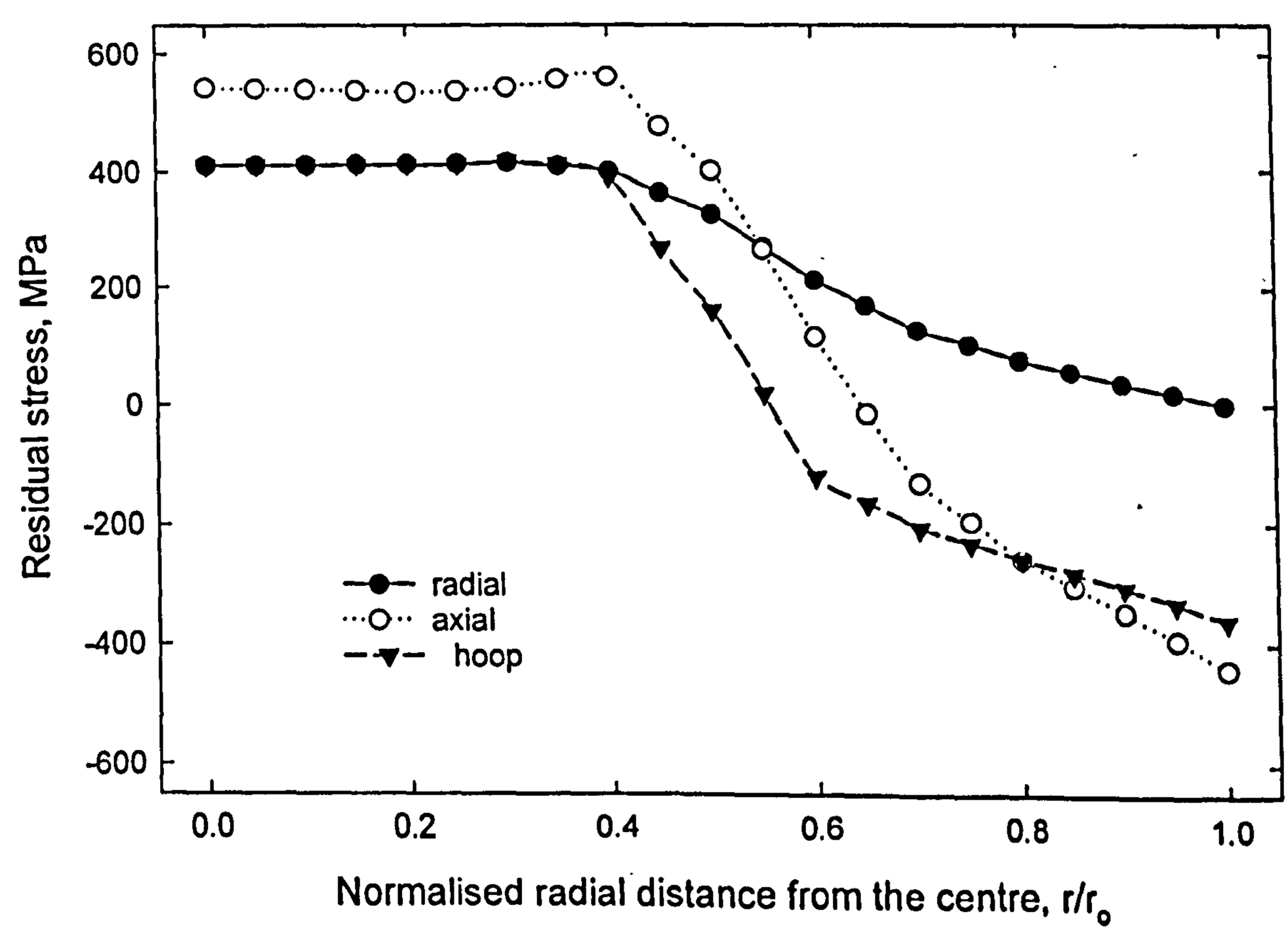

(b) L/D = 1.0, L = 60mm, D = 60mm

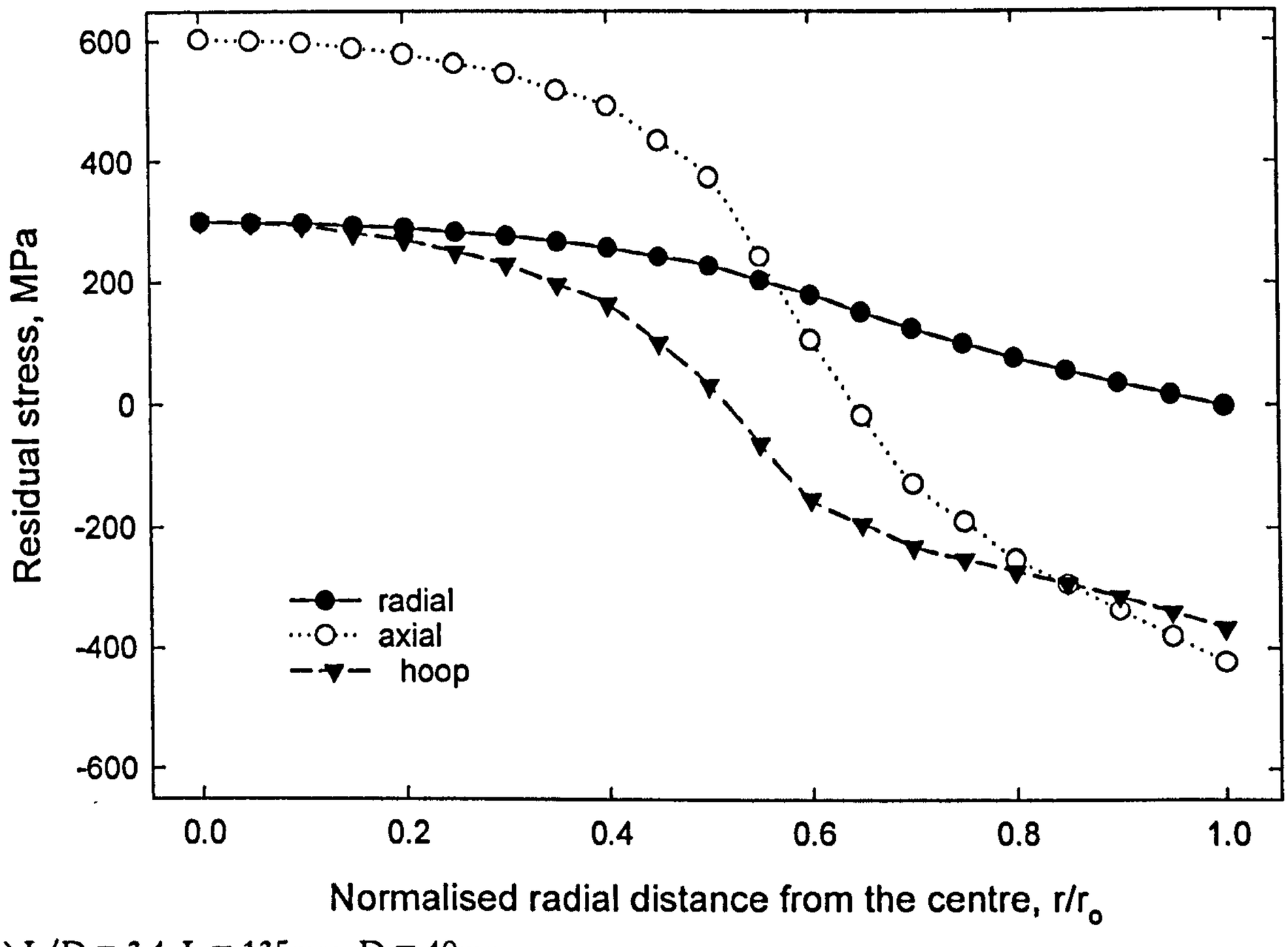

(c) L/D = 3.4, L = 135mm, D = 40mm

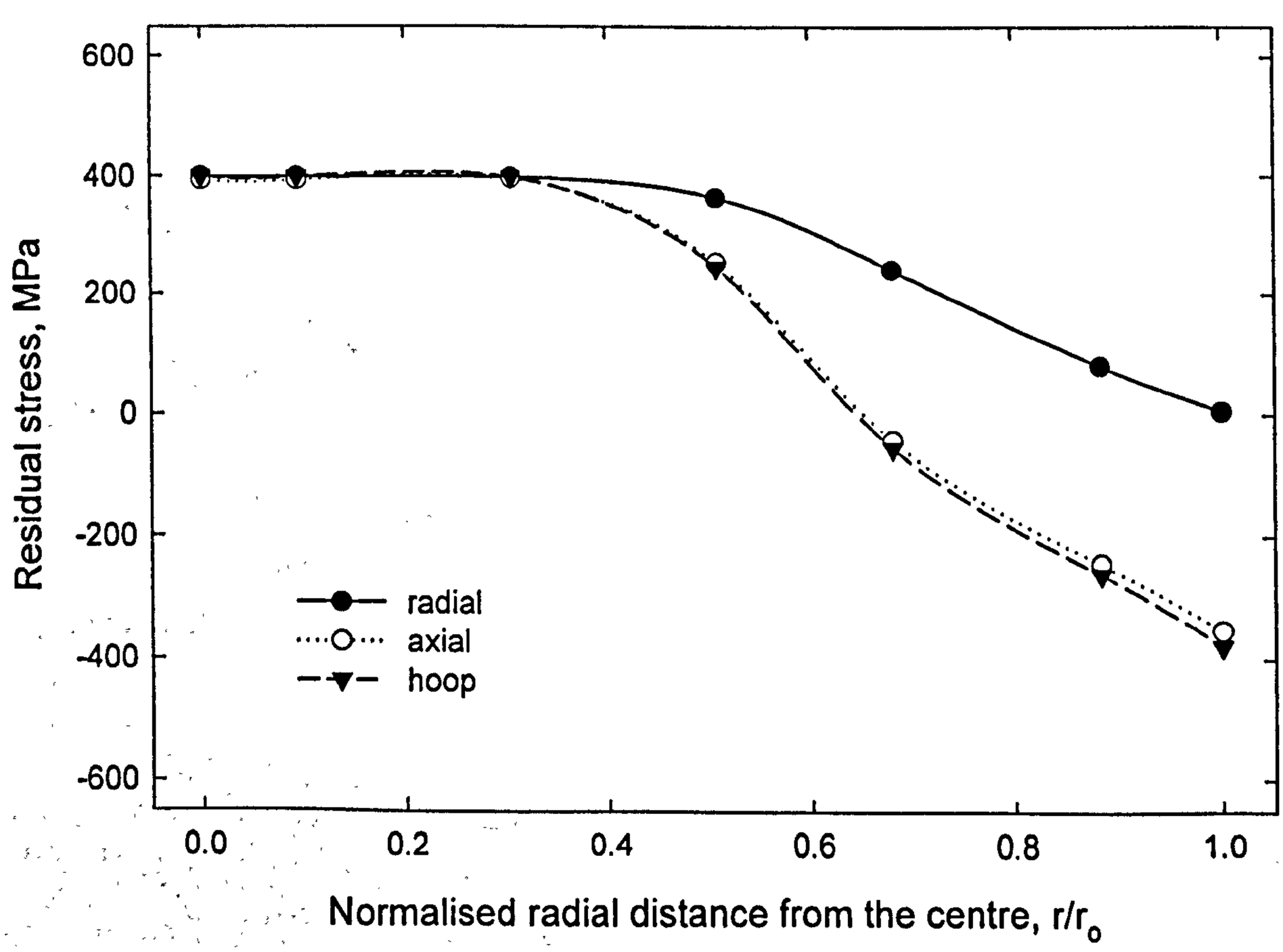

(d) Sphere diameter 30mm

Figure 3.3 Residual stresses across radial line of quenched cylindrical bars and sphere.

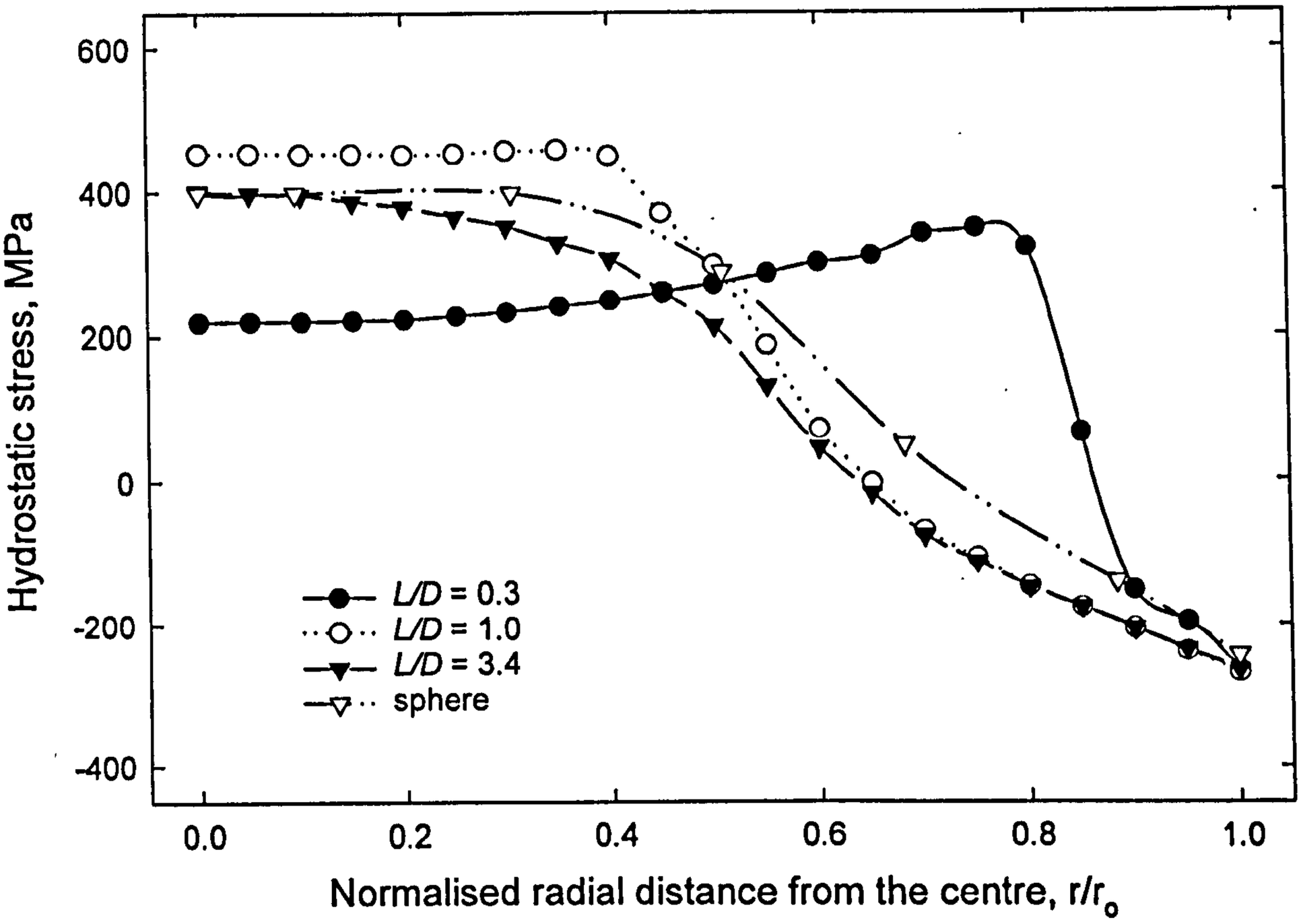

Figure 3.4 Hydrostatic stresses across radial line of quenched cylindrical bars and sphere.

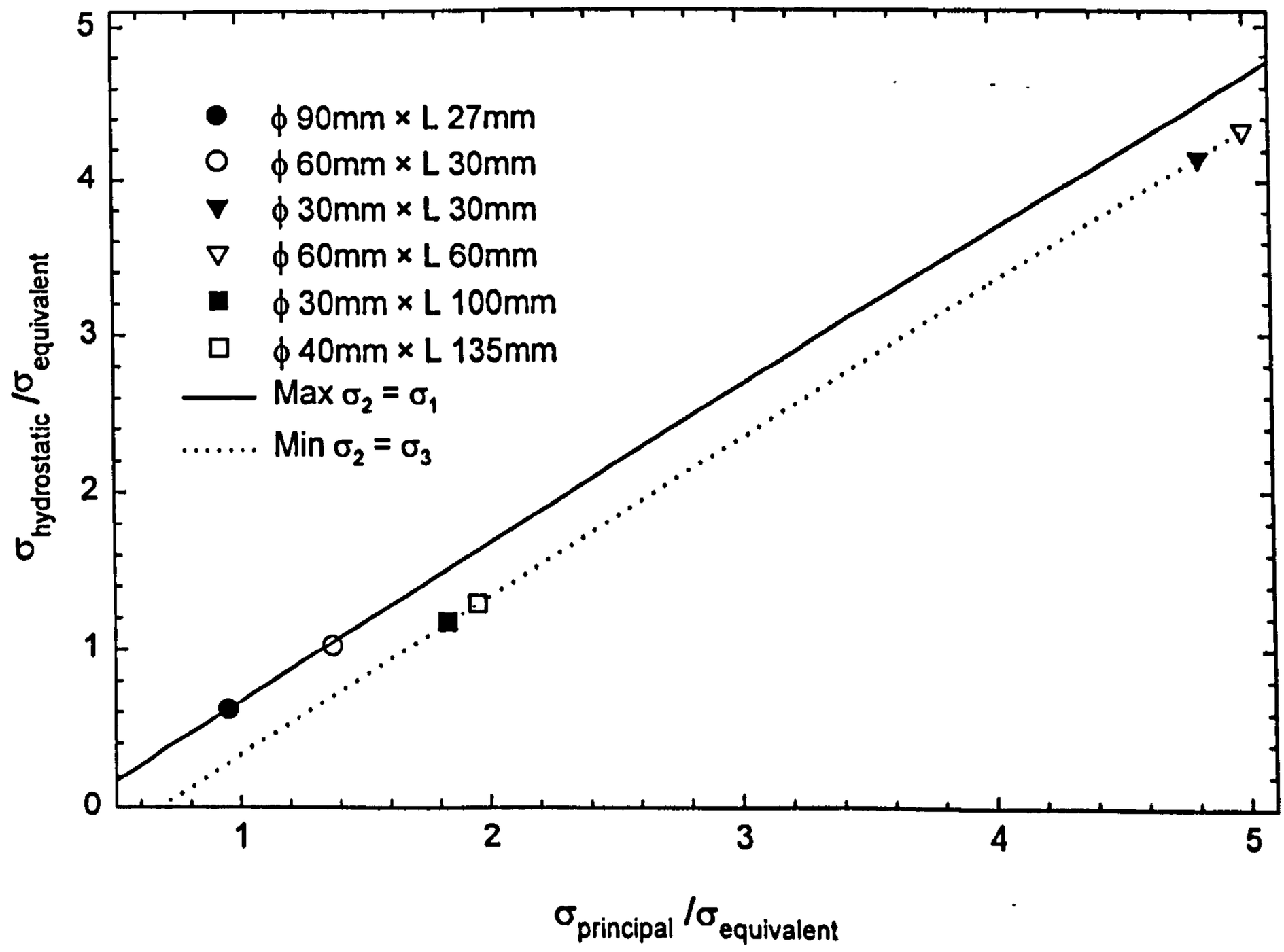

Figure 3.5 Effect of geometry on hydrostatic and principal stress.

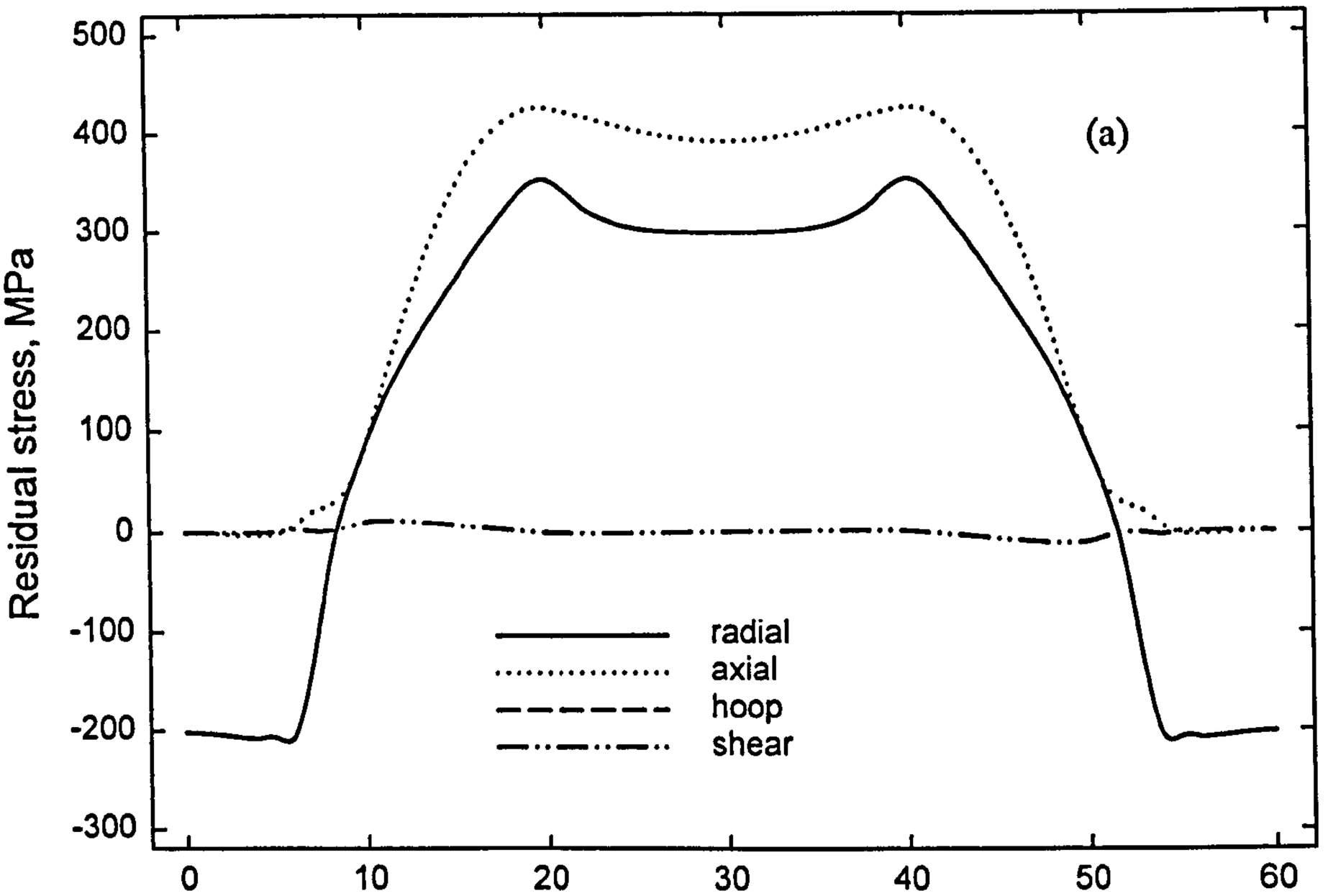

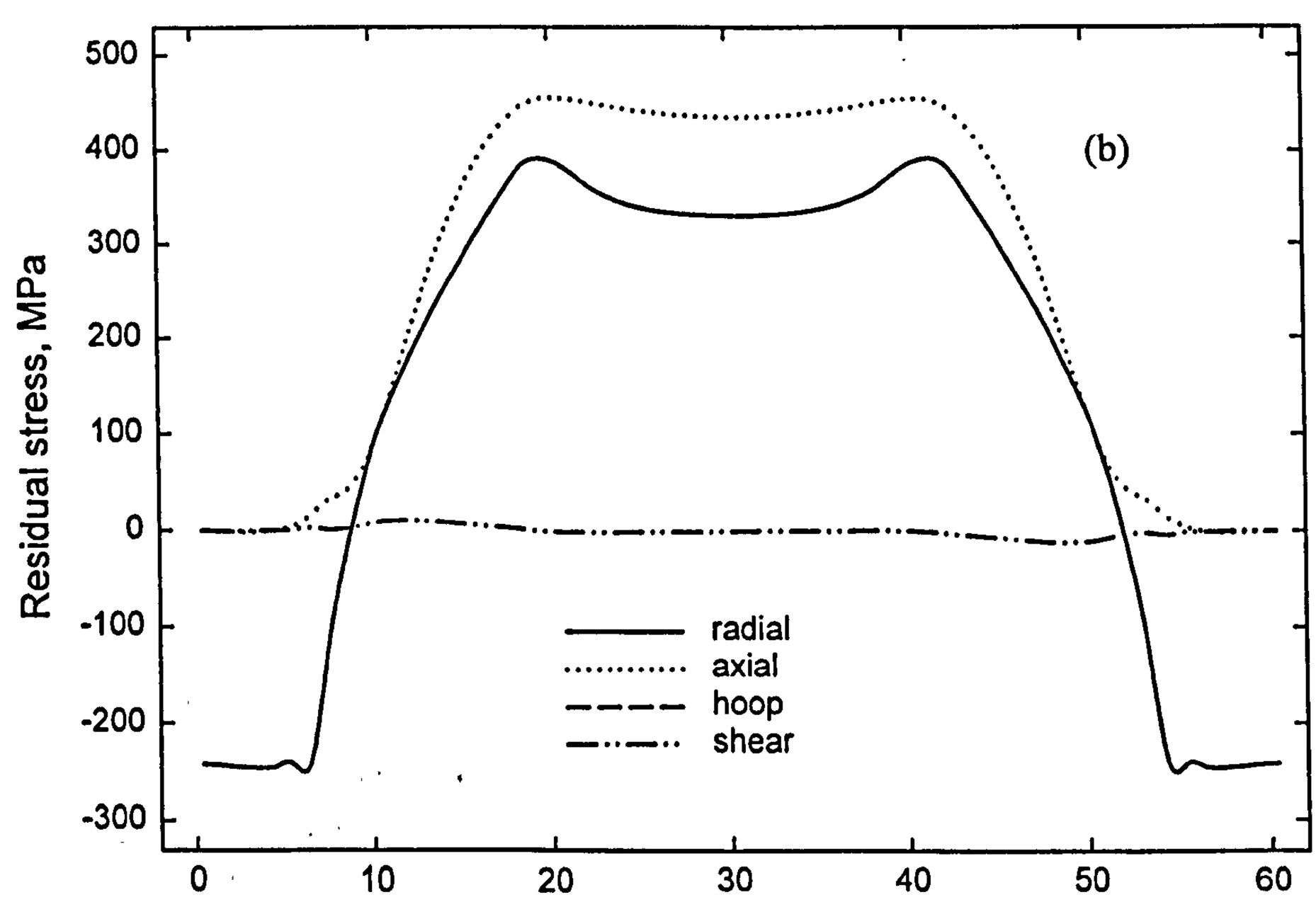

Figure 3.6 Residual stress distributions along the longitudinal axis of a quenched cylinder, diameter 60mm, length 60mm (a) of type 321 and (b) 316L stainless steel.

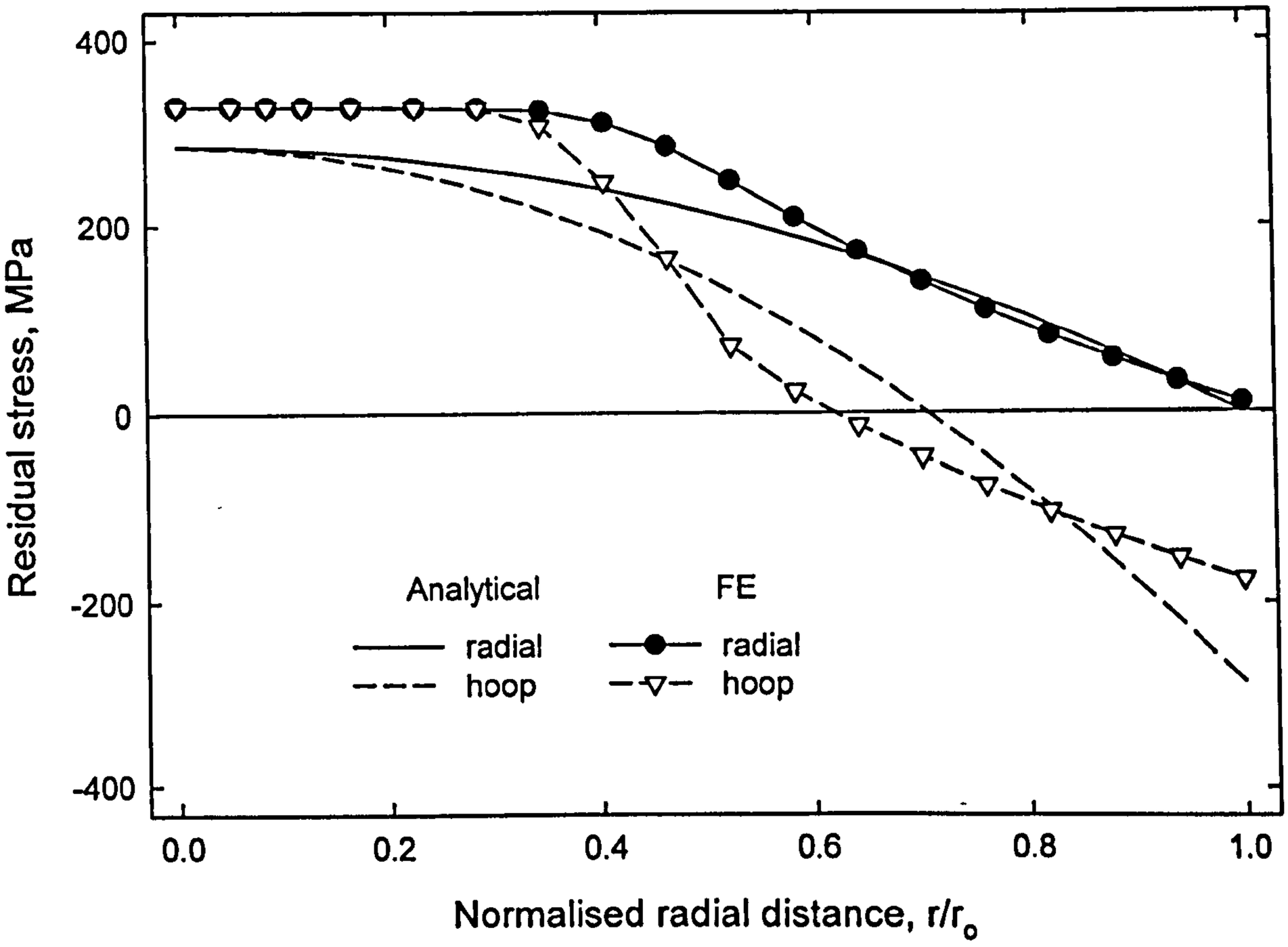

Figure 3.7 Comparison between the FE predicted and analytical distribution of residual stresses across the radial plane from the centre of a solid stainless steel sphere, diameter 30mm. Heat transfer coefficient, h = 7000 W/m^2 K, initial temperature 850°C and kinematic hardening model.

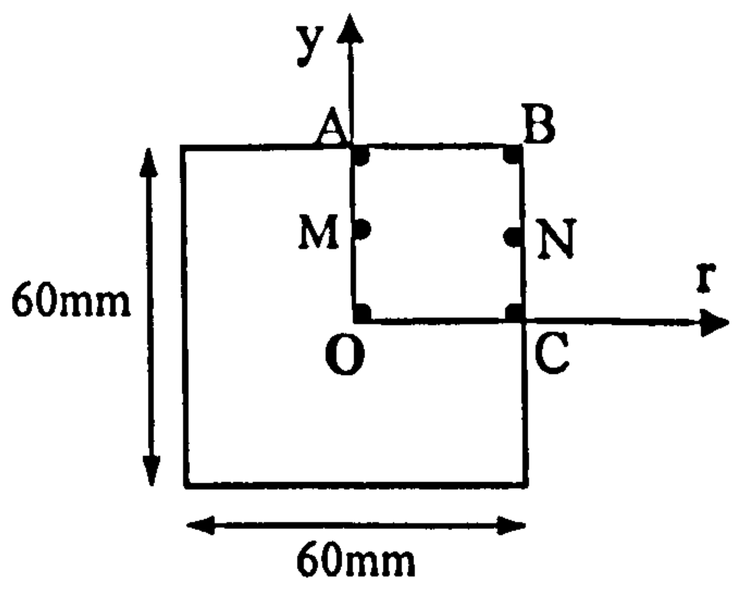

Figure 3.8 Section through a cylinder showing the locations used in Table 3.2.

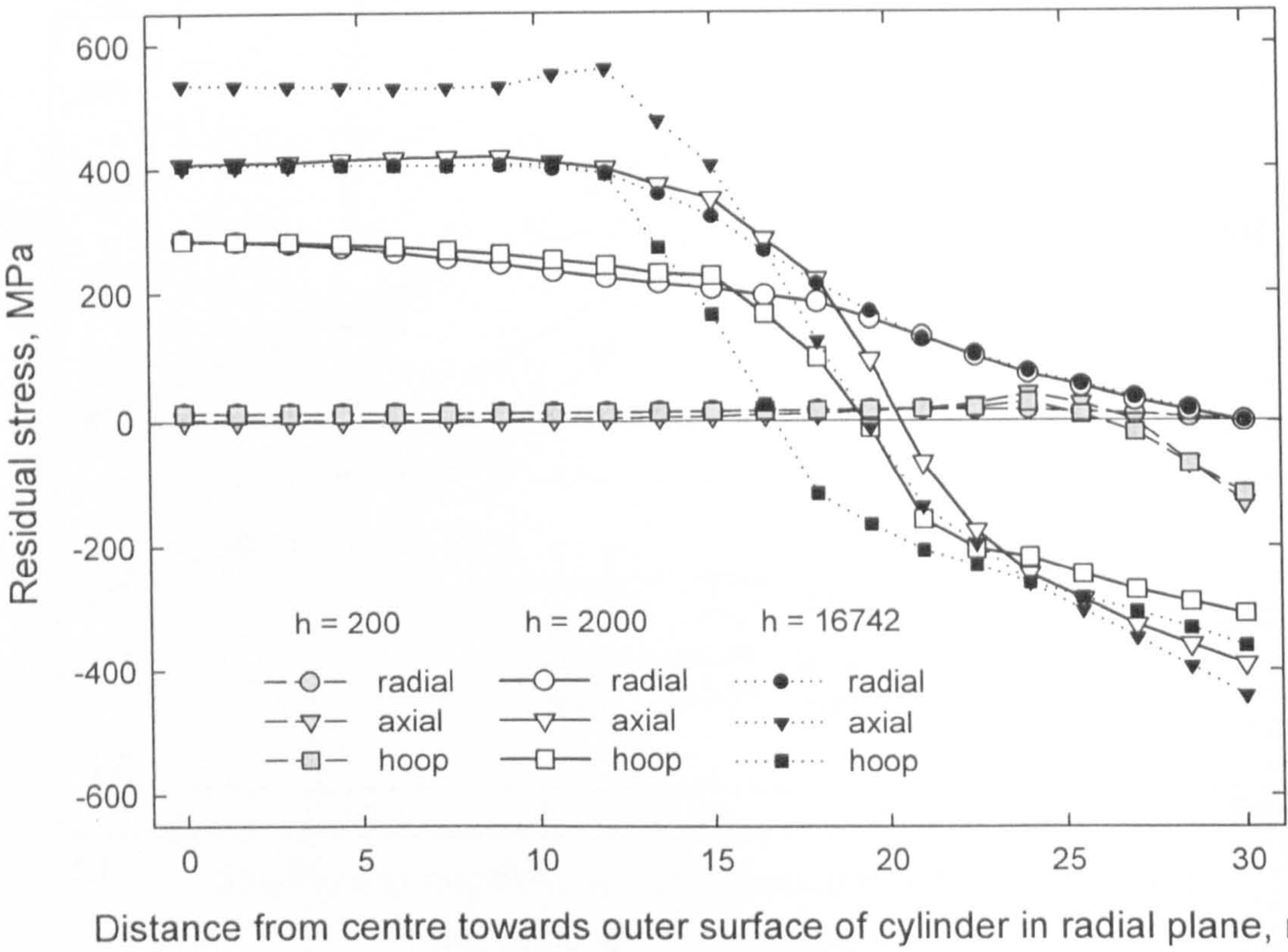

Figure 3.9 Effect of heat transfer coefficient h (W/m^2 K) on the predicted residual stress distribution.

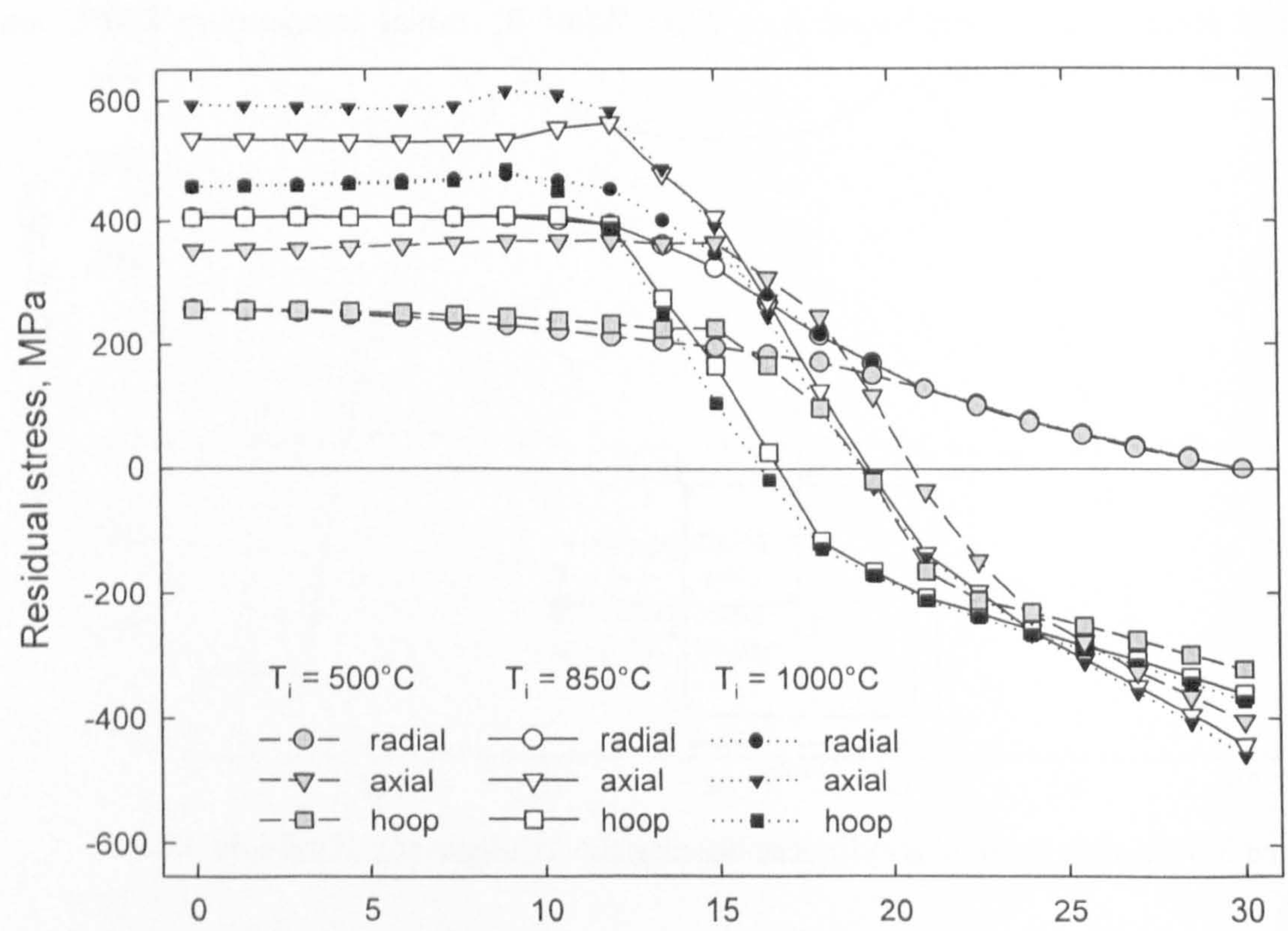

Figure 3.10 Effect of initial temperature on the predicted residual stress distribution.

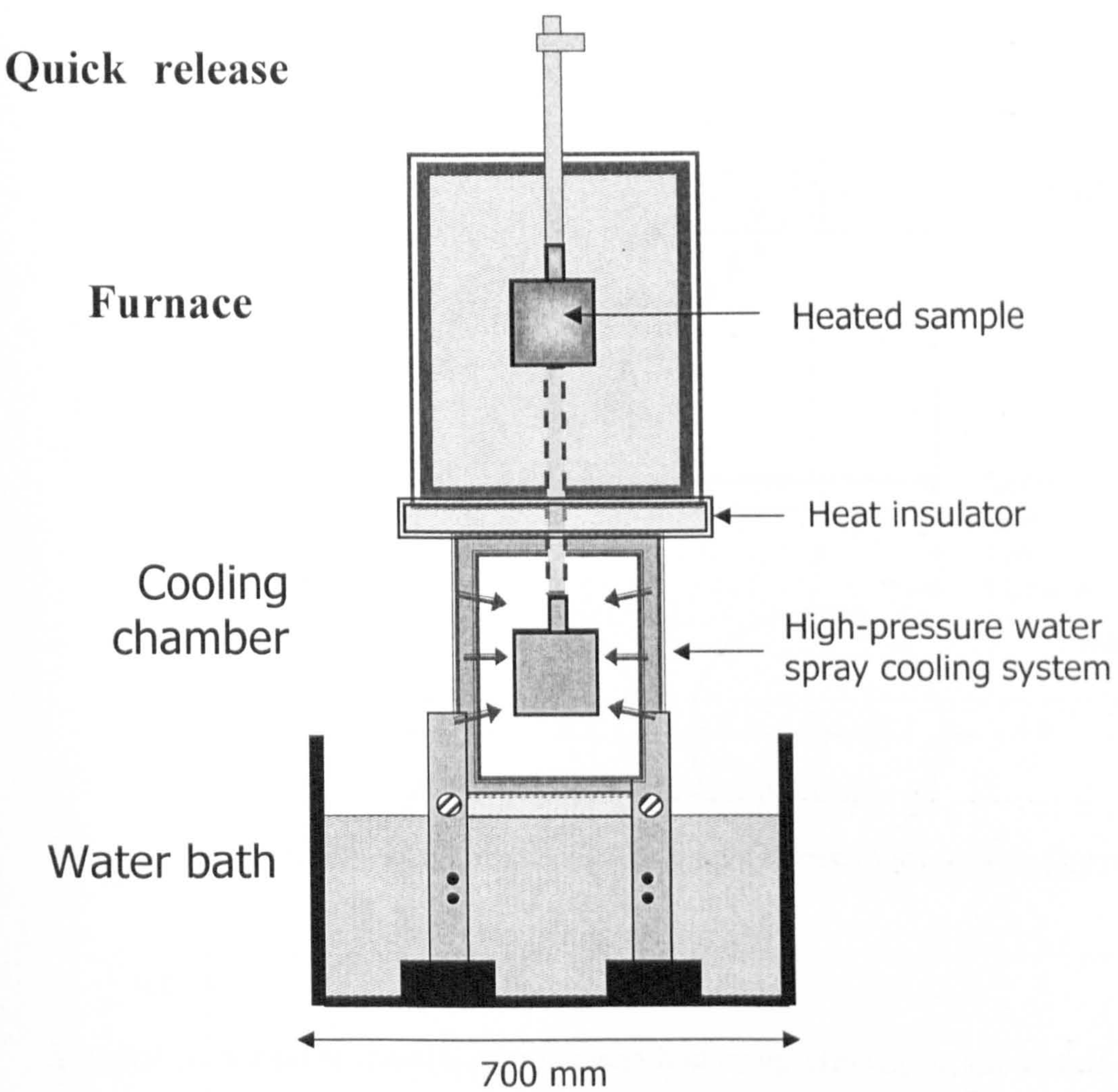

Figure 3.11 Schematic layout of the quenching rig.

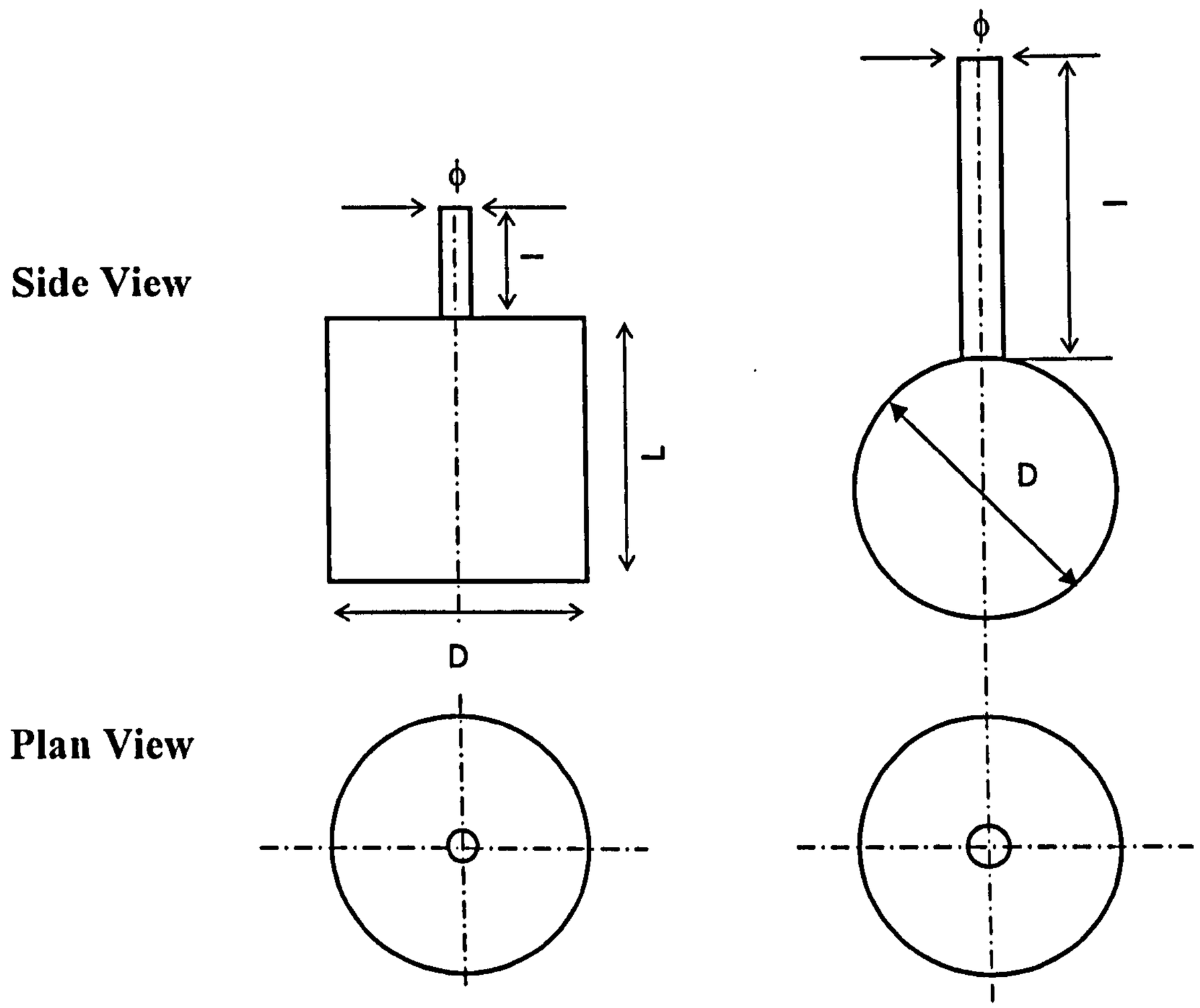

Figure 3.12 Schematic of generic quenched specimens, cylinder, diameter *D*, length *L* and sphere, diameter *D*.

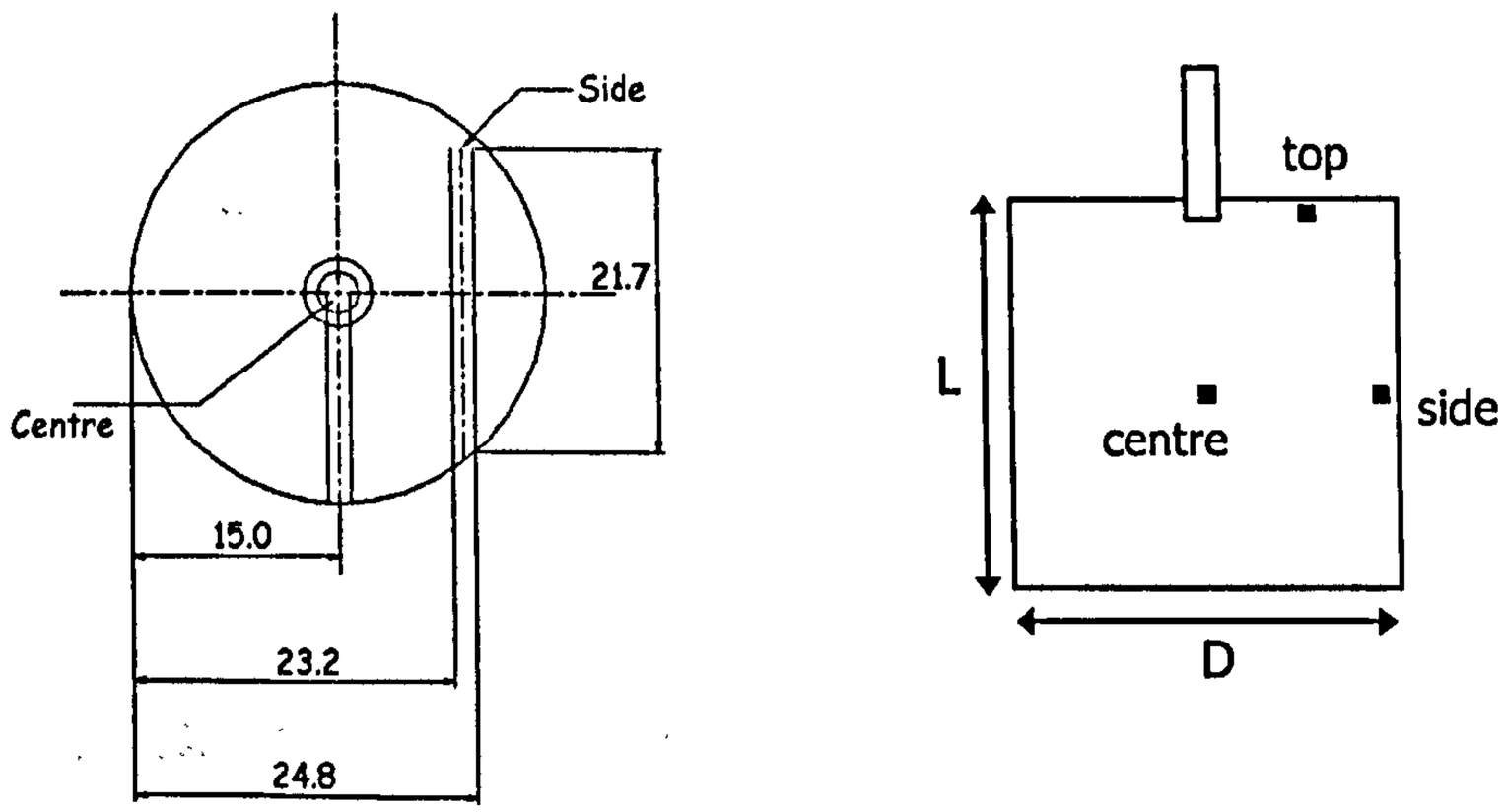

Figure 3.13 Plan view of a solid sphere, diameter 30mm illustrating the positions of thermocouples for temperature measurements during heating and subsequent quenching. Also shown is a vertical section of a generic cylindrical body, diameter *D*, length *L* to illustrate the locations of thermocouples during quenching test.

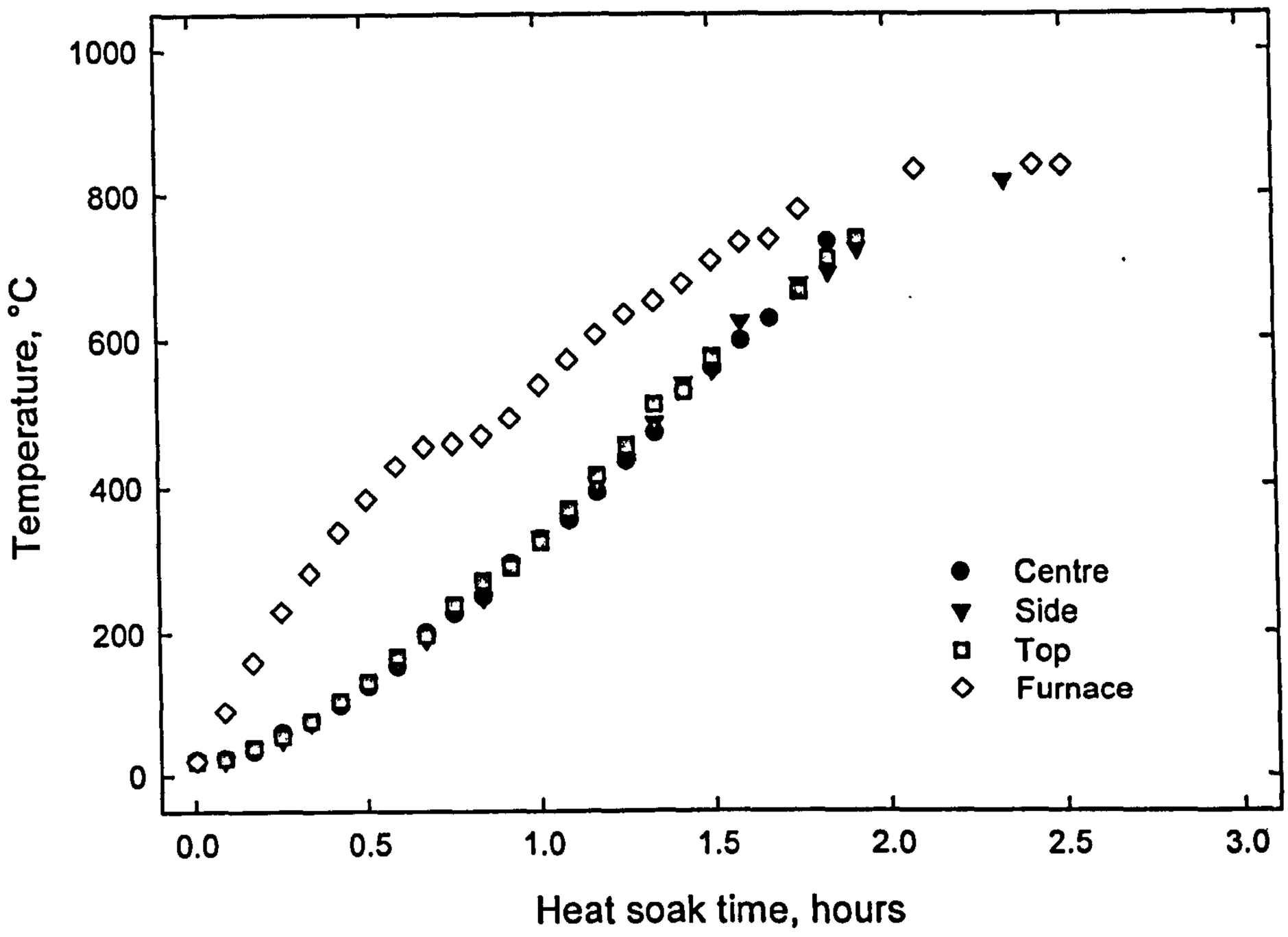

Figure 3.14 Temperature distributions in a quenched cylinder (*s2*) during preheating.

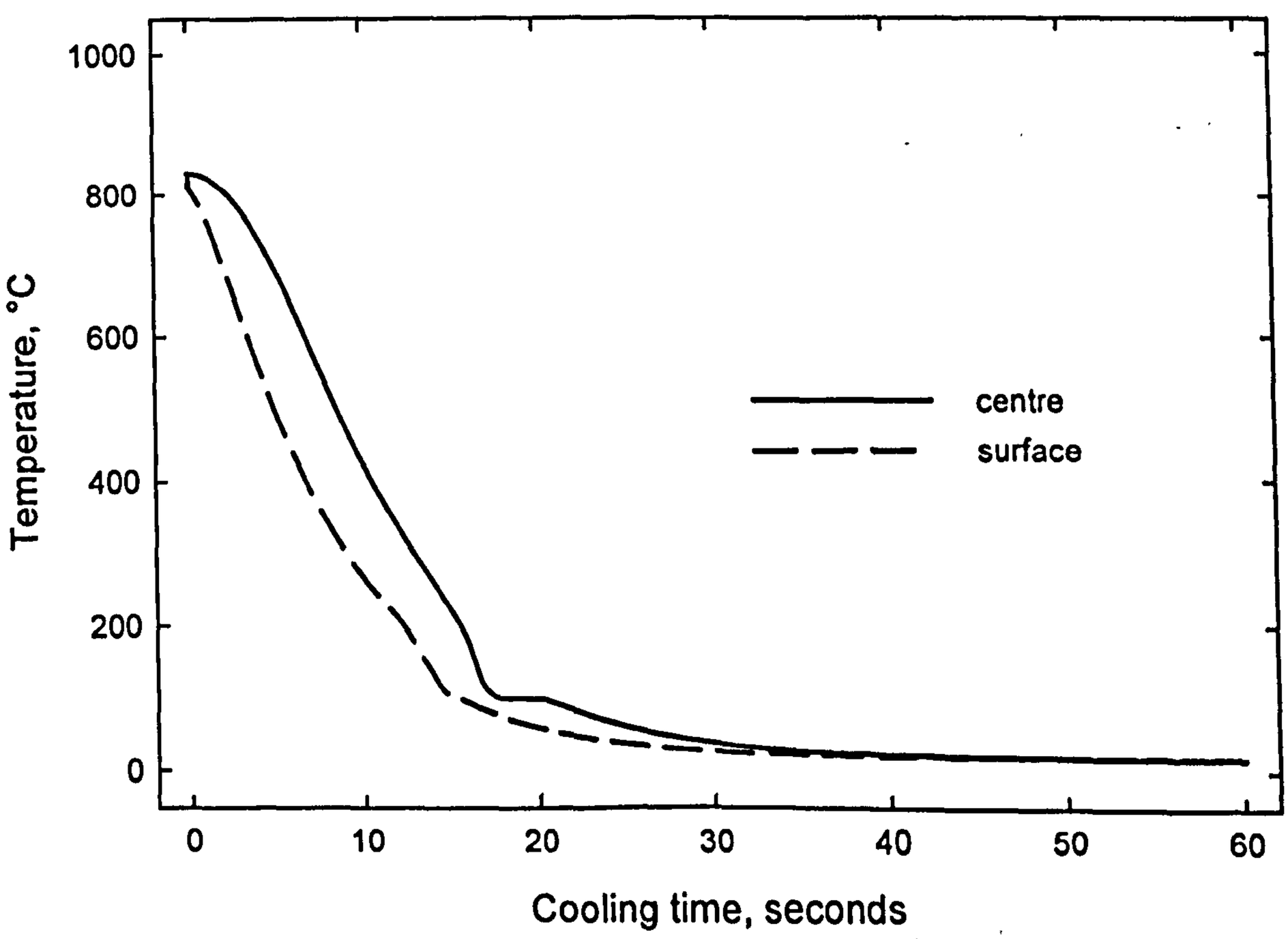

Figure 3.15 Typical temperature-time curve measured during cooling at the centre and surface of a quenched sphere, 30 mm diameter (*s22*).

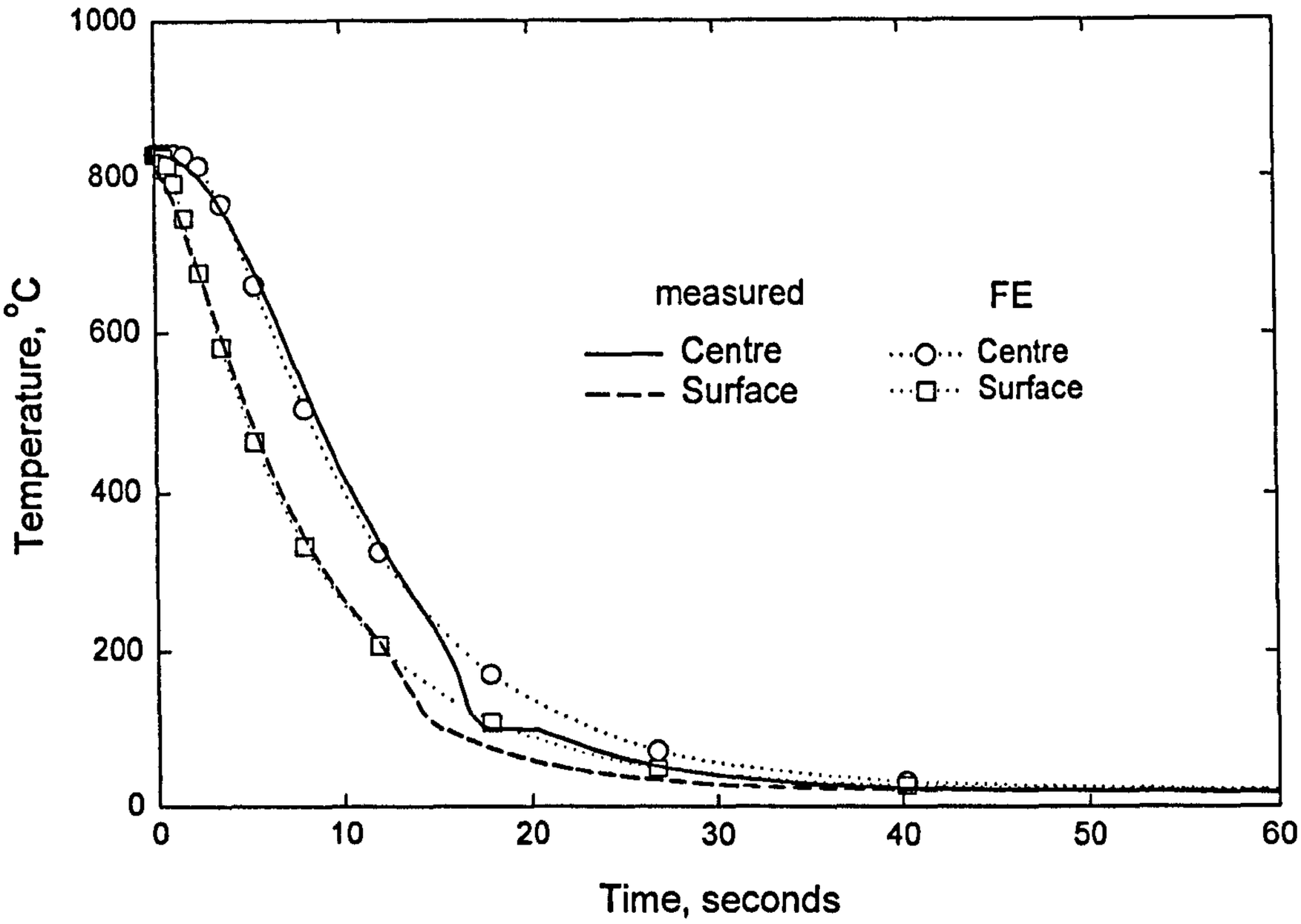

Figure 3.16 Typical temperature-time curve measured during cooling at the centre and surface of a quenched sphere (*s22*), 30 mm diameter, compared with finite element results. Heat transfer coefficient, $h = 7000$ W/m^2 K.

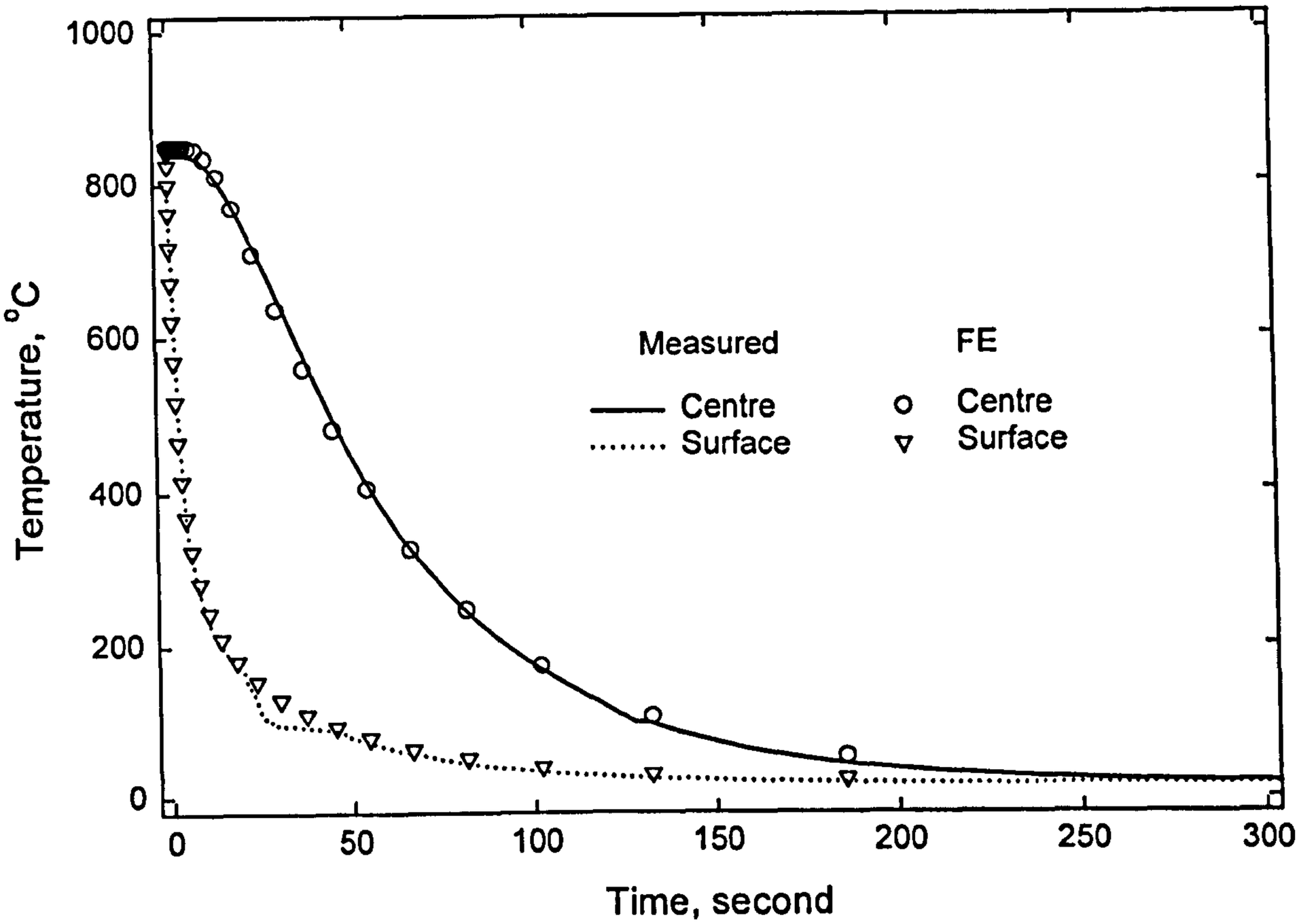

Figure 3.17 Typical temperature-time curve measured during quenching at the centre and surface of a quenched cylinder (*s26*), diameter 60mm, length 160mm. Comparison is made with finite element simulation. Heat transfer coefficient, $h = 7000$ W/m^2 K.

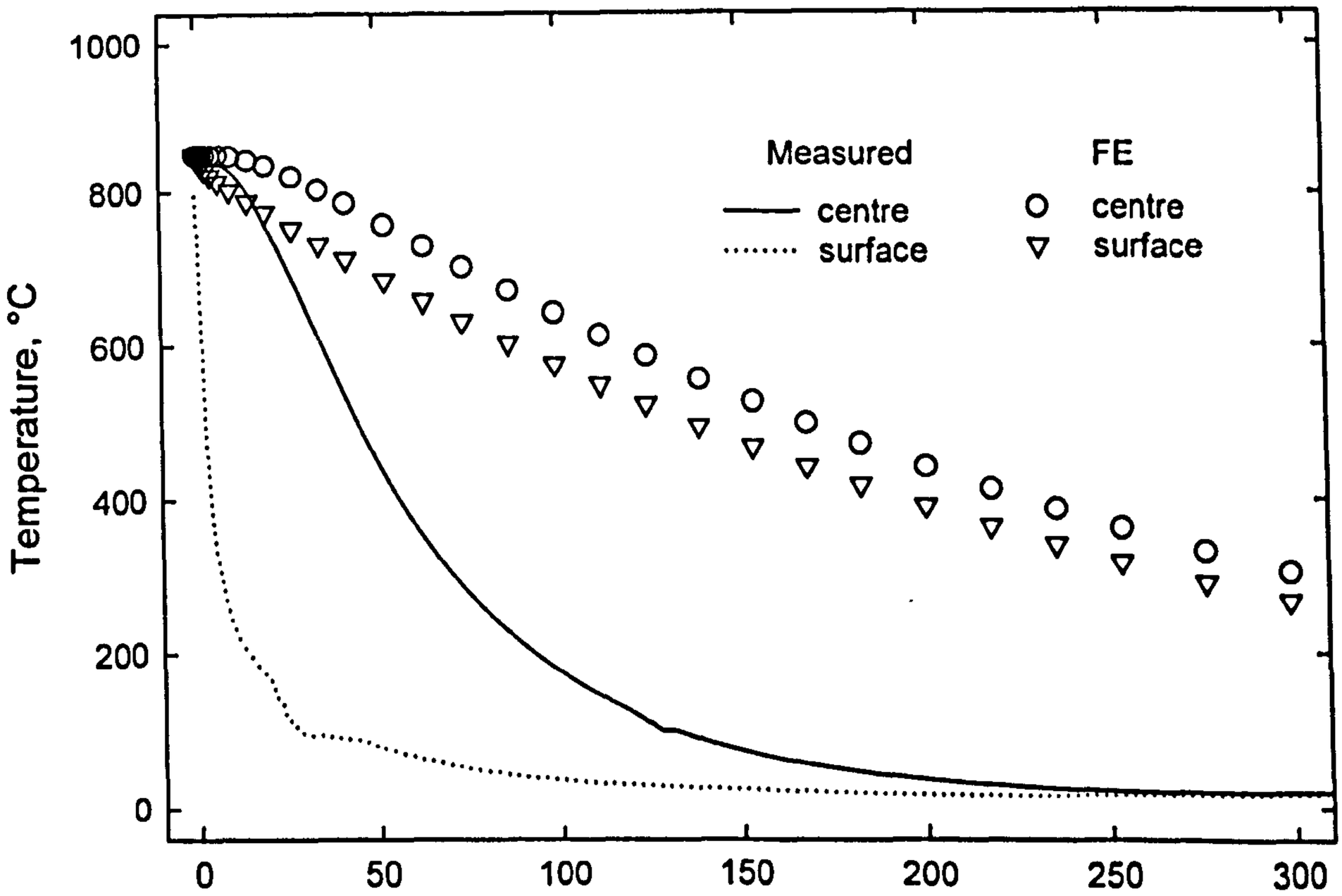

Figure 3.18 FE predicted temperature-time curve with heat transfer coefficient, $h = 200$ W/m^2 K compared with measured temperature fields for sample *s26*.

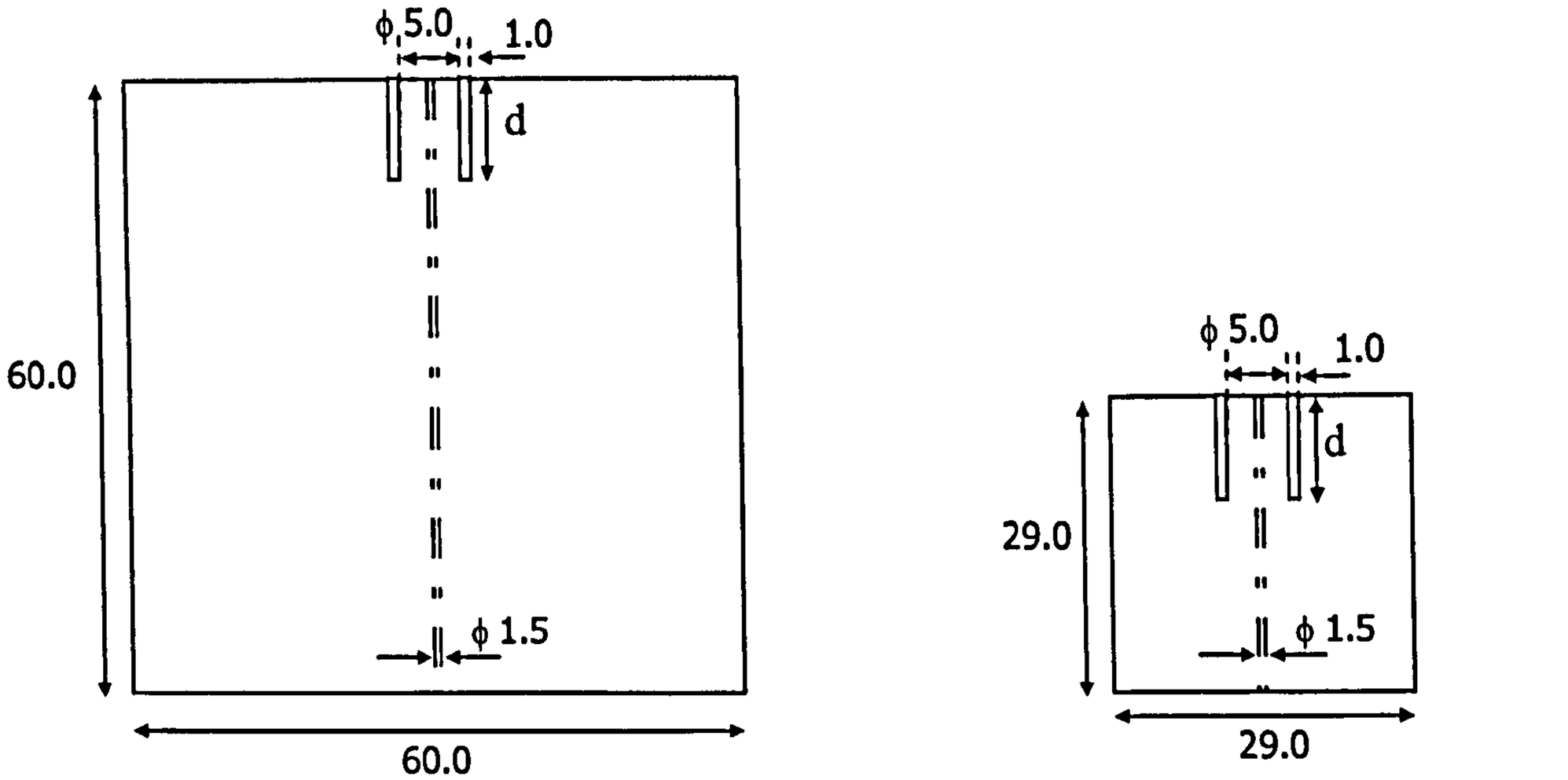

(a) Large quenched pre-trepanned cylinders *s40-s44*

(b) Small quenched pre-trepanned cylinders *s34-s38*

Figure 3.19 Schematic of the preparation of trepanned cylinders. For (a) large cylinders the edm depths *d* were 0, 15.5, 30.0, 45.5, 60.0 corresponding to samples s44, s40, s41, s42, s43, respectively listed in Table 3.3. For (b) small cylinders the edm depths *d* were 0, 8.5, 15.5, 21.5, 28.0 corresponding to samples s38, s34, s35, s36, s37, respectively (see Table 3.3). All dimensions in mm. As shown the drilling diameter was 1.5mm, the edm trepan diameter was 5.0mm and the thickness of copper electrode was 1.0mm.

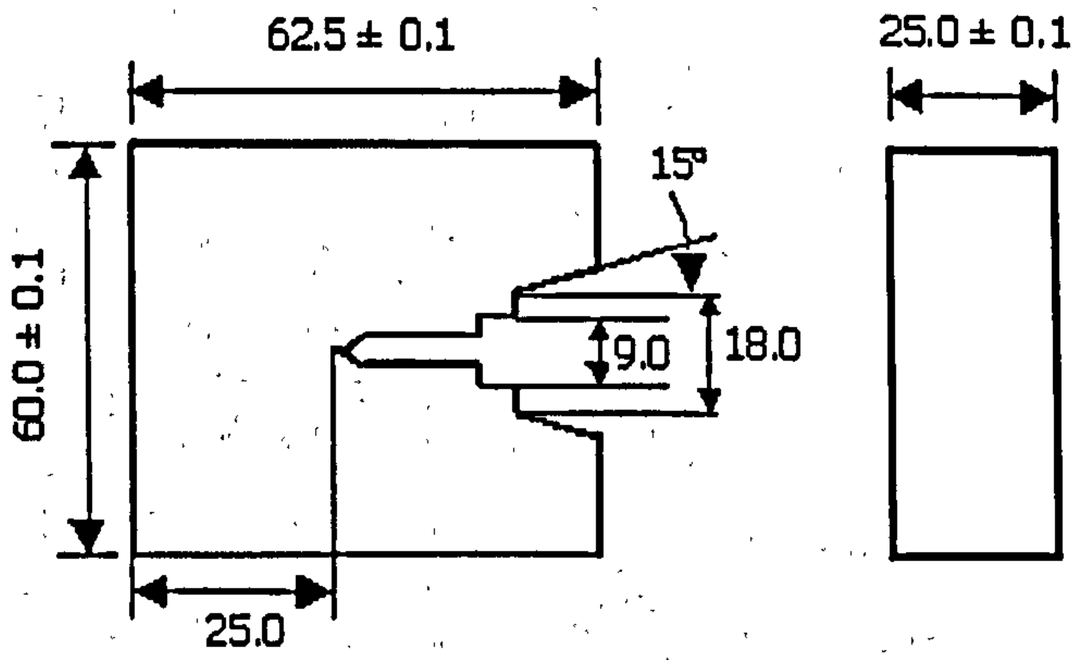

Figure 3.20 Side punch C(T) specimen (dimensions in mm).

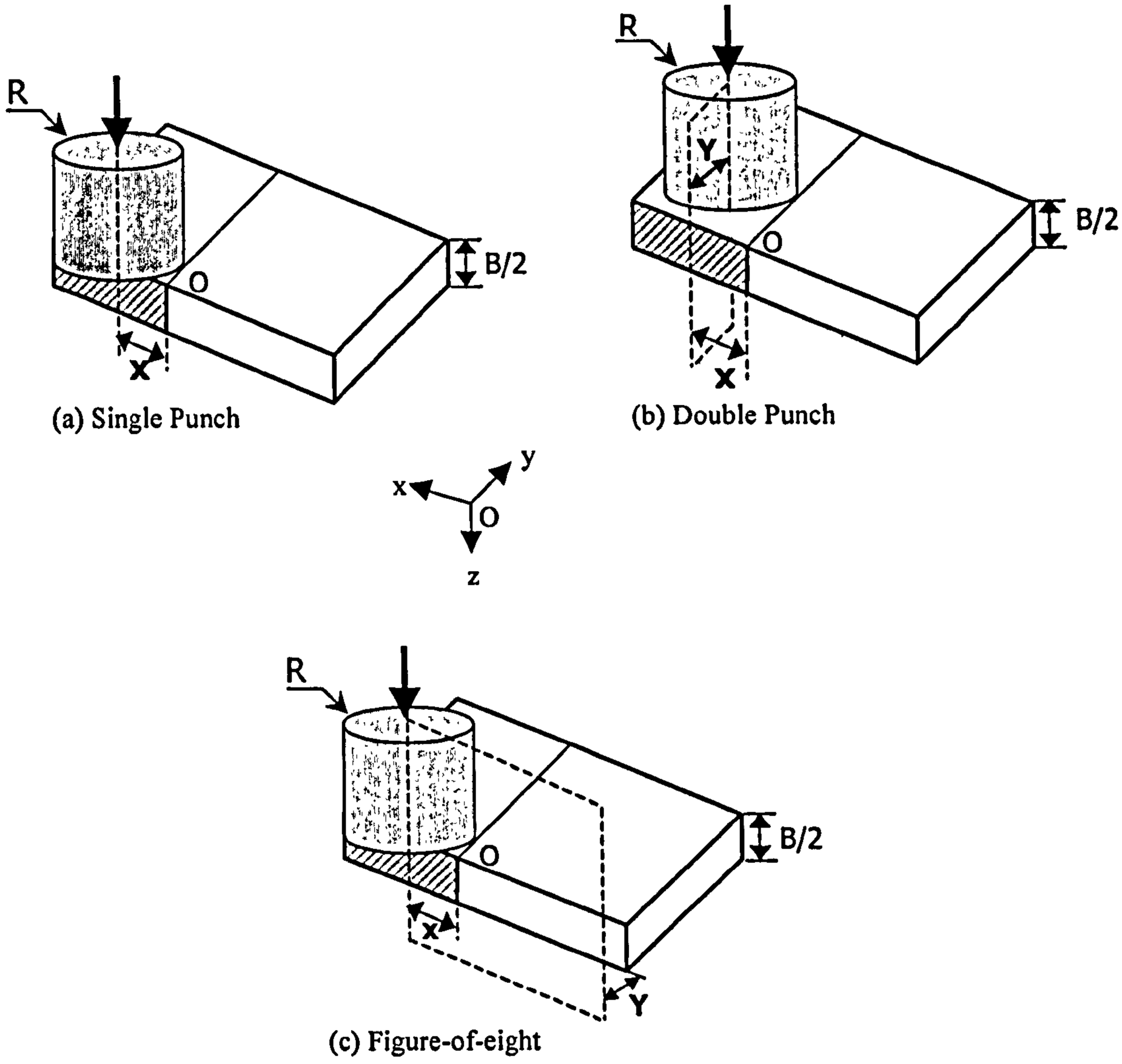

Figure 3.21 Schematic of the side-punching process on C(T) specimen. A quarter of the specimen is shown.

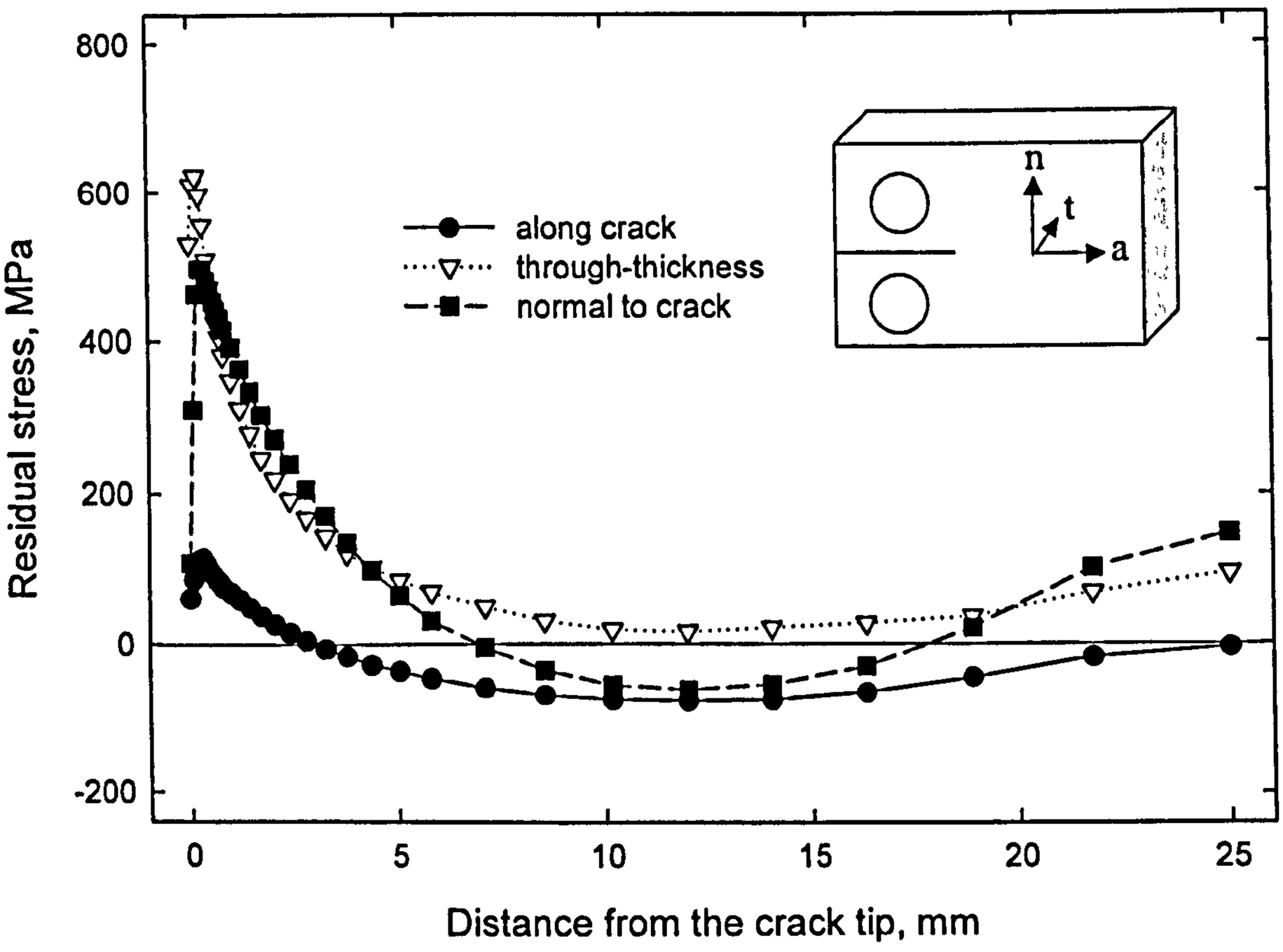

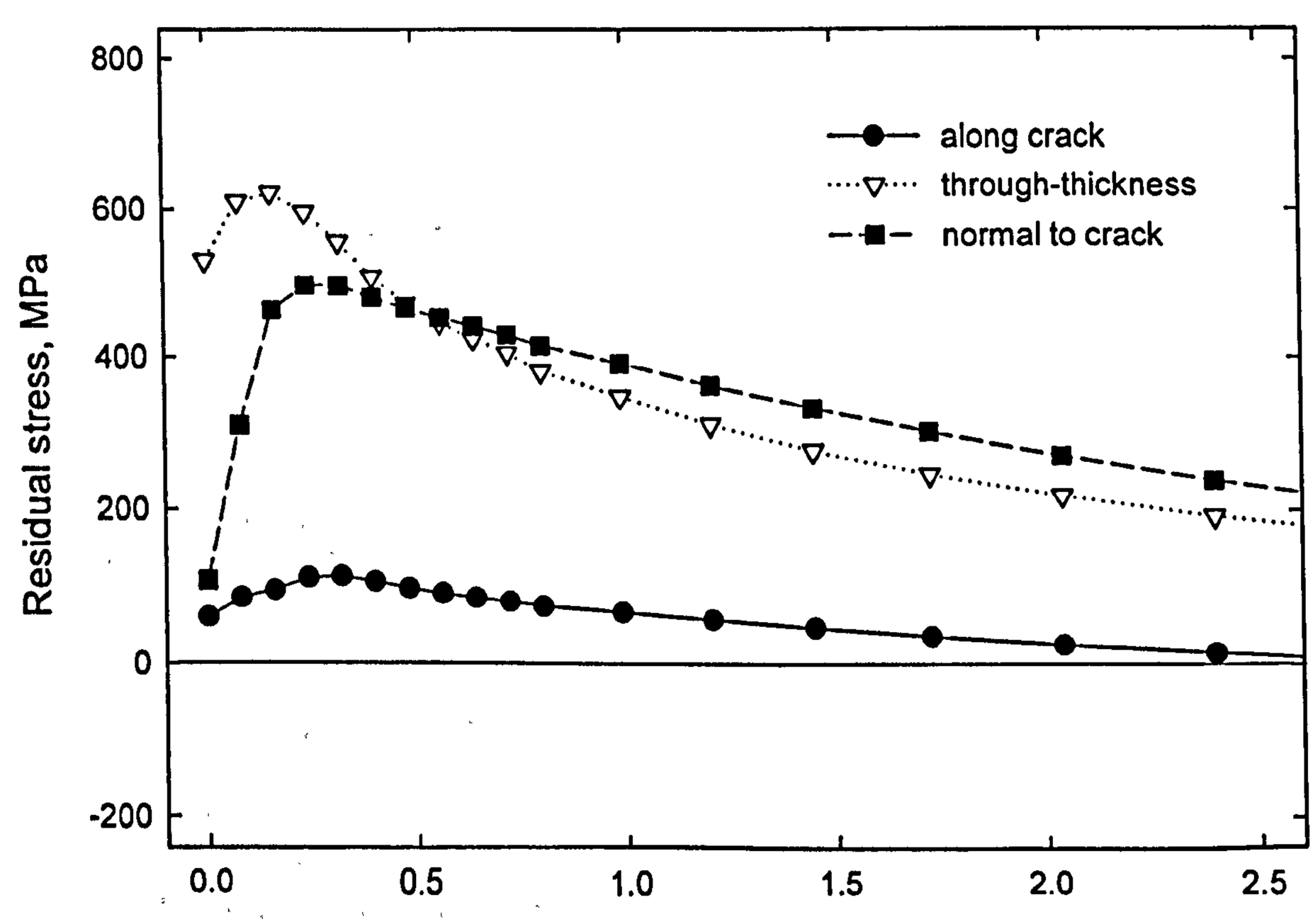

Figure 3.22 Residual stress distribution across the ligament from the notch tip of the C(T) specimen under various loading conditions for single punch. For clarity distribution in the first 2.5mm from the notch tip is also shown.

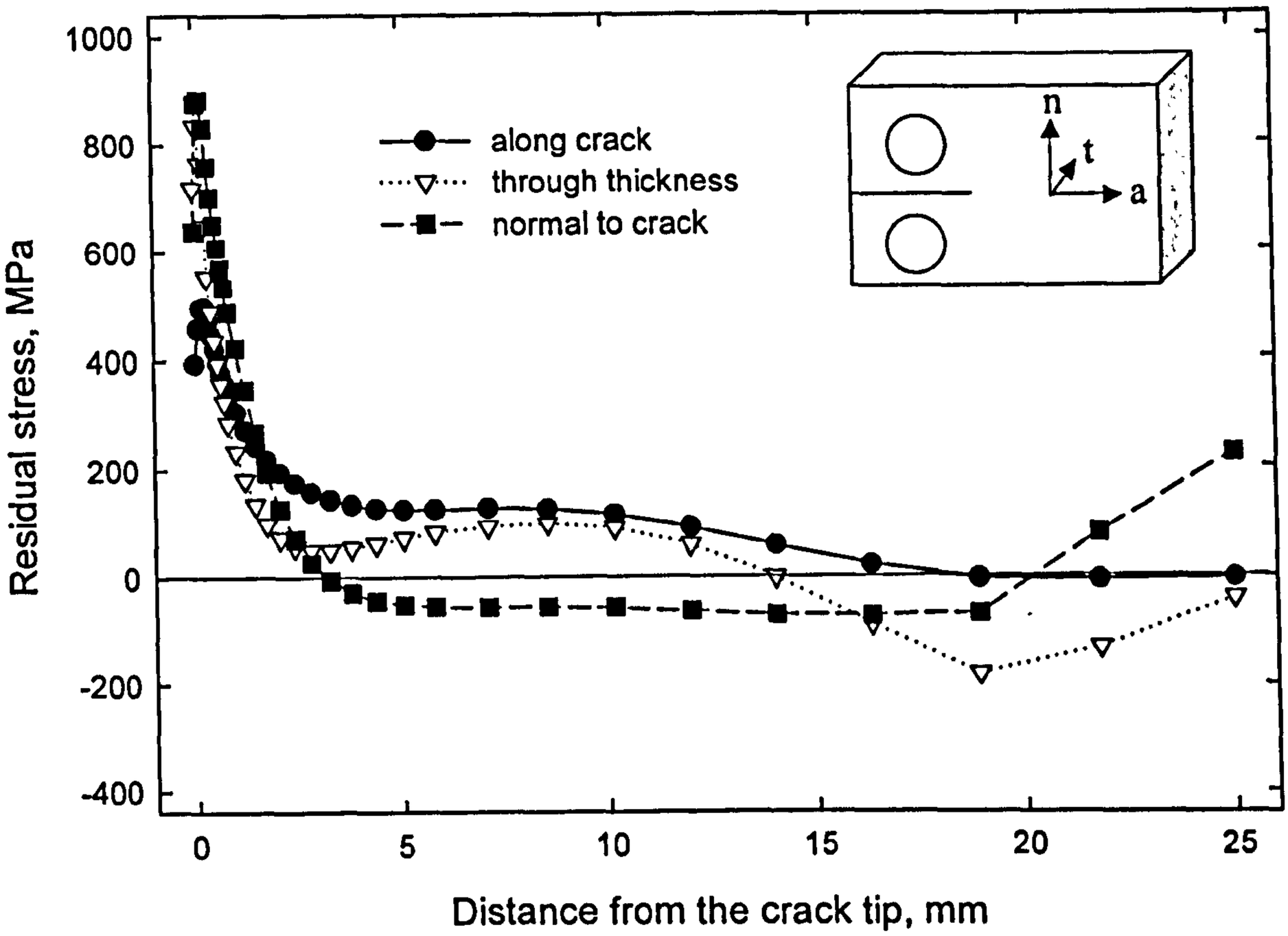

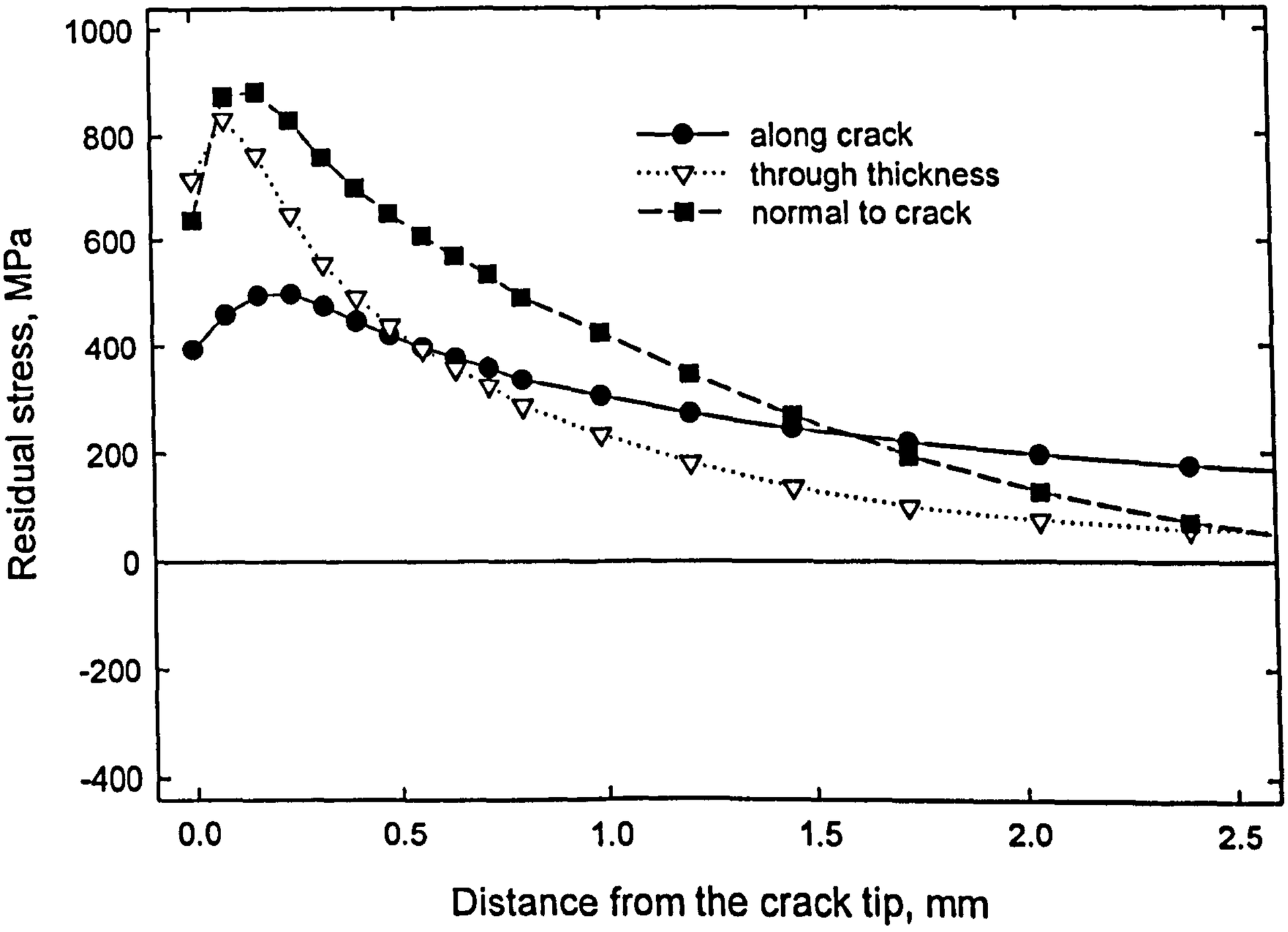

Figure 3.23 Residual stress distribution across the ligament from the notch tip of the C(T) specimen under various loading conditions for double punch. For clarity distribution in the first 2.5mm from the notch tip is also shown.

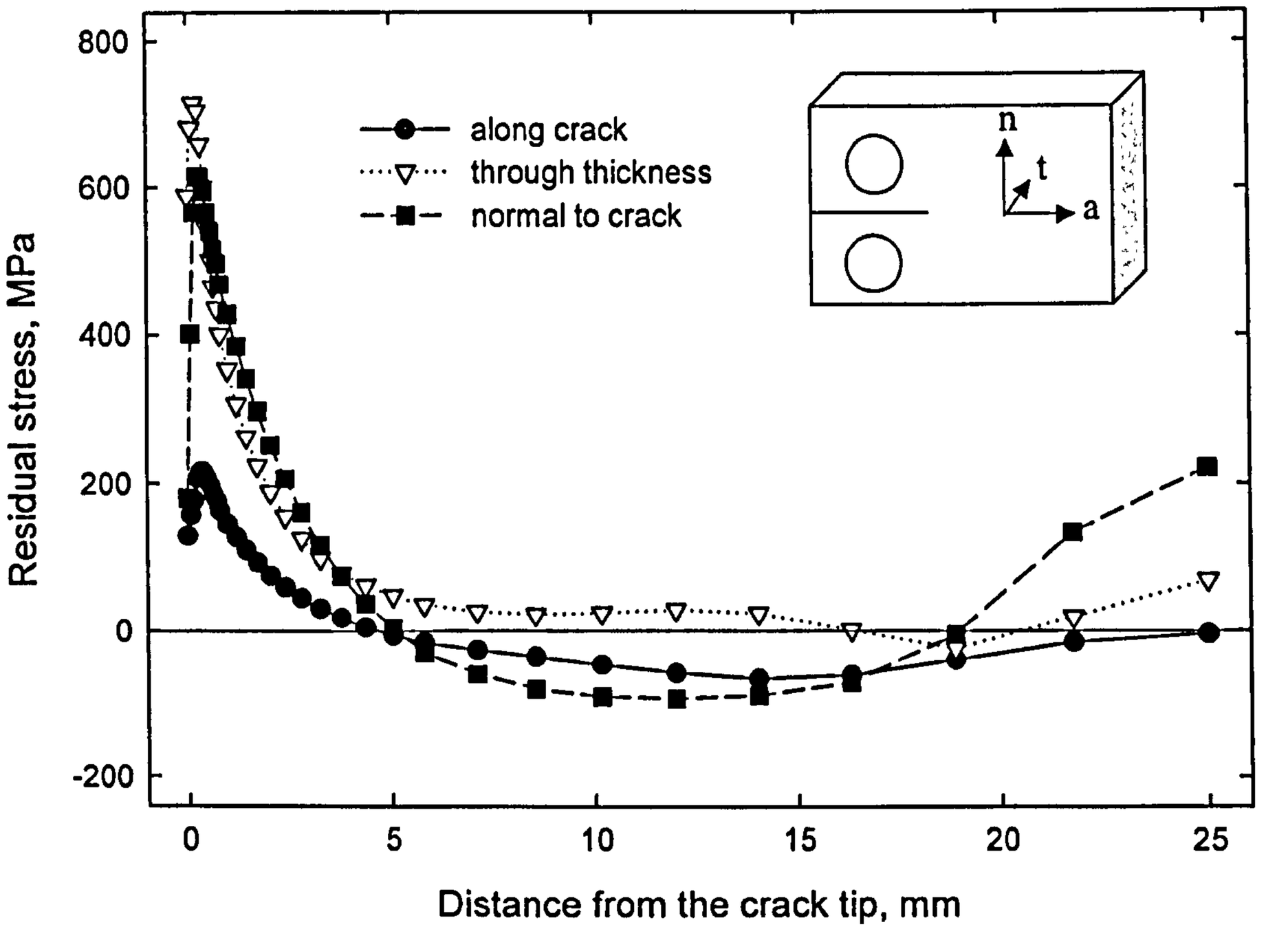

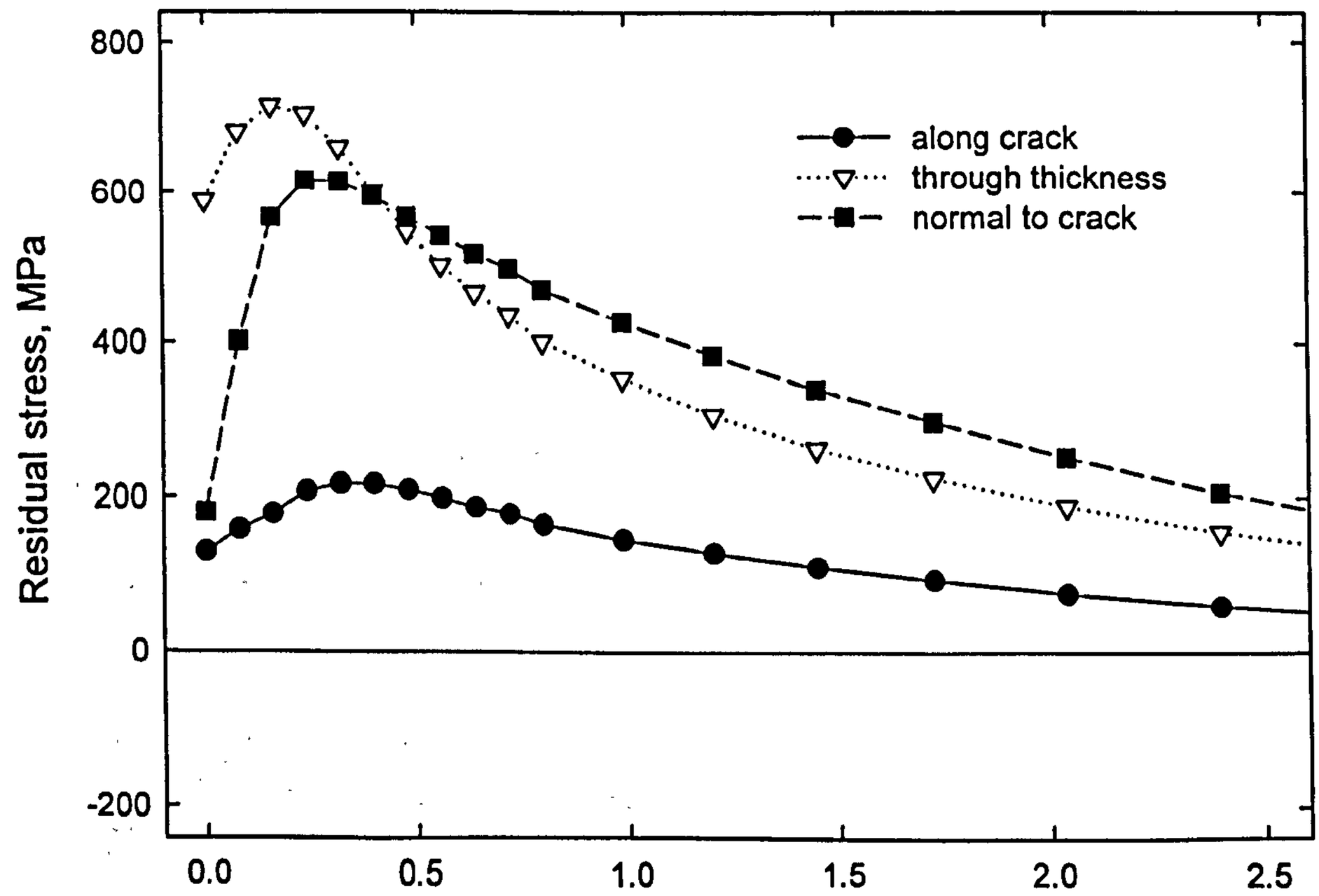

Figure 3.24 Residual stress distribution across the ligament from the notch tip of the C(T) specimen under various loading conditions for figure-of-eight punch. For clarity distribution in the first 2.5mm from the notch tip is also shown.

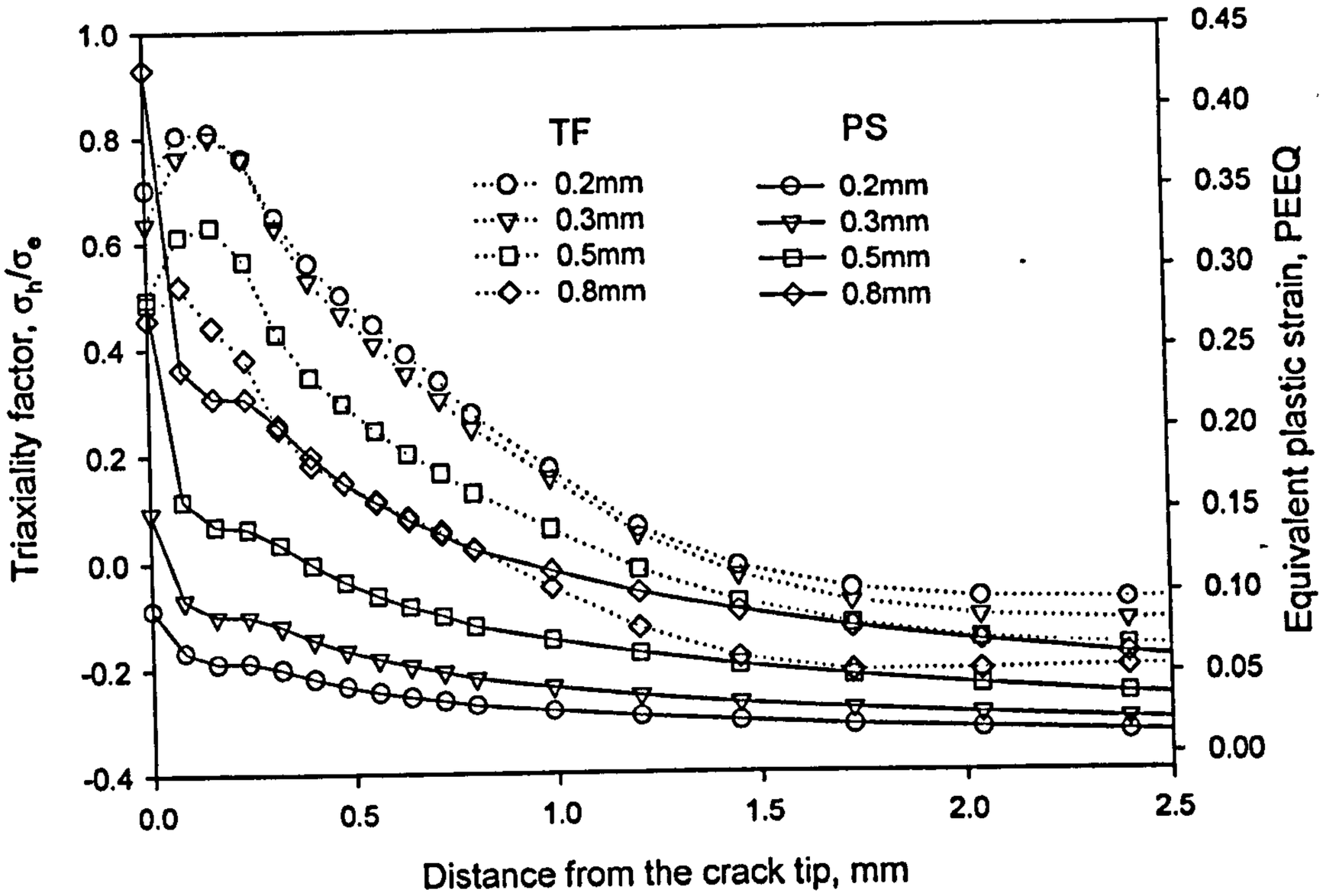

(a) Single Punch

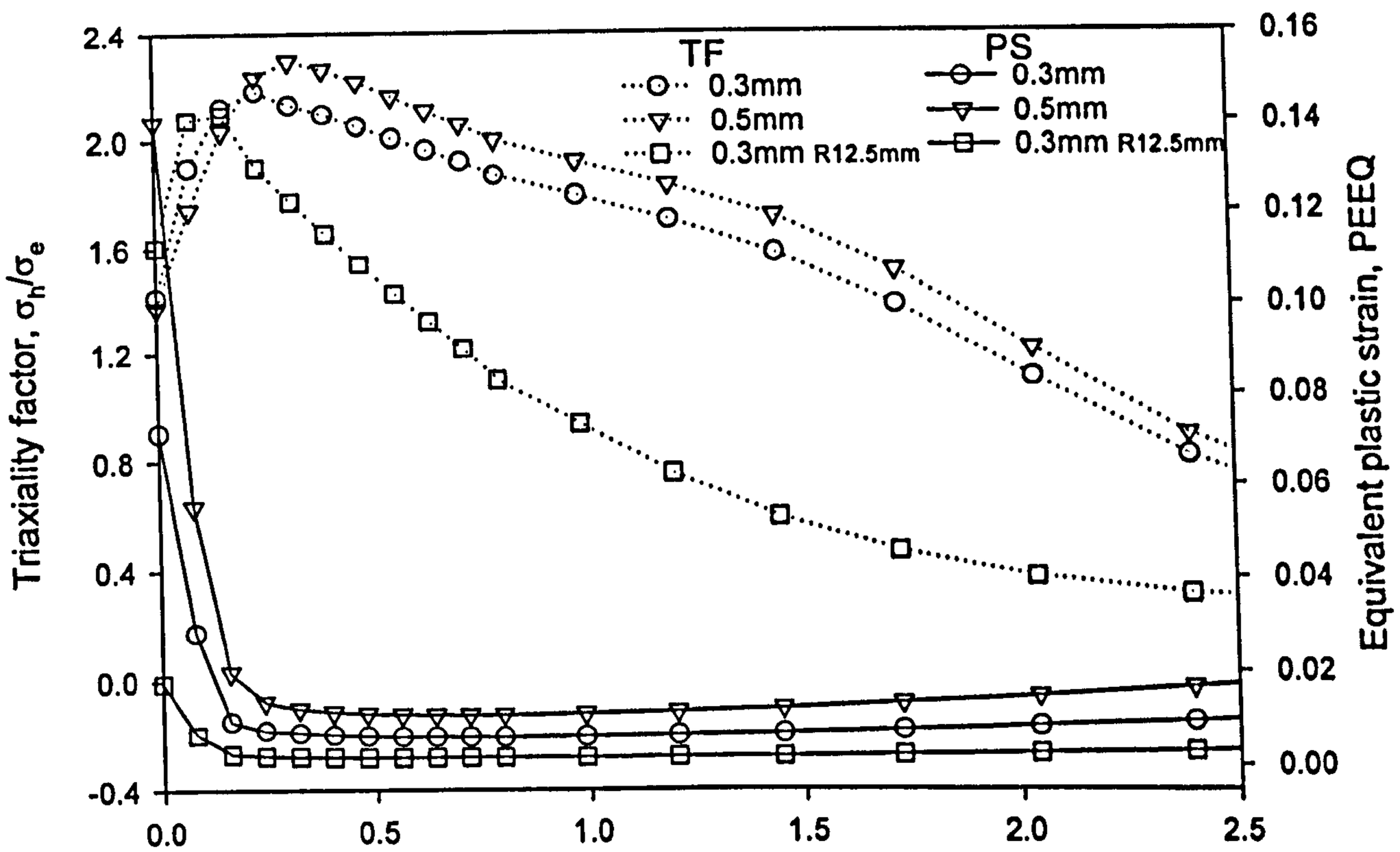

(b) Double Punch

Figure 3.25 Distributions of triaxiality factor (TF) and equivalent plastic strain (PS) across the ligament from the notch tip of the side punch C(T) specimen under various loading conditions for (a) single and (b) double punch. Only the distribution in the first 2.5mm from the notch tip is shown for clarity.

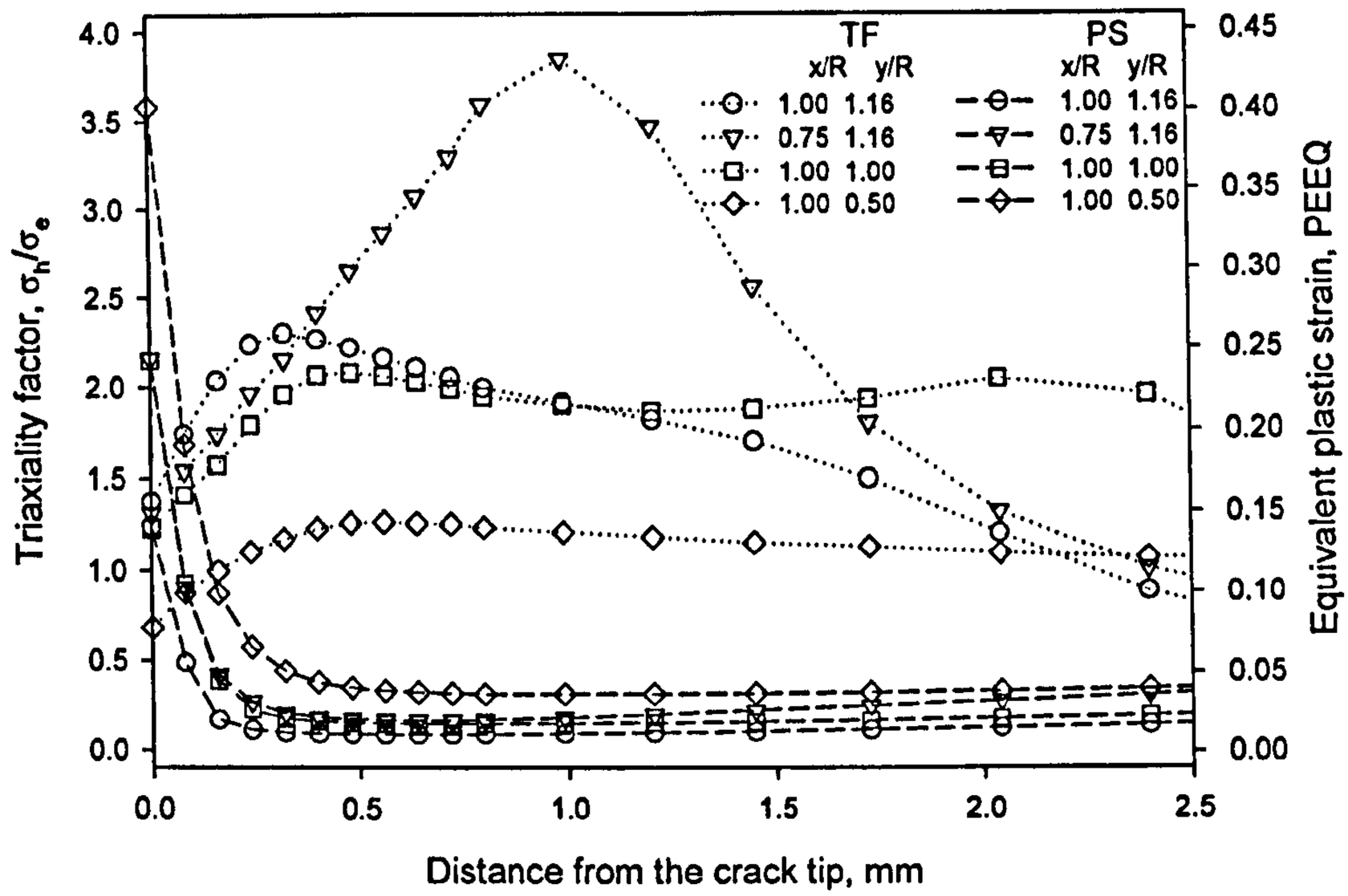

Figure 3.26 Effect of positions of punch on distributions of triaxiality factor and equivalent plastic strain across the ligament from the notch tip of the side punch C(T) specimen. Figure-of-eight punch: x/R=1, y/R=0.5. See Figure 3.27 for illustration of x/R and y/R ratios.

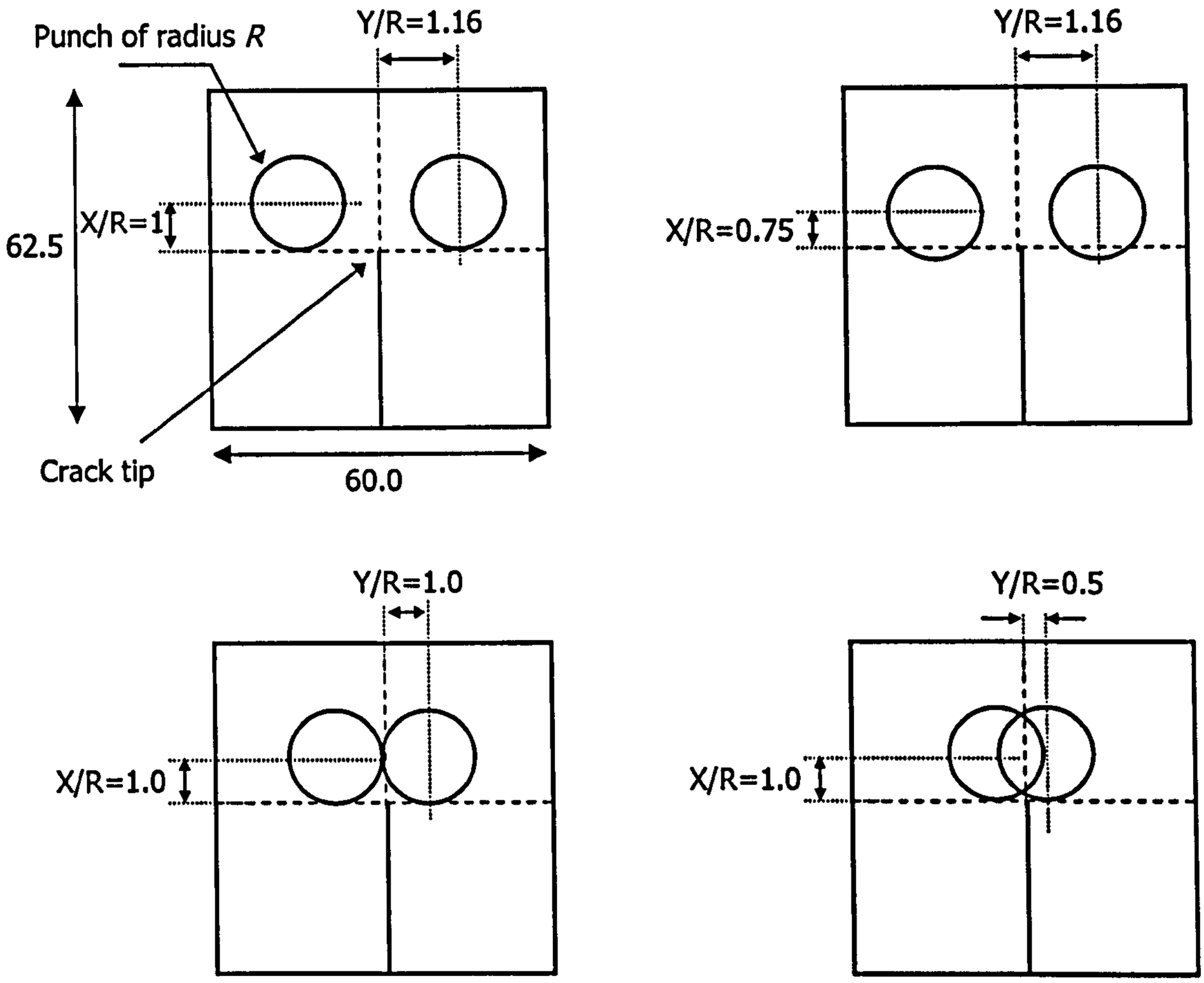

Figure 3.27 Illustration of variation of *X* and *Y* on double punch. X is the distance between the crack tip and the punch centre; Y is the distance between the crack plane and the punch centre.

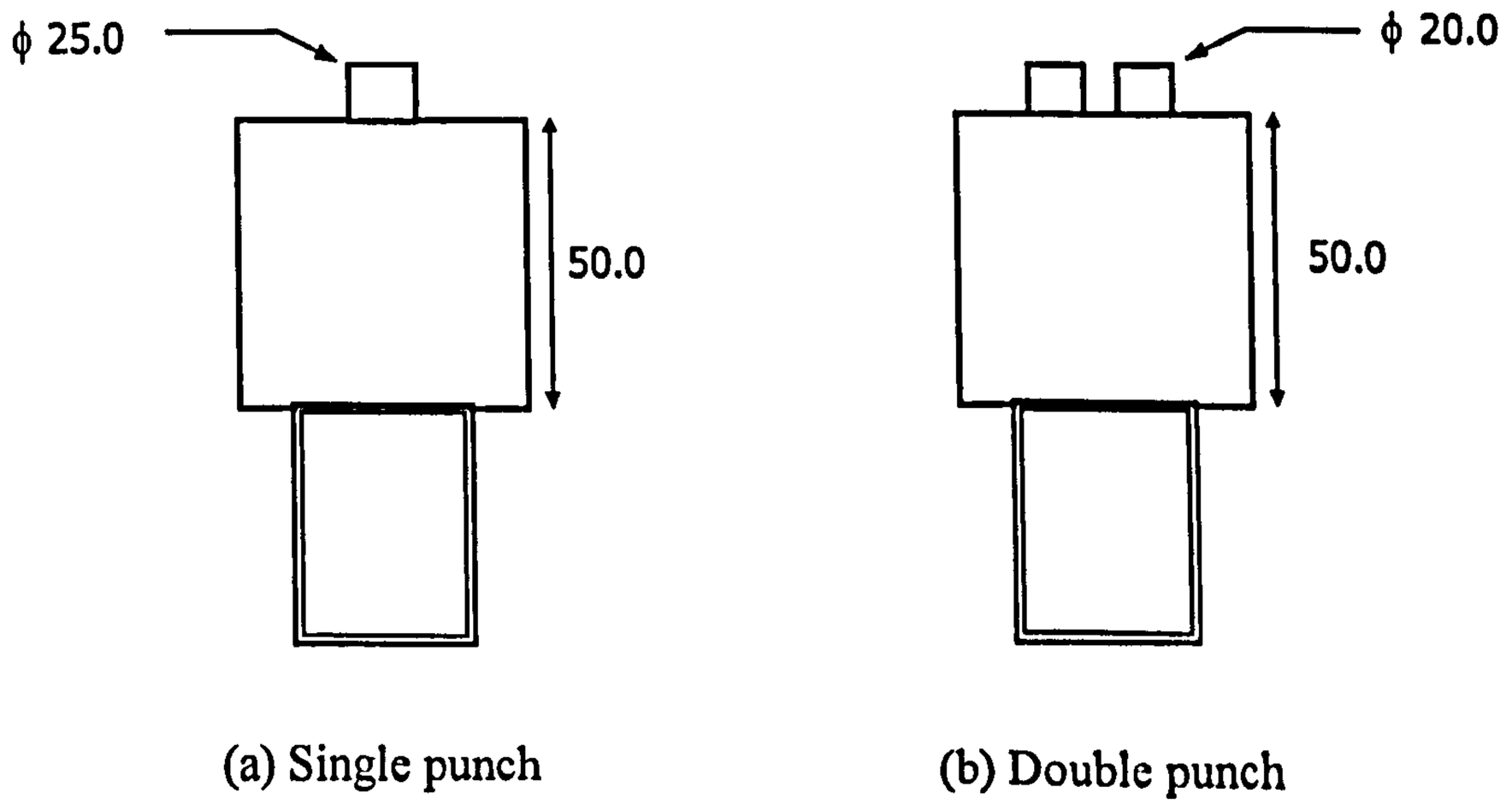

(a) Single punch (b) Double punch

Figure 3.28 Schematic of (a) single and (b) double punching tools.

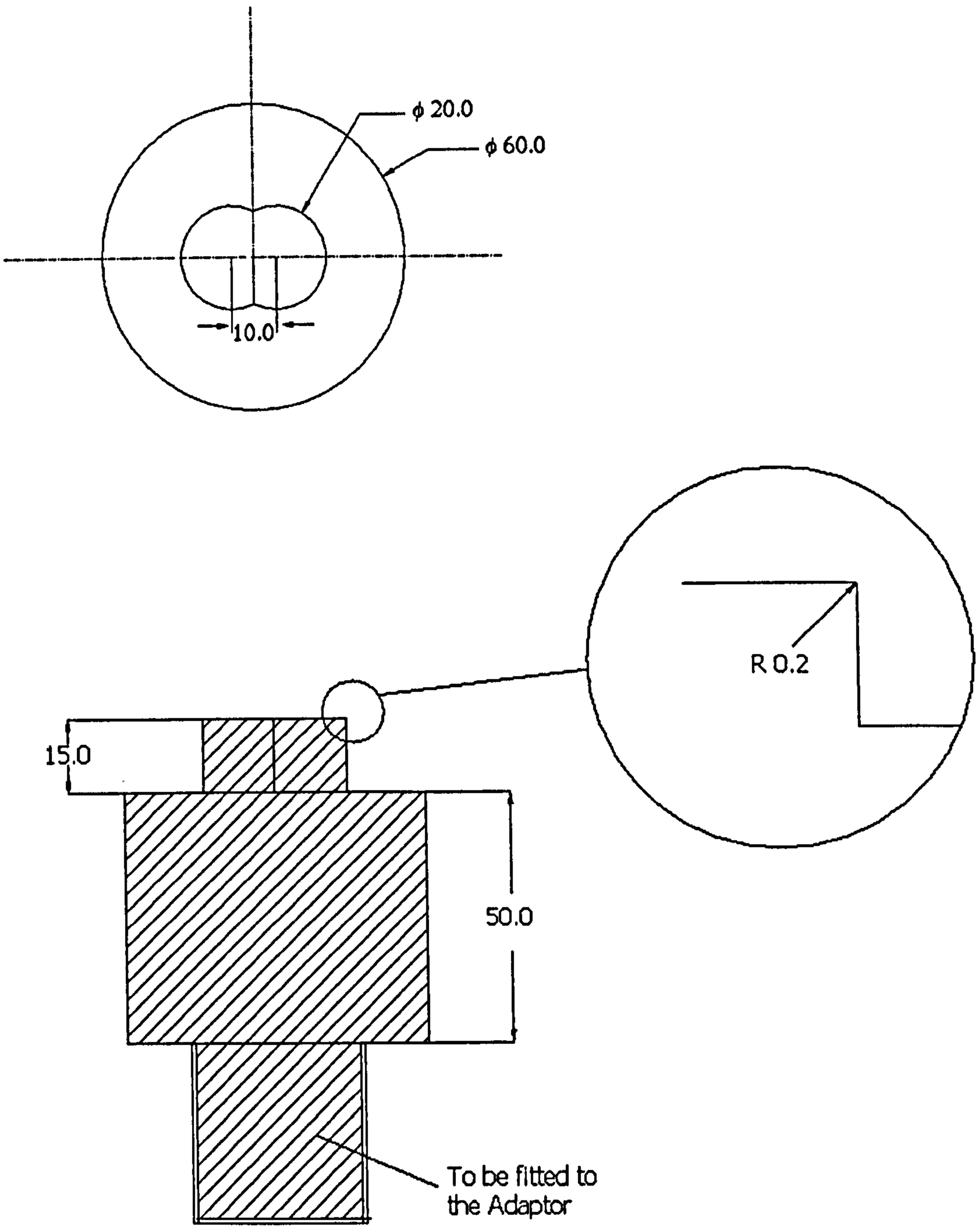

Figure 3.29 "Figure of eight" shape punching tool. Dimensions in "mm".

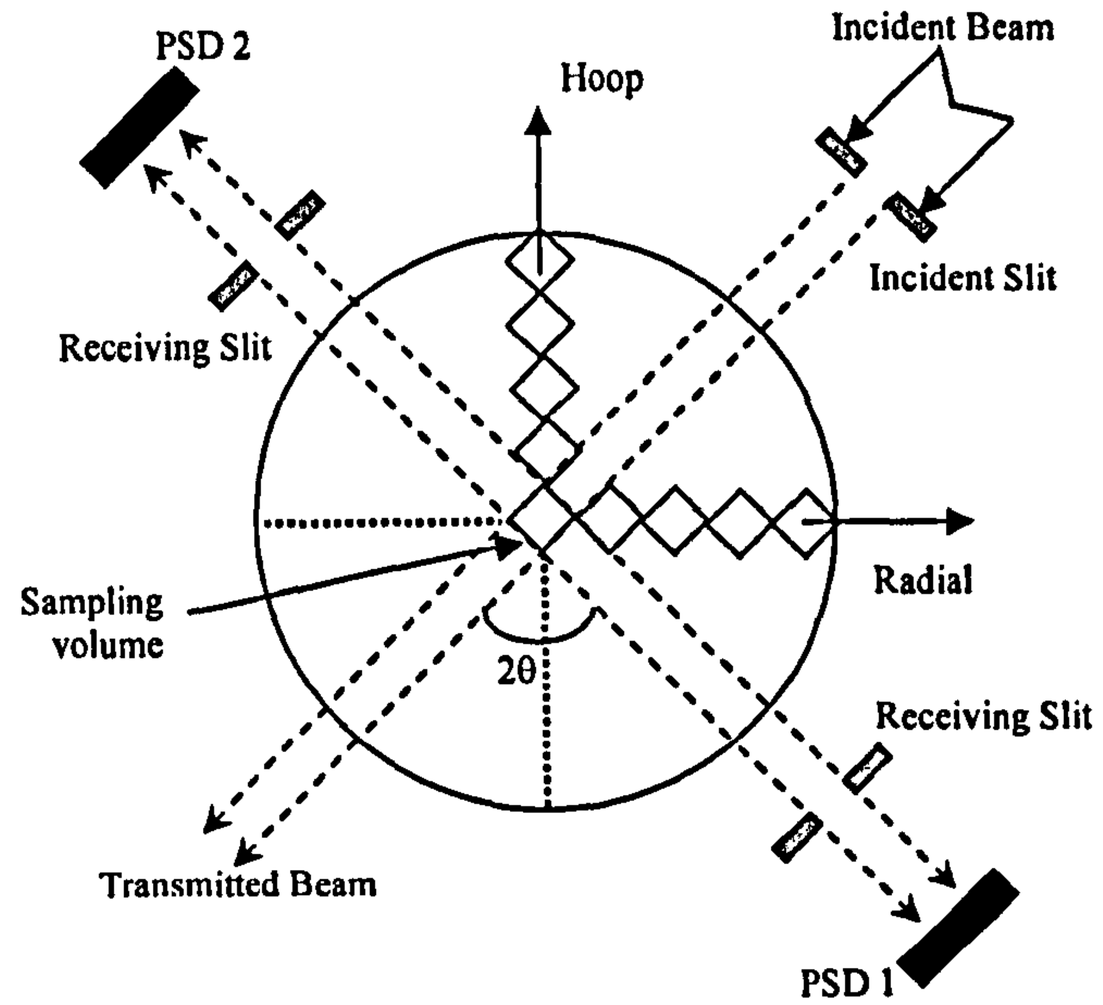

Figure 4.1 Schematic layout of the ENGIN neutron diffractometer on the PEARL beam line at the ISIS facilities.

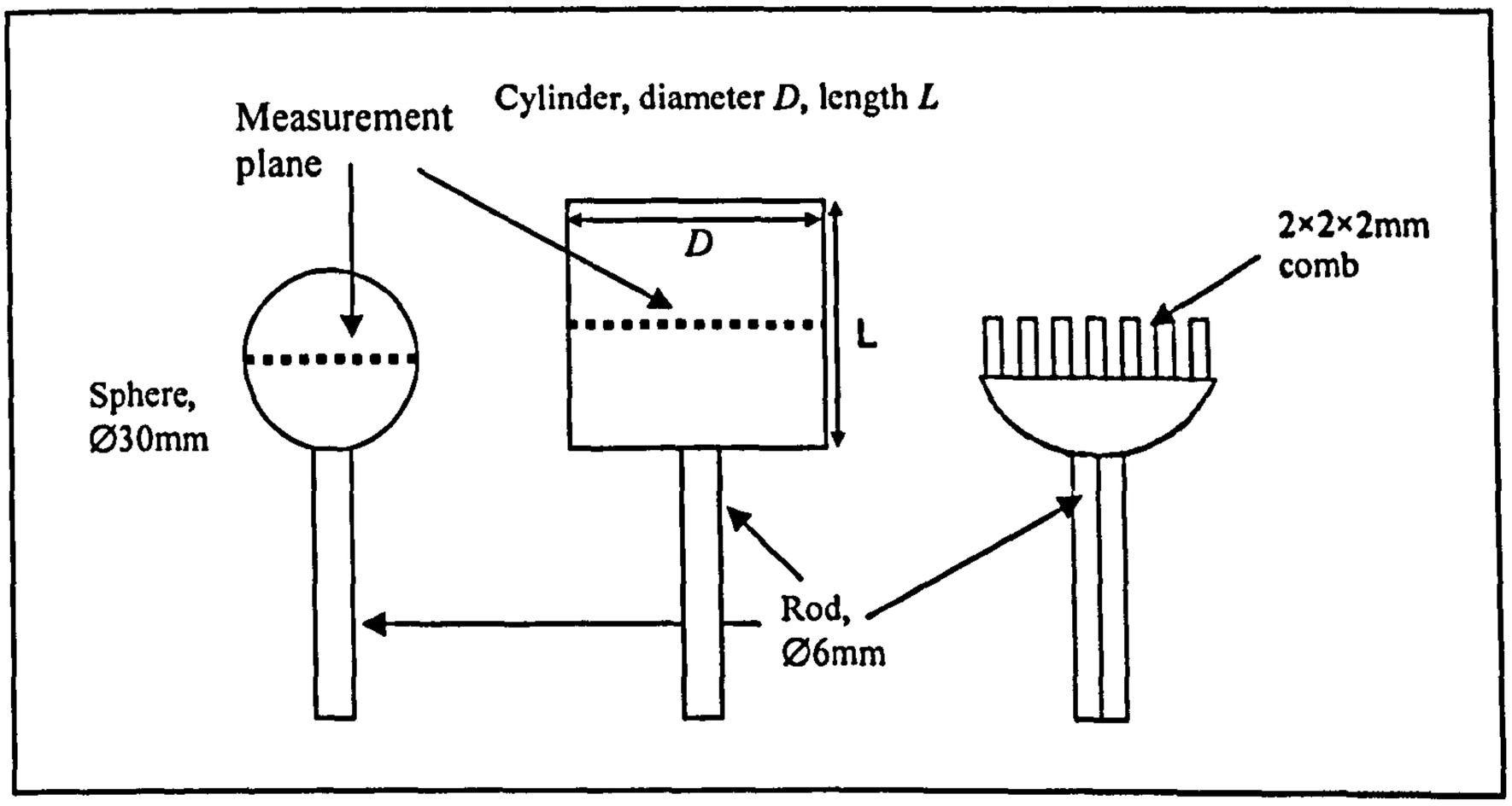

Figure 4.2 Schematic diagrams showing types 316H and 316L stainless steel solid sphere, diameter 30mm, the solid cylinder, diameter *D*, length *L* and the reference comb sample used for the ND measurements. Note different cylinder sizes were used. The *D*, *L* pair consisted of 60, 60; 60, 160; 30, 30 and 29, 29. All dimensions in mm.

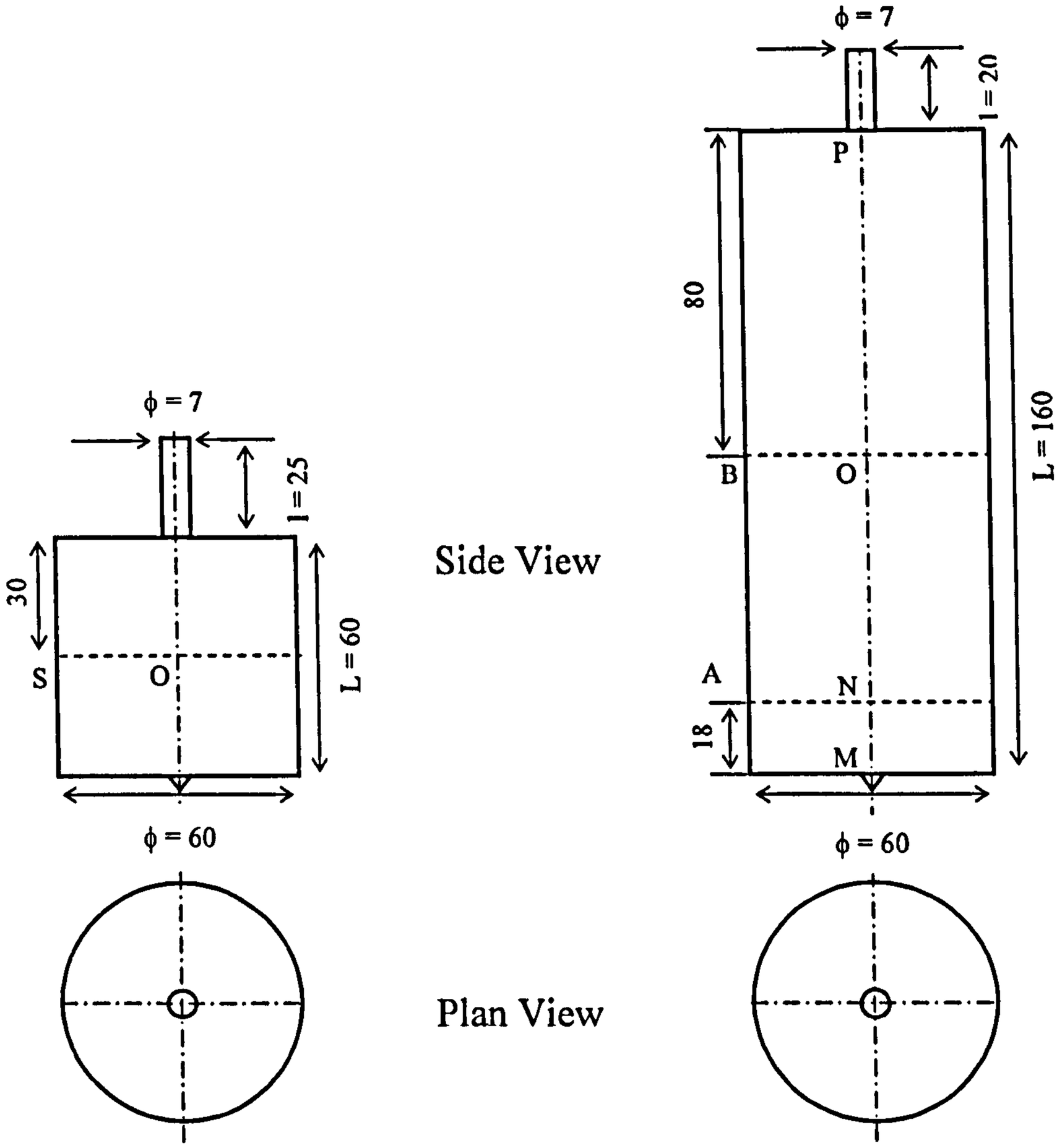

(a) Sample *s19*, dia 60mm, len 60mm

(b) Sample *s27*, diameter 60mm, length 160mm

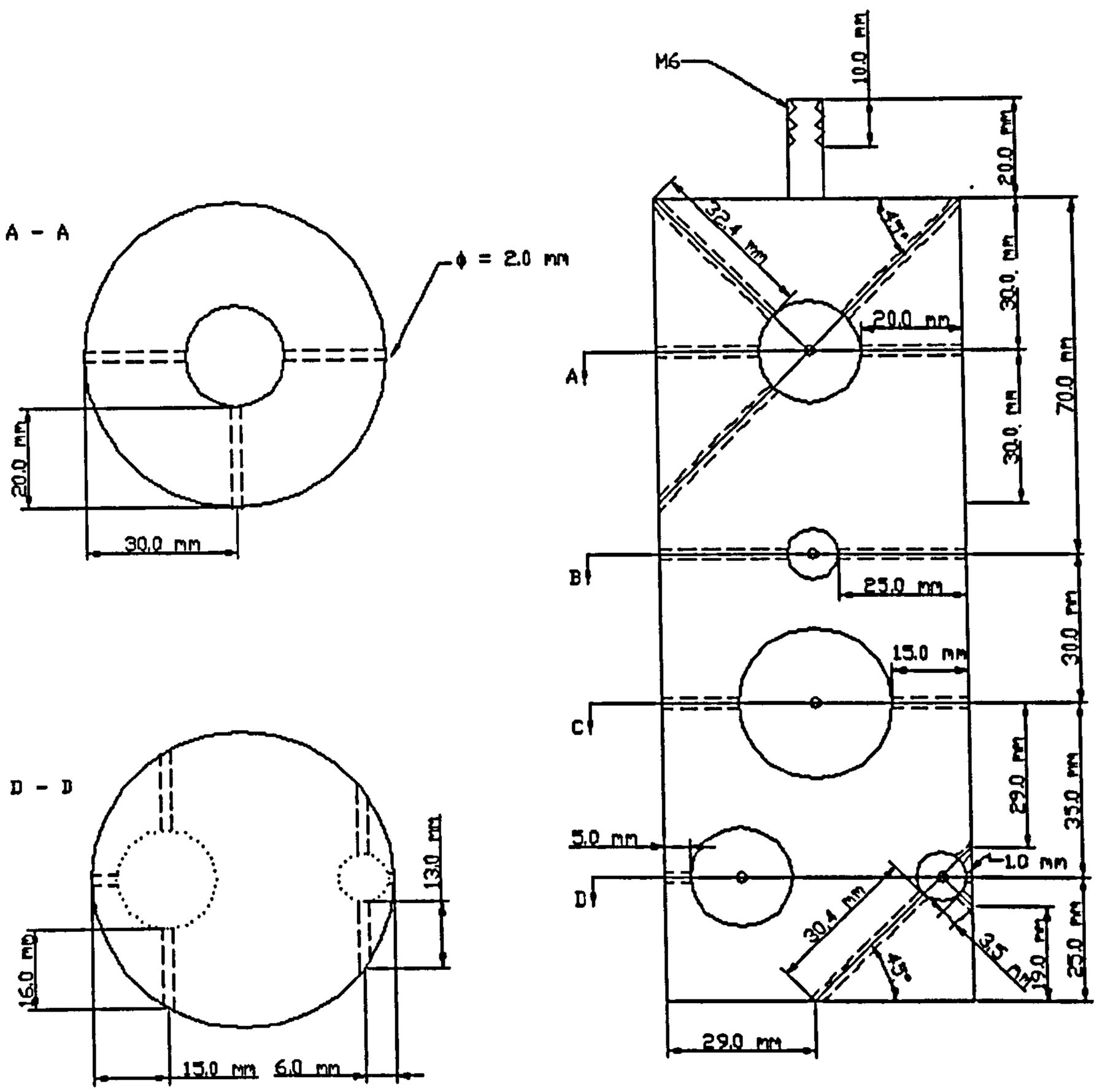

(c) Sample *s26*, diameter 60mm, length 160mm.The drilled holes of diameter 2.0mm are represented by dashed lines. The circles represent imaginary spheres within the specimen with reduced path lengths for ND measurements.

Figure 4.3 Schematic of quenched 316H stainless steel cylinders *s19*, *s27* and *s26* respectively.

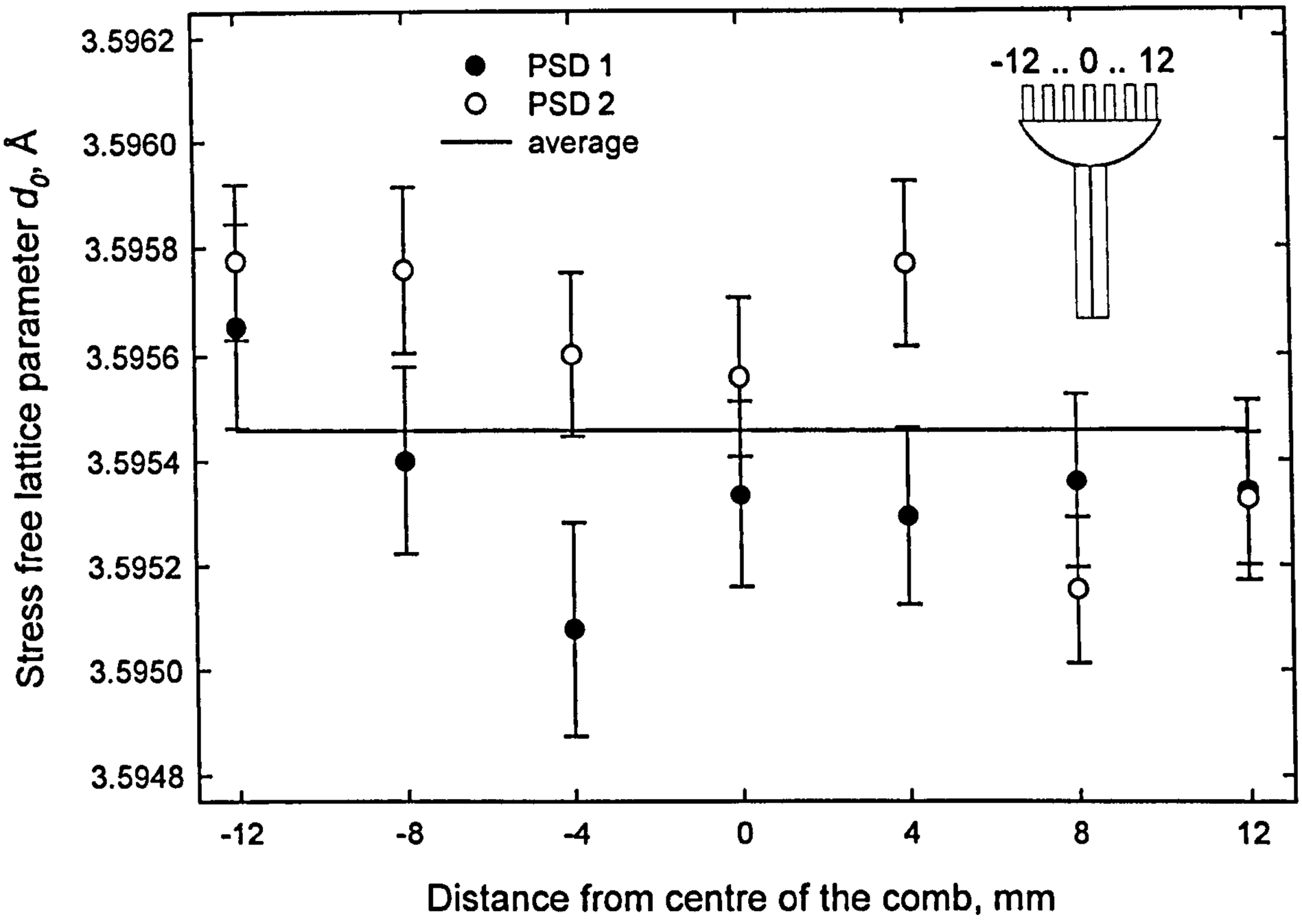

Figure 4.4 Summary of the measured stress-free lattice parameter d_0 across the seven fingers on the comb *s9* used to determine residual elastic strain on quenched sample *s8*.

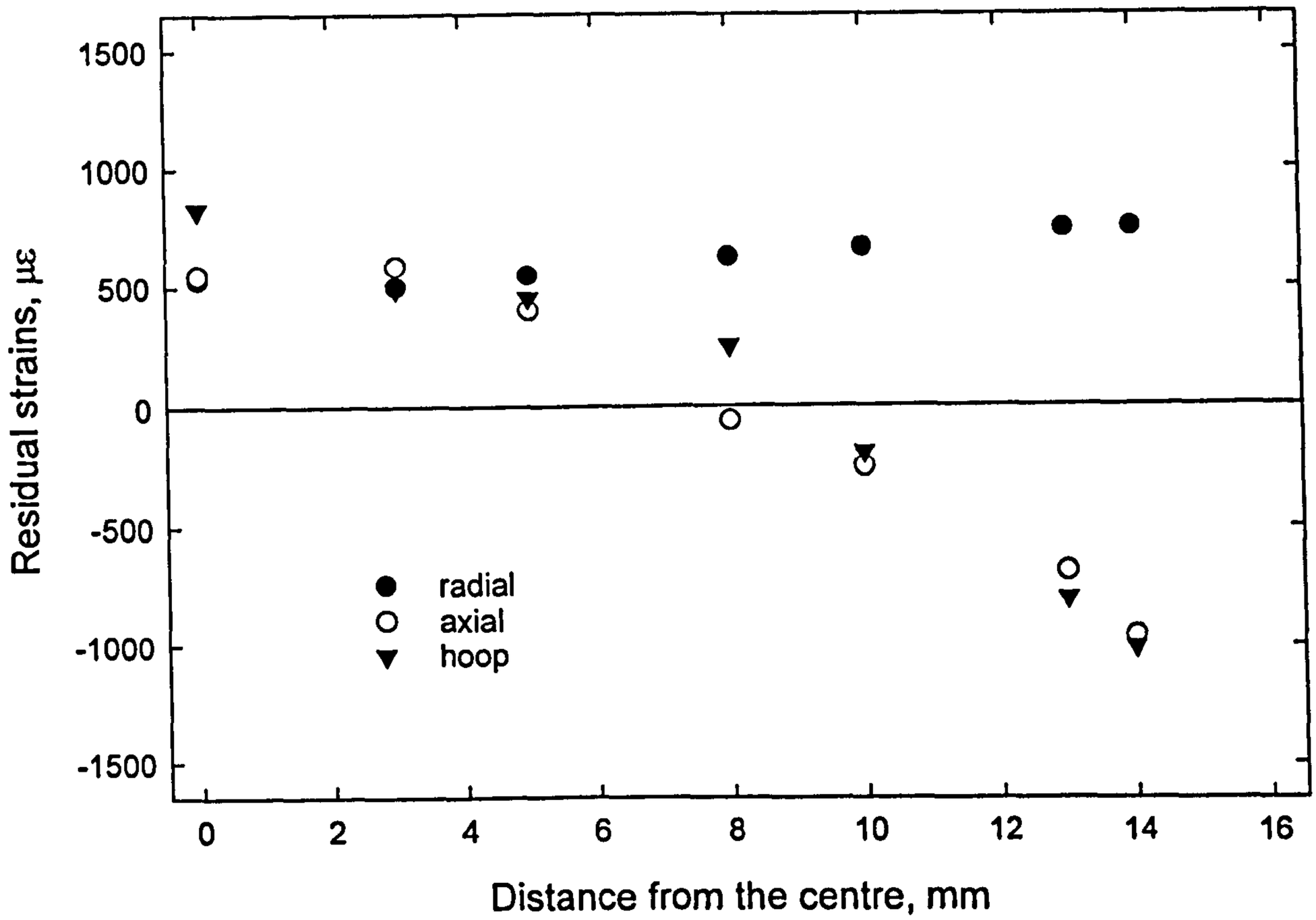

Figure 4.5 Summary of ND measured residual strains in quenched sphere *s8*.

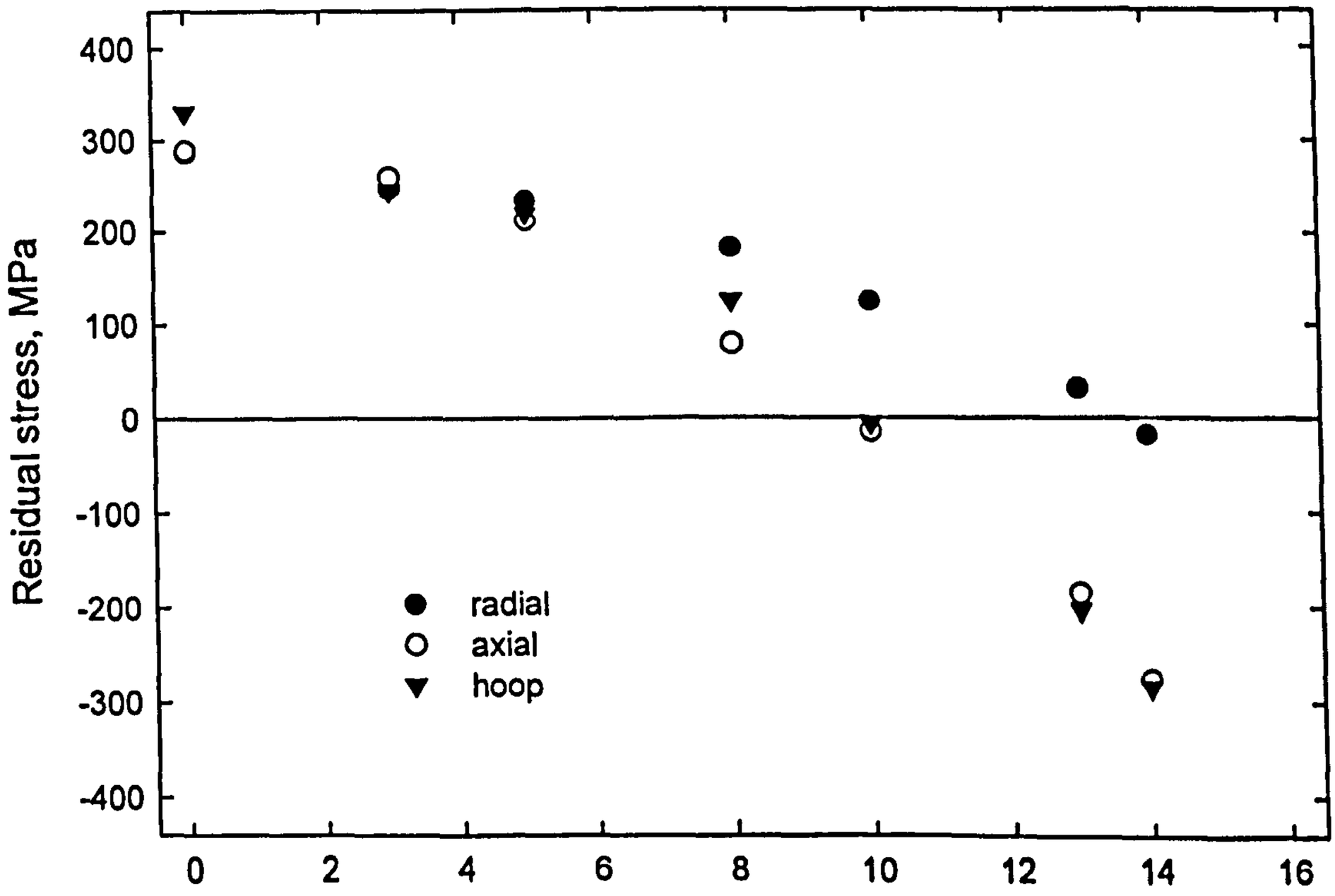

Figure 4.6 Measured residual stress distributions across radial plane in quenched sphere *s8*.

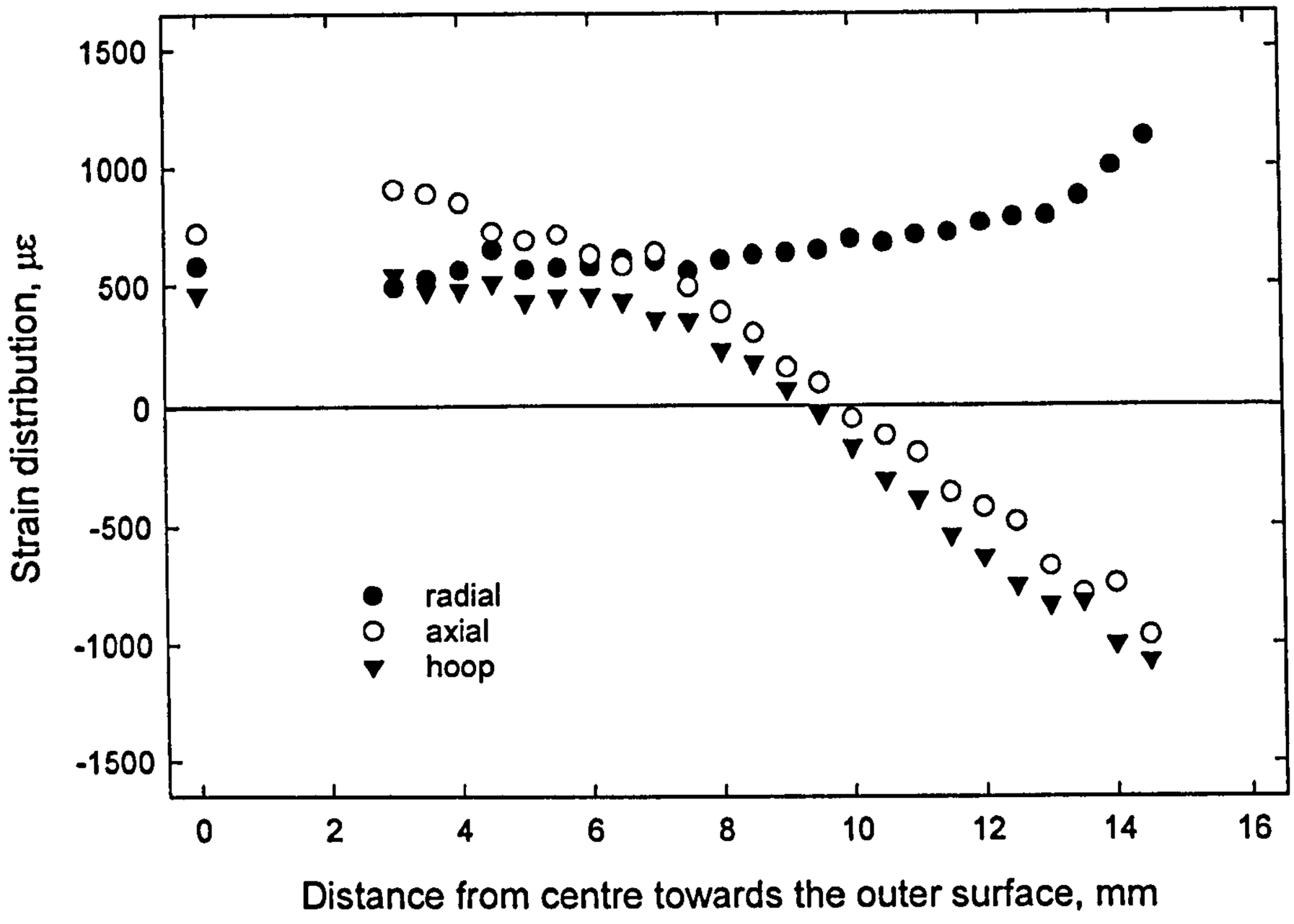

Figure 4.7 Summary of ND measured residual strains in a quenched sphere *s22*.

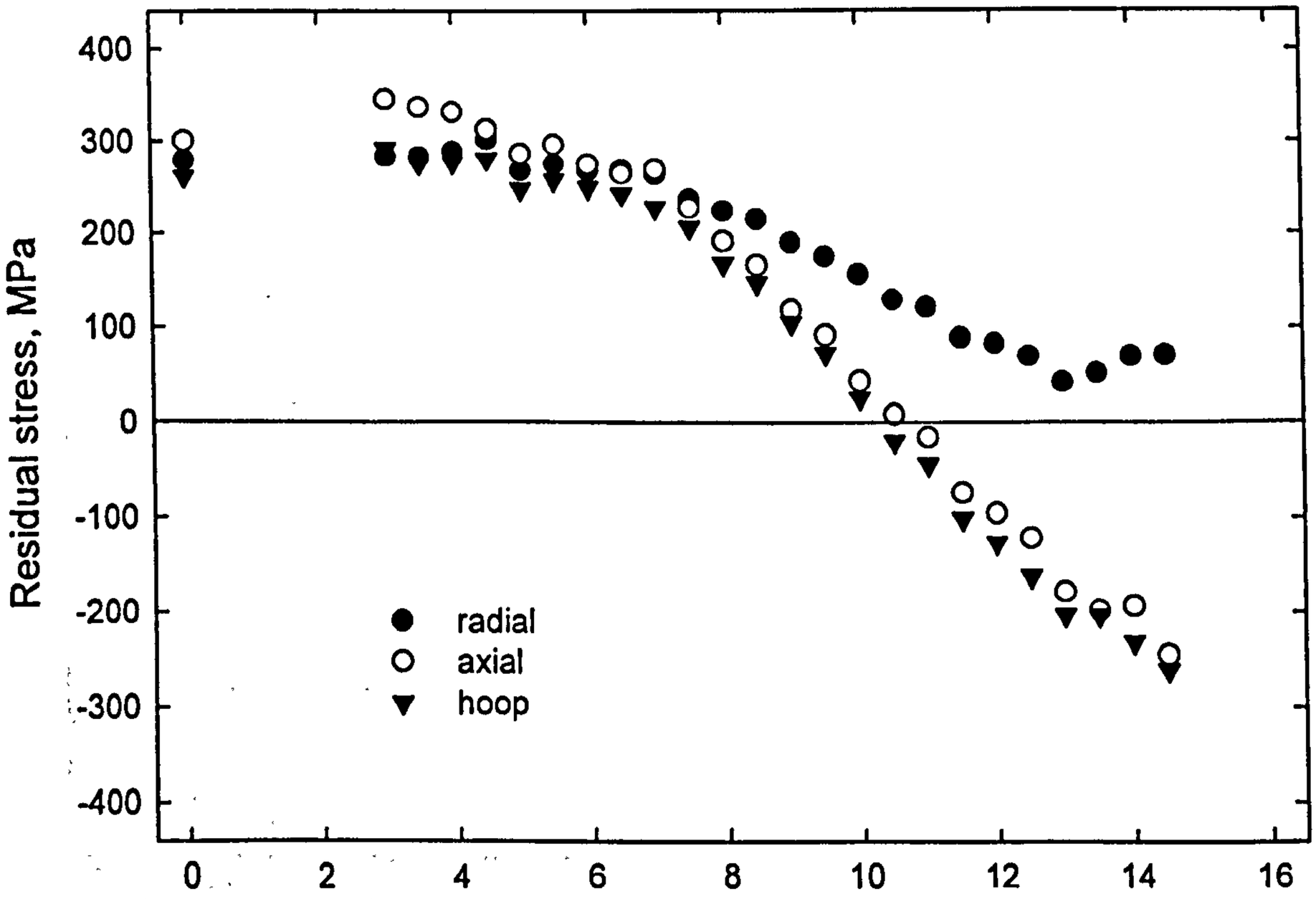

Figure 4.8 Measured residual stress distributions across radial plane in quenched sphere *s22*.

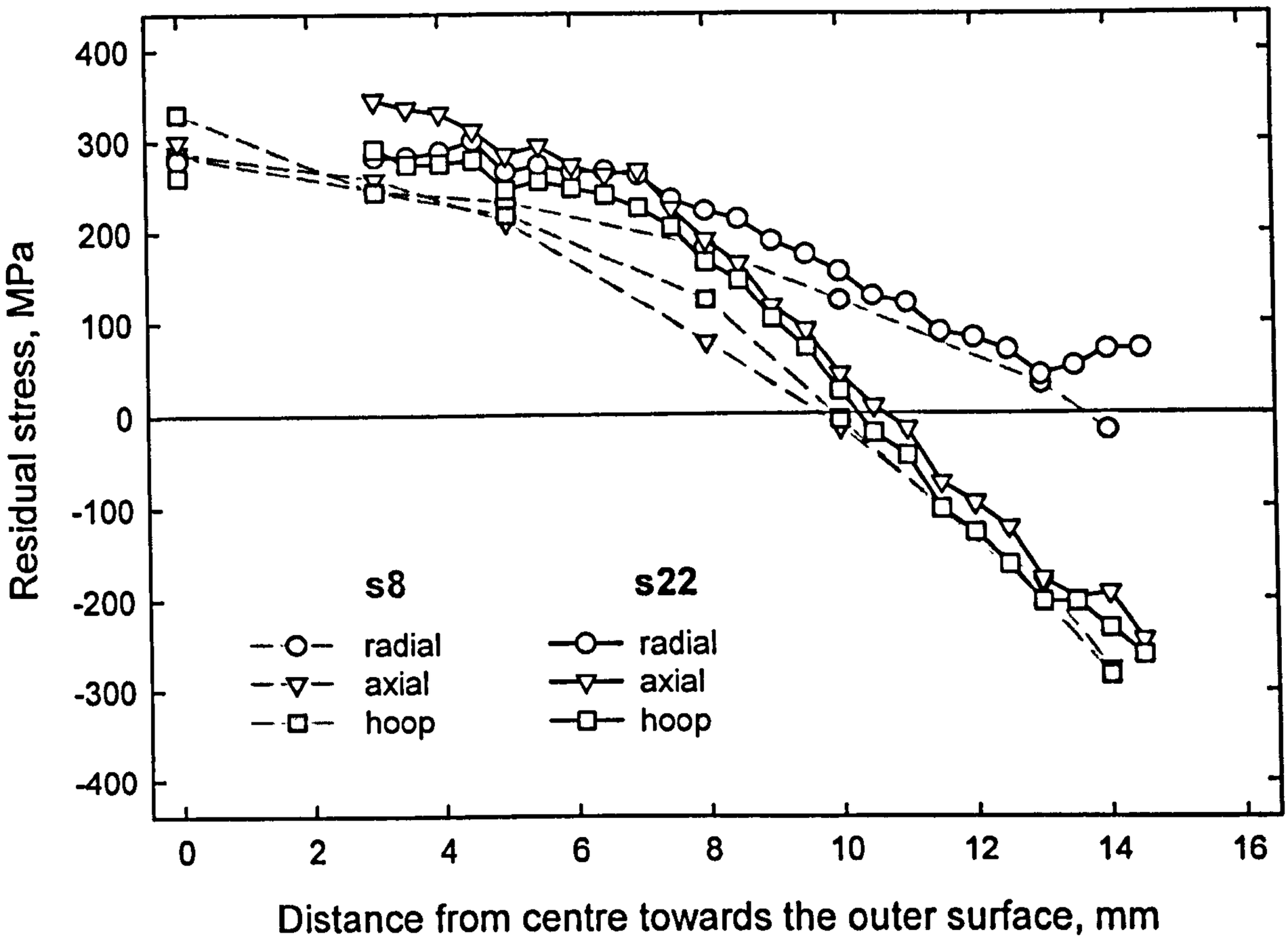

Figure 4.9 Comparison of residual stress distribution across equatorial plane between quenched spheres *s8* (type 316L) and *s22* (type 316H).

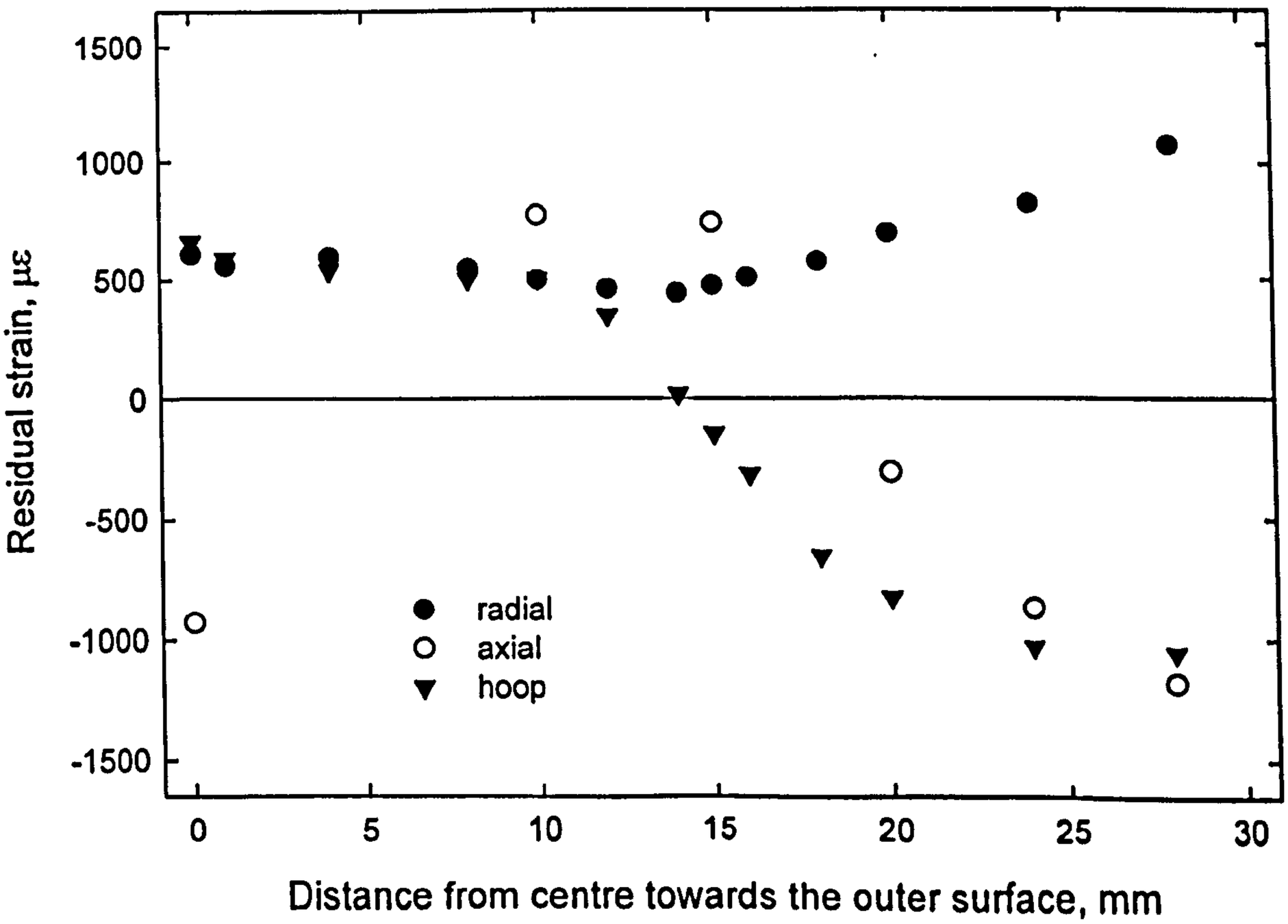

Figure 4.10 Summary of ND measured strains in quenched cylinder *s19* across OS (see Figure 4.3a).

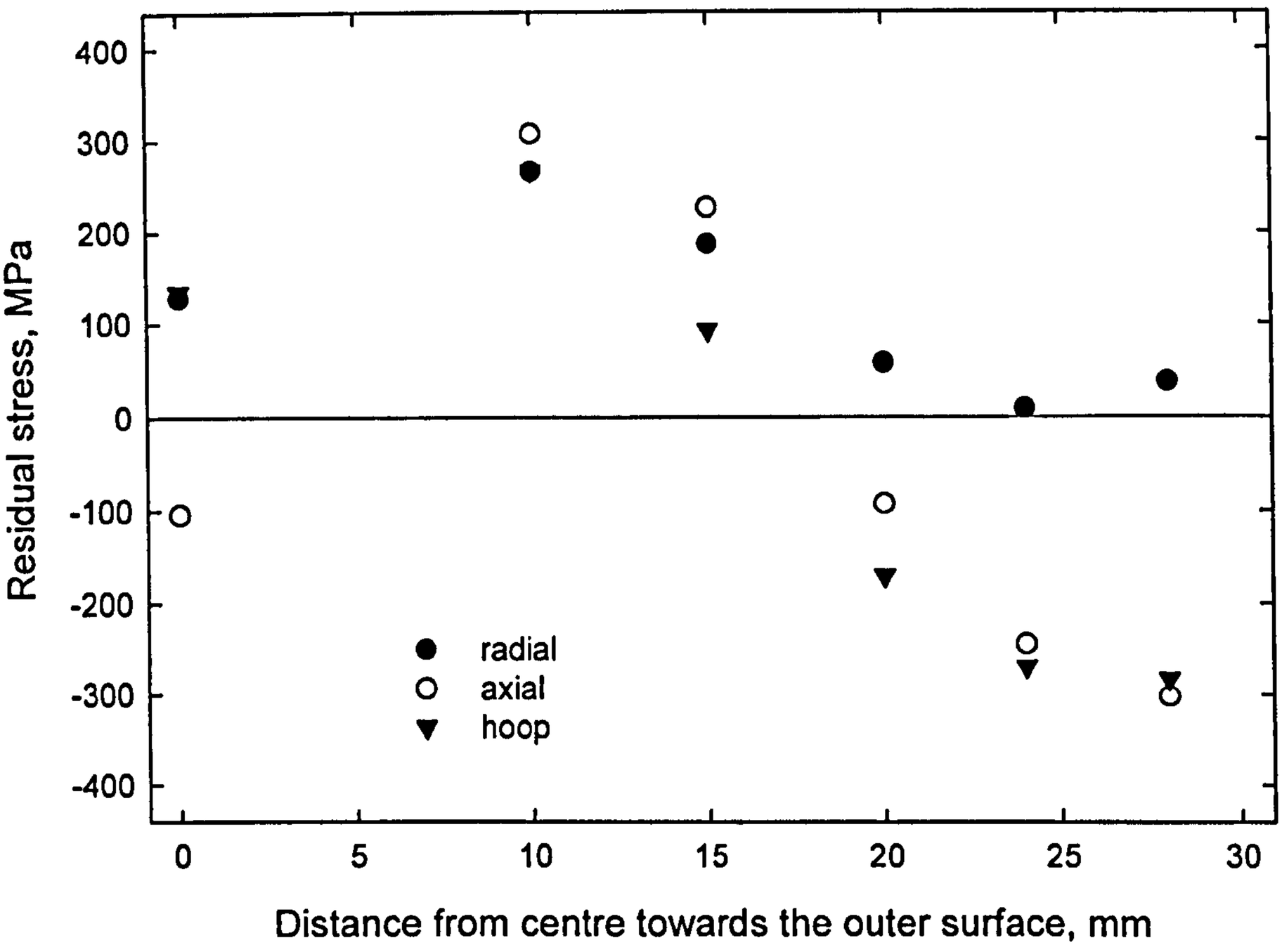

Figure 4.11 Measured residual stress distribution across OS (see Figure 4.3a) in a quenched stainless steel solid cylinder *s19*.

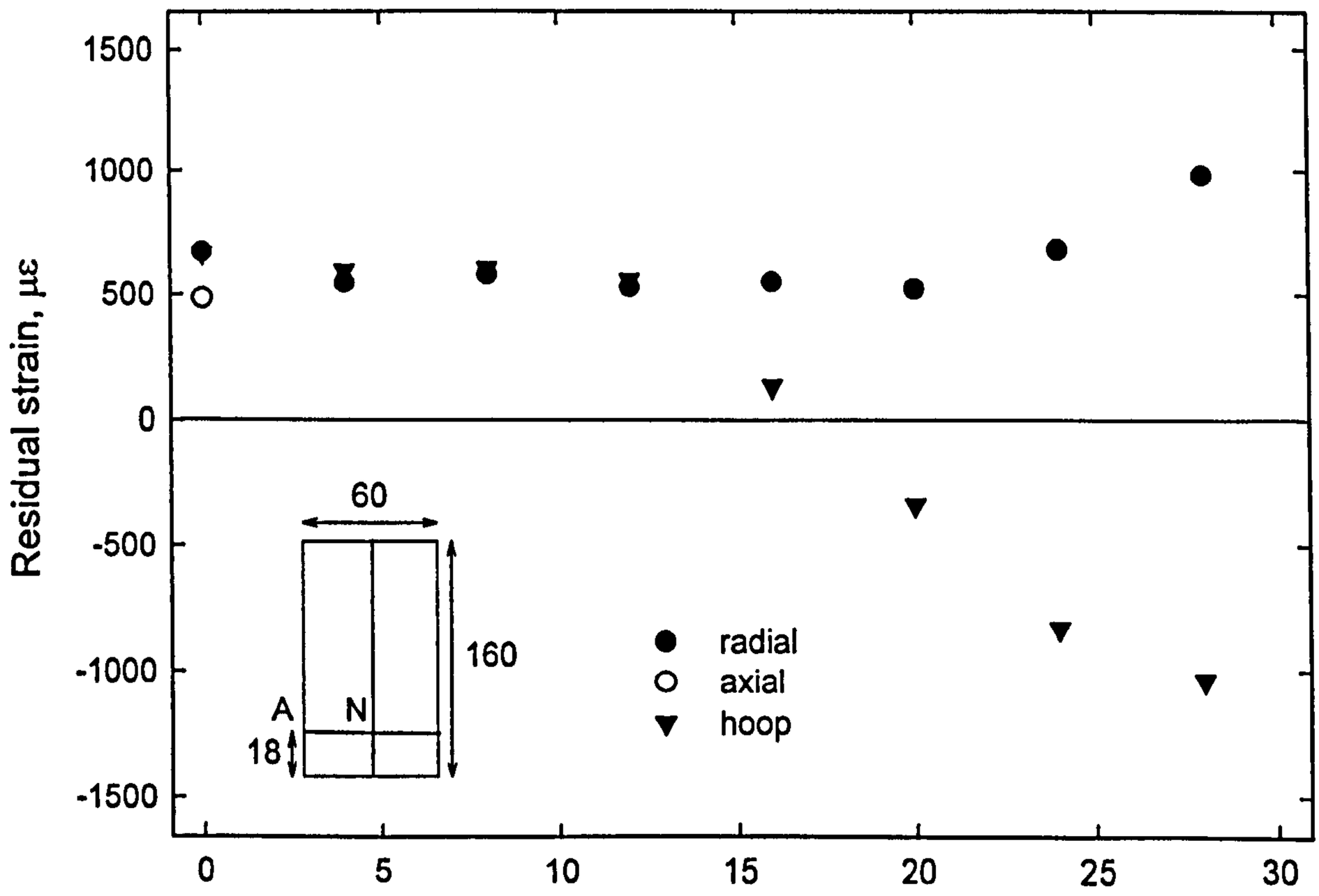

Figure 4.12 Summary of ND measured residual strains in a quenched cylinder *s27* at 18mm offset from the flat of the cylinder across NA (see Figure 4.3b).

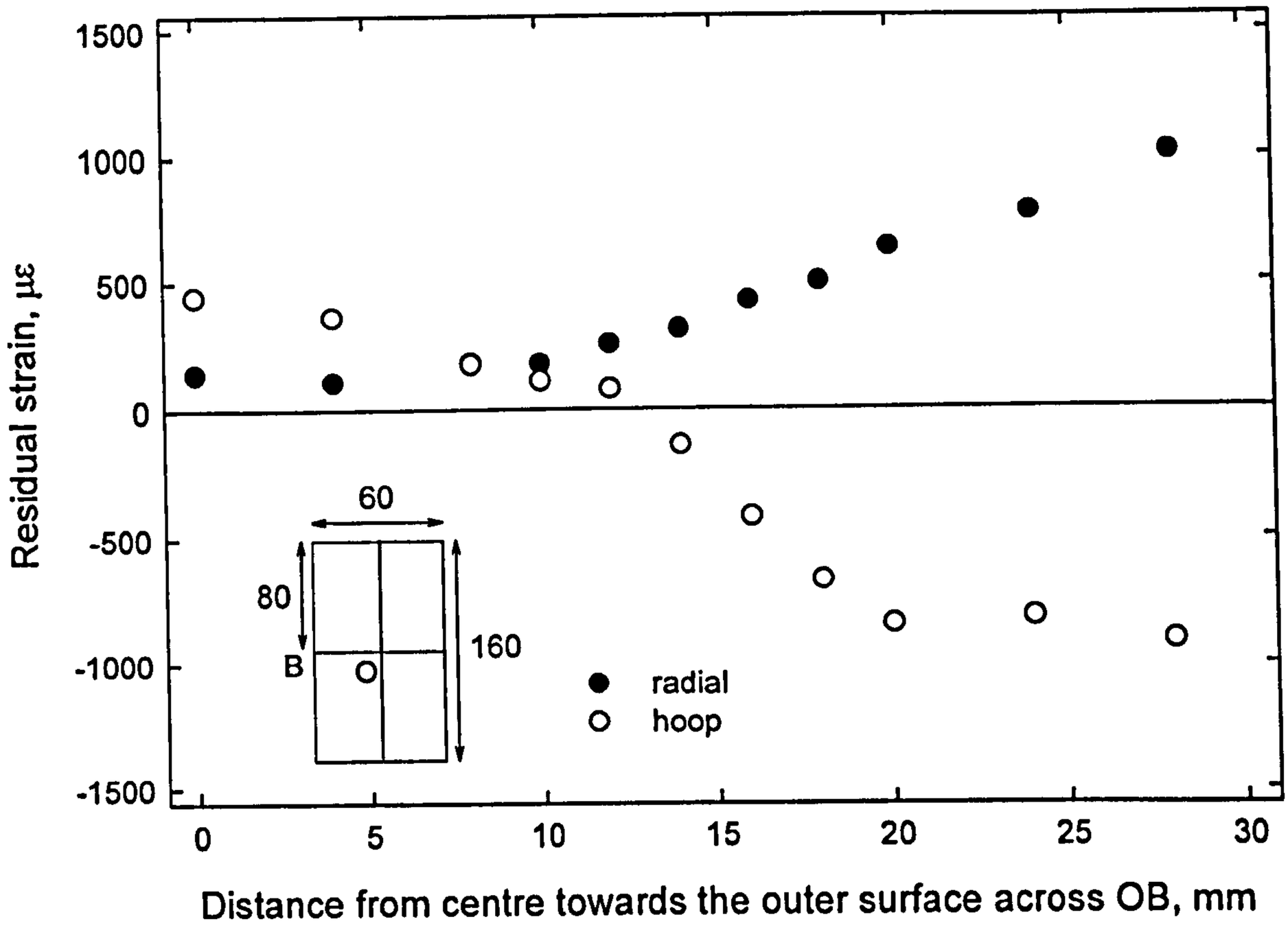

Figure 4.13 Summary of ND measured residual strains in a quenched cylinder *s27* across OB (see Figure 4.3b).

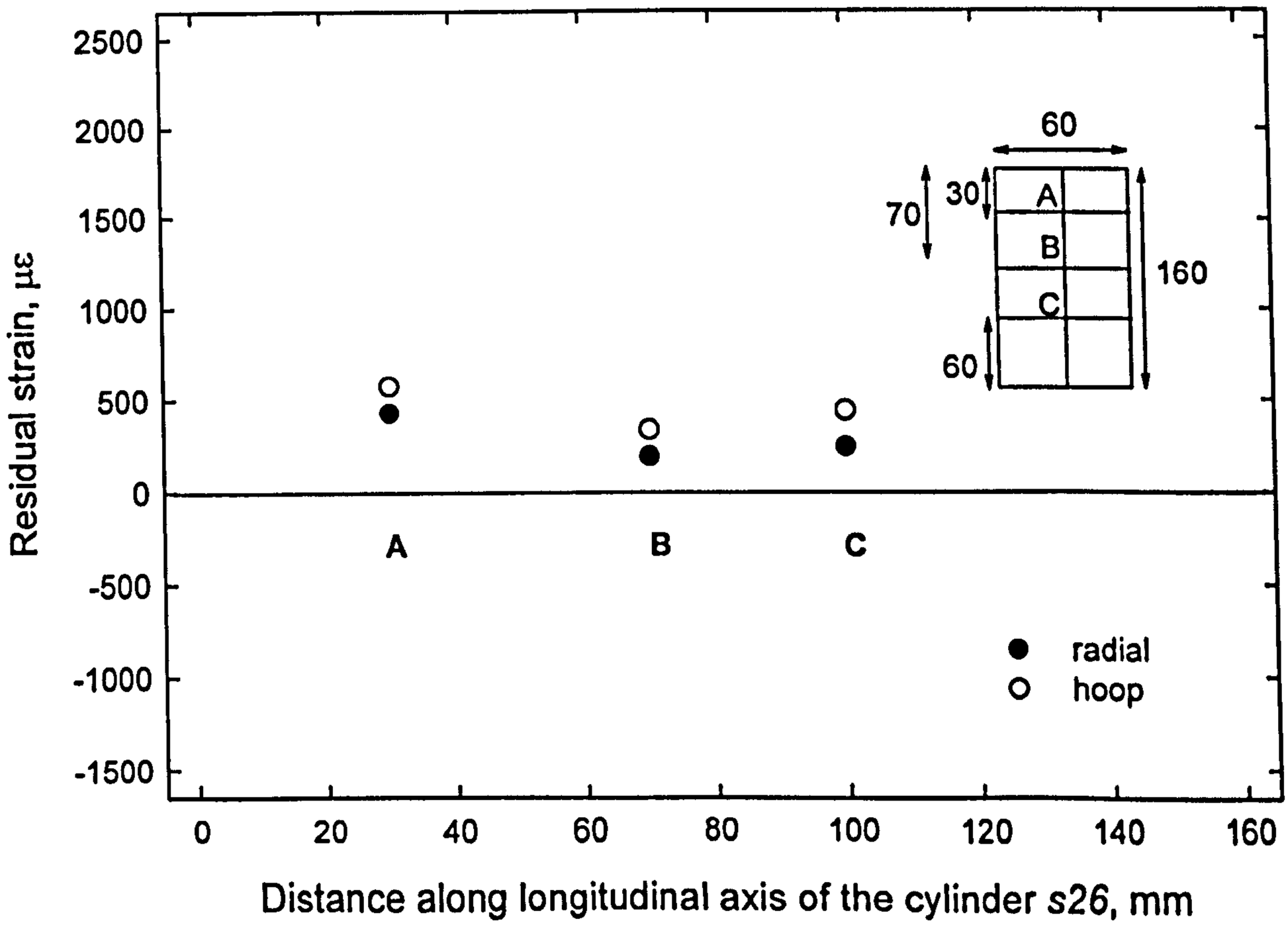

Figure 4.14 Summary of ND measured residual strains in a quenched cylinder *s26* along the longitudinal axis at positions A, B and C (see Figure 4.3c).

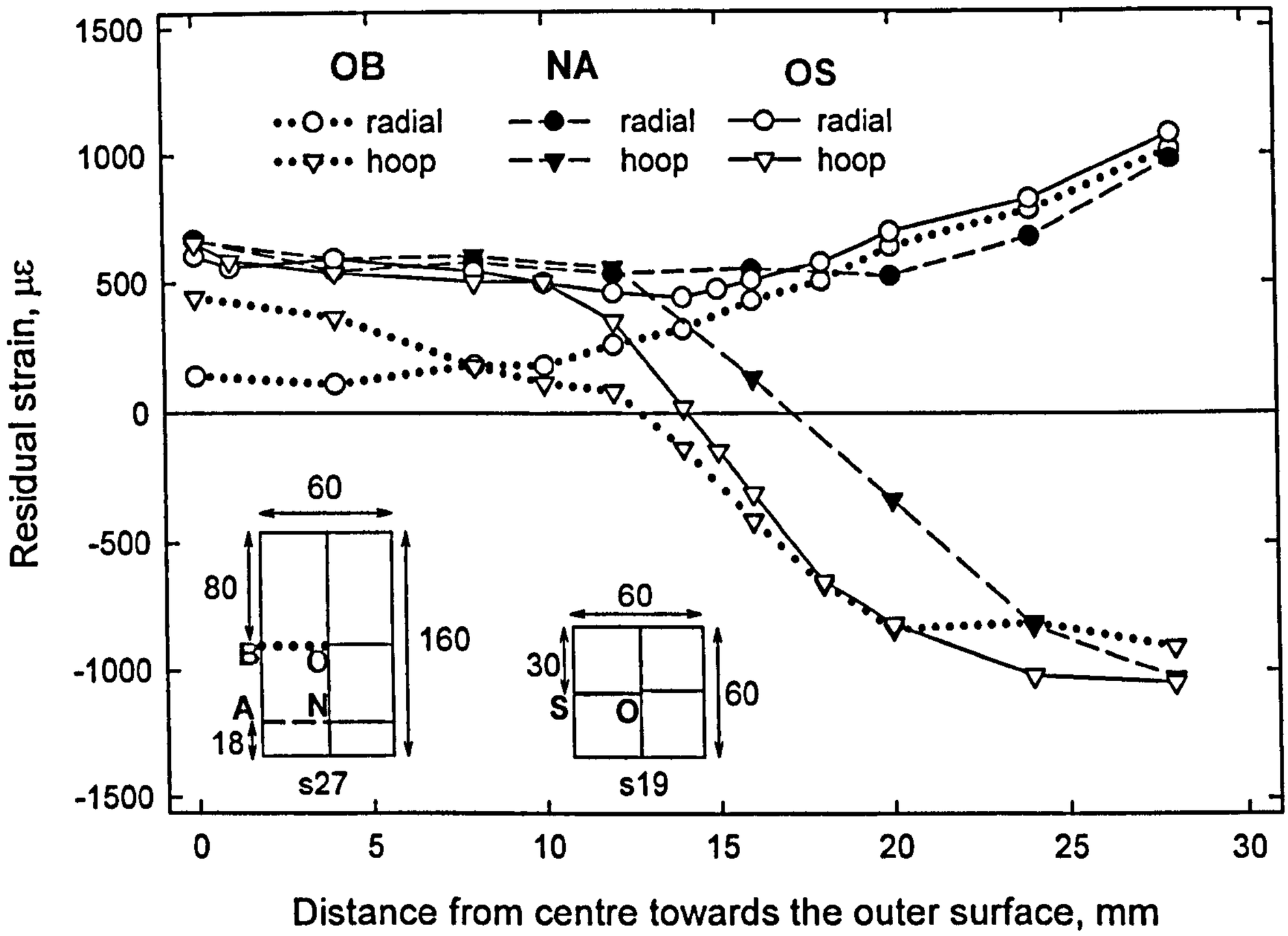

Figure 4.15 Comparison of measured residual strain distributions in cylinder *s27* across OB and NA (see Figure 4.3b) and cylinder *s19* across OS (see Figure 4.3a).

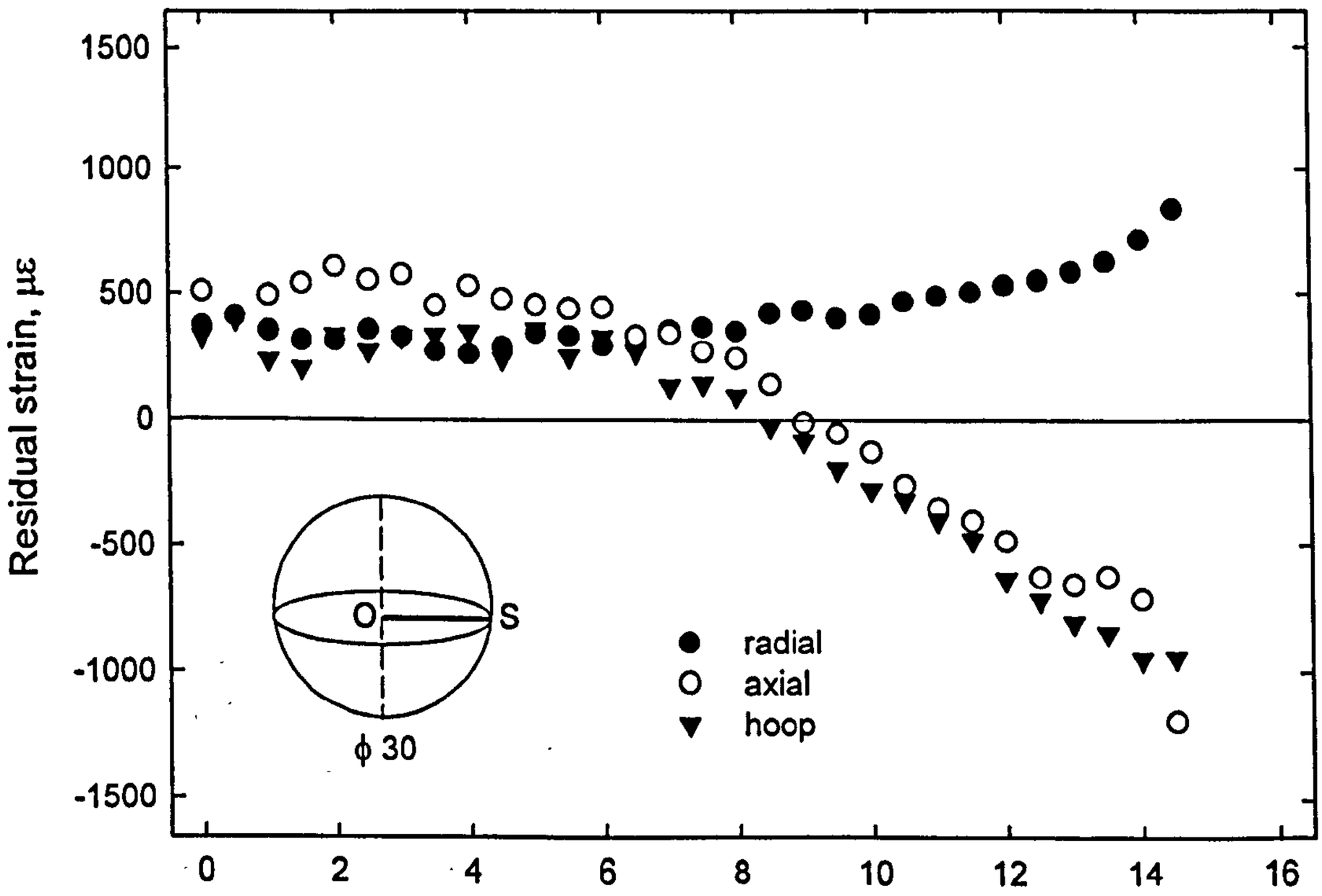

Figure 4.16 Summary of ND measured residual strains in a quenched and aged (at 550°C for 3200 hours) 316H solid SS sphere *s24*.

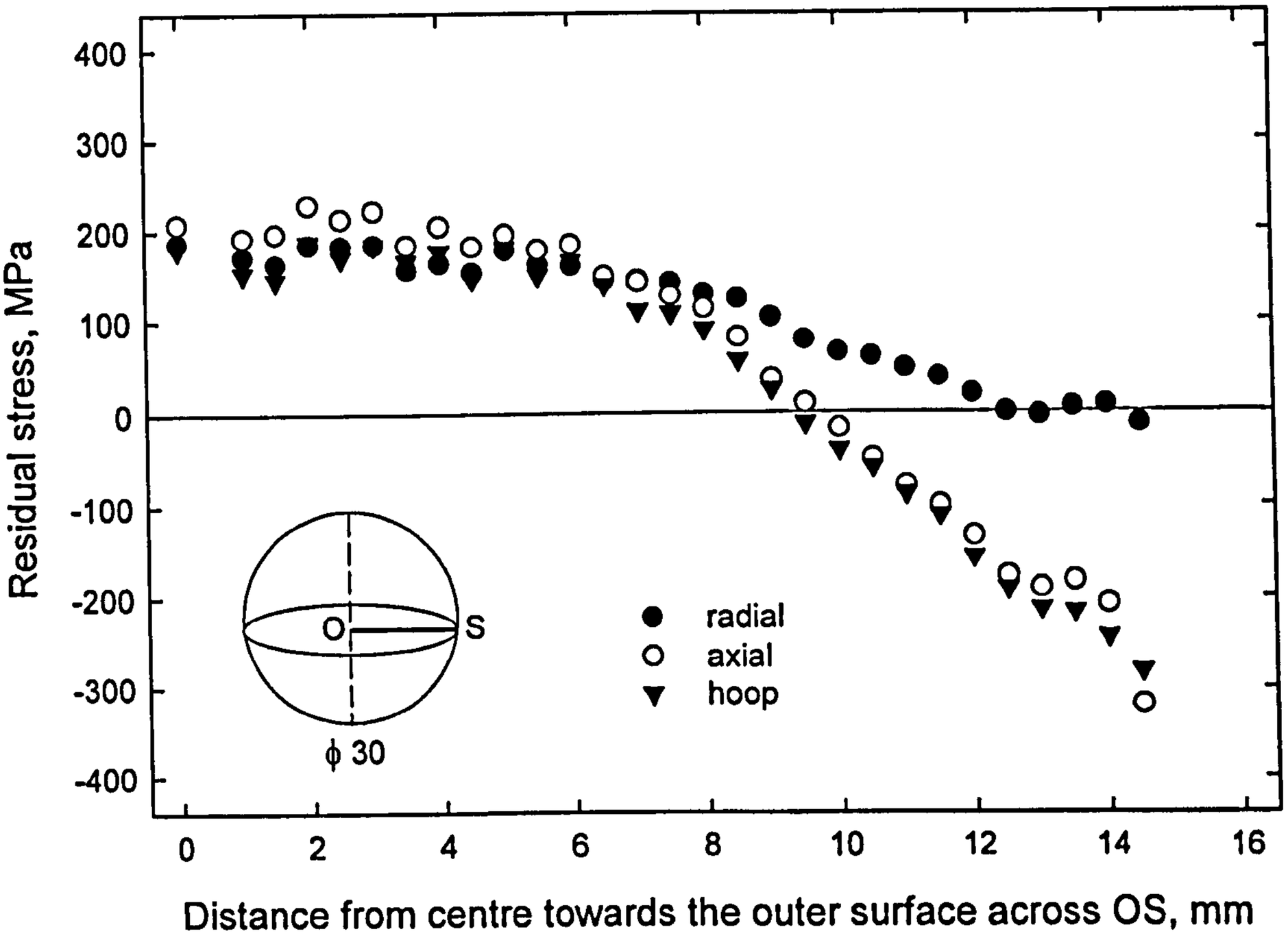

Figure 4.17 Measured residual stress distribution across the radial plane in a quenched and aged (3200 hours at 550°C) 316H SS solid sphere *s24*.

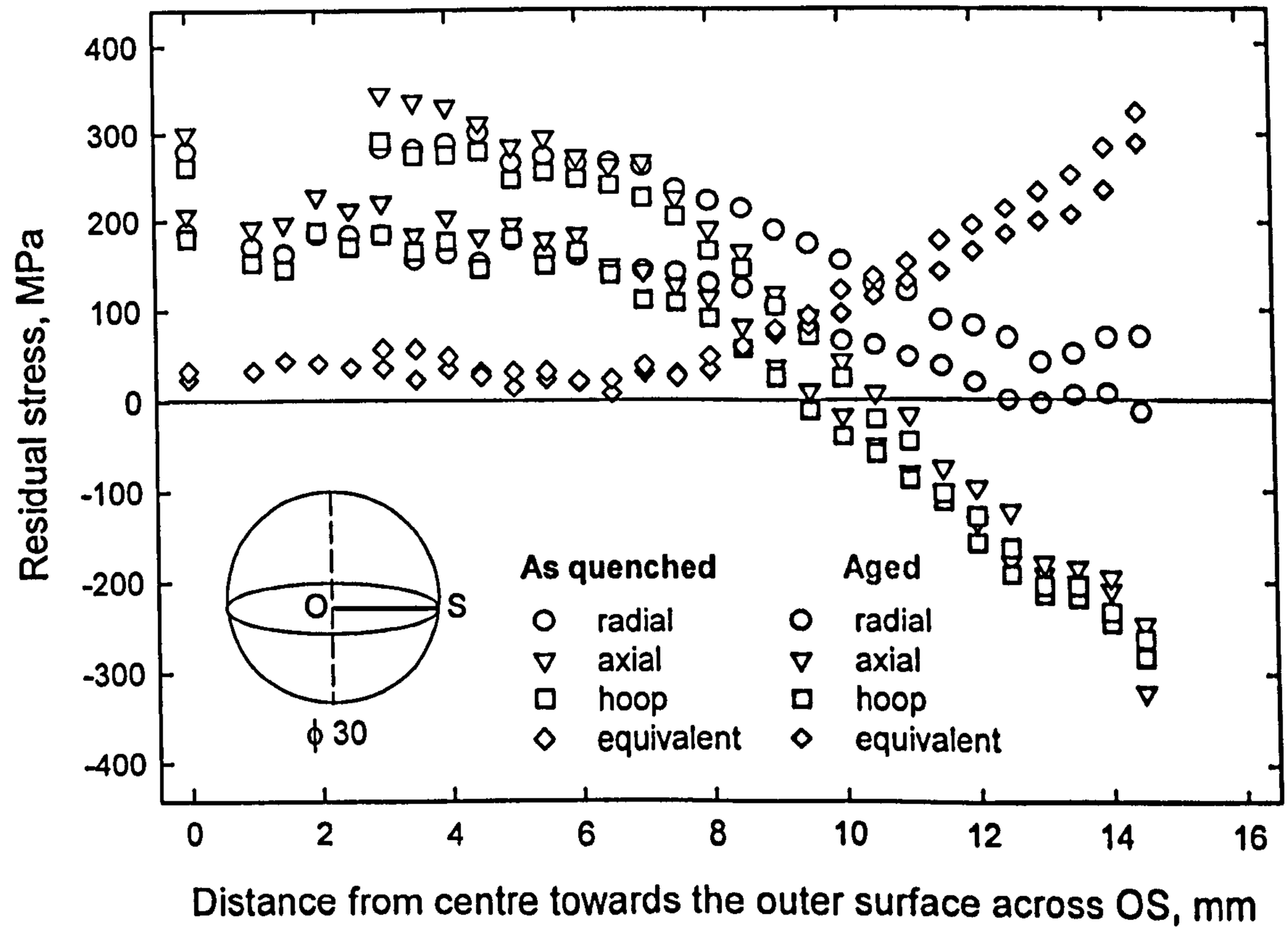

Figure 4.18 Comparison of residual stress distributions between as-quenched 316H SS solid sphere *s22* and quenched and aged 316H SS solid sphere *s24* across OS.

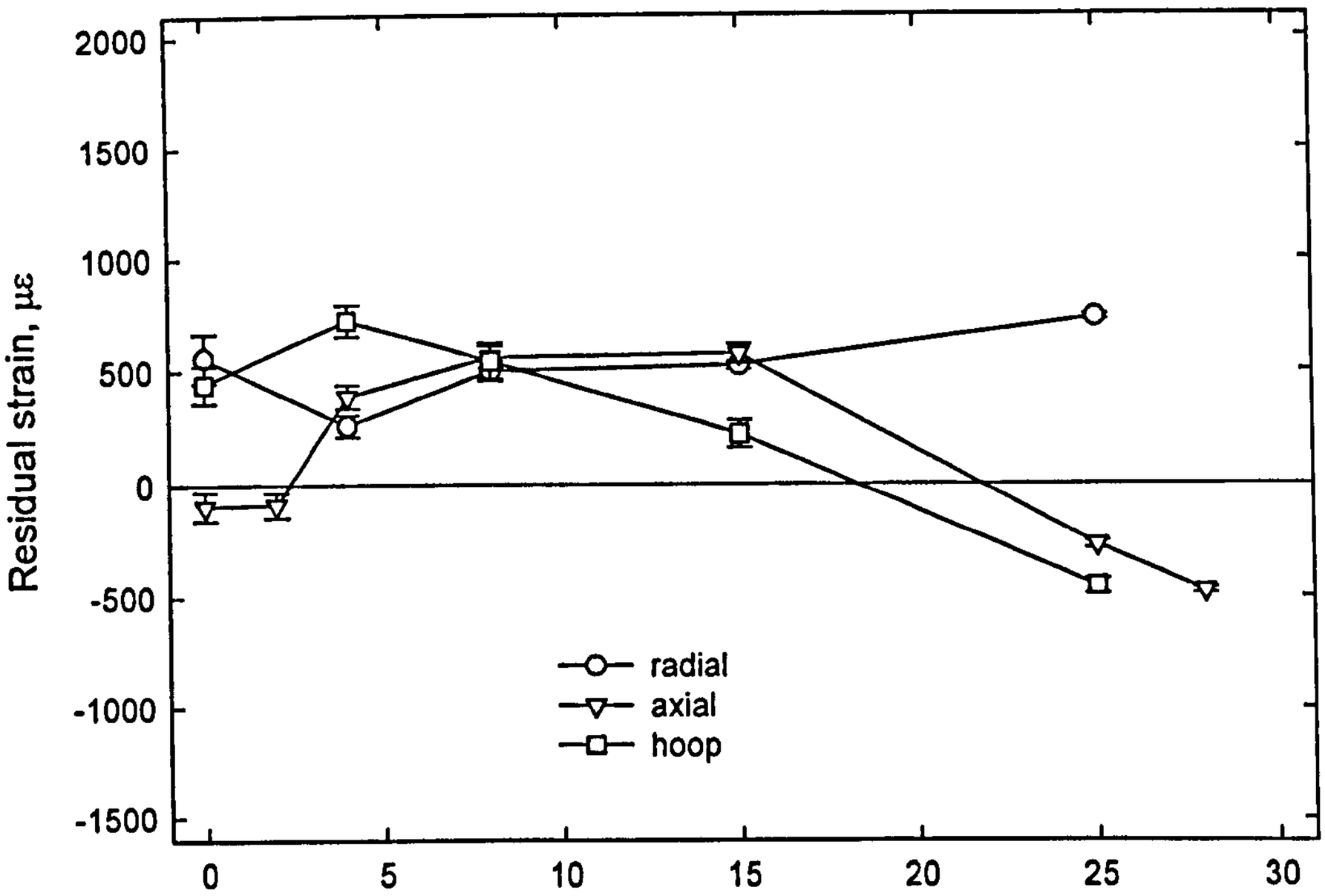

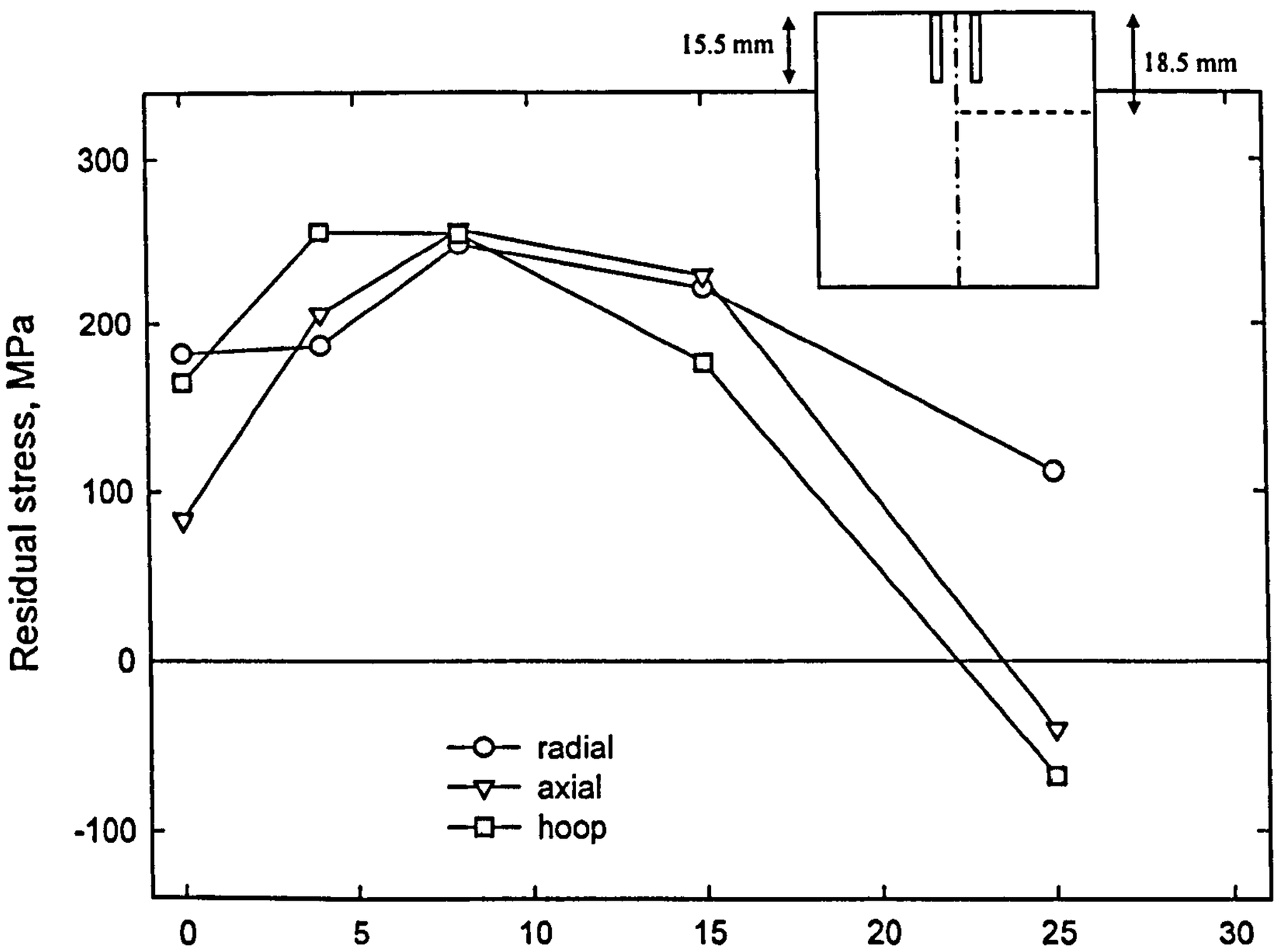

Figure 4.19 Distribution of residual (a) strain and (b) stress across a radial plane 18.5mm below the top surface in a quenched cylinder bar *s40* with 1.5mm diameter drill and 5mm diameter trepanned up to 15.5mm depth.

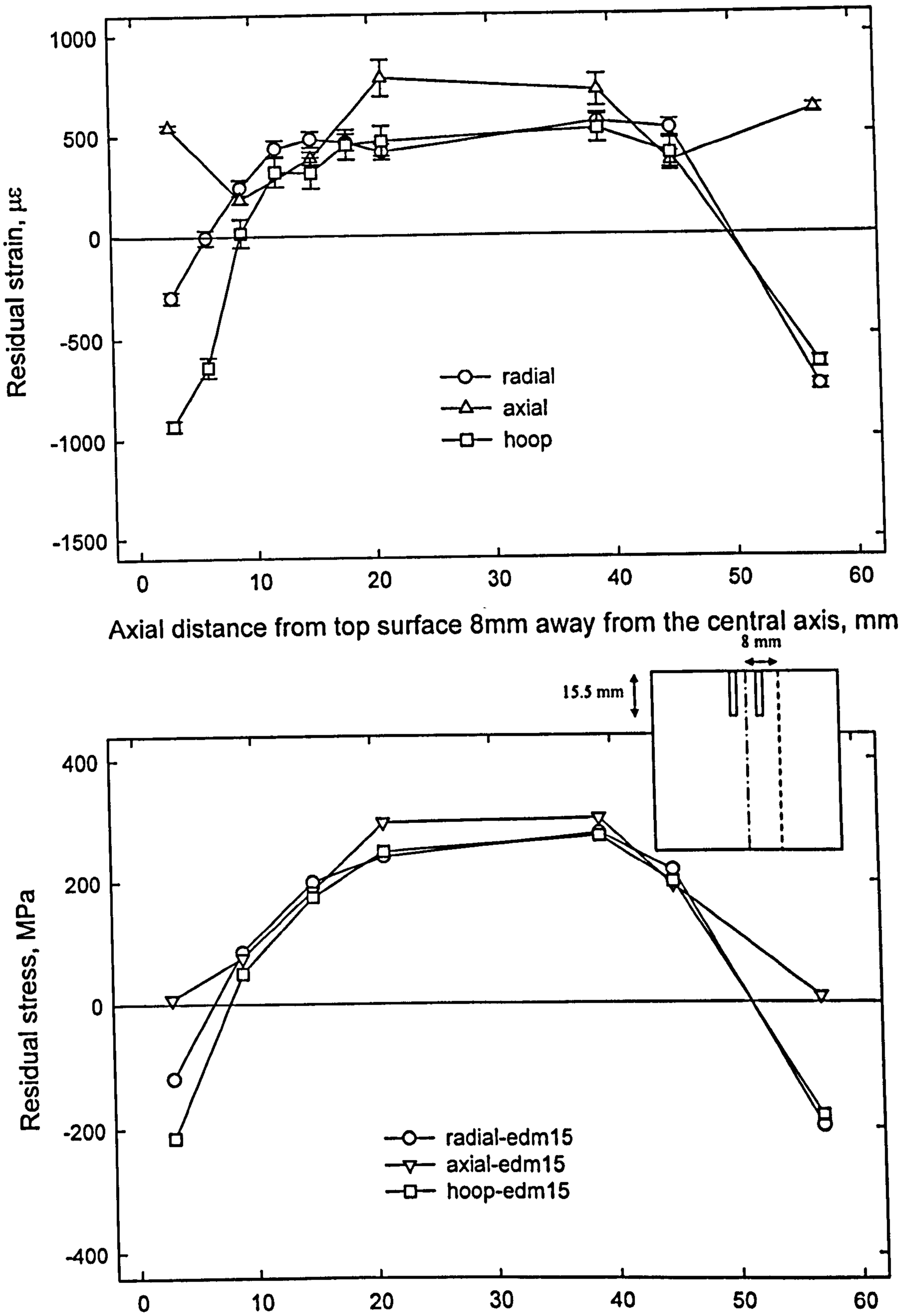

Figure 4.20 Distribution of residual (a) strain and (b) stress along an axial line 8mm away from the centreline in a quenched cylinder bar *s40* with 1.5mm diameter drill and 5mm diameter trepanned up to 15.5mm depth.

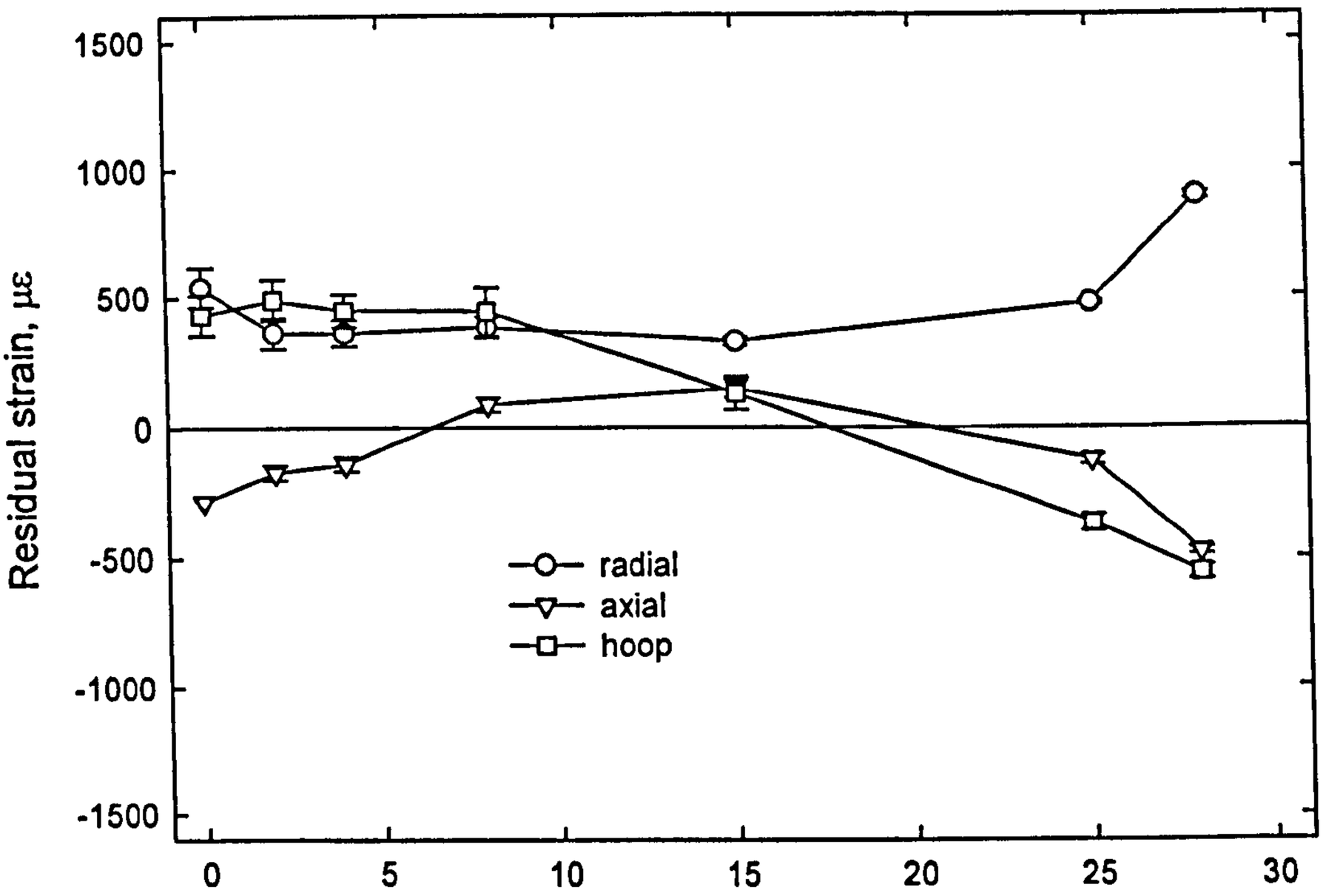

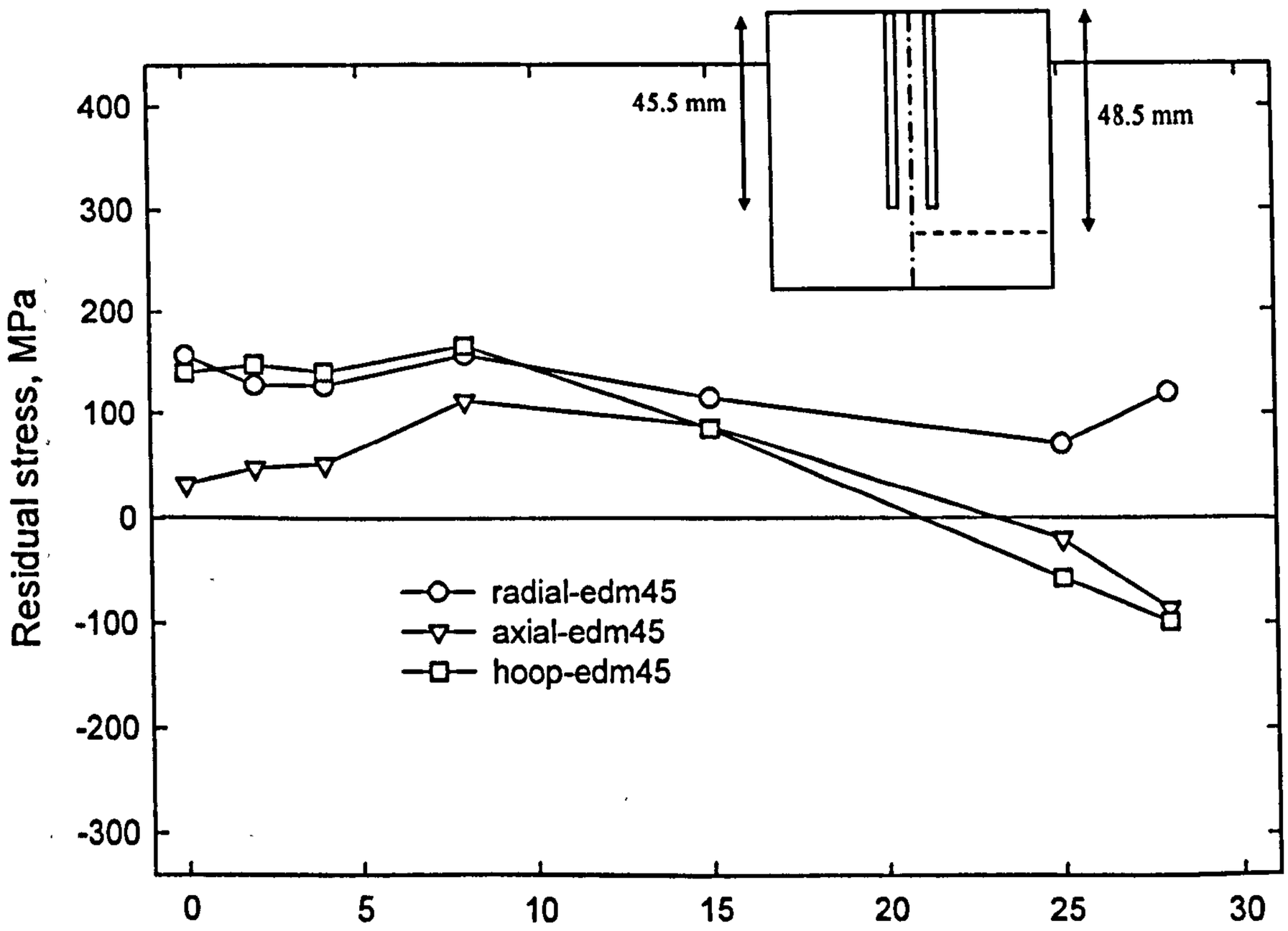

Figure 4.21 Distribution of residual (a) strain and (b) stress across a radial plane 48.5mm below the top surface in a quenched cylinder bar *s42* with 1.5mm diameter drill and 5mm diameter trepanned up to 45.5mm depth.

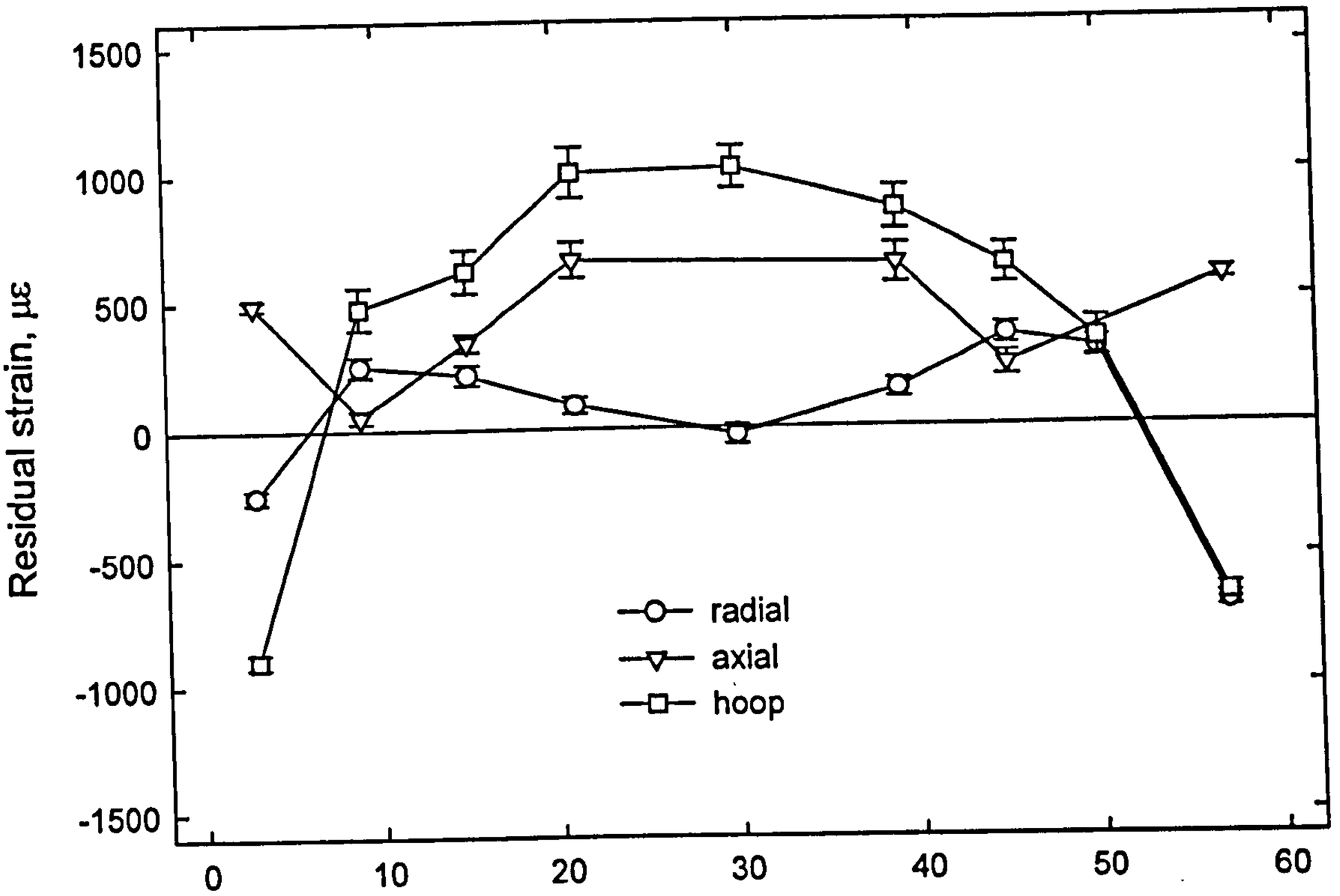

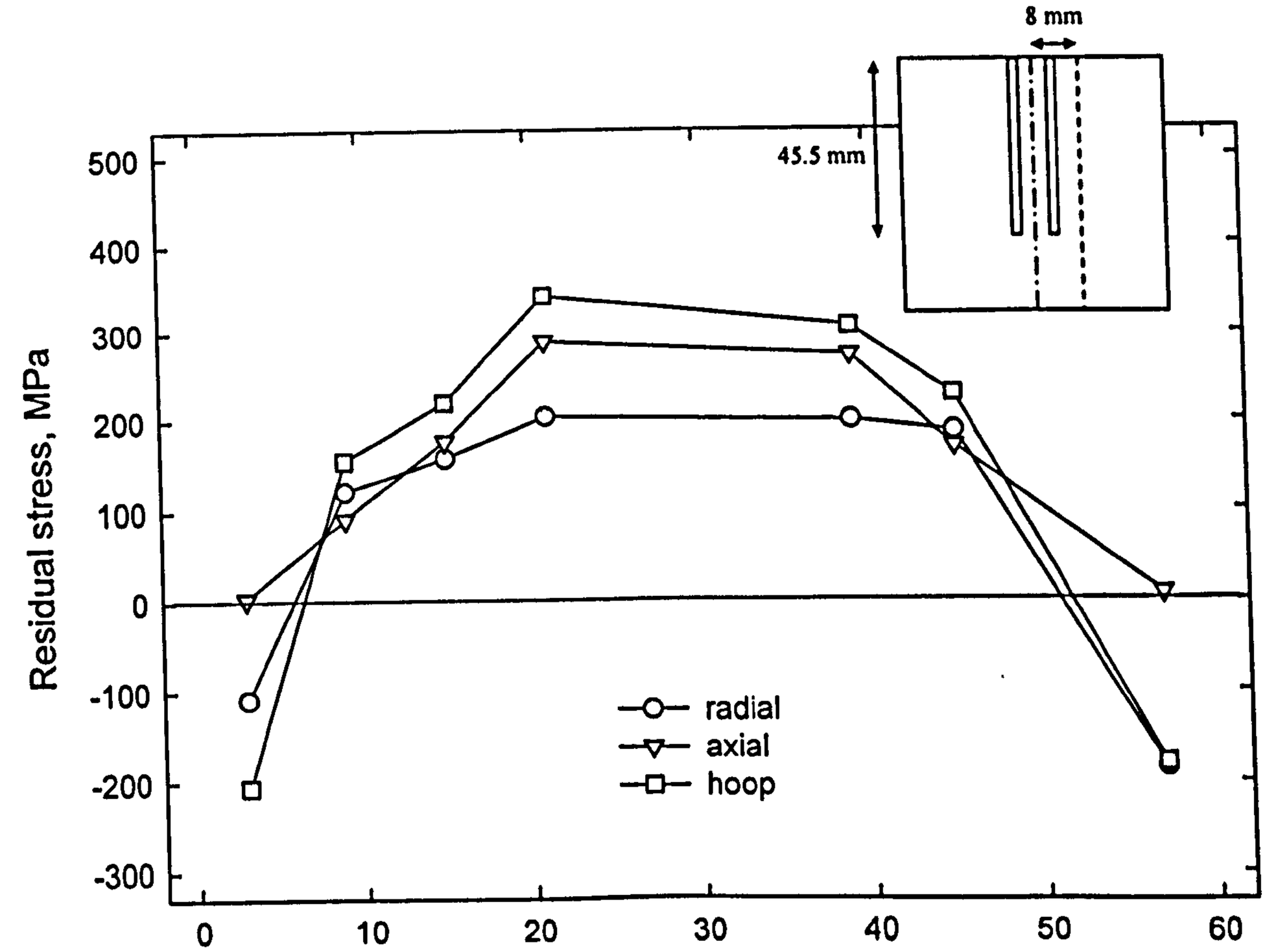

Figure 4.22 Distribution of residual (a) strain and (b) stress along an axial line 8mm away from the centreline in a quenched cylinder bar *s42* with 1.5mm diameter drill and 5mm diameter trepanned up to 45.5mm depth.

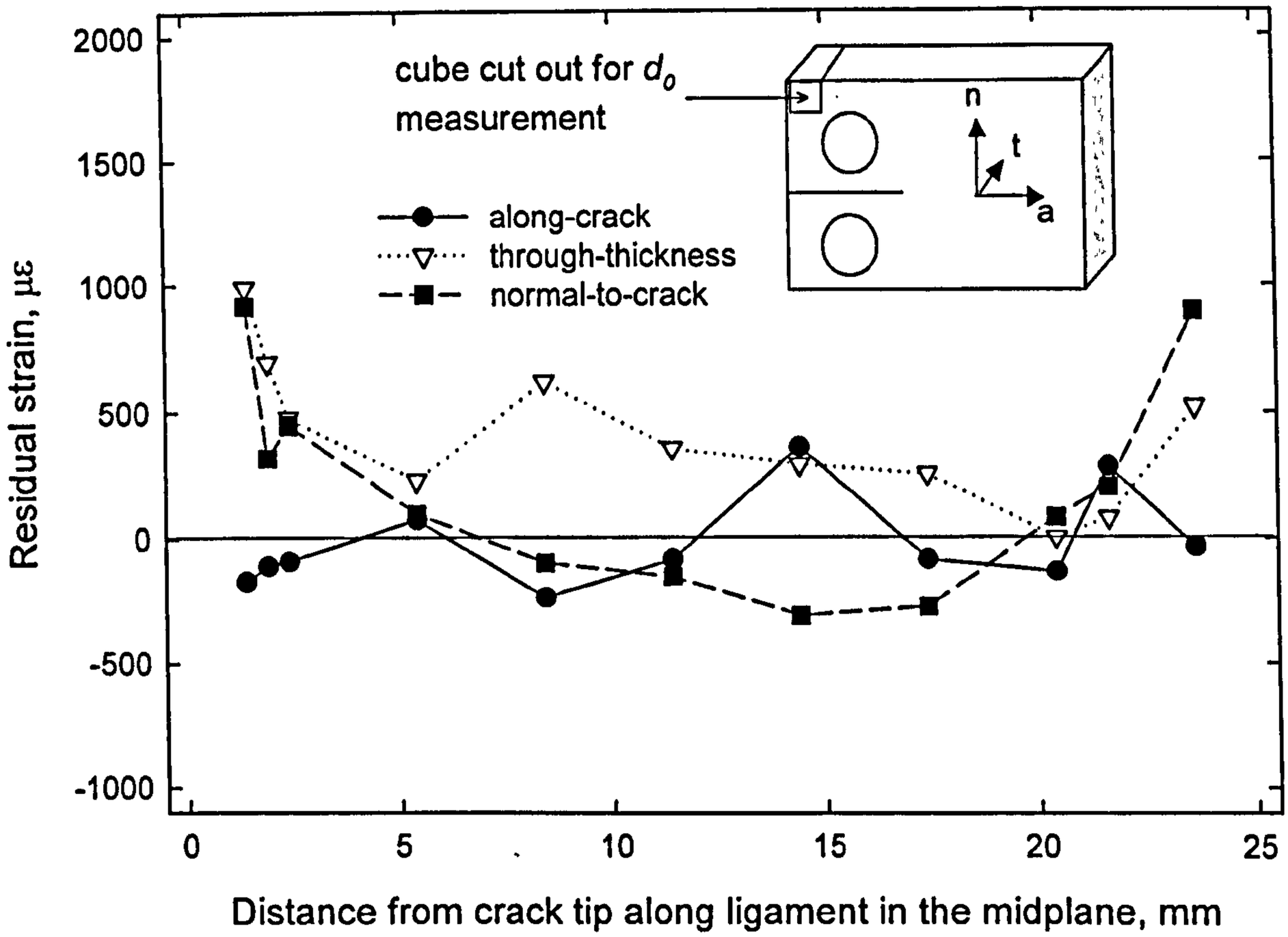

Figure 4.23 Measured residual strain distribution along the ligament ahead of crack tip in the mid-plane of an as-punched C(T) specimen.

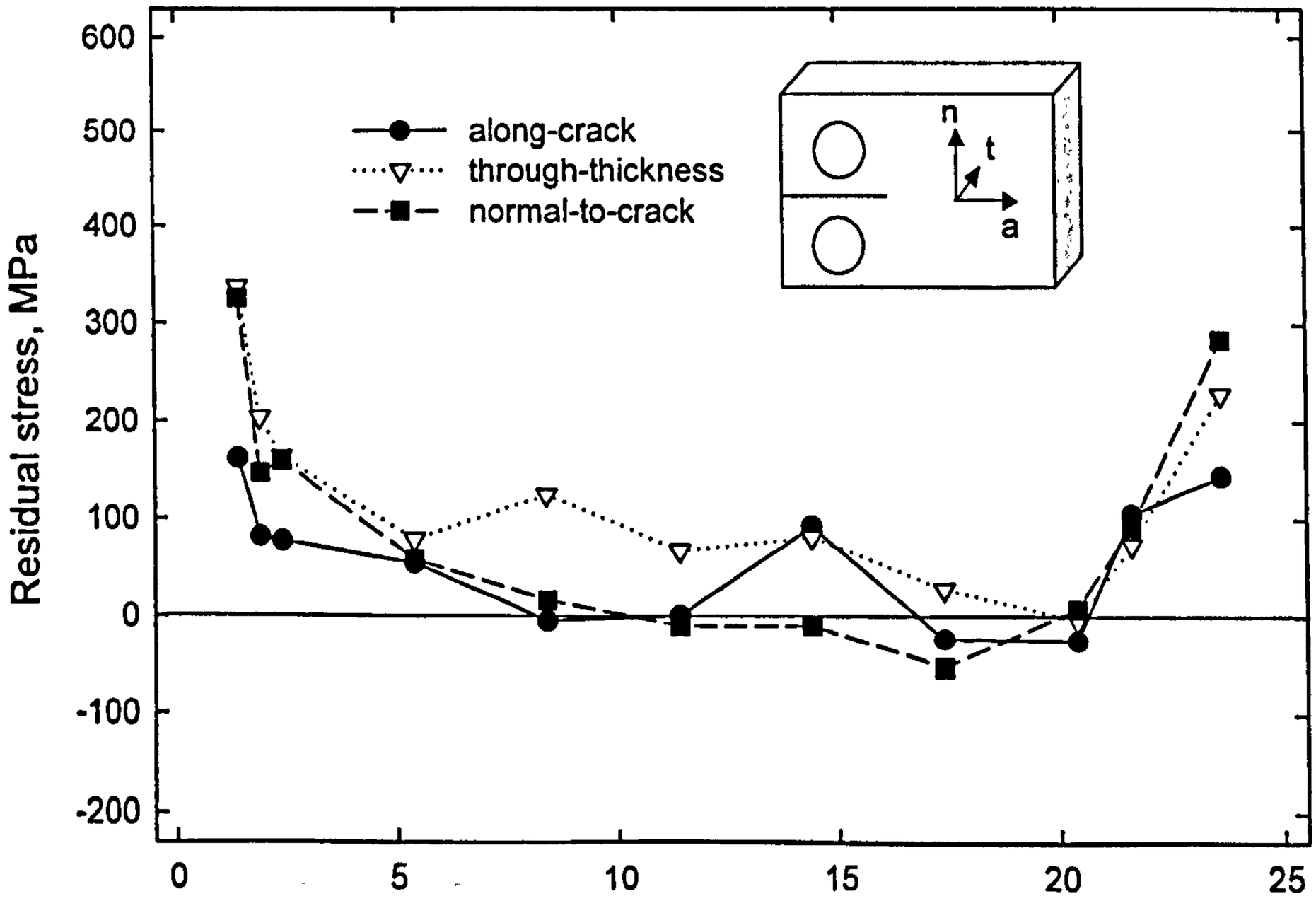

Figure 4.24 Measured residual stress distribution along the ligament ahead of crack tip in the mid-plane of an as-punched C(T) specimen.

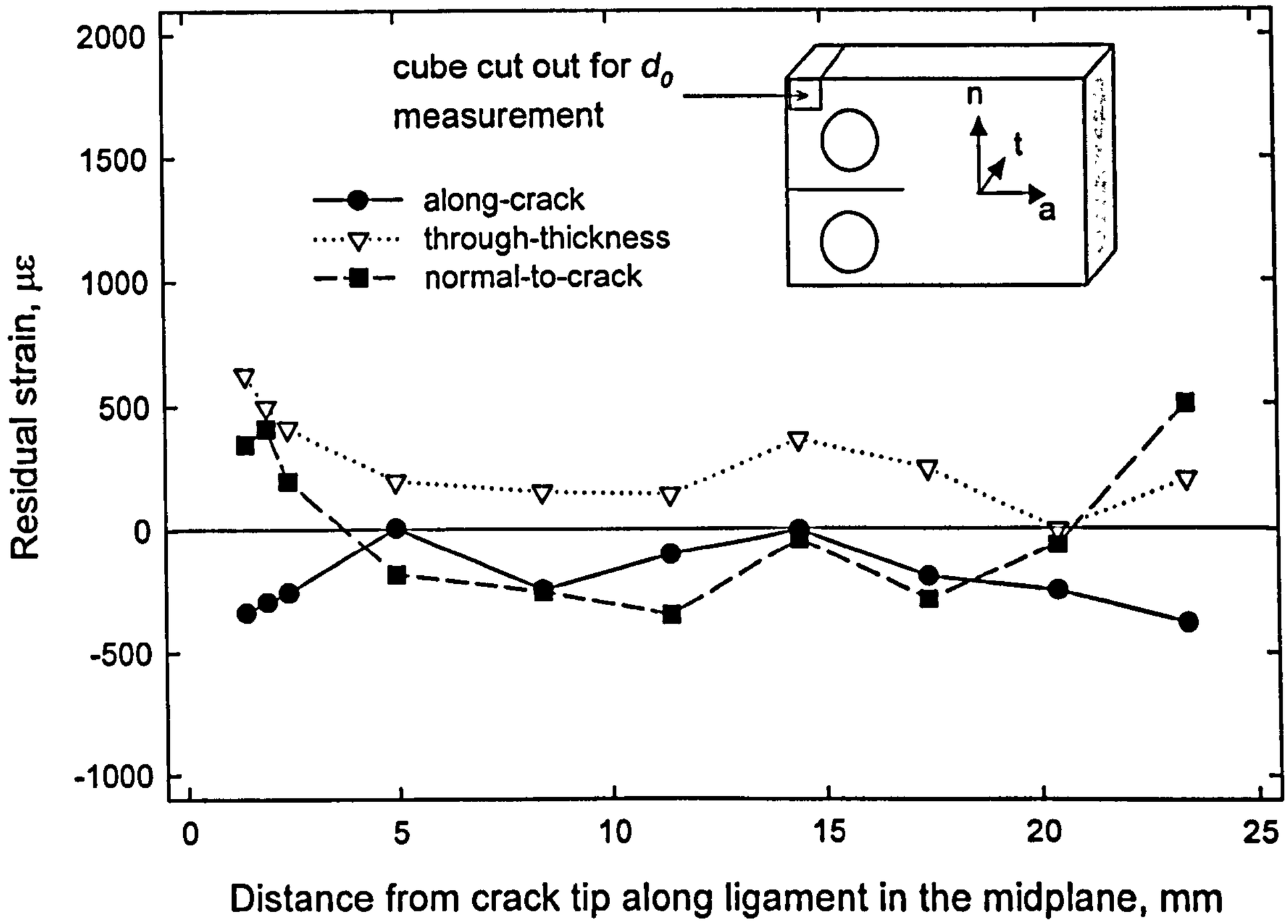

Figure 4.25 Measured residual strain distribution along the ligament ahead of crack tip in the mid-plane of a punched and thermally aged C(T) specimen.

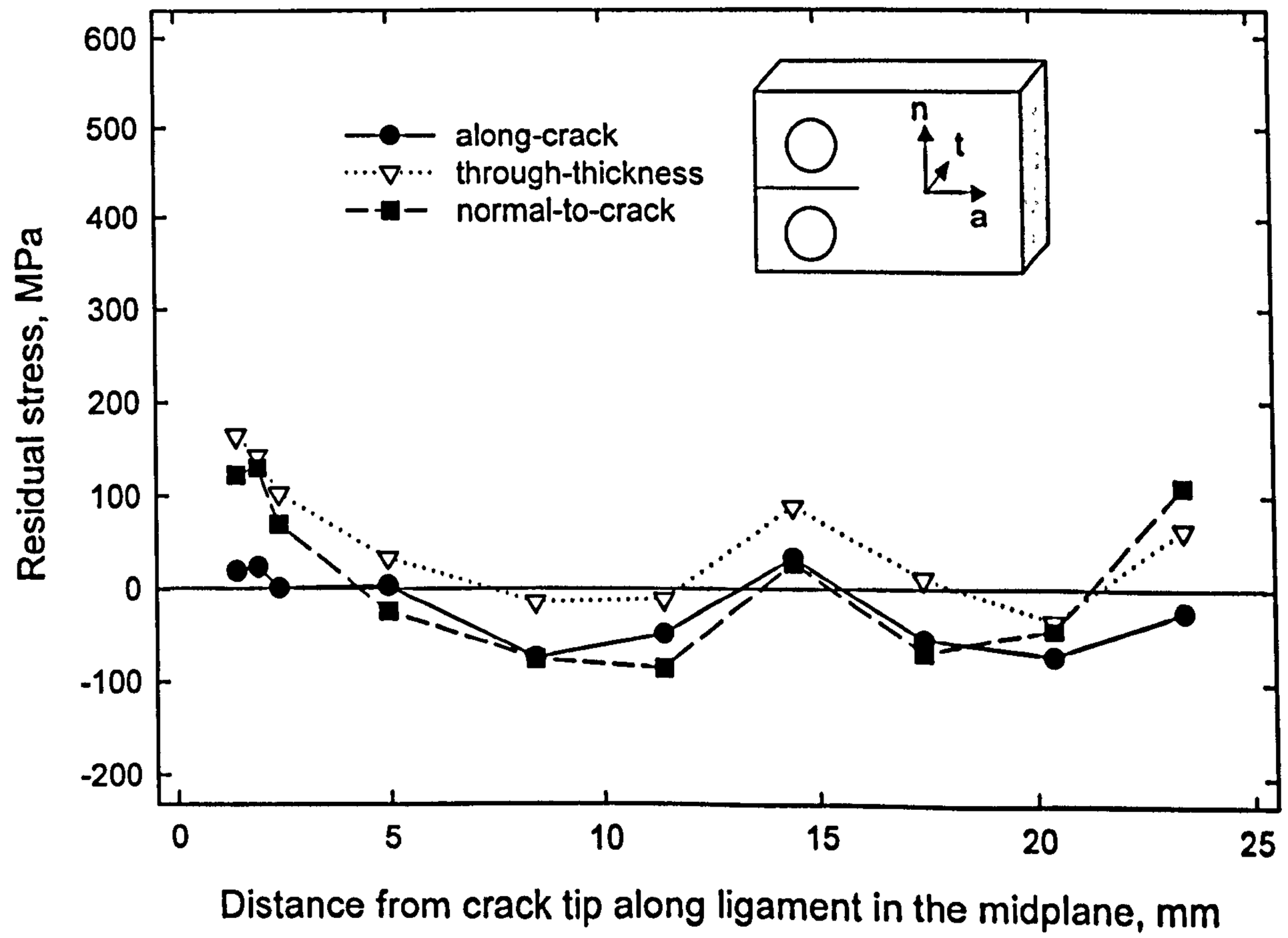

Figure 4.26 Measured residual stress distribution along the ligament ahead of crack tip in the mid-plane of a punched and thermally aged C(T) specimen.

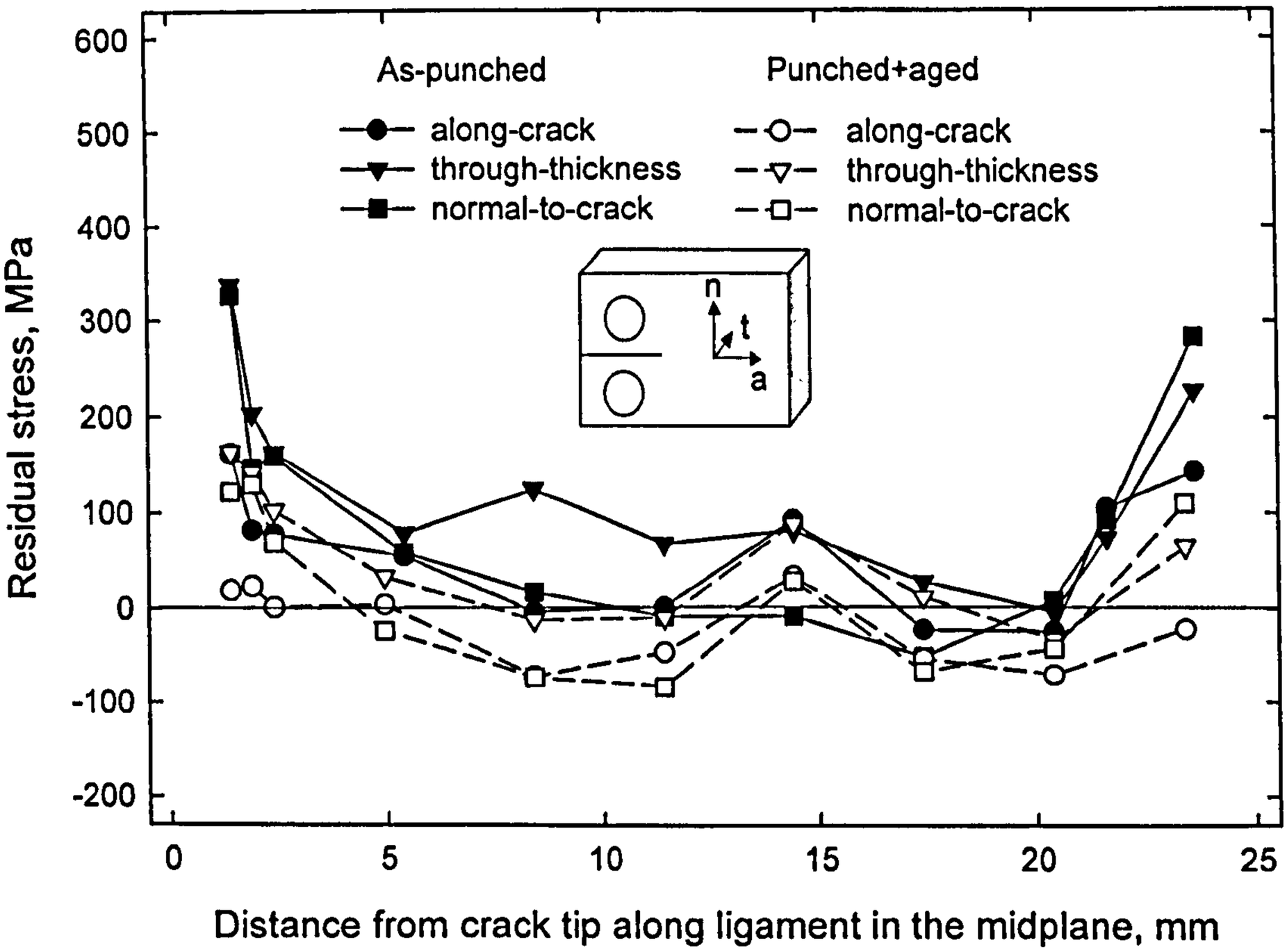

Figure 4.27 Comparison of measured residual stress distribution along the ligament ahead of crack tip in the mid-plane between the as-punched and punched and thermally aged C(T) specimens.

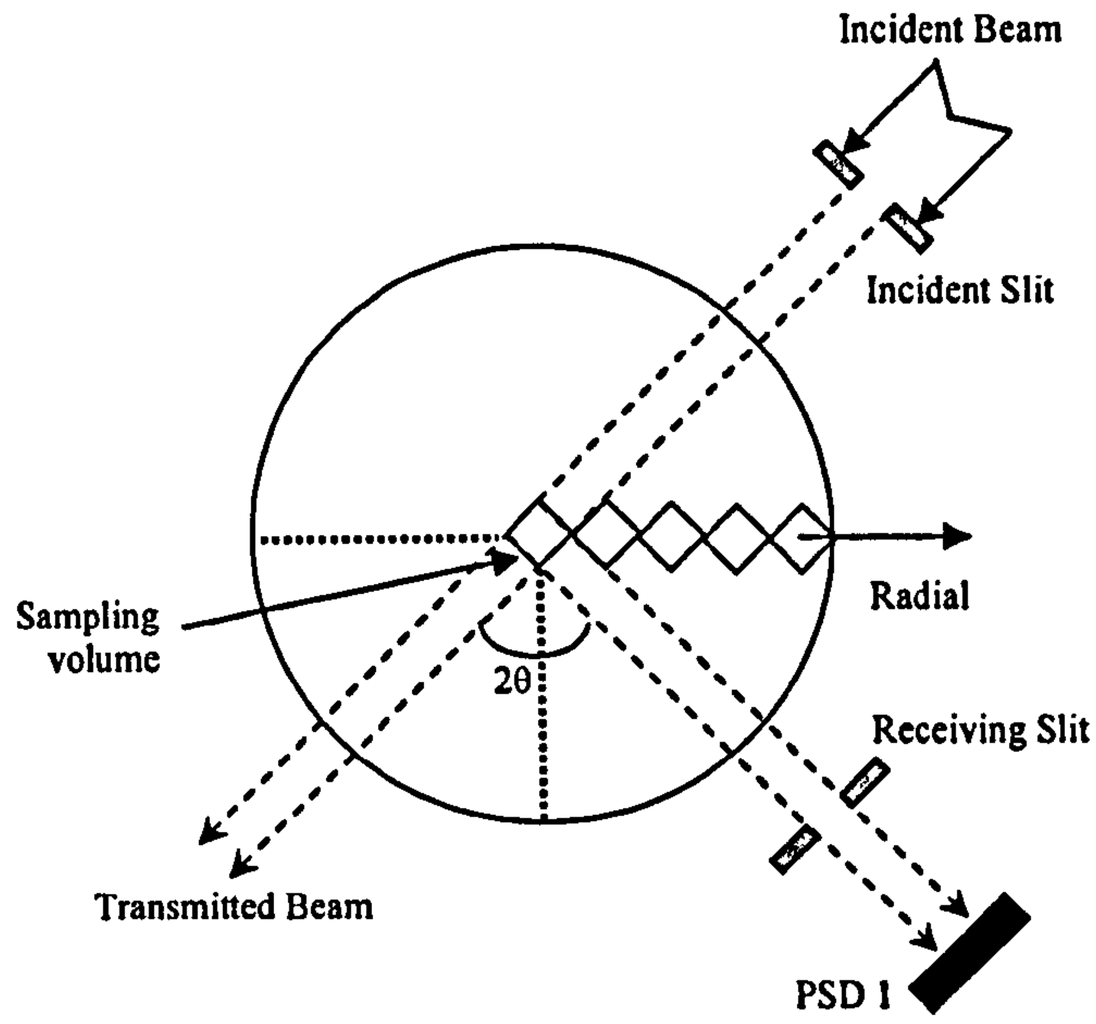

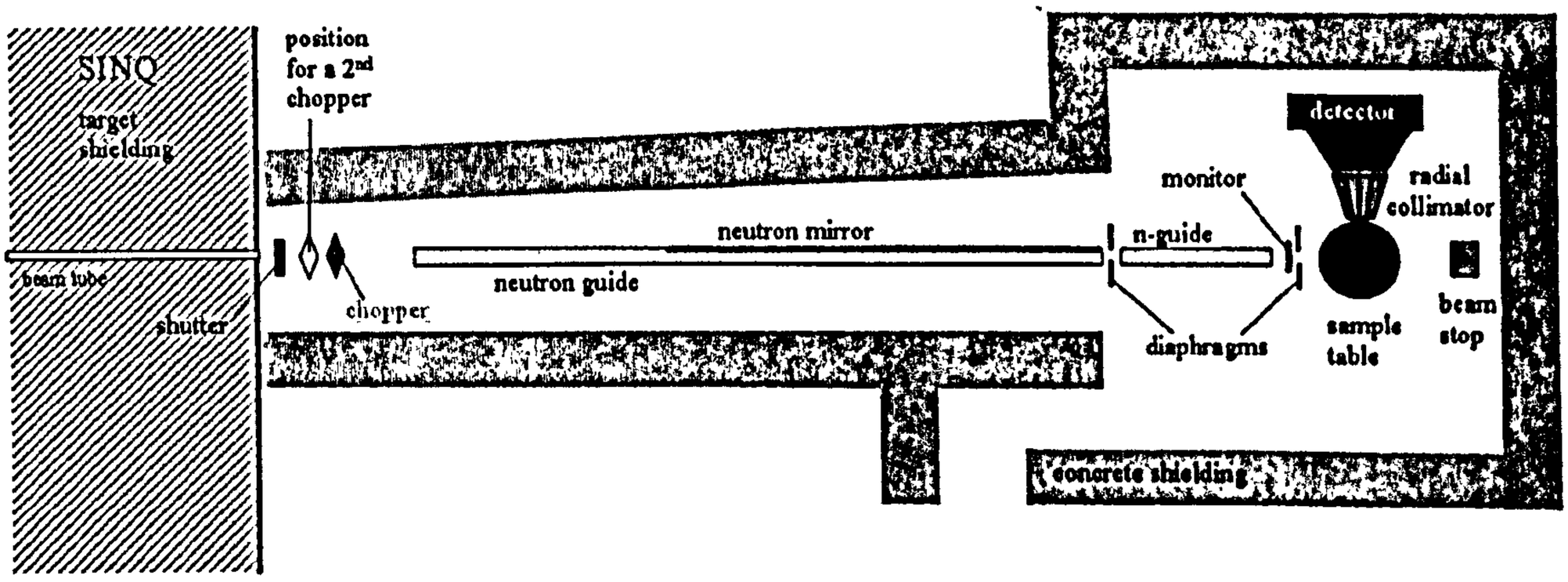

Figure 4.28 Schematic layout of the POLDI neutron diffractometer at the PSI facility.

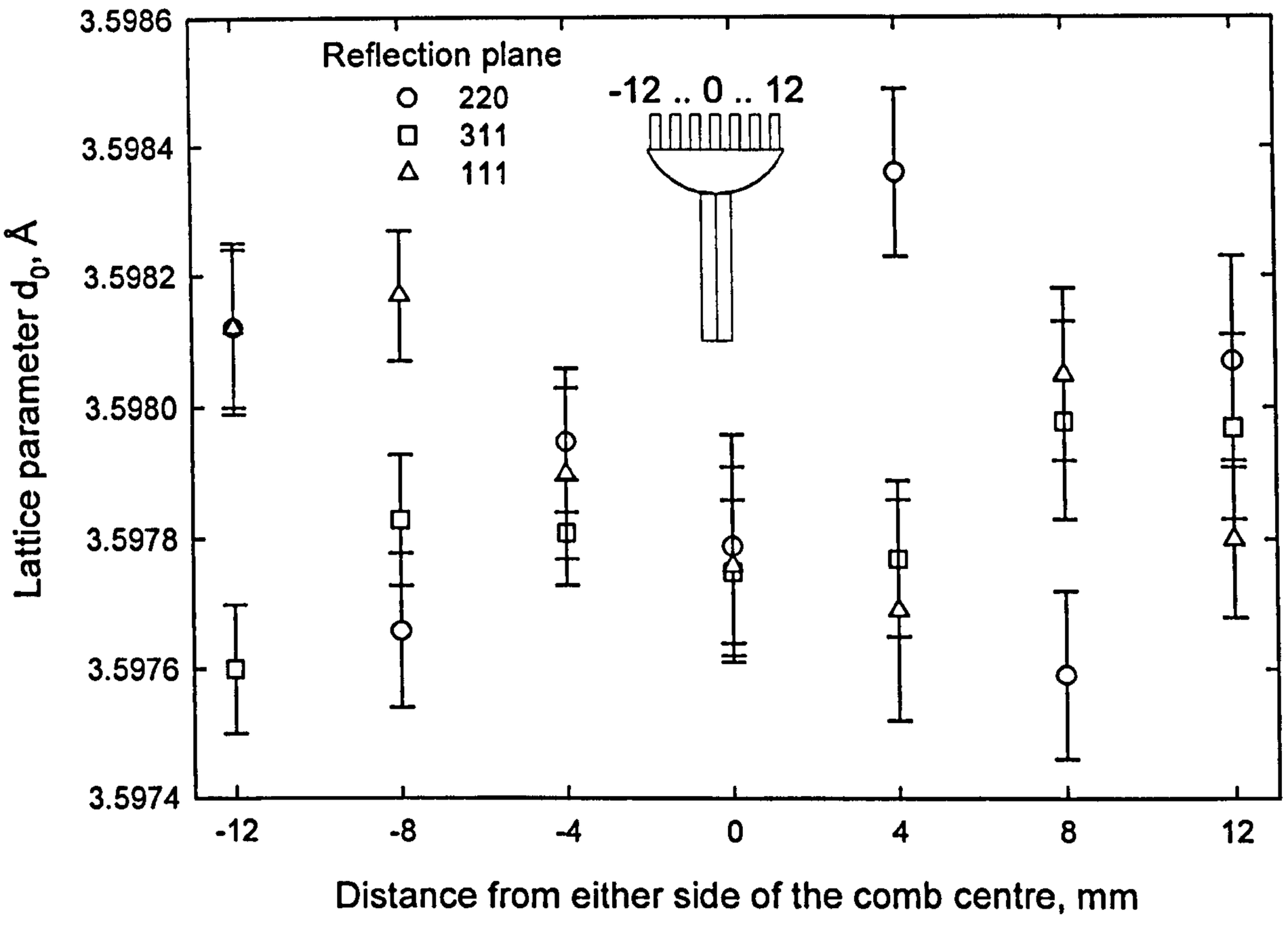

Figure 4.29 Summary of measured stress-free lattice parameter d_0 across comb *s30* used to determine the residual elastic strain distribution across sample *s29*.

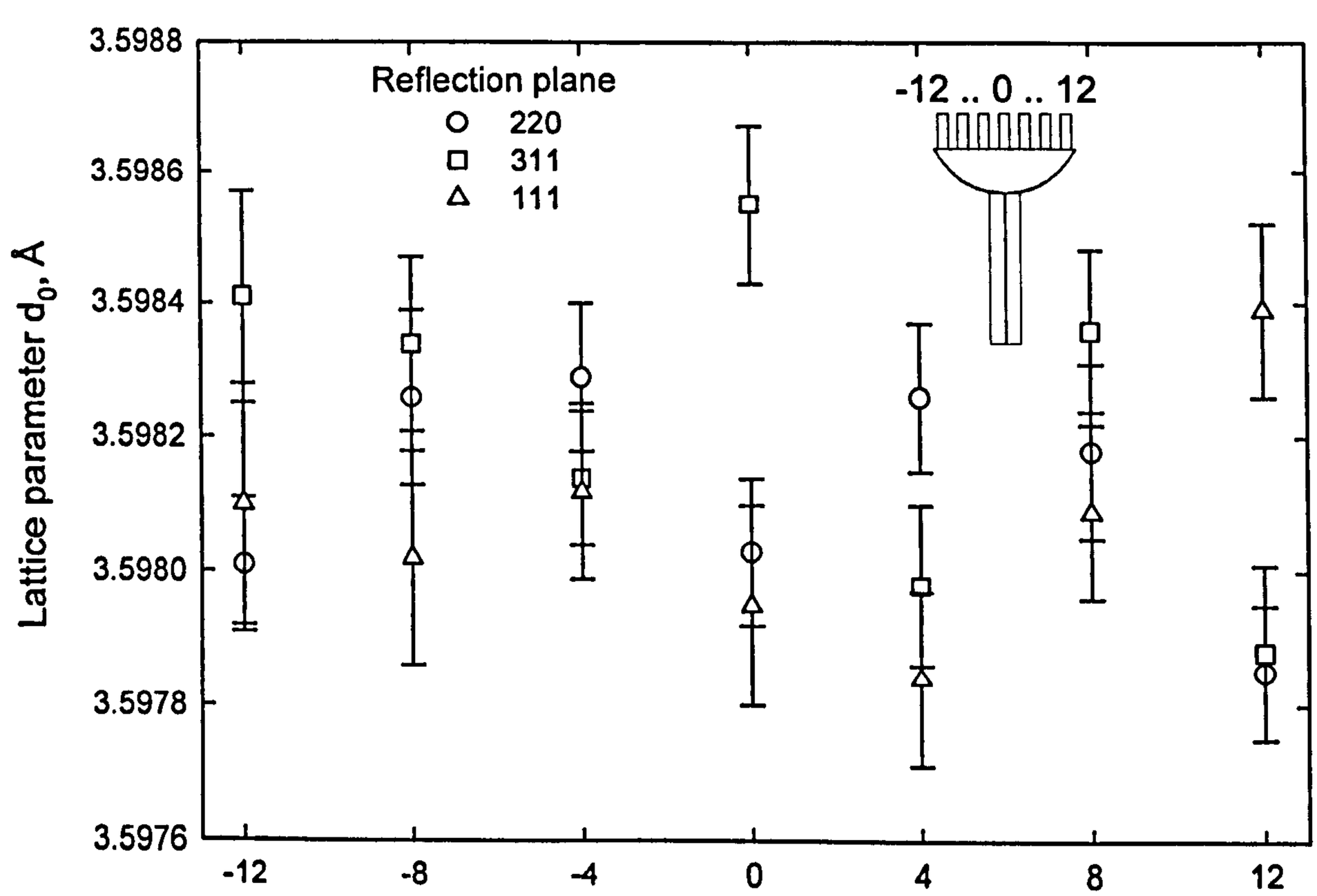

Figure 4.30 Summary of measured stress-free lattice parameter d_0 across comb *s31* used to determine the residual elastic strain distribution across sample *s28*.

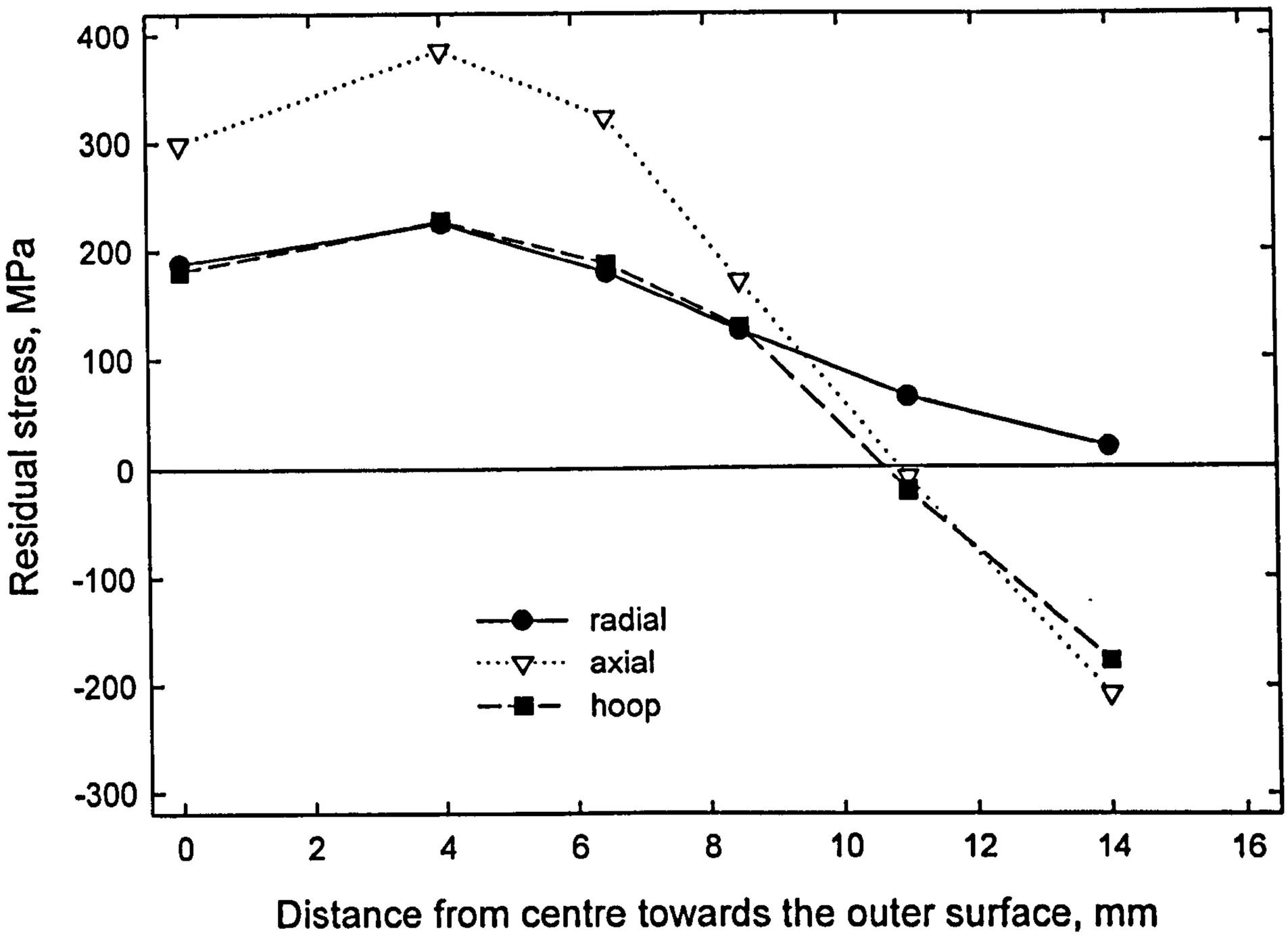

Figure 4.31 Measured and predicted residual stress distribution across the equatorial plane of a quenched and short-term (1.25 hours) thermally aged cylinder *s29*.

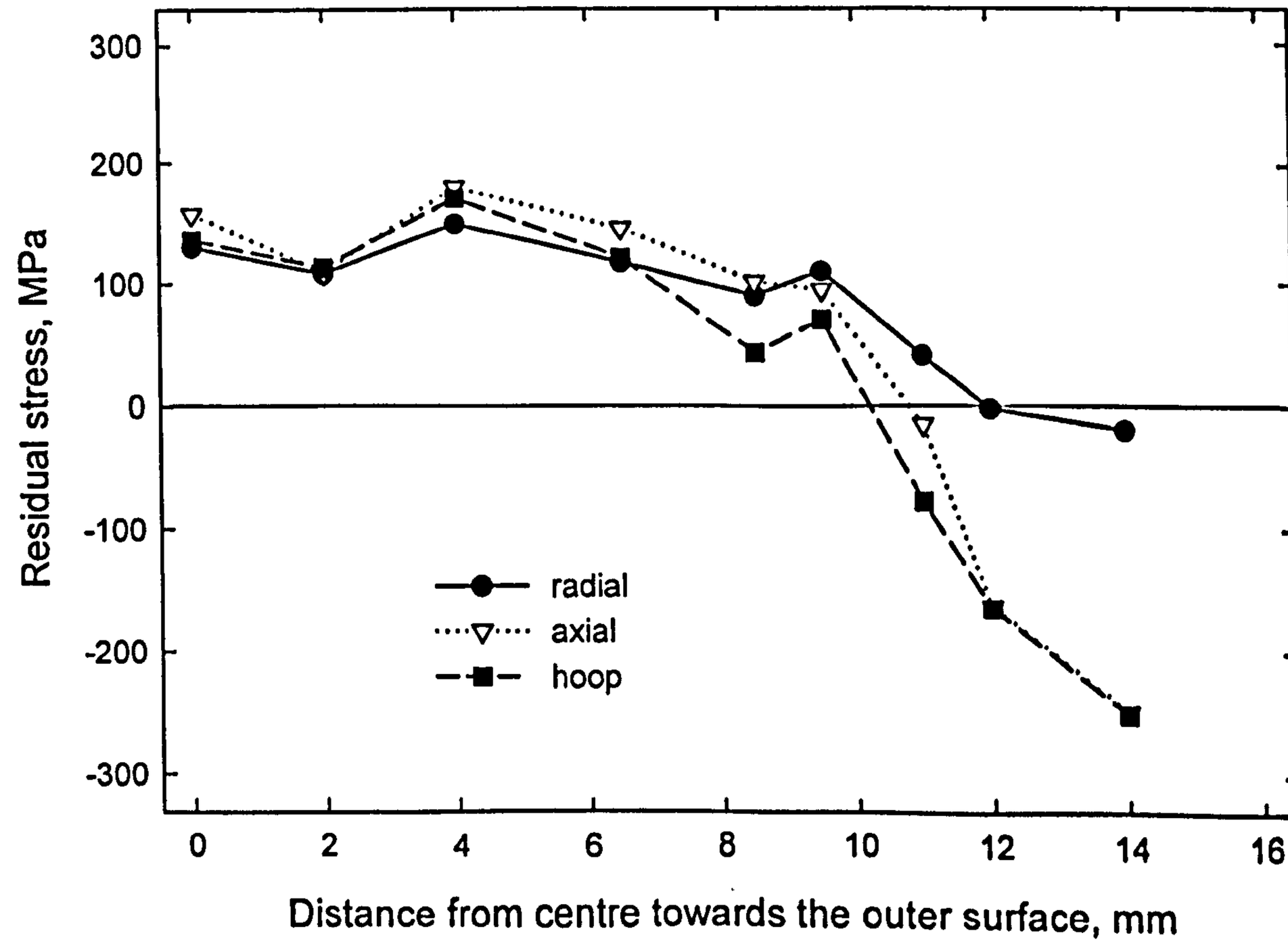

Figure 4.32 Measured and predicted residual stress distribution across the equatorial plane of a quenched and long-term (1800 hours) thermally aged cylinder *s28*.

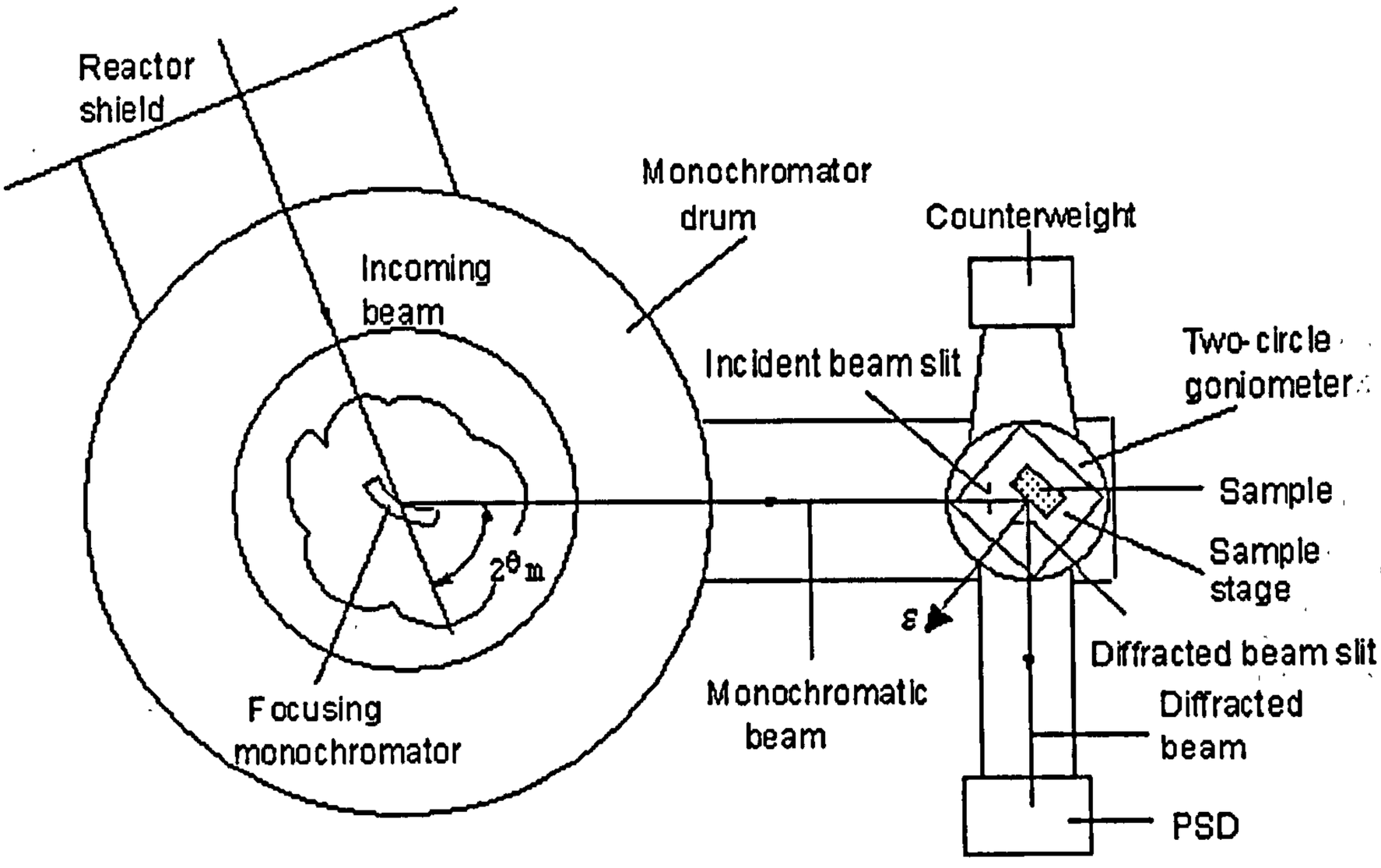

Figure 4.33 Description of residual stress instrument REST at NFL, Sweden (http://www.studsvik.uu.se/)

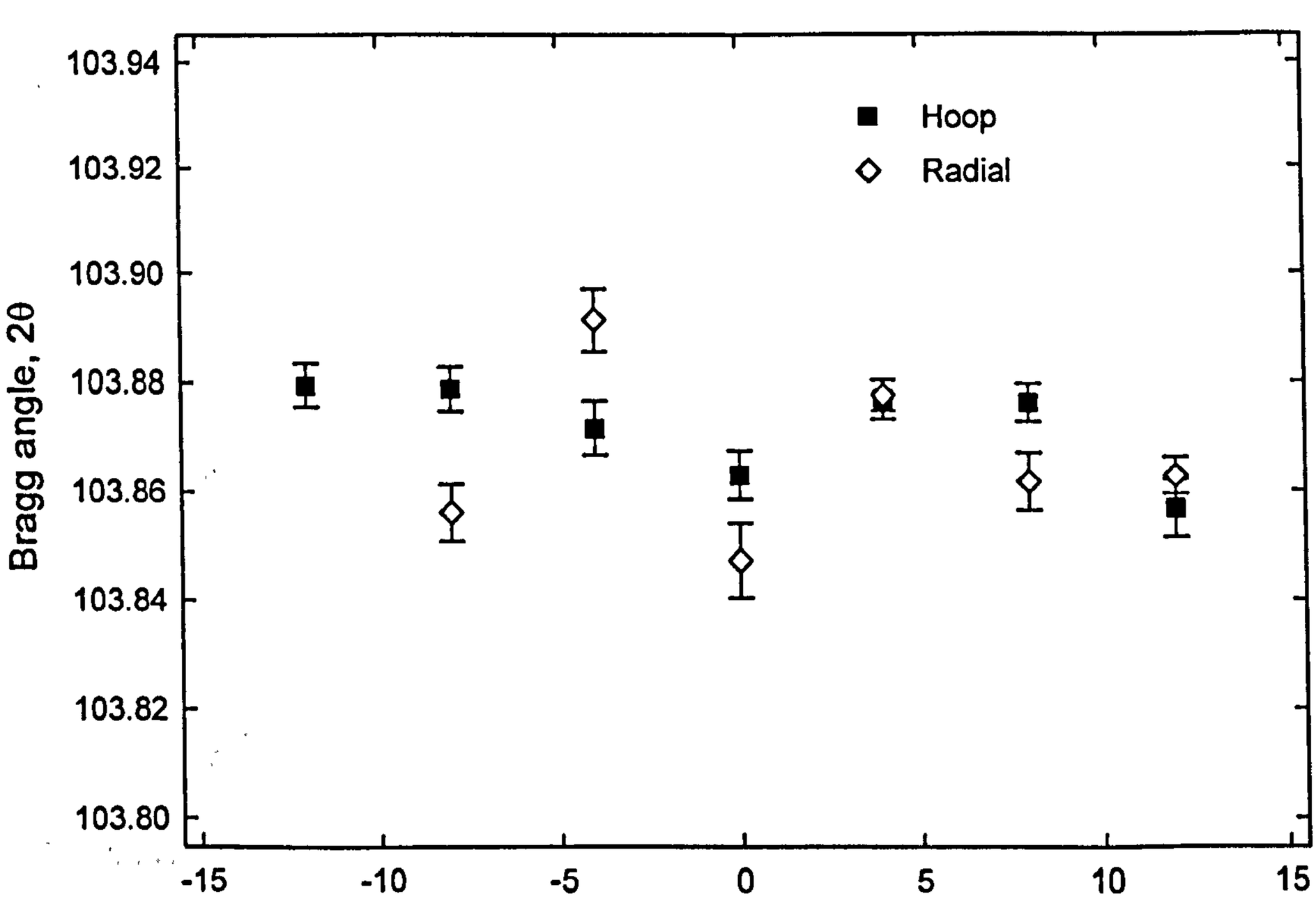

Figure 4.34 Summary of the measured Bragg angles across the seven fingers on the comb *s25* used to determine the stress free parameter.

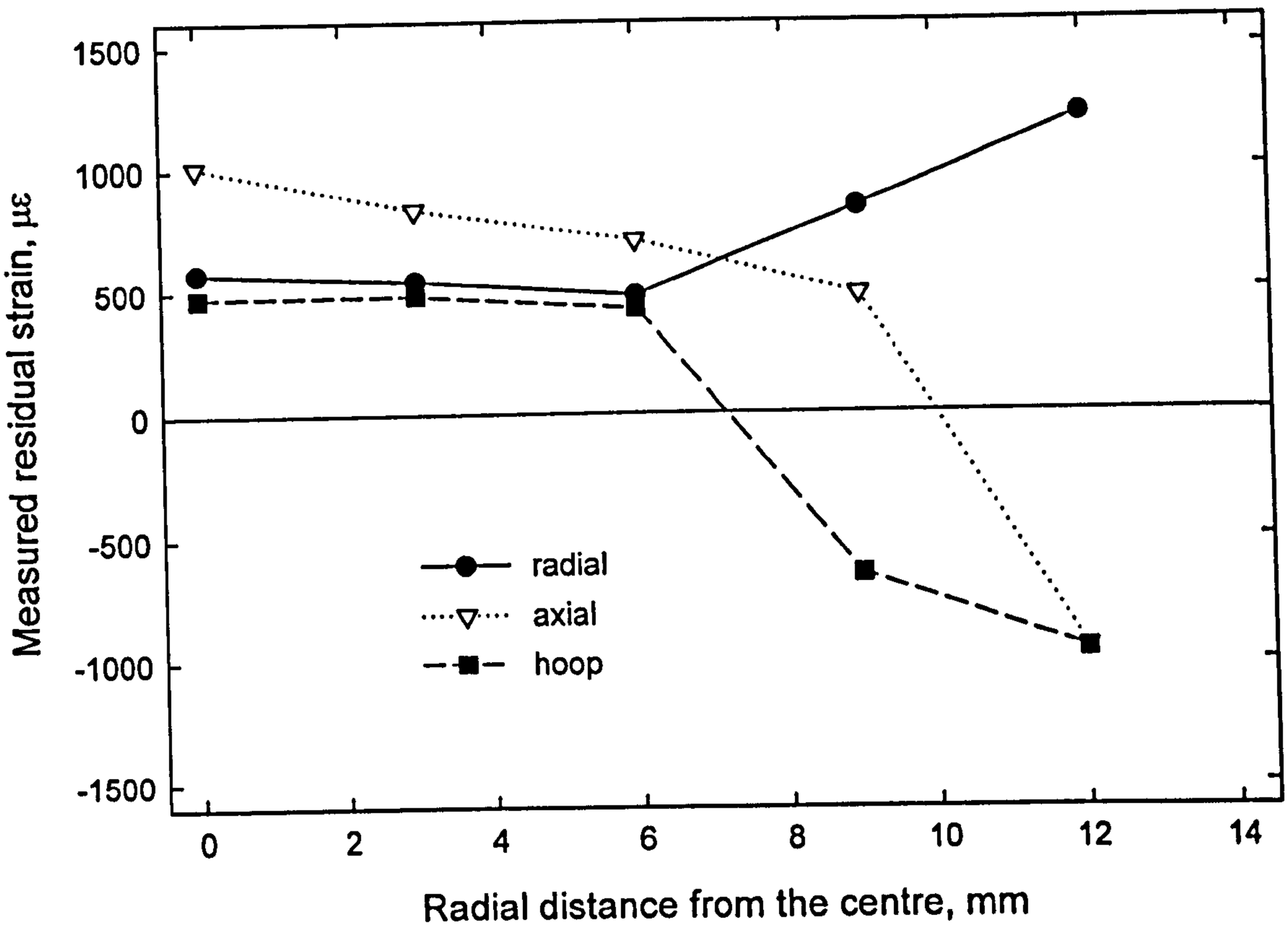

Figure 4.35 Summary of ND measured residual strains for a quenched stainless steel solid cylindrical bar *s39*, diameter 29mm, length 29mm, across the equatorial plane from the centre to the surface of the bar.

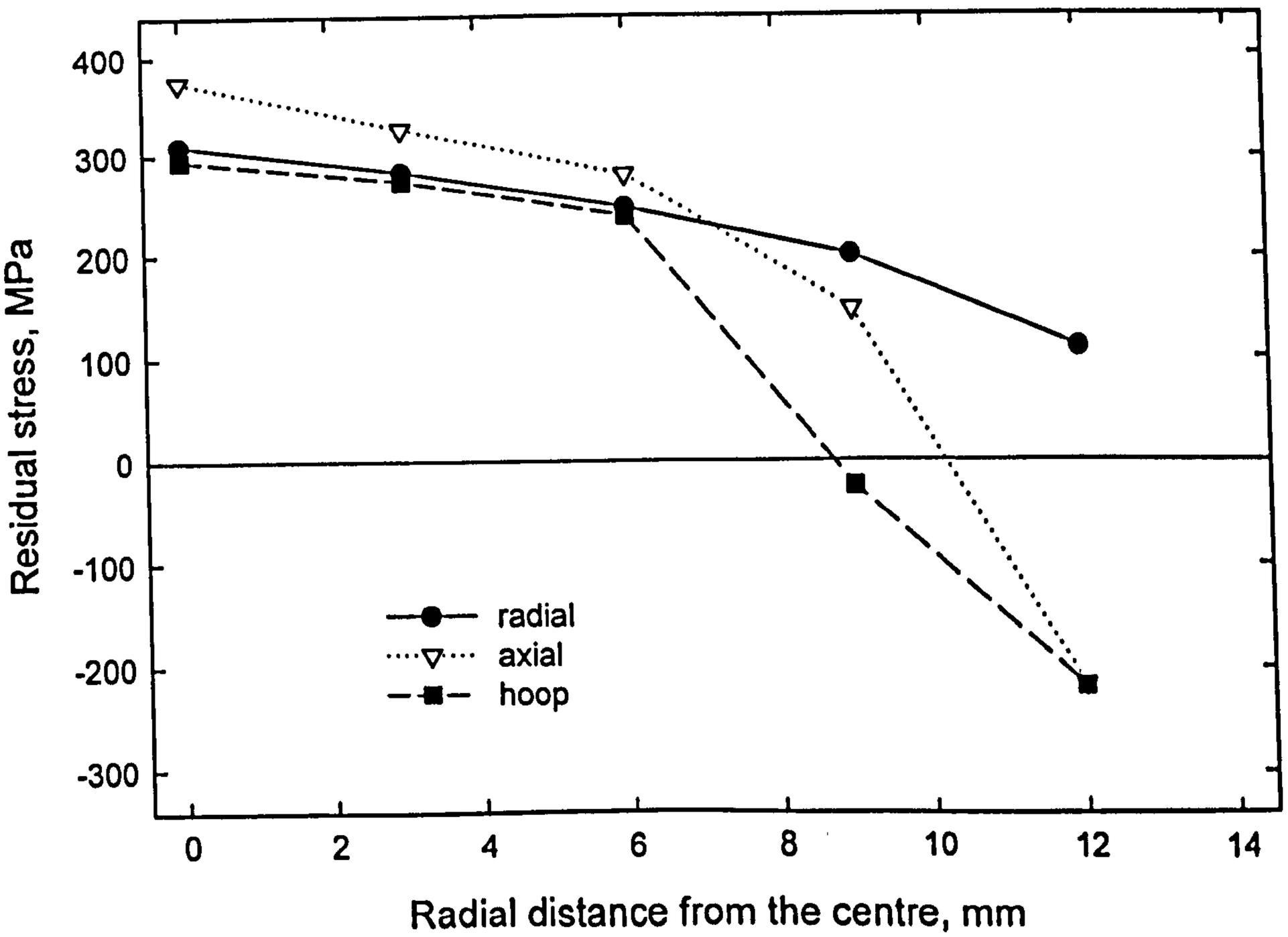

Figure 4.36 Measured residual stress distribution across the equatorial plane of a quenched cylinder *s39*, diameter 29mm, length 29mm, measured from the centre to the surface of the bar.

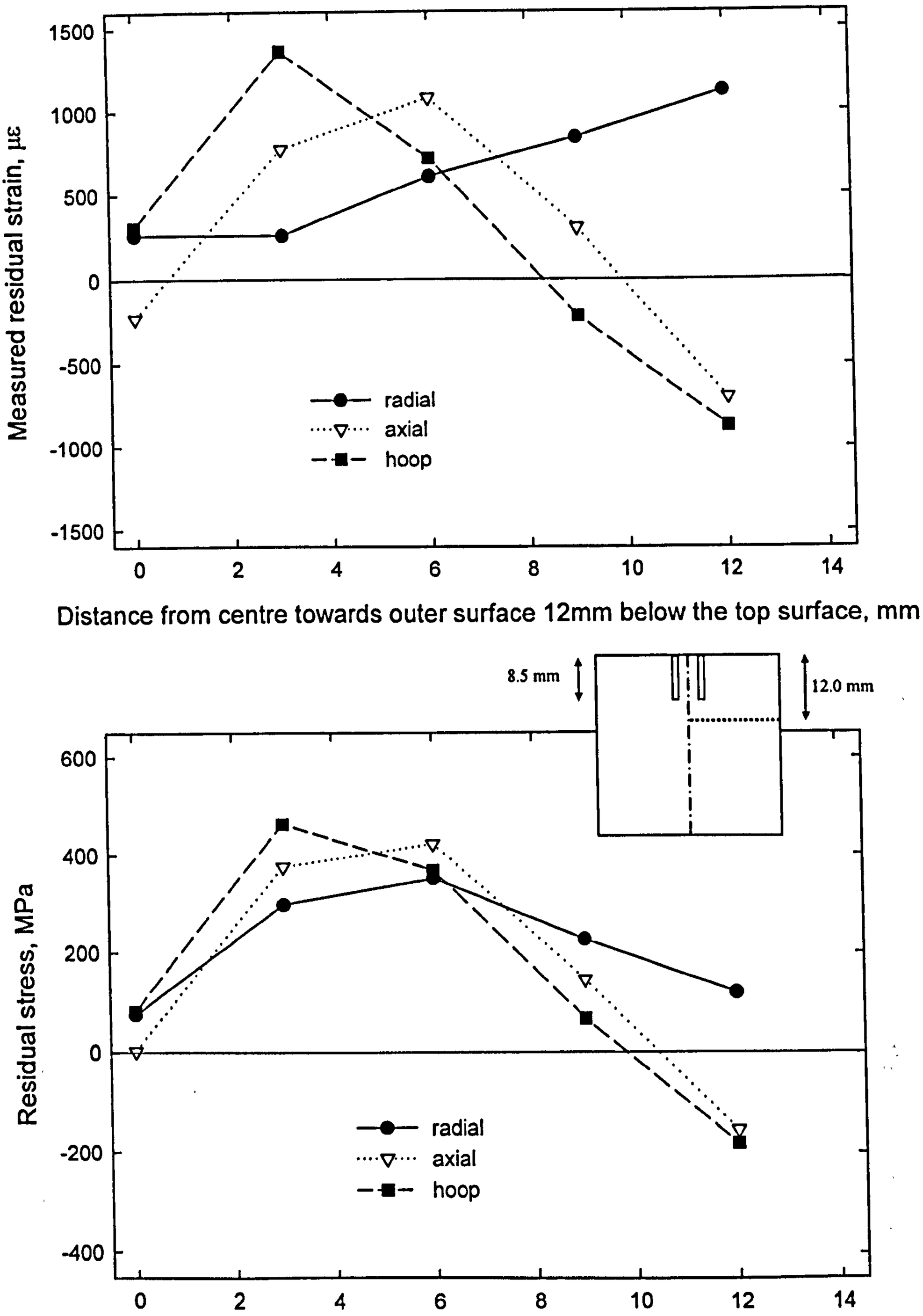

Figure 4.37 Distribution of residual (a) strain and (b) stress across a radial plane 12mm below the top surface in a quenched cylinder bar *s34* with 1.5mm diameter drill and 5mm diameter trepanned up to 8.5mm depth.

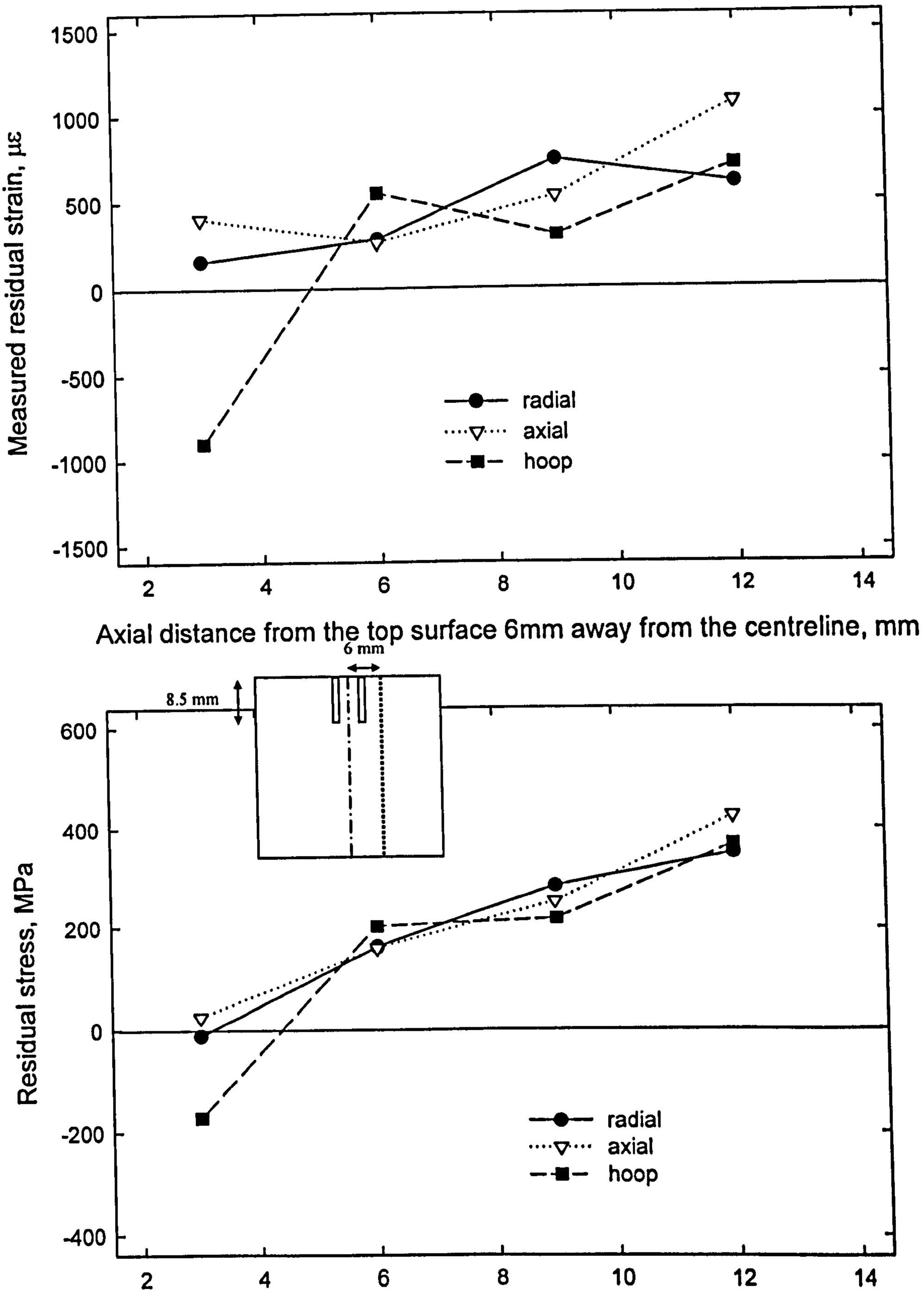

Figure 4.38 Distribution of residual (a) strain and (b) stress along an axial line 6mm away from the centreline in a quenched cylinder bar *s34* with 1.5mm diameter drill and 5mm diameter trepanned up to 8.5mm depth.

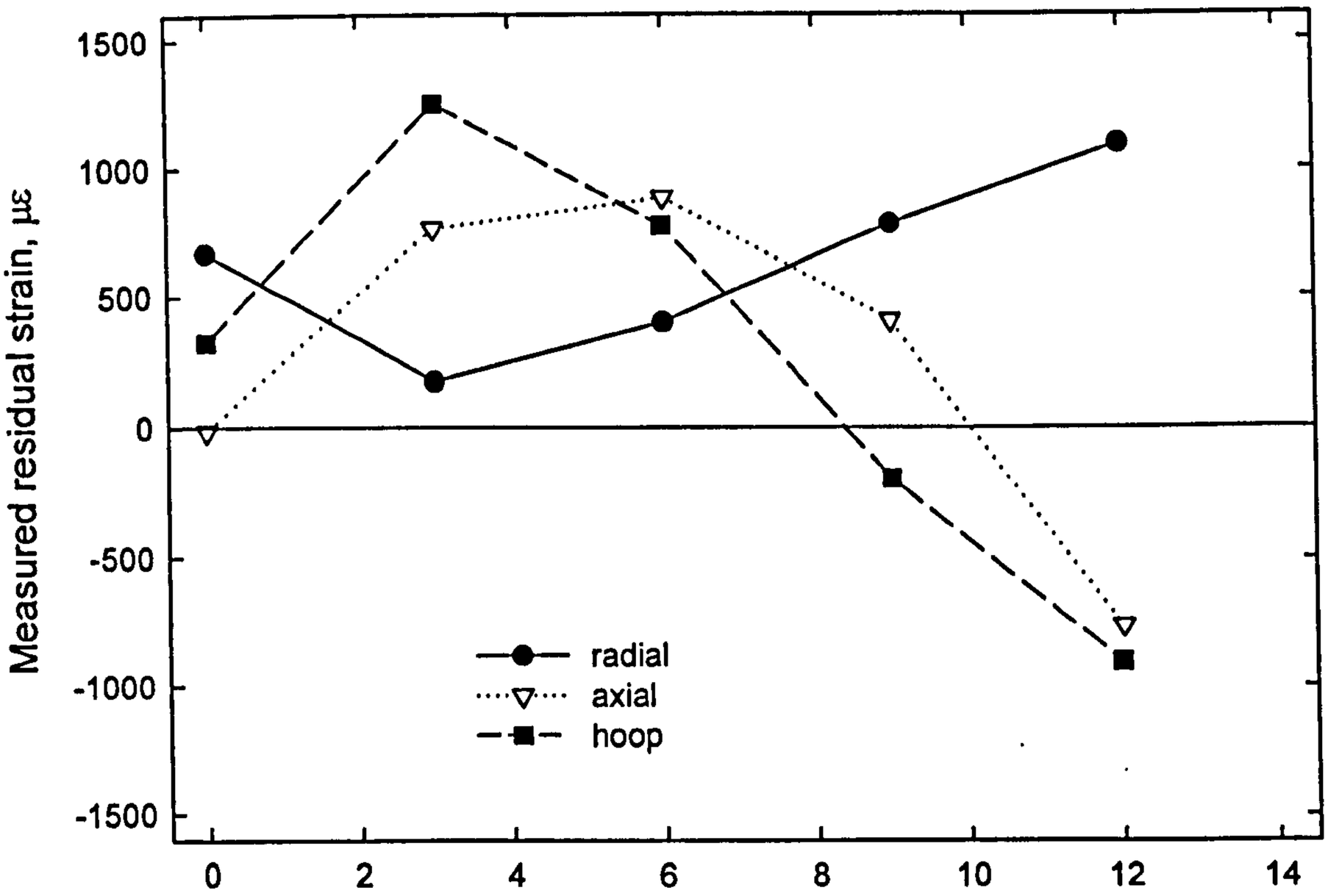

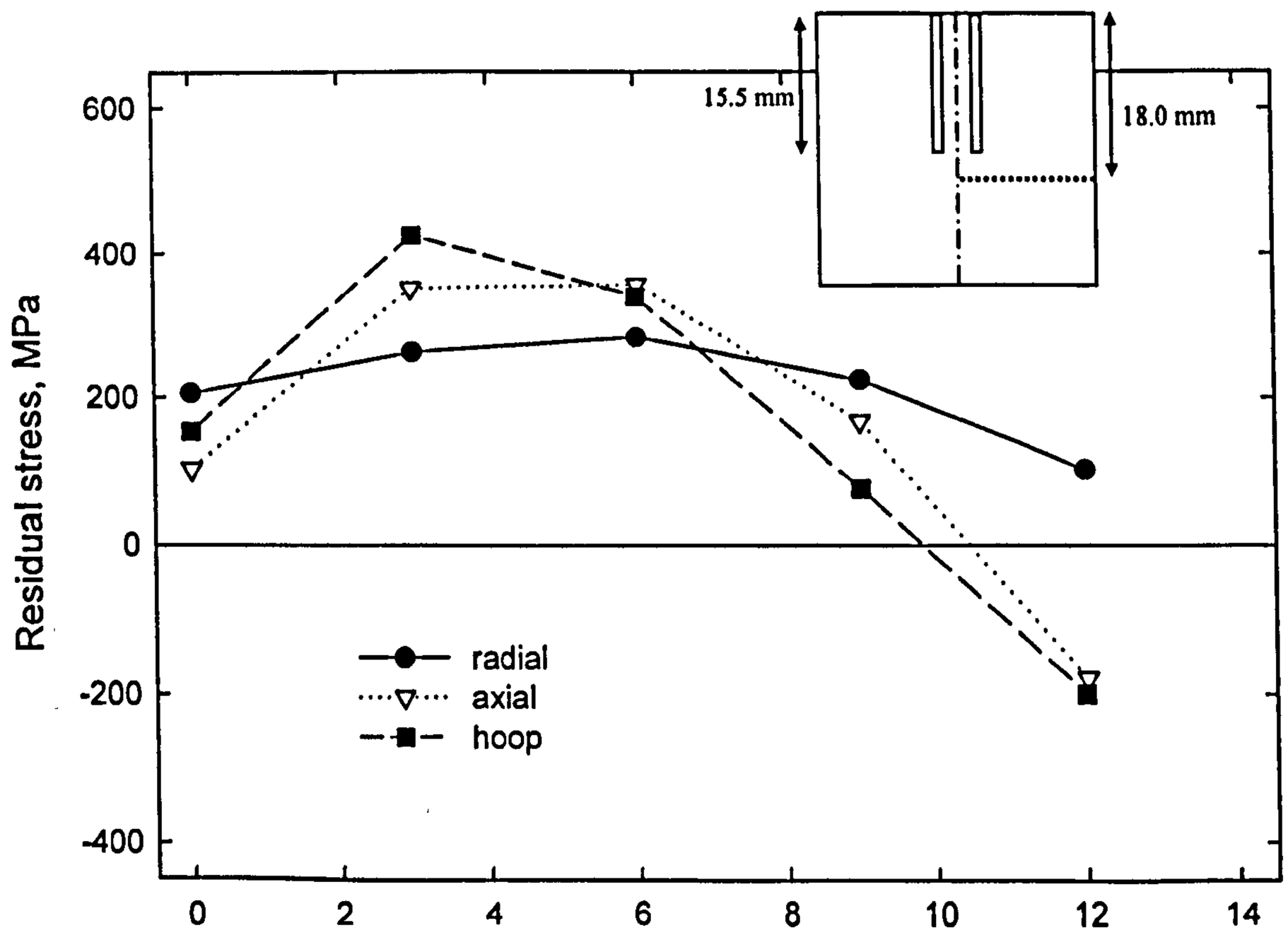

Figure 4.39 Distribution of residual (a) strain and (b) stress across a radial plane 18mm below the top surface in a quenched cylinder bar *s35* with 1.5mm diameter drill and 5mm diameter trepanned up to 15.5mm depth.

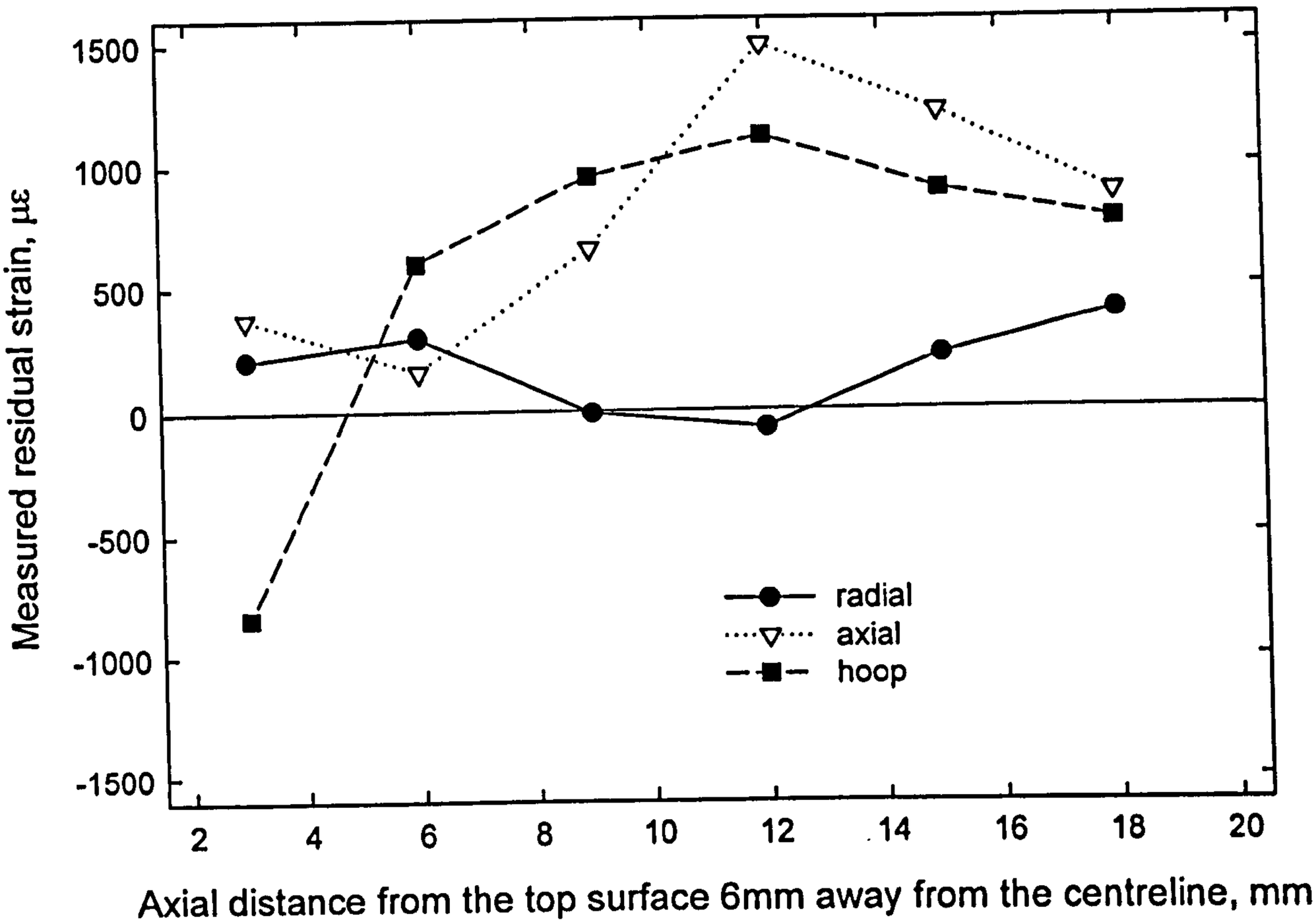

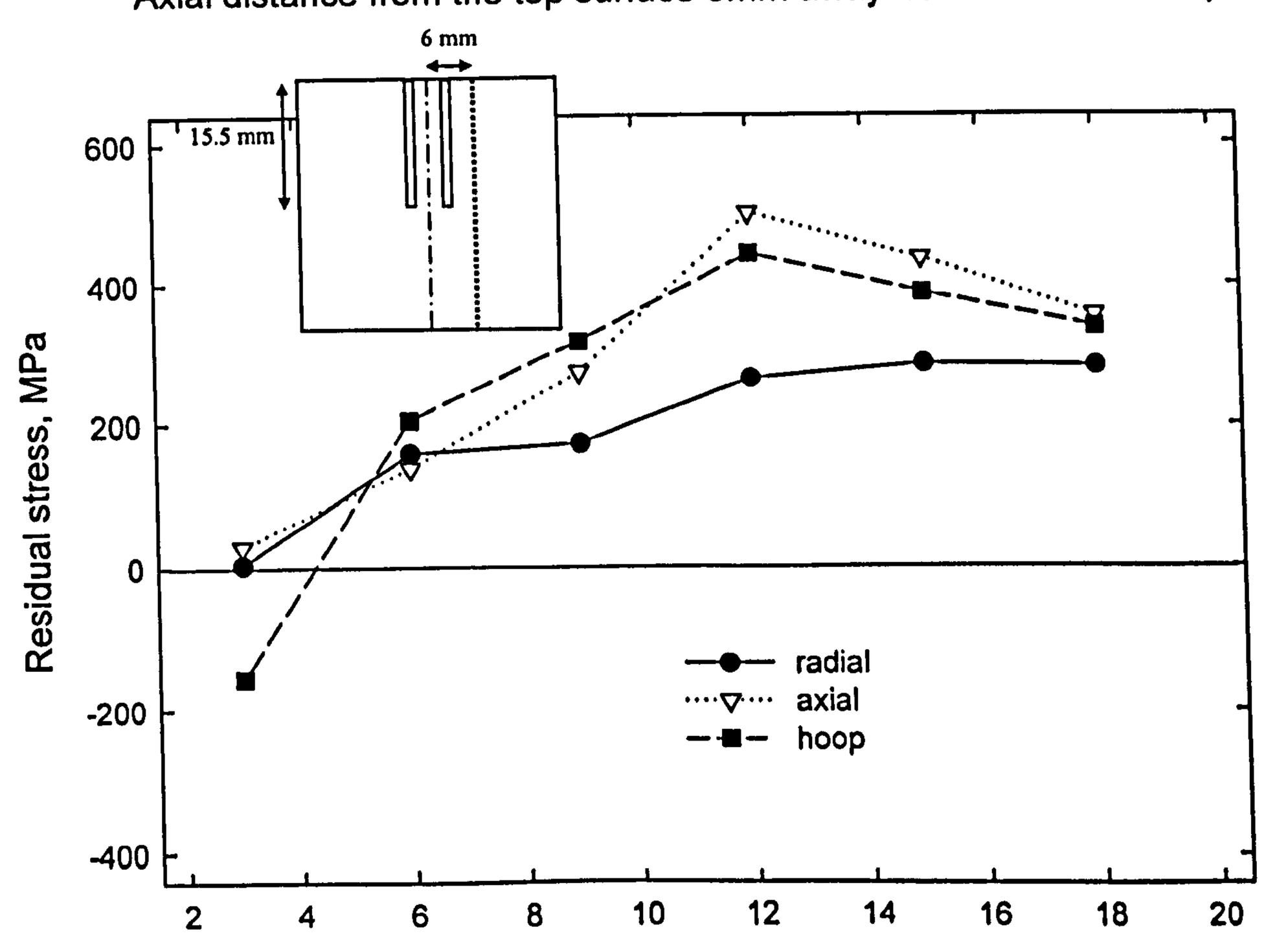

Figure 4.40 Distribution of residual (a) strain and (b) stress along an axial line 6mm away from the centreline in a quenched cylinder bar *s35* with 1.5mm diameter drill and 5mm diameter trepanned up to 15.5mm depth.

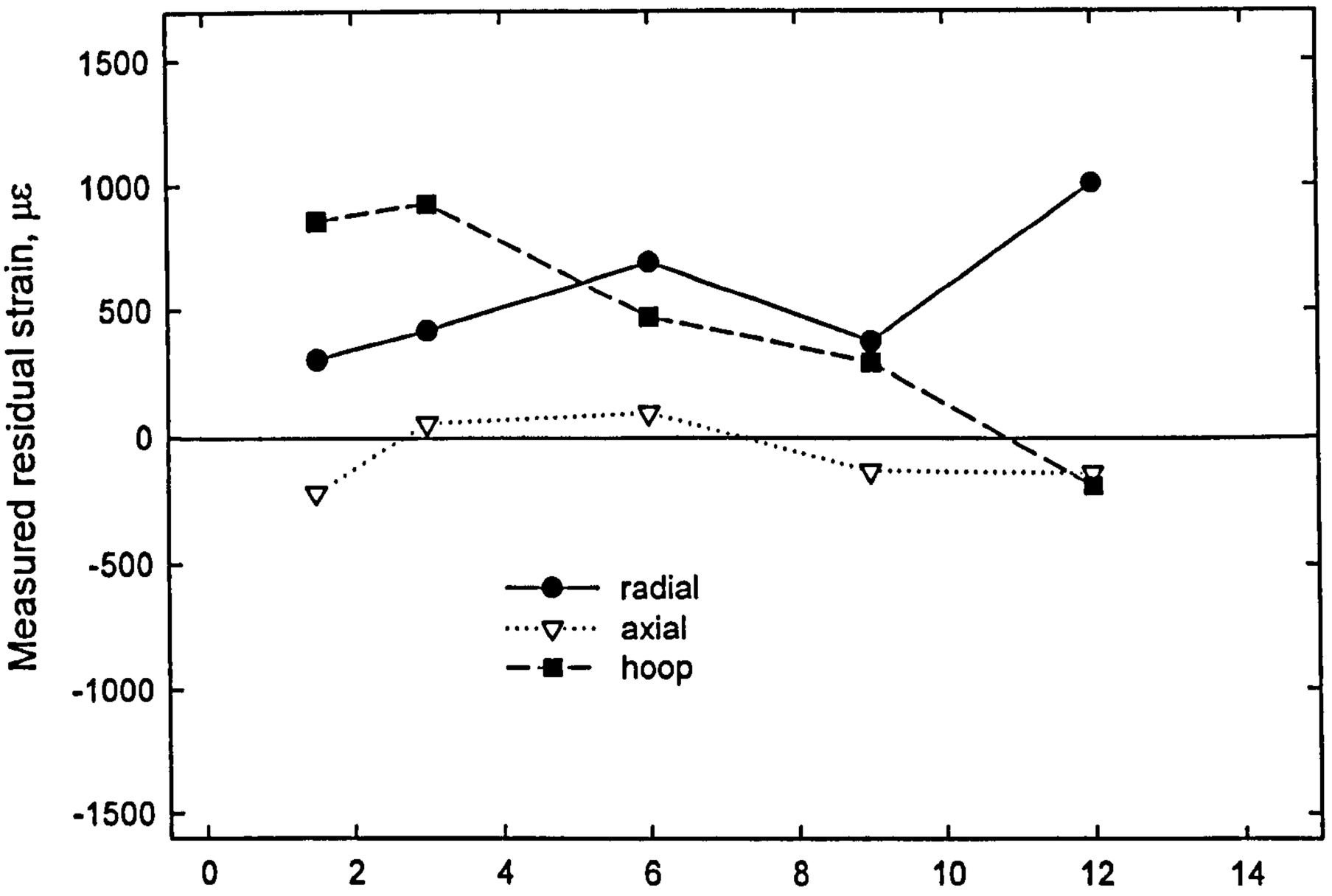

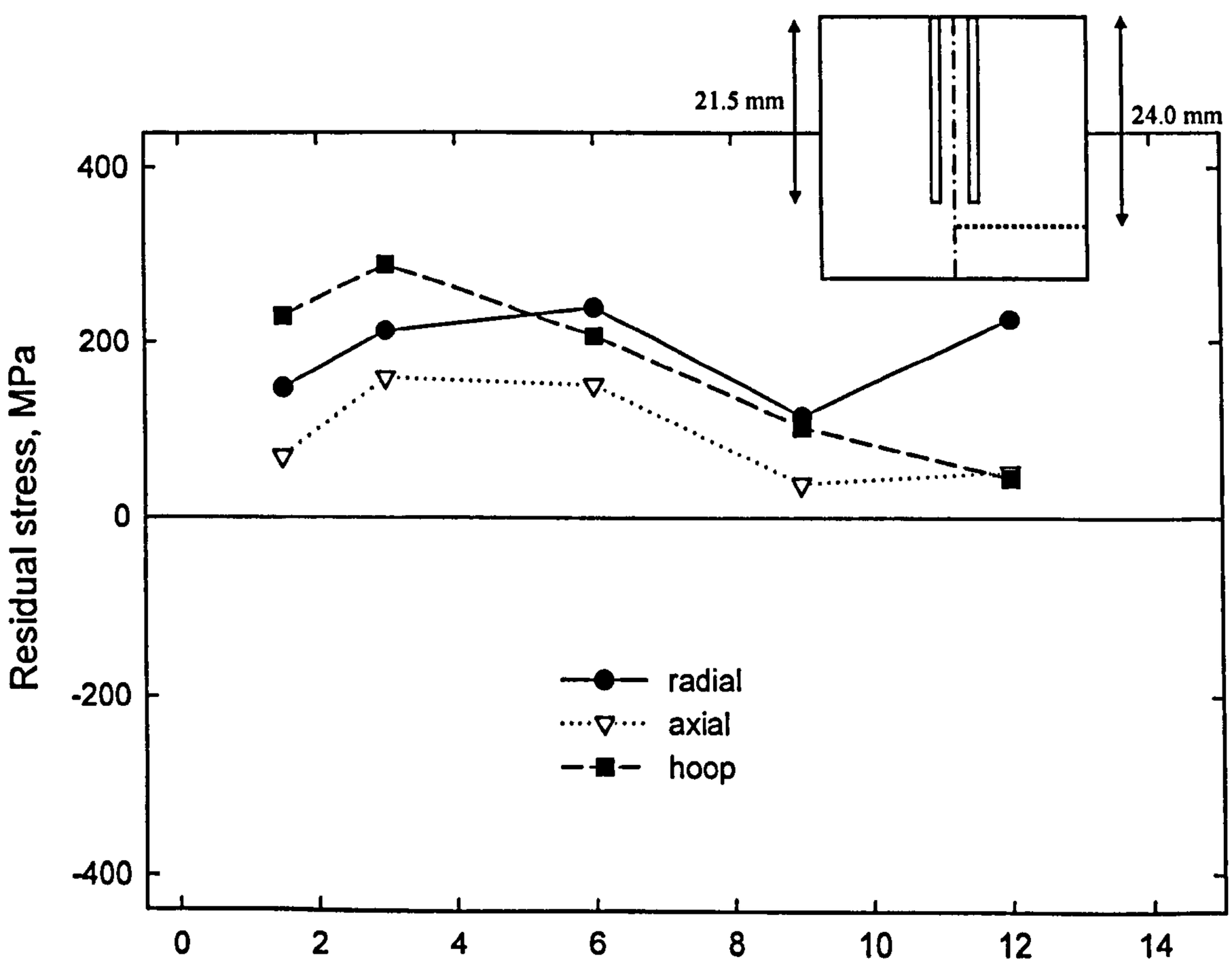

Figure 4.41 Distribution of residual (a) strain and (b) stress across a radial plane 24mm below the top surface in a quenched cylinder bar *s36* with 1.5mm diameter drill and 5mm diameter trepanned up to 21.5mm depth.

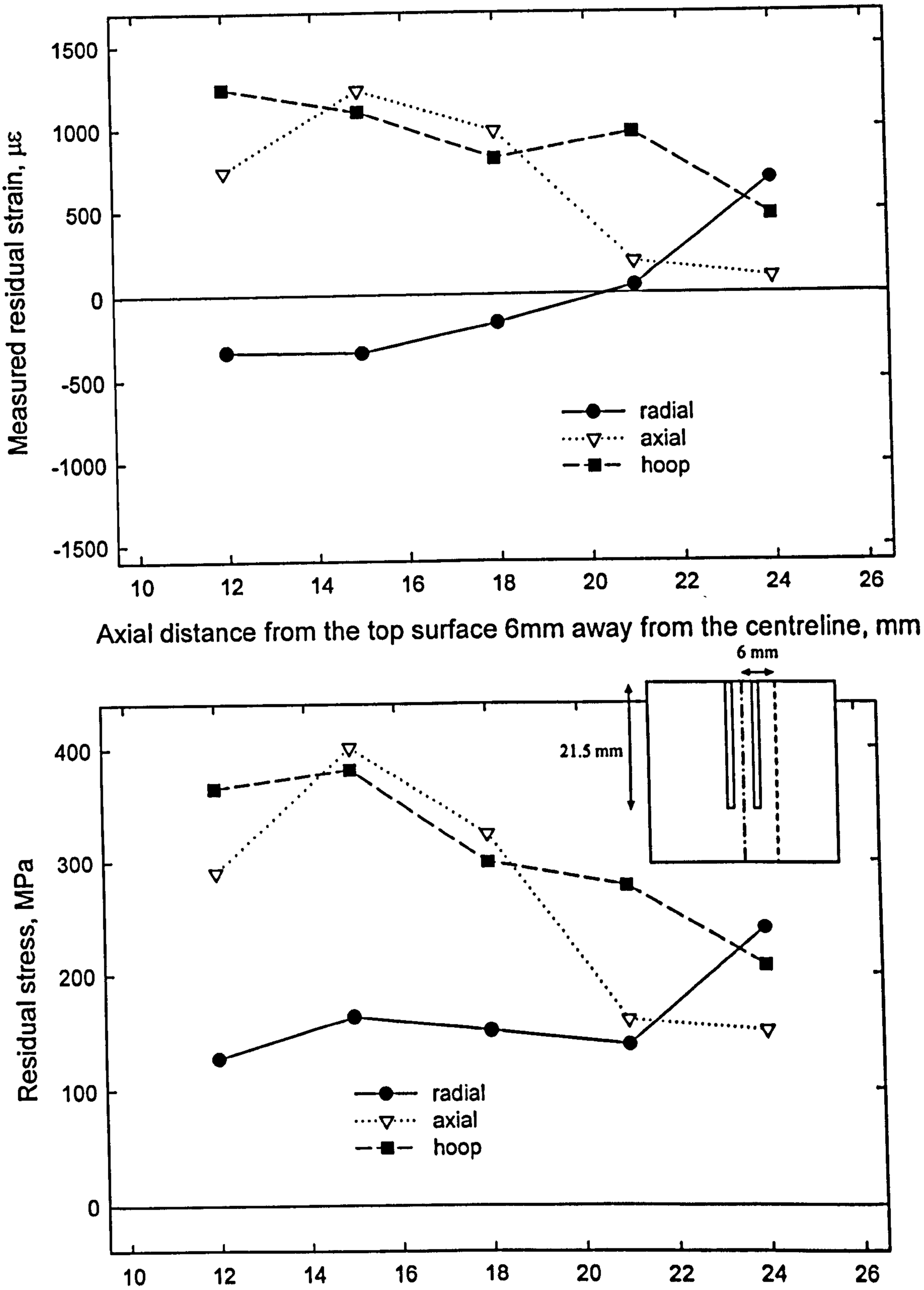

Figure 4.42 Distribution of residual (a) strain and (b) stress along an axial line 6mm away from the centreline in a quenched cylinder bar *s36* with 1.5mm diameter drill and 5mm diameter trepanned up to 21.5mm depth.

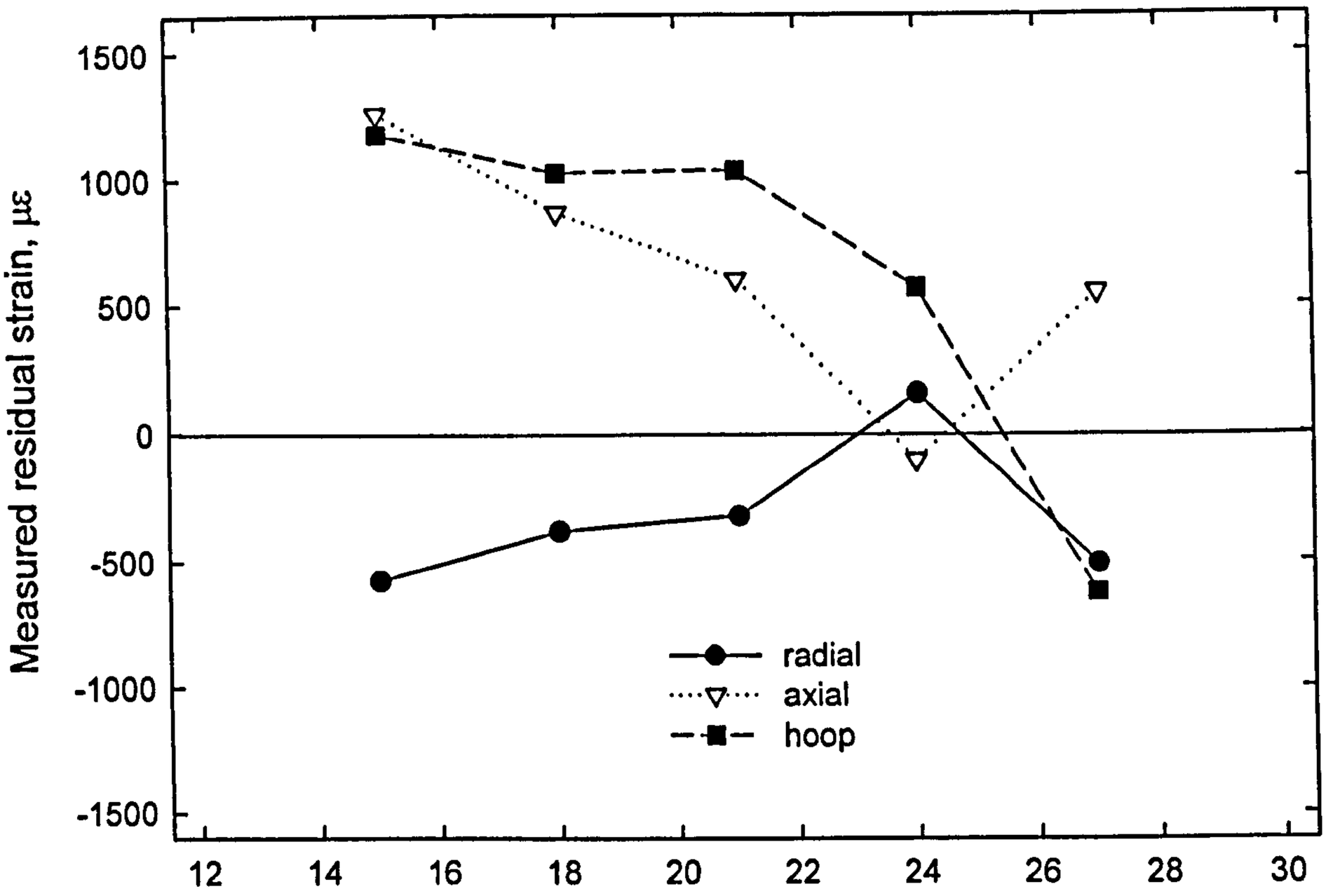

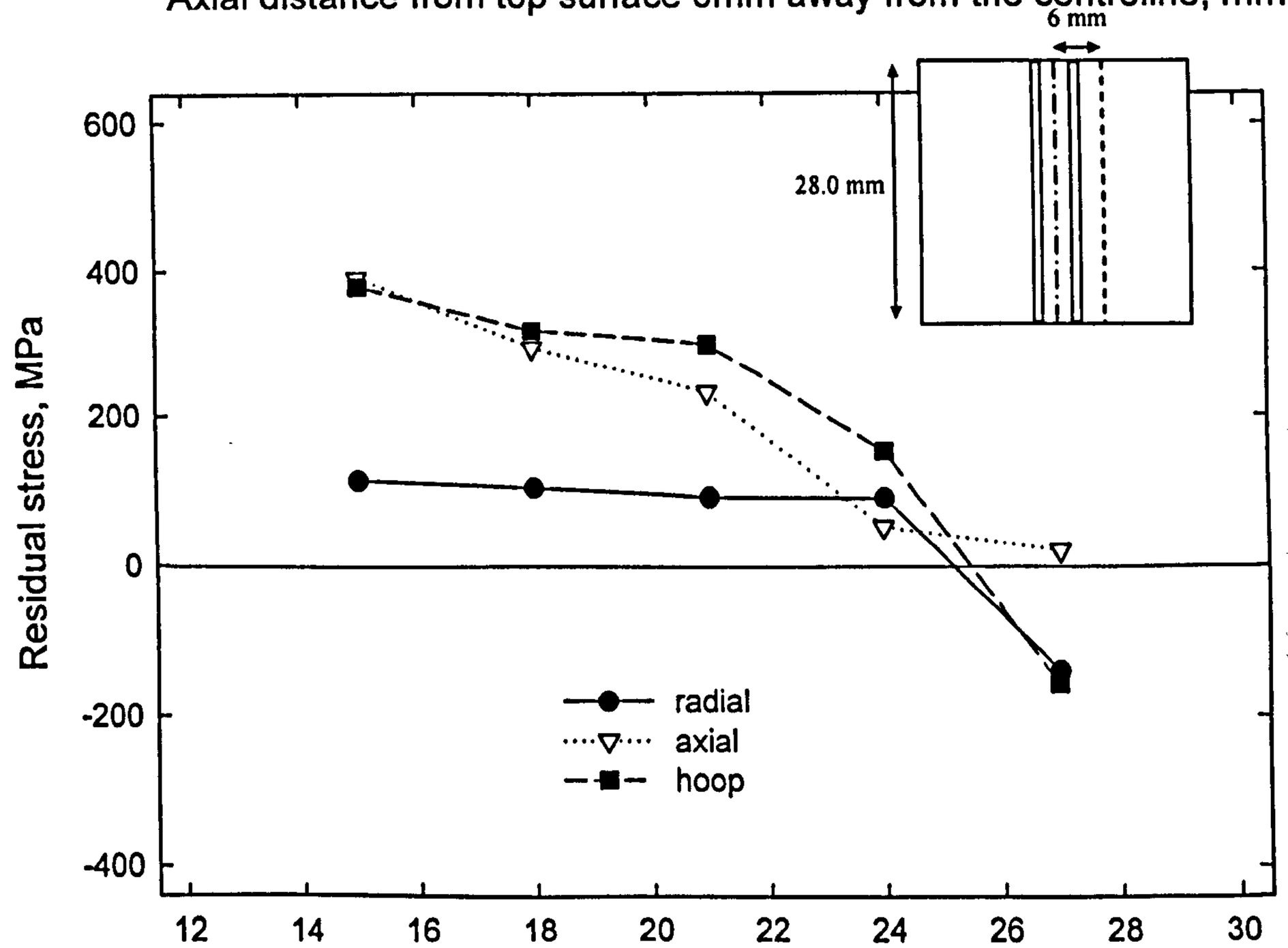

Figure 4.43 Distribution of residual (a) strain and (b) stress along an axial line 6mm away from the centreline in a quenched cylinder bar *s37* with 1.5mm diameter drill and 5mm diameter trepanned up to 28mm depth.

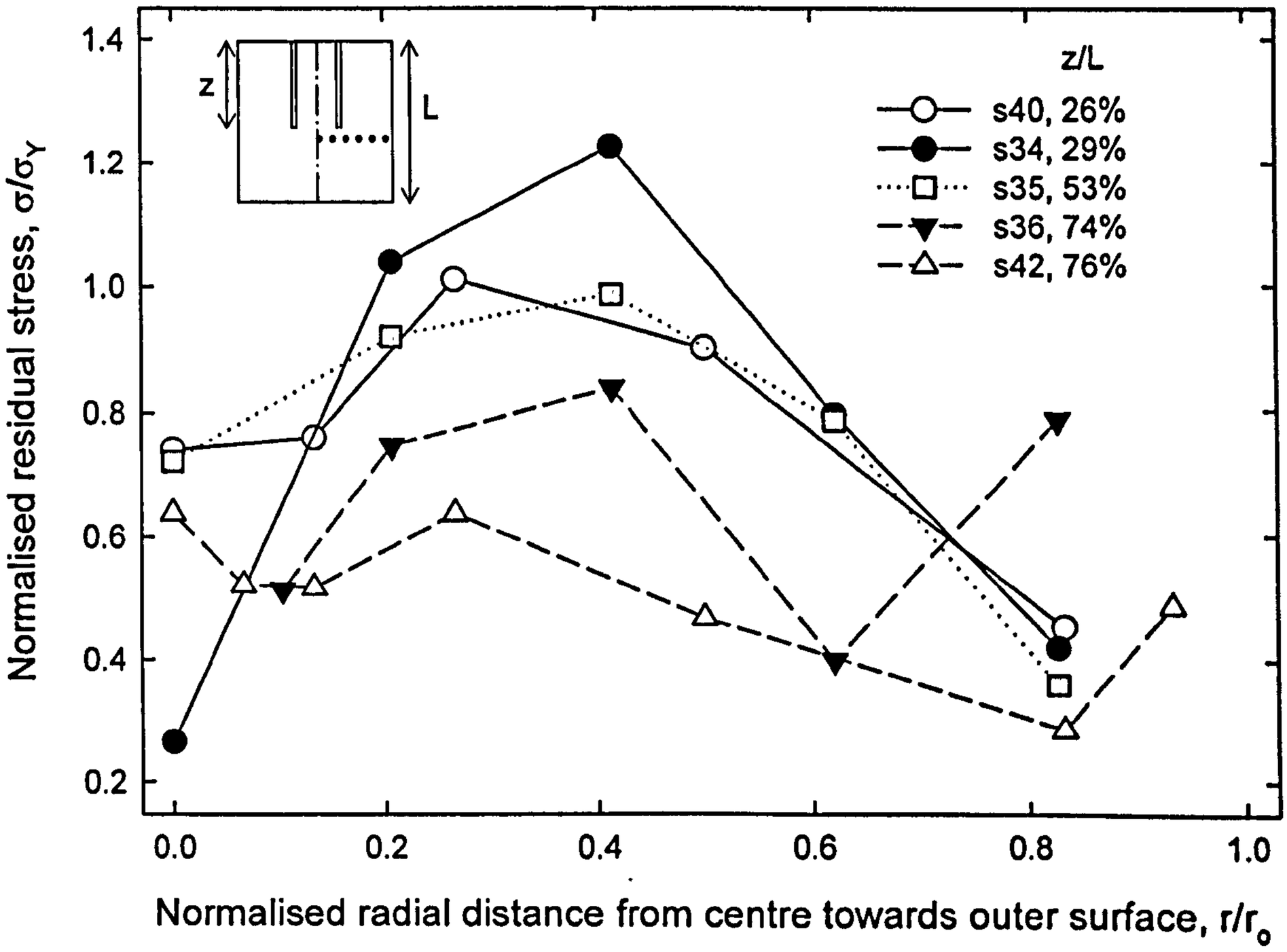

(a) Radial component

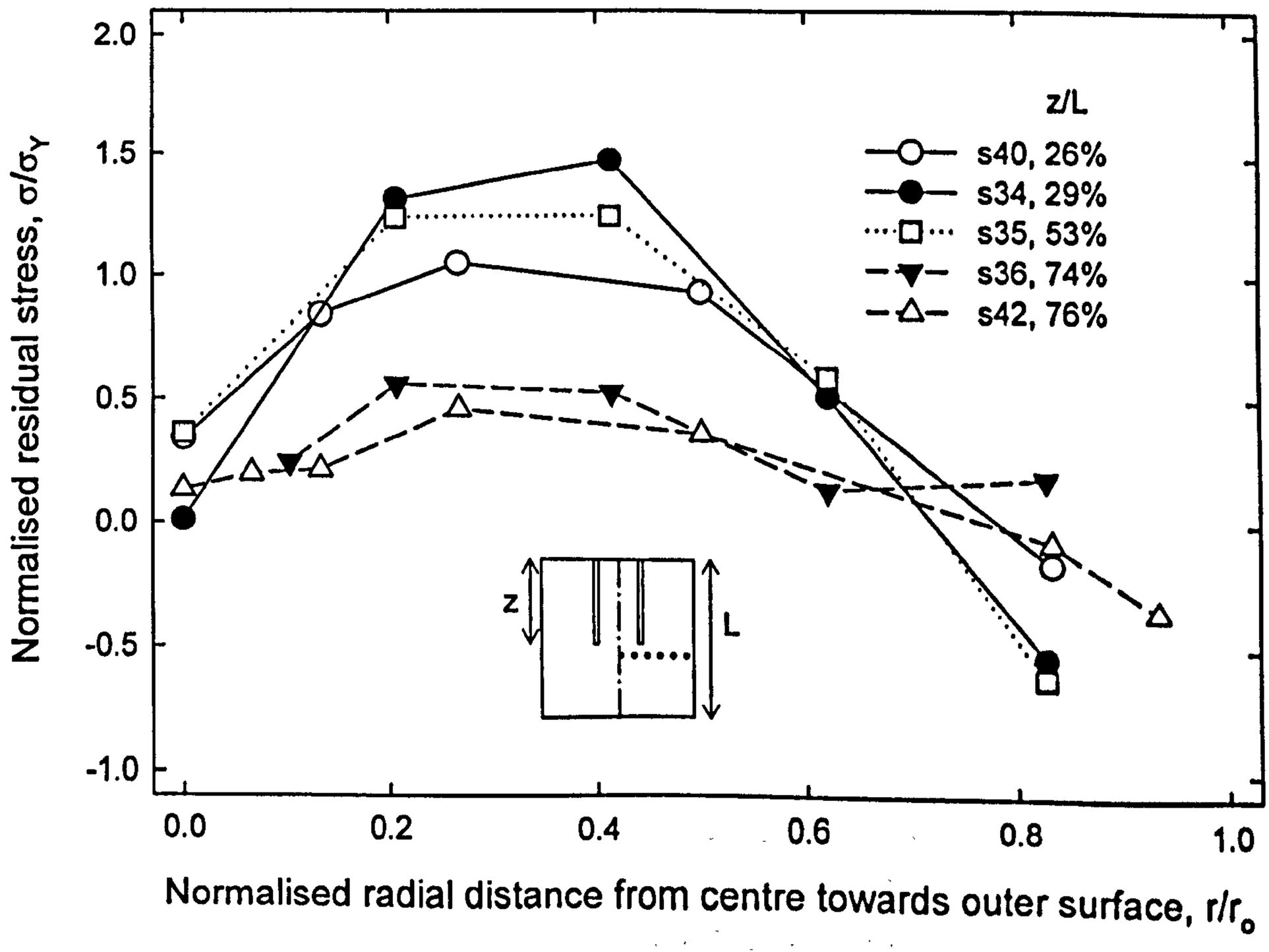

(b) Axial component

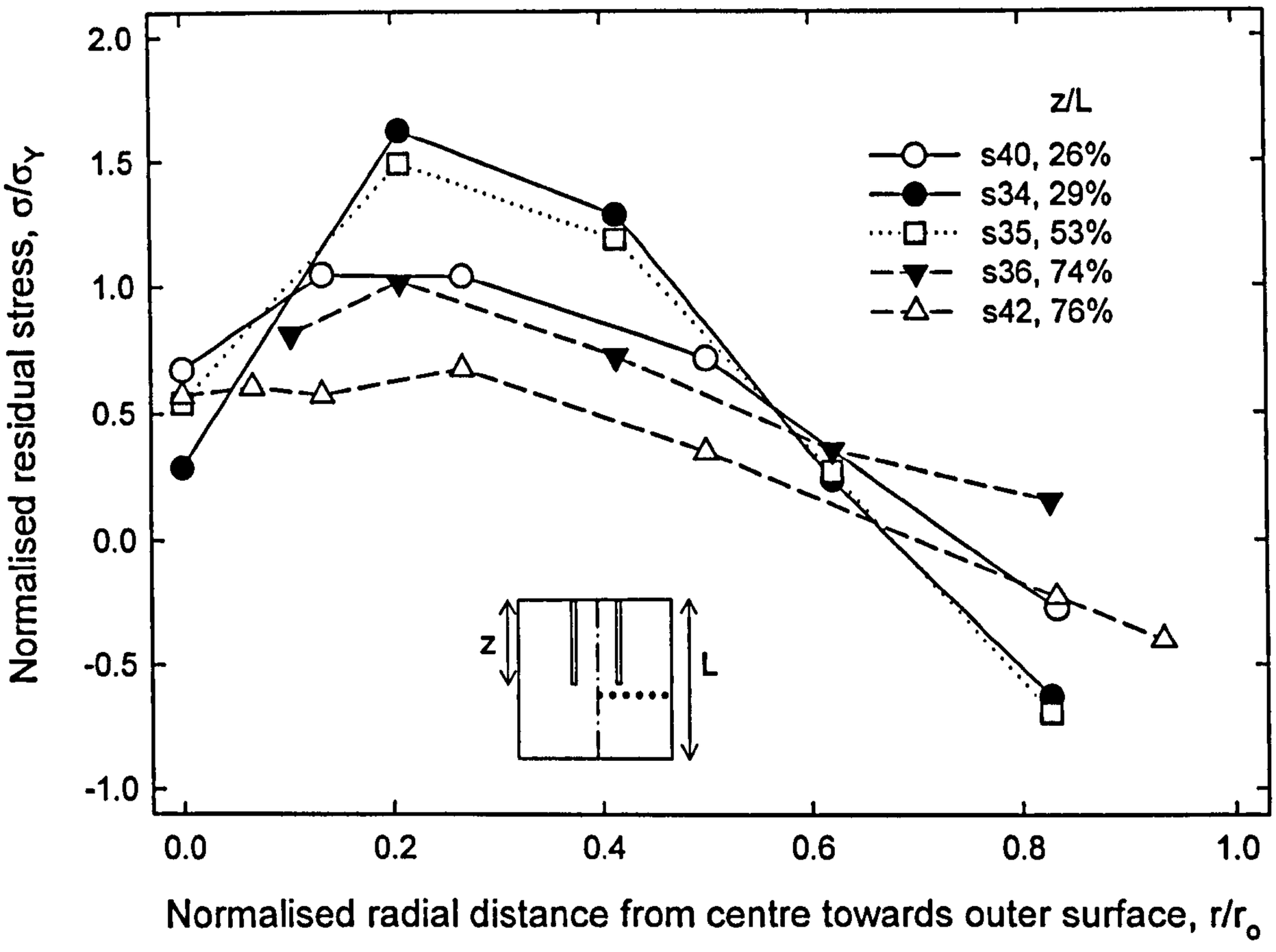

(c) Hoop component

Figure 4.44 Effect of edm depth on the measured residual stress distribution across a radial plane ahead of the edm front.

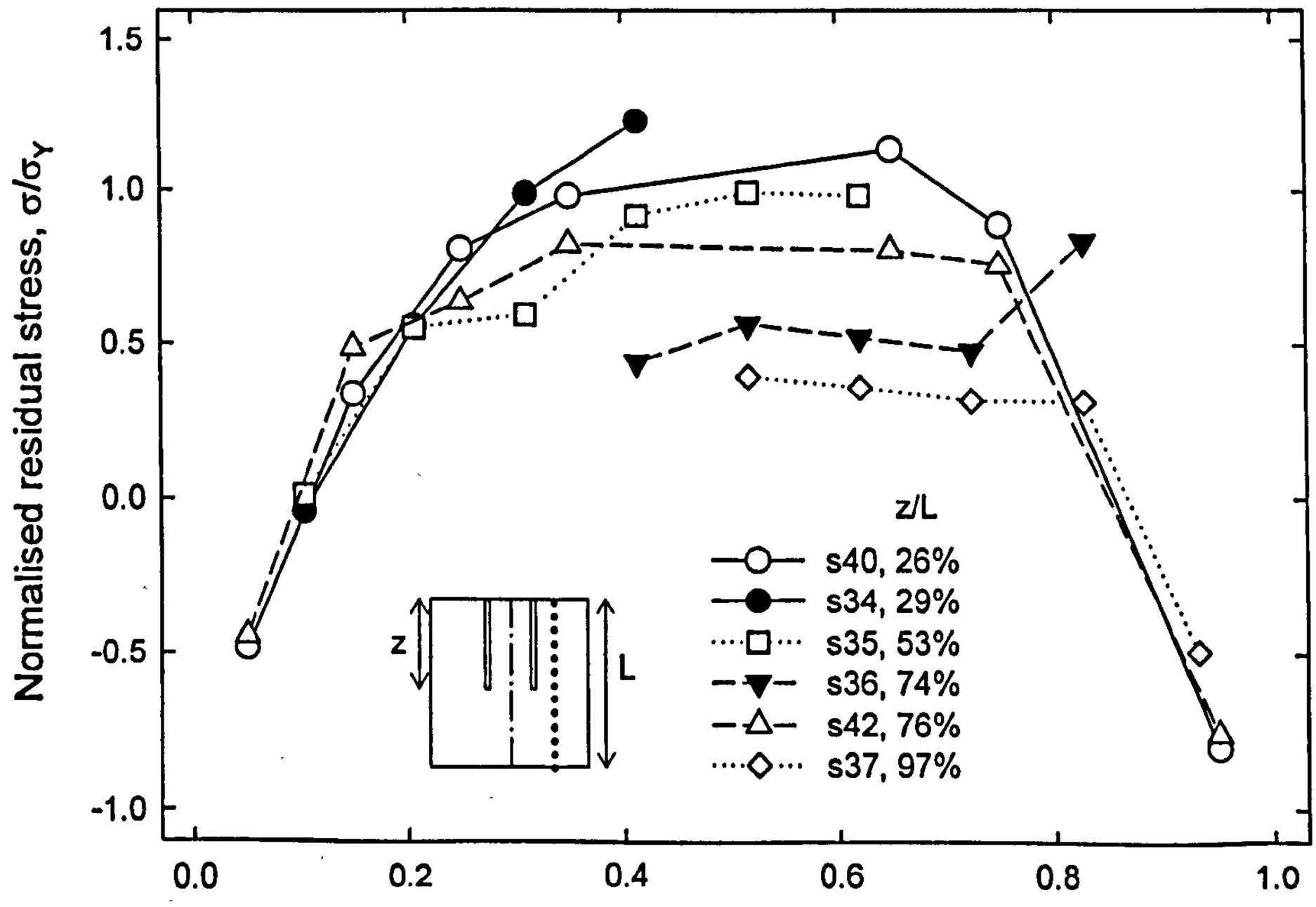

(a) Radial component

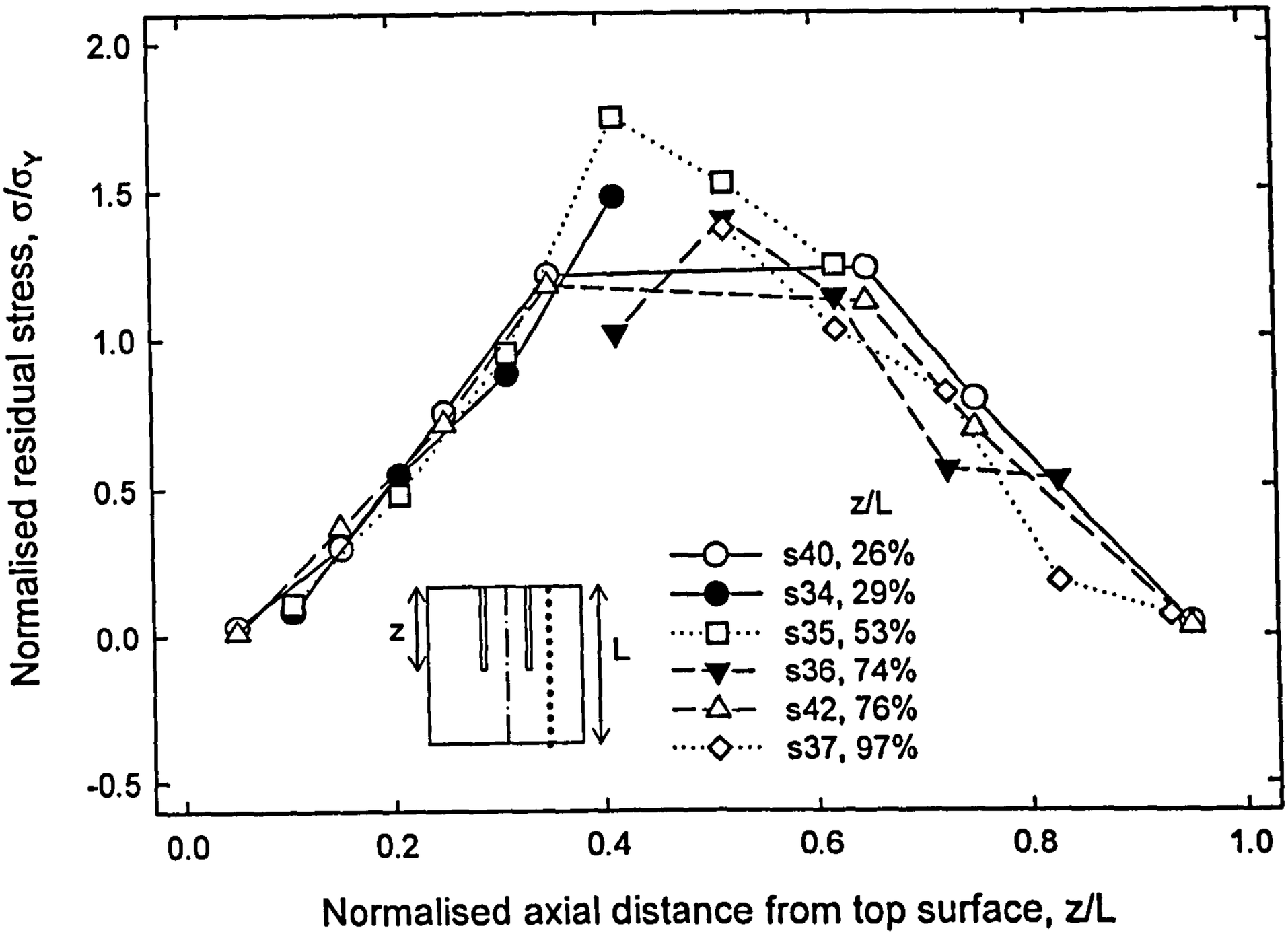

(b) Axial component

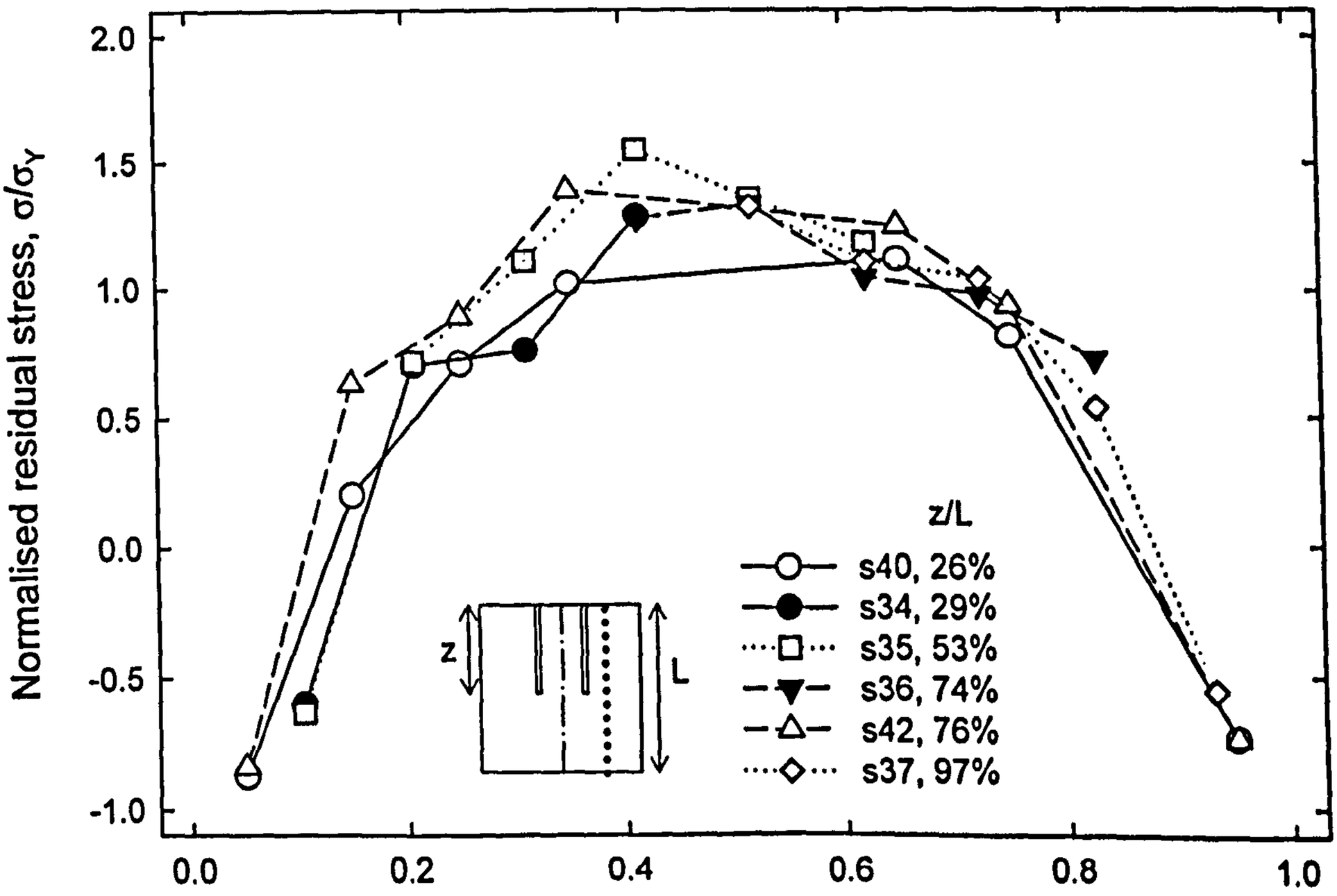

(c) Hoop component

Figure 4.45 Effect of edm depth on the measured residual stress distribution along an axial line 6-8mm away from the centreline.

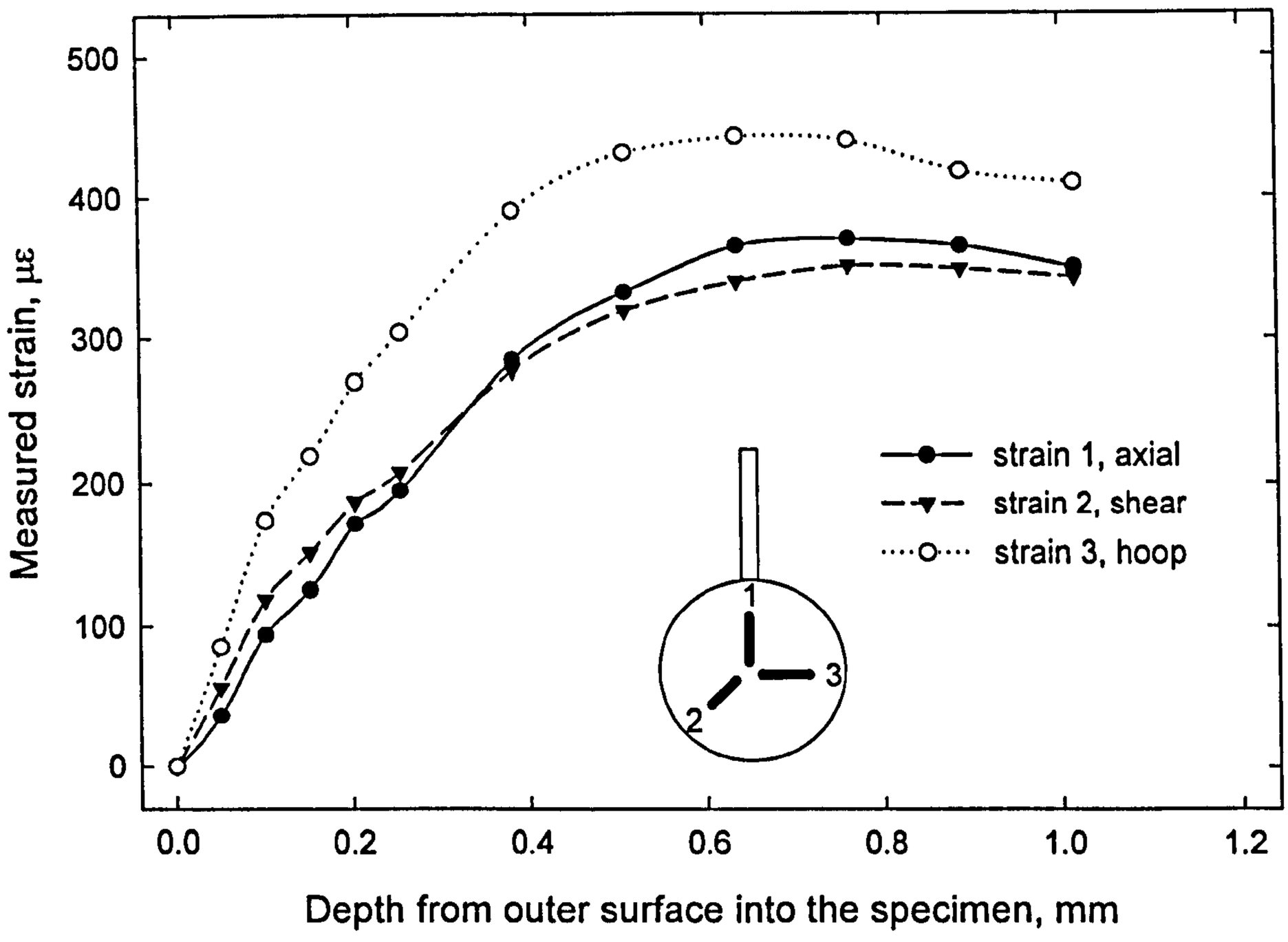

Figure 5.1 Incremental centre hole measured residual strains of a 30mm diameter sphere *s8*.

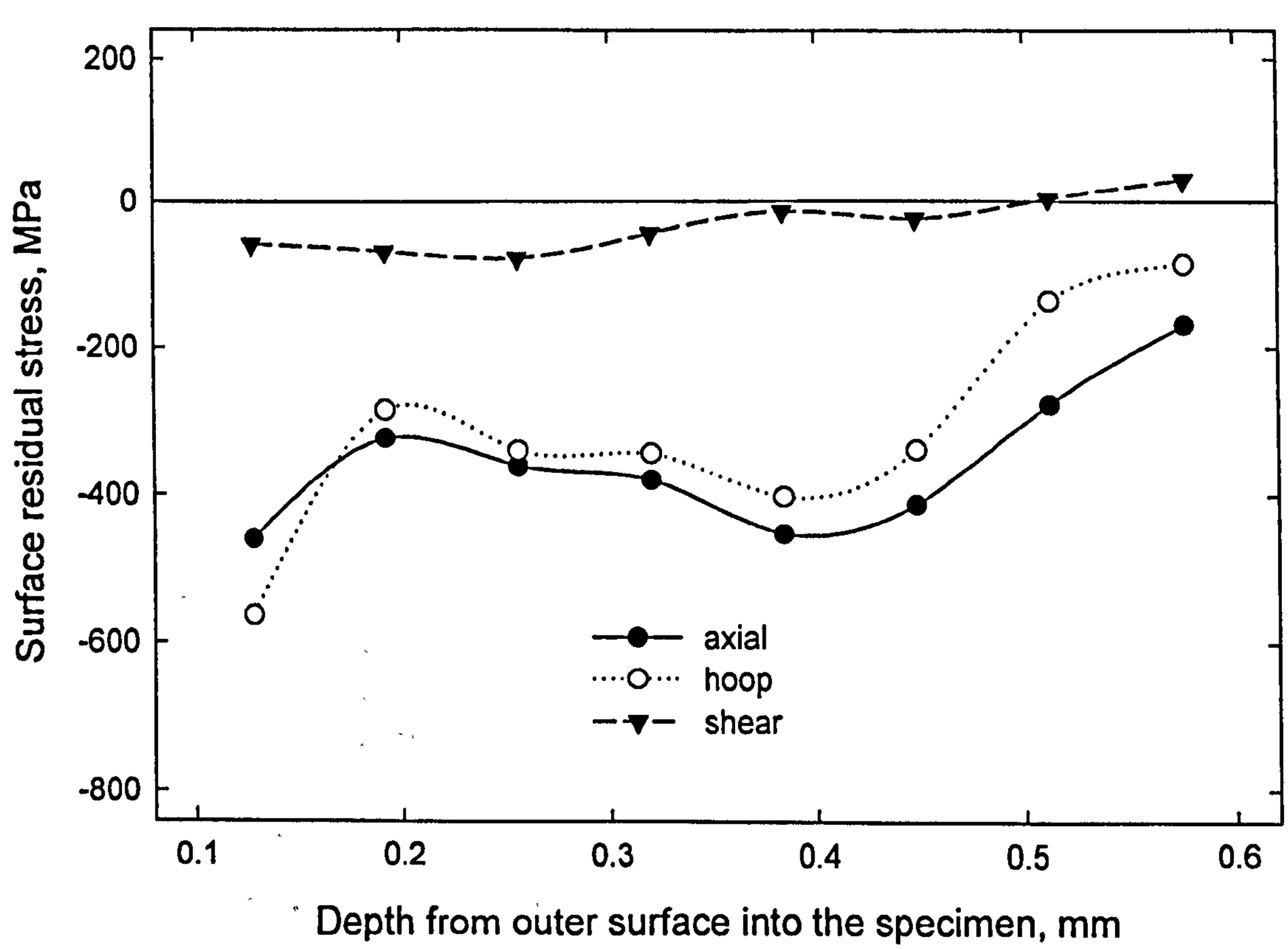

Figure 5.2 Centre hole surface residual stress result for a 30mm diameter sphere *s8*.

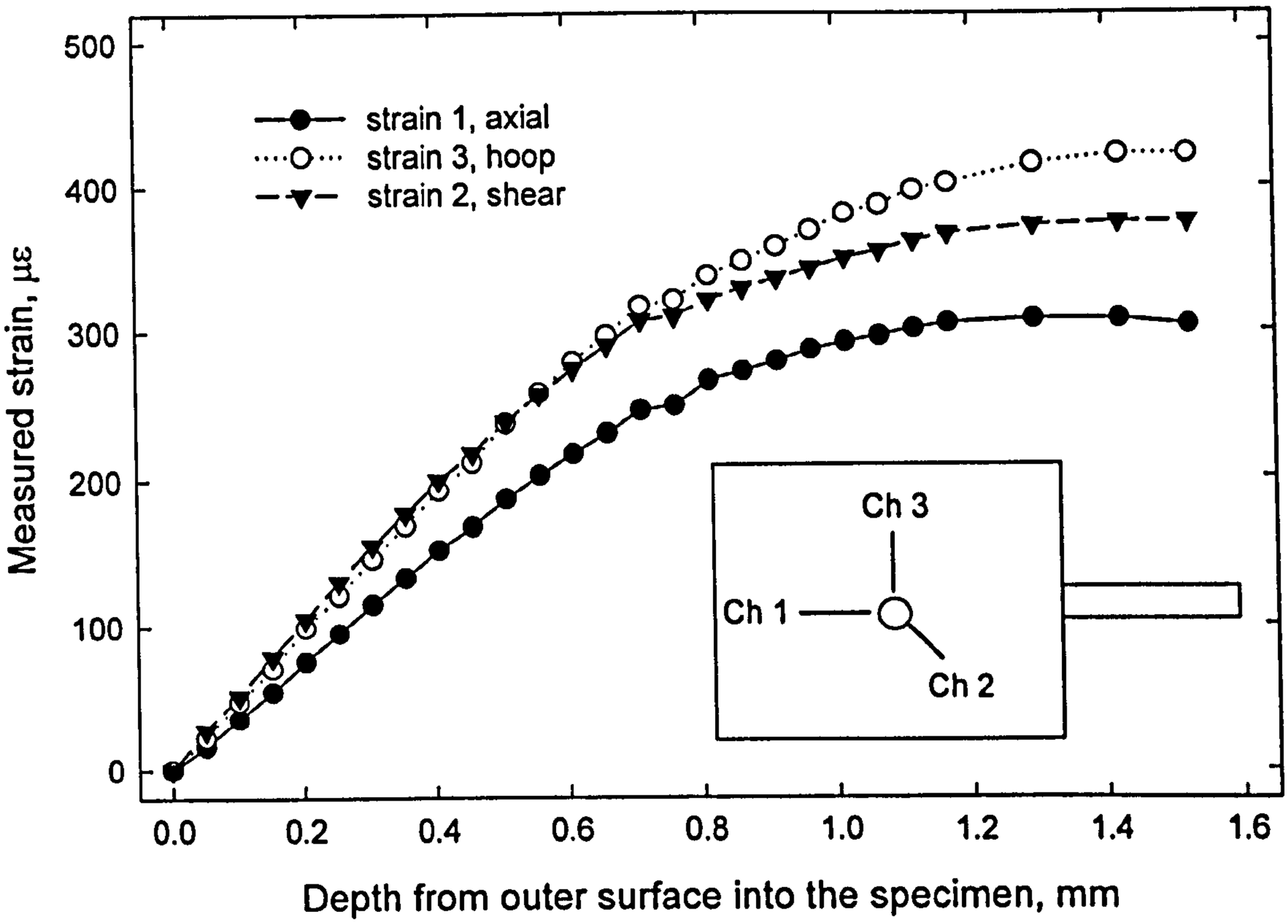

Figure 5.3 Incremental centre hole measured residual strains of a quenched cylinder, diameter 60mm, length 60mm *s12*.

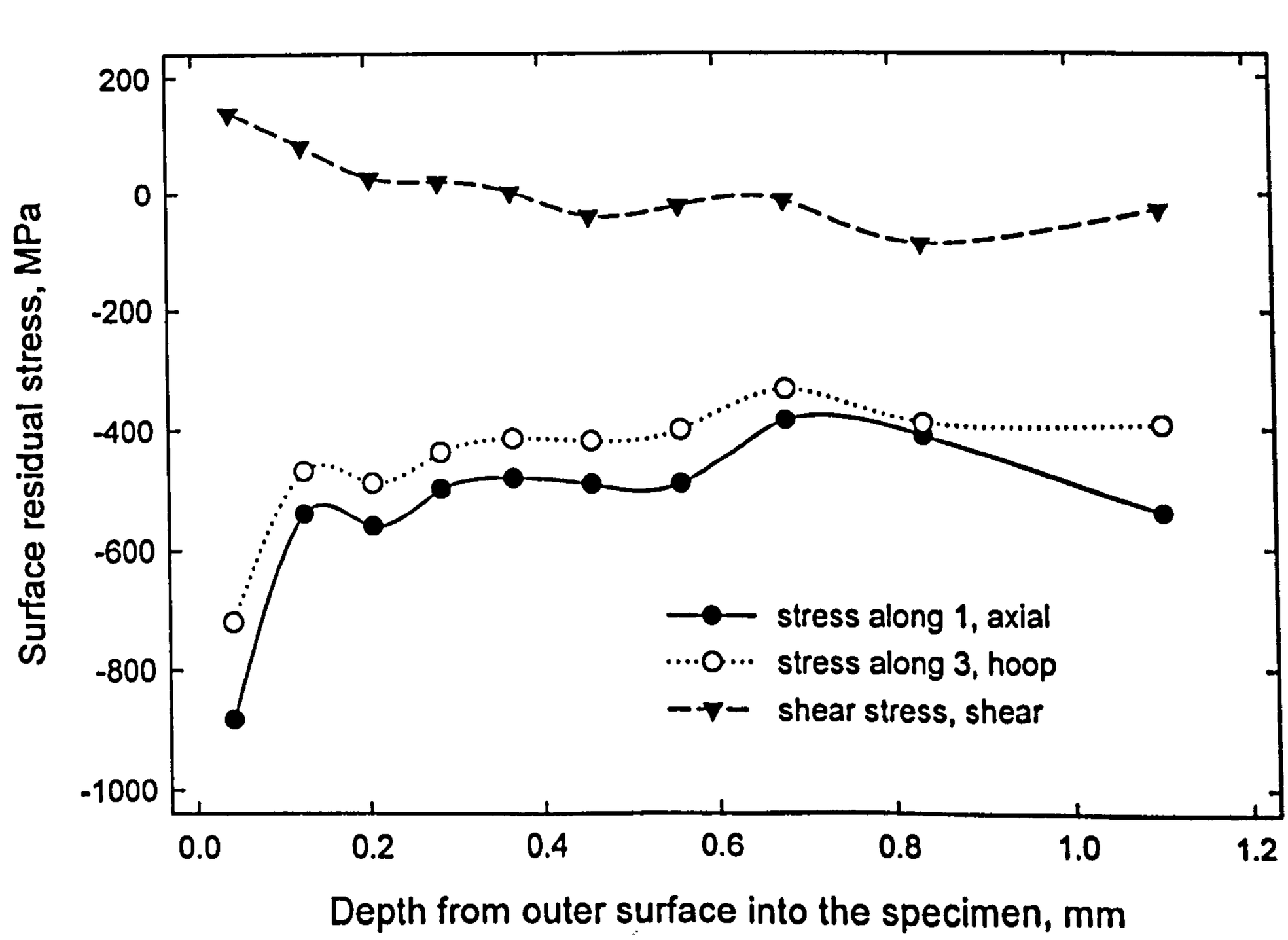

Figure 5.4 Surface residual stress result for a 60mm diameter cylinder *s12*.

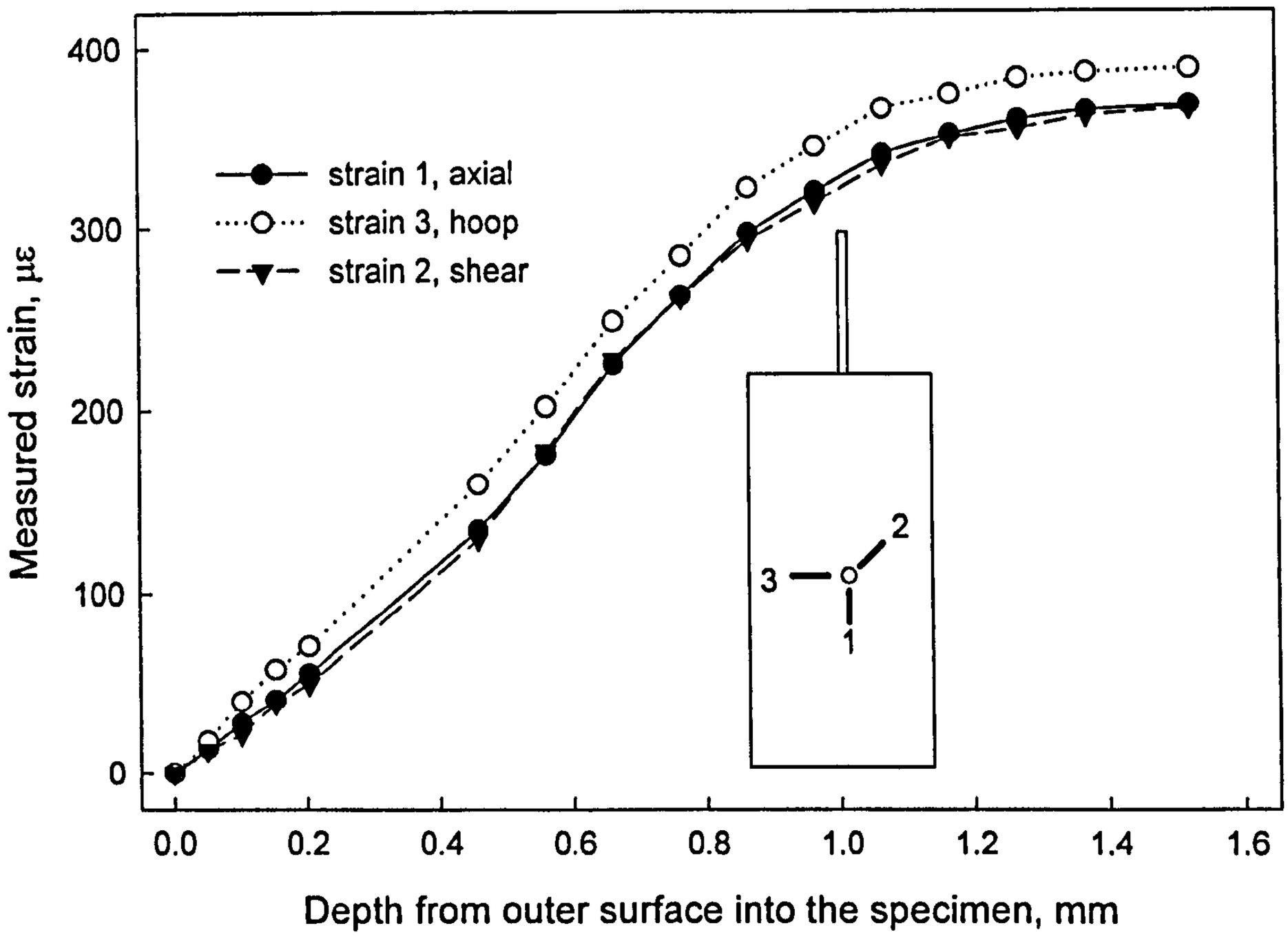

Figure 5.5 Incremental centre hole measured residual strains of a quenched cylinder, diameter 30mm, length 100mm *s1*.

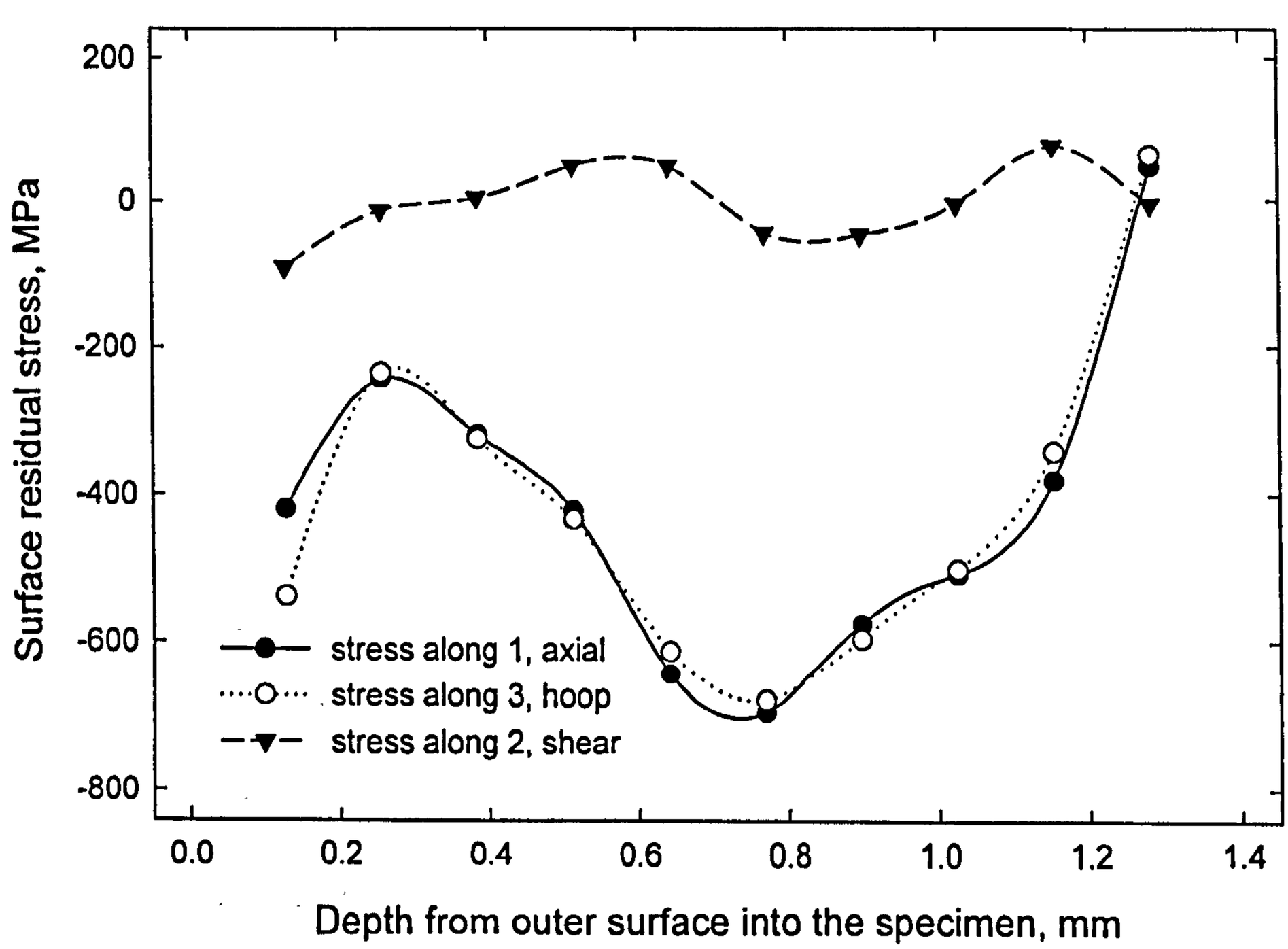

Figure 5.6 Surface residual stress result for a quenched cylinder, diameter 30mm, length 100mm (sample *s1*).

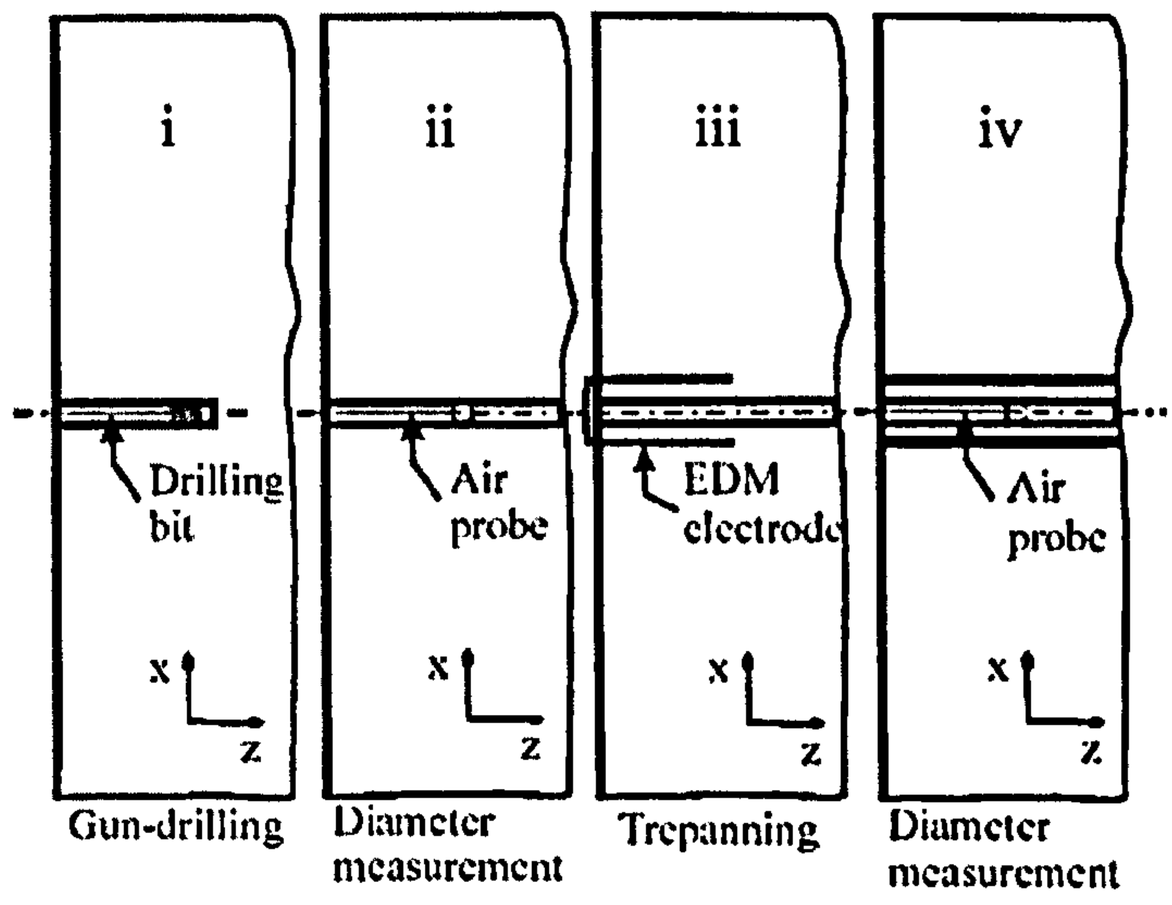

Figure 5.7 Schematic illustration of the deep hole drilling (DHD) method.

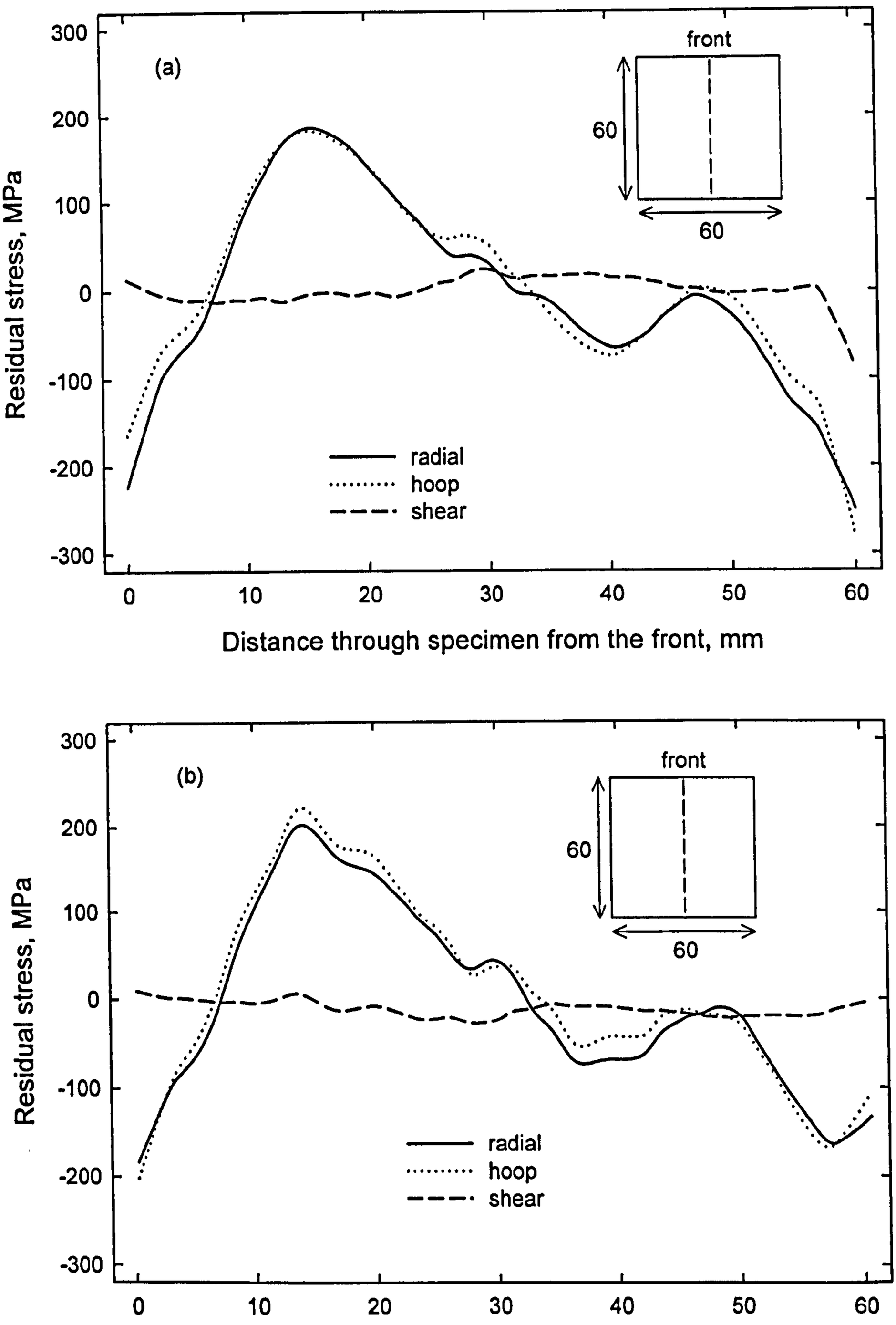

Figure 5.8 Residual stress distributions measured from the font through the quenched cylinders fabricated from stainless steel of type (a) 321 (*s12*) and (b) 316L (*s2*).

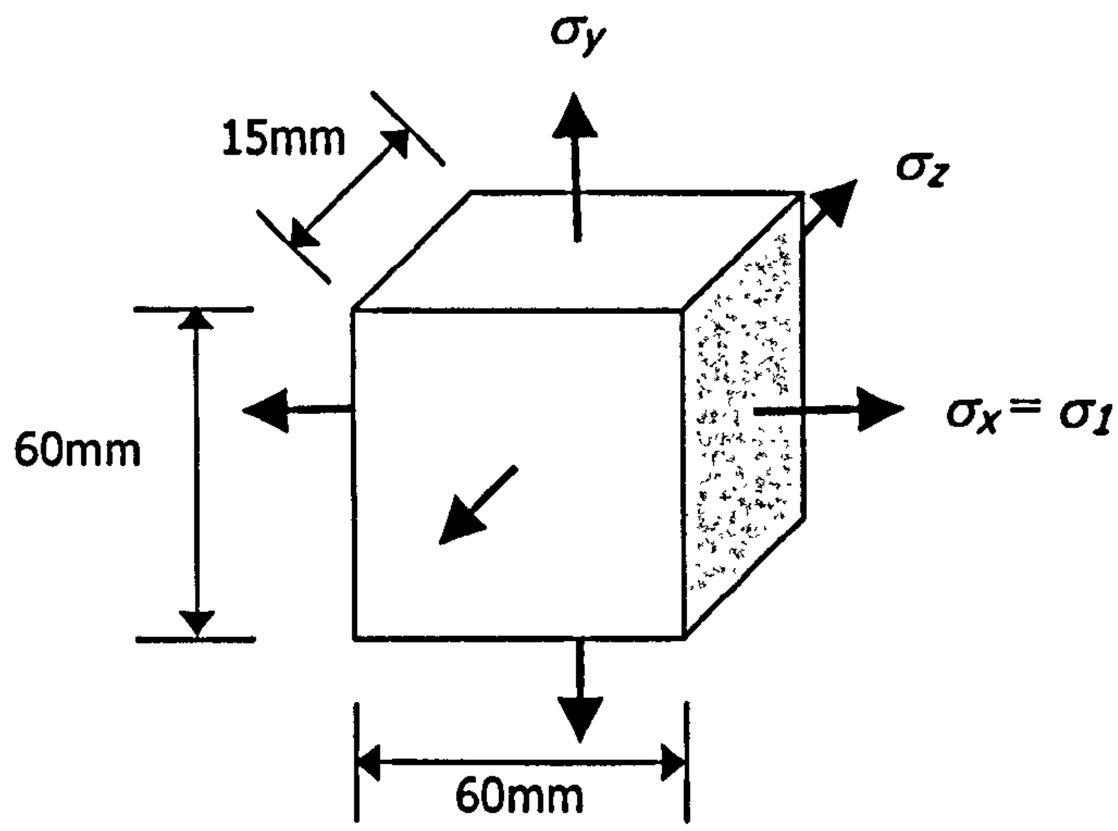

Figure 6.1 Three dimensional, prismatic block of material in the deep hole technique zone of validity study.

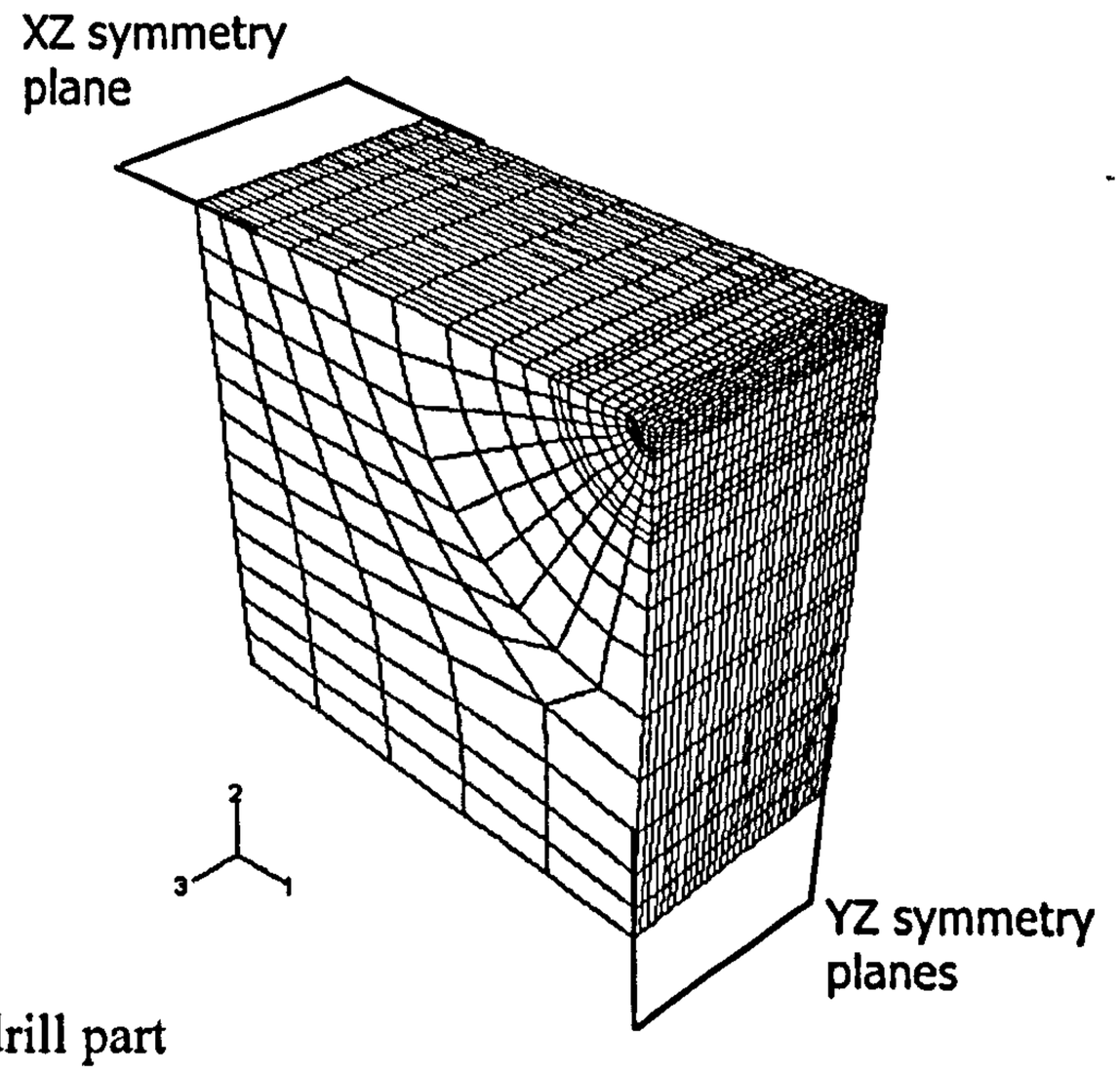

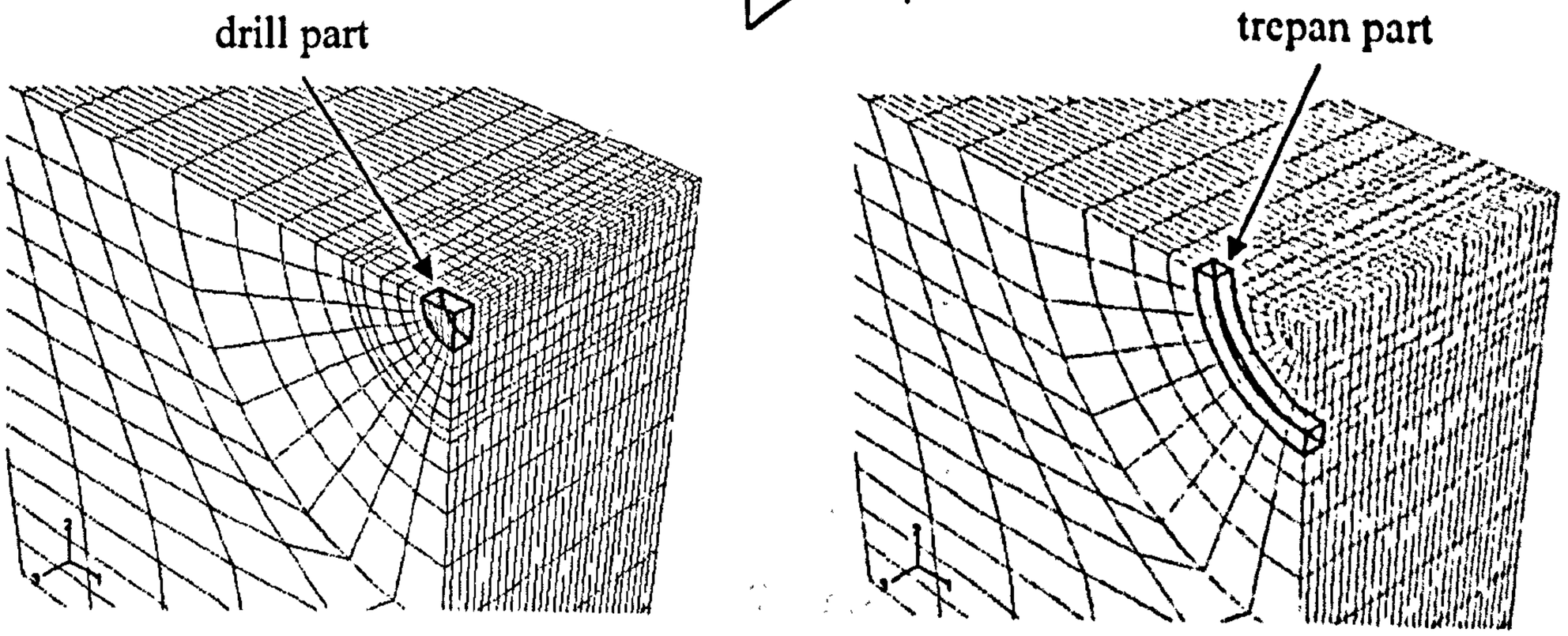

Figure 6.2 Finite element model of the 3D block used in the deep hole validity zone study.

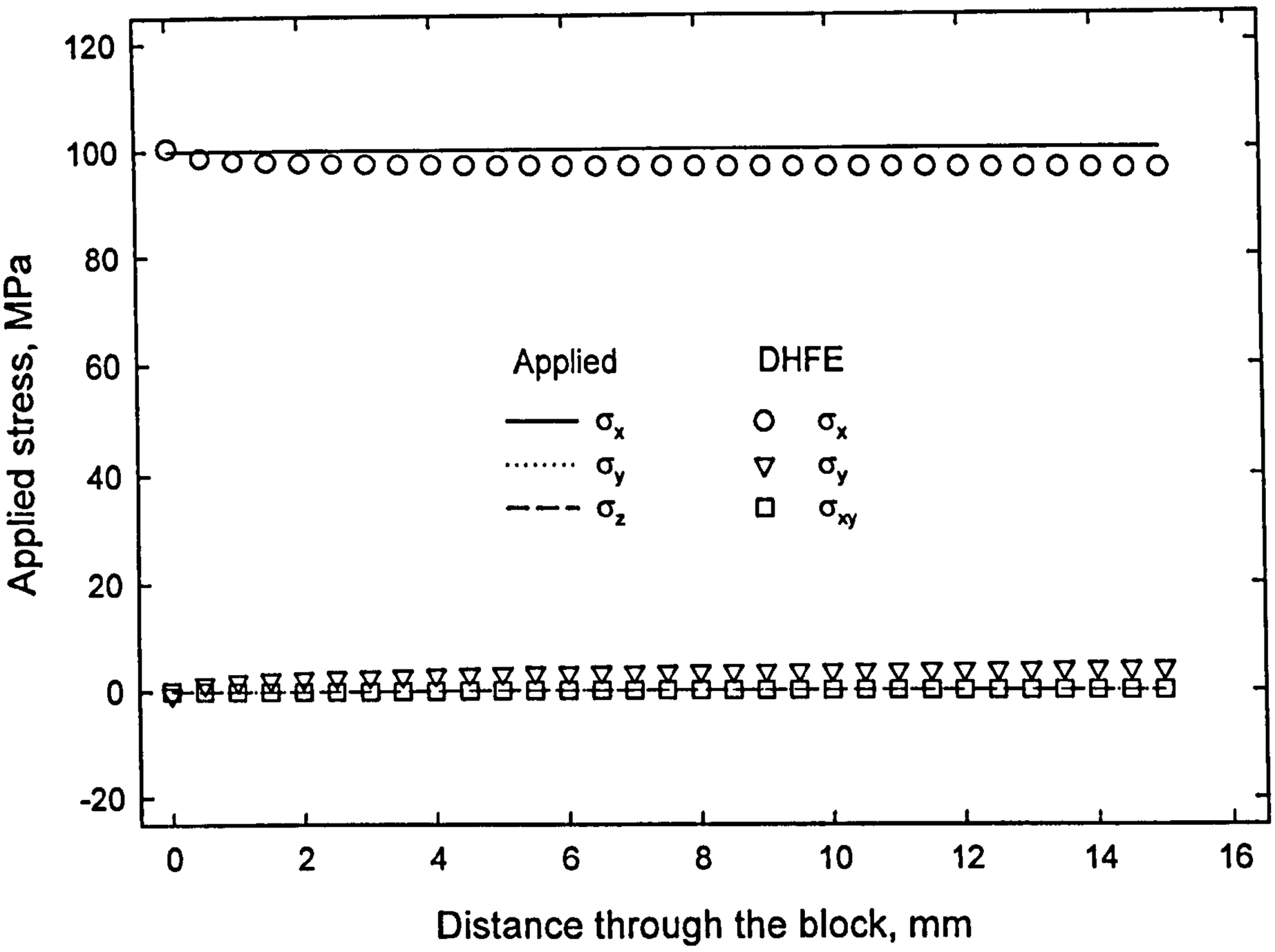

(a) Loading case b, σ_x = 100MPa

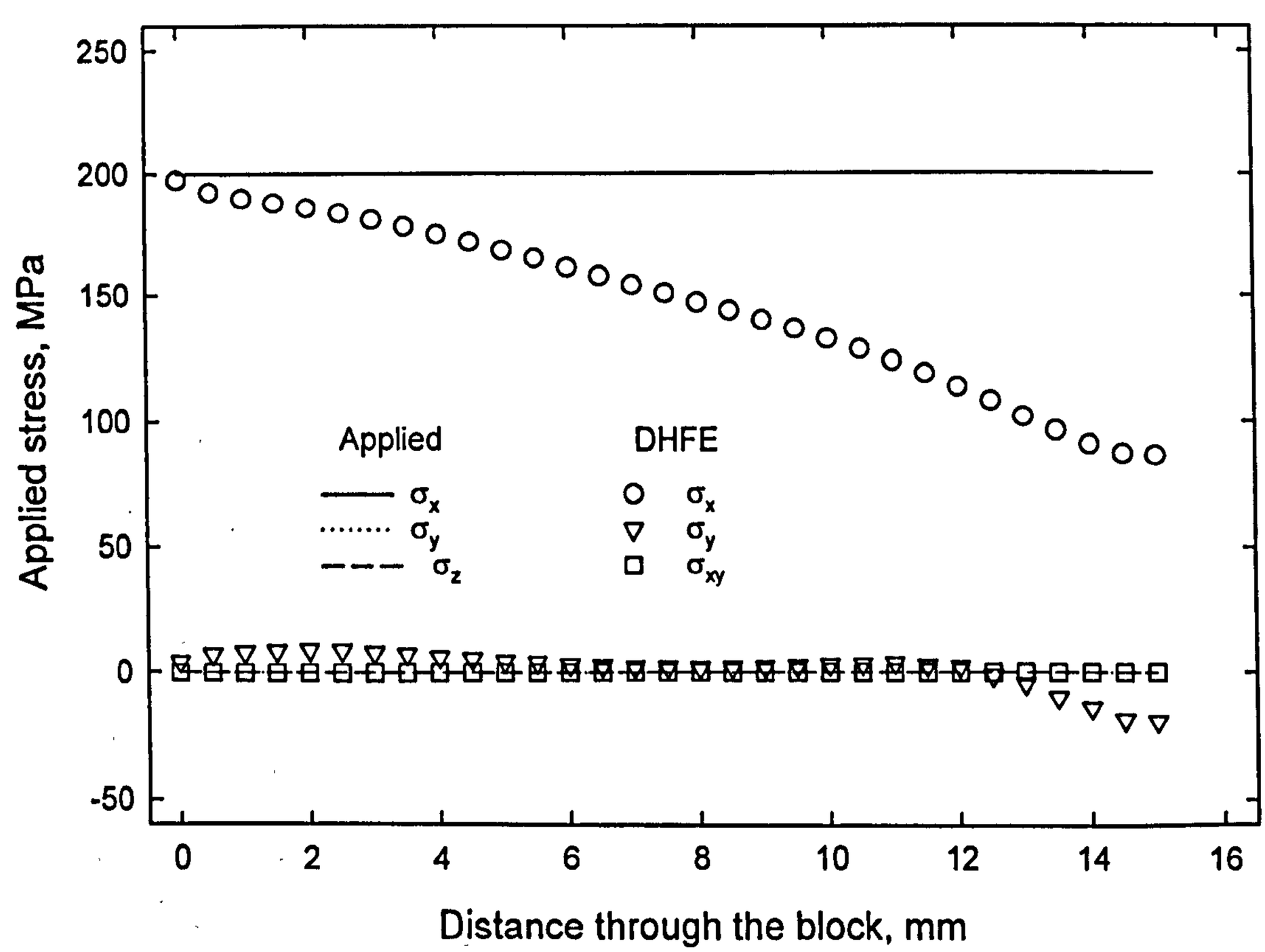

(b) Loading case d, σ_x = 200MPa

Figure 6.3 Through-thickness applied and reconstructed deep hole stress distribution for uniaxial loading case with triaxiality factor of 0.333.

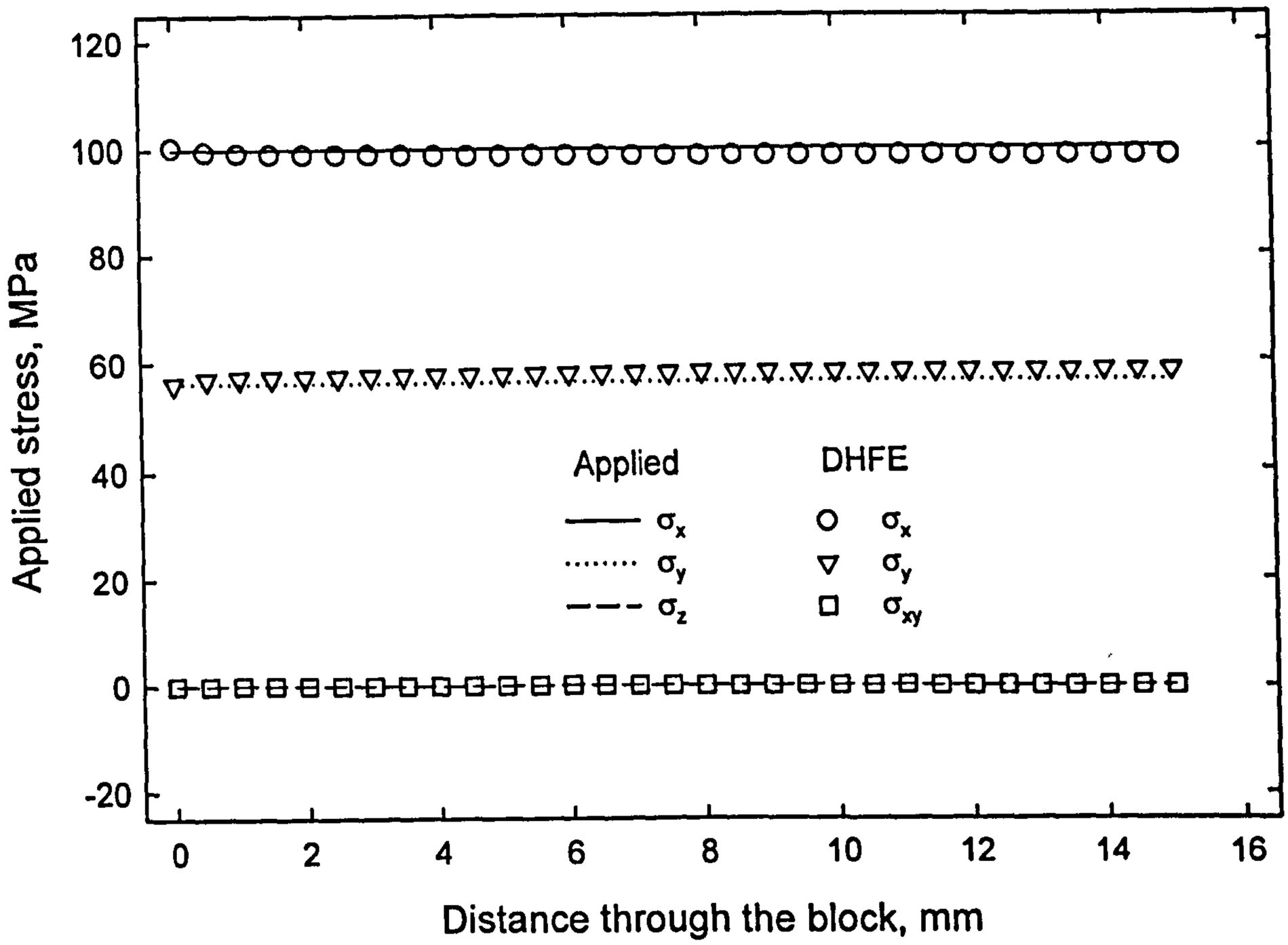

(a) Loading case g, σ_x=100MPa, σ_y=56MPa

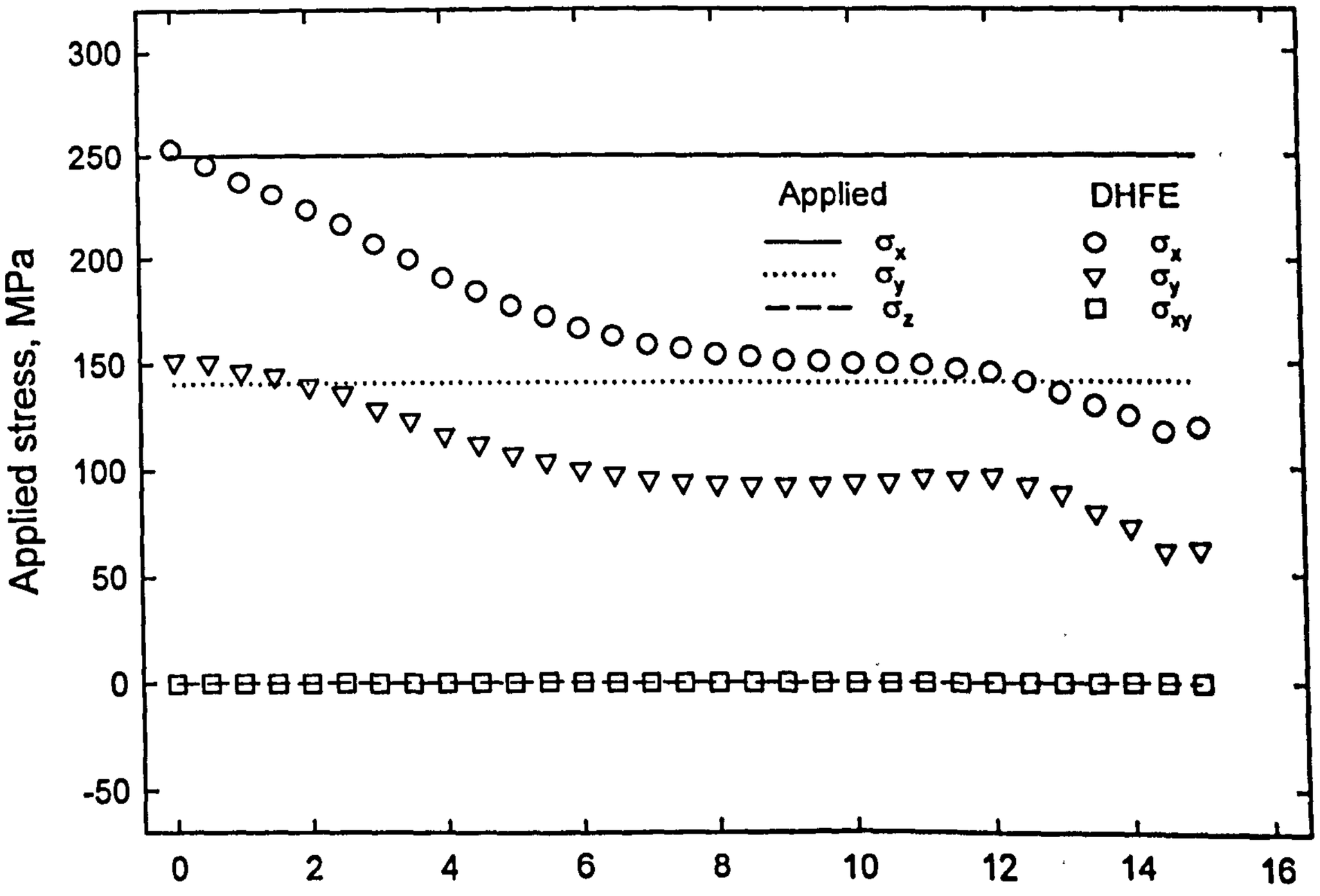

(b) Loading case j, σ_x=250MPa, σ_y=141MPa

Figure 6.4 Through-thickness applied and reconstructed deep hole stress distribution for biaxial loading case with triaxiality factor of 0.6.

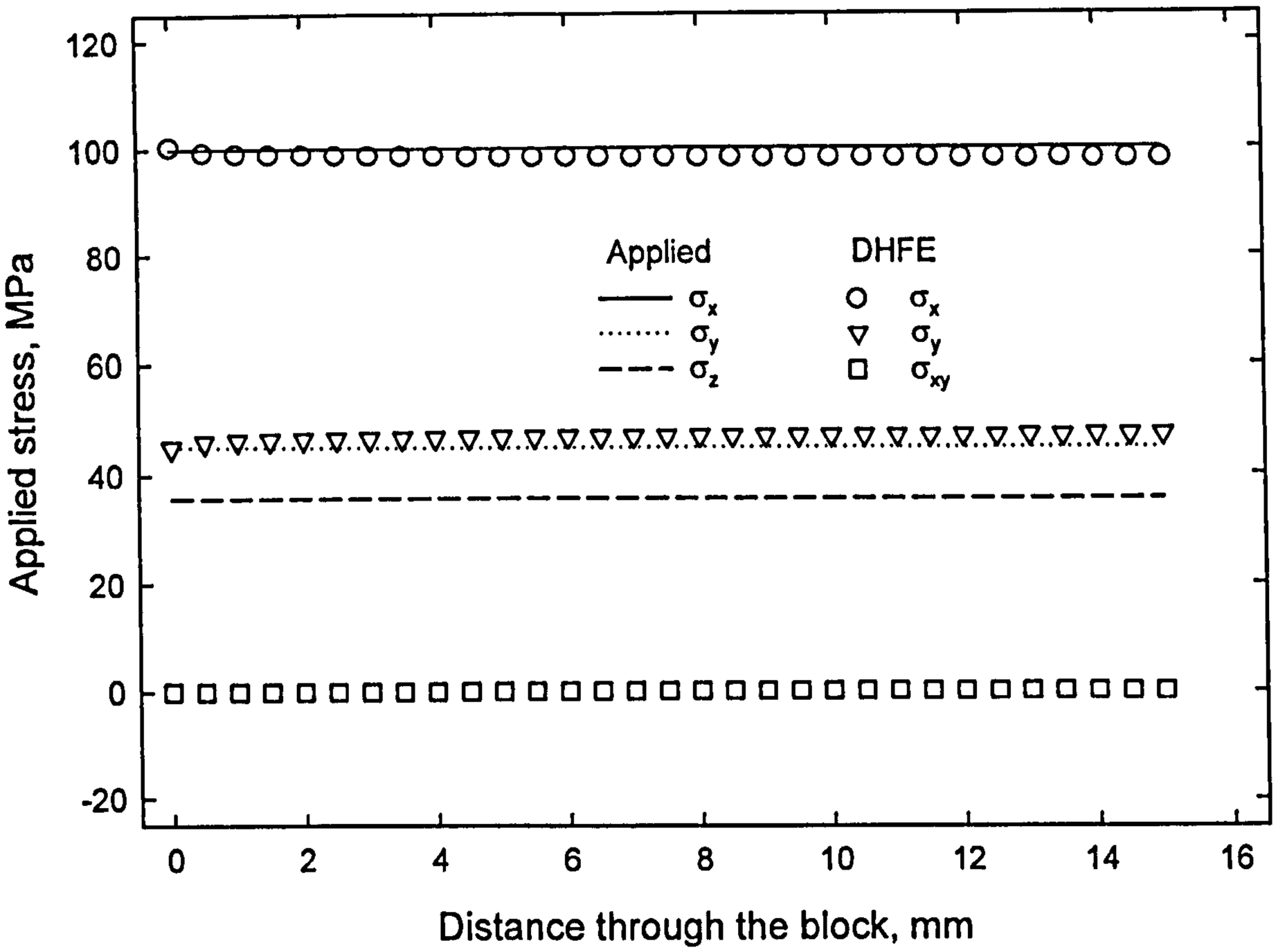

(a) Loading case l, σ_x=100MPa, σ_y=45MPa, σ_z=36MPa

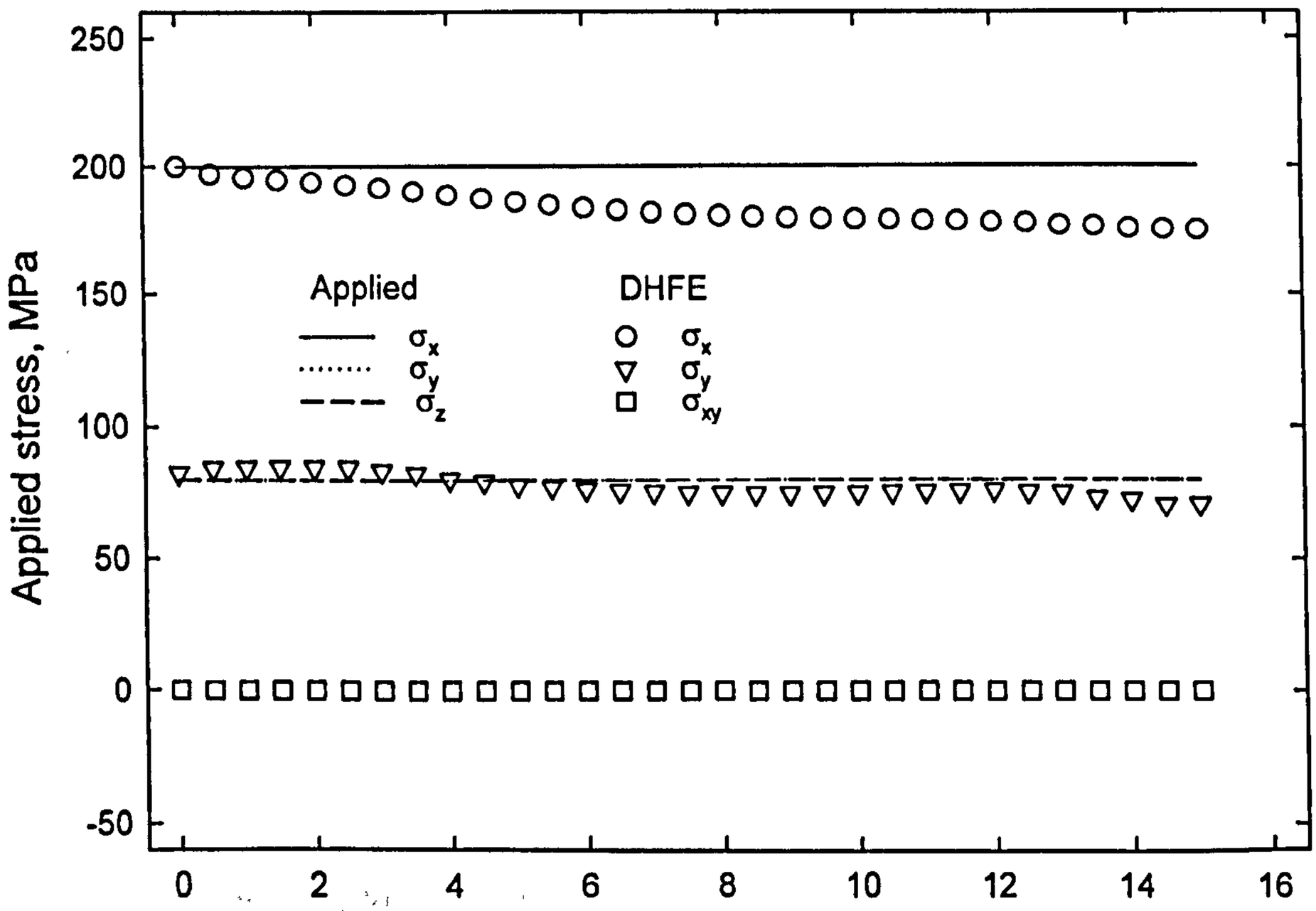

(b) Loading case q, σ_x=200MPa, σ_y=80MPa, σ_z=80MPa

Figure 6.5 Through-thickness applied and reconstructed deep hole stress distribution for triaxial loading case with triaxiality factor of 1.

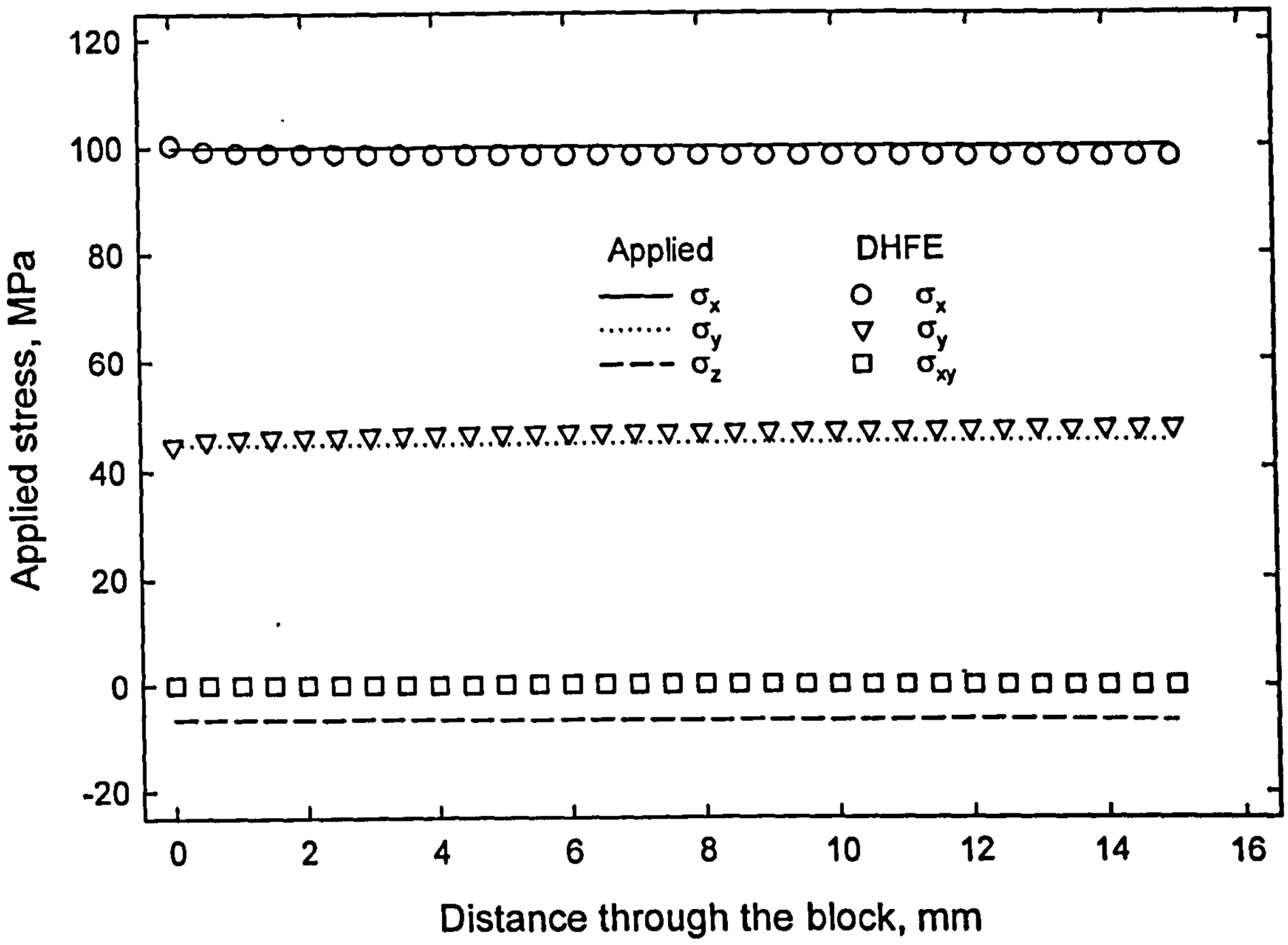

(a) Loading case u, σ_x=100MPa, σ_y=45MPa, σ_z= -7MPa

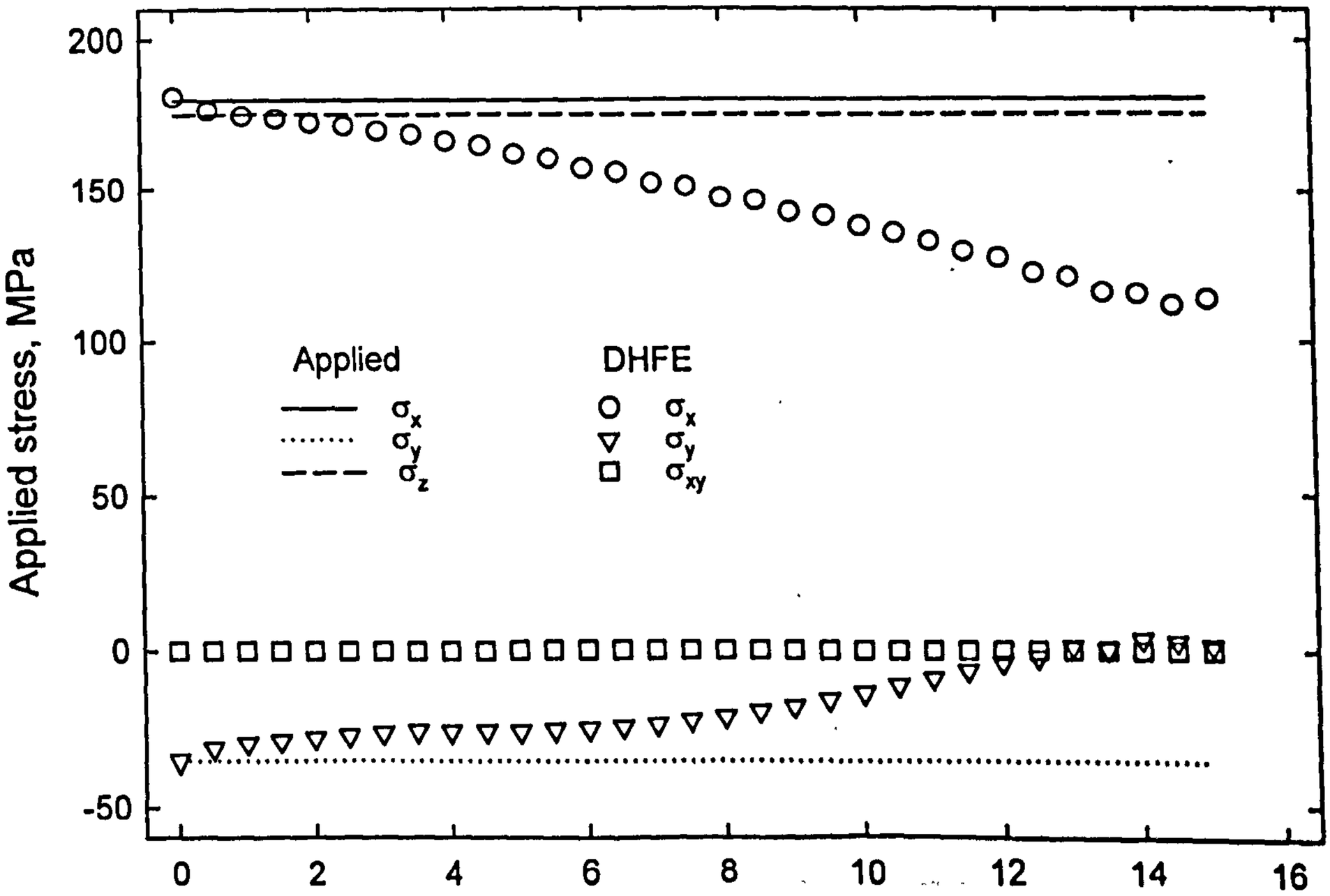

(b) Loading case y, σ_x=180MPa, σ_y= -35MPa, σ_z=175MPa

Figure 6.6 Through-thickness applied and reconstructed deep hole stress distribution for triaxial loading case with triaxiality factor of 0.5.

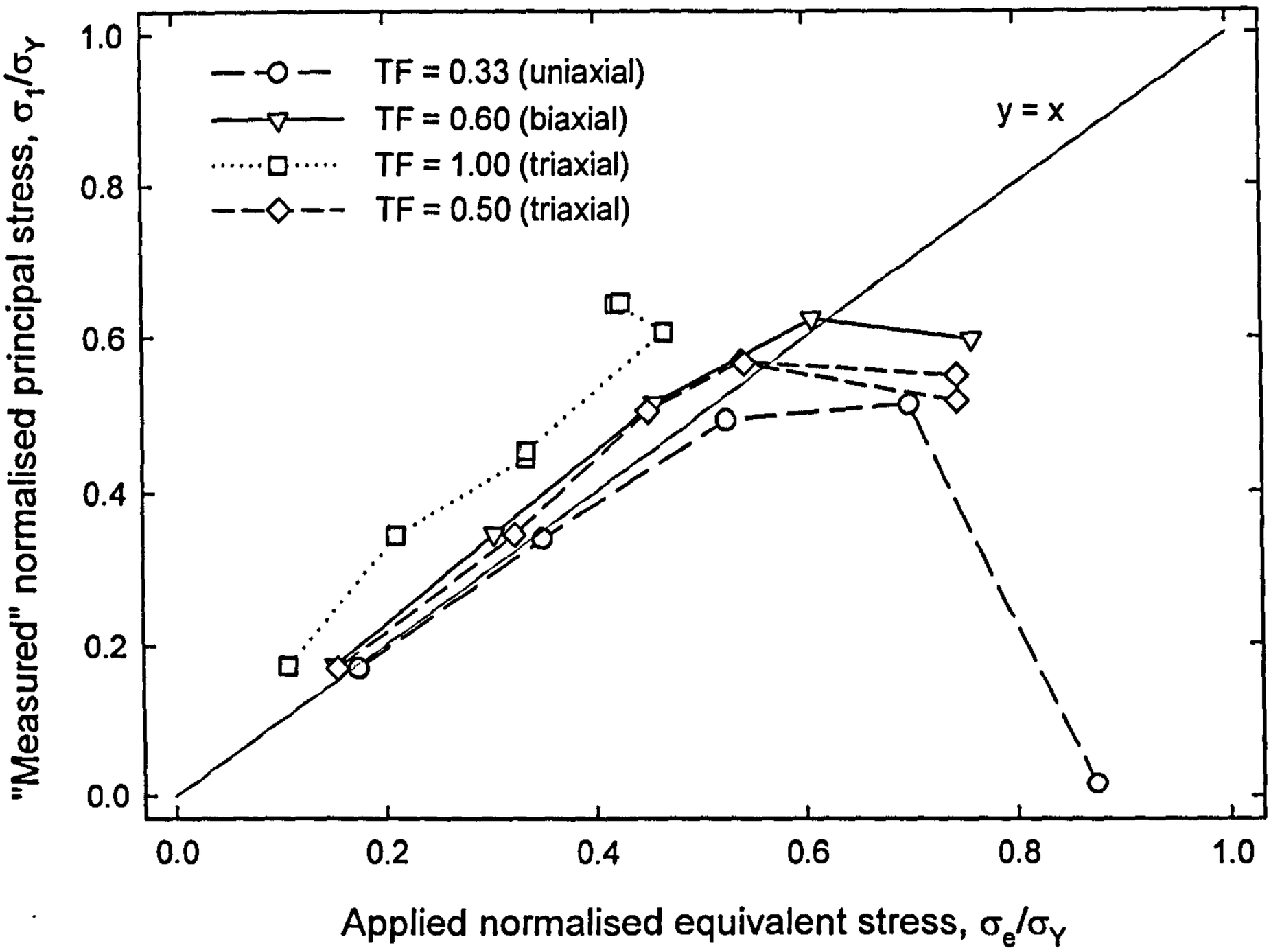

Figure 6.7 Summary of "measured" principal stress versus applied equivalent stress normalised by yield stress.

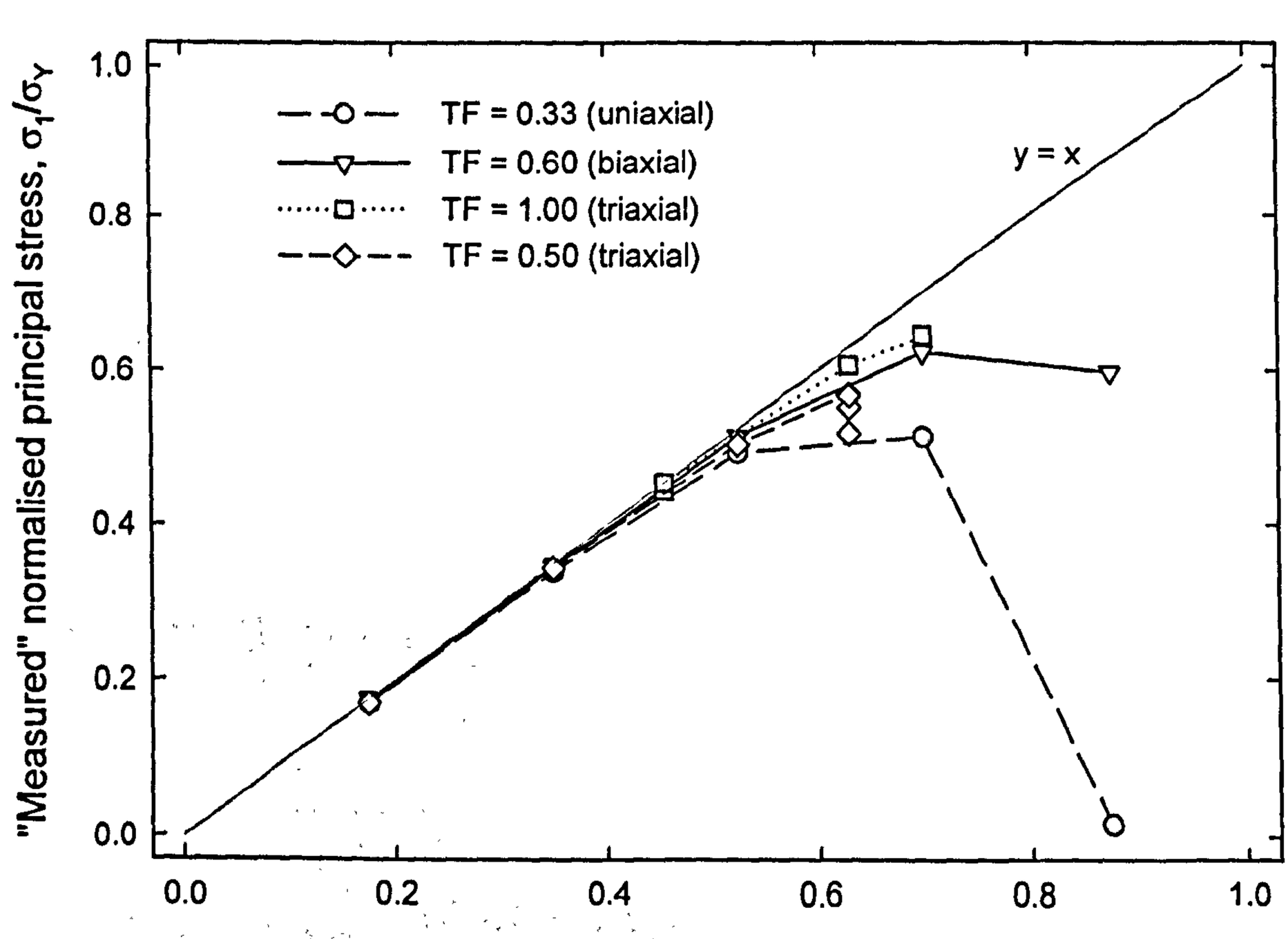

Figure 6.8 Summary of "measured" versus applied principal stress normalised by yield stress.

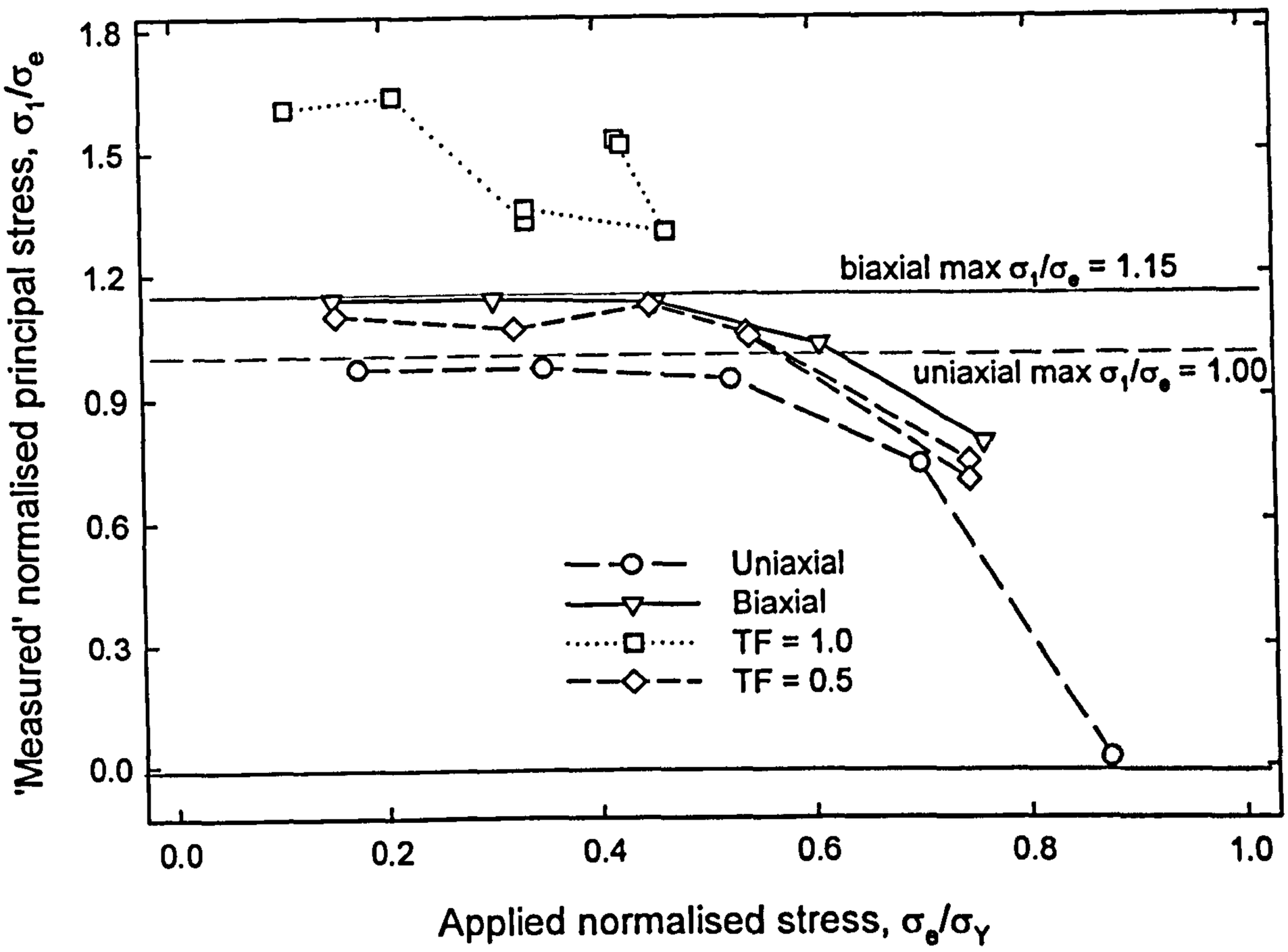

Figure 6.9 Summary of "measured" principal stress normalised by equivalent stress versus applied stress normalised by yield stress.

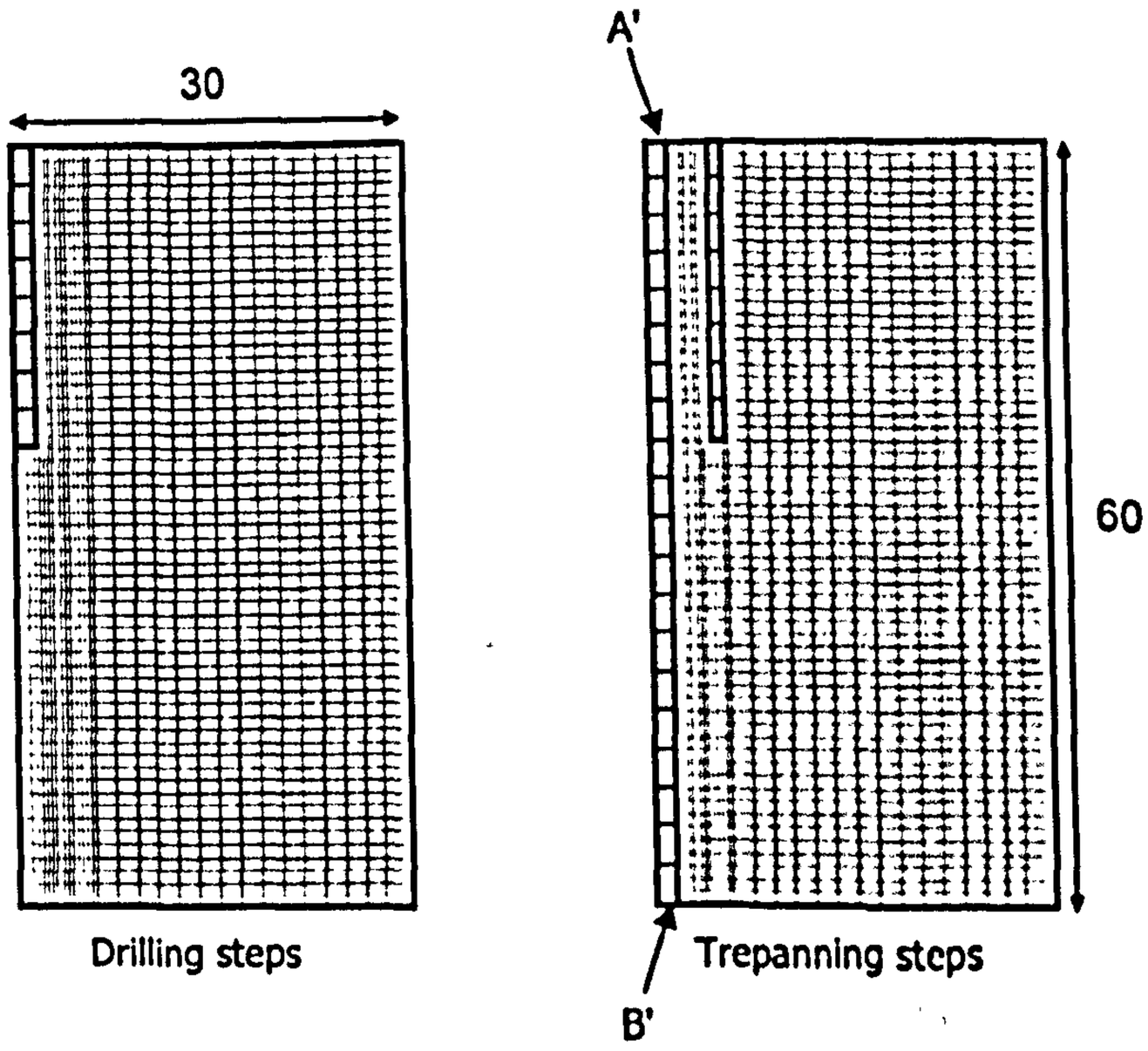

Figure 6.10 Axi-symmetric model of the quenched cylinder illustrating the drilling and trepanning steps of deep hole drilling measurement technique. The edge A'B' represents the inner surface of the gun-drilled reference hole used to measure the diametral distortions.

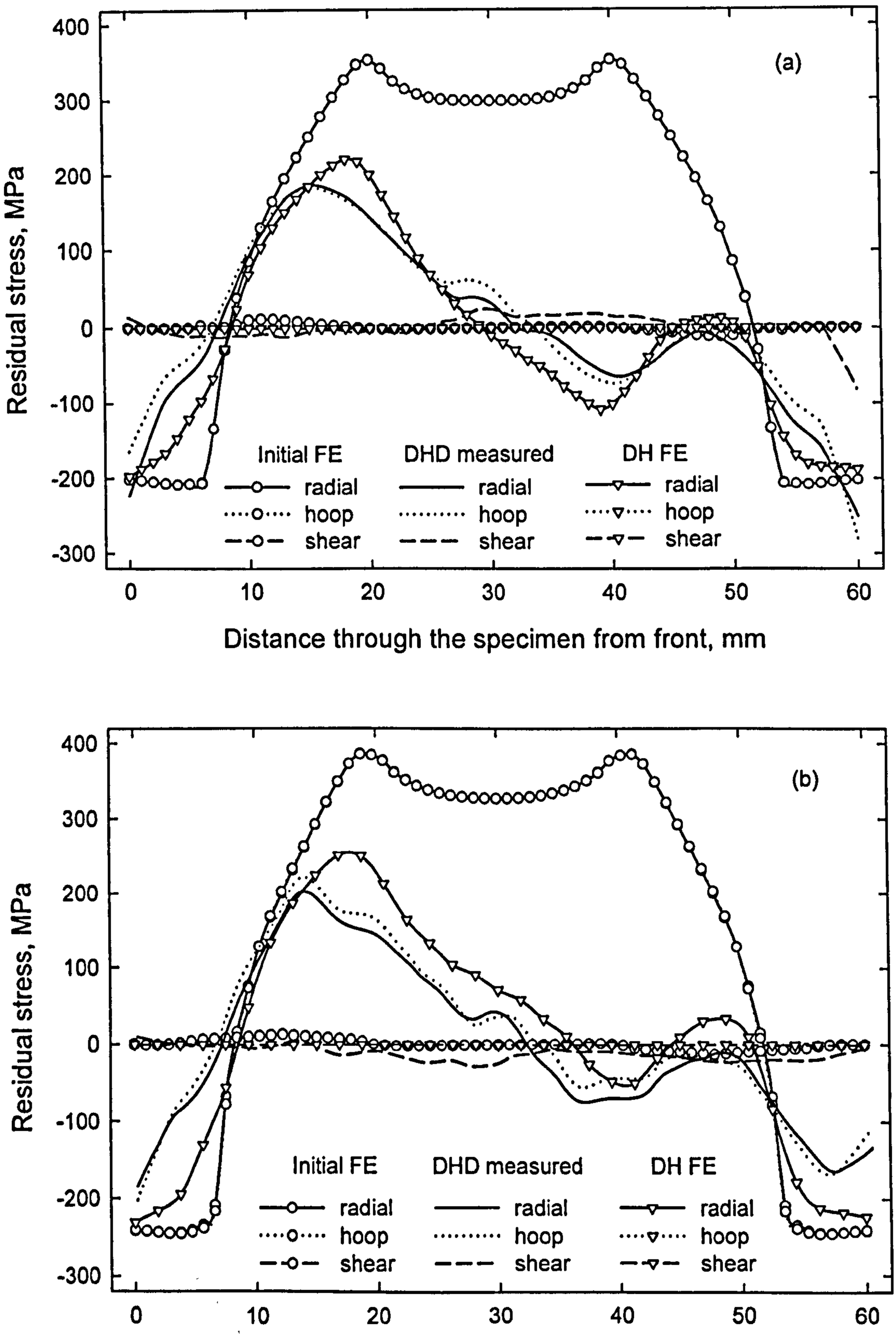

Figure 6.11 Deep hole measured residual stresses compared with the finite element predicted residual stresses due to simulation of deep hole method. The predicted initial quenched residual stresses (Figure 3.6) are also shown. (a) type 321, (b) type 316L.

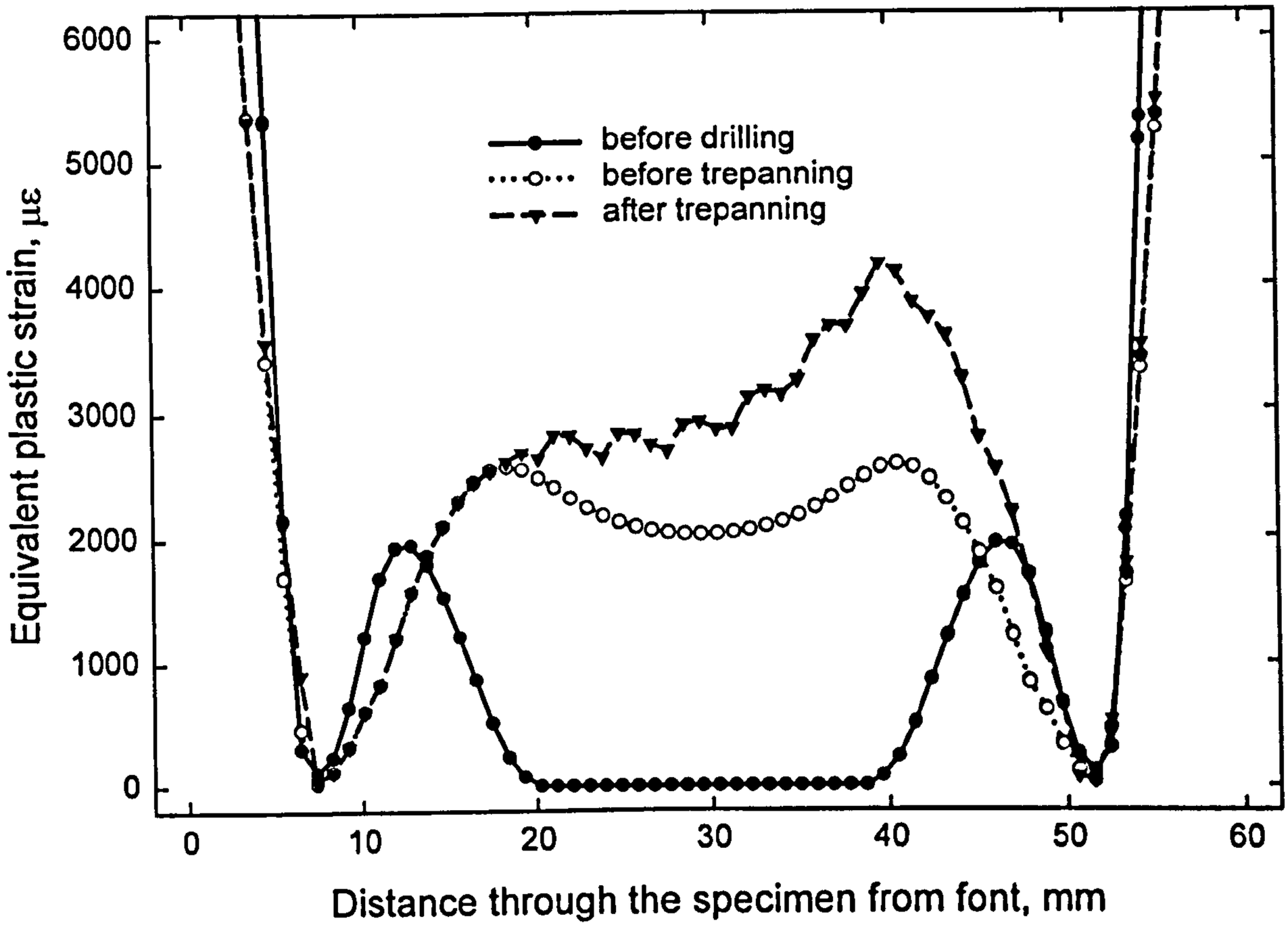

Figure 6.12 FE predicted distribution of equivalent plastic strain along the edge of drilled region A'B' (see Figure 6.10) before drilling, before trepanning and after trepanning.

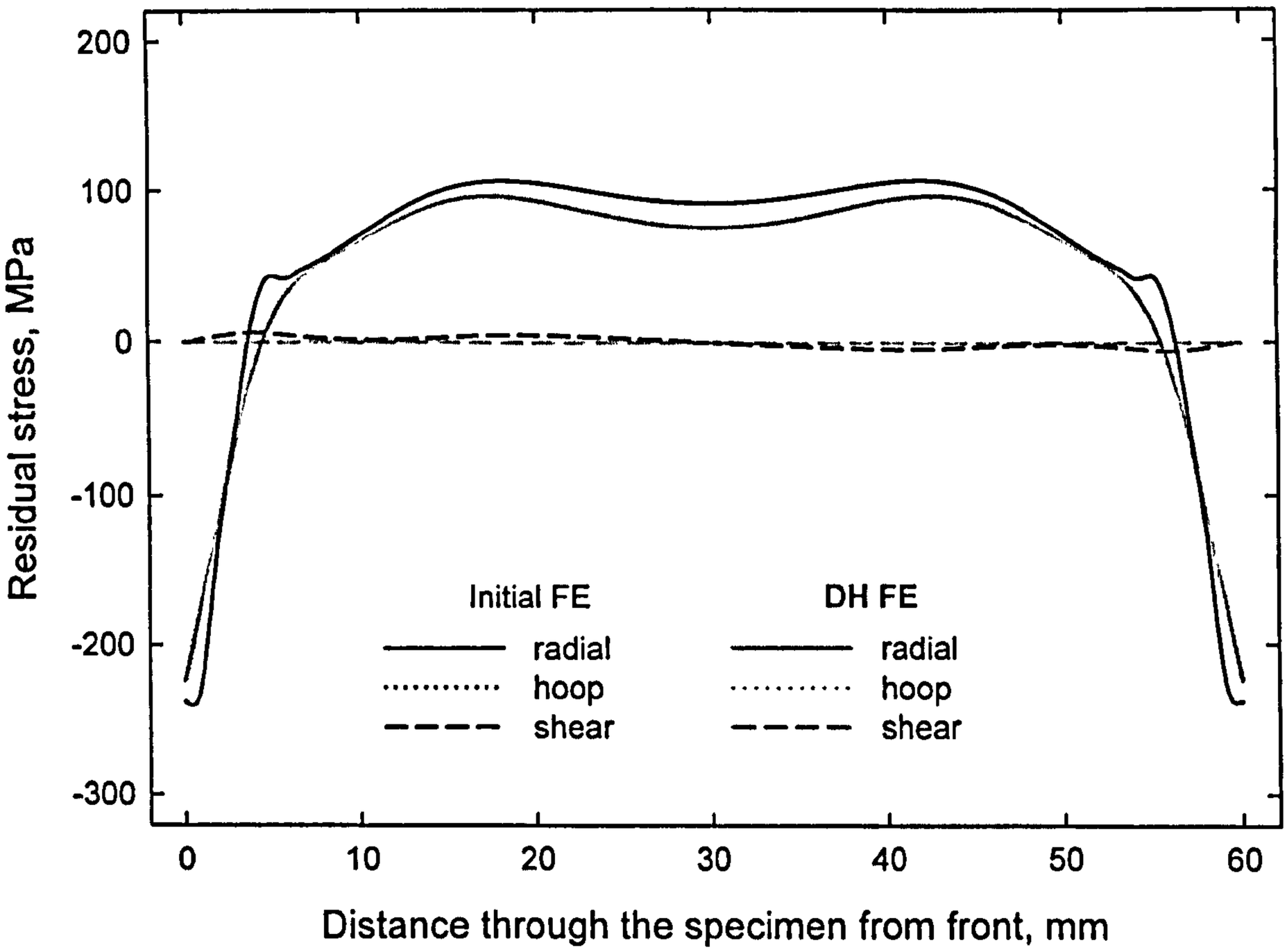

Figure 6.13 Initial FE predicted and deep hole simulated residual stress distributions along the longitudinal axis of type 316L stainless steel cylinder, with heat transfer coefficient, $h = 400$ W/m^2 K and kinematic hardening.

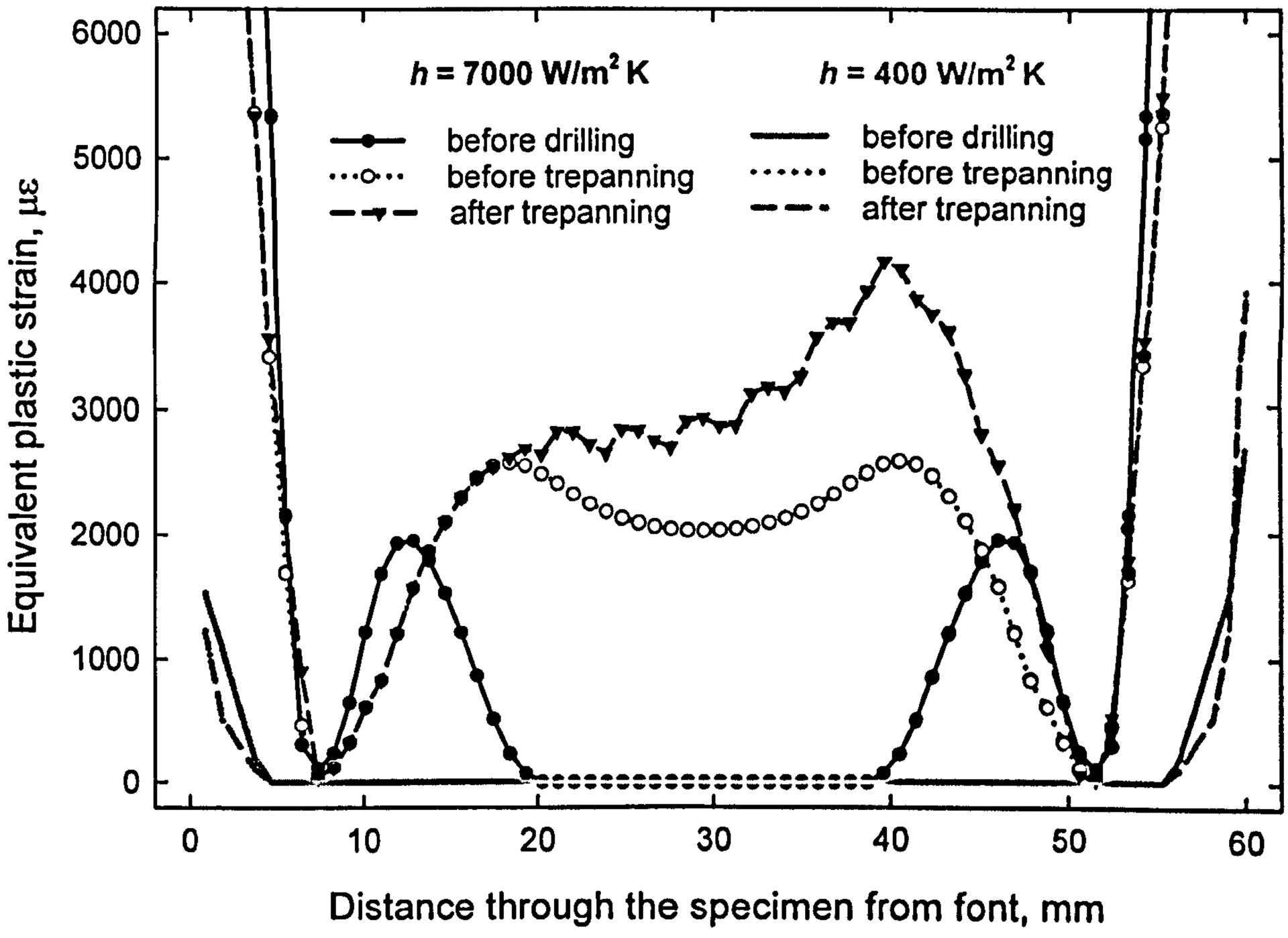

Figure 6.14 FE predicted distribution of equivalent plastic strain along the edge of drilled region A'B' (see Figure 6.10) before drilling, before trepanning and after trepanning. Comparison is made between the distributions for heat transfer coefficients, $h = 7000$ W/m^2 K and $h = 400$ W/m^2 K.

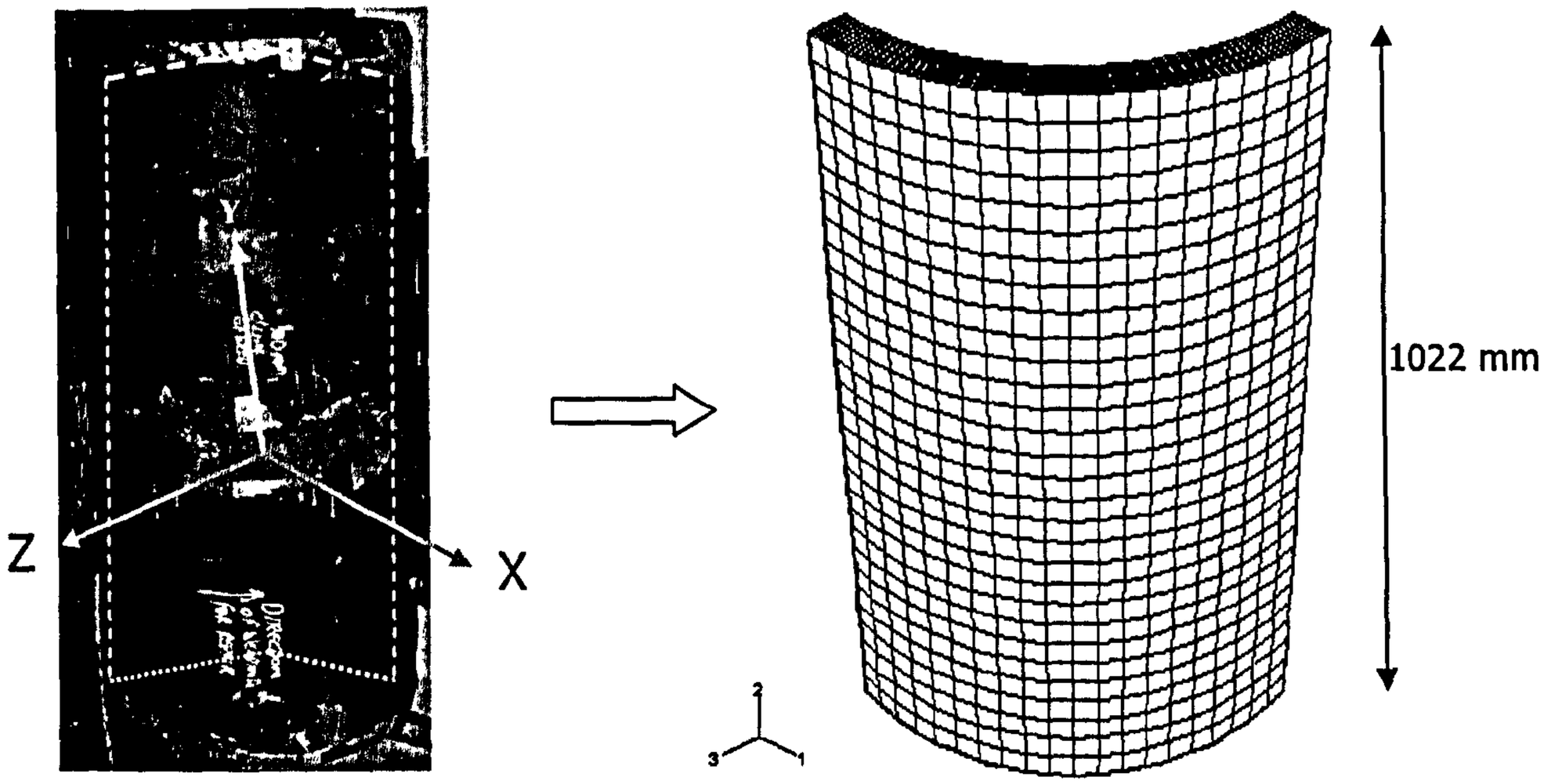

Figure 6.15 Welded pipe geometry, ¼ model of the full pipe, inner diameter = 362mm, outer diameter = 432mm, wall thickness = 35mm.

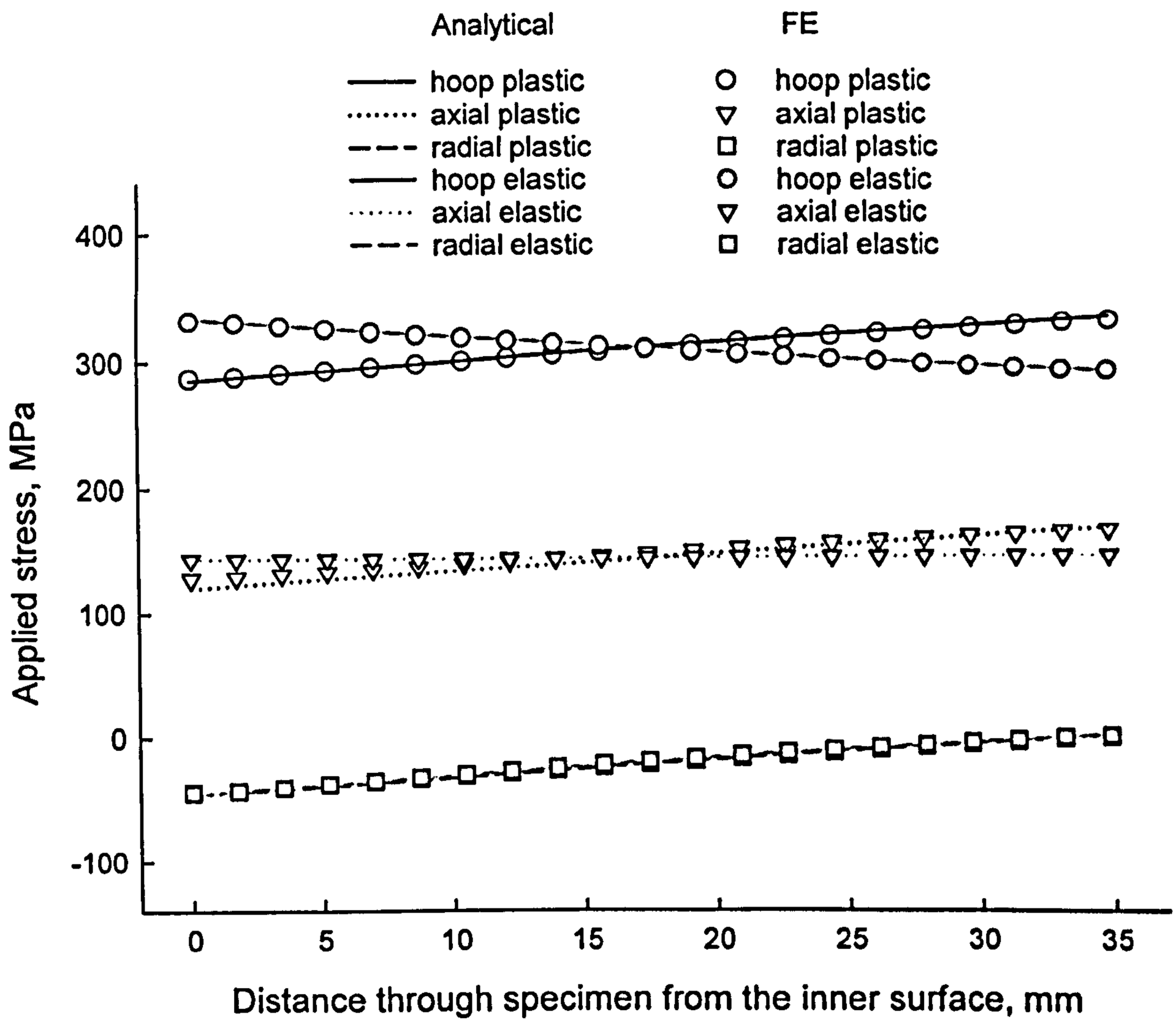

Figure 6.16 Stress distributions through the pipe with no weld cap from the inner surface. The theoretical result assuming an elastic case compares very well with the finite element predicted stress distribution.

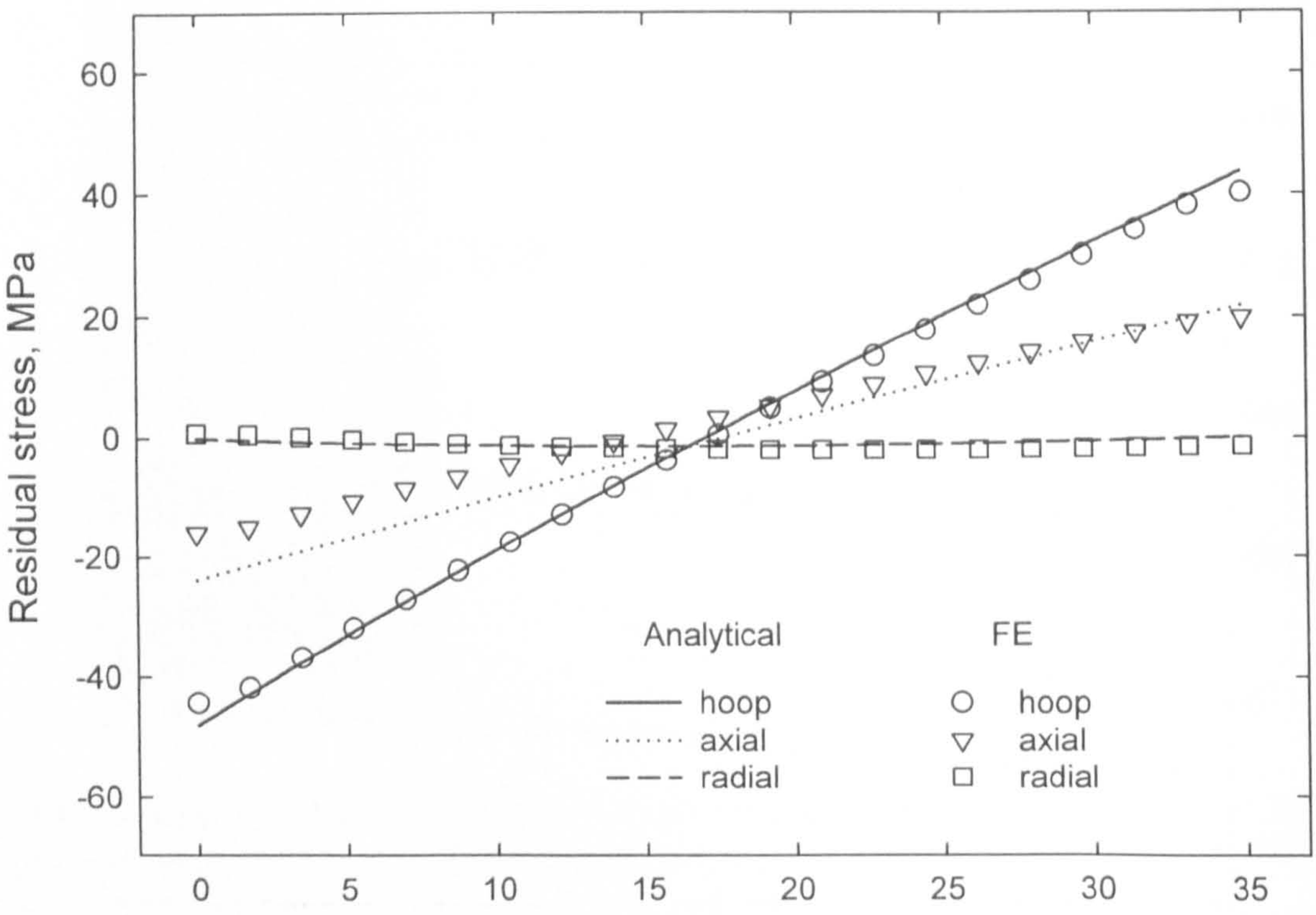

Figure 6.17 Calculated and finite element predicted autofrettage residual stress distribution through the pipe thickness.

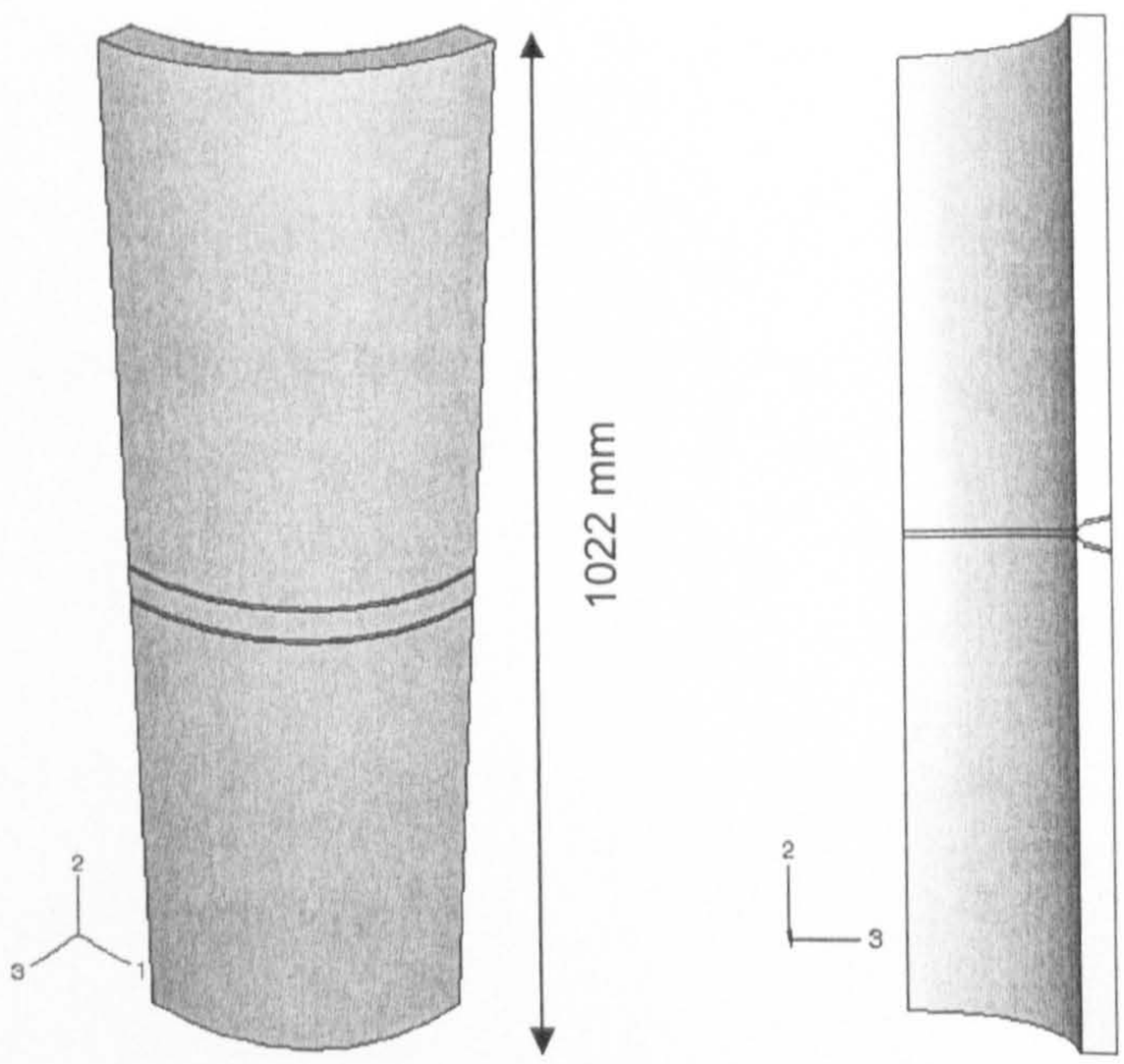

Figure 6.18 Illustration of the outer and inner surface of the welded pipe model.

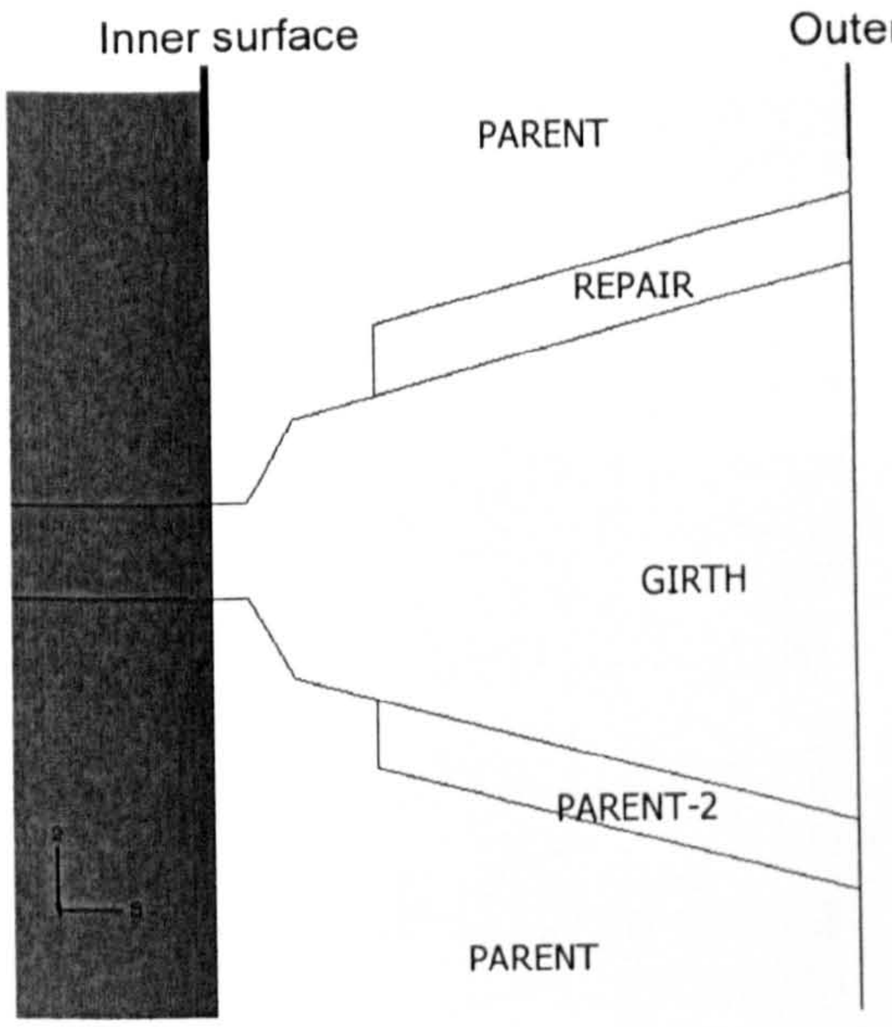

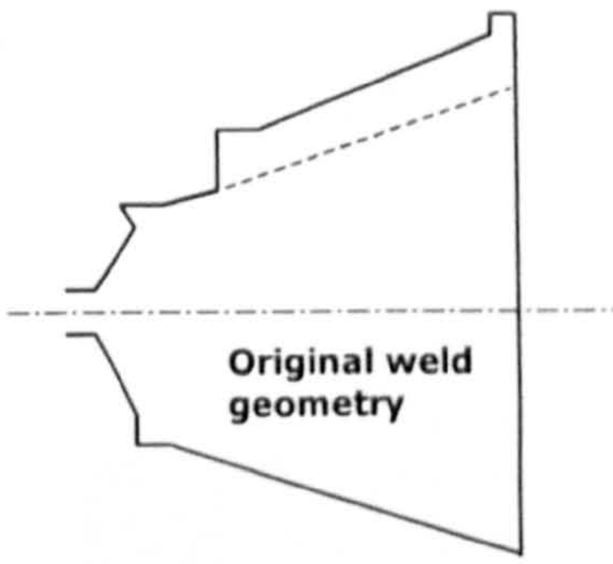

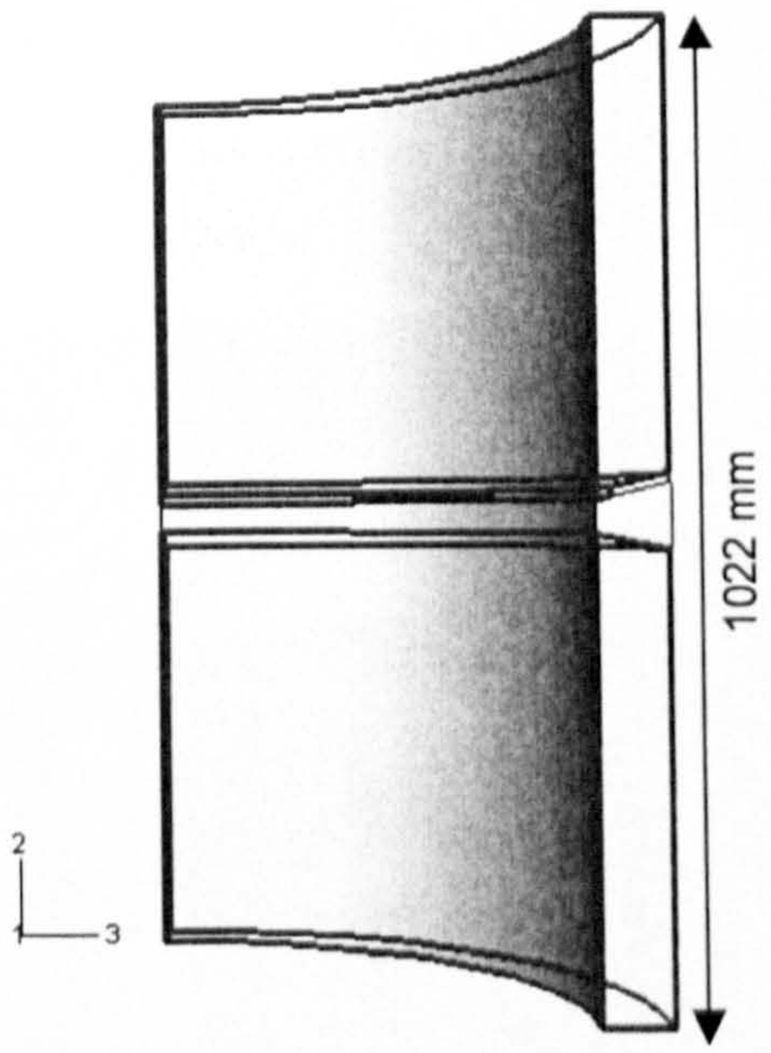

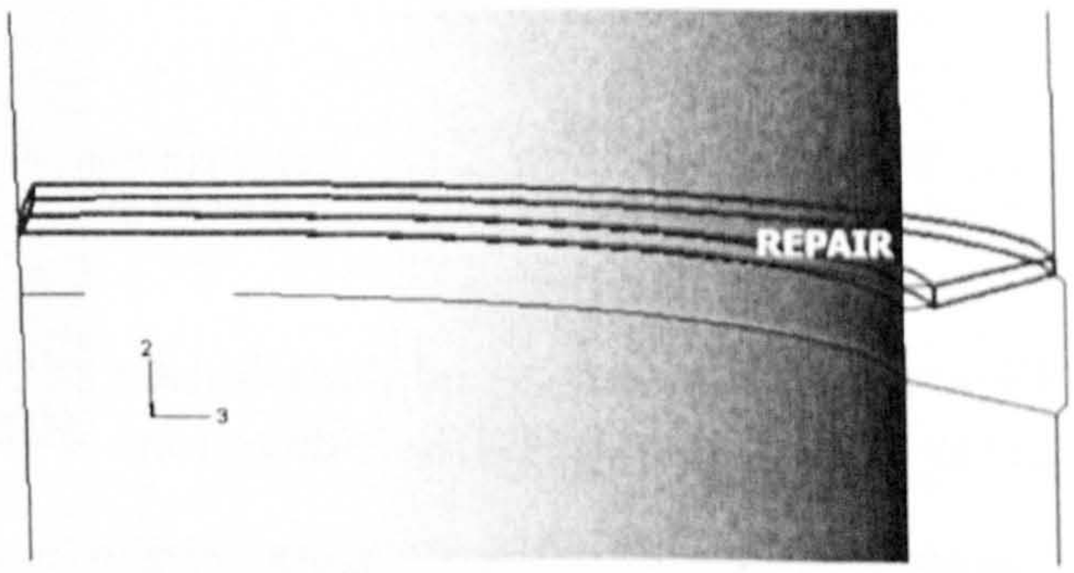

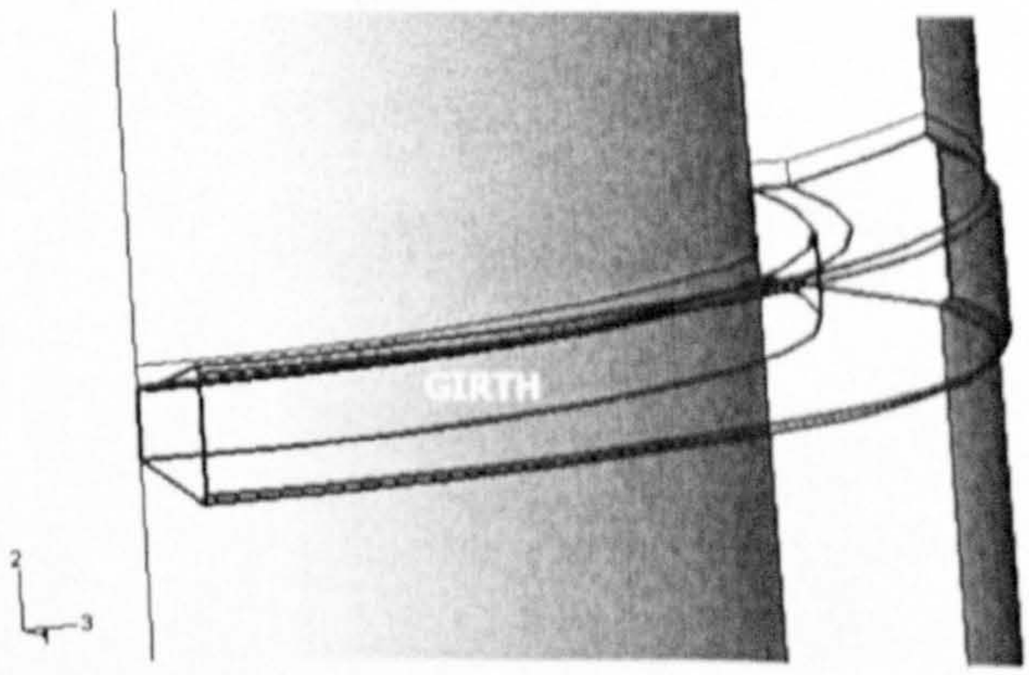

Figure 6.19 Illustration of the three regions – Parent, Repair and Girth, highlighted. Also shown is the original unmodified weld profile on the top right hand corner.

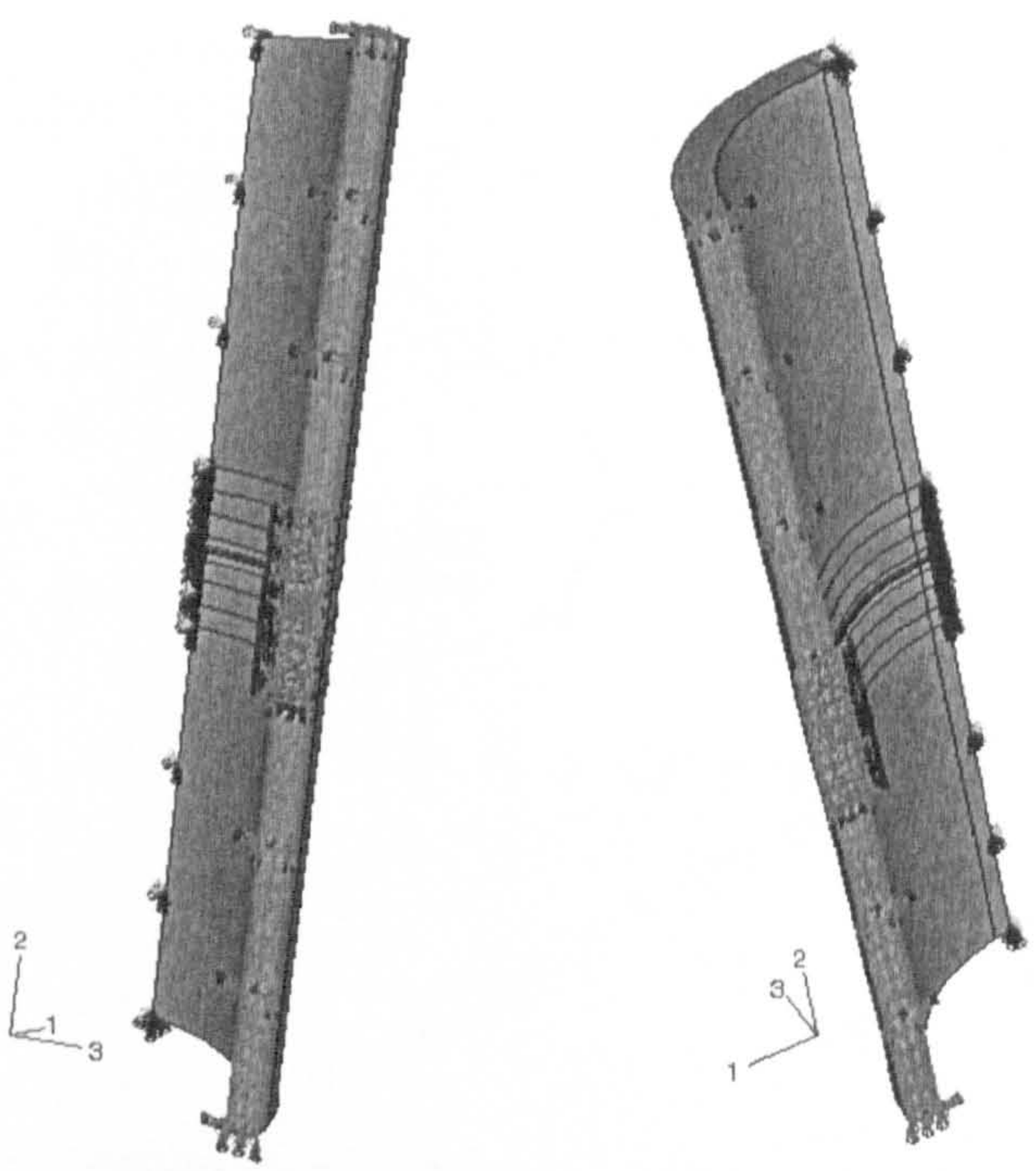

(a) Symmetry boundary condition in 1-direction

(b) Symmetry boundary condition in 3-direction

(c) Displacement BC with a node fixed in 2-direction

Figure 6.20 Boundary conditions consist of a) 1-Symmetry BC, b) 3-Symmetry BC and c) Fixed displacement BC in 2-direction.

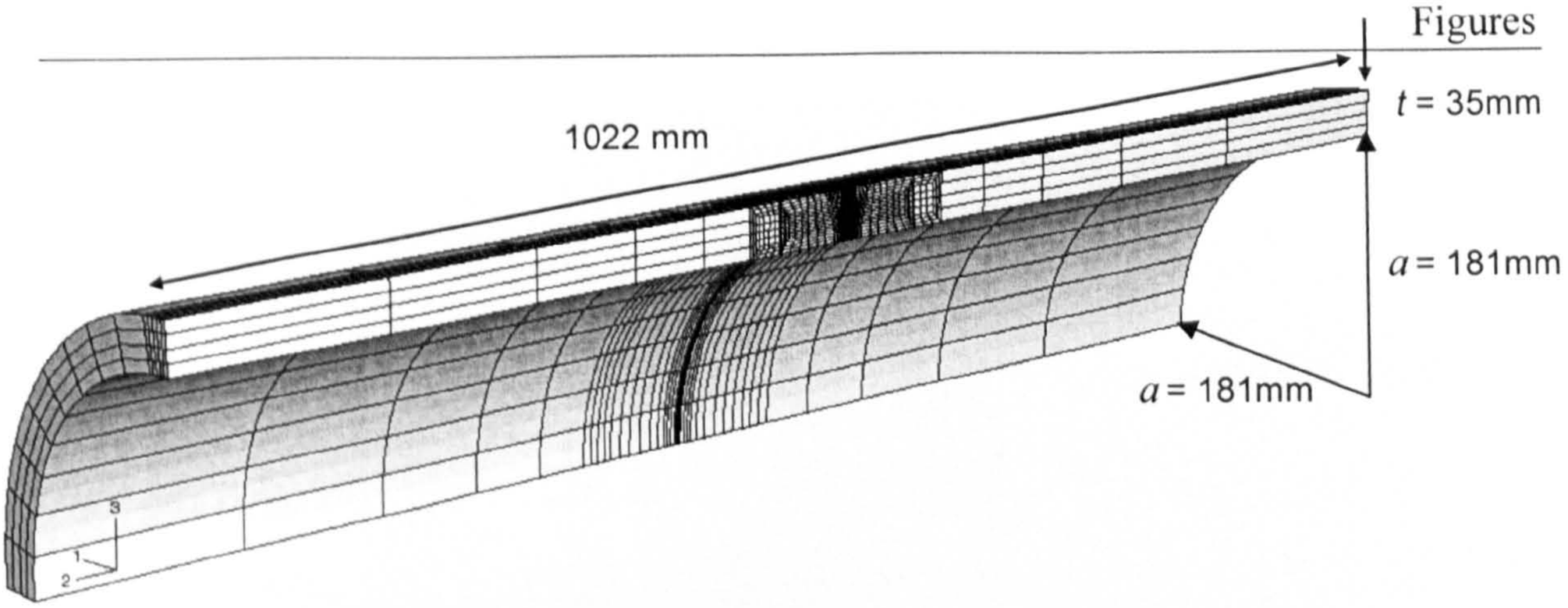

Figure 6.21 3D mesh showing the drilling and trepanning regions.

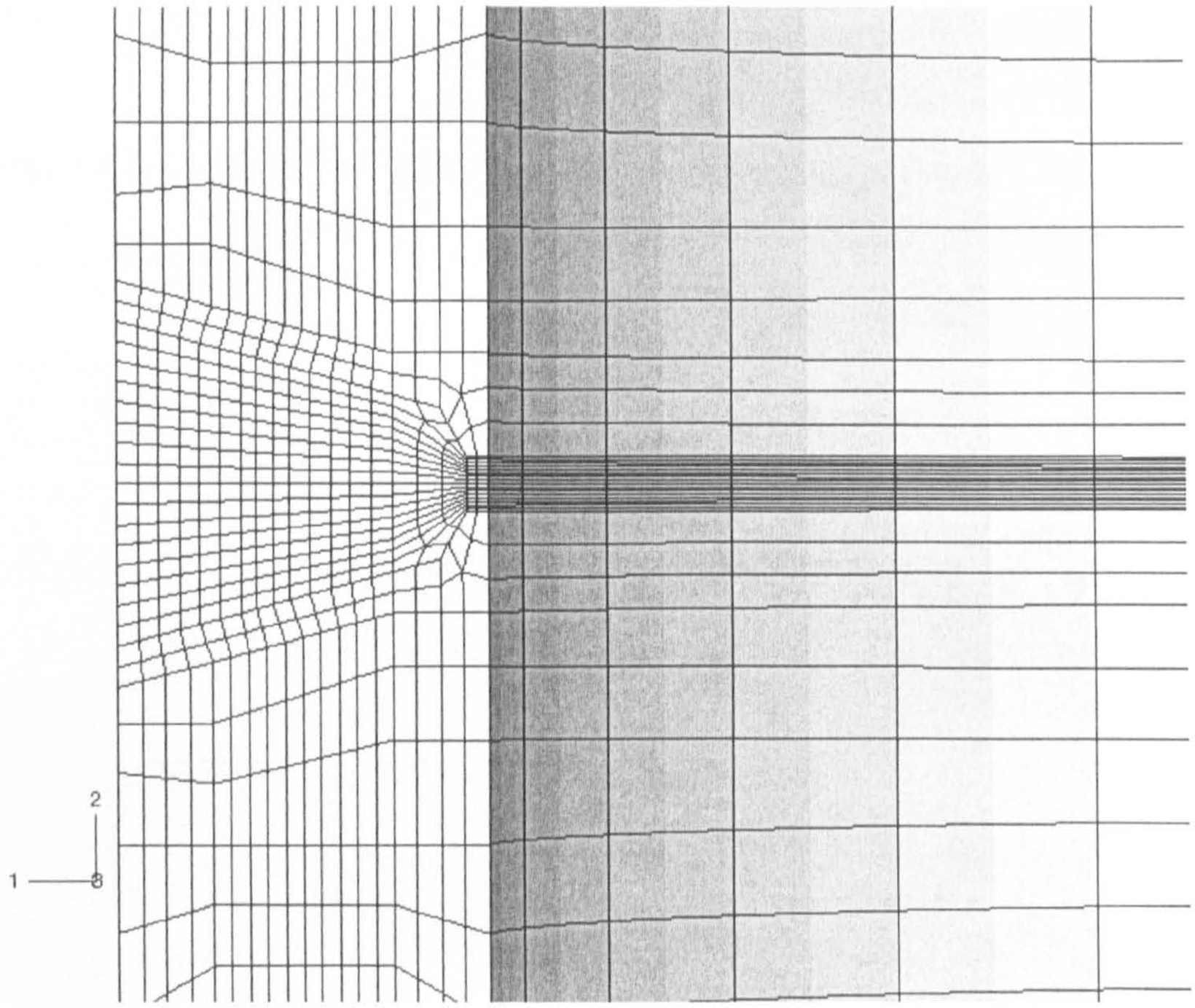

Figure 6.22 Figure showing detailed mesh of the welded region.

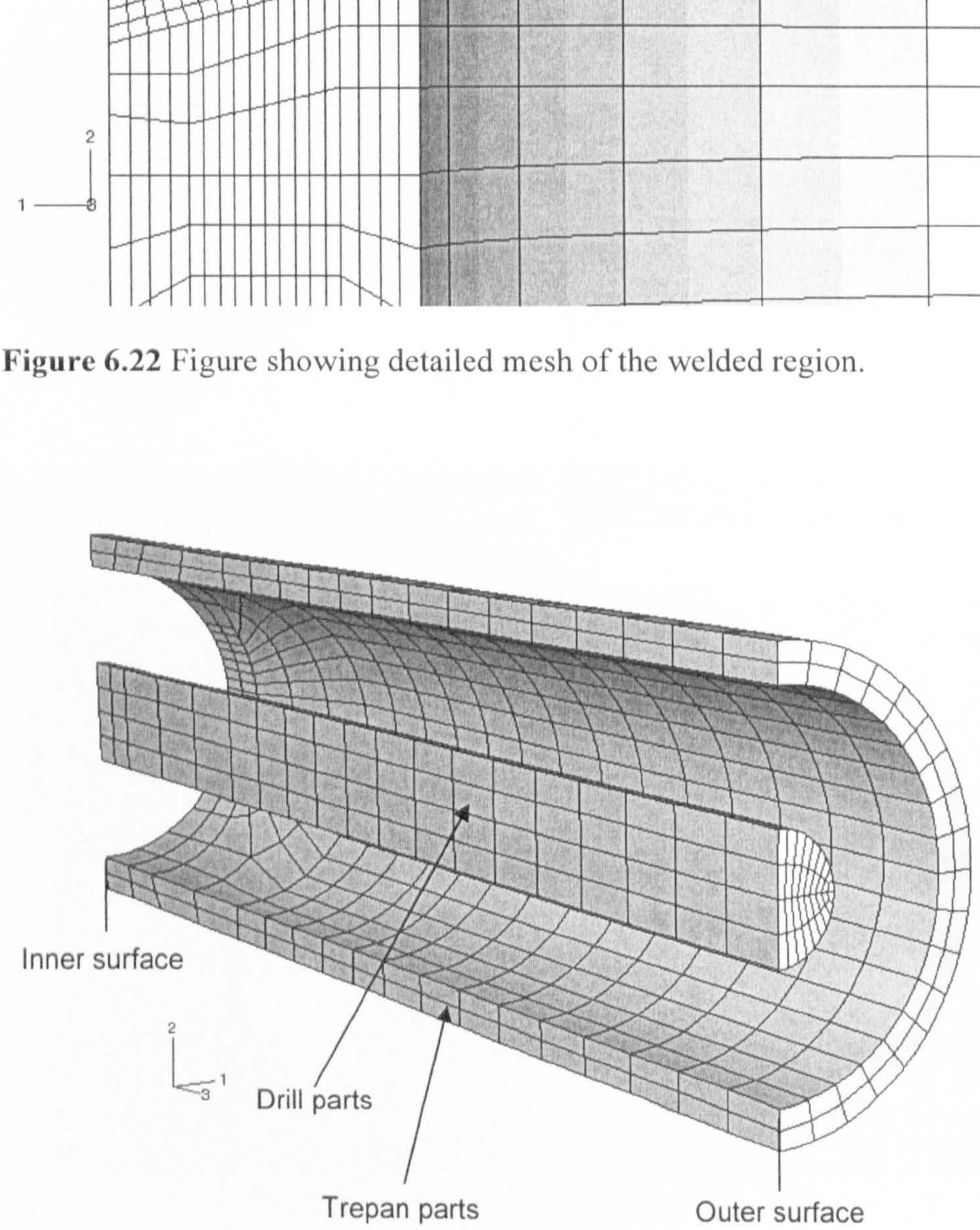

Figure 6.23 Illustration of drill and trepan parts.

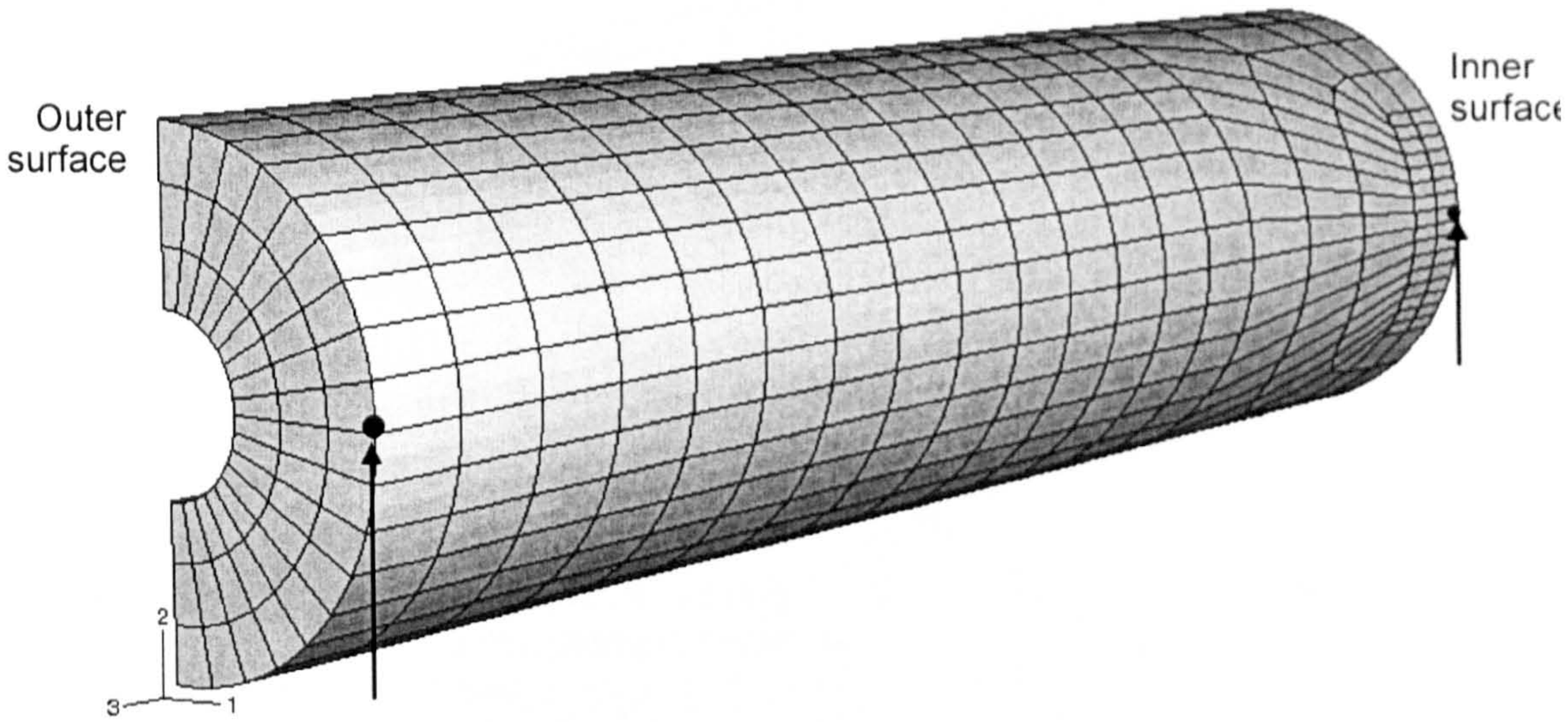

Figure 6.24 Core illustrating the additional boundary conditions on two nodes required in the deep hole simulation in the pipe axial (2-direction) shown by the arrows on the outer and inner surface.

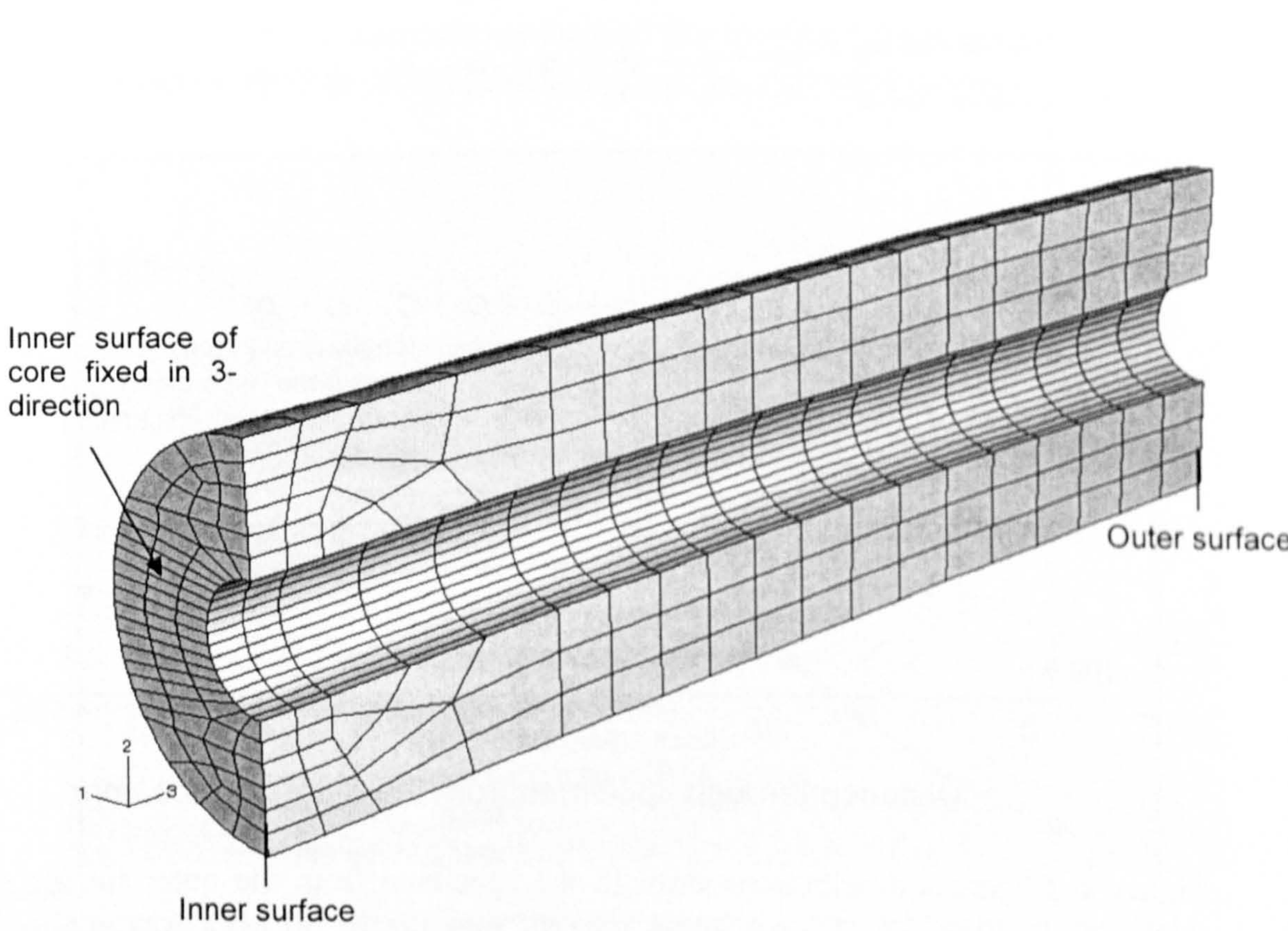

Figure 6.25 Back bush fixed in the normal (3-direction) during the deep hole simulation.

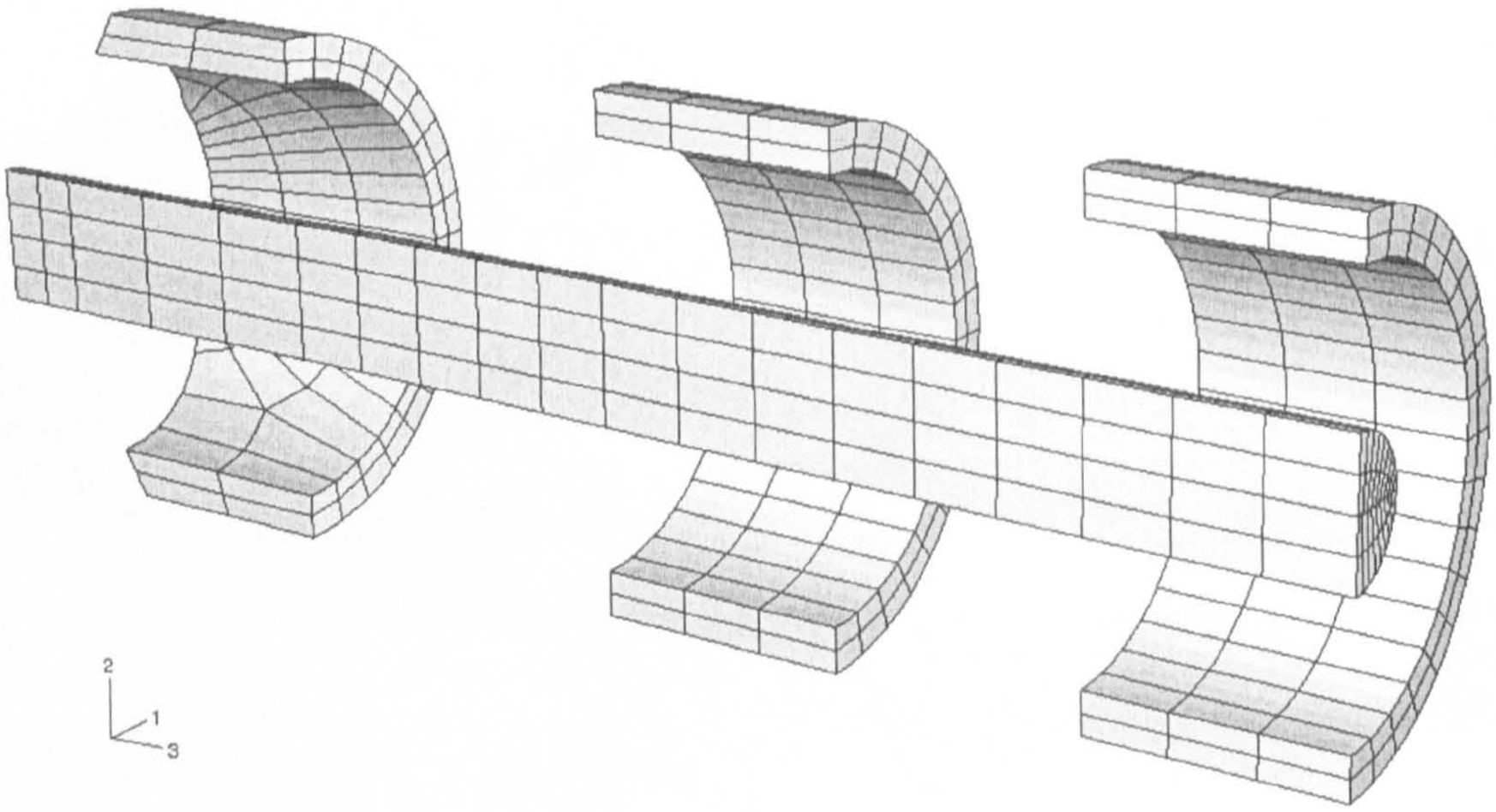

Figure 6.26 Illustration of single-step drilling and 6-step trepanning process.

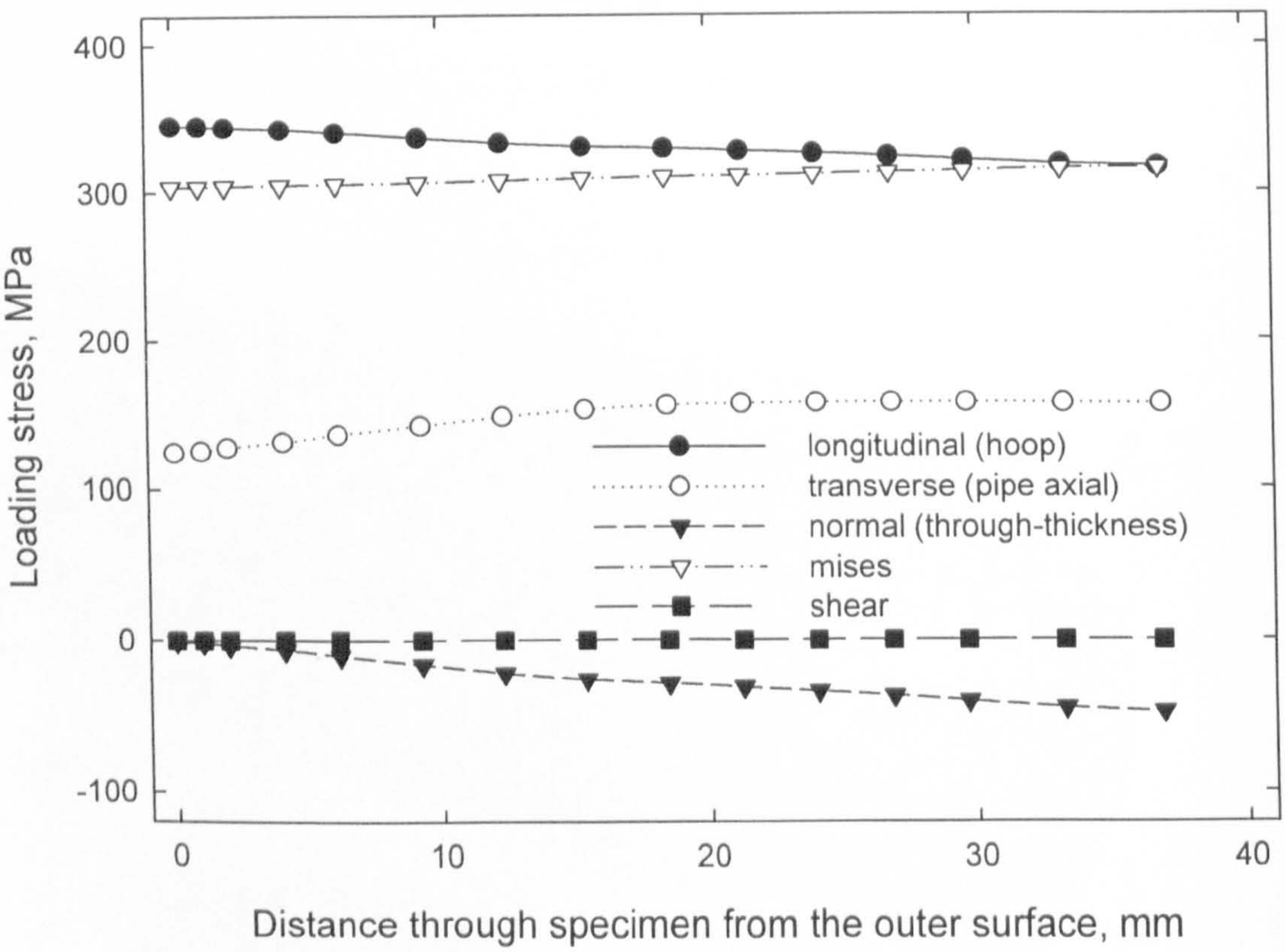

Figure 6.27 Stress distributions through the specimen from the outer surface (along thick line in Figure 6.21). An initial internal pressure of 50 MPa was applied, with tensile load of 117.9 MPa at both free ends to simulate the end cap conditions.

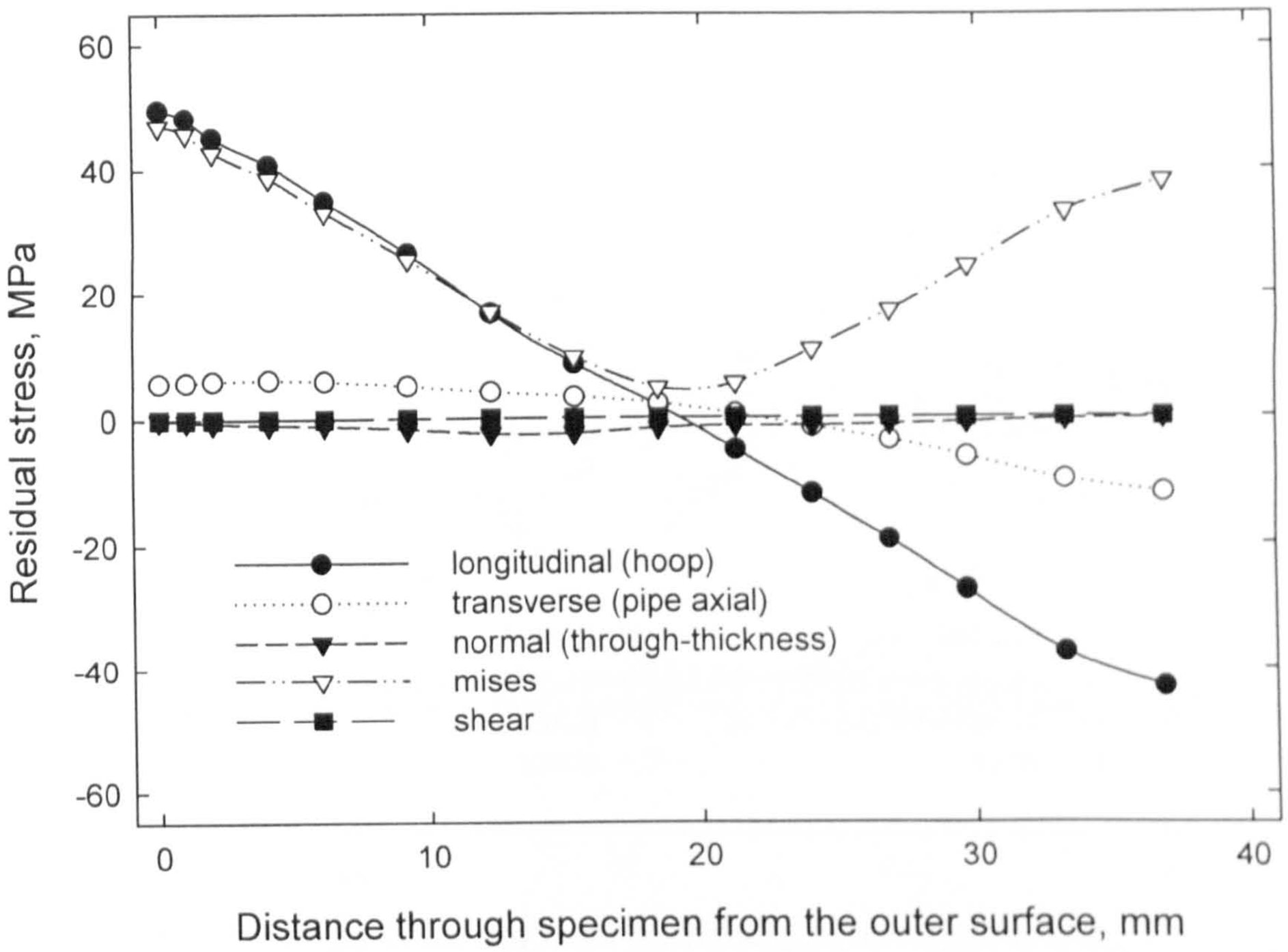

Figure 6.28 Residual stress distributions through the specimen from the outer surface. The residual stresses result in the specimen after loading unloading sequence.

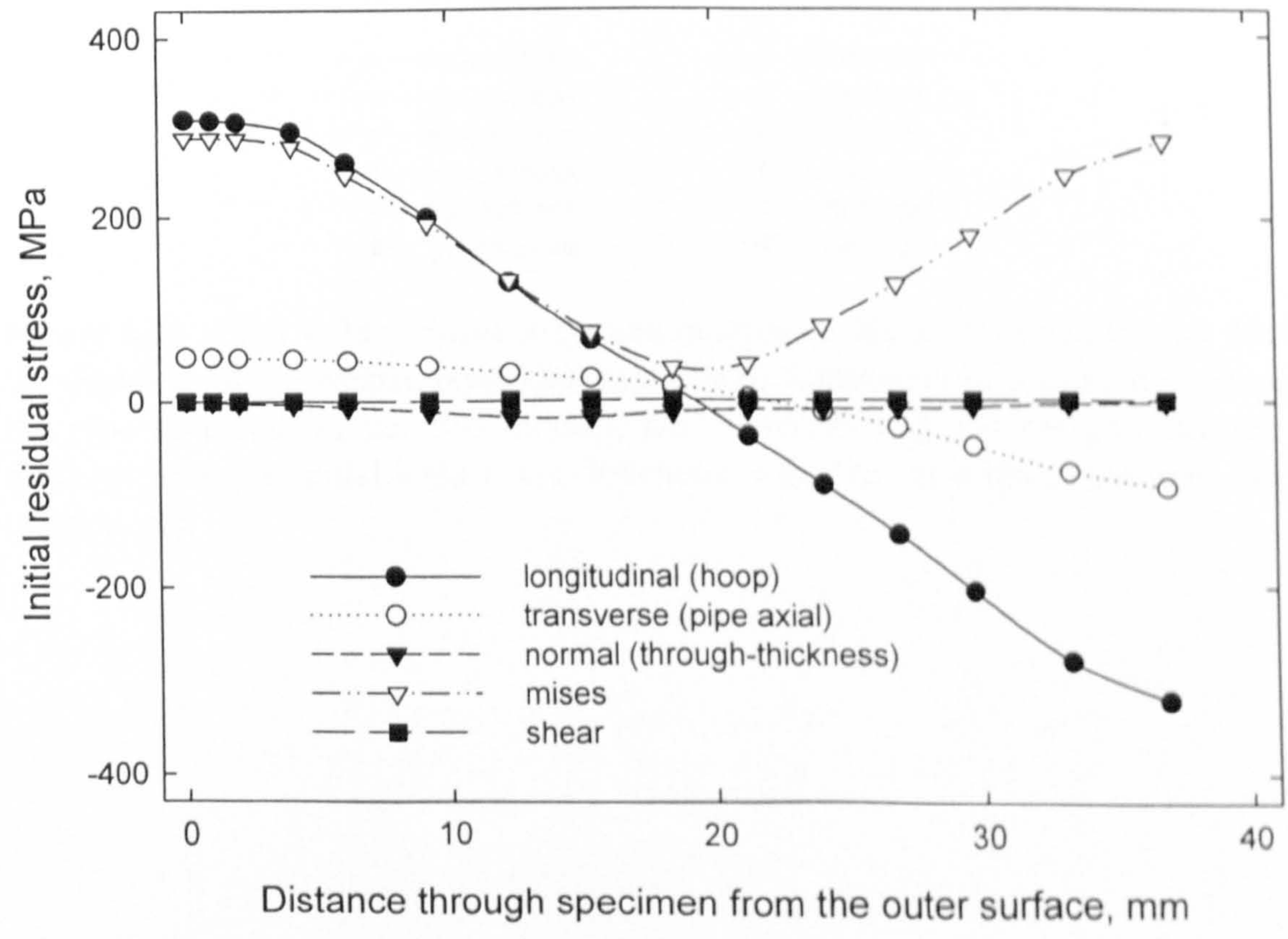

Figure 6.29 Initial applied residual stress distributions through the specimen.

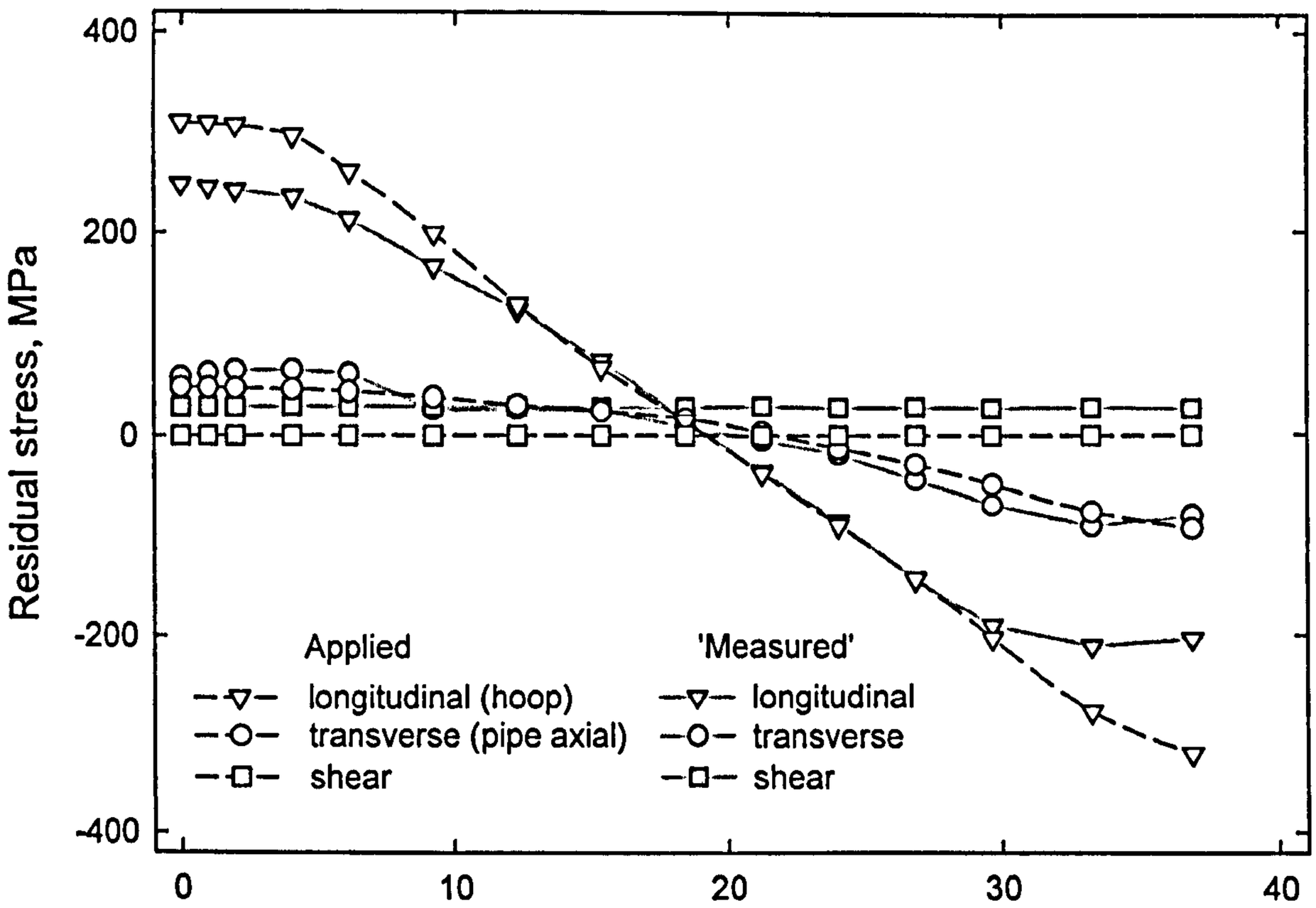

Figure 6.30 Comparison of the initial applied residual stresses with the deep hole reconstructed residual stresses.

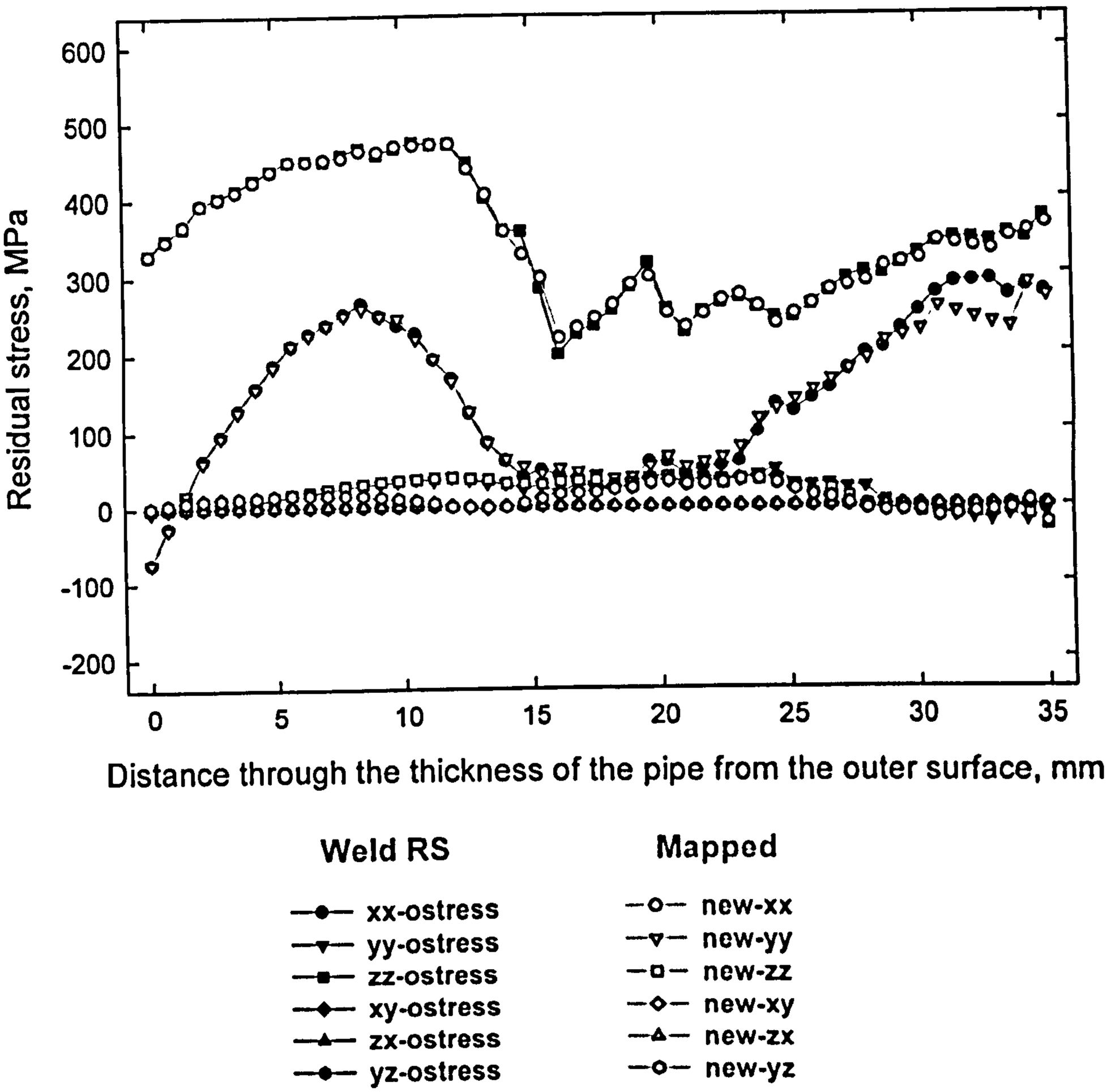

Figure 6.31 Initial weld residual stress and mapped residual stress distribution through the thickness of the welded pipe. Note that due to differences in coordinate systems of the pipe specimen in the two models, the coordinates in the mapped stresses are different from the initial weld stress directions, e.g., "zz" in original becomes "xx" in mapped, etc.

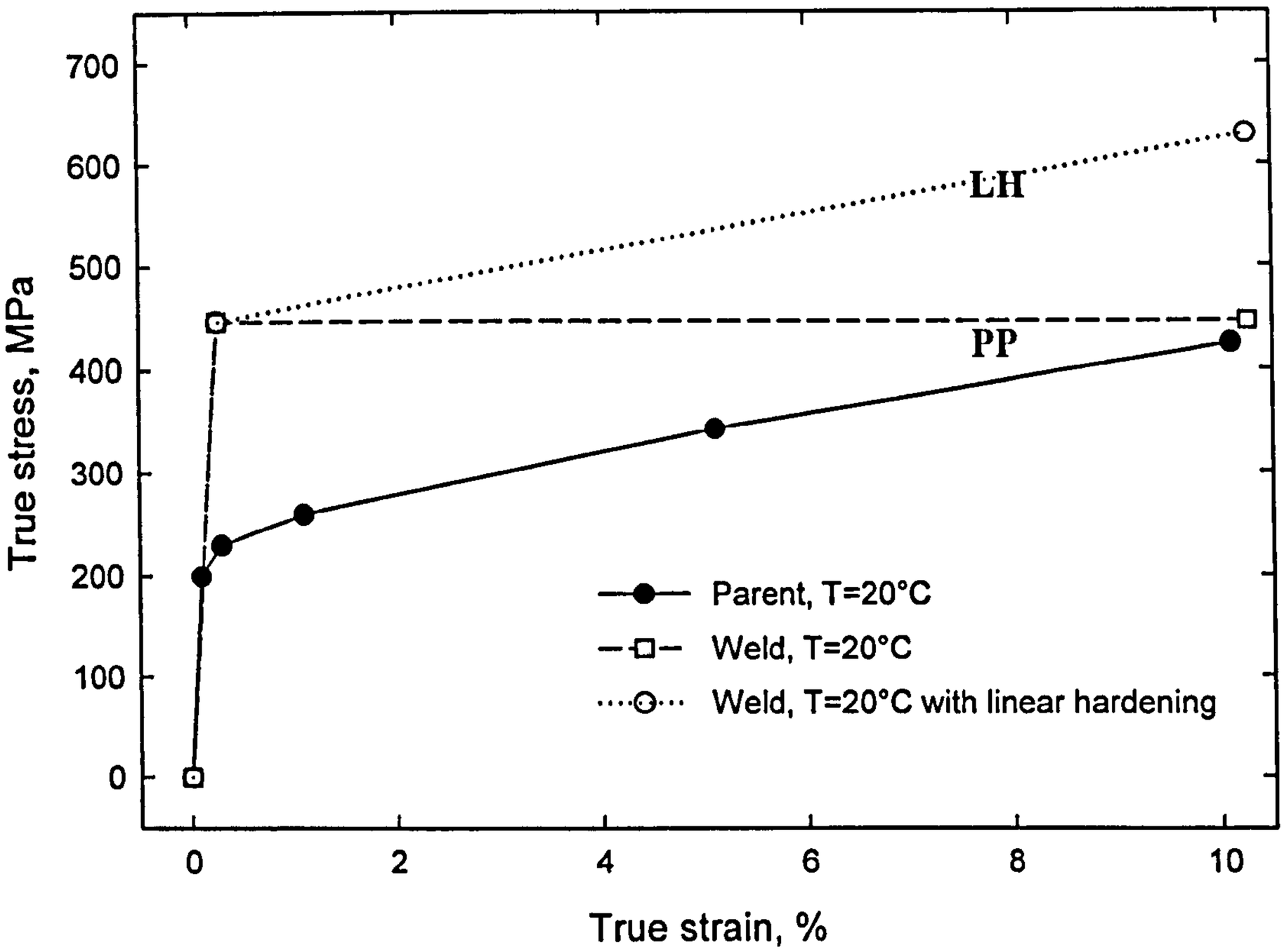

Figure 6.32 Parent and girth weld material properties at room temperature. Also shown is the fictitious weld material property with an identical linear hardening (LH) as the parent material.

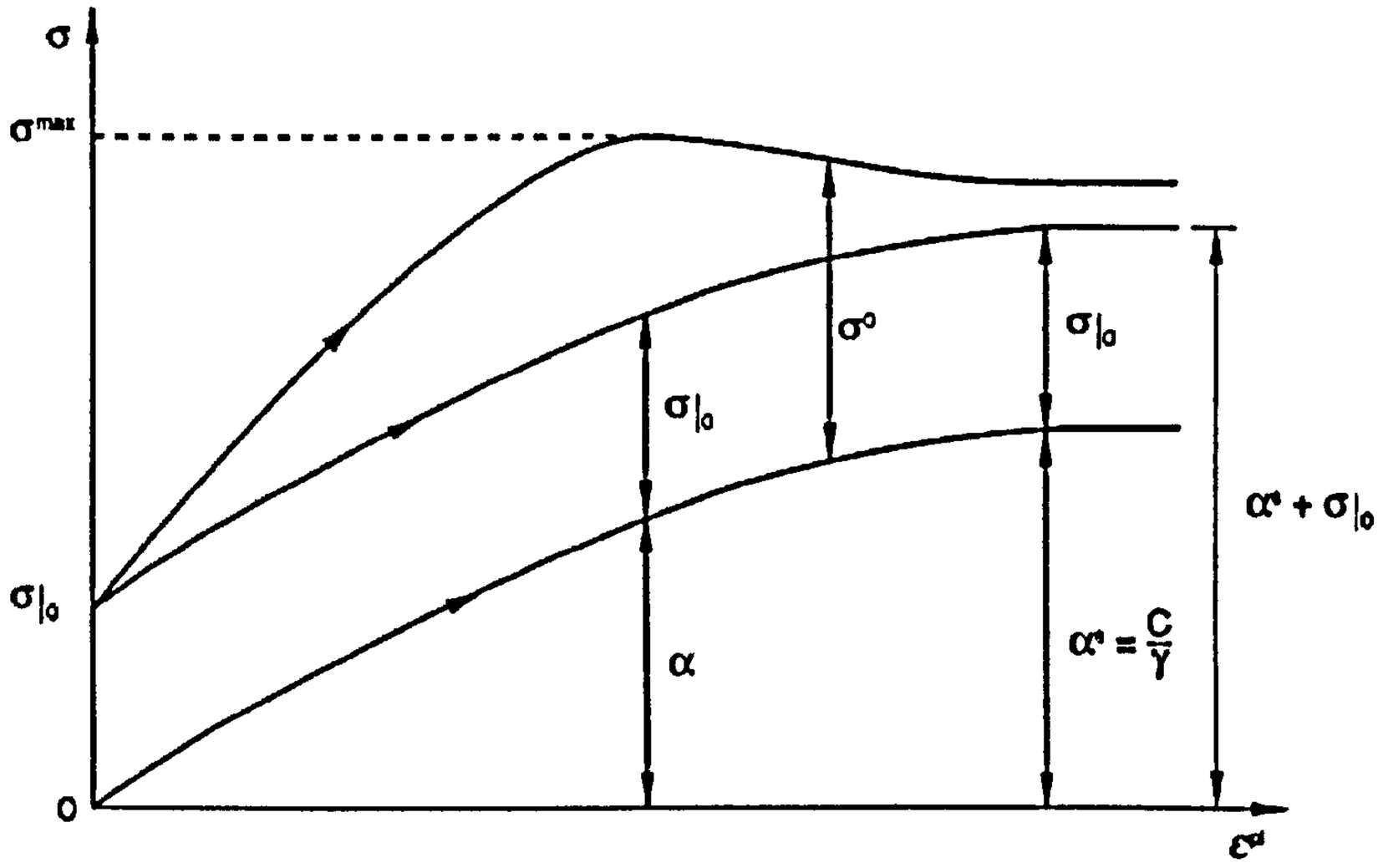

Figure 6.33 Non-linear kinematic hardening model based on VORSAC data.

$$\sigma^0 = \sigma|_0 + Q_\infty(1 - e^{-b\bar{\varepsilon}^{pl}})$$

where $\sigma|_0(\theta, f_i)$ is the yield surface size at zero plastic strain, and $Q_\infty(\theta, f_i)$ and $b(\theta, f_i)$ are additional material parameters that must be calibrated from cyclic test data.

Weld at T=20°C:

$\sigma|_0 = 350\times10^6$ Pa; C = 5003×10^6; $\gamma = 24.42$; Q = 0.0; b = 0.25

Parent at T=20°C:

$\sigma|_0 = 218\times10^6$ Pa; C = 4629×10^6; $\gamma = 20.0$; Q = 0.0; b = 0.25

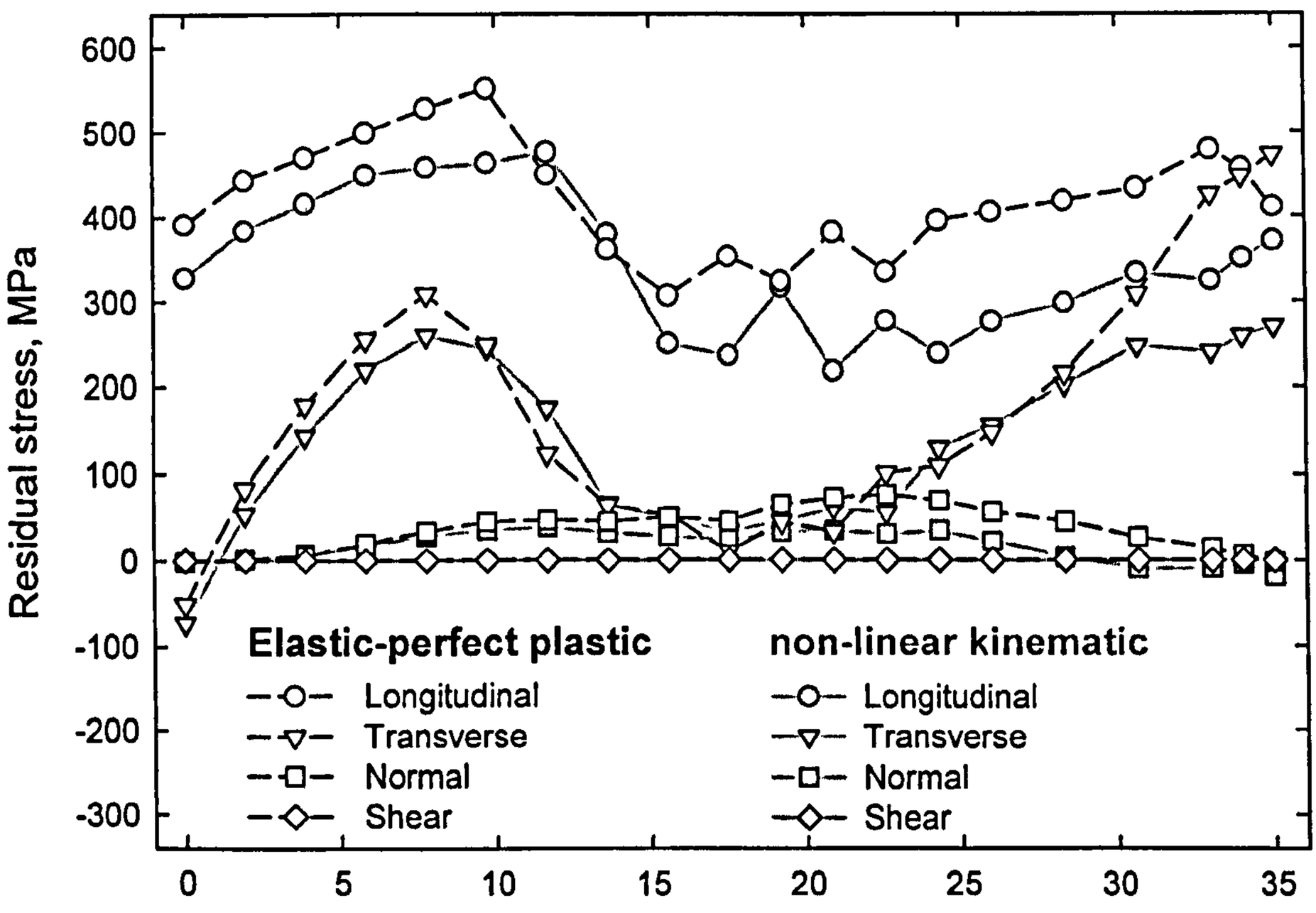

Figure 6.34 Comparison of mapped equilibrium residual stress distribution through the thickness of the pipe specimen along a line, based on two material properties, elastic-perfect plastic and non-linear kinematic hardening models.

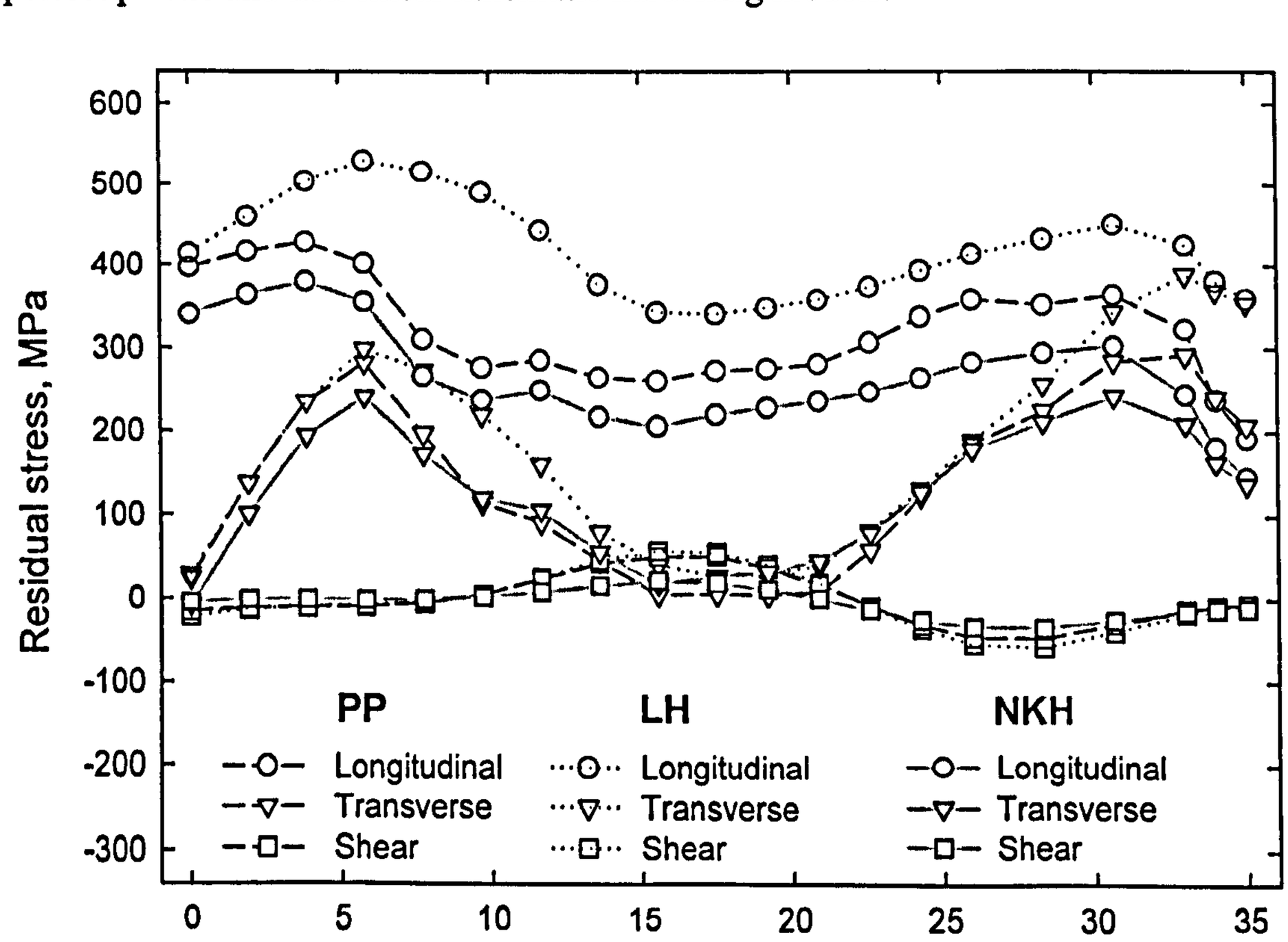

Figure 6.35 Reconstructed deep hole simulated residual stresses.

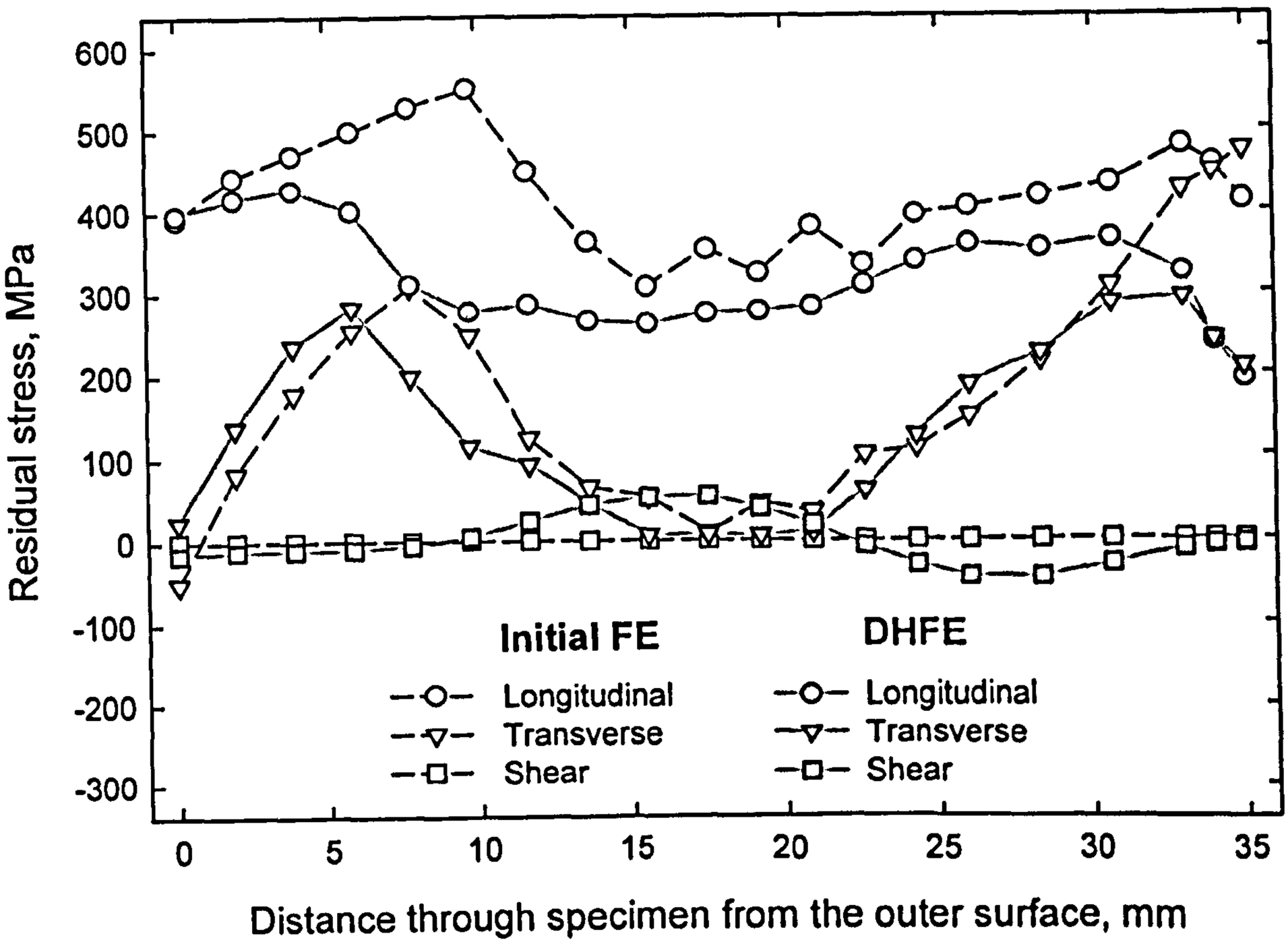

Figure 6.36 Comparison of initial FE residual stresses with reconstructed deep hole simulated residual stresses for elastic perfect plastic (PP) material model.

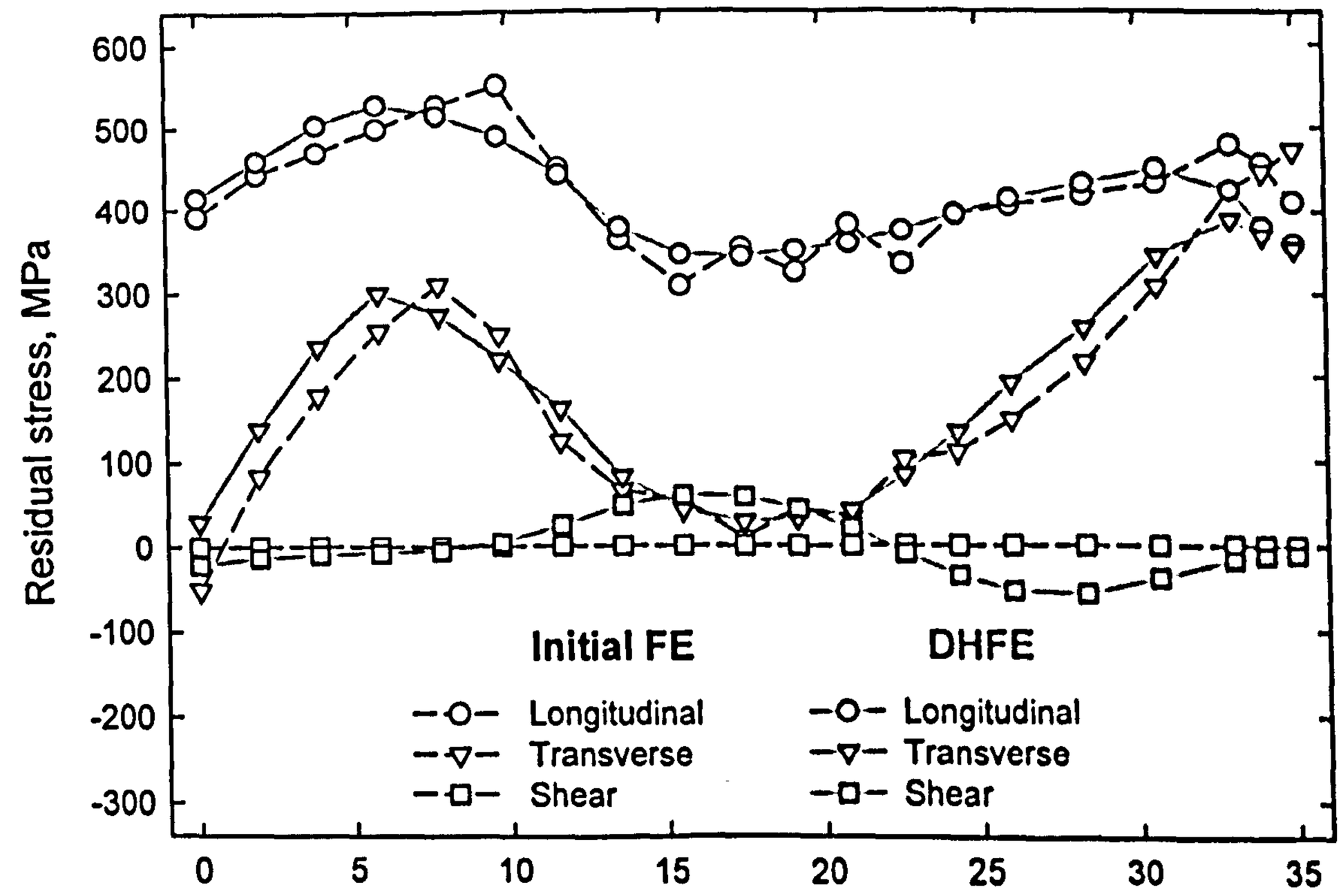

Figure 6.37 Comparison of initial FE residual stresses with reconstructed deep hole simulated residual stresses for linear hardening (LH) material model.

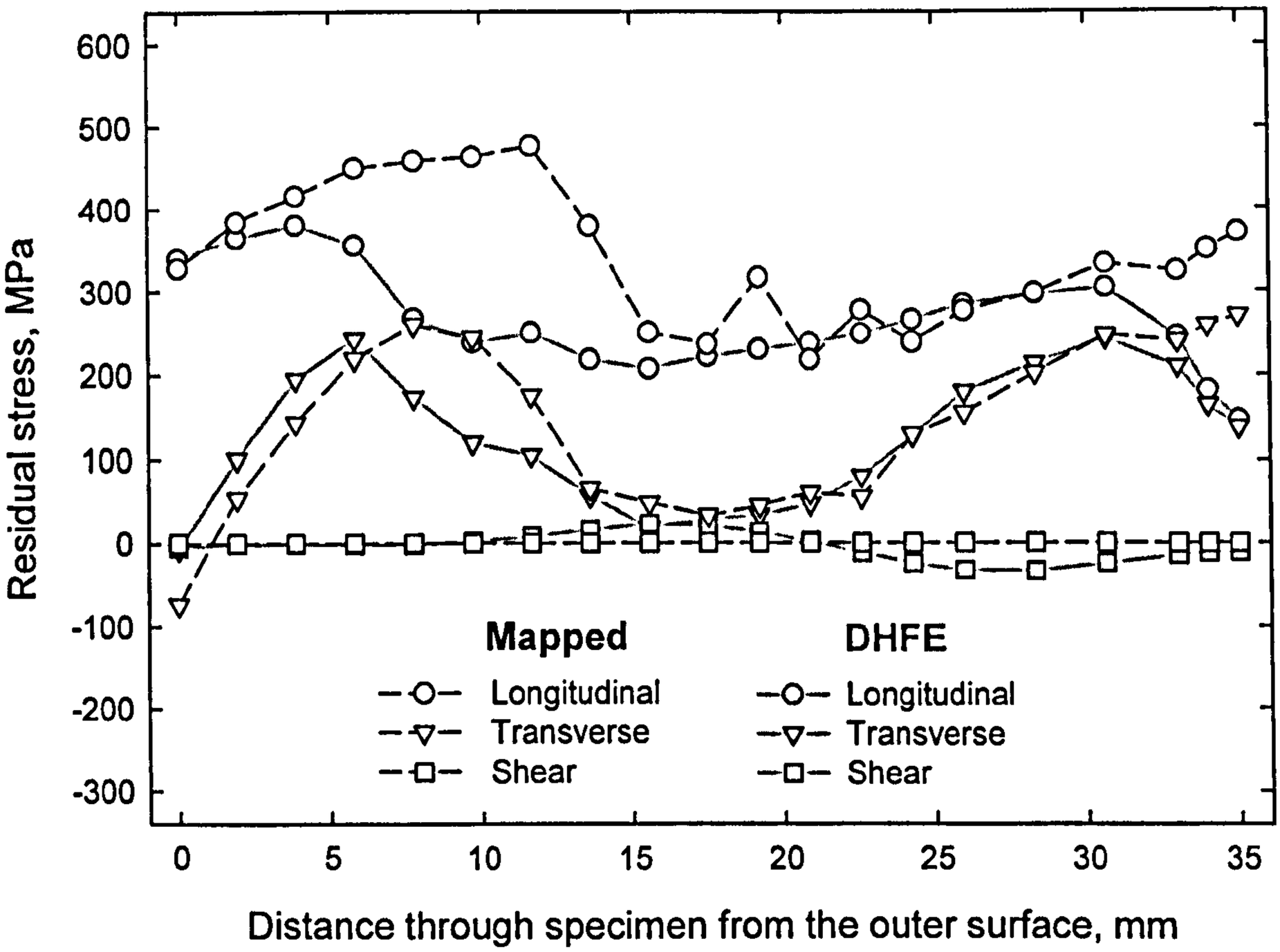

Figure 6.38 Comparison of initial FE residual stresses with reconstructed deep hole simulated residual stresses for non-linear kinematic hardening (NKH) material model.

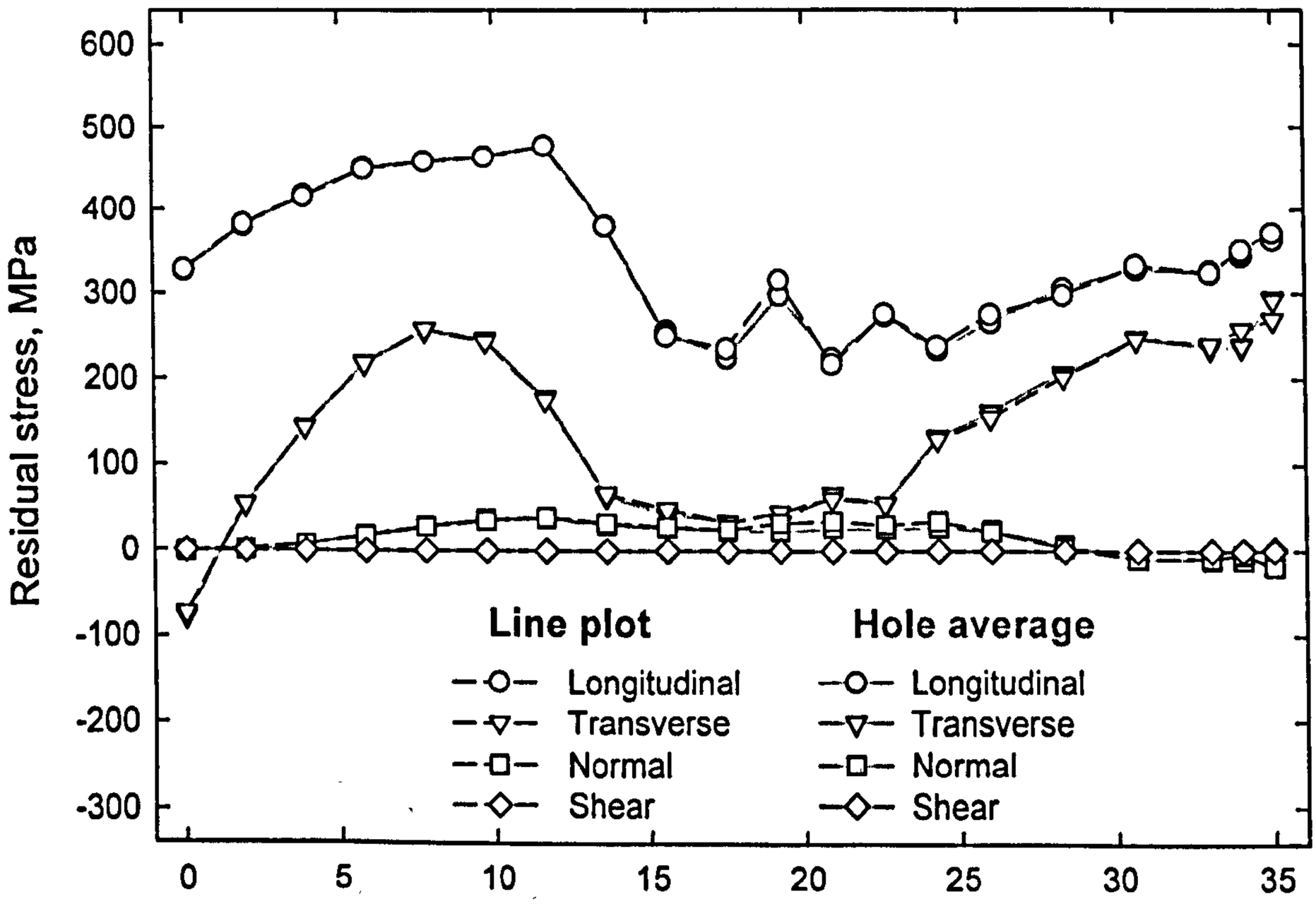

Figure 6.39 Initial FE predicted residual stresses through the thickness of the pipe from outer surface along a line compared with a hole-average.

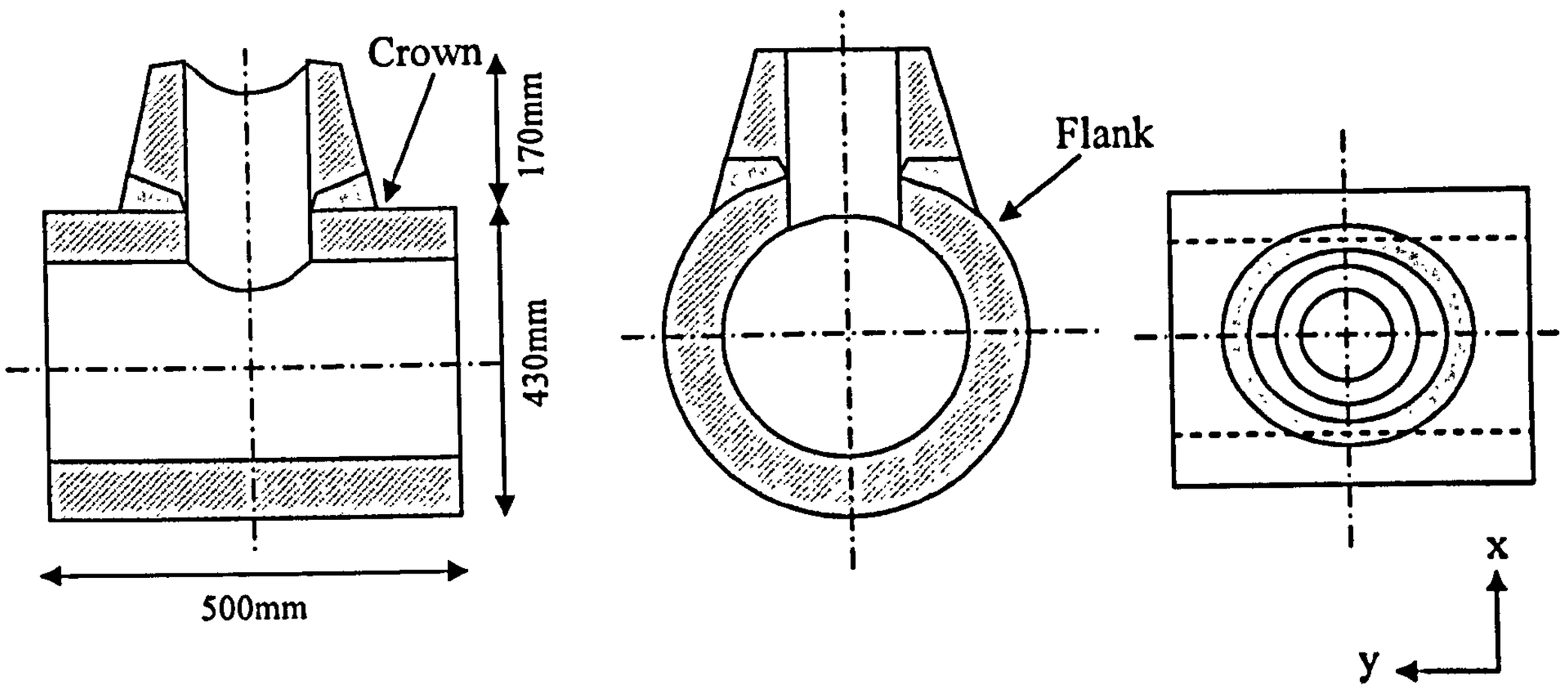

Figure 6.40 Nozzle Arrangement, Mock-up specimen S4.

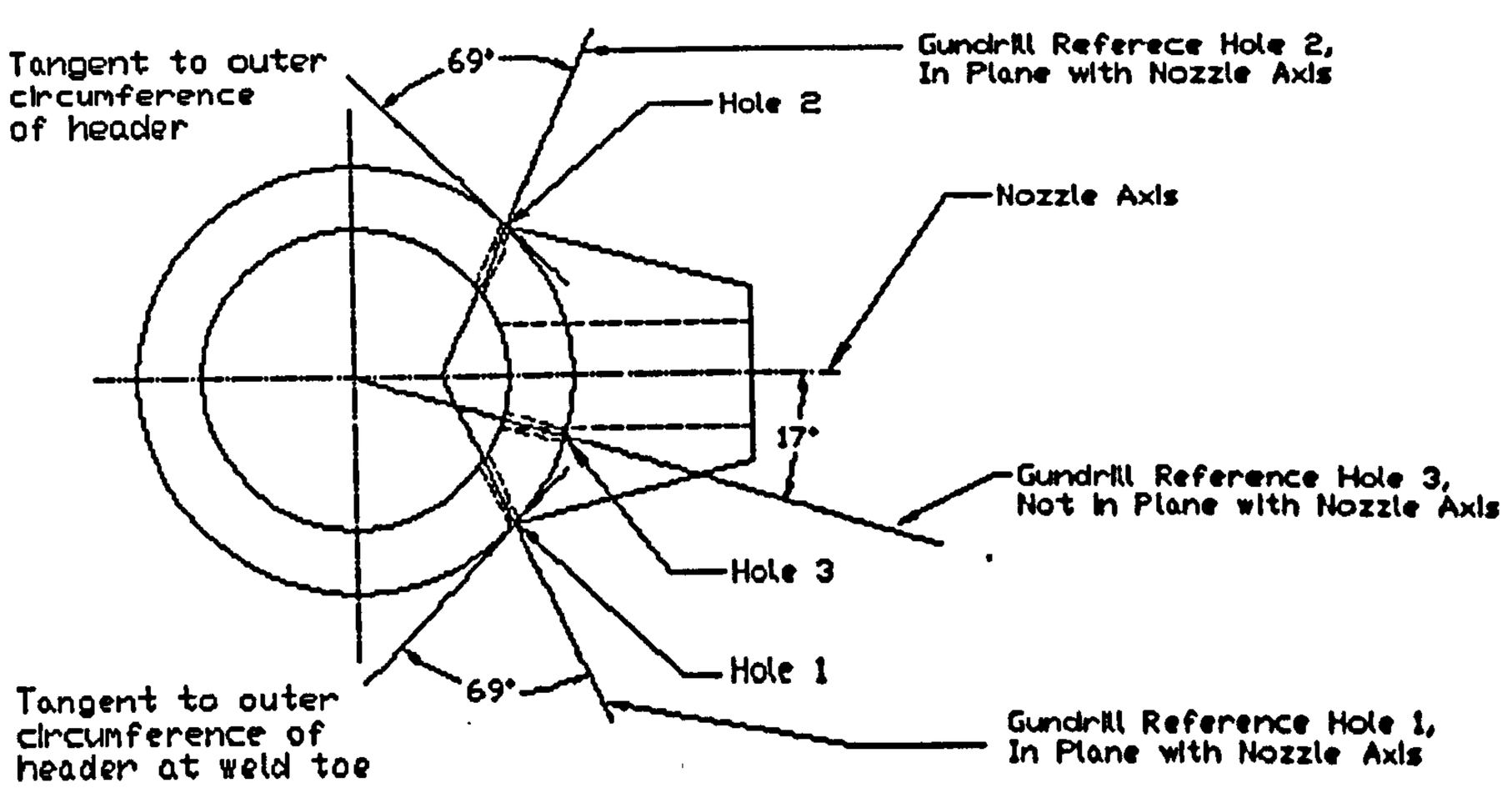

Figure 6.41 Location of deep hole measurements on mock-up S4 specimen.

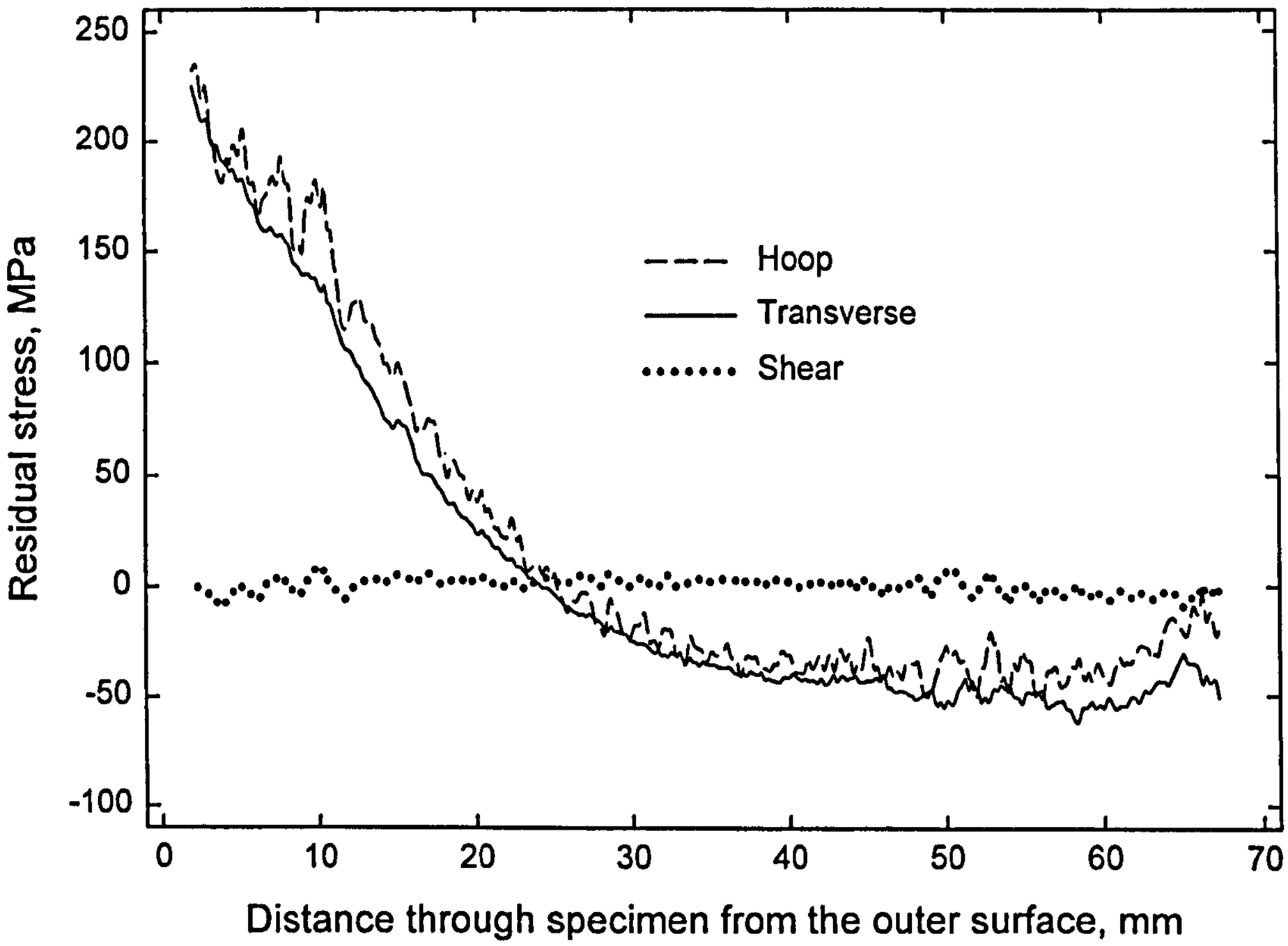

(a) At the flank (Hole 2)

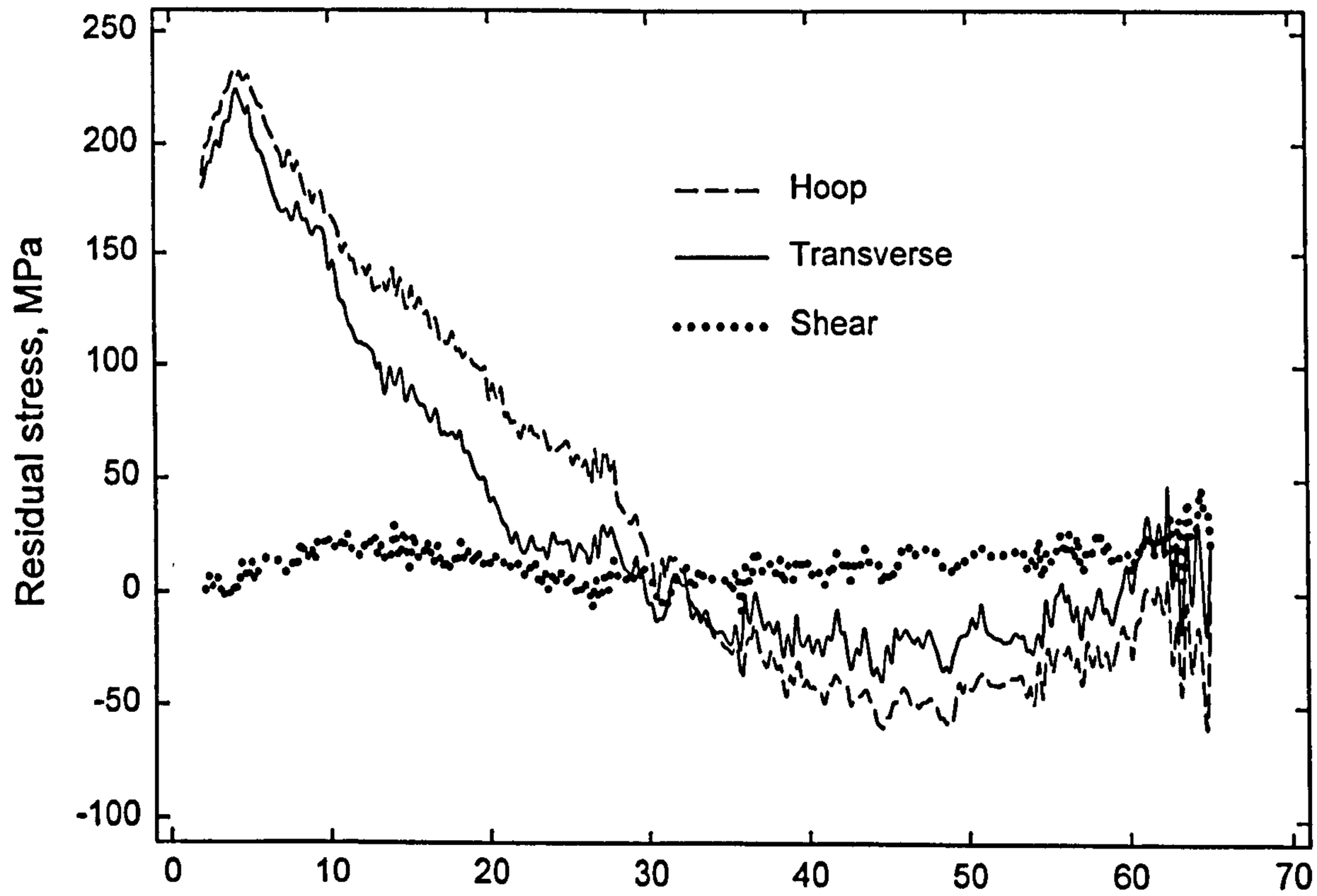

(b) Near the crown (Hole 3)

Figure 6.42 Measured residual stresses after thermal soak test at 550°C for 19,644 h.

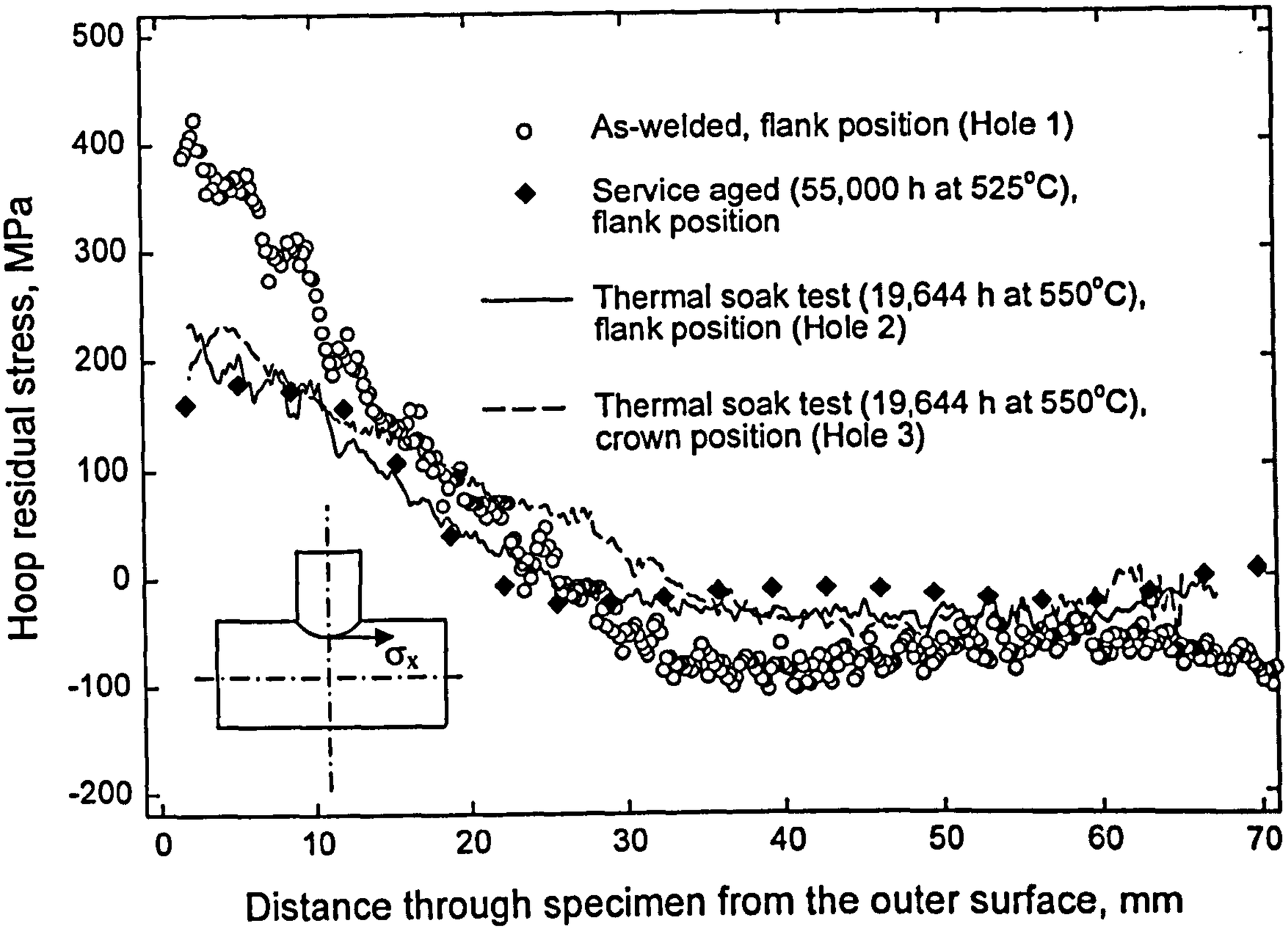

(a) Hoop residual stresses

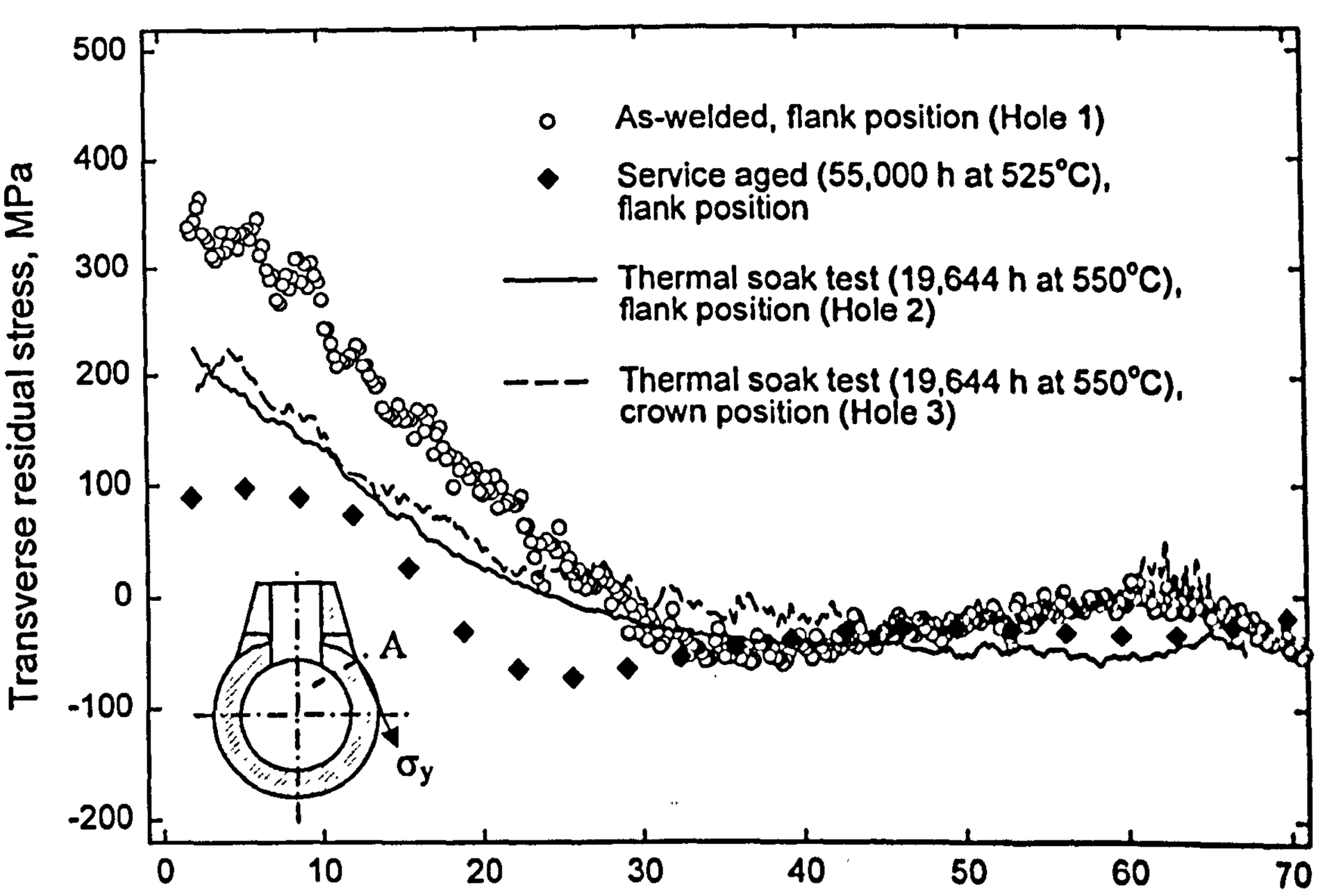

(b) Transverse residual stresses

Figure 6.43 Comparison of measured residual stresses at the nozzle after the thermal soak test (19,644 h at 550°C) with the as-welded state and measured stresses from a service-aged (55,000 h at 525°C) component.

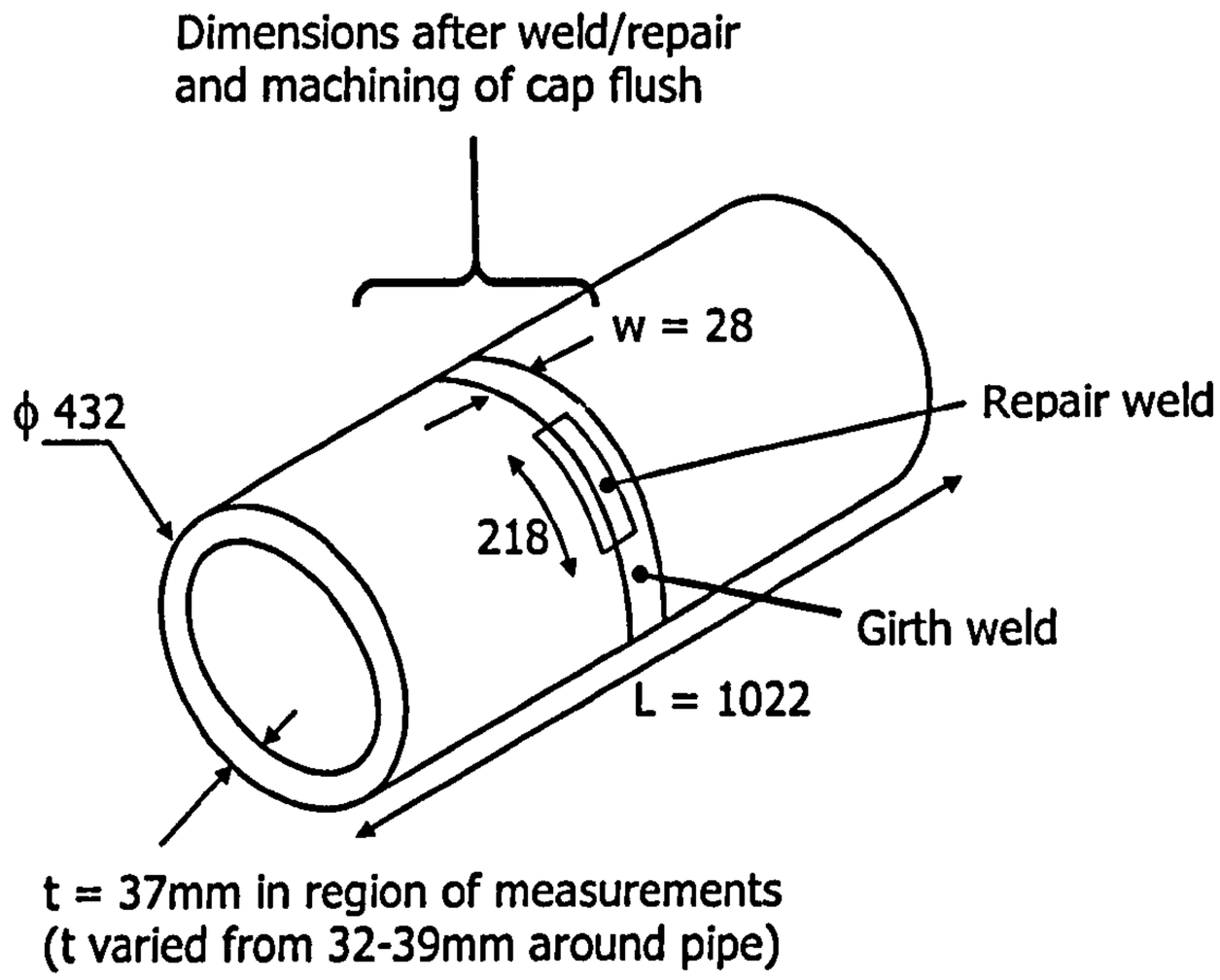

Figure 6.44 Arrangement of stainless steel pipe girth weld (dimensions in mm).

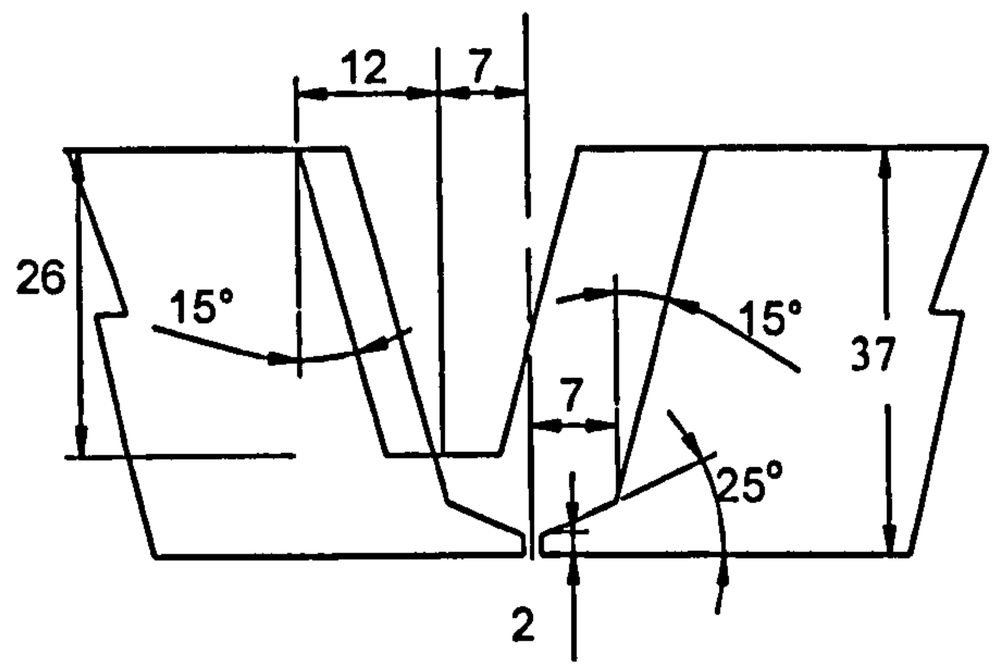

(a) Schematic of axial cross-section through original and repair weld preparations (dimensions in mm).

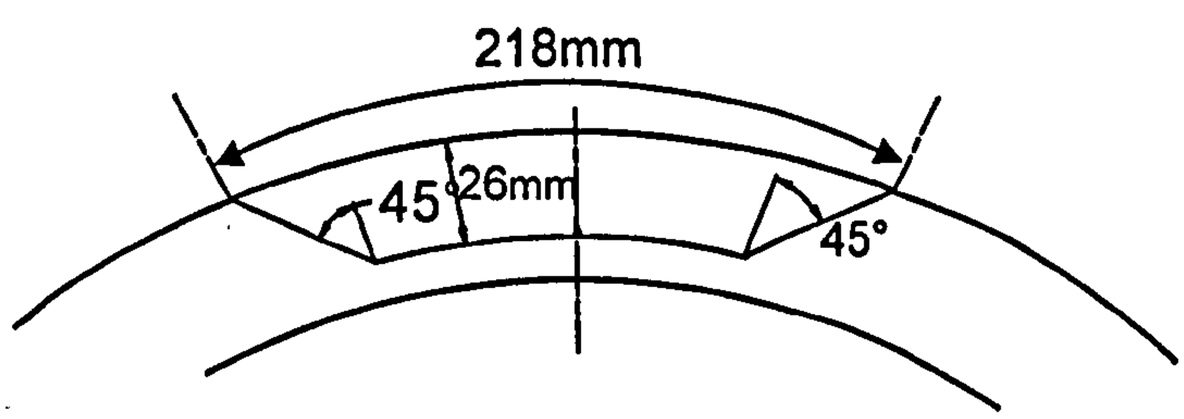

(b) Schematic of hoop cross-section through repair weld excavation.

Figure 6.45 Set-up of butt-weld and offset repair weld (all dimensions in mm).

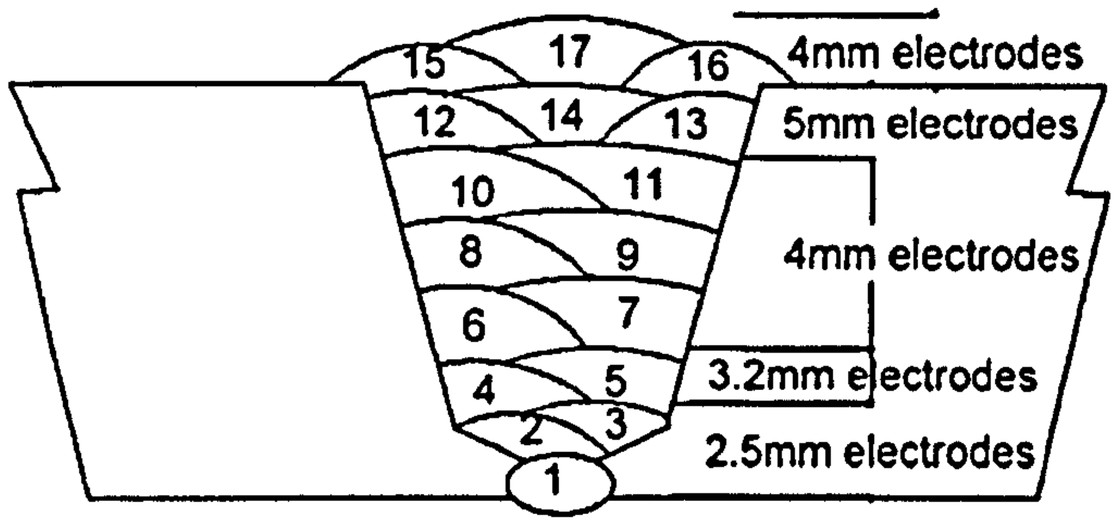

(a) Original weld

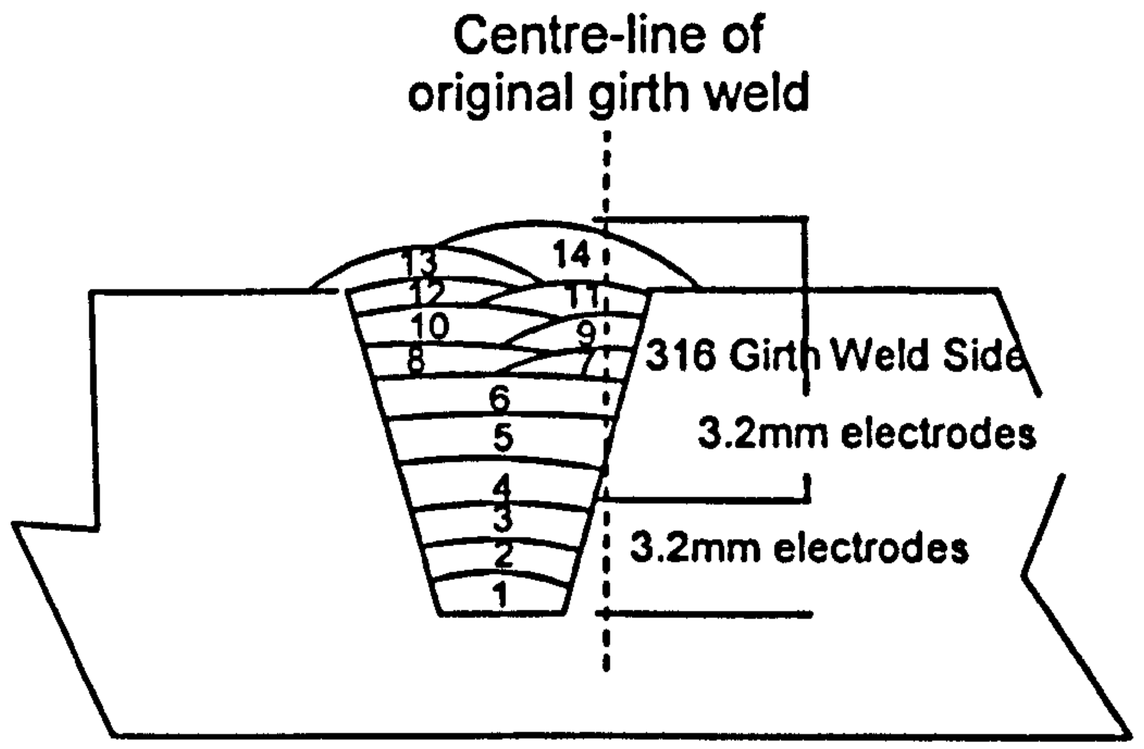

(b) Repair weld

Figure 6.46 Bead run sequence.

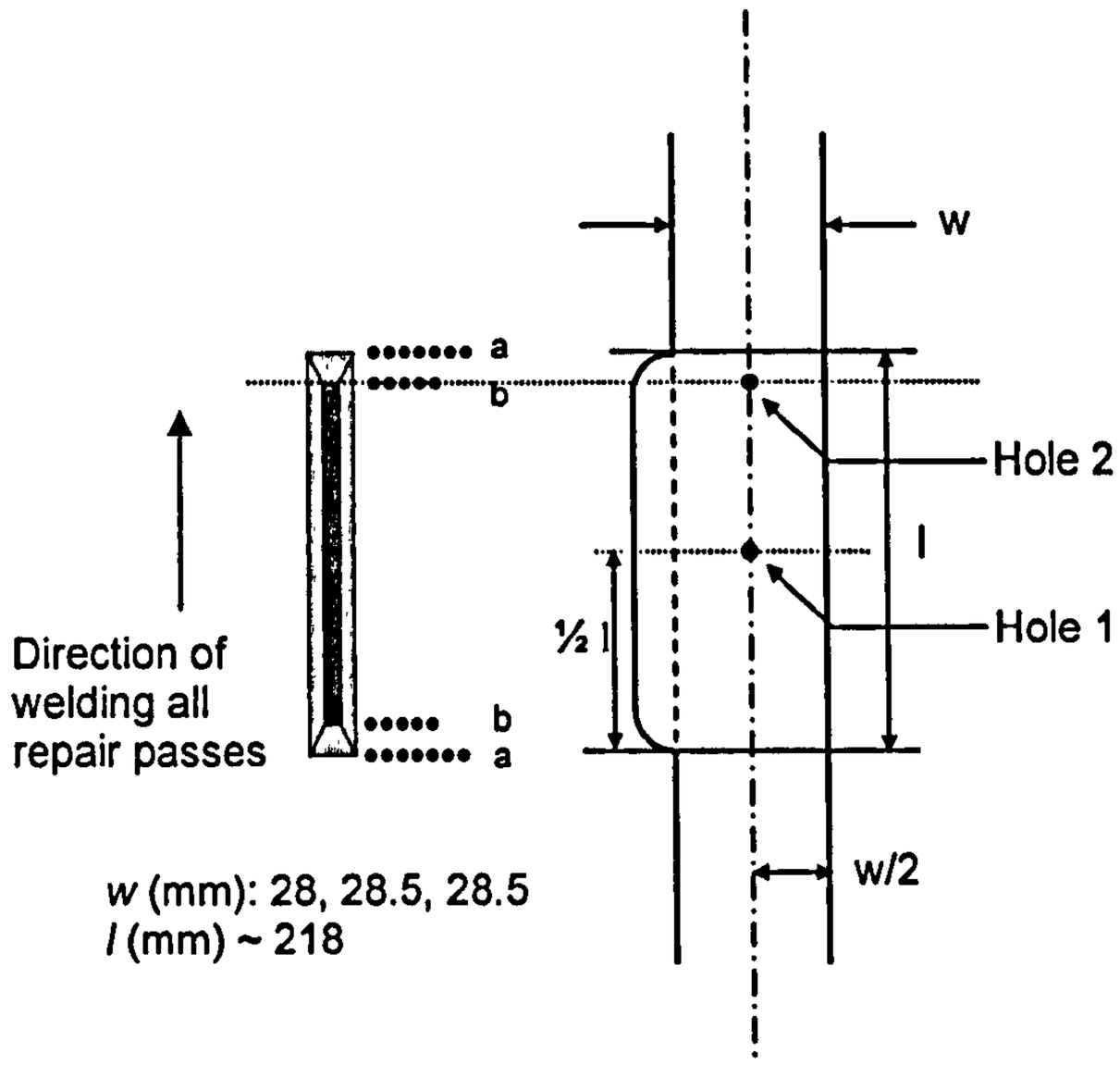

Figure 6.47 Locations of Deep Hole Measurements.

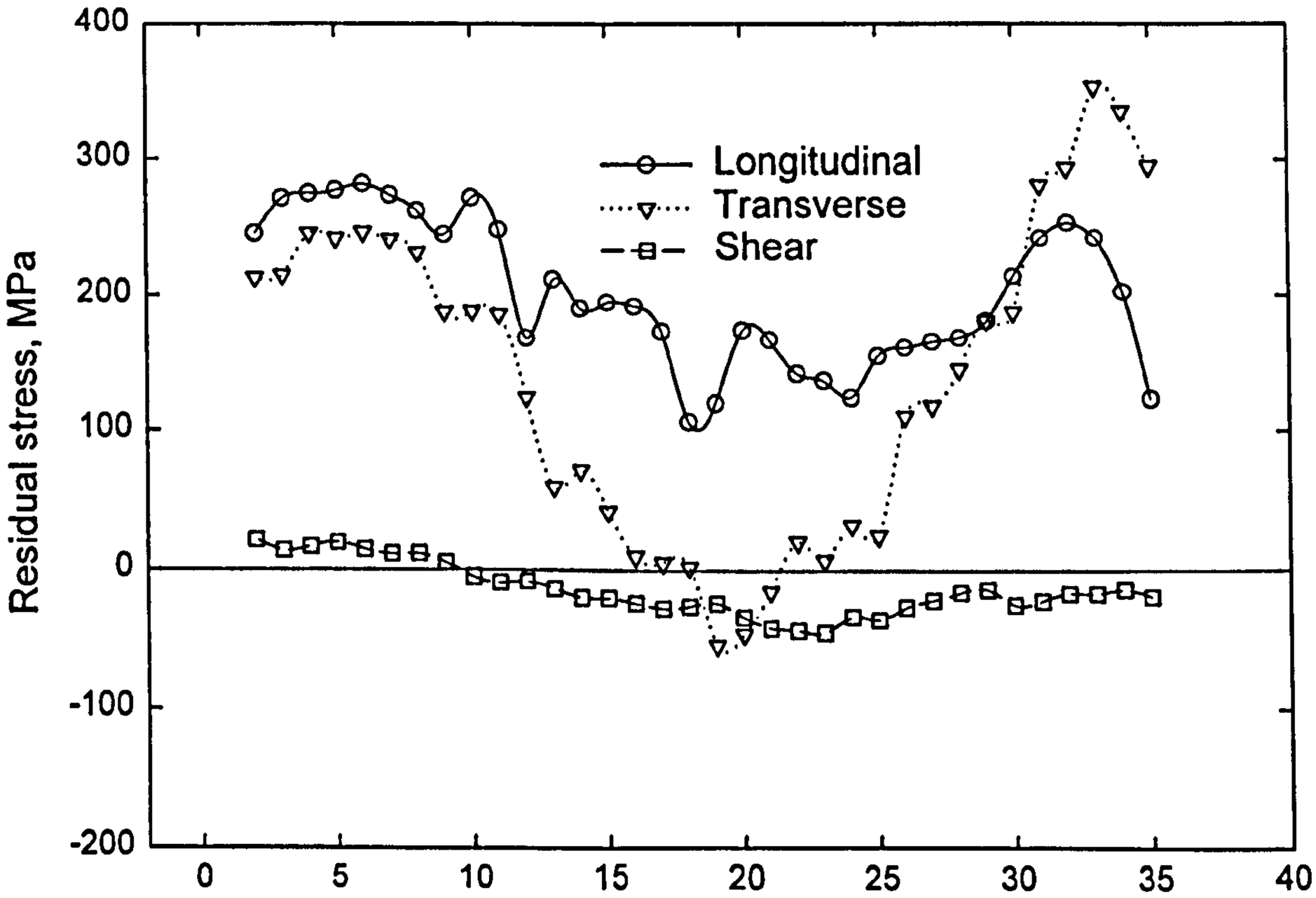

Figure 6.48 Measured residual stresses near the intersection of the girth centreline with the mid-length of the repair weld (Hole 1).

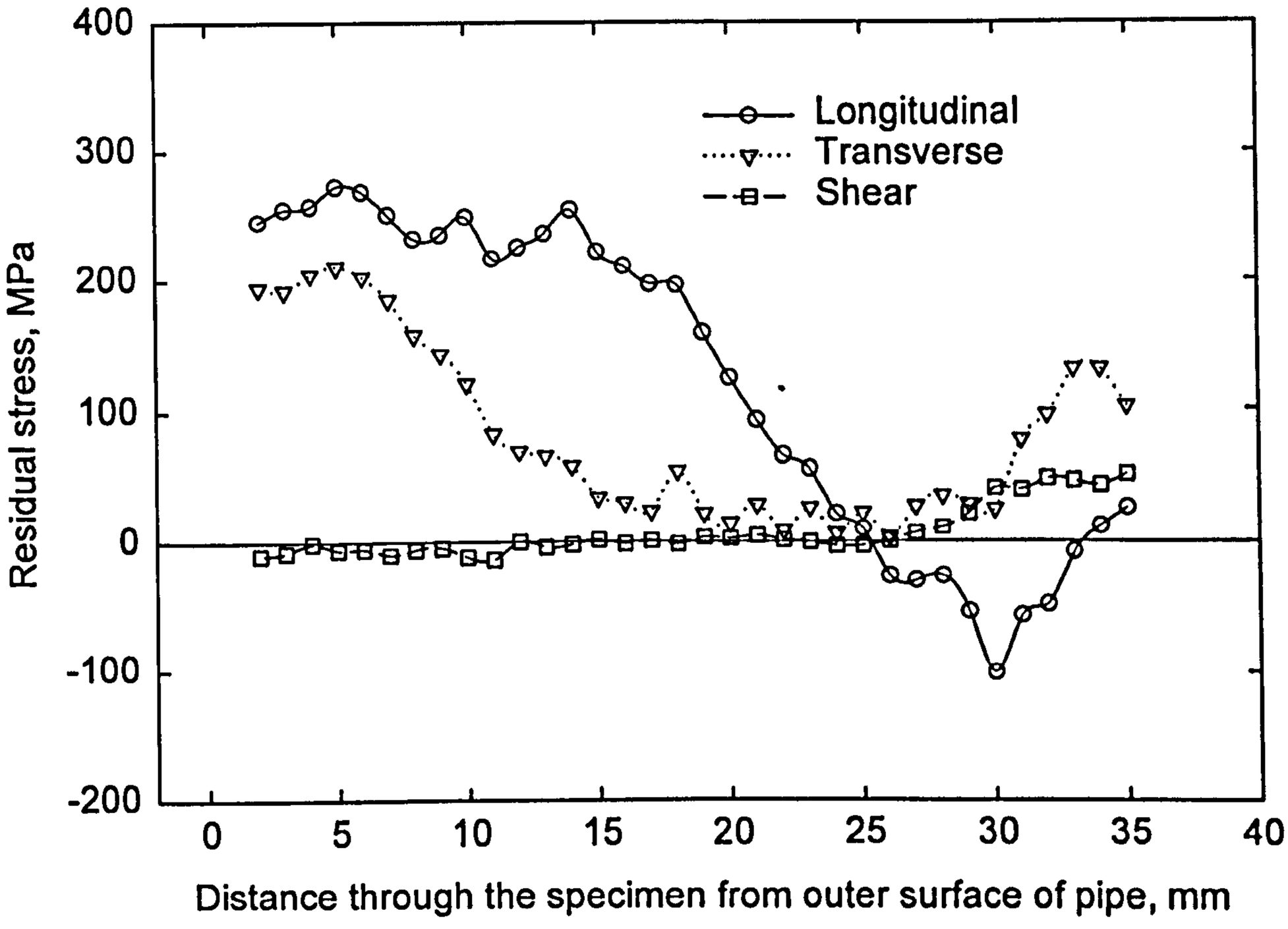

Figure 6.49 Measured residual stresses along the girth weld centreline at the stop end of the repair weld (Hole 2).

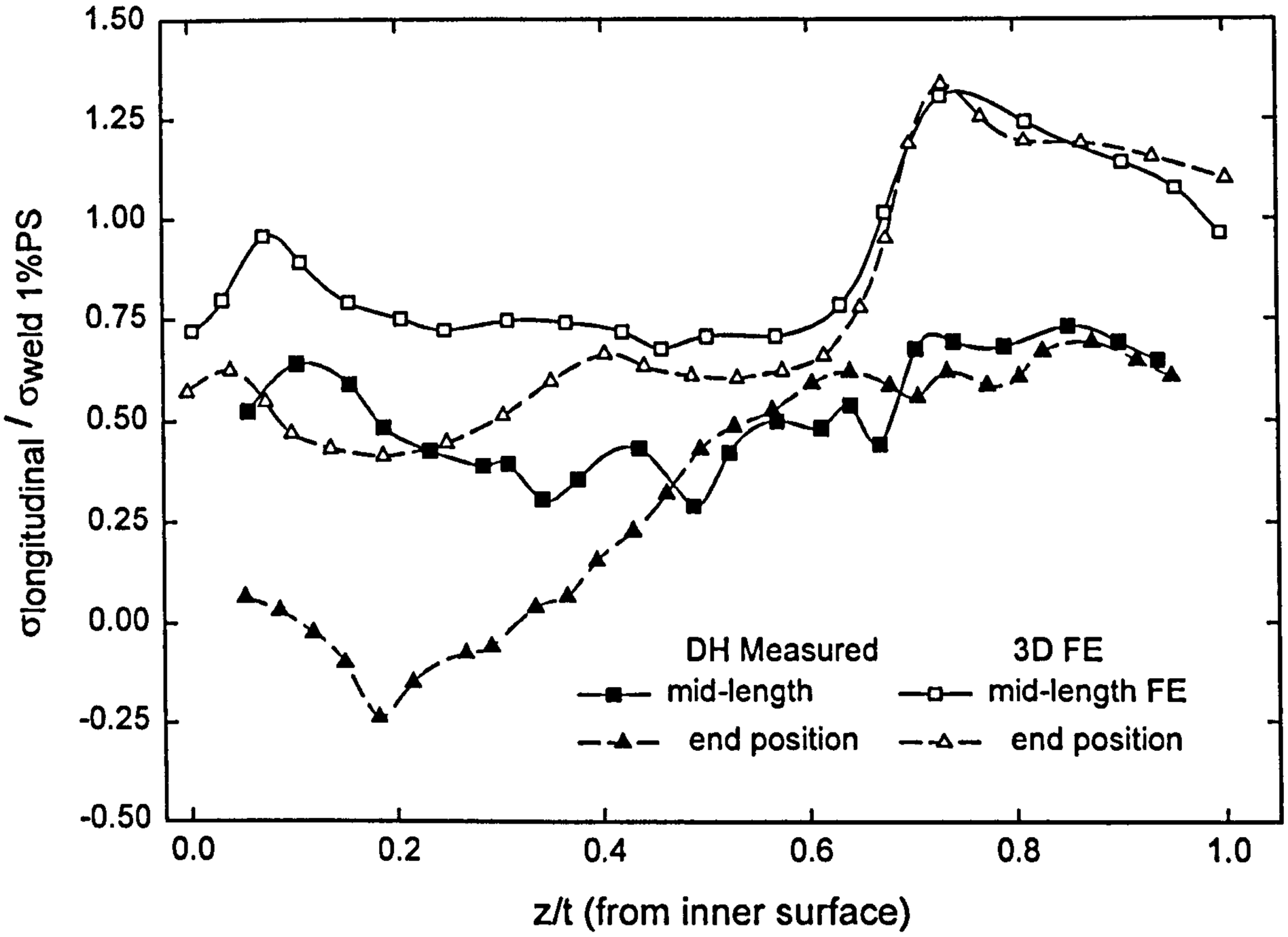

(a) Longitudinal

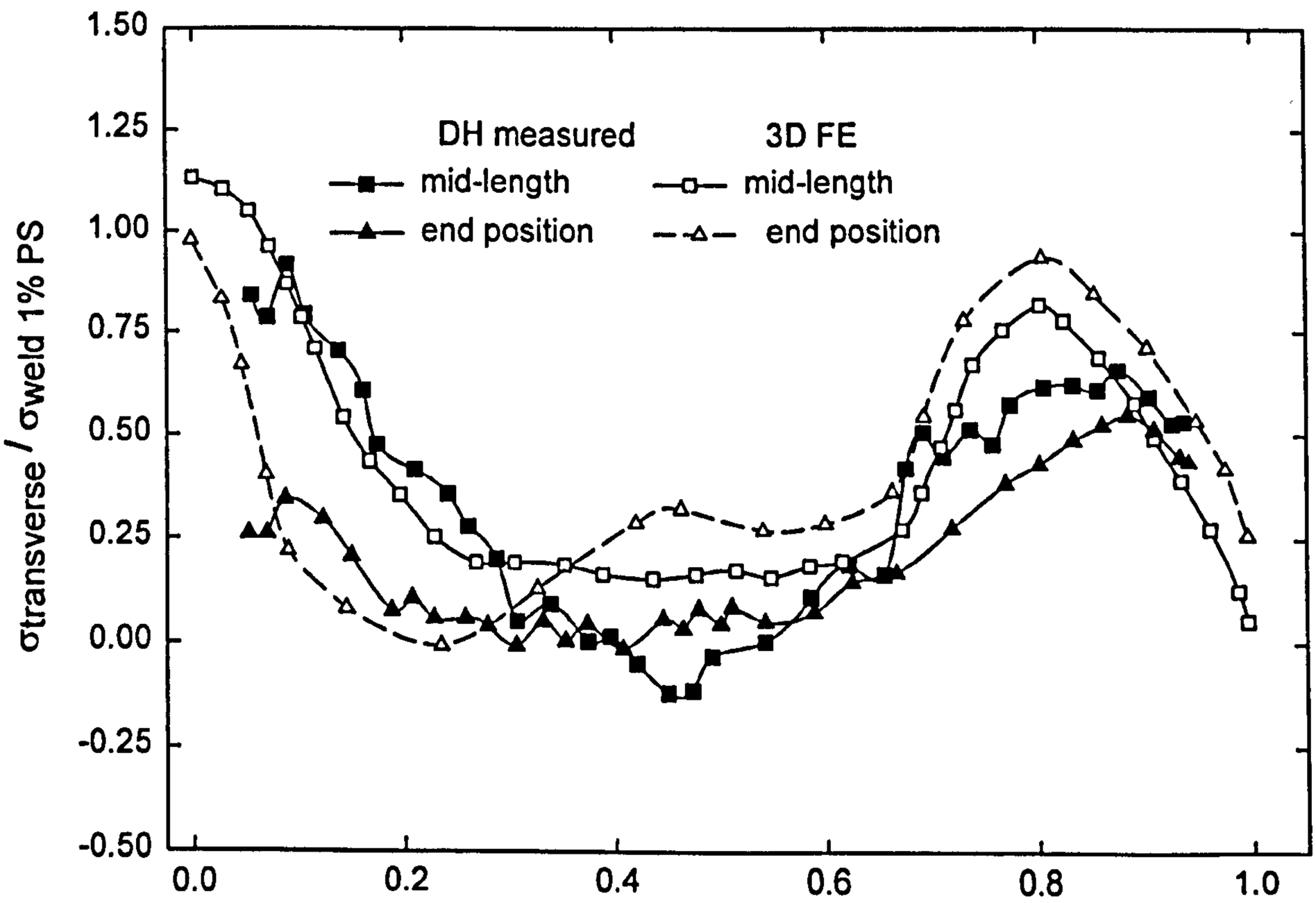

(b) Transverse

Figure 6.50 Measured residual stresses in a 218mm long, offset, 316 Stainless Steel repair weld compared with 3D FE predictions for a similar Esshete Repair.

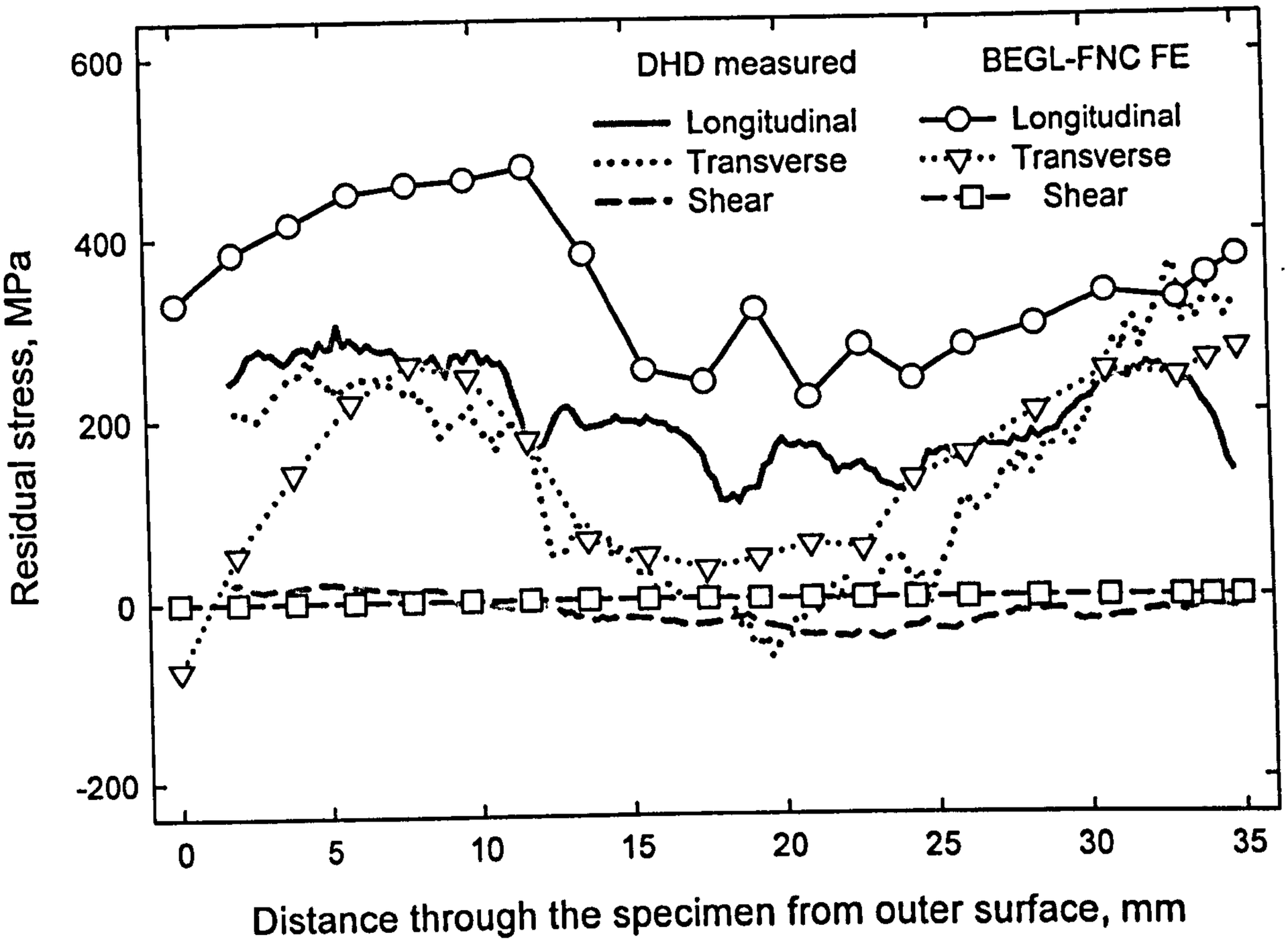

Figure 6.51 Measured residual stresses at mid-length of repair weld (Hole 1) compared with predicted residual stresses mapped from BEGL-FNC model (see Figure 6.38).

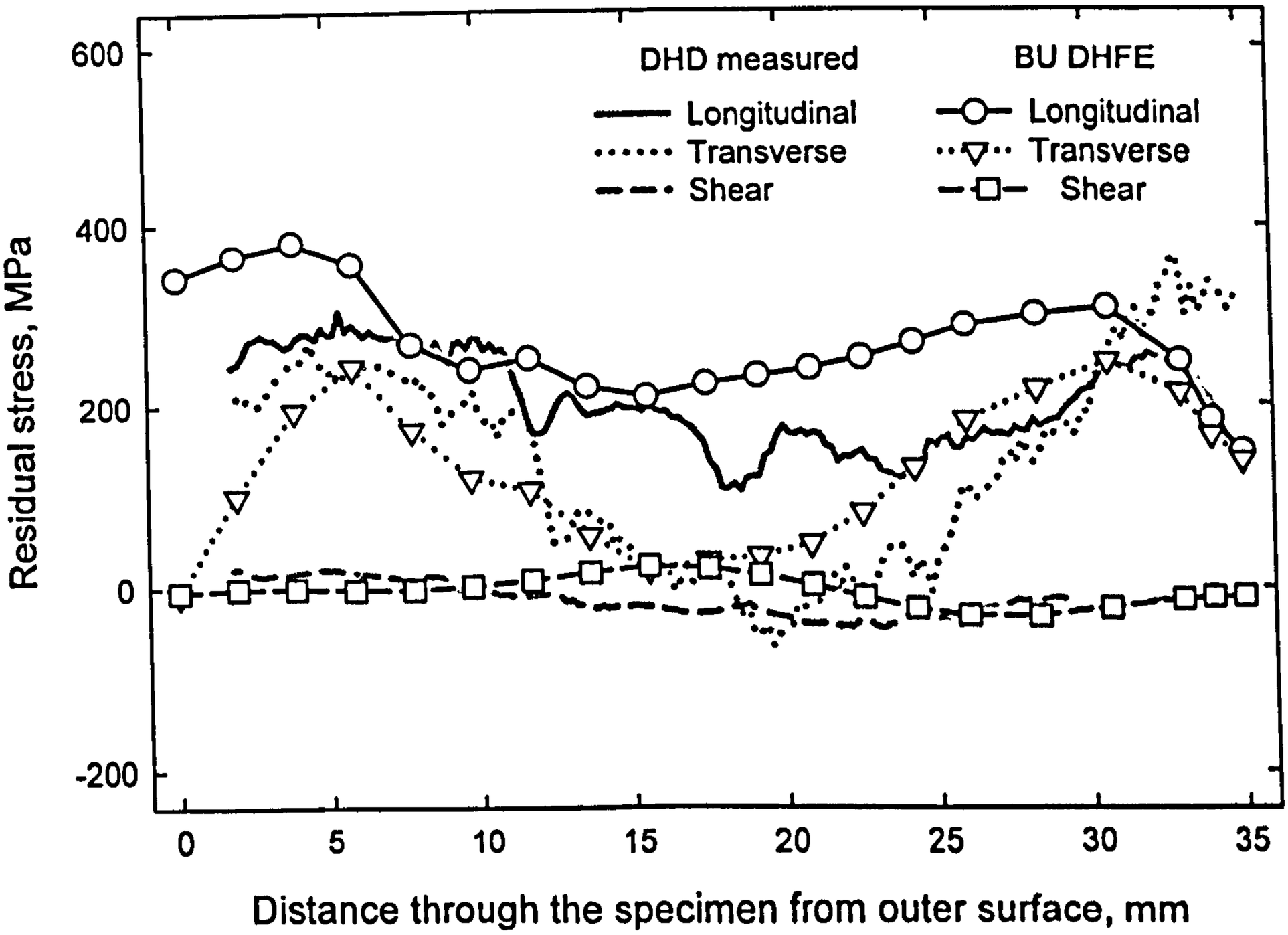

Figure 6.52 Comparison of measured residual stresses at mid-length of the repair weld (Hole 1) with the DH FE reconstructed residual stresses (see Figure 6.38).

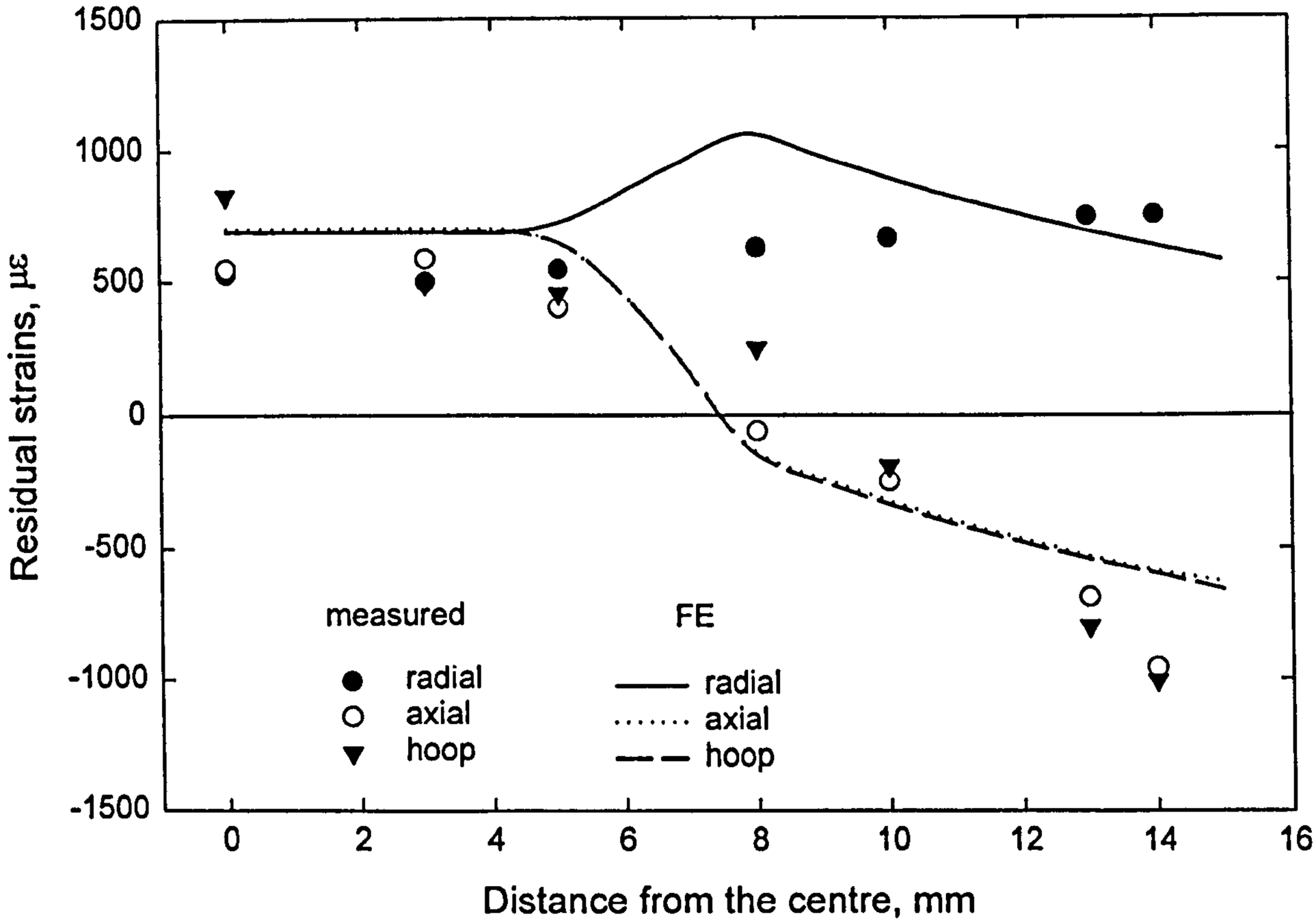

Figure 7.1 Summary of the measured strains and FE strains with heat transfer coefficient $h = 7000$ W/m^2 K and kinematic hardening model in quenched sphere *s8*.

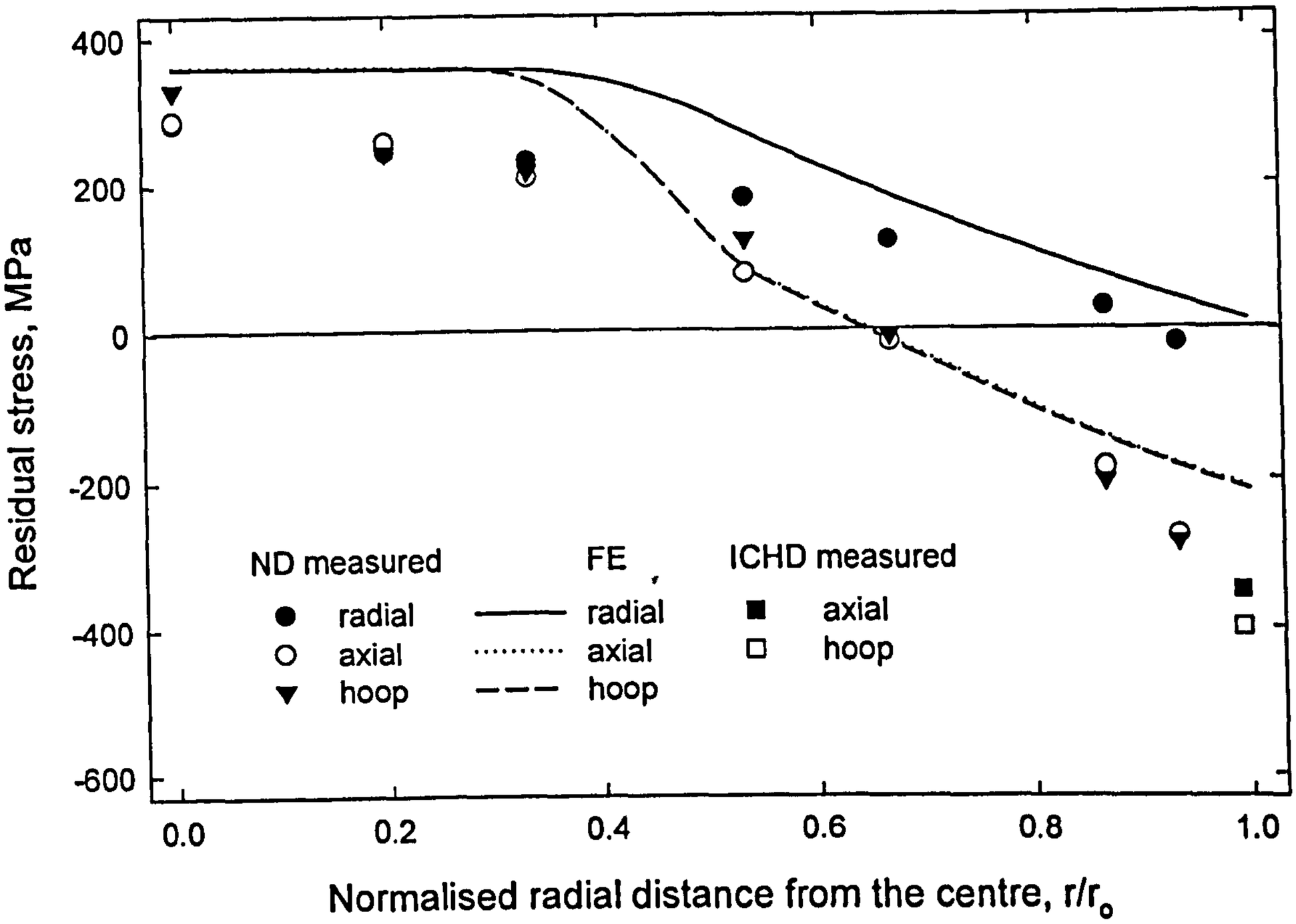

a) Isotropic hardening

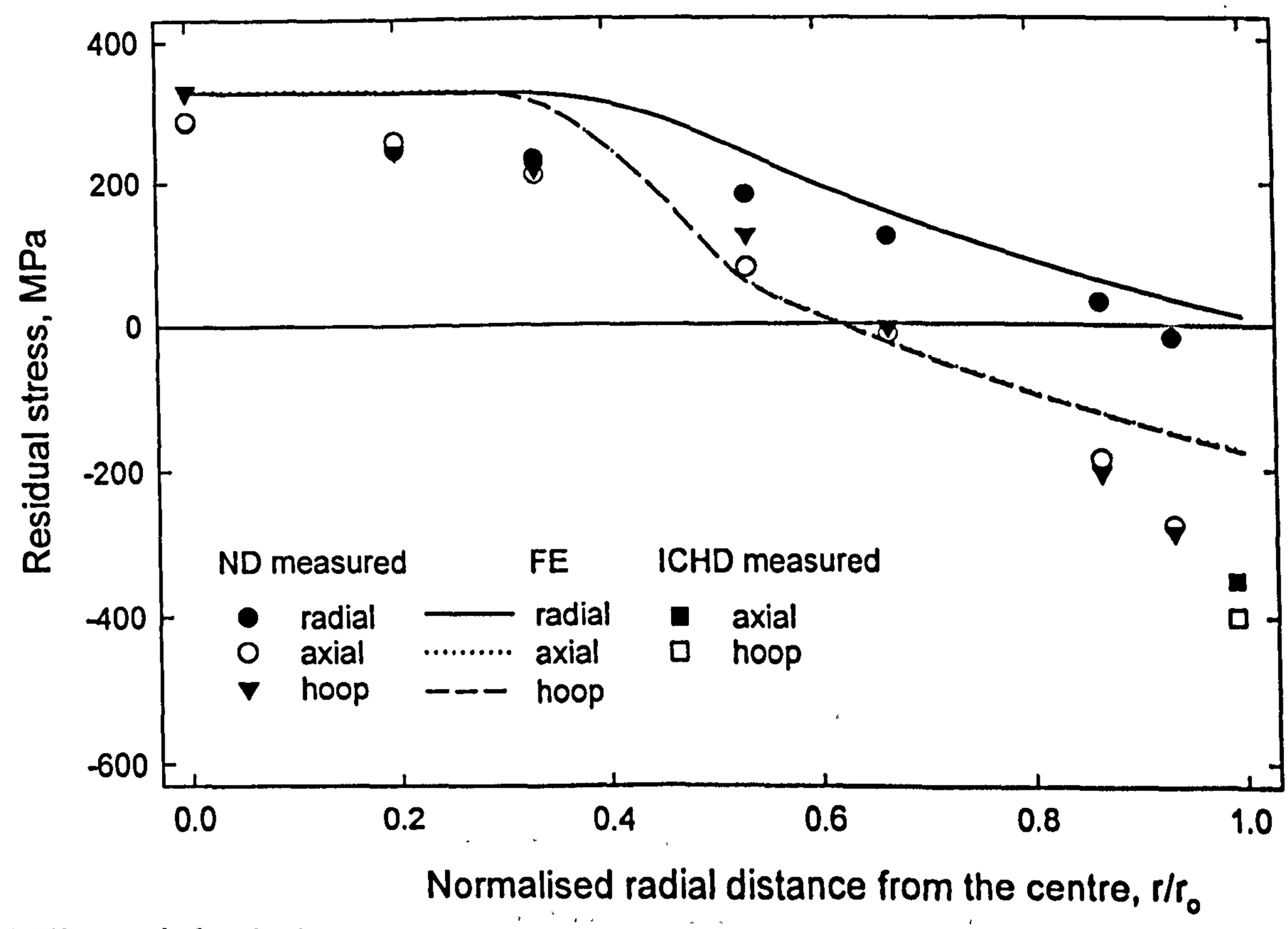

b) Kinematic hardening

Figure 7.2 Measured residual stresses compared with FE predictions with heat transfer coefficient $h = 7000$ W/m^2 K in quenched sphere *s8*.

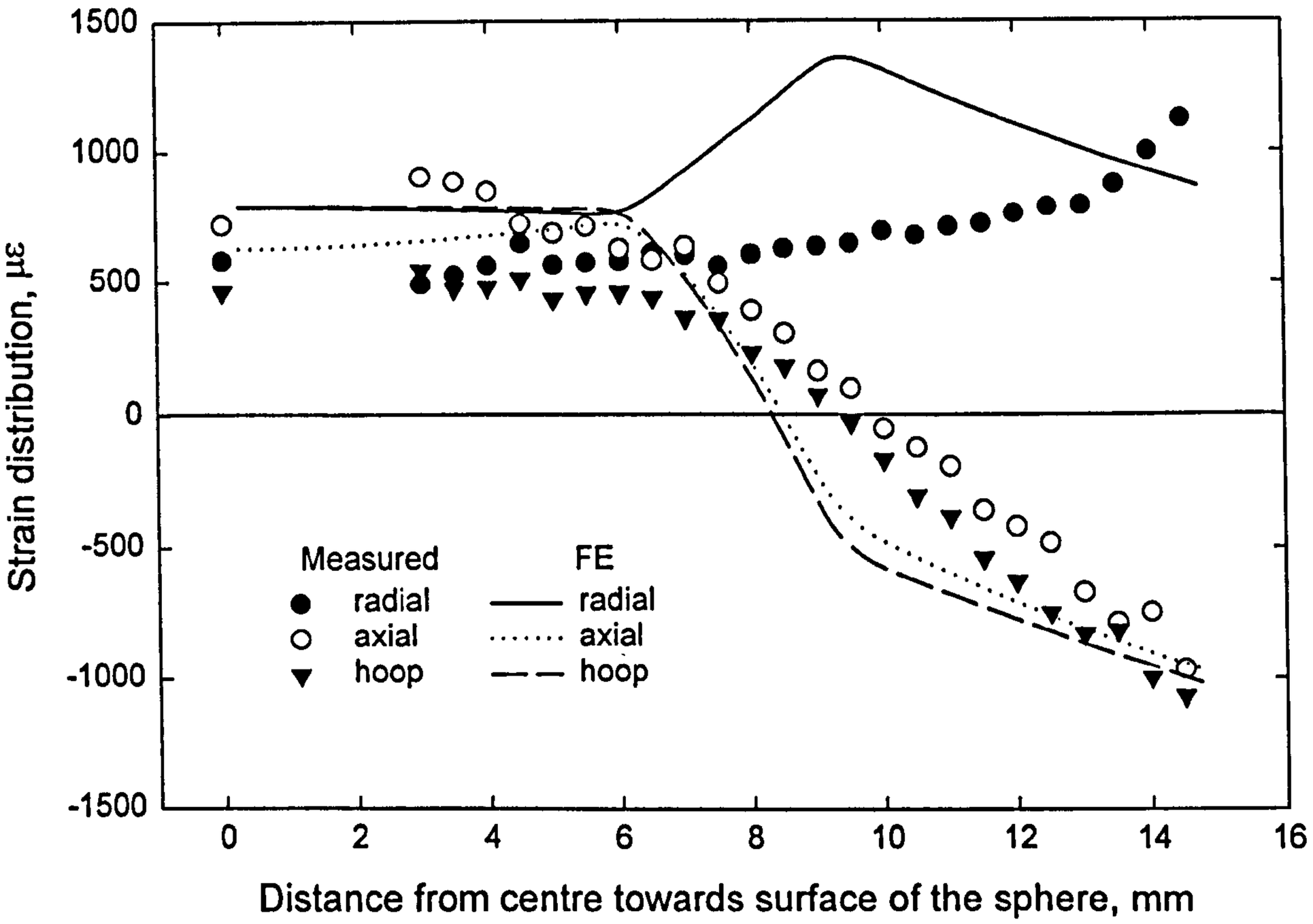

Figure 7.3 Summary of ND measured and FE predicted strains for a 30 mm diameter quenched stainless steel solid sphere *s22*.

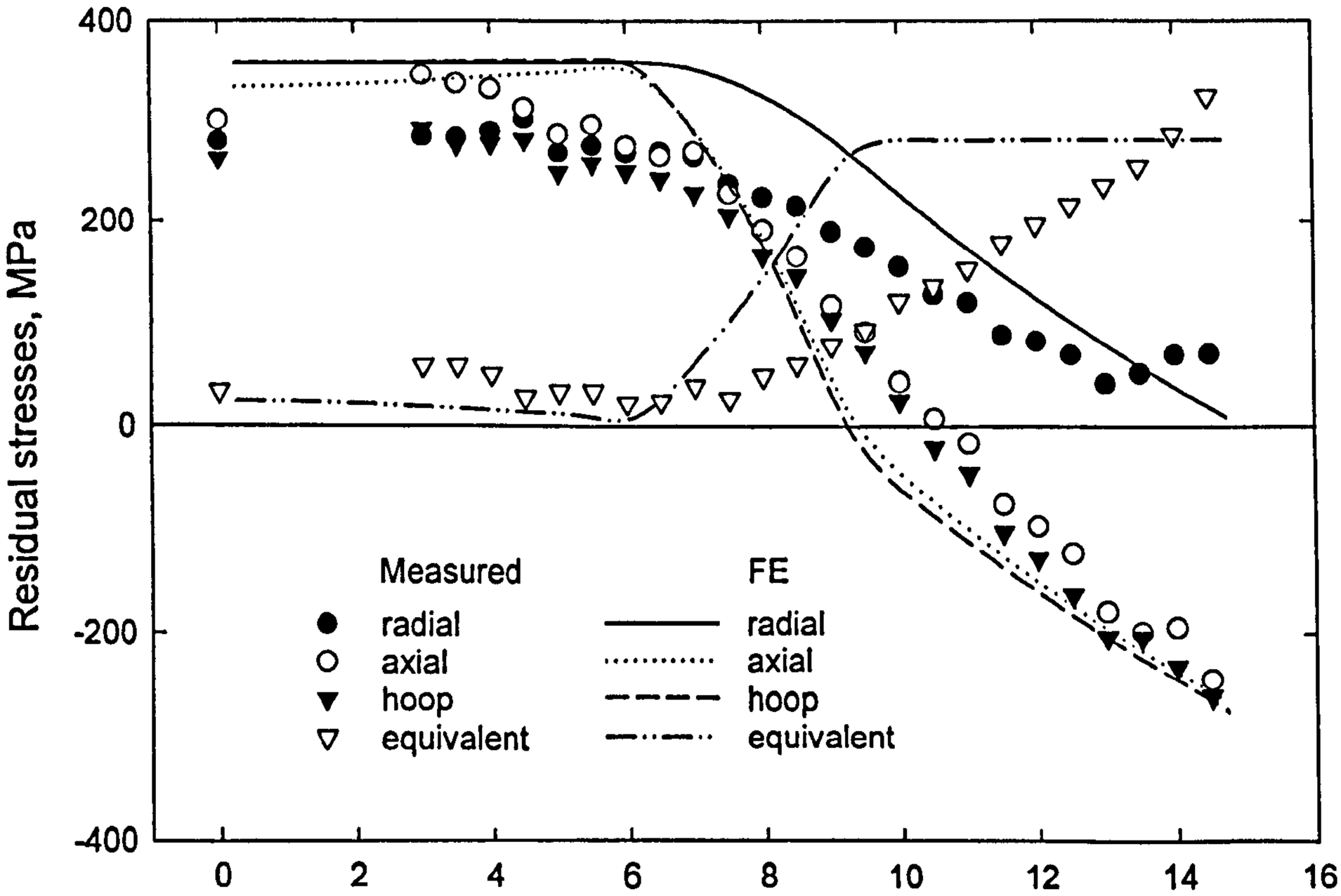

Figure 7.4 ND measured and FE predicted residual stresses in a 30 mm diameter quenched stainless steel solid sphere *s22*.

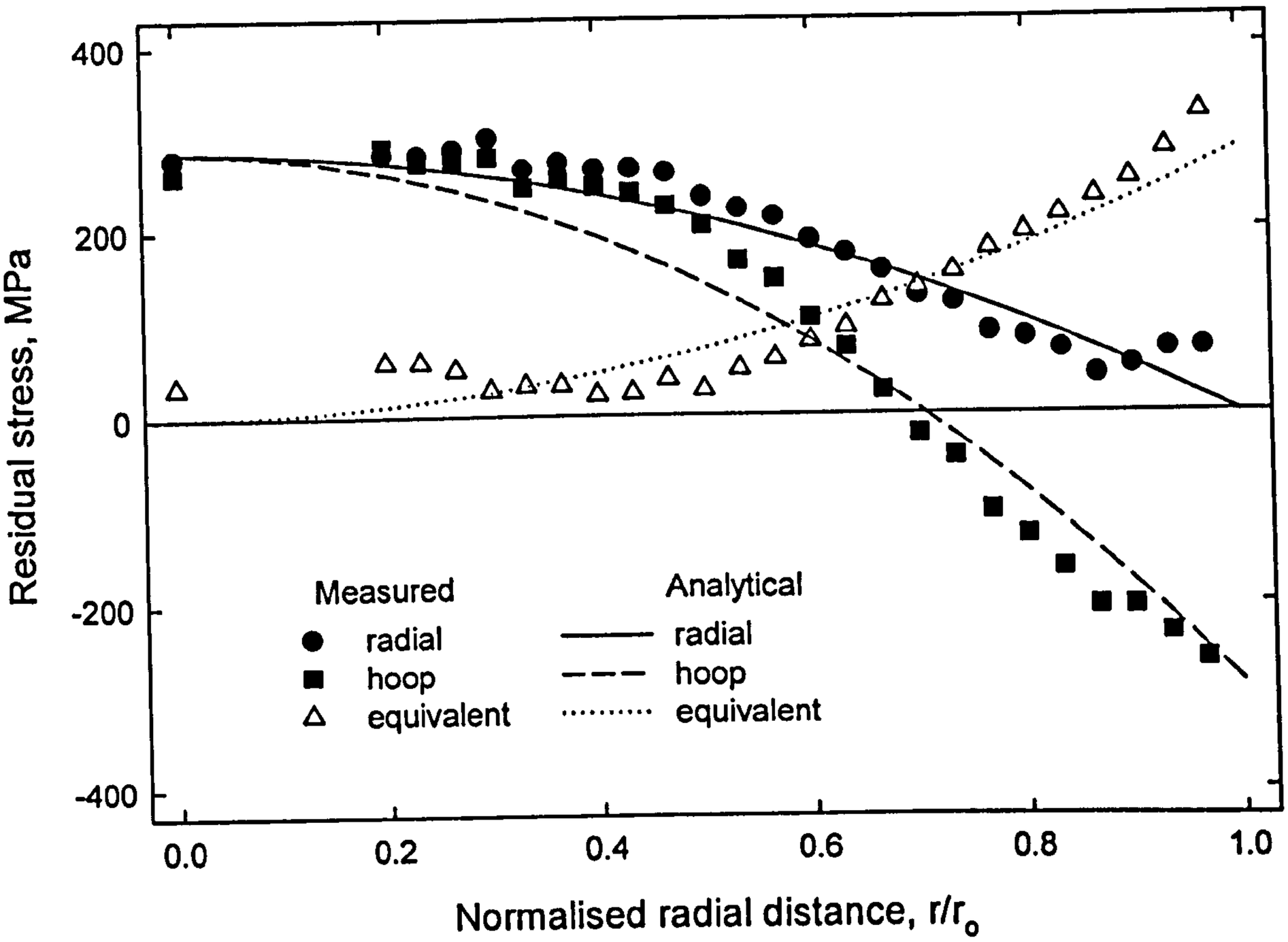

Figure 7.5 ND measured residual stress results in a 30 mm diameter stainless steel solid sphere *s22*, compared with an analytical distribution [McKenzie and Moakler 1973].

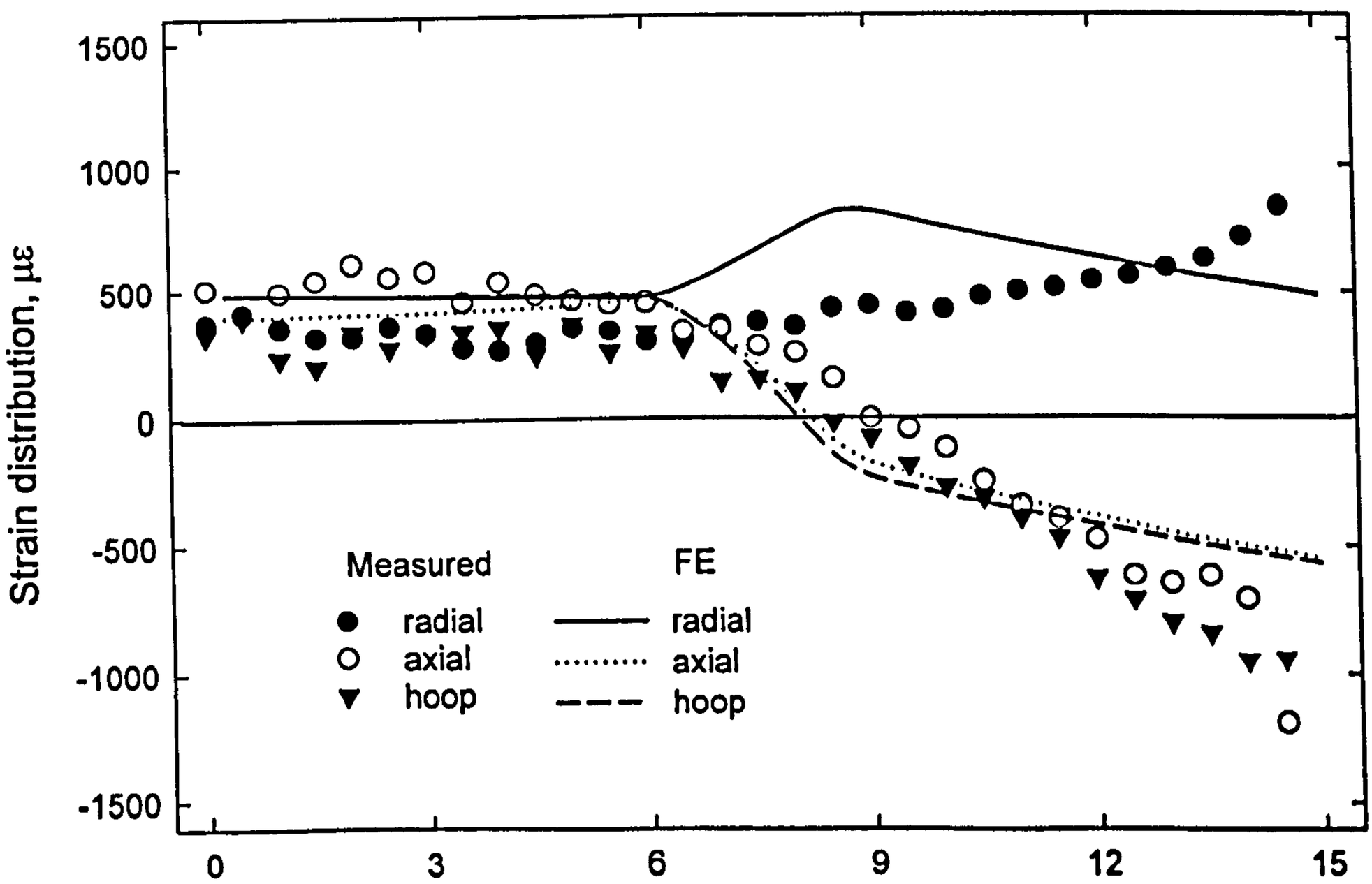

Figure 7.6 Summary of ND measured and FE predicted residual strain distributions across the equatorial plane of a thermally aged quenched SS solid sphere *s24*, diameter 30mm measured from the centre to the surface of the sphere.

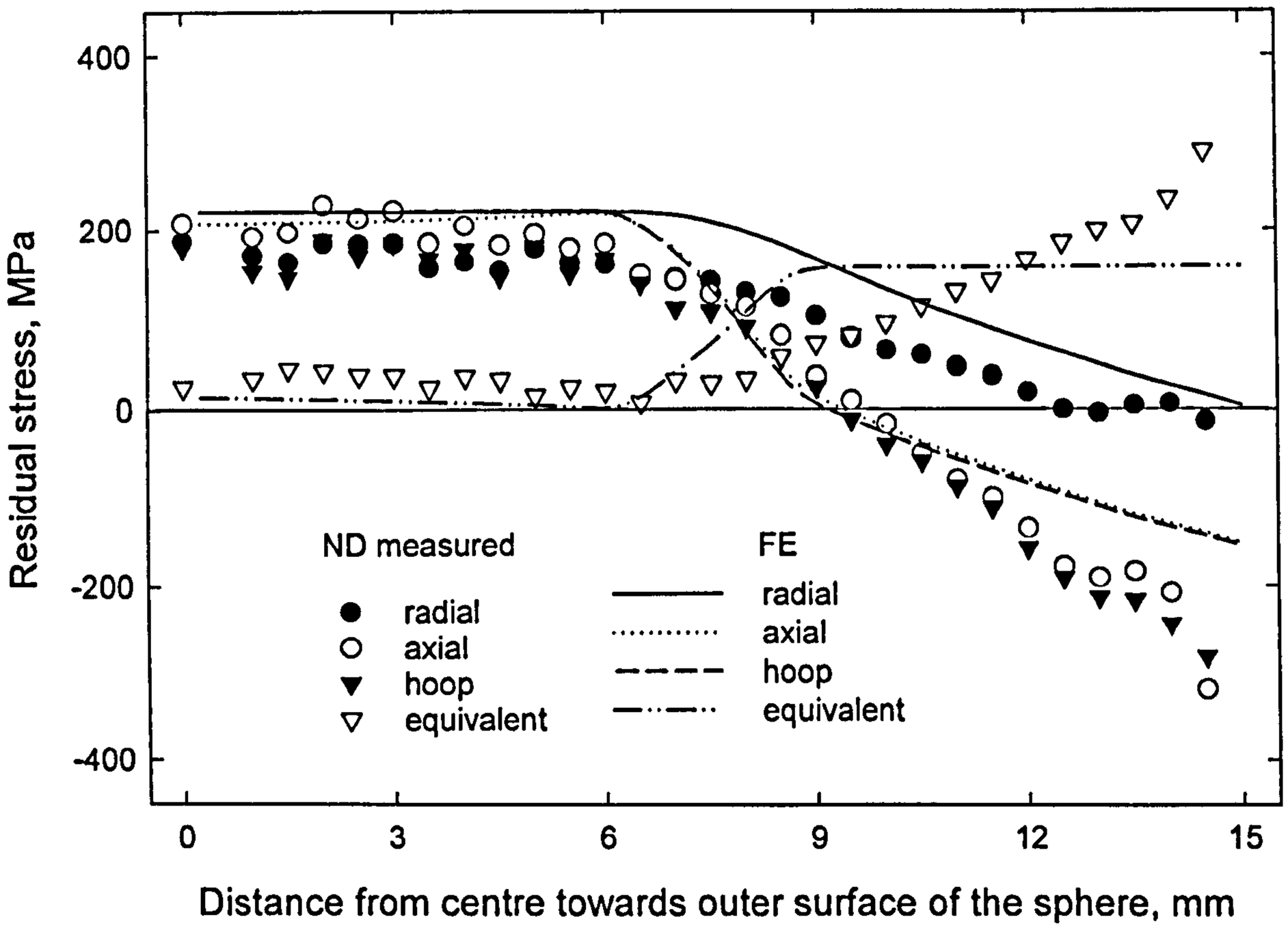

Figure 7.7 Measured and predicted residual stress distribution across the equatorial plane of a quenched sphere, diameter 30mm followed by thermal ageing at 550°C for 3200 hours, *s24*, measured from the centre to the surface of the sphere. The heat transfer coefficient, $h = 7000$ W/m^2 K, initial temperature = 850°C, kinematic hardening model

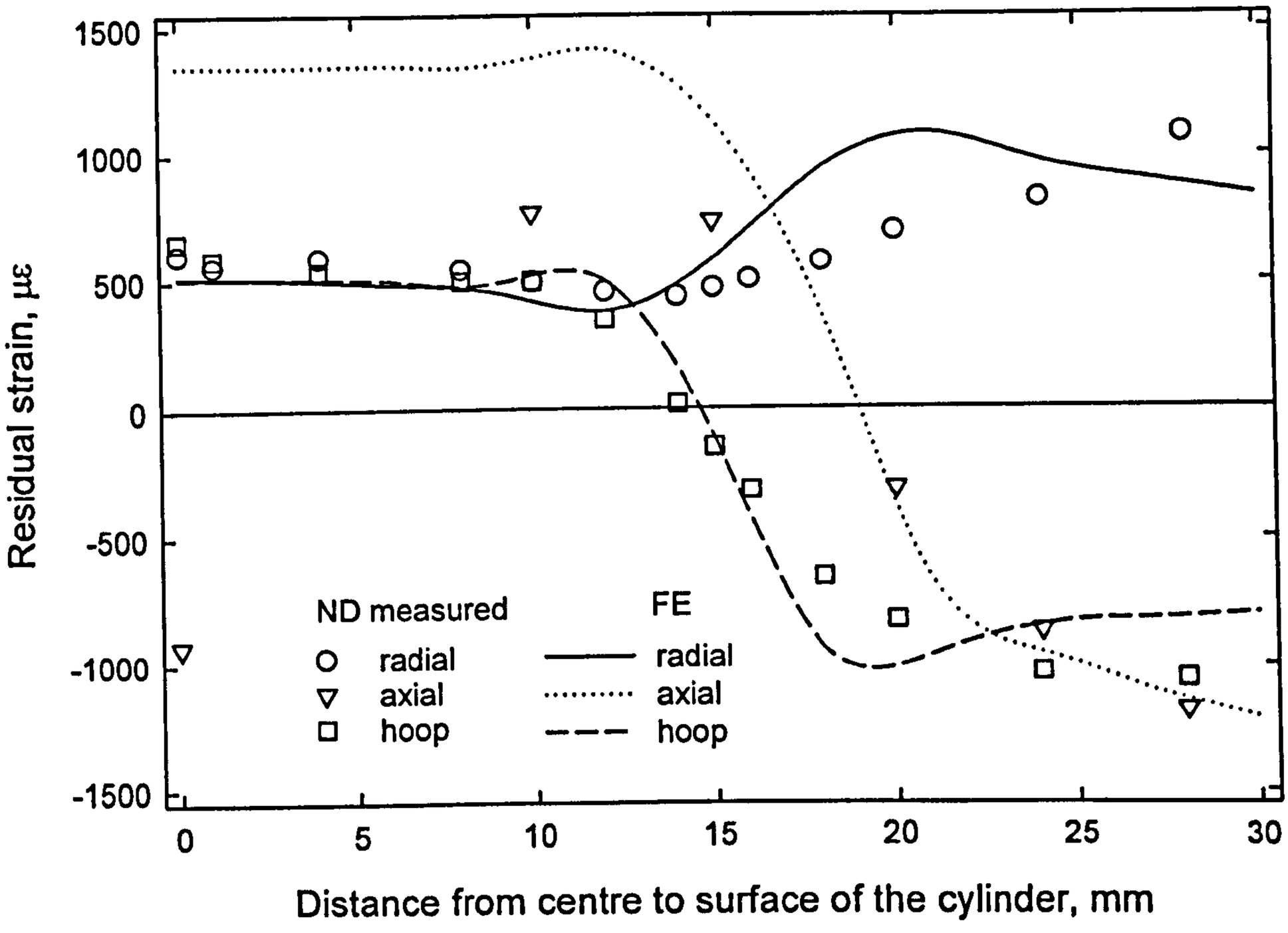

Figure 7.8 Summary of ND measured and FE predicted strains for a quenched stainless steel solid cylindrical bar *s19*, diameter 60mm, length 60mm across OS (see Figure 4.3a). The heat transfer coefficient, h = 7000 W/m^2 K, initial temperature = 850°C, kinematic hardening model.

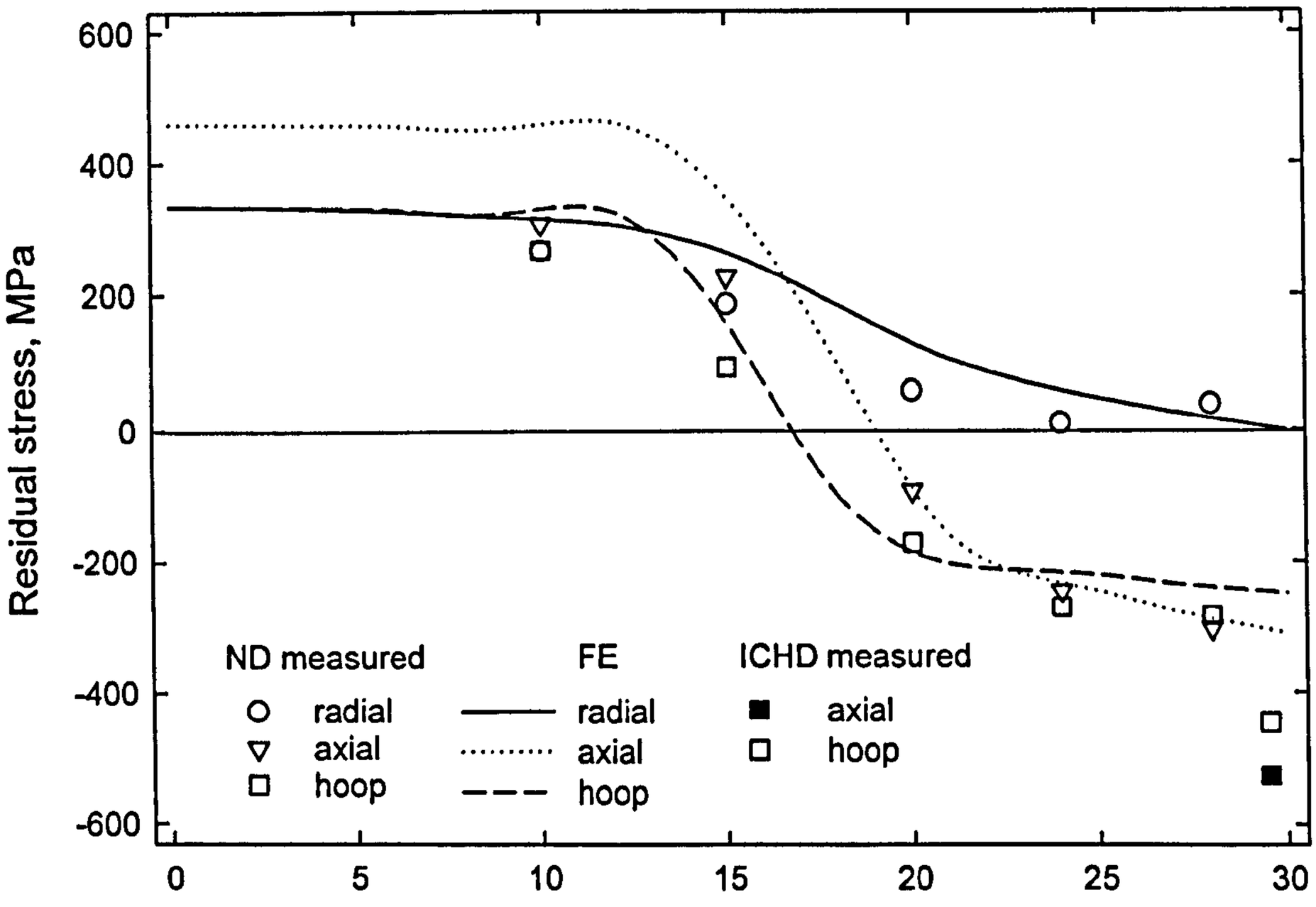

Figure 7.9 ND measured and FE predicted residual stresses in a quenched stainless steel solid cylinder *s19*, diameter 60mm, length 60mm across OS (see Figure 4.3a). The heat transfer coefficient, h = 7000 W/m^2 K, initial temperature = 850°C, with kinematic hardening model. Also shown is the ICHD measured of a similar quenched cylinder sample *s12*.

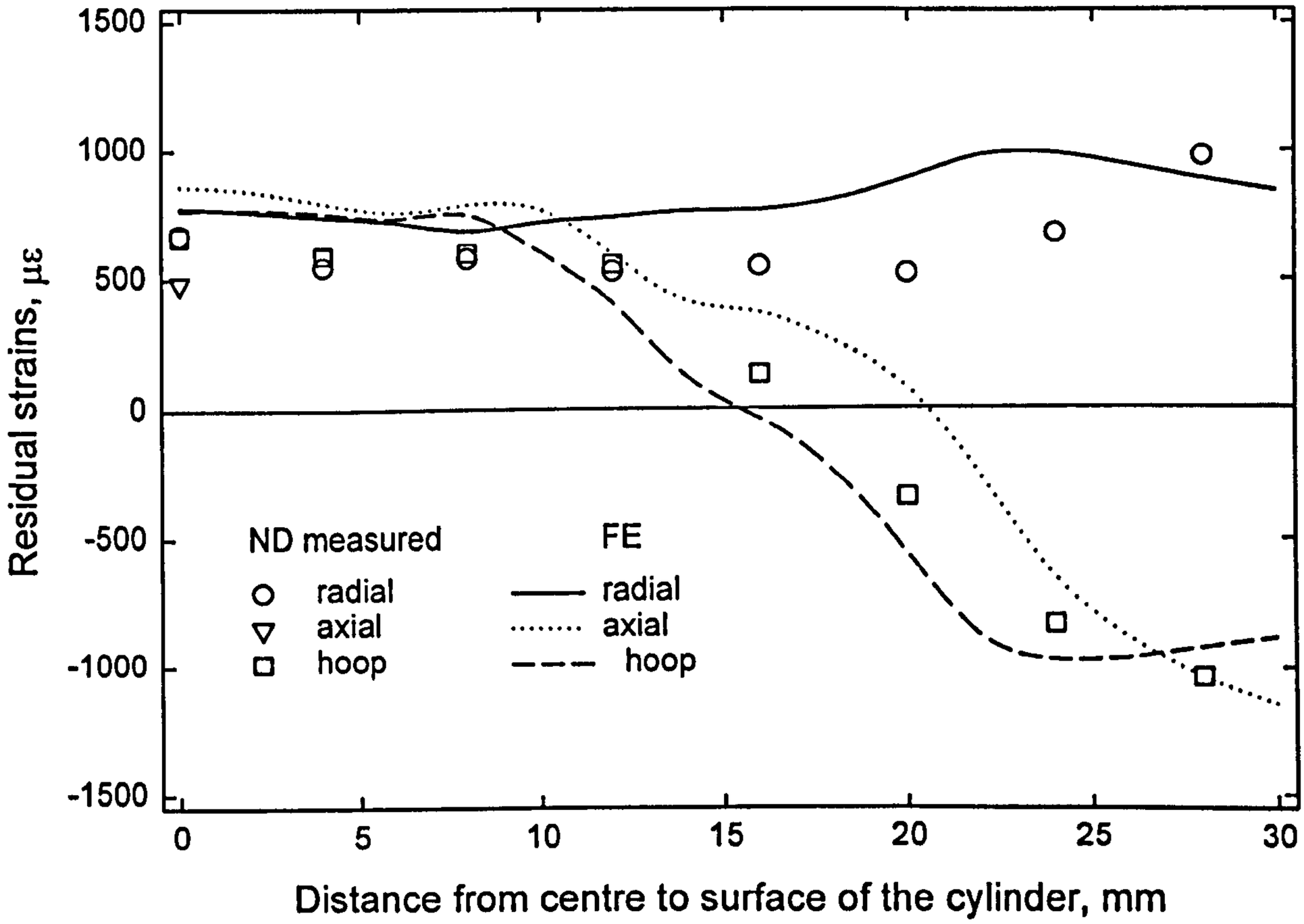

Figure 7.10 Summary of ND measured and FE predicted strains for a quenched stainless steel solid cylindrical bar *s27*, diameter 60mm, length 160mm, at 18mm offset from the end, across NA (see Figure 4.3(b)). The heat transfer coefficient, h = 7000 $W/m^2 K$, initial temperature = 850°C, kinematic hardening model.

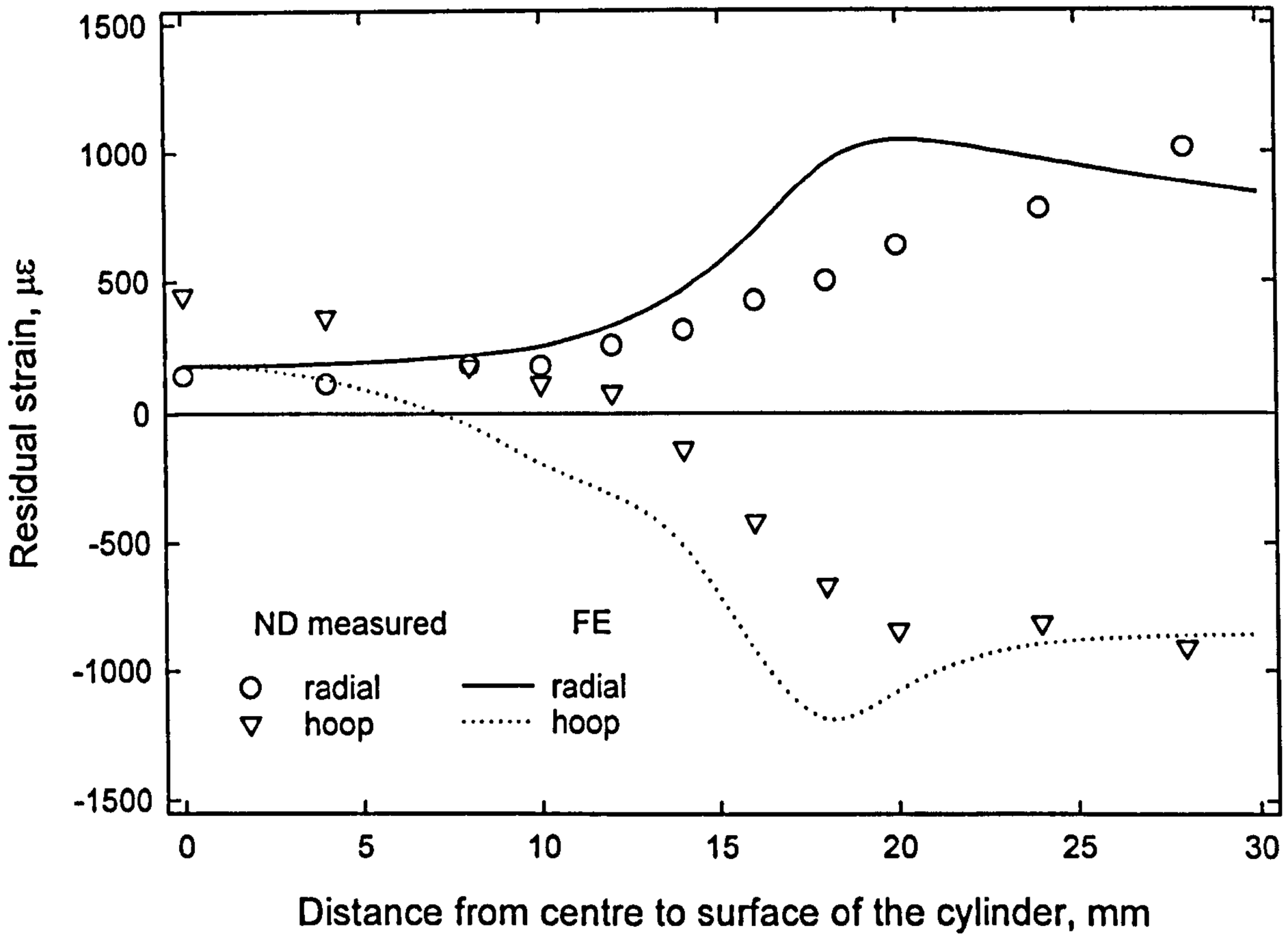

Figure 7.11 Summary of ND measured and FE predicted strains for a quenched stainless steel solid cylindrical bar *s27*, diameter 60mm, length 160mm, across OB (see Figure 4.3(b)). The heat transfer coefficient, h = 7000 W/m^2 K, initial temperature = 850°C, kinematic hardening model.

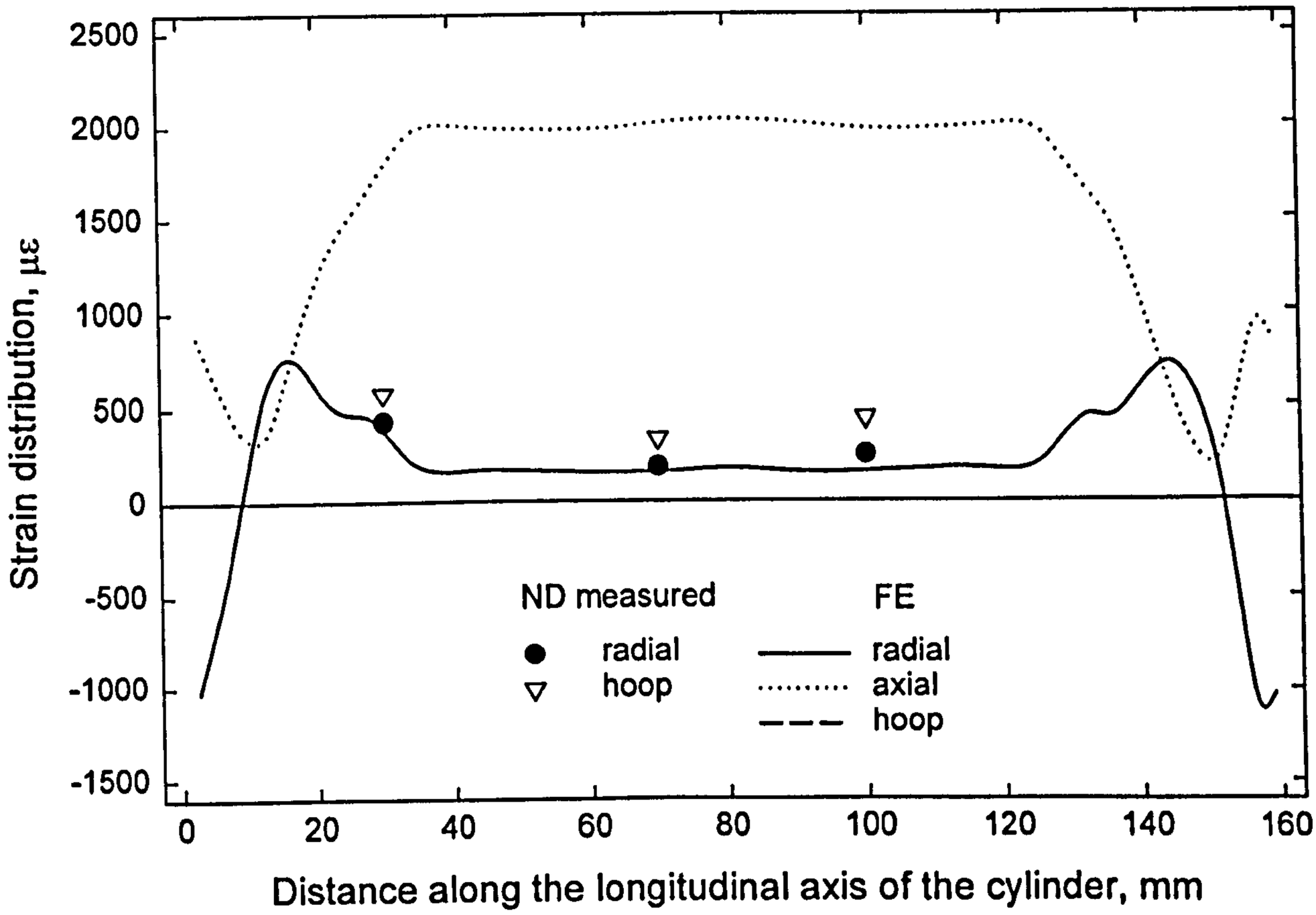

Figure 7.12 Summary of ND measured and FE predicted strains for a quenched stainless steel solid cylindrical bar, diameter 60mm, length 160mm, along the longitudinal axis. The measurements are at positions A, B and C on specimen *s26* (see Figure 4.3(c)). The heat transfer coefficient, h = 7000 W/m^2 K, initial temperature = 850°C, kinematic hardening model.

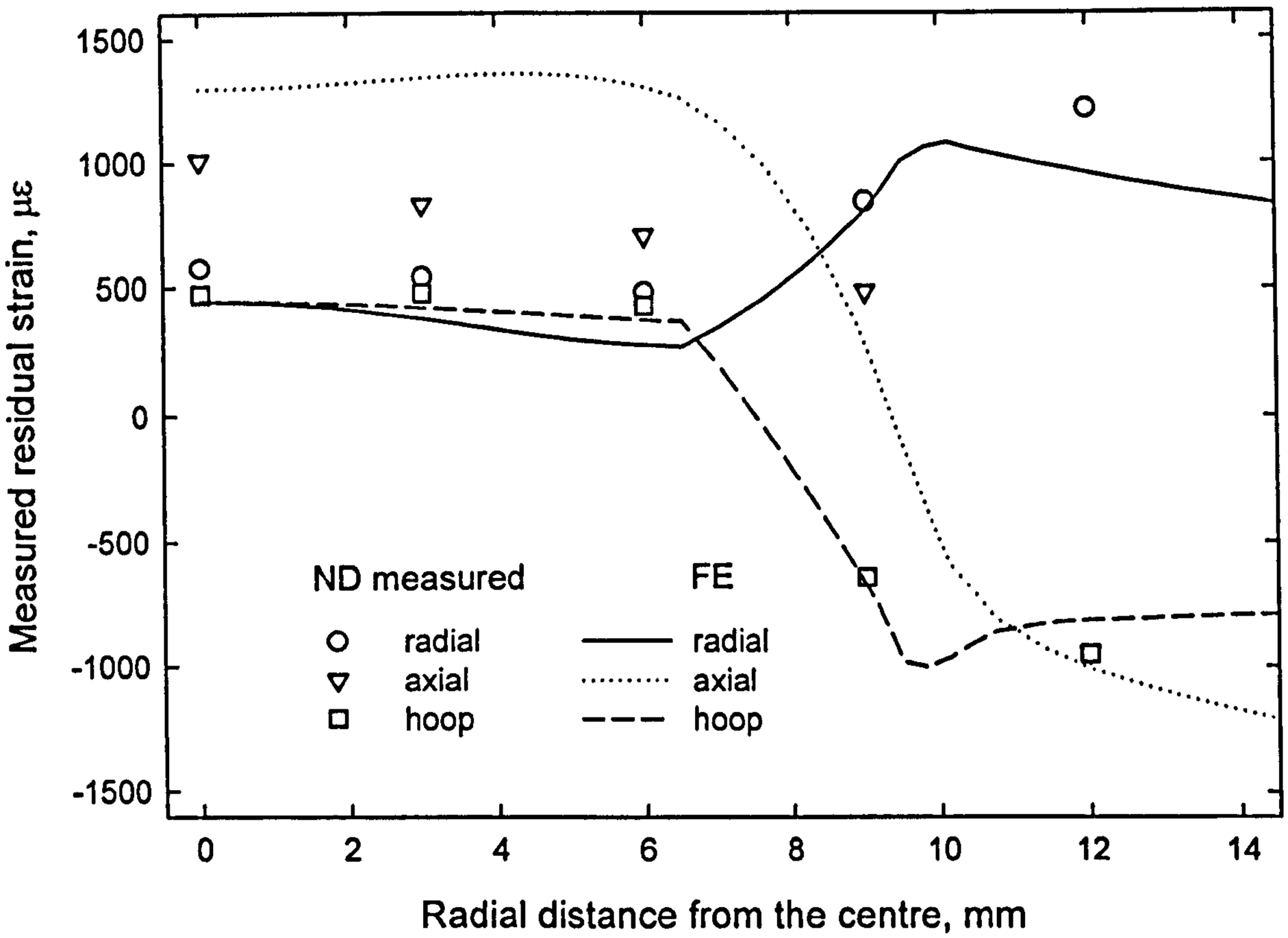

Figure 7.13 Summary of ND measured and FE predicted strains for a quenched stainless steel solid cylindrical bar *s39*, diameter 29mm, length 29mm, across the equatorial plane from the centre to the surface of the bar.

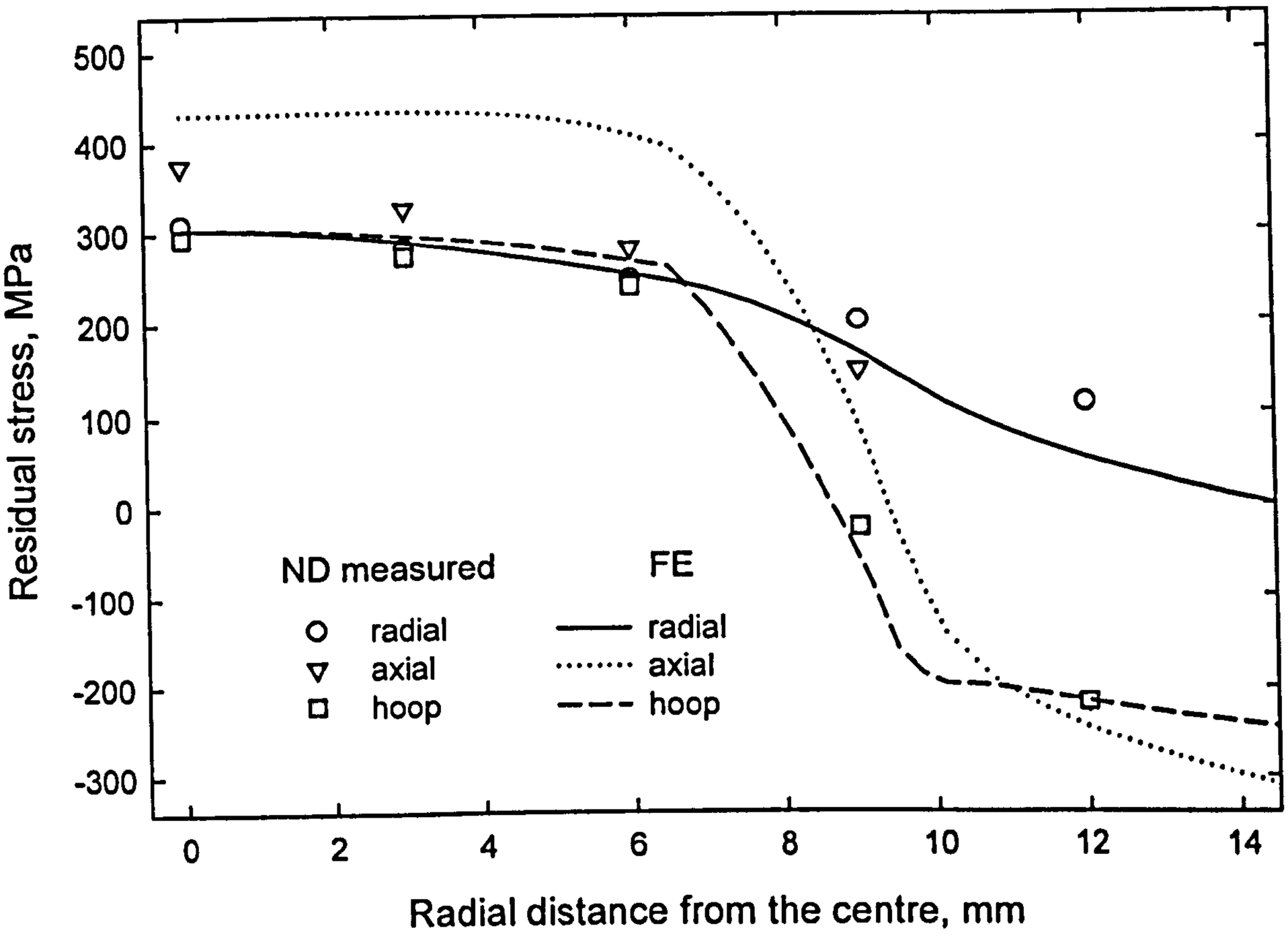

Figure 7.14 Measured and predicted residual stress distribution across the equatorial plane of a quenched cylinder *s39*, diameter 29mm, length 29mm, measured from the centre to the surface of the bar. The heat transfer coefficient, h = 7000 W/m^2 K, initial temperature = 850°C, kinematic hardening model.

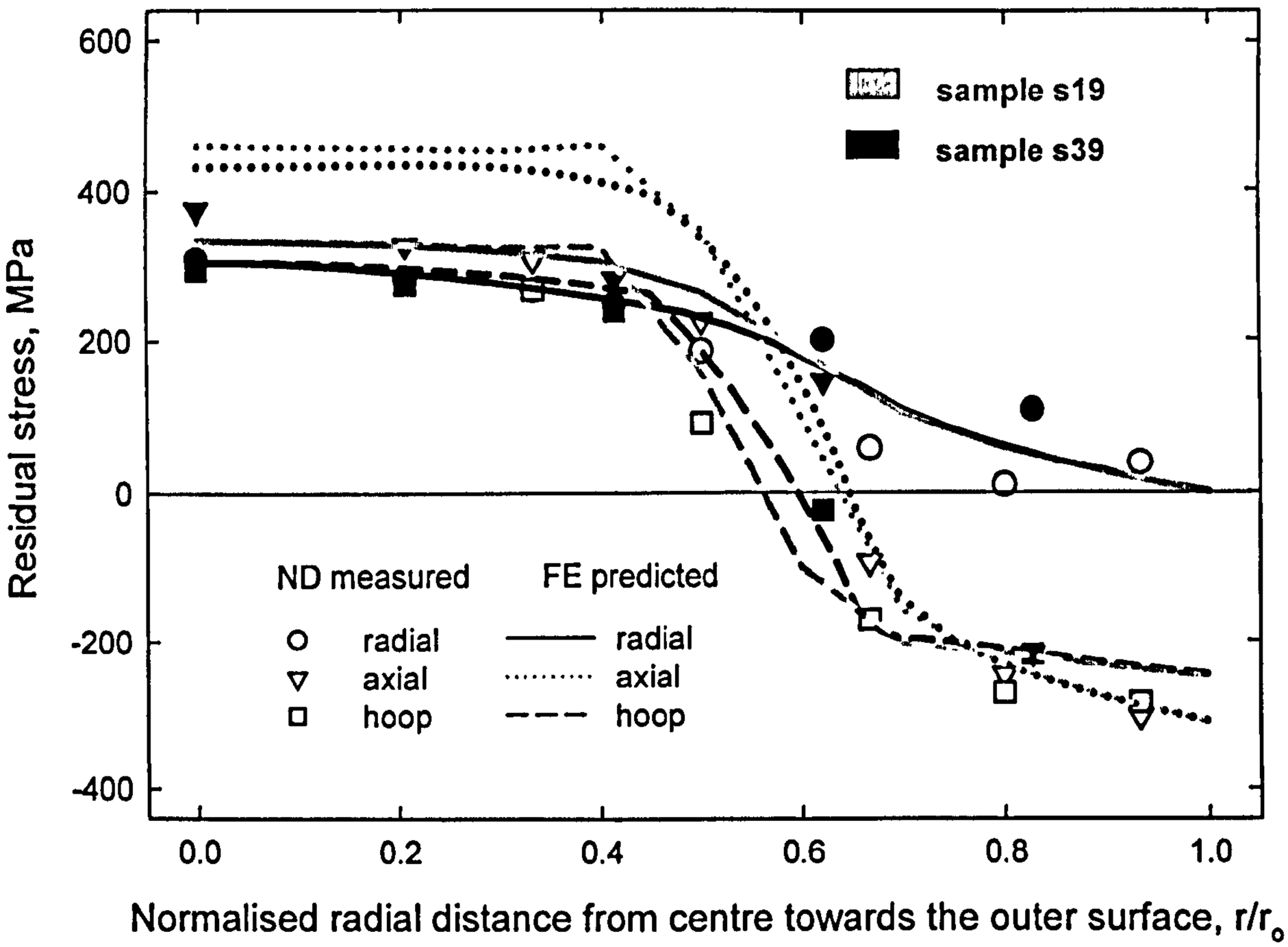

Figure 7.15 Comparison of residual stress distribution in *s19* and *s39*.

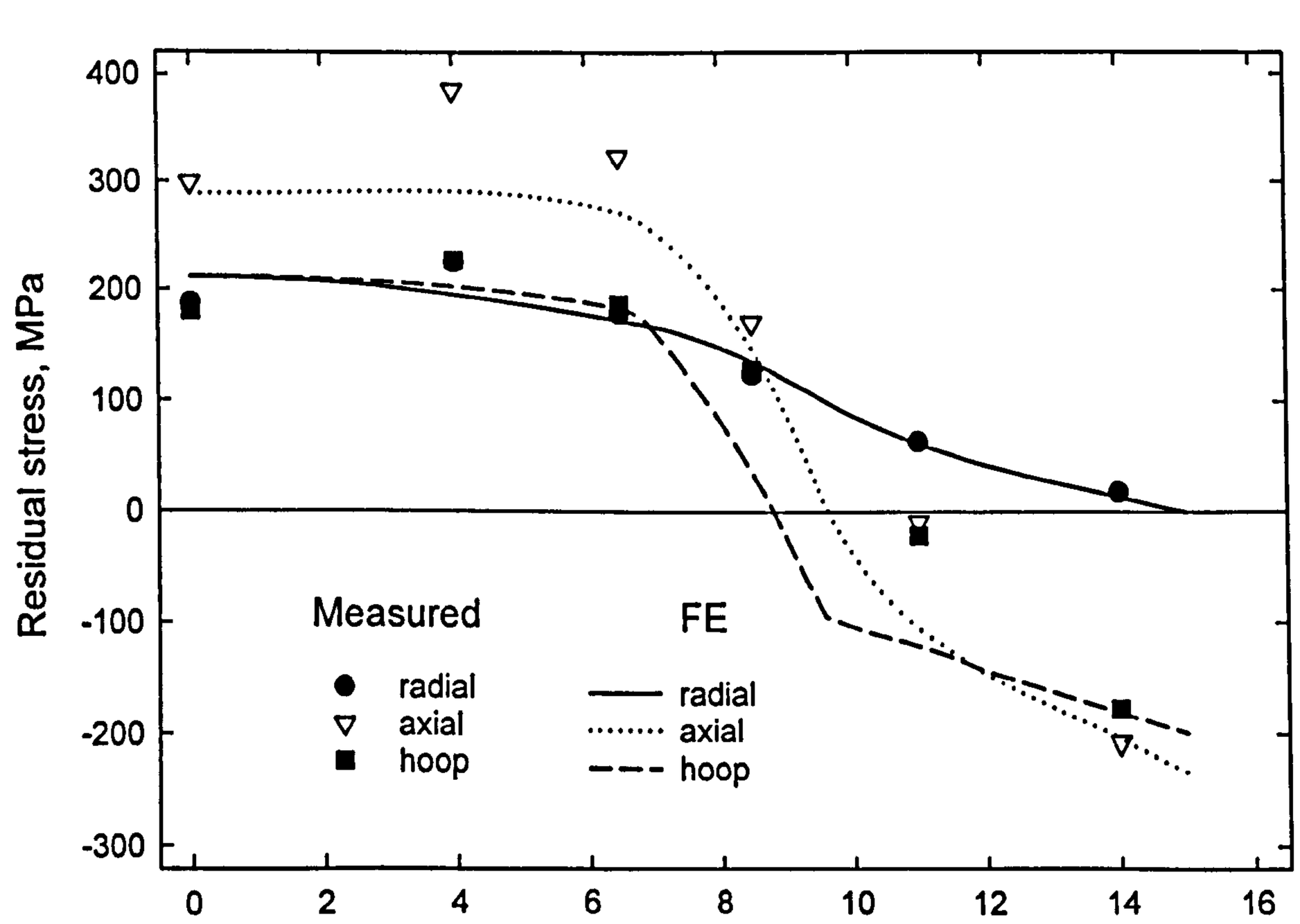

Figure 7.16 Measured and predicted residual stress distribution across the equatorial plane of a quenched and short-term (1.25 hours) thermally aged cylinder *s29*.

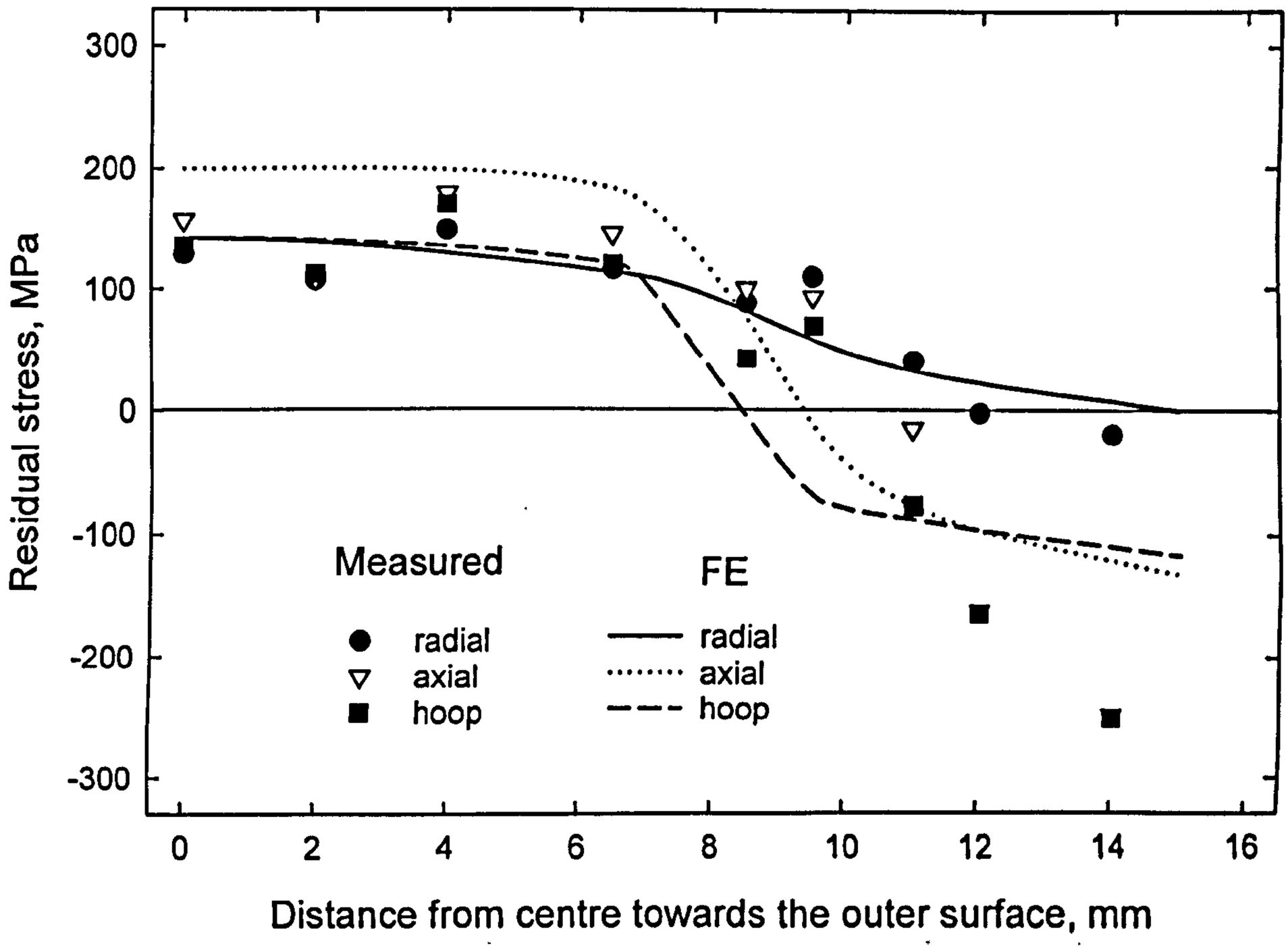

Figure 7.17 Measured and predicted residual stress distribution across the equatorial plane of a quenched and long-term (1800 hours) thermally aged cylinder *s28*.

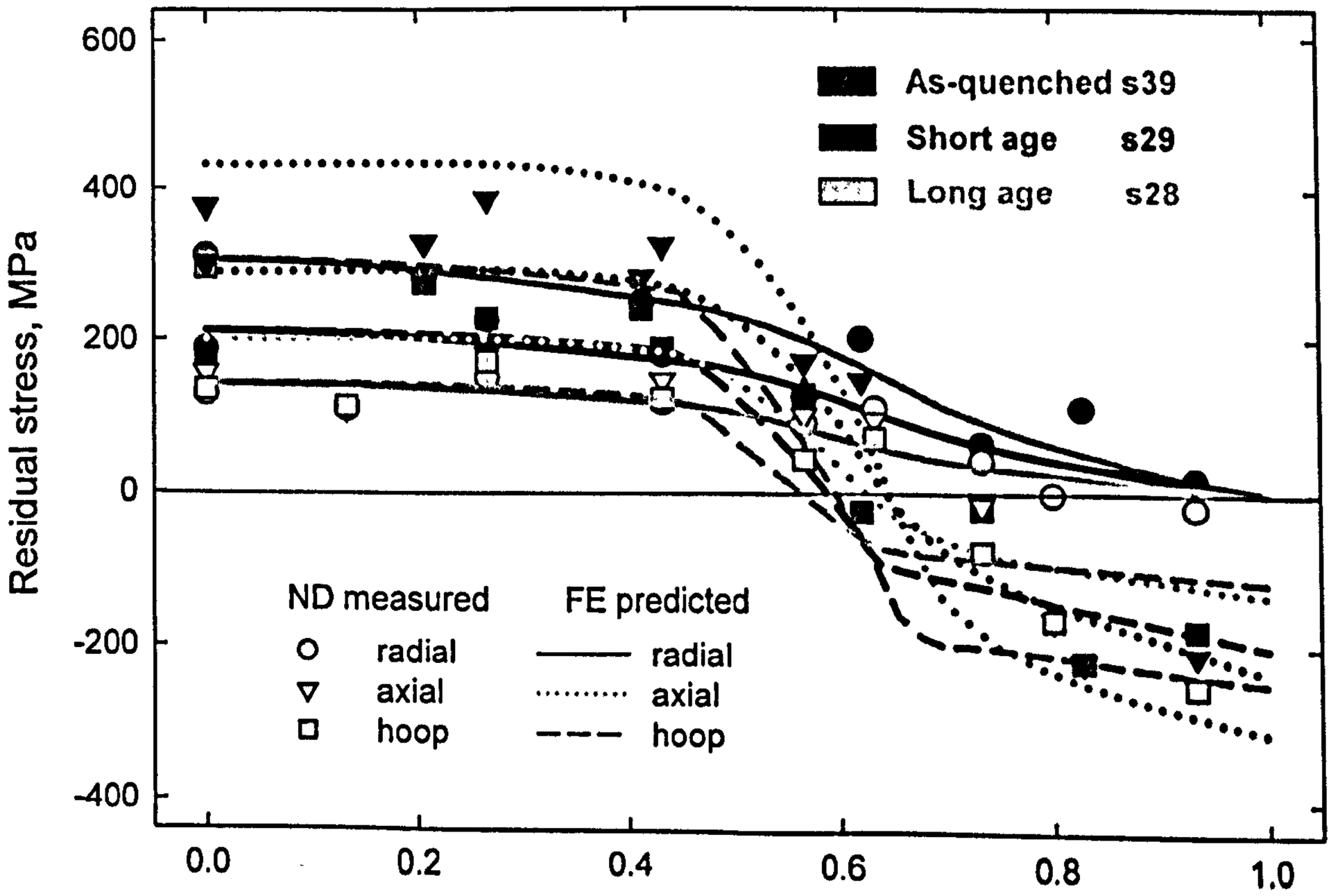

Figure 7.18 Comparison of residual stress distribution between cylinders *s29*, *s28* and *s39*.

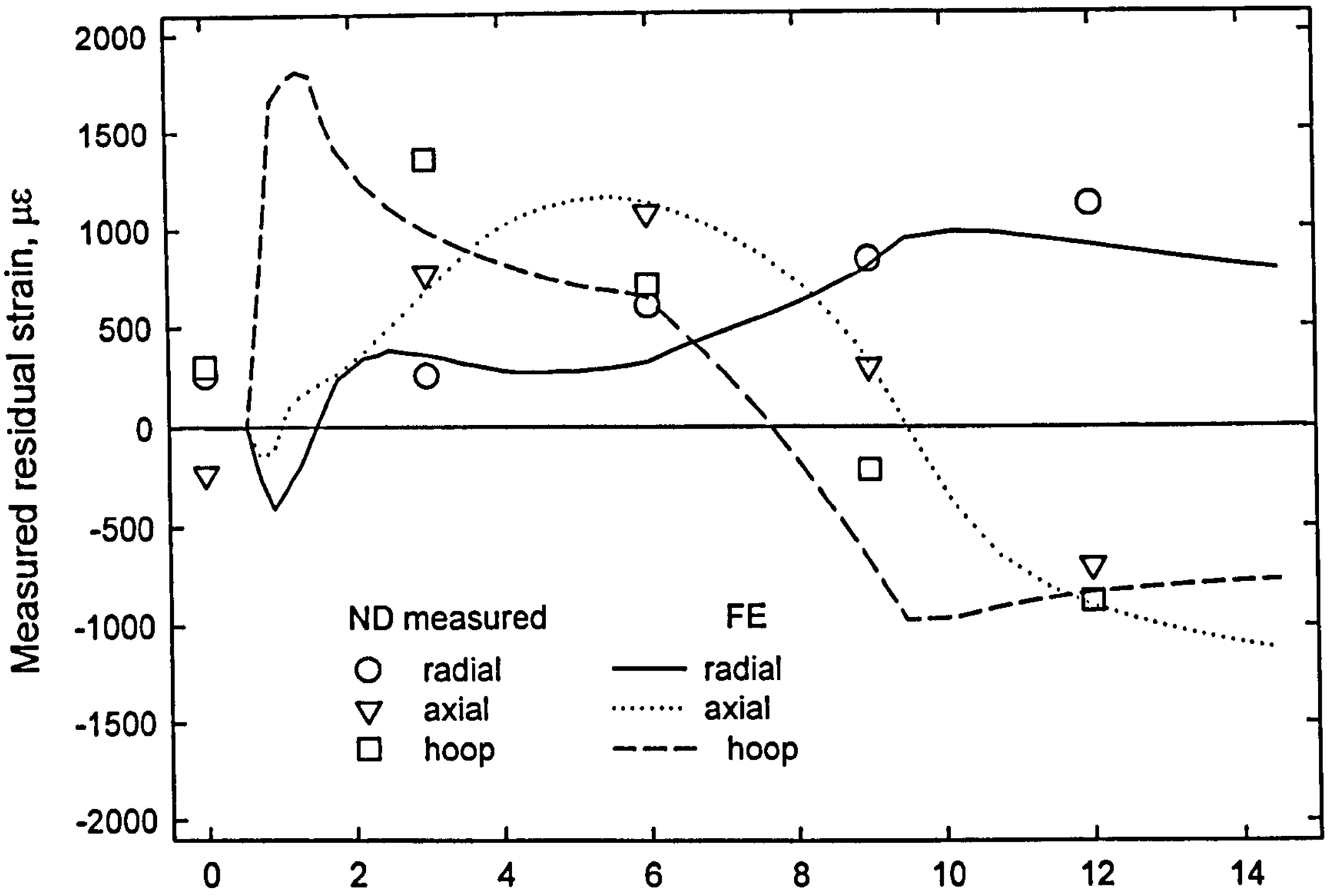

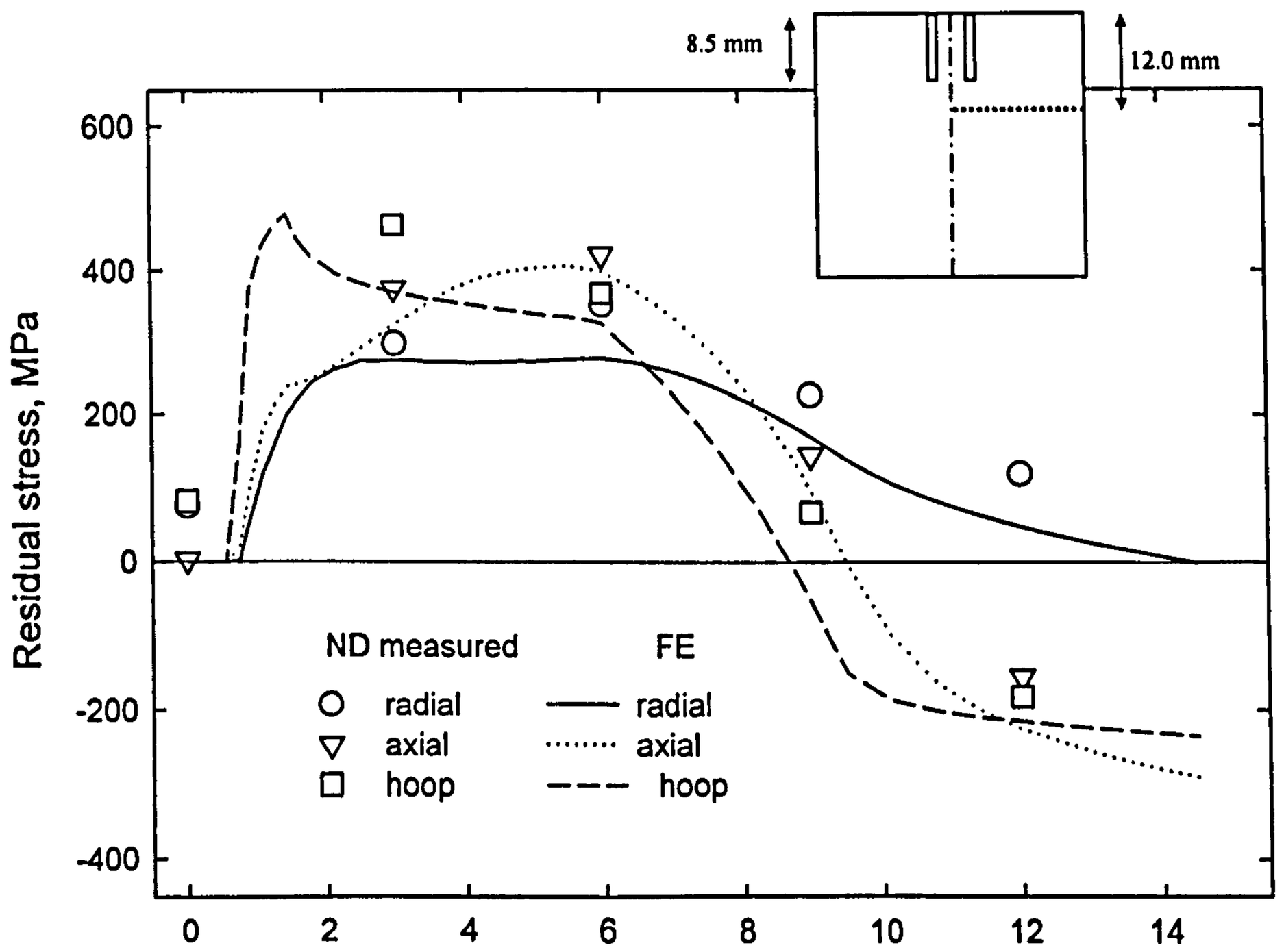

Figure 7.19 Distribution of residual (a) strain and (b) stress across a radial plane 12mm below the top surface in a quenched cylinder bar *s34* with 1.5mm diameter drill and 5mm diameter trepanned up to 8.5mm depth.

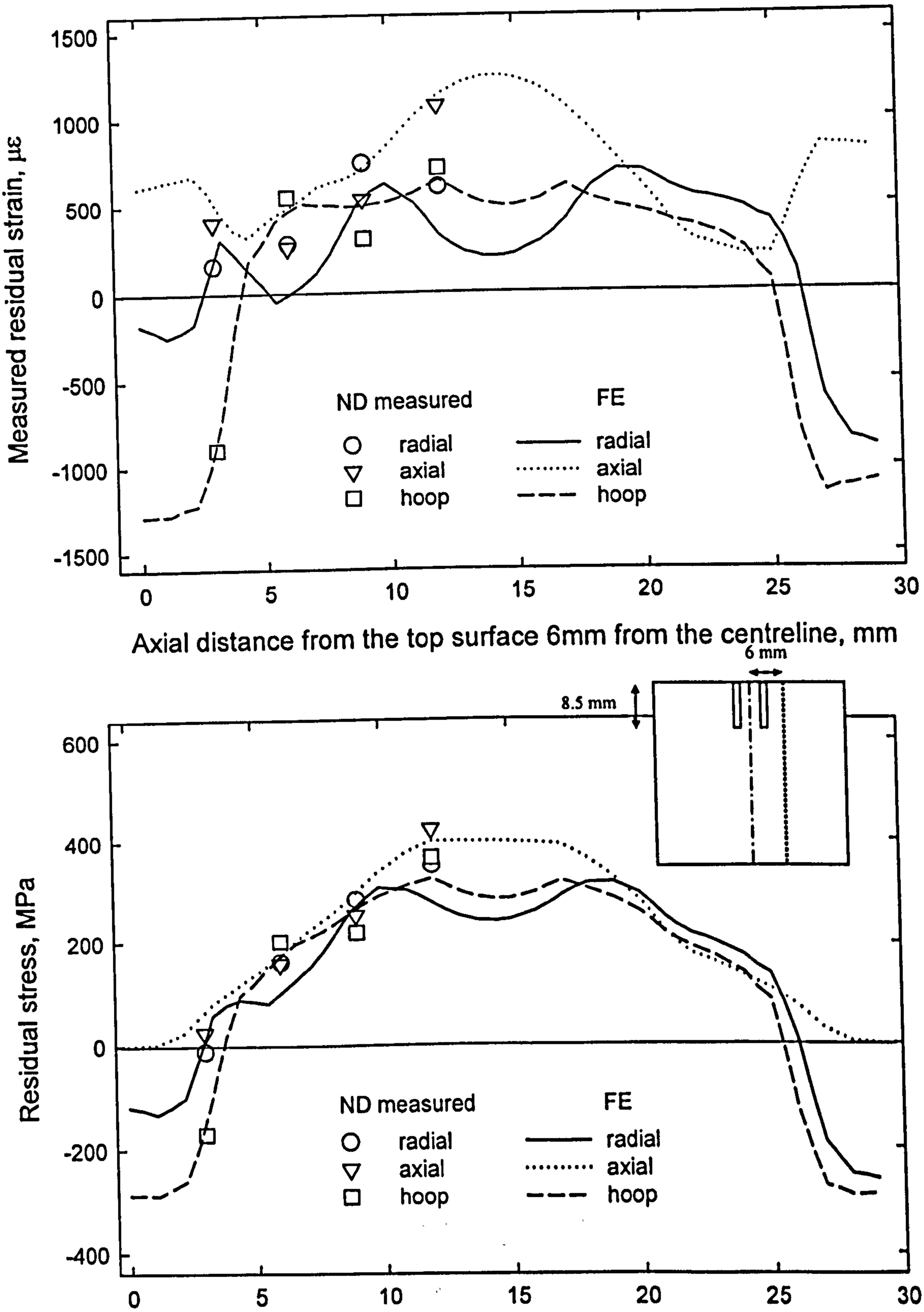

Figure 7.20 Distribution of residual (a) strain and (b) stress along an axial line 6mm away from the centreline in a quenched cylinder bar *s34* with 1.5mm diameter drill and 5mm diameter trepanned up to 8.5mm depth.

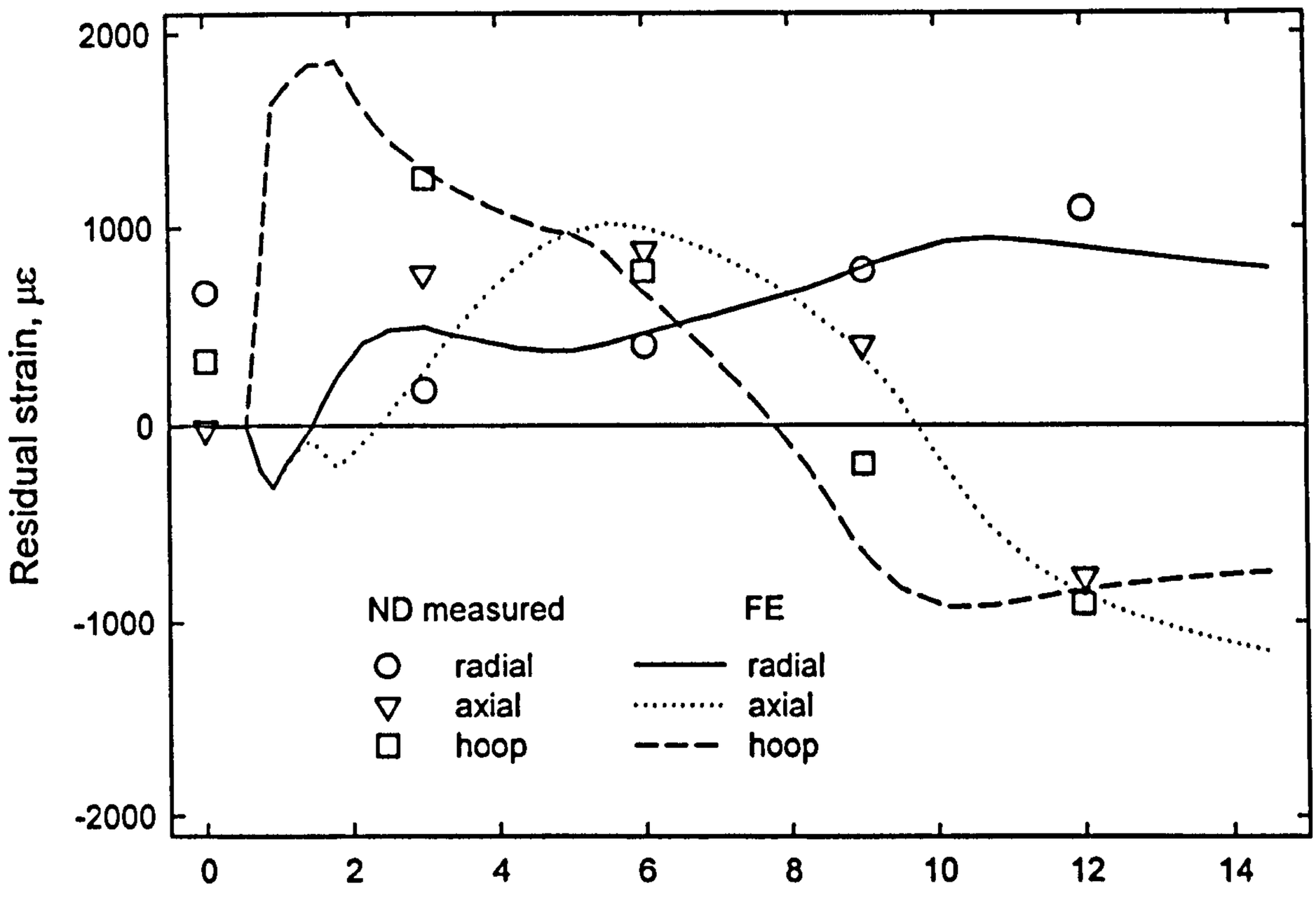

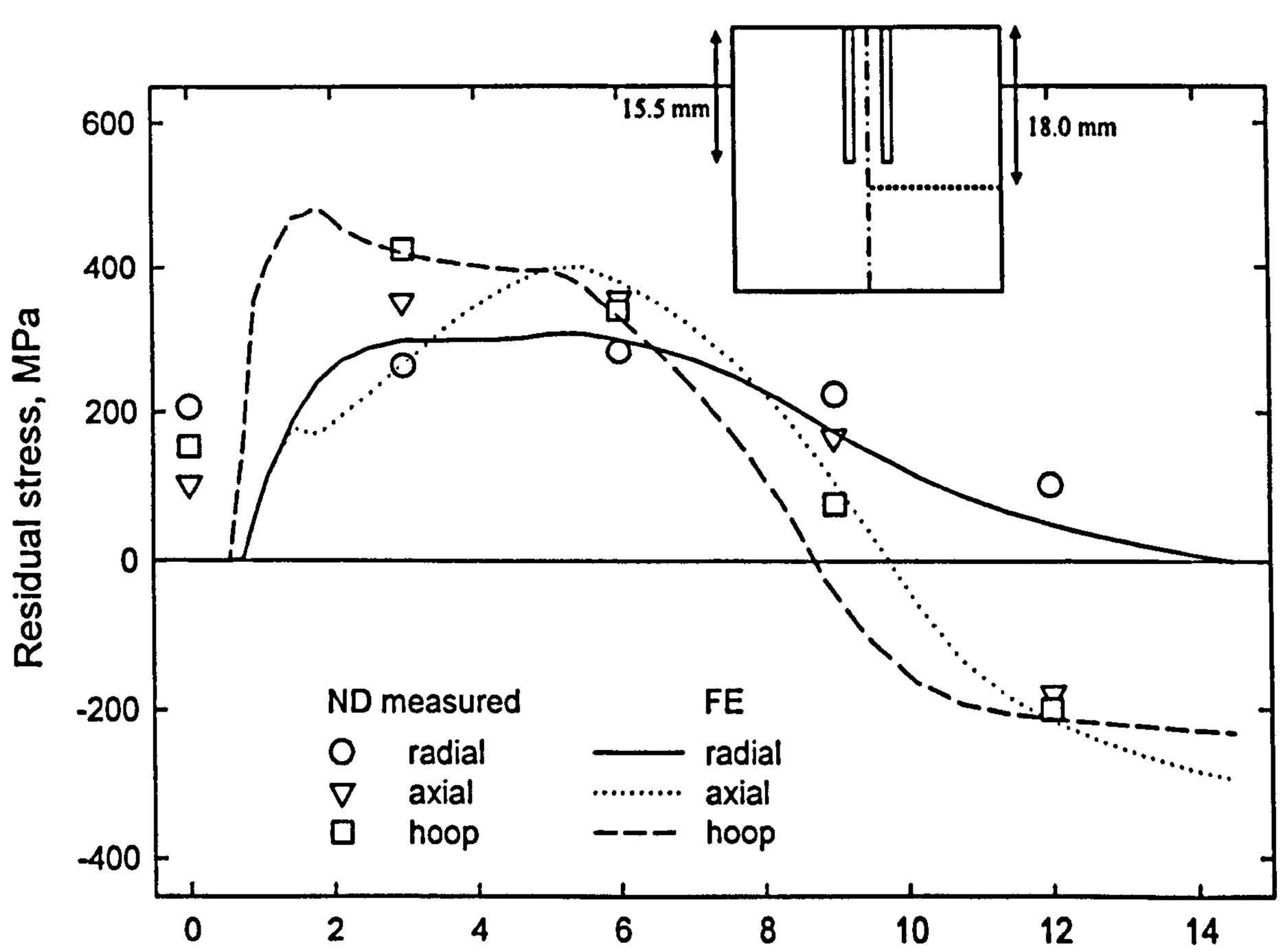

Figure 7.21 Distribution of residual (a) strain and (b) stress across a radial plane 18mm below the top surface in a quenched cylinder bar *s35* with 1.5mm diameter drill and 5mm diameter trepanned up to 15.5mm depth.

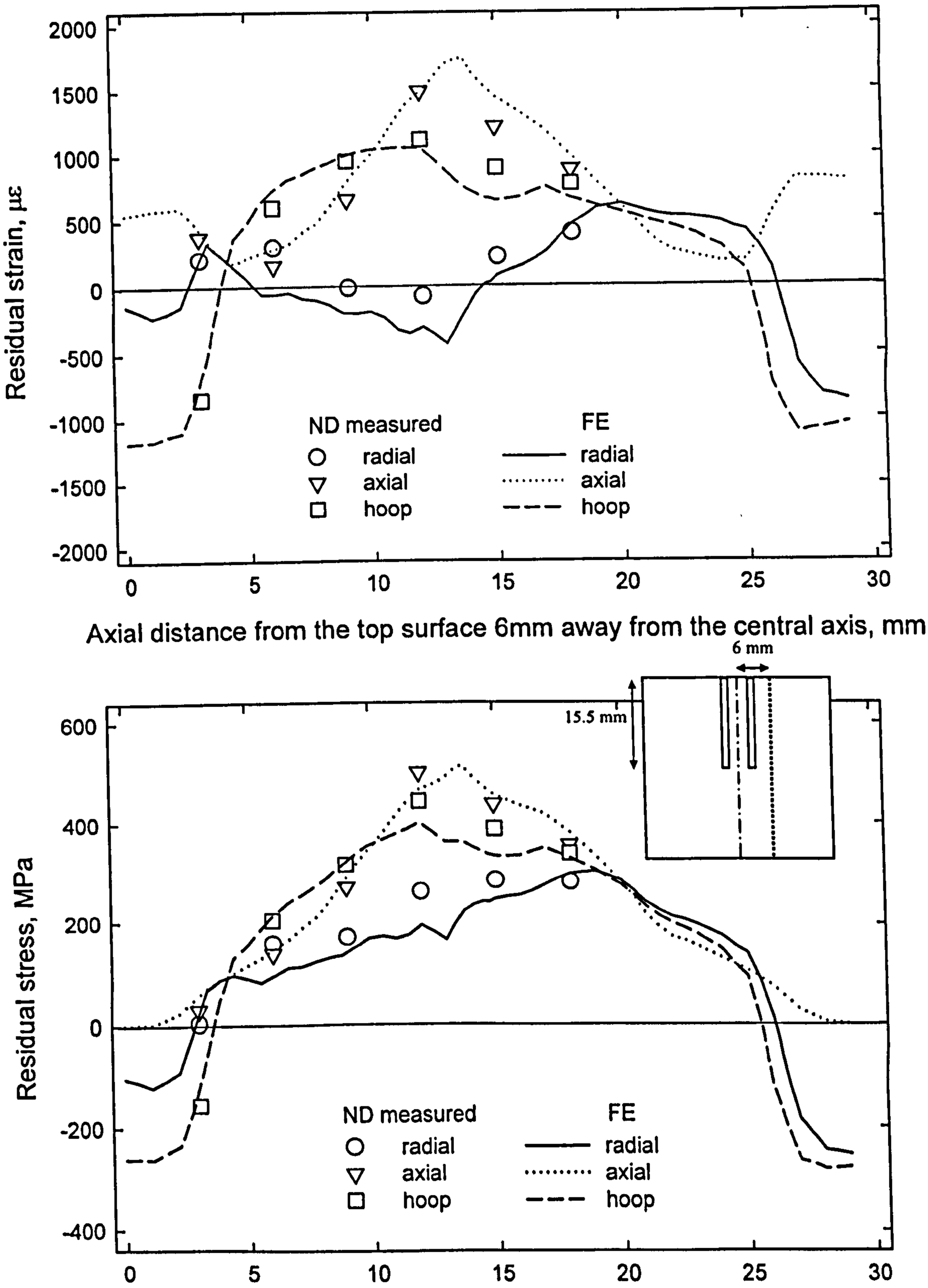

Figure 7.22 Distribution of residual (a) strain and (b) stress along an axial line 6mm away from the centreline in a quenched cylinder bar *s35* with 1.5mm diameter drill and 5mm diameter trepanned up to 15.5mm depth.

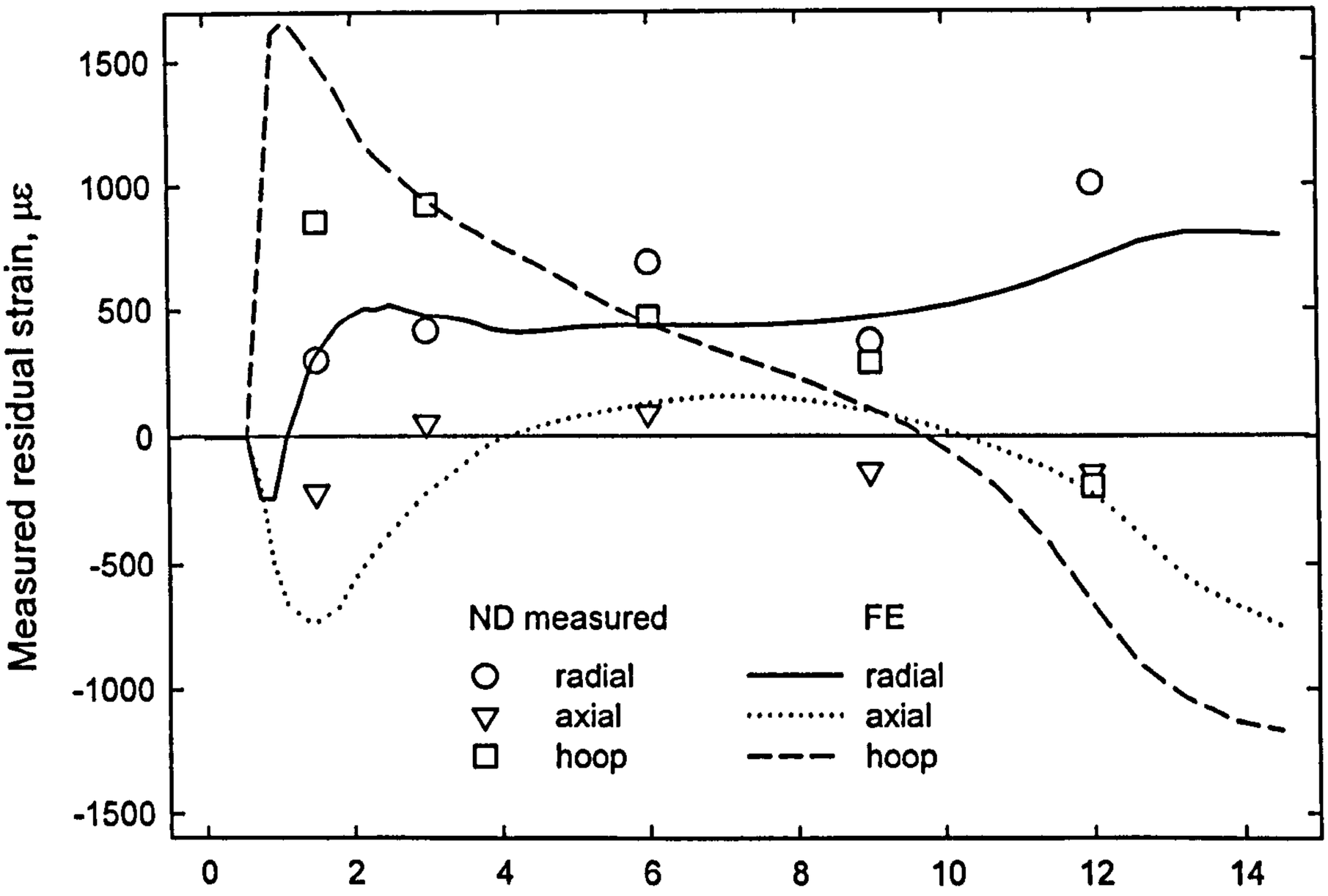

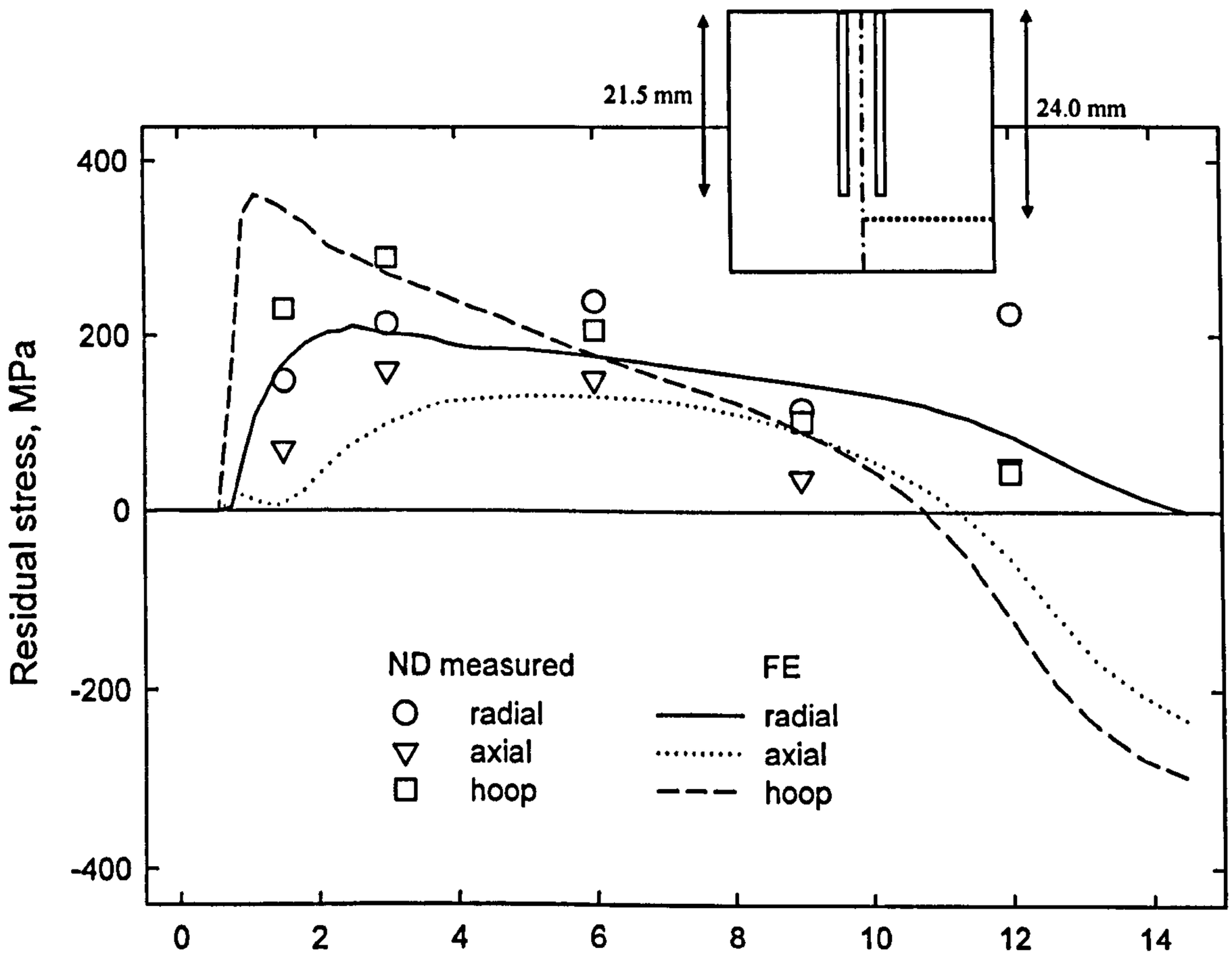

Figure 7.23 Distribution of residual (a) strain and (b) stress across a radial plane 24mm below the top surface in a quenched cylinder bar *s36* with 1.5mm diameter drill and 5mm diameter trepanned up to 21.5mm depth.

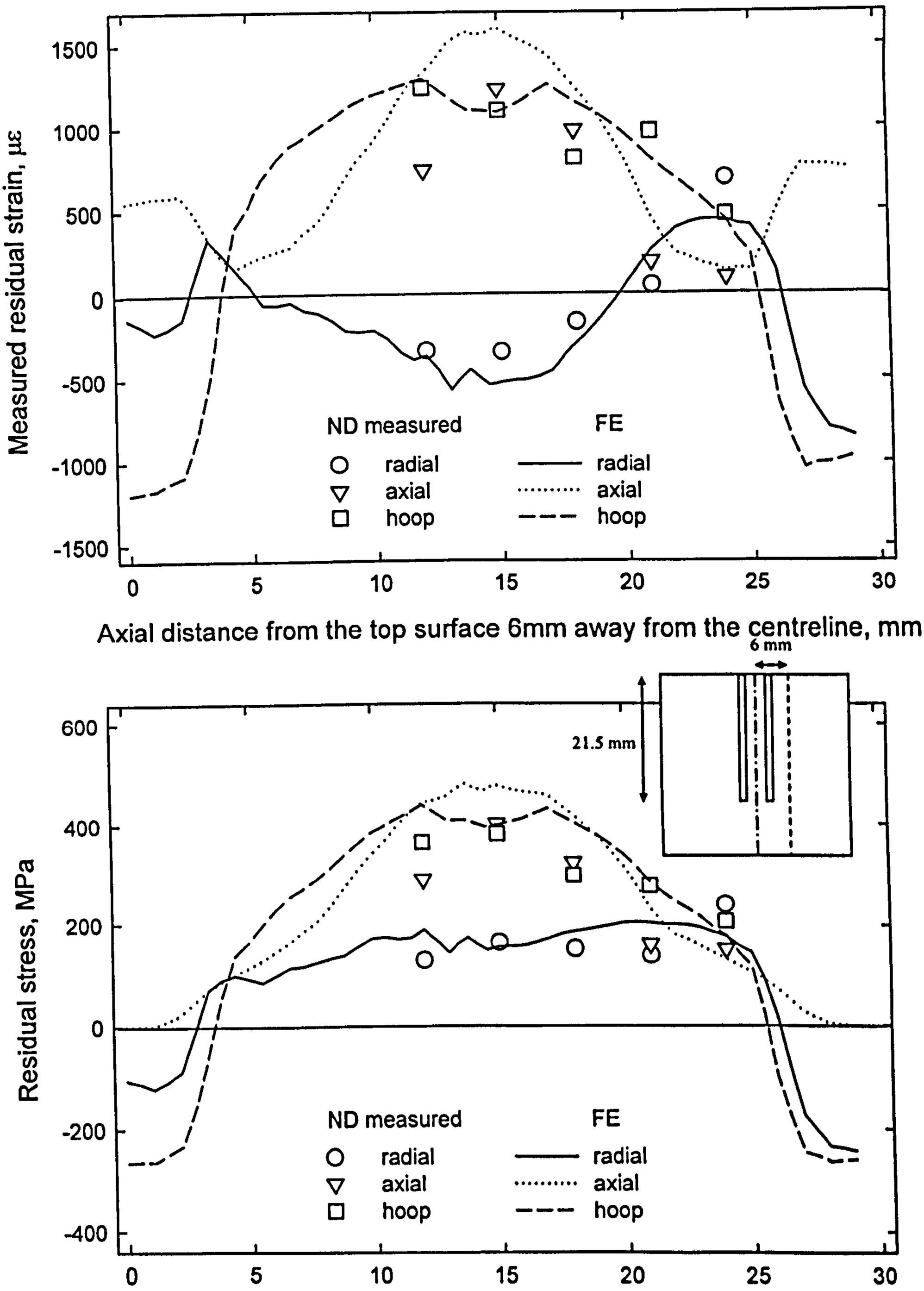

Figure 7.24 Distribution of residual (a) strain and (b) stress along an axial linc 6mm away from the centreline in a quenched cylinder bar *s36* with 1.5mm diameter drill and 5mm diameter trepanned up to 21.5mm depth.

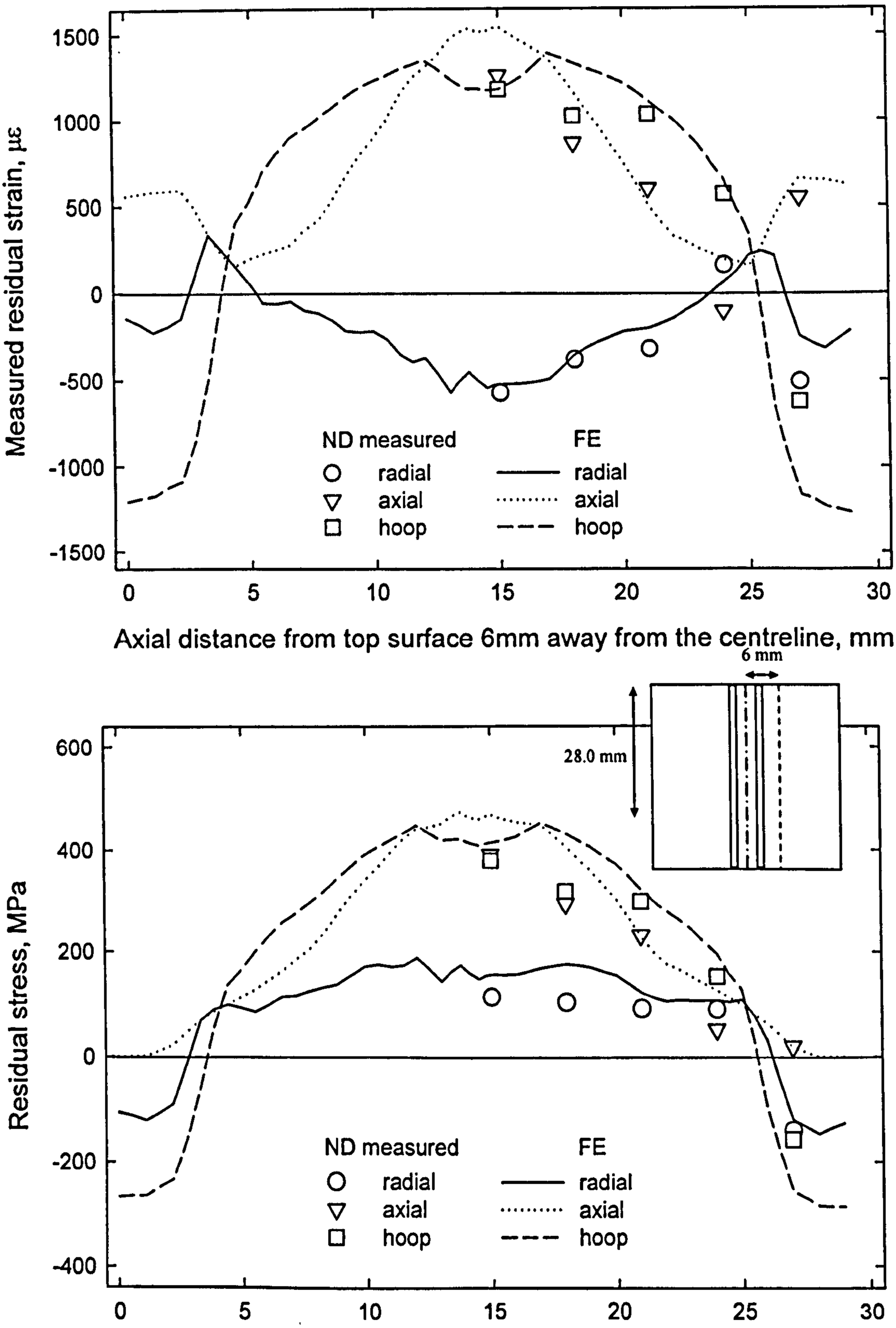

Figure 7.25 Distribution of residual (a) strain and (b) stress along an axial line 6mm away from the centreline in a quenched cylinder bar *s37* with 1.5mm diameter drill and 5mm diameter trepanned up to 28mm depth.

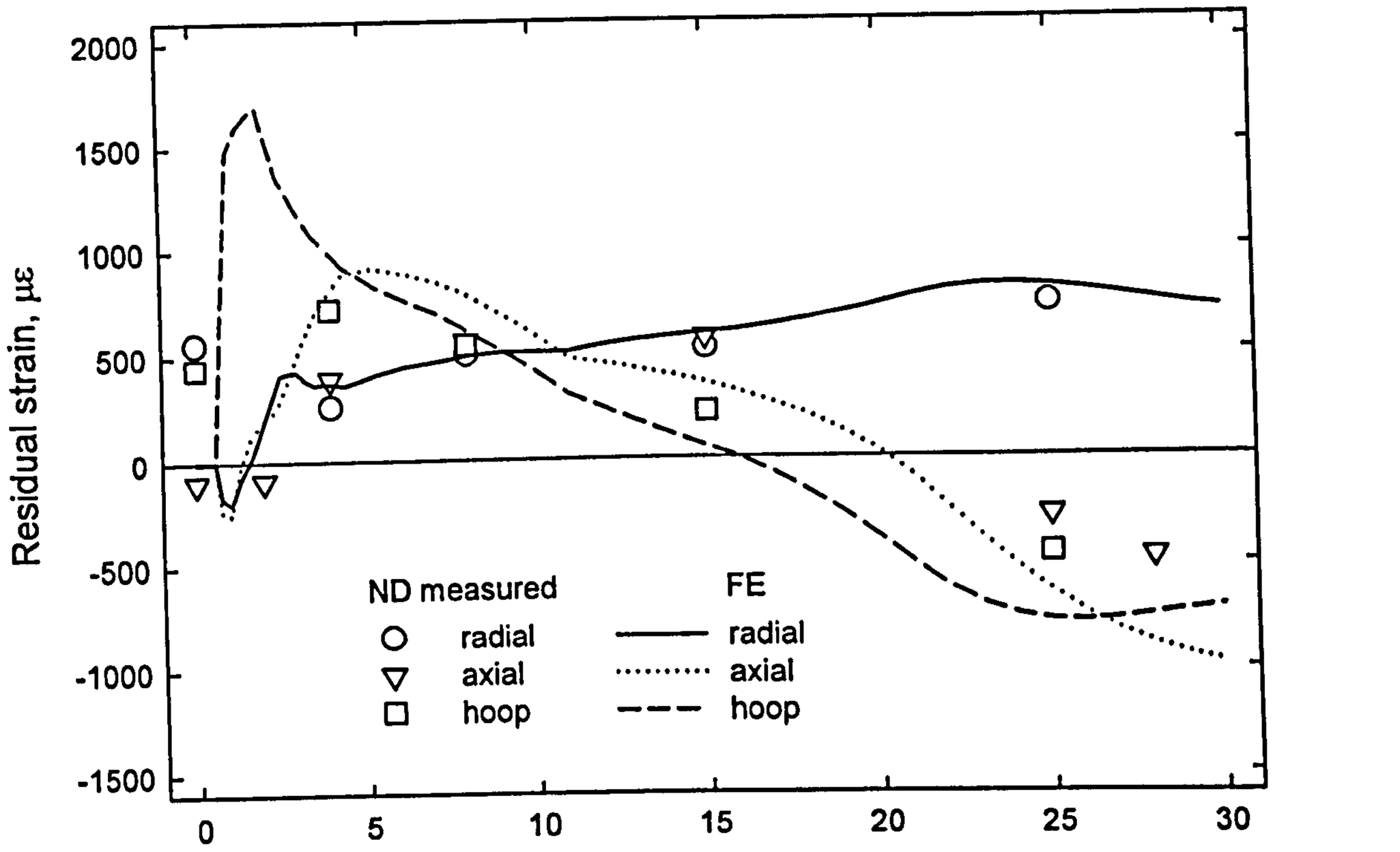

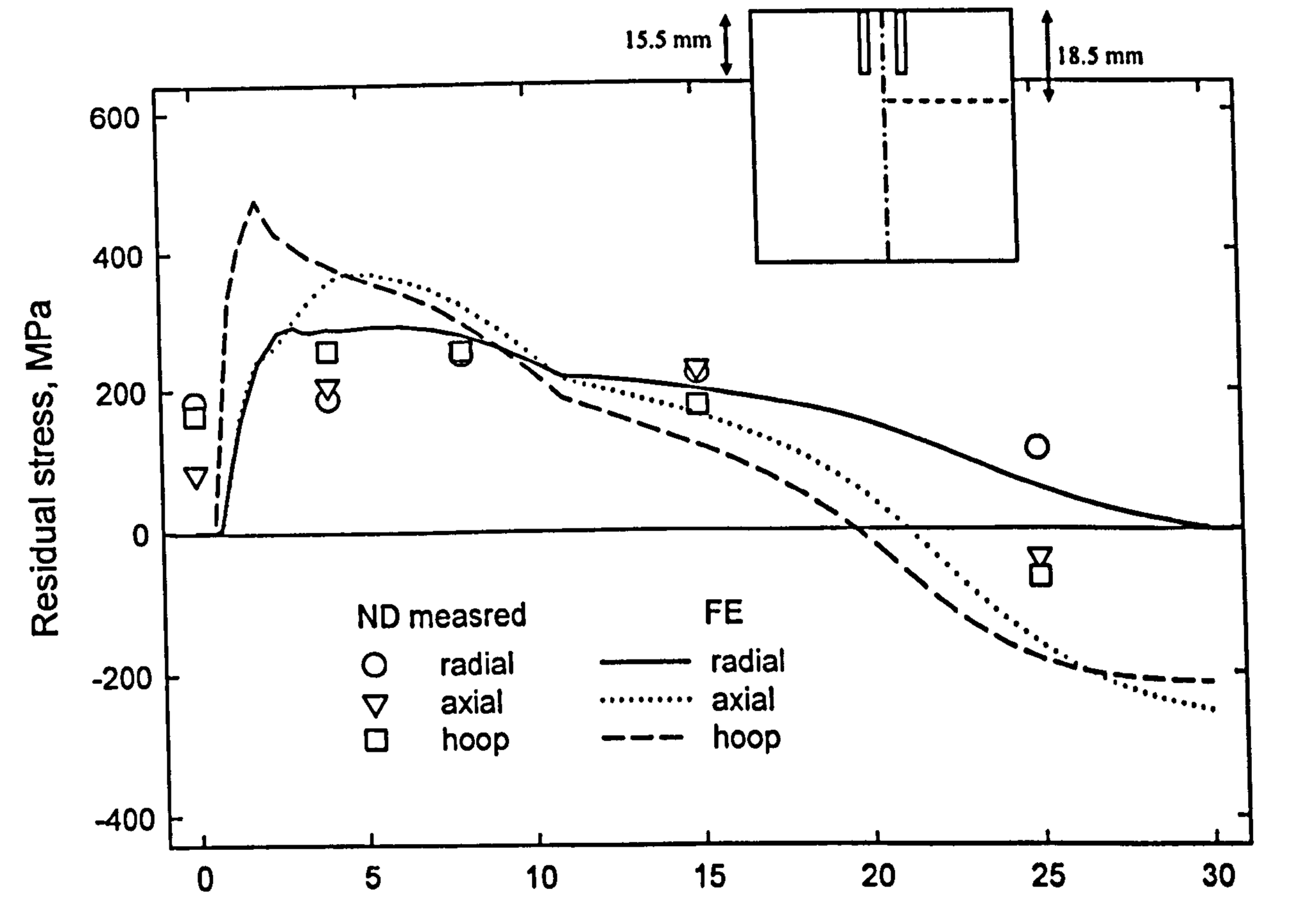

Figure 7.26 Distribution of residual (a) strain and (b) stress across a radial plane 18.5mm below the top surface in a quenched cylinder bar *s40* with 1.5mm diameter drill and 5mm diameter trepanned up to 15.5mm depth.

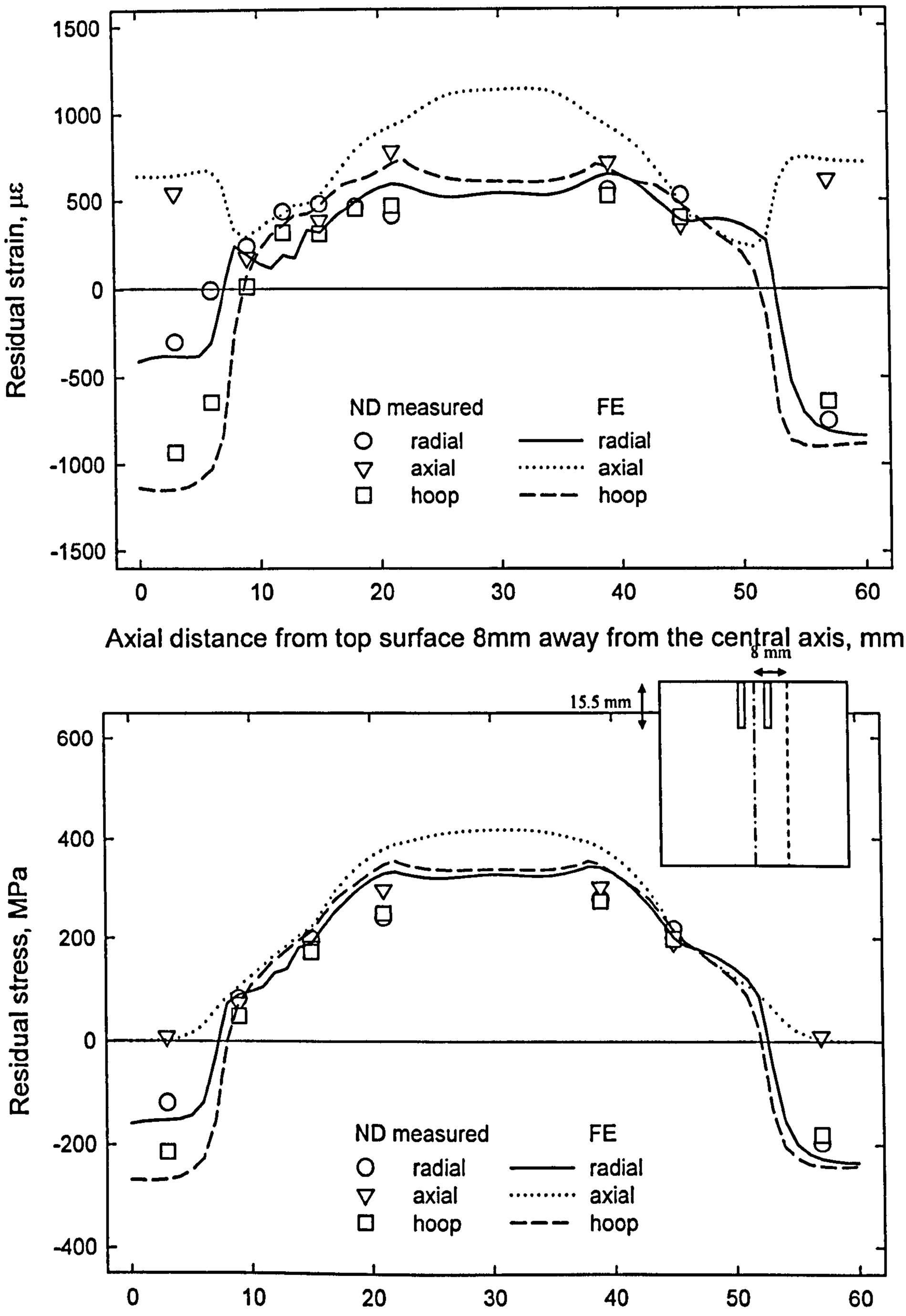

Figure 7.27 Distribution of residual (a) strain and (b) stress along an axial line 8mm away from the centreline in a quenched cylinder bar *s40* with 1.5mm diameter drill and 5mm diameter trepanned up to 15.5mm depth.

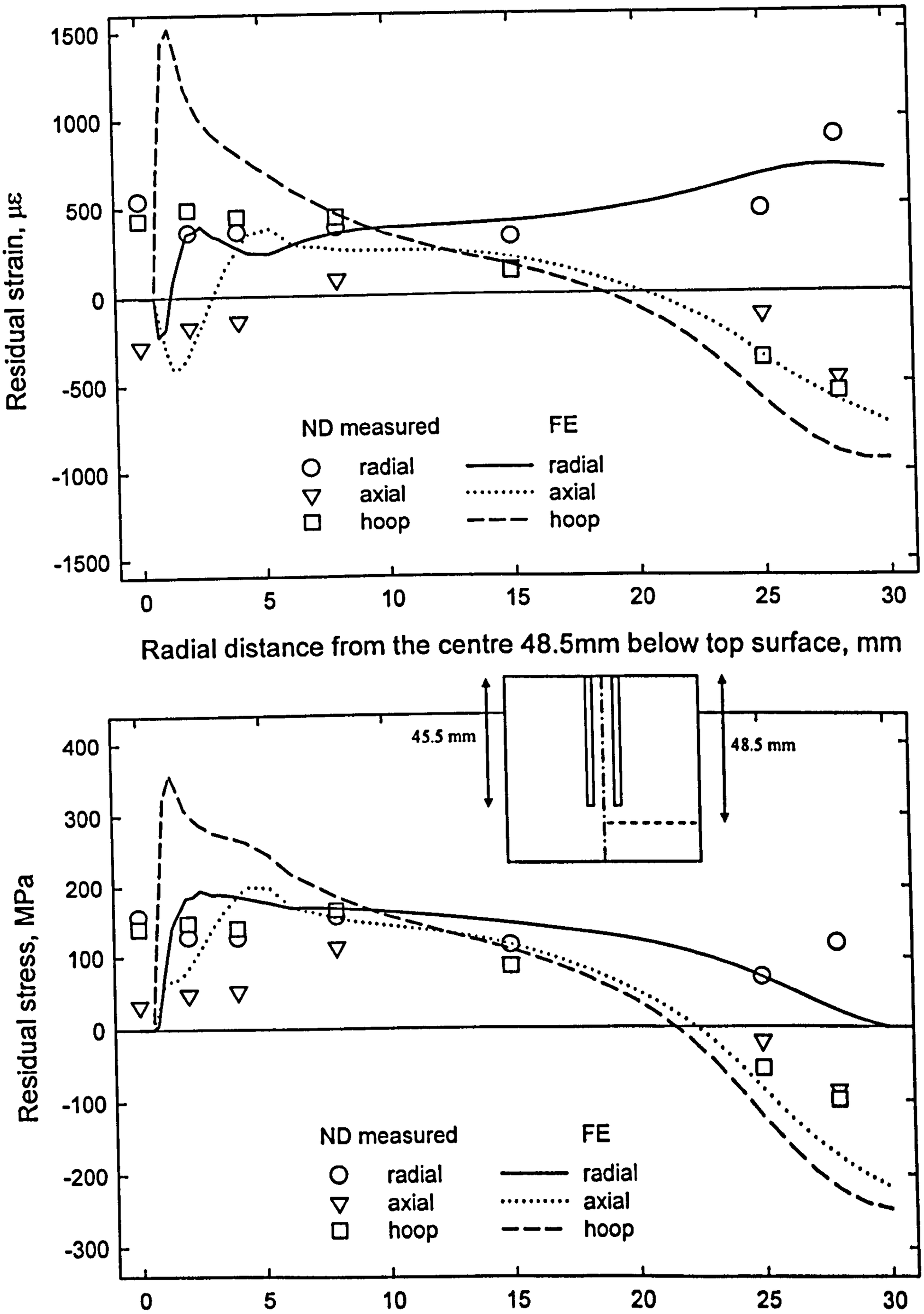

Figure 7.28 Distribution of residual (a) strain and (b) stress across a radial plane 48.5mm below the top surface in a quenched cylinder bar *s42* with 1.5mm diameter drill and 5mm diameter trepanned up to 45.5mm depth.

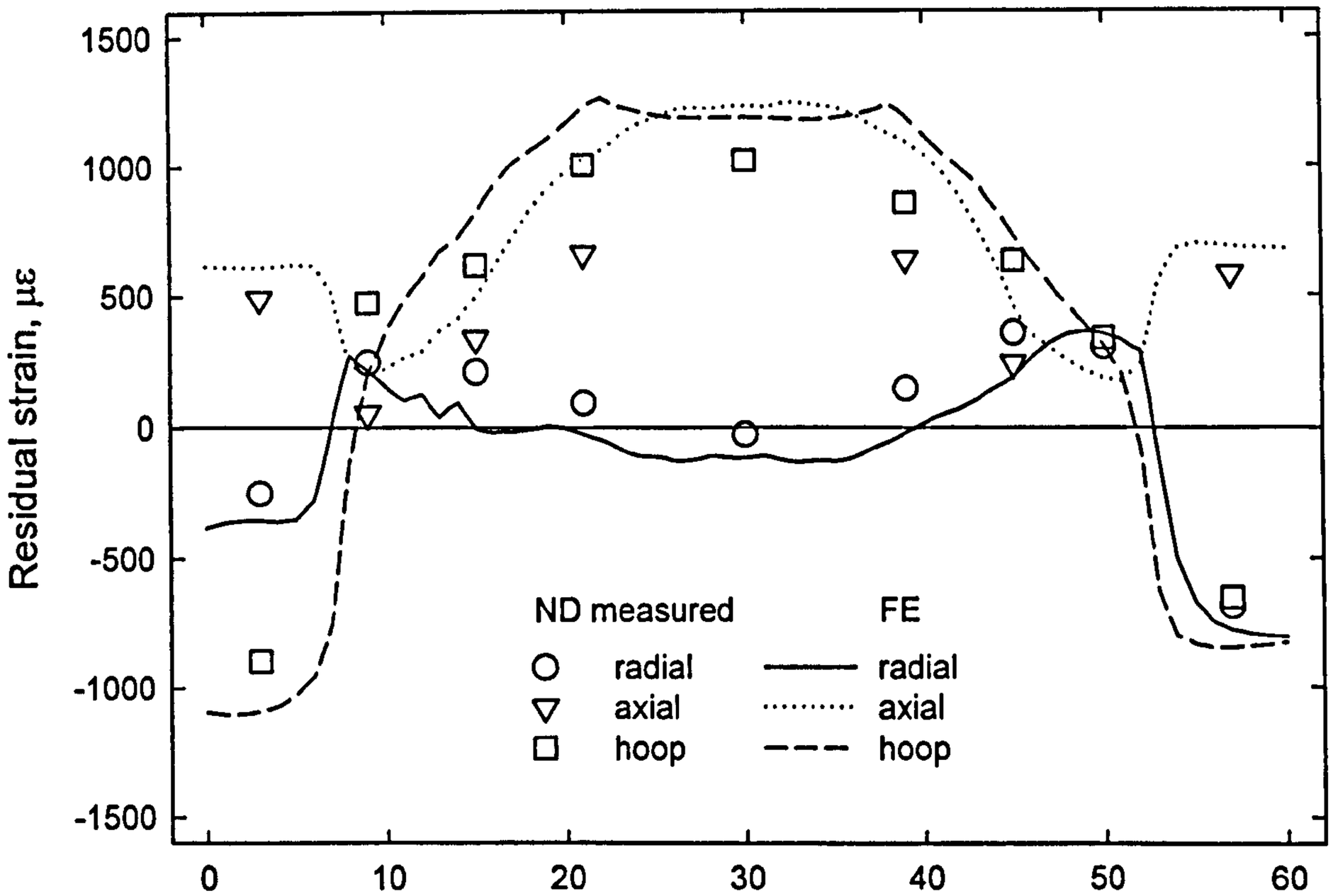

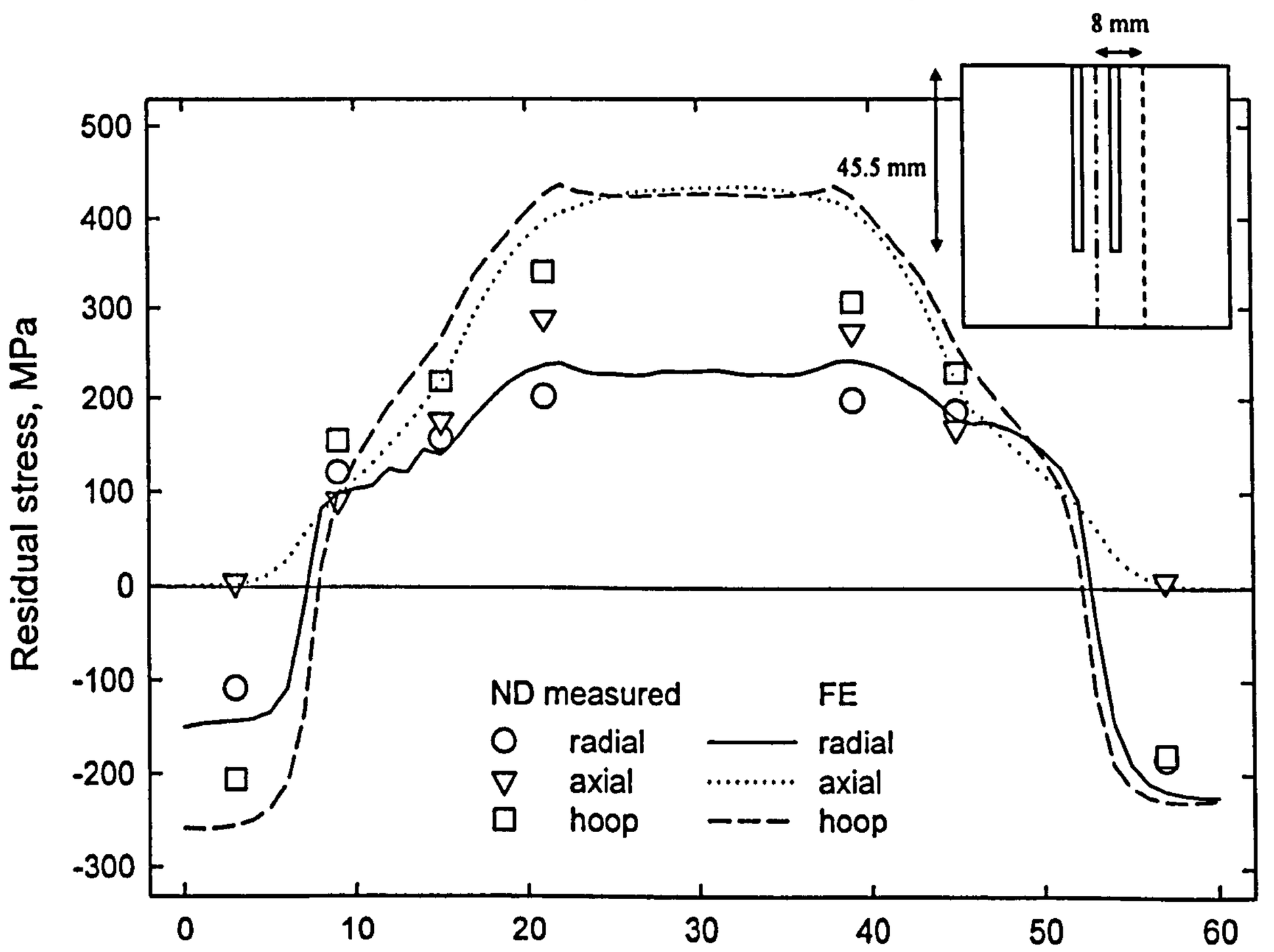

Figure 7.29 Distribution of residual (a) strain and (b) stress along an axial line 8mm away from the centreline in a quenched cylinder bar *s42* with 1.5mm diameter drill and 5mm diameter trepanned up to 45.5mm depth.

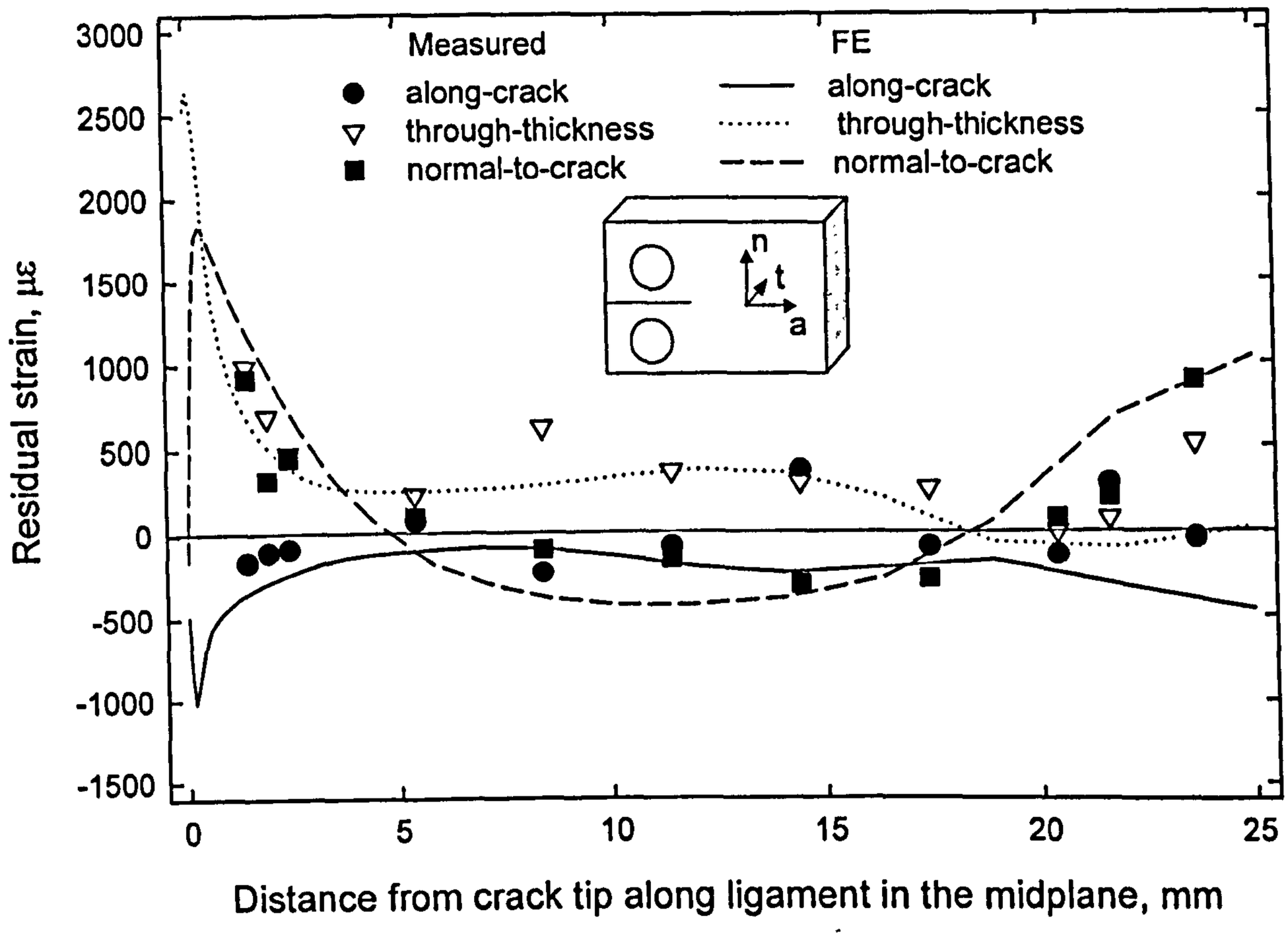

Figure 7.30 Measured and FE predicted residual strain distribution along the ligament ahead of the crack tip in the mid-plane of an as-punched C(T) specimen.

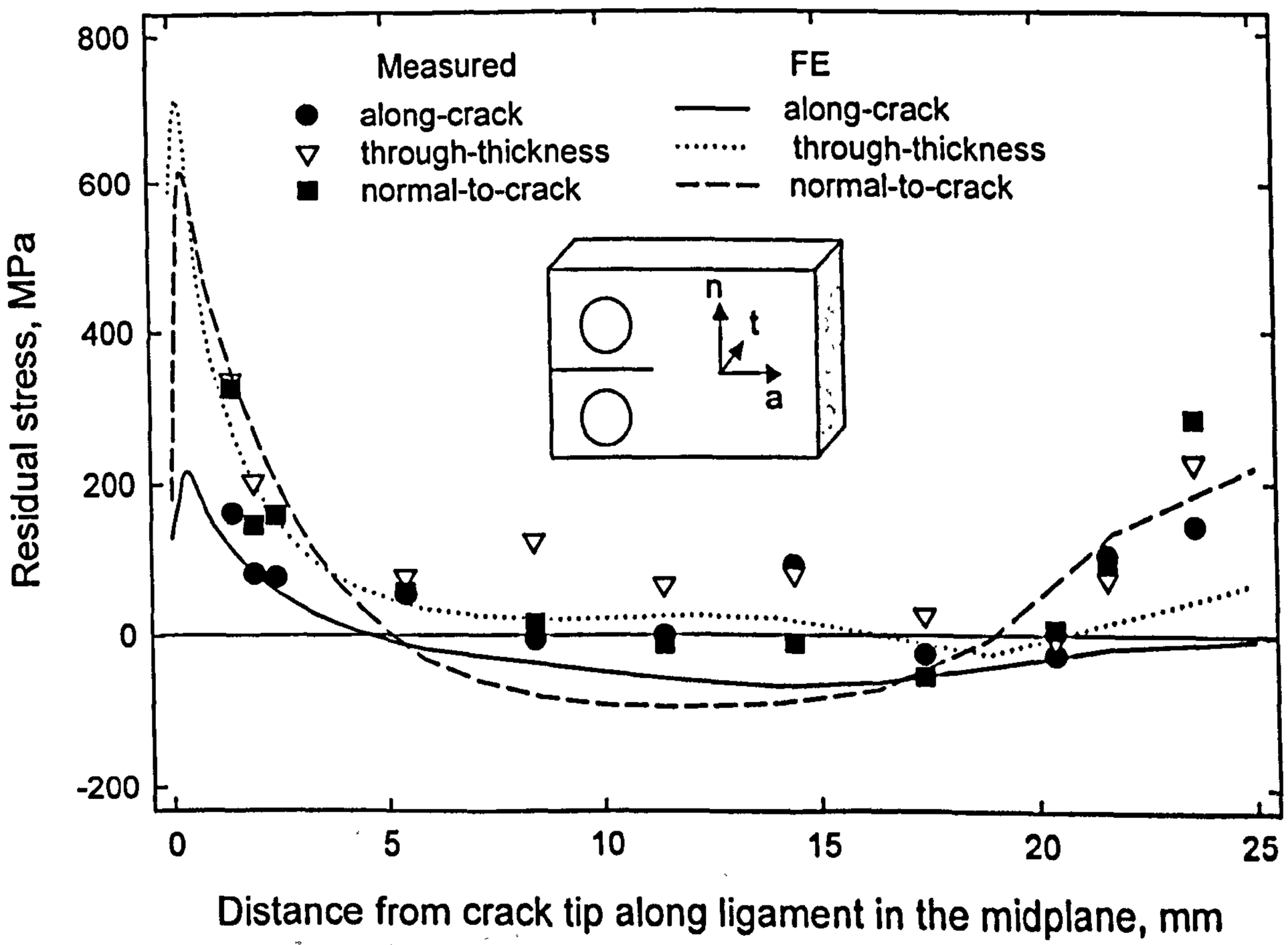

Figure 7.31 Measured and FE predicted residual stress distribution along the ligament ahead of the crack tip in the mid-plane of an as-punched C(T) specimen.

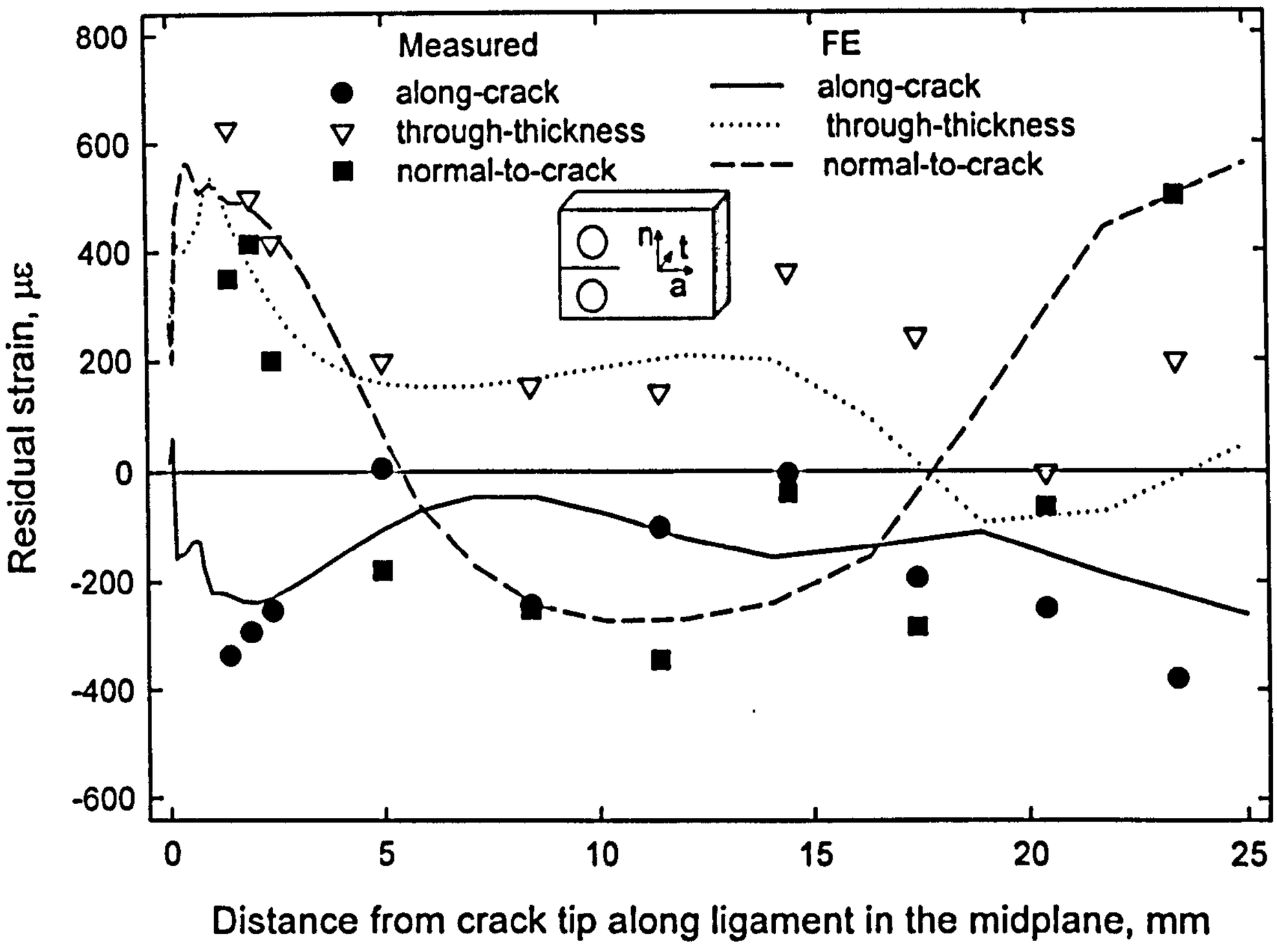

Figure 7.32 Measured and FE predicted residual strain distribution along the ligament ahead of the crack tip in the mid-plane of a punched and aged C(T) specimen.

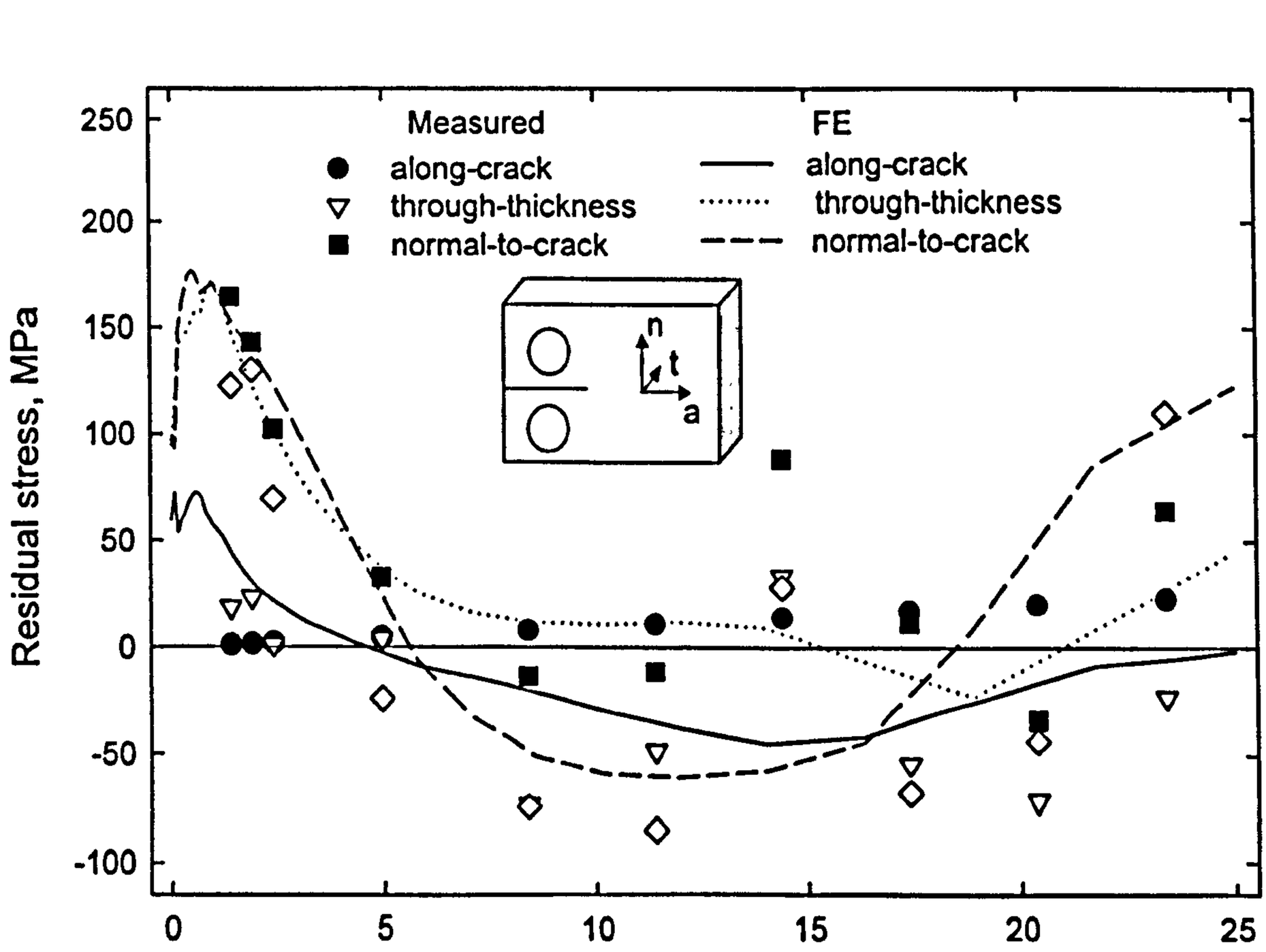

Figure 7.33 Measured and FE predicted residual stress distribution along the ligament ahead of the crack tip in the mid-plane of a punched and aged C(T) specimen.

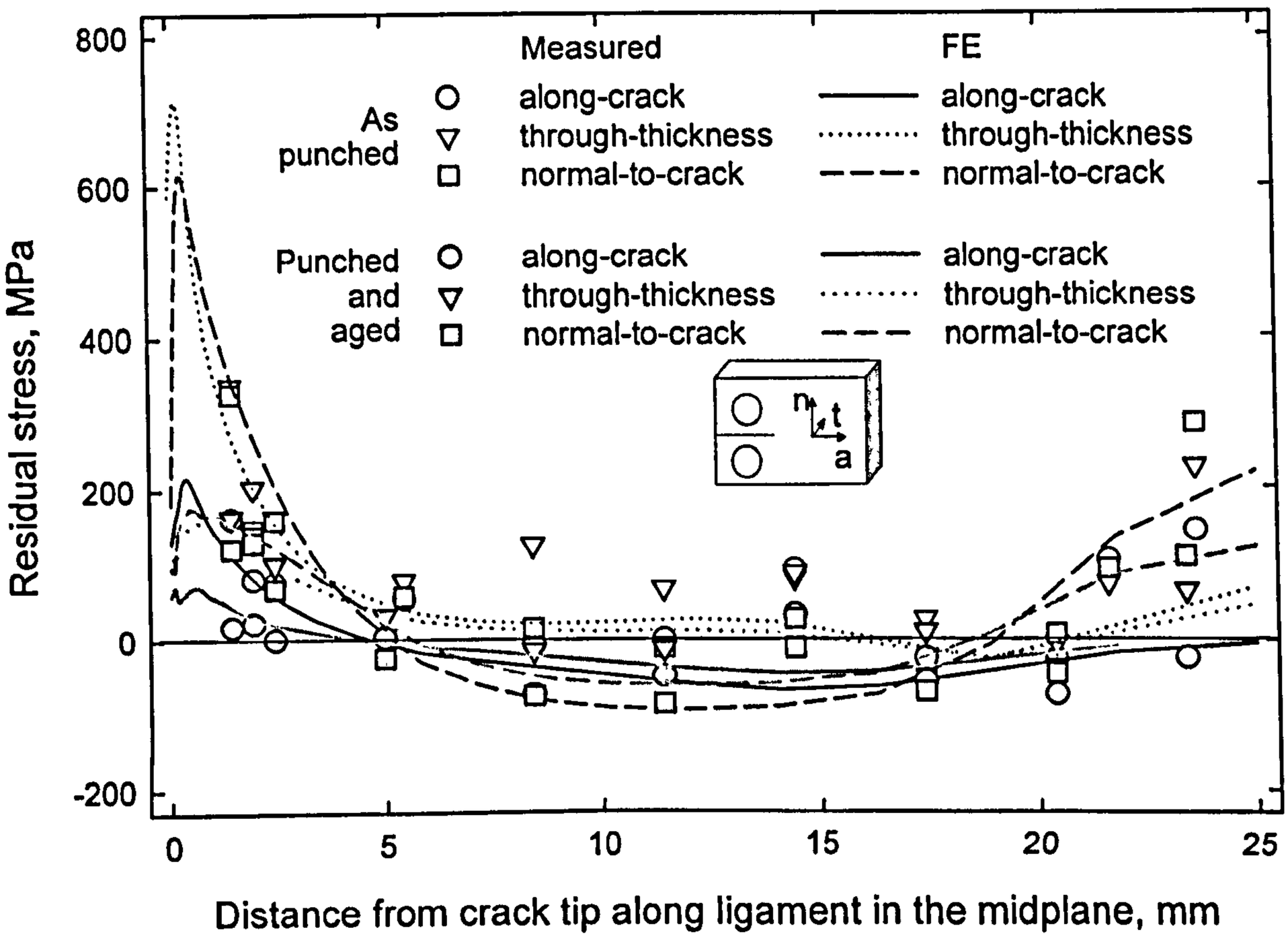

Figure 7.34 Comparison of residual stress distribution along the ligament ahead of crack tip in the mid-plane between as-punched and punched and thermally aged (at 550°C for 3900hours) C(T) specimens.

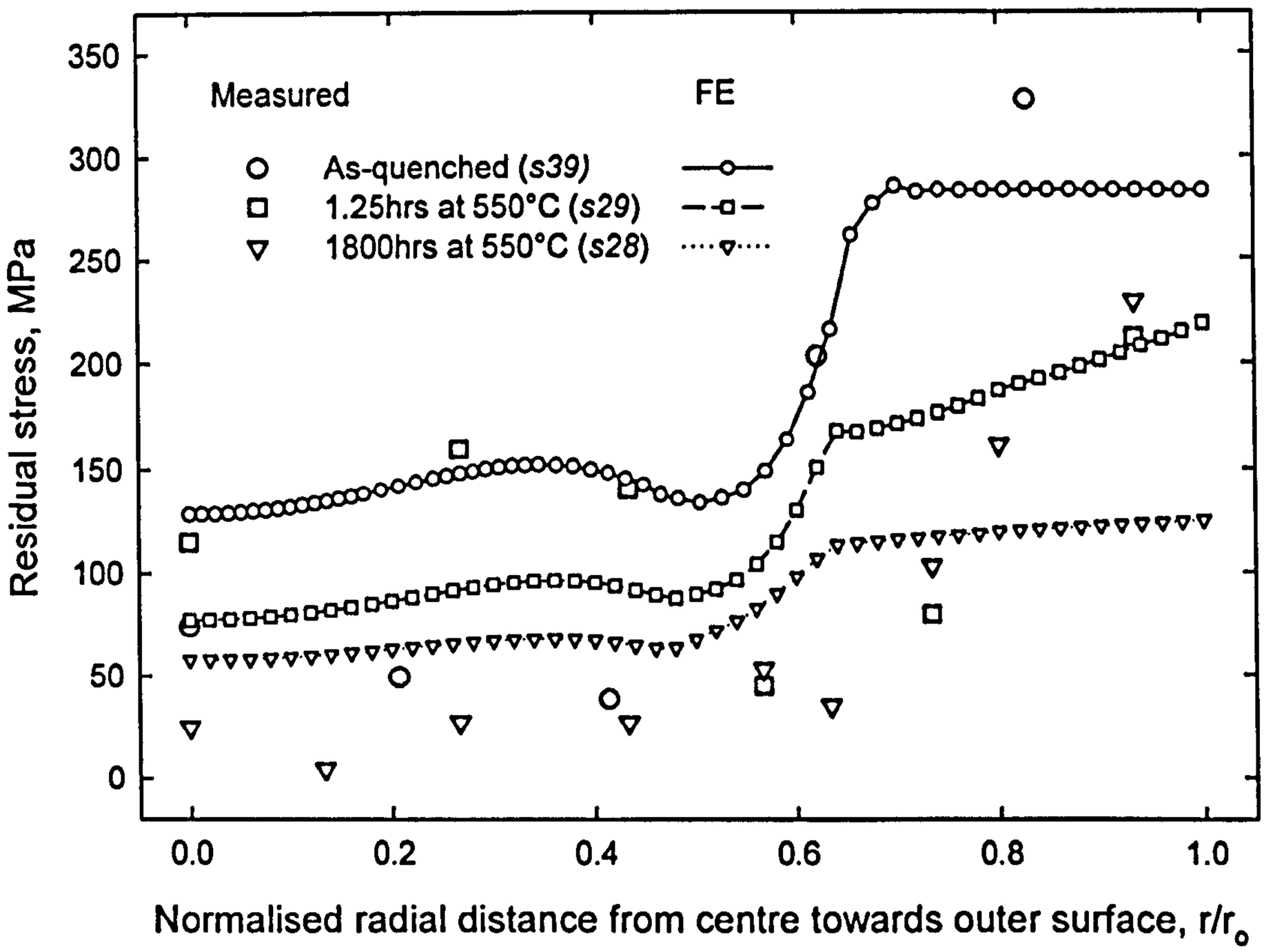

Figure 8.1 Measured and FE predicted von Mises equivalent residual stress distribution across the radial plane in a quenched cylinder during thermal exposure.

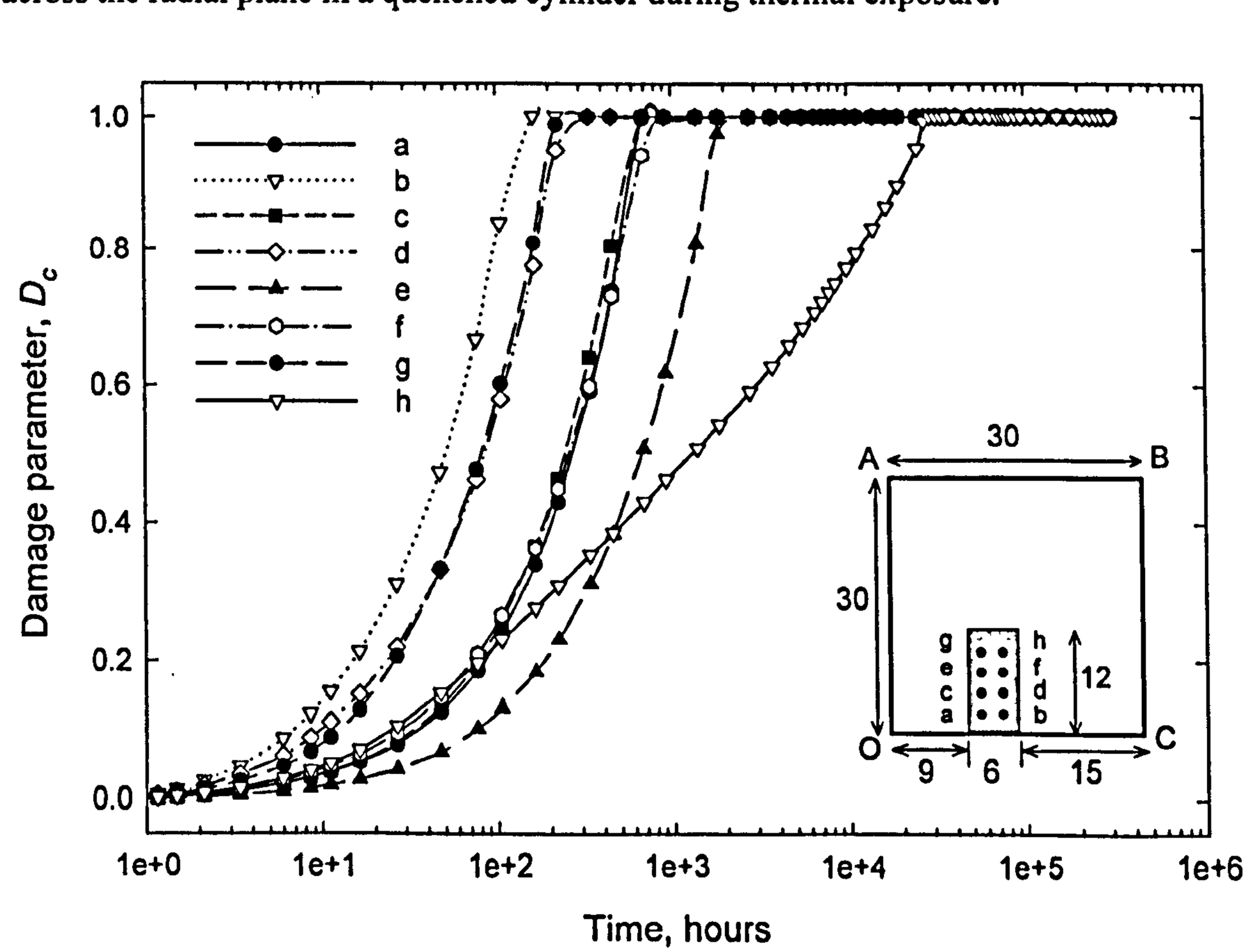

(a) set 1: $p = 2.38$, $q = 1.04$

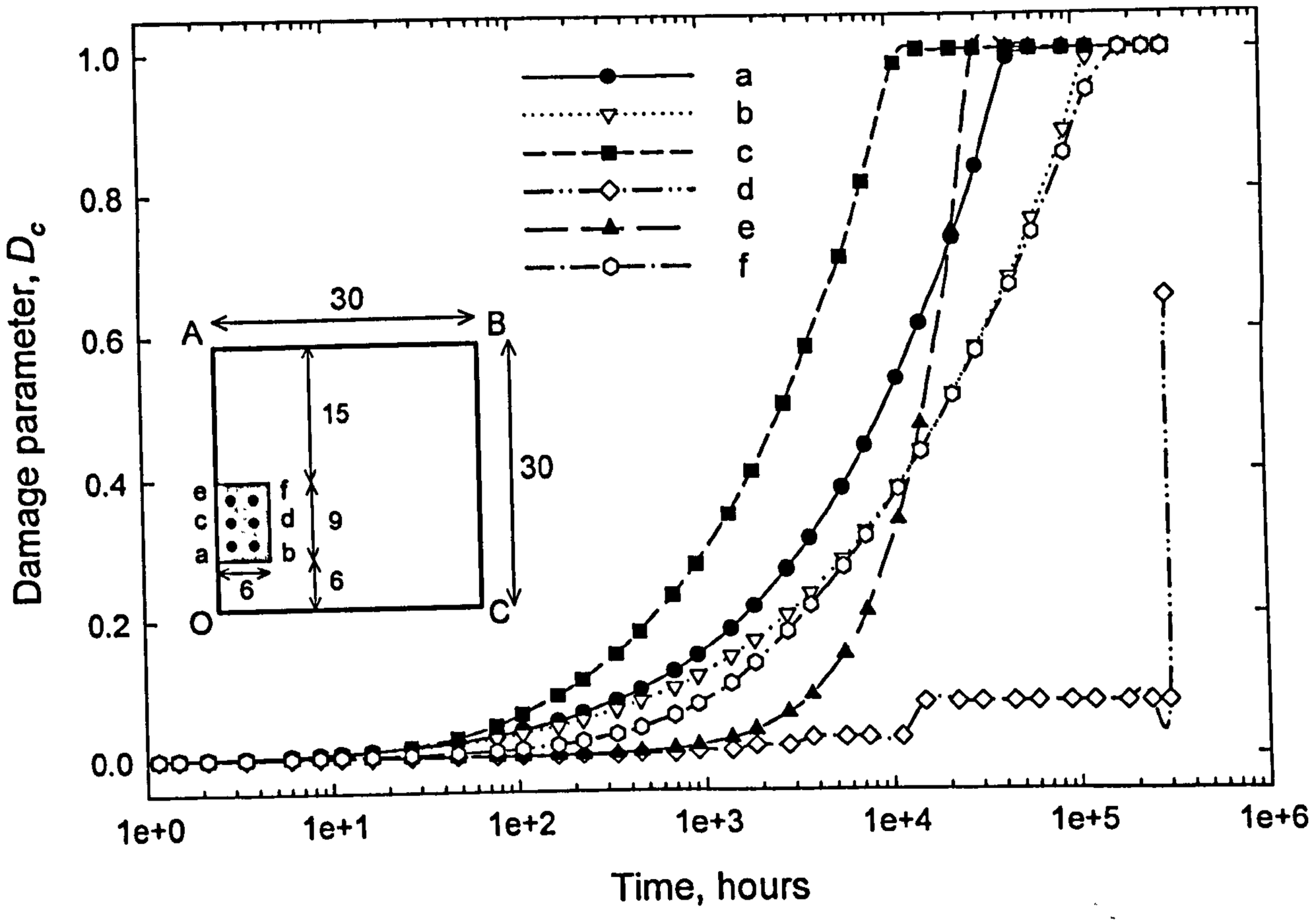

(b) set 2: $p = 0.15$, $q = 1.25$

Figure 8.2 Predicted damage in a selected region of a quenched cylinder, diameter 60mm, length 60mm subjected to thermal exposure at 550°C.

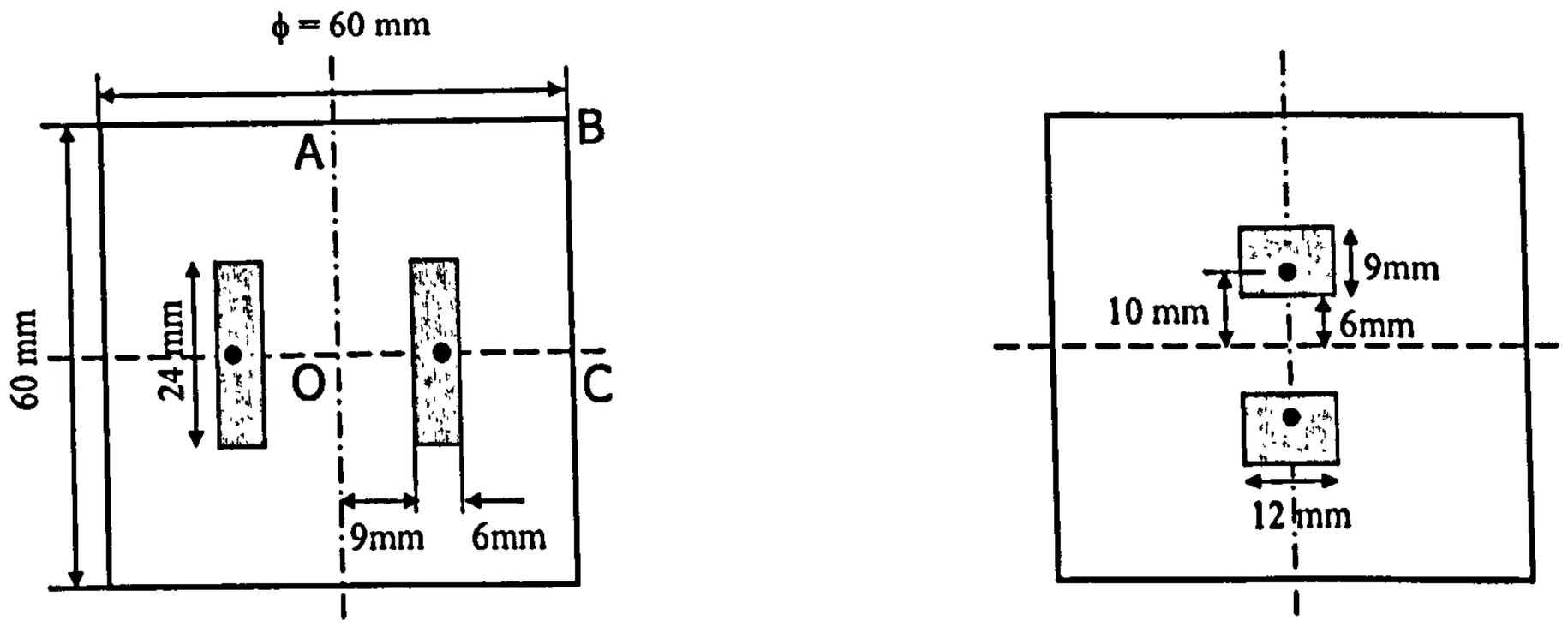

(a) Set 1 (b) Set 2

Figure 8.3 Region of creep damage accumulation predicted in a quenched cylinder bar followed by thermal ageing at 550°C for 2880hours and 4320hours under empirical functions set 1 and set 2 respectively.

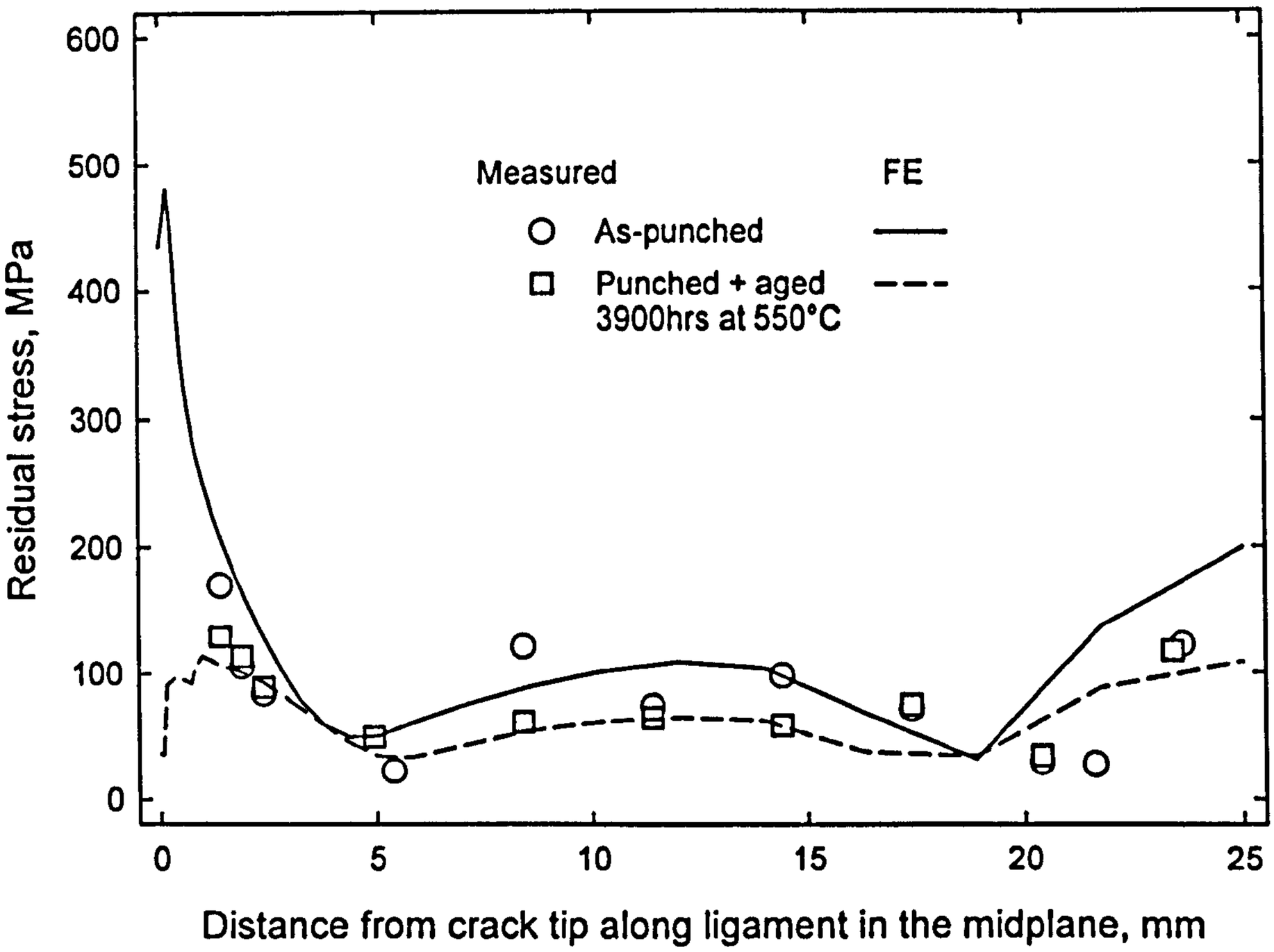

Figure 8.4 Measured and FE predicted von Mises equivalent residual stress distribution along the ligament ahead of crack tip in the mid-plane of a figure-of-eight punched C(T) specimen during thermal ageing.

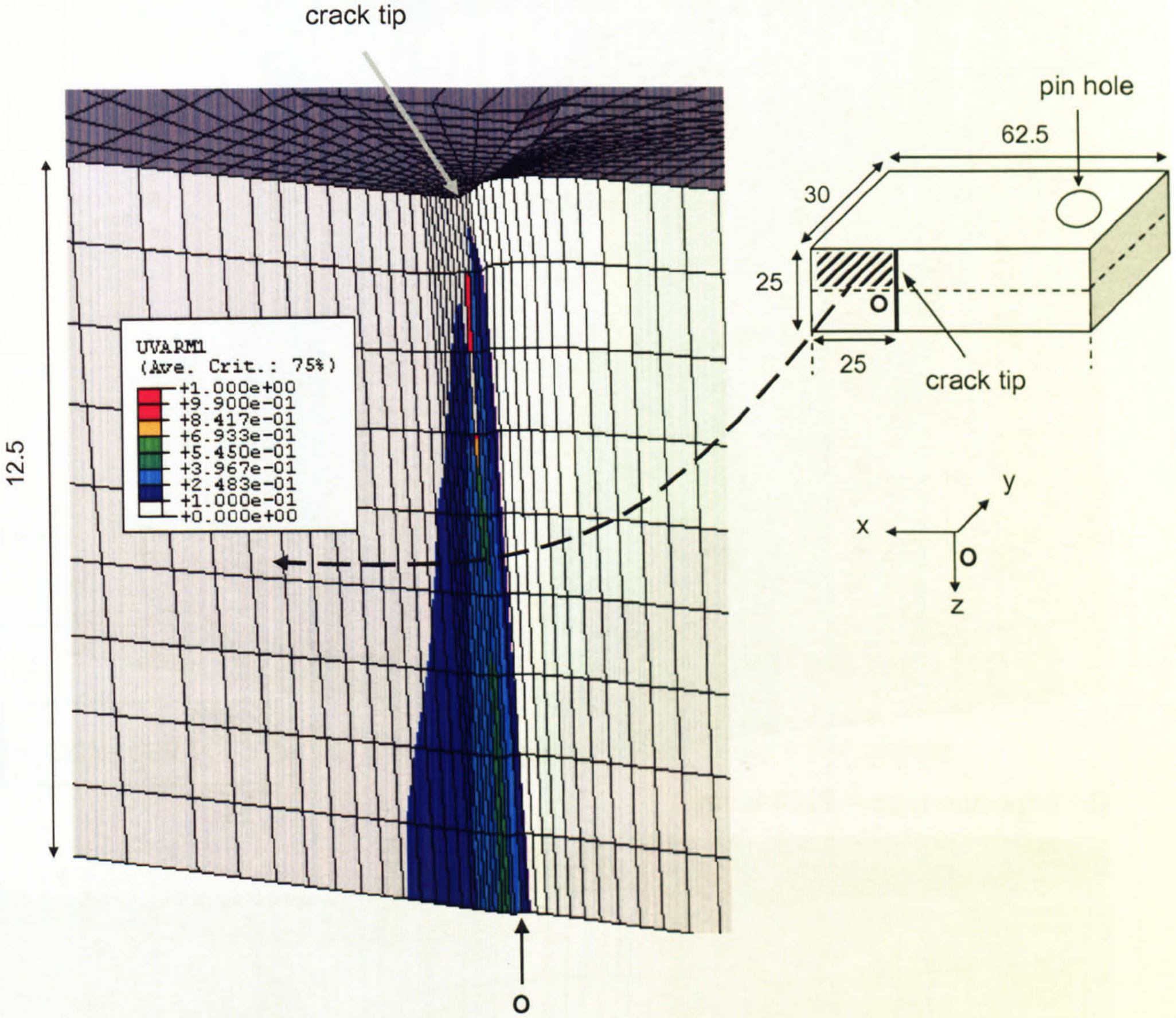

(a) Exposure time = 200 hours

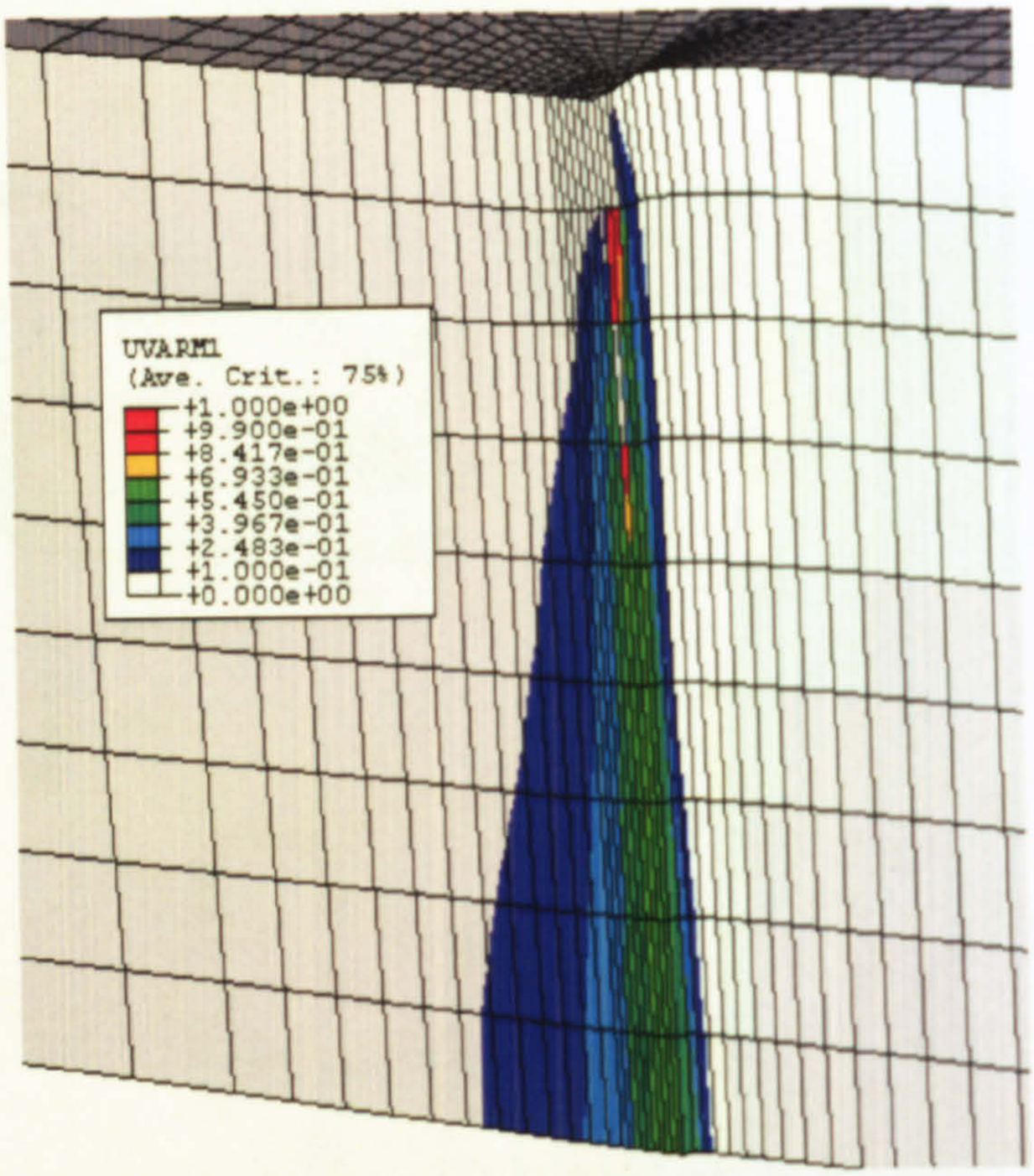

(b) Exposure time = 2100 hours

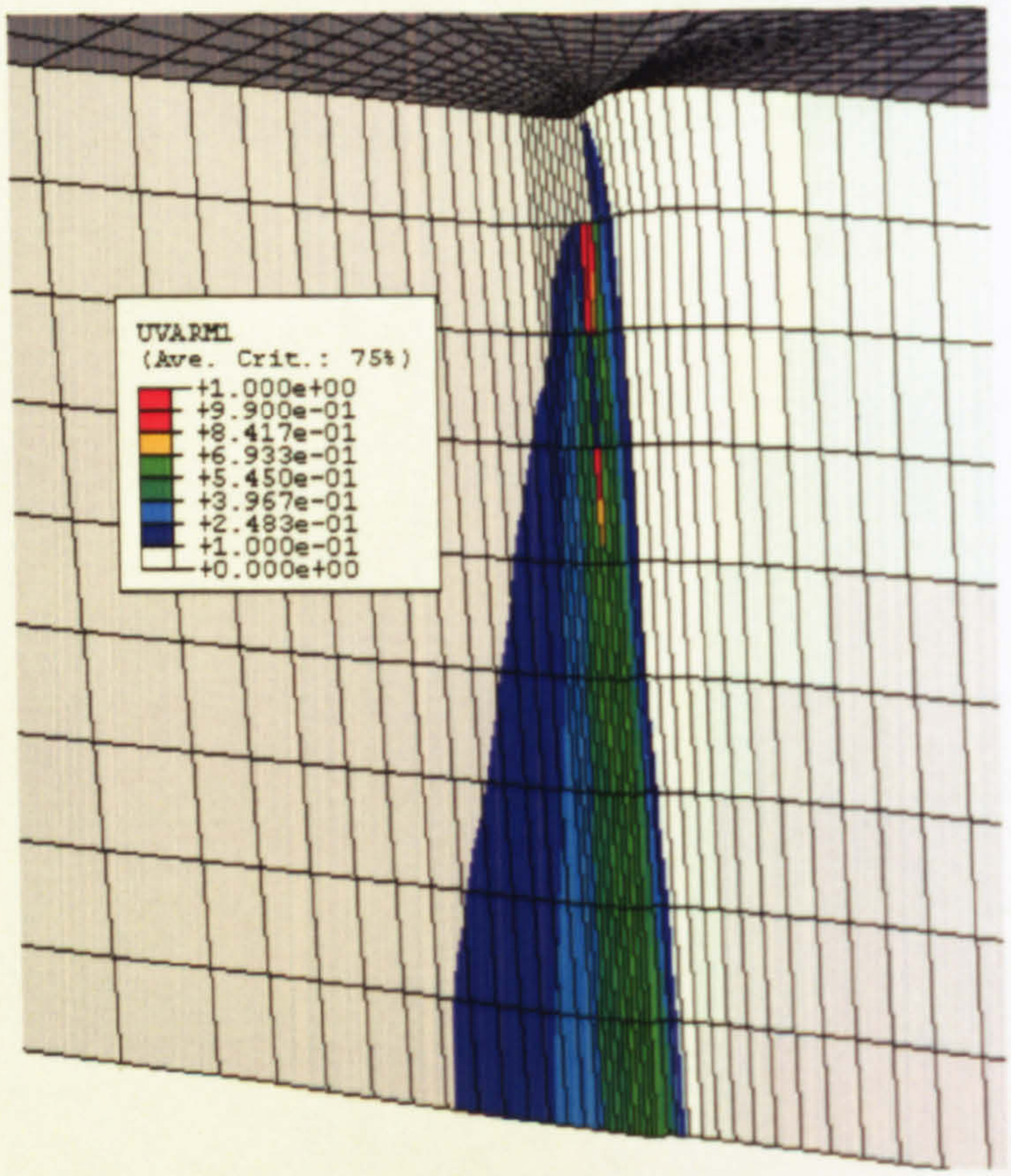

(c) Exposure time = 3900 hours

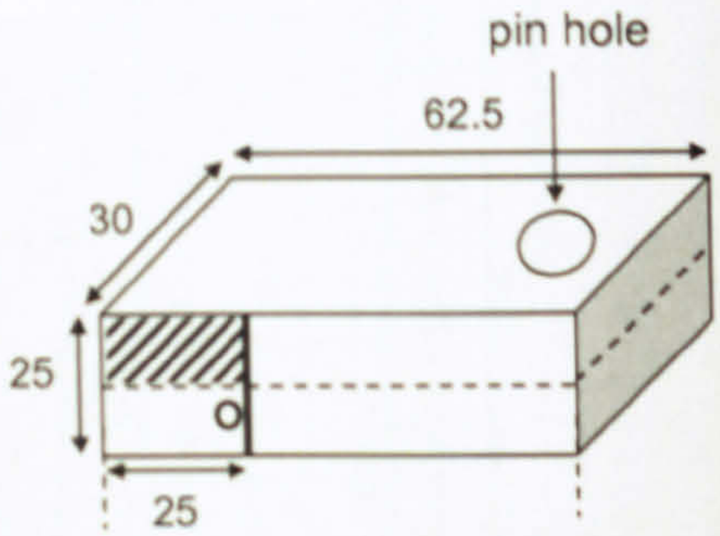

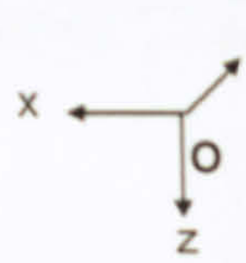

Figure 8.5 Contour plots illustrating the development of predicted damage parameter in thermally exposed single punch C(T) specimens with time.

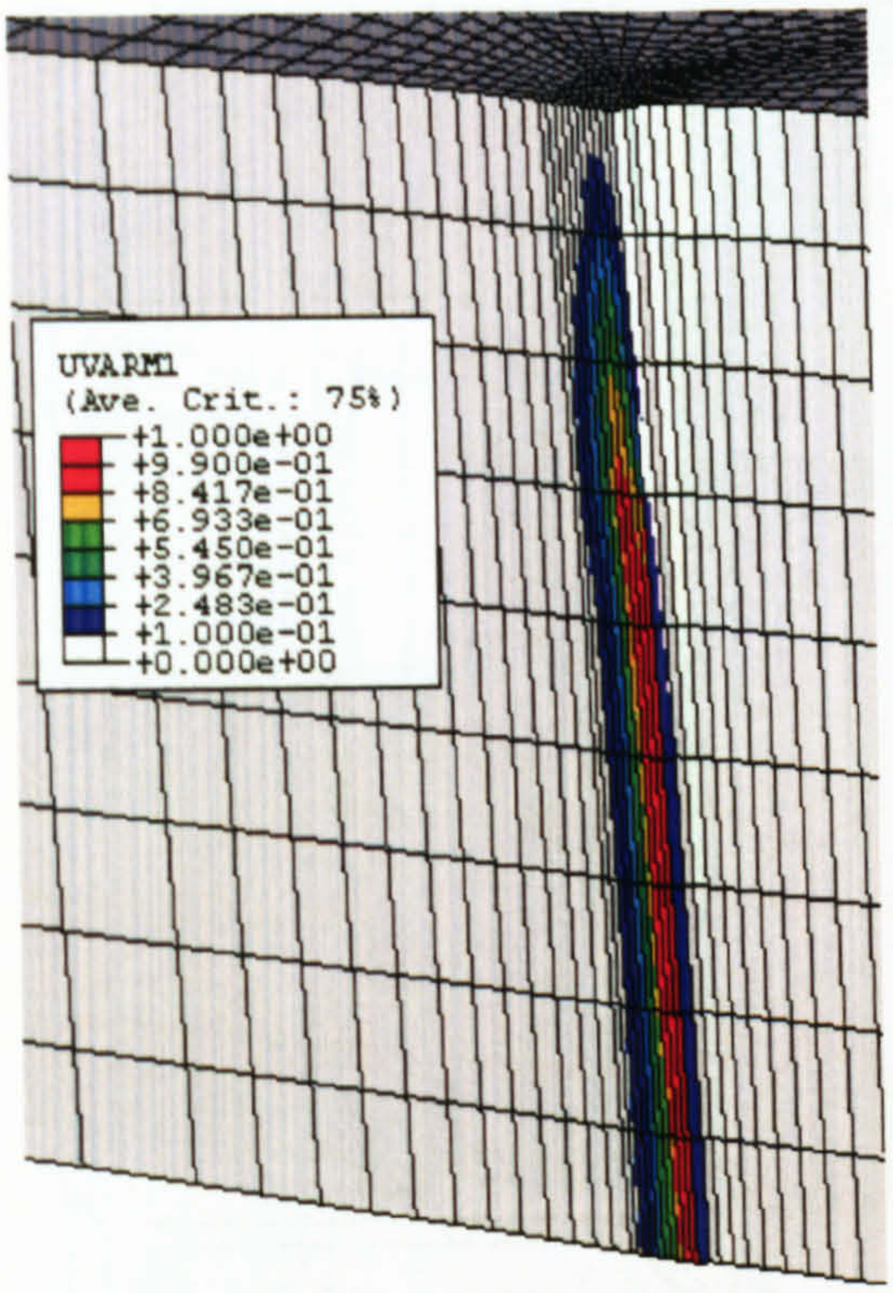

(a) Exposure time = 1.5 hours

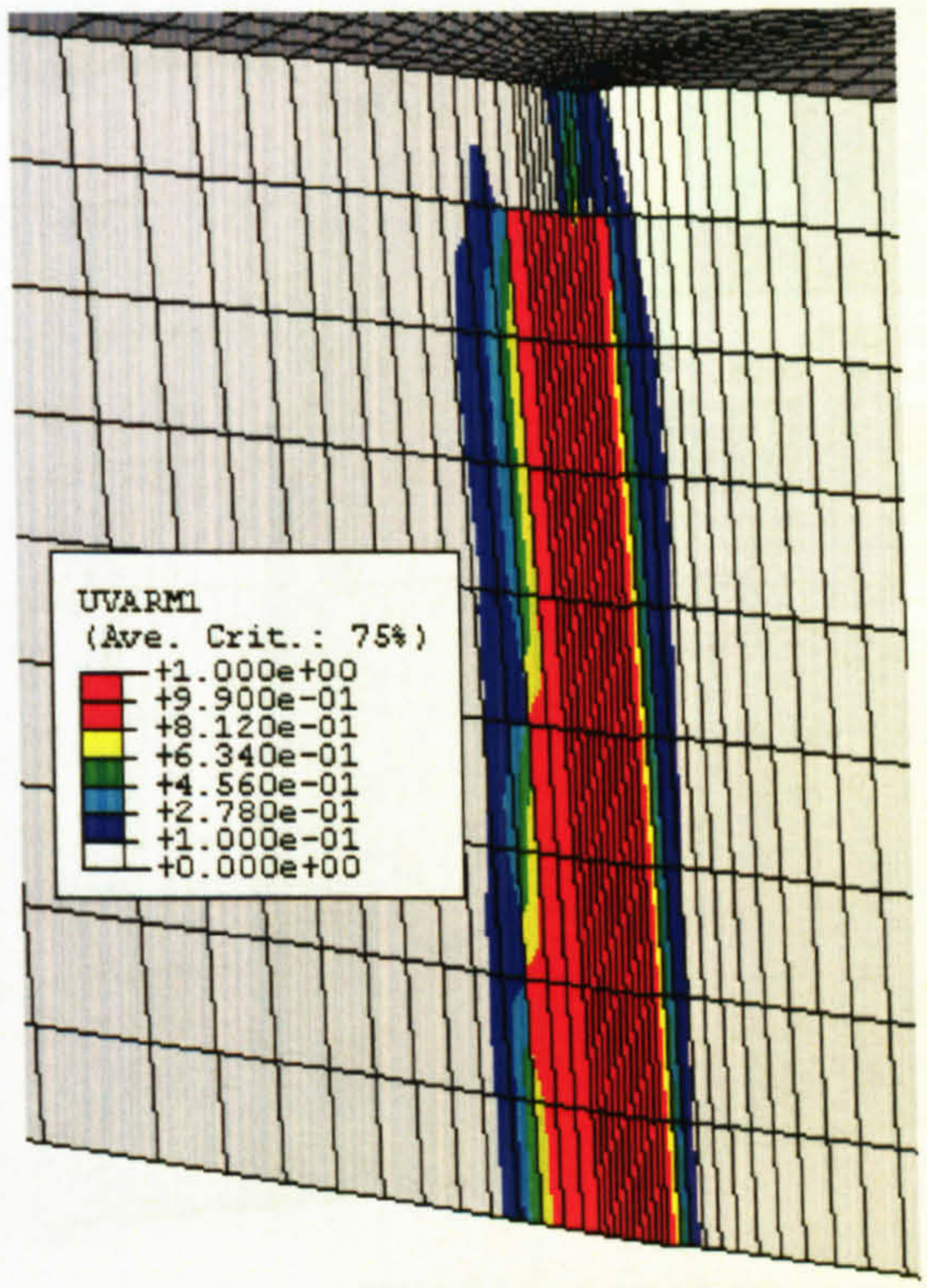

(b) Exposure time = 2100 hours

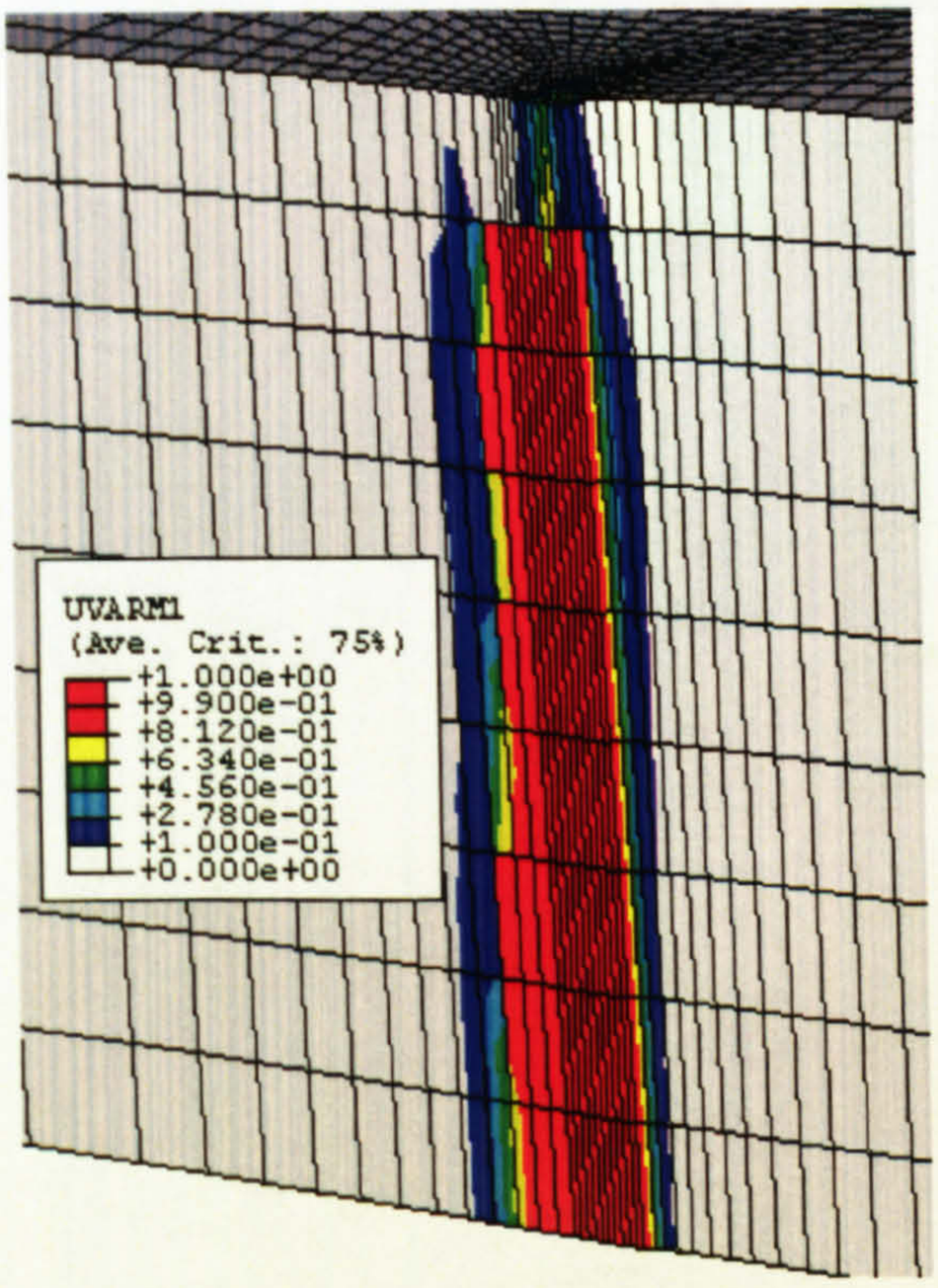

(c) Exposure time = 3900 hours

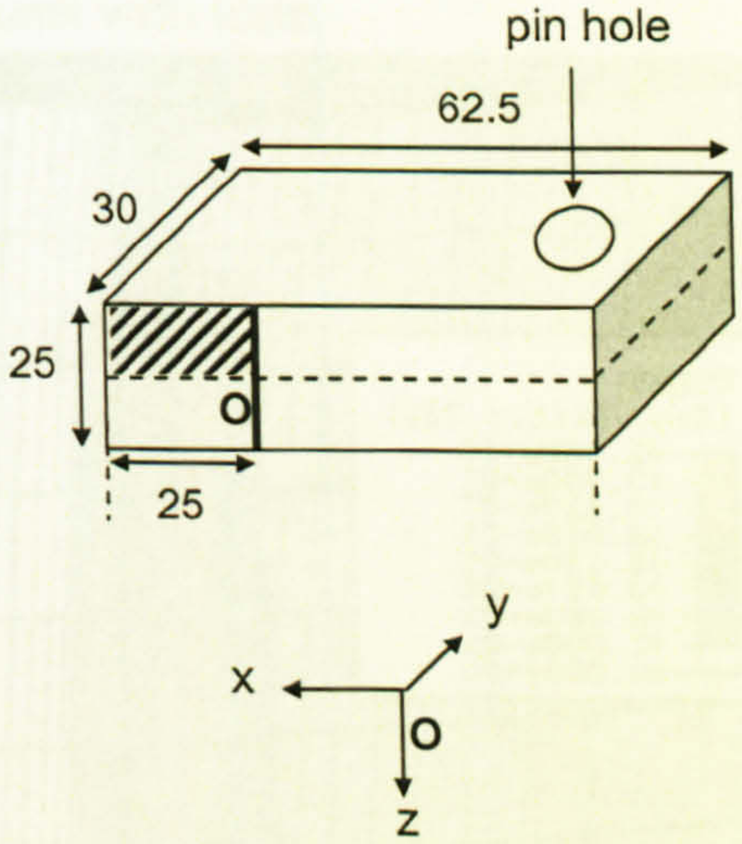

Figure 8.6 Contour plots illustrating the development of predicted damage parameter in thermally exposed double punch C(T) specimens with time.

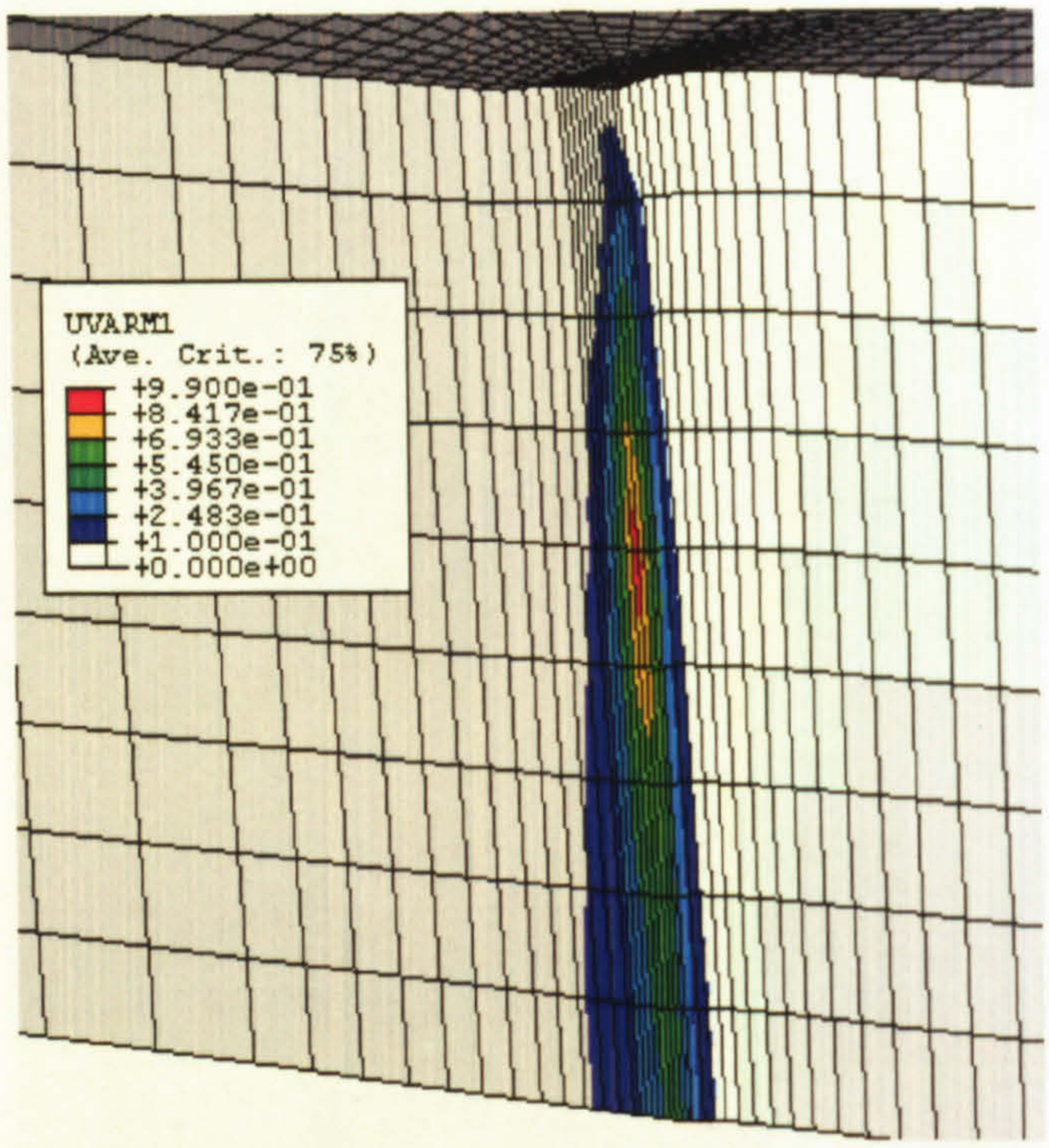

(a) Exposure time = 20 hours

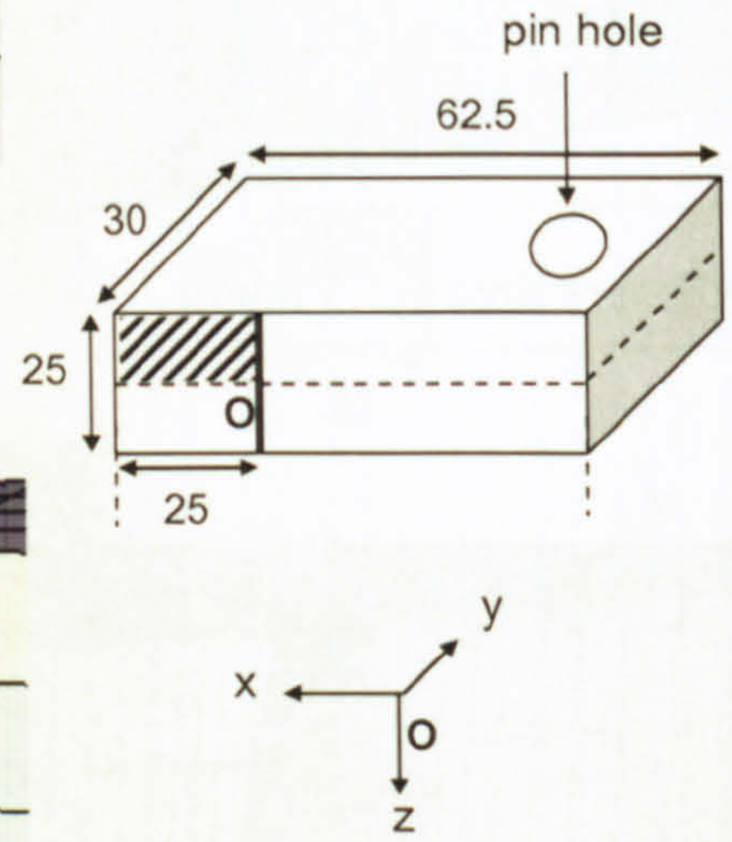

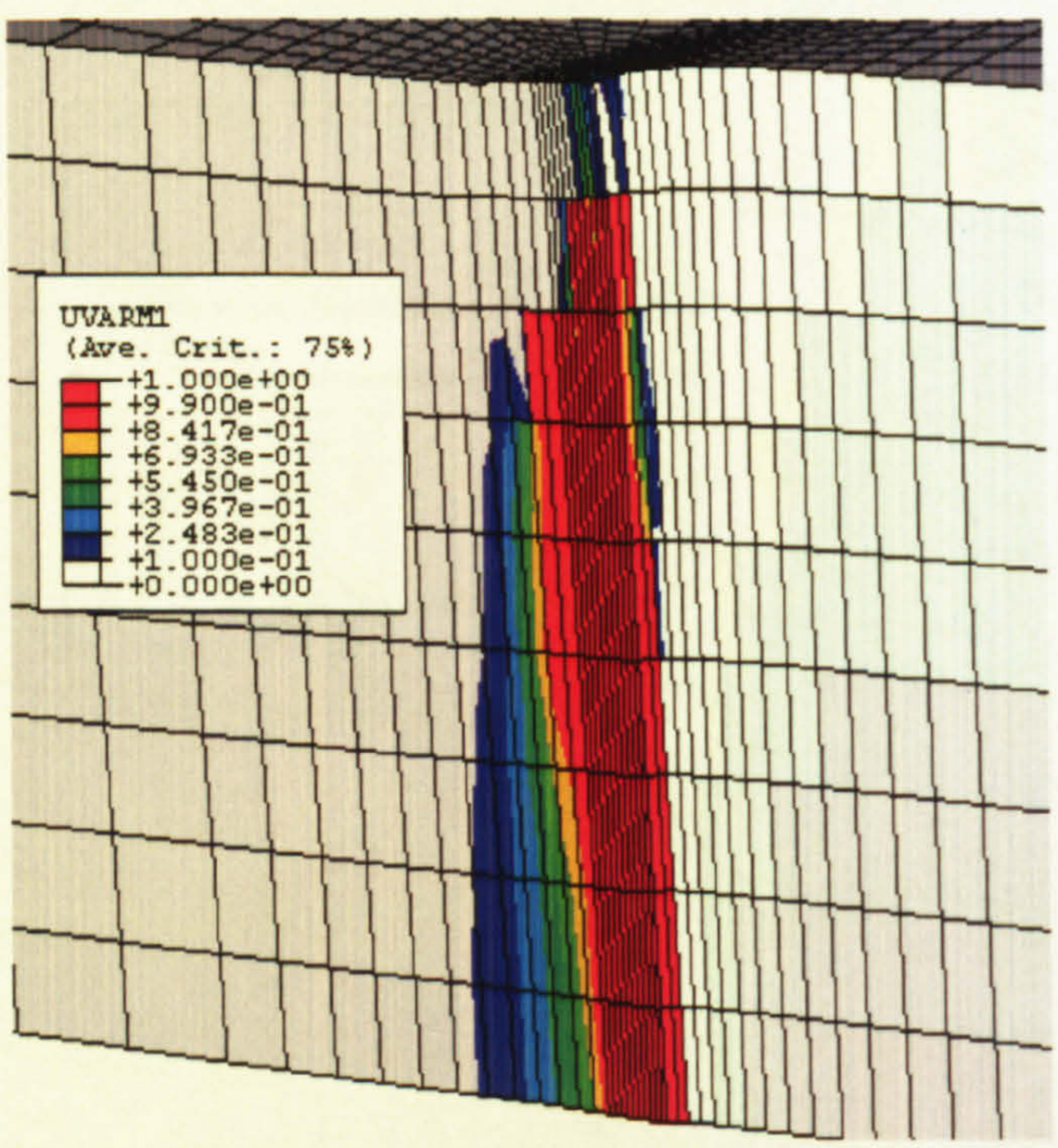

(b) Exposure time = 2100 hours

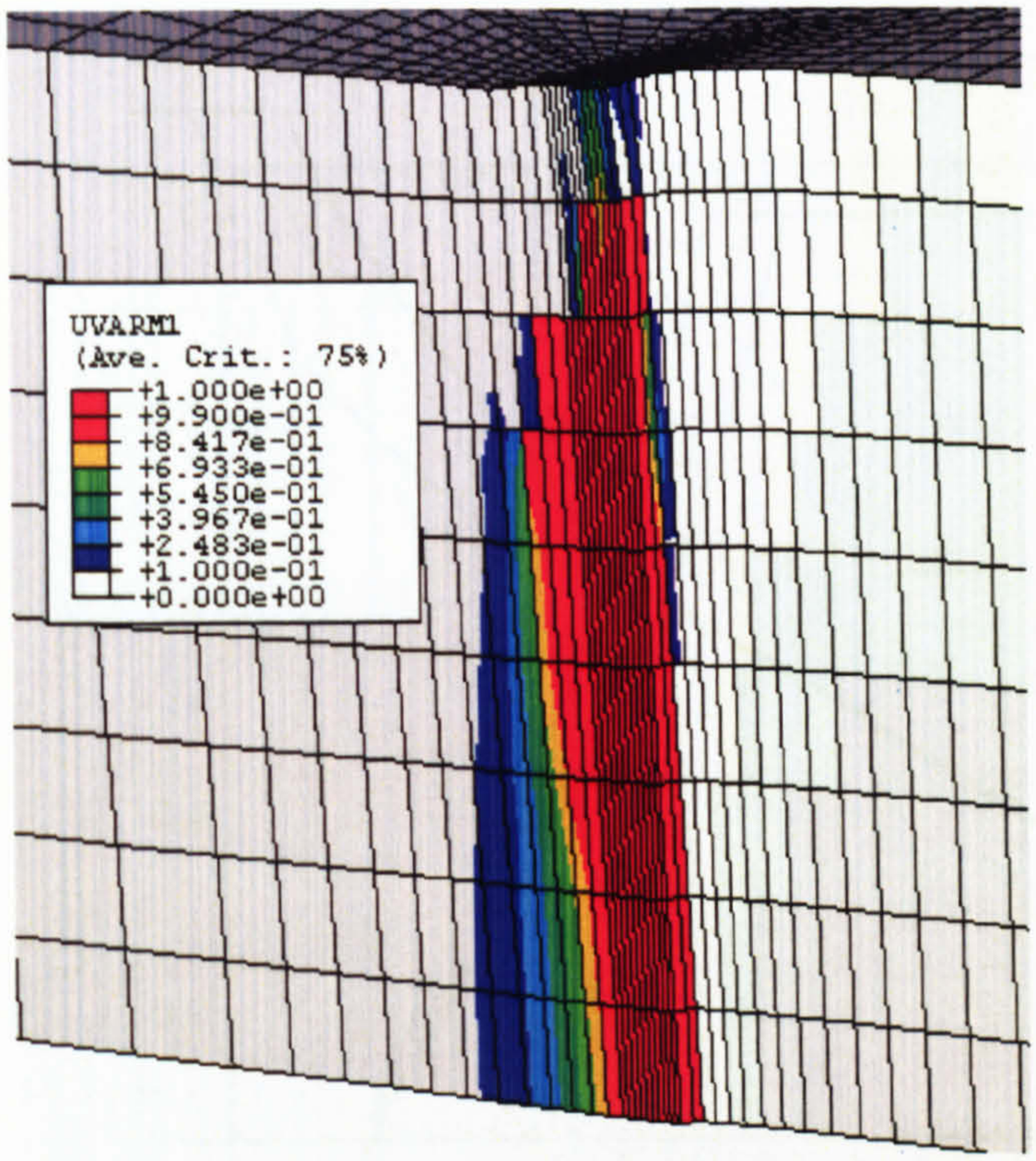

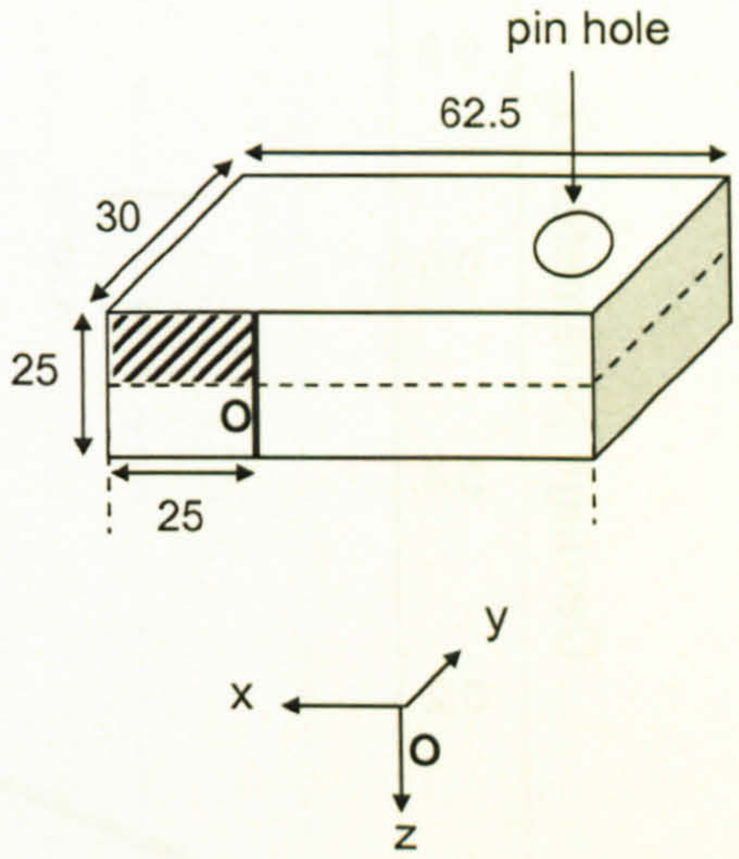

(c) Exposure time = 3900 hours

Figure 8.7 Contour plots illustrating the development of predicted damage parameter in thermally exposed figure-of-eight punch C(T) specimens with time.

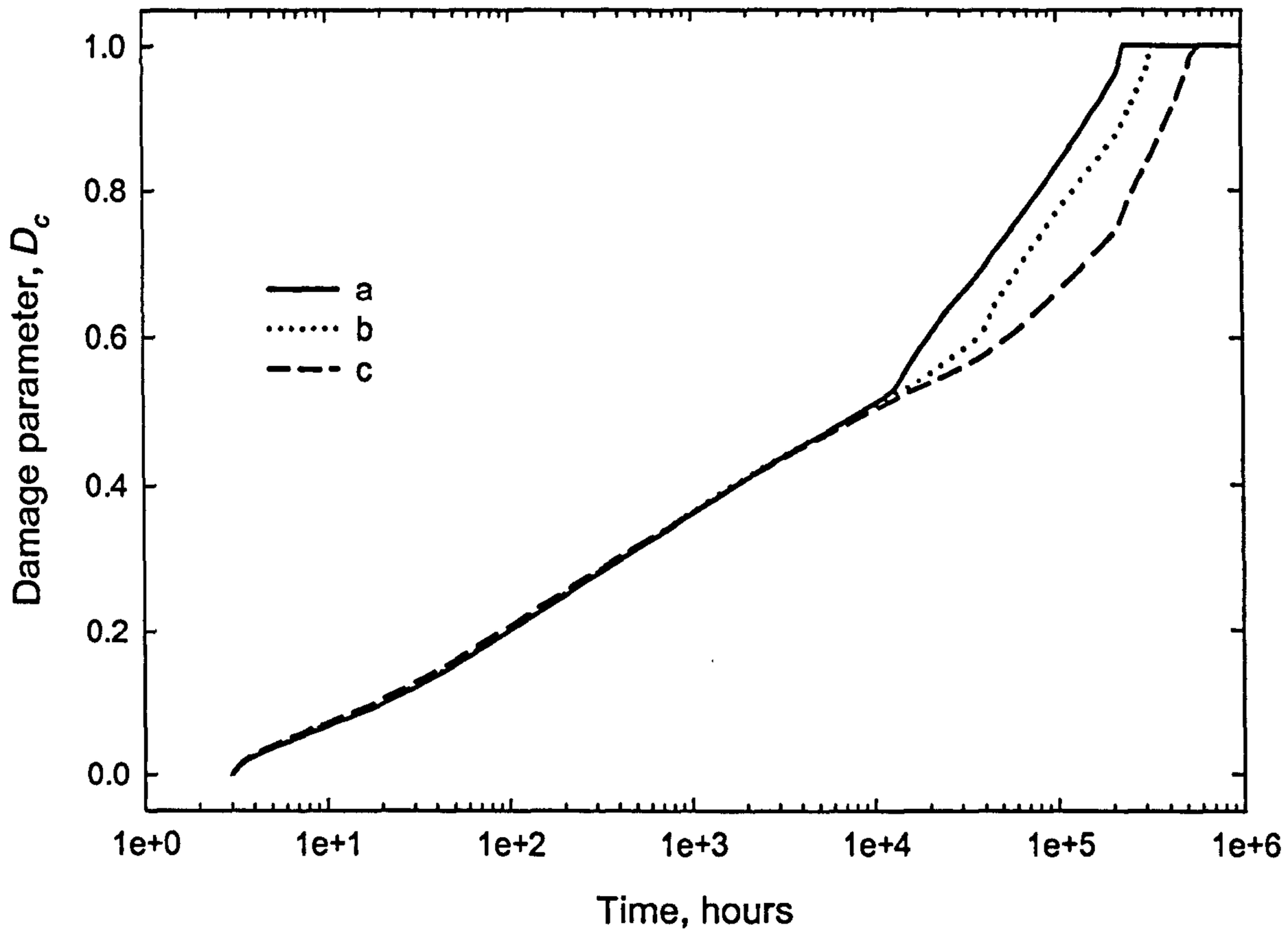

(a) Single punch

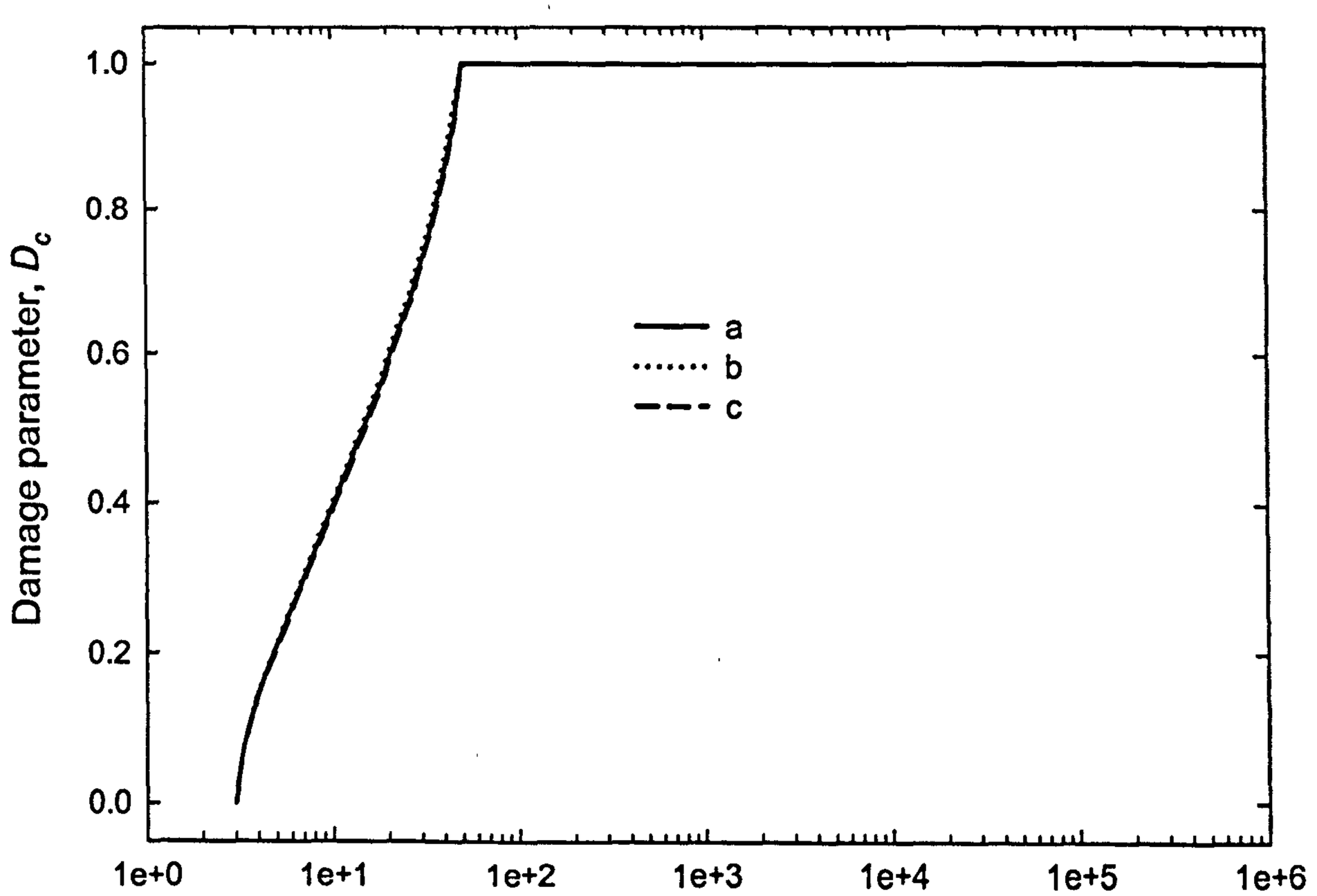

(b) Double punch

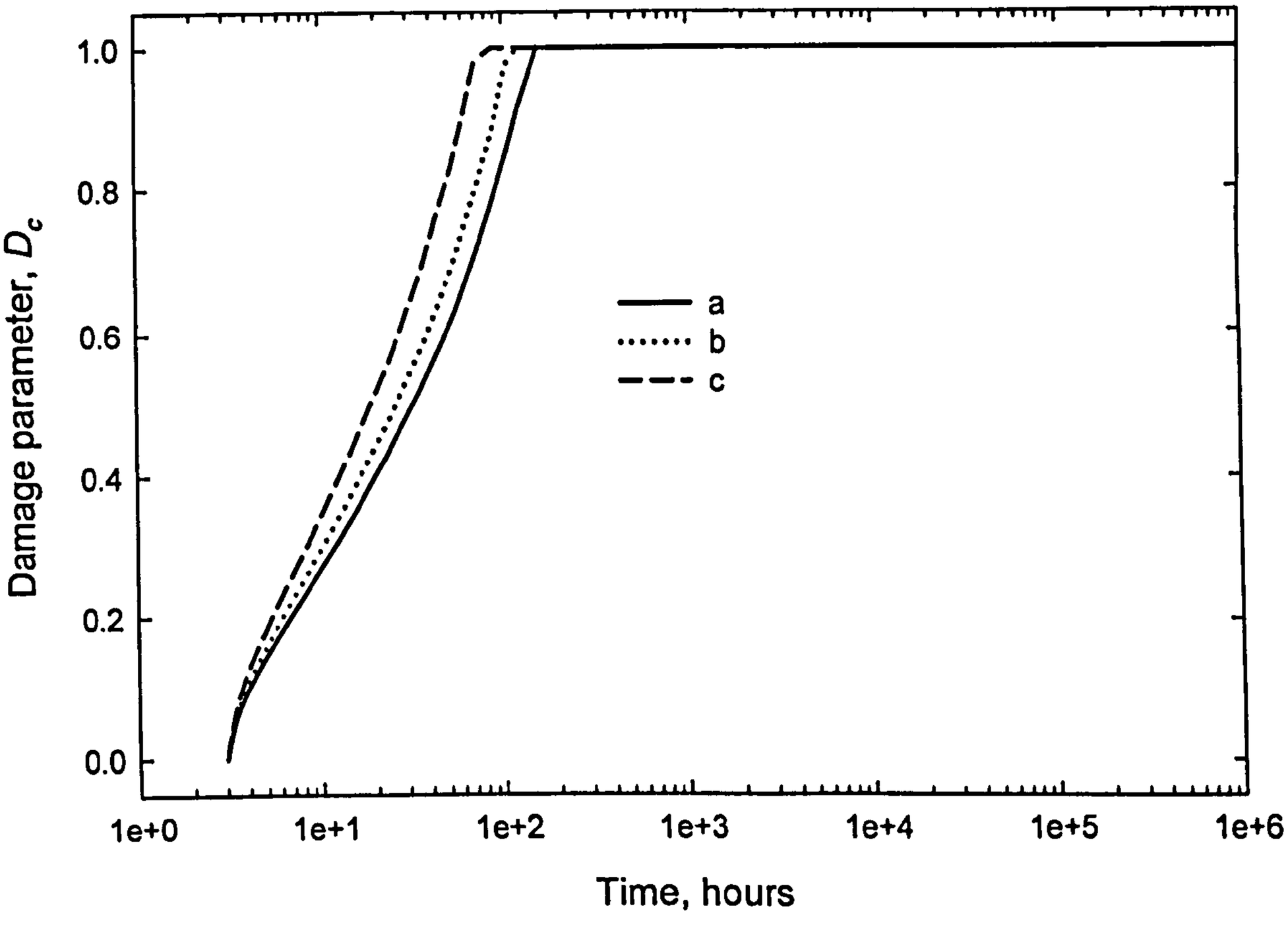

(c) Figure-of-eight punch

Figure 8.8 Predicted damage in a selected region of punched C(T) specimen subjected to thermal exposure at 550°C. See Figure 8.9 for illustration of the selected positions "a", "b" and "c".

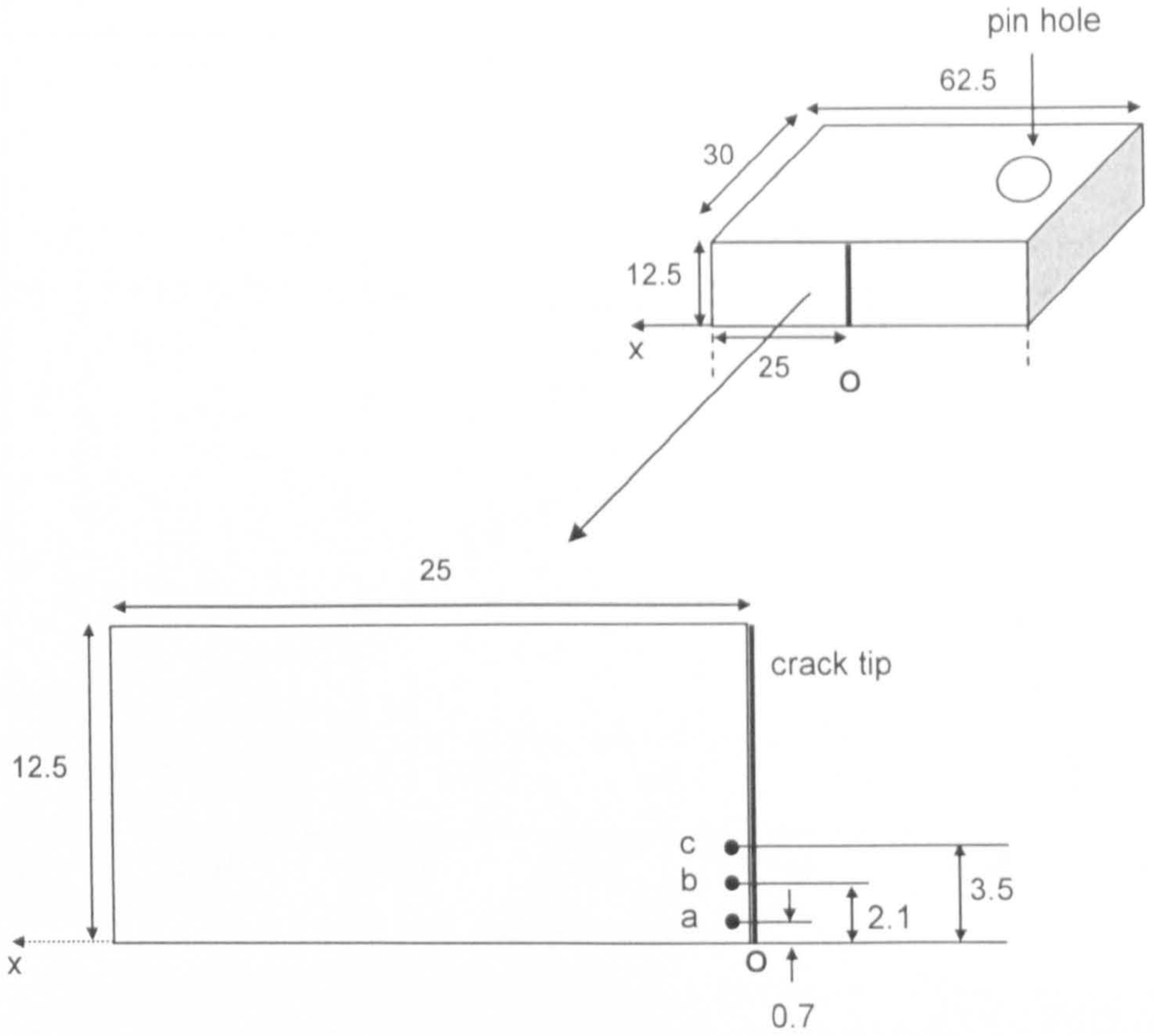

Figure 8.9 Illustration of the selected location in the punched specimen where the creep damage parameter is shown in Figure 8.8.

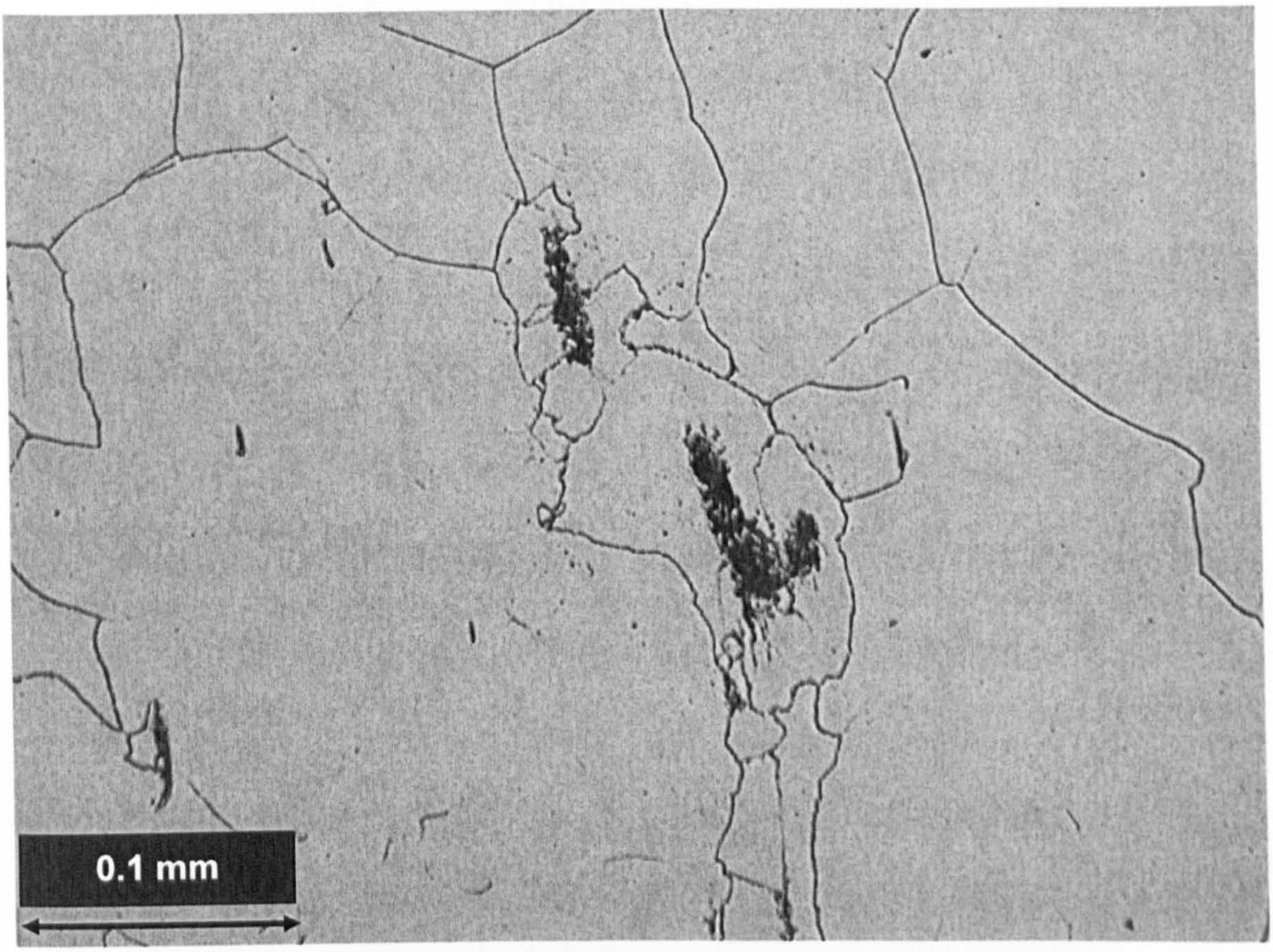

(a) Radial plane 12 mm off centre

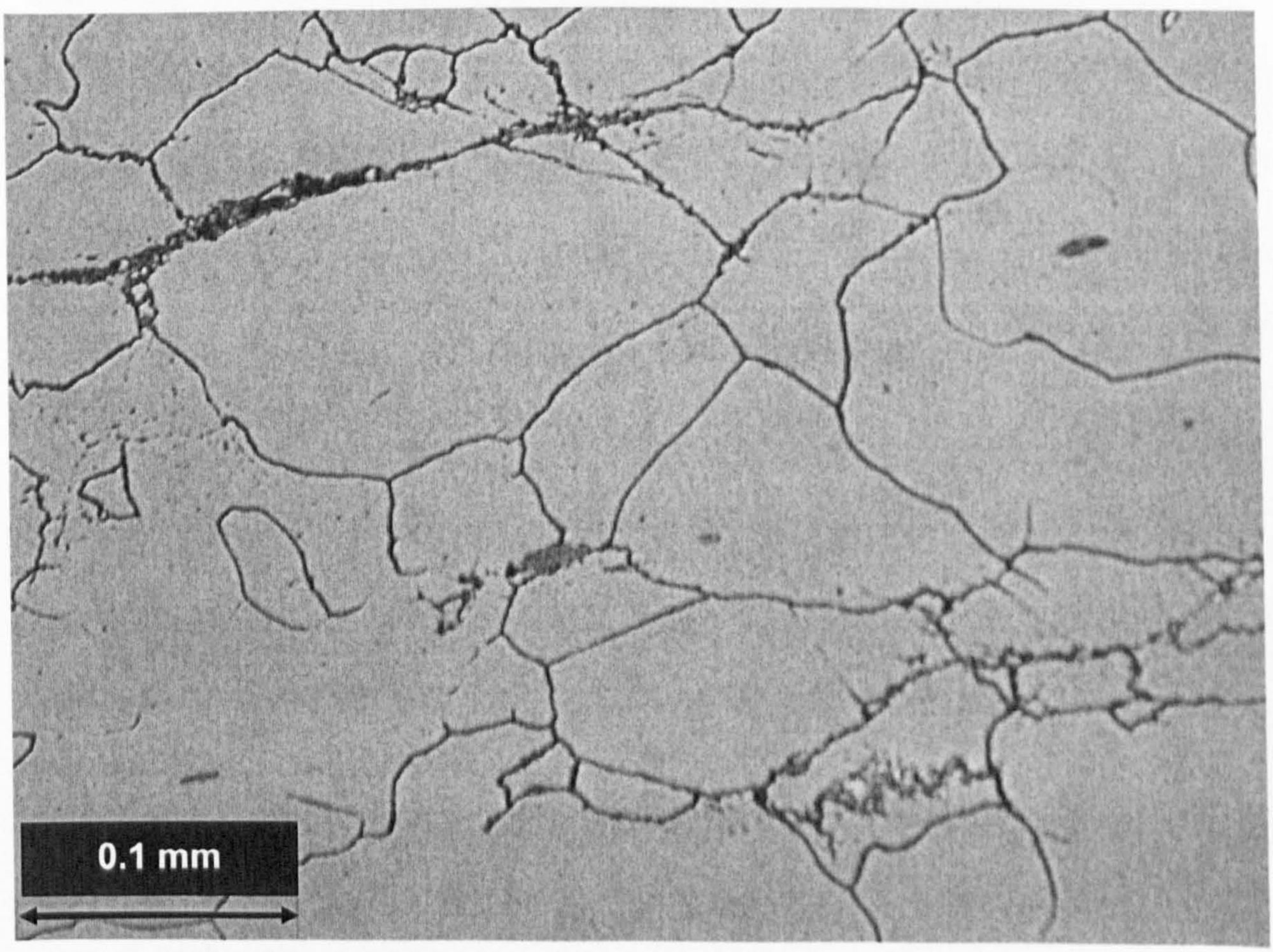

(b) Axial plane 10 mm off centre

Figure 8.10 Micrographs of quenched and thermally aged cylinder *s17*.

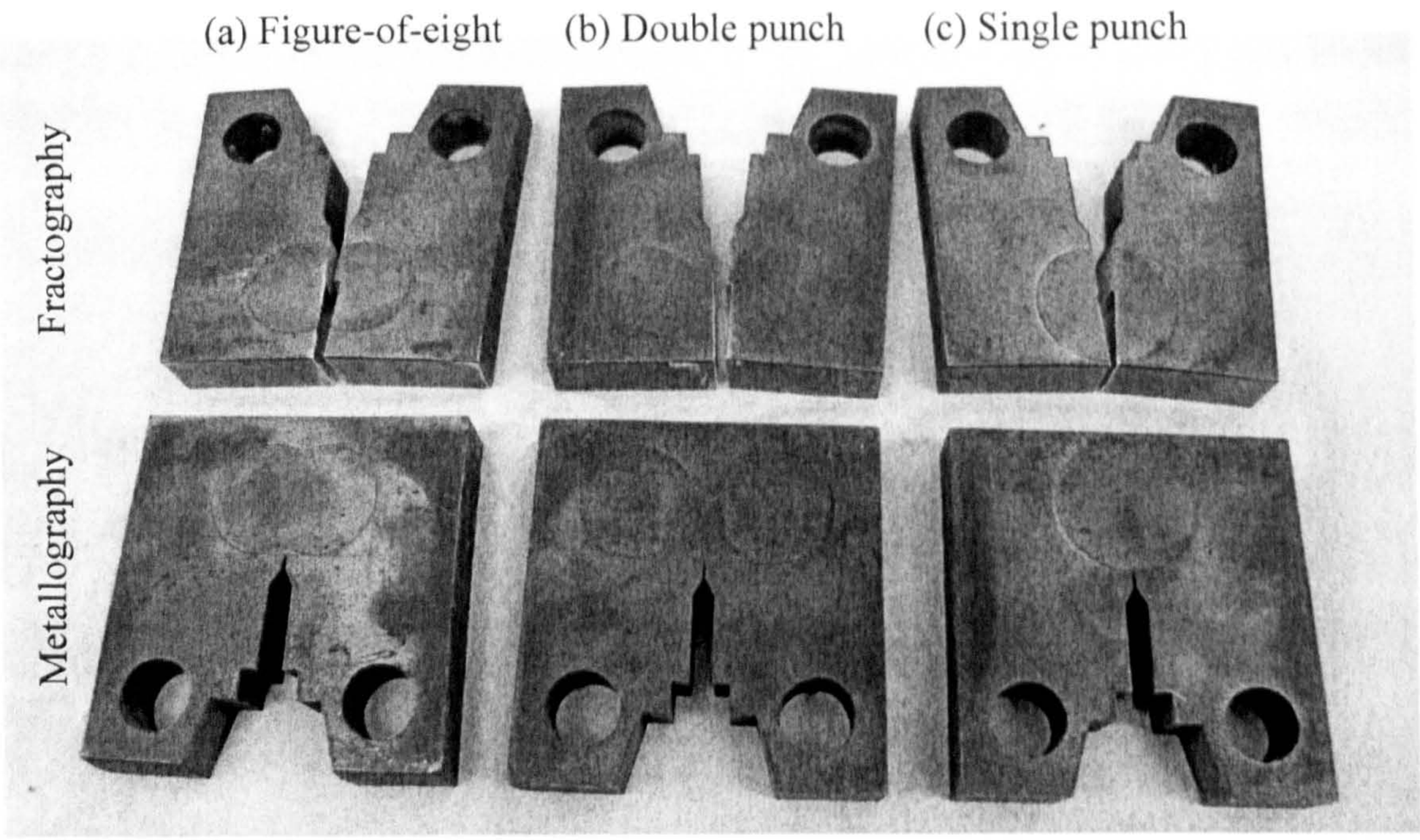

Figure 8.11 Side punched and thermally aged C(T) specimens including (a) figure-of-eight, (b) double and (c) single punch cases left to right. The top fractured samples are used for fractography and the bottom samples for metallography study.

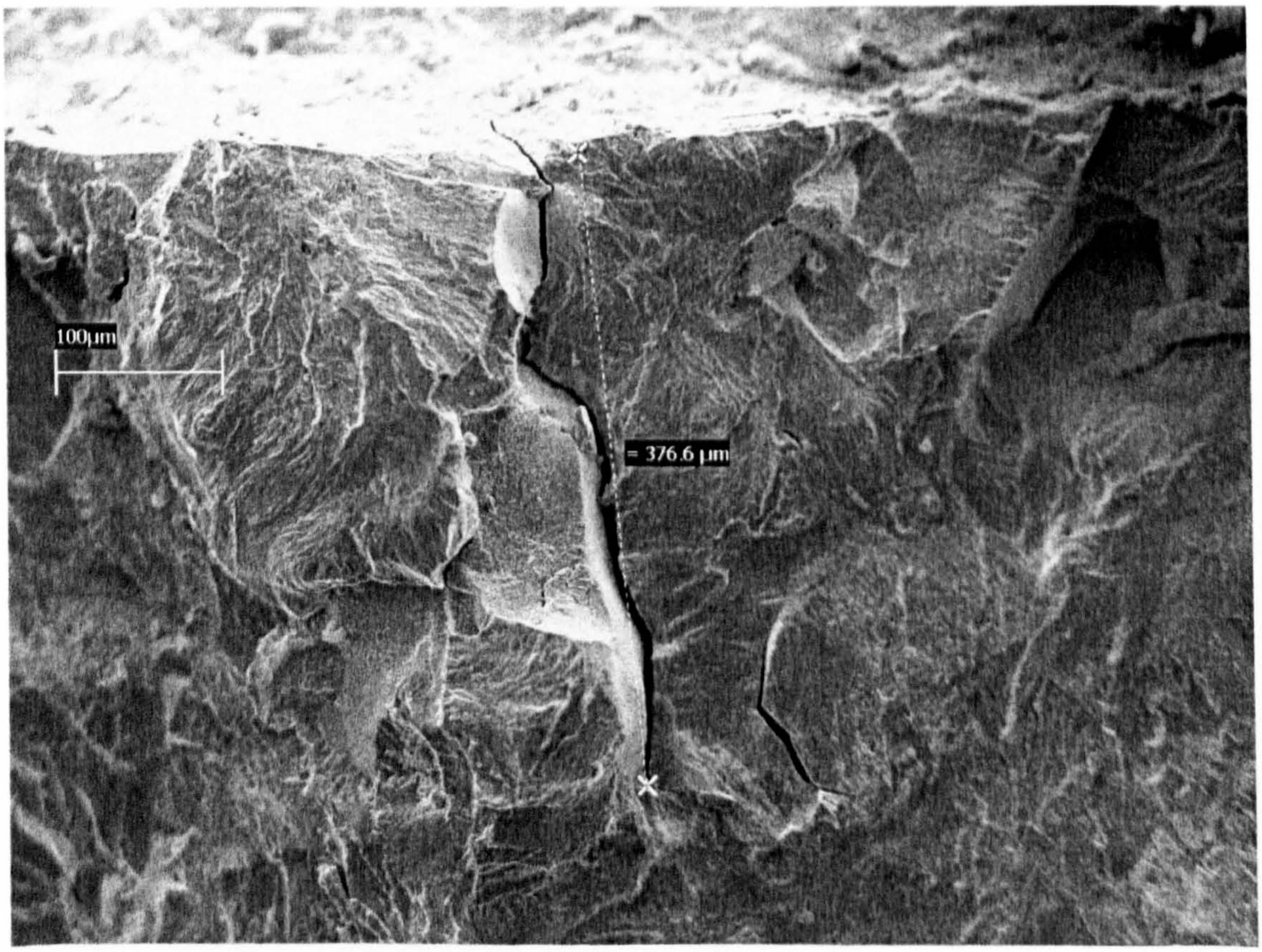

(a) Z=2.9, X=0.3 (grain boundary cracks have cavities)

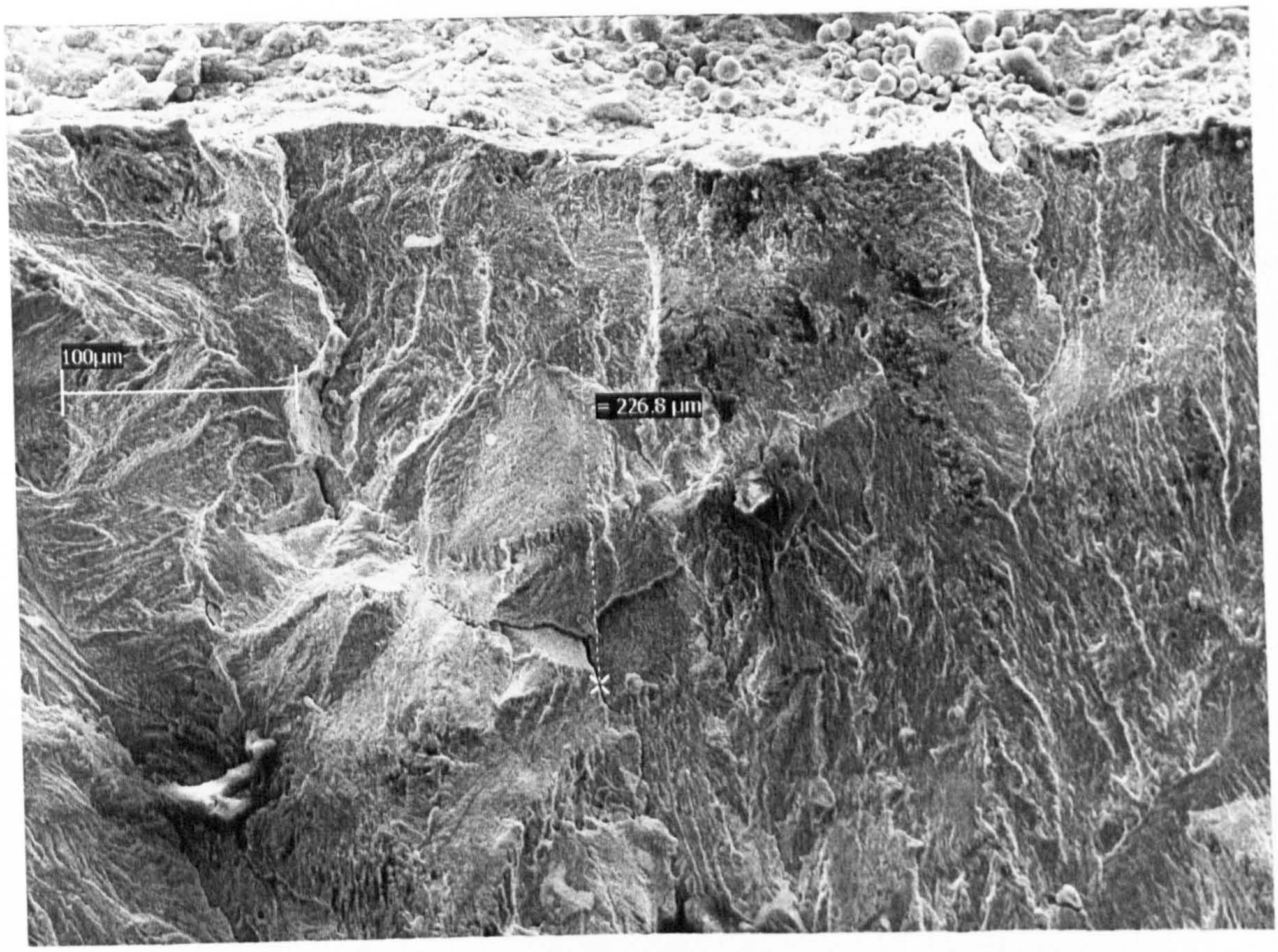

(b) Z=11.7, X=0.22

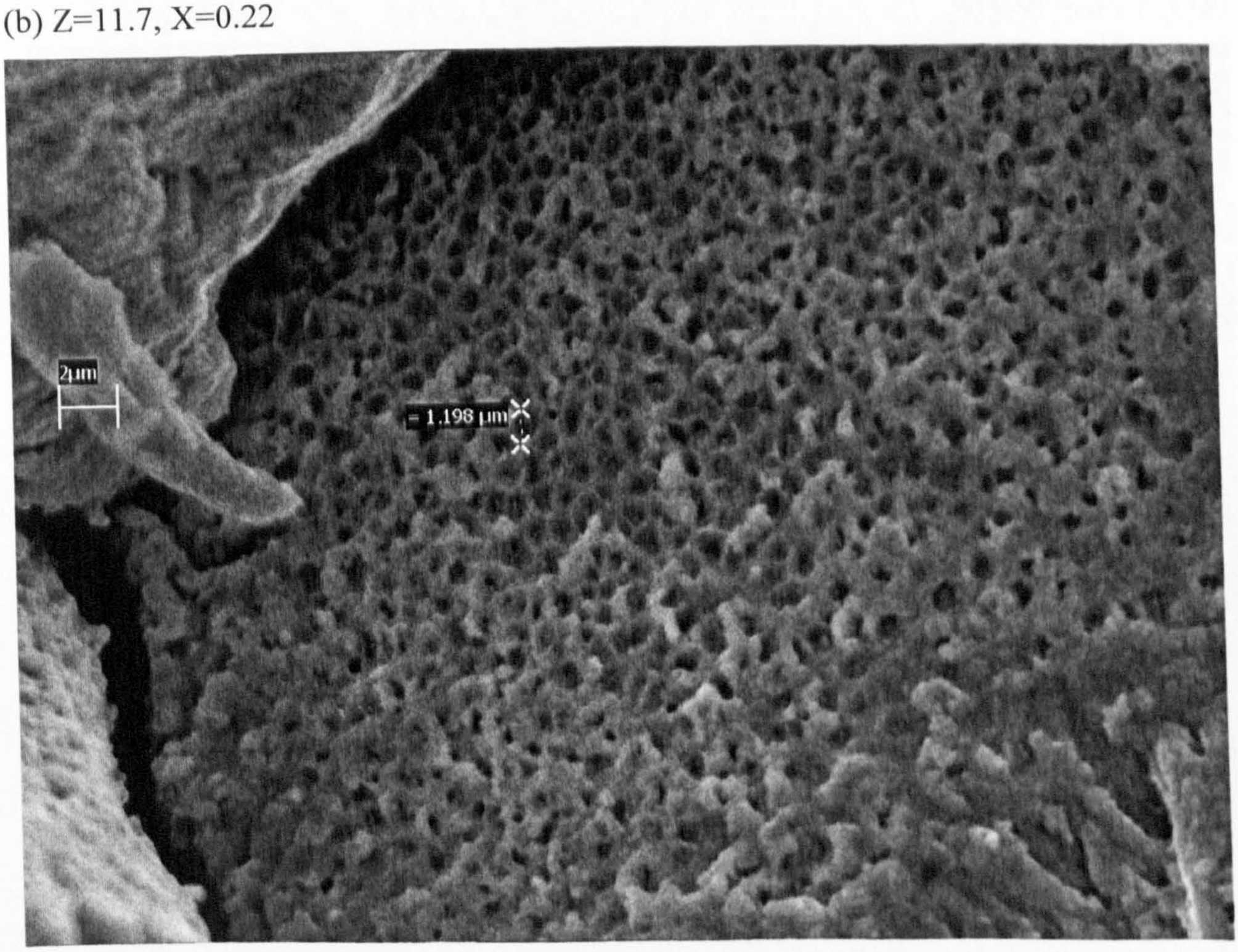

(c) Z=11.7, X=0.22

Figure 8.12 Scanning electron micrograph showing creep cavities in figure-of-eight side punched C(T) fracture surface. See Figure 8.15 for illustration of X and Z.

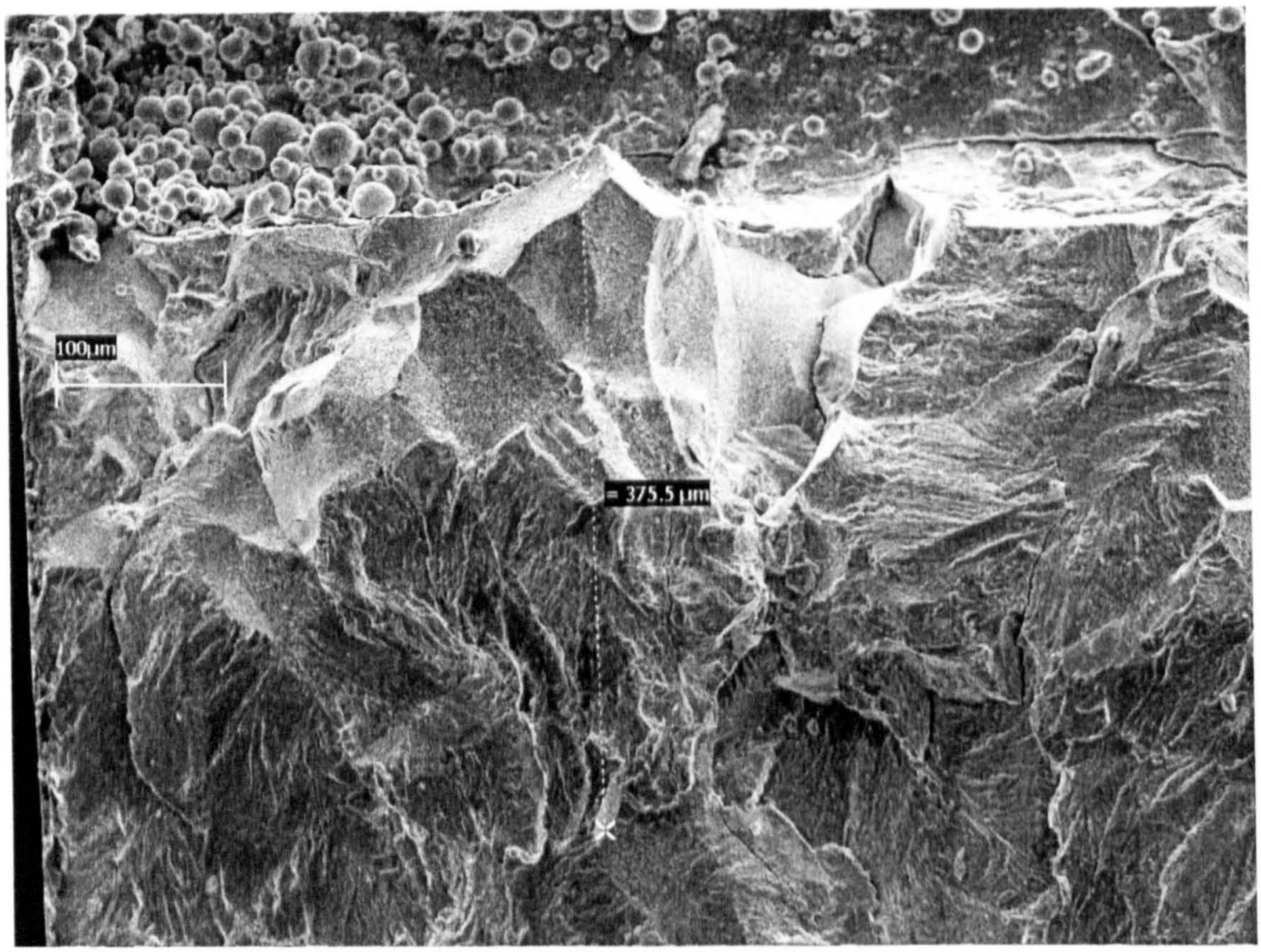

(a) Z=0.4, X=0.375

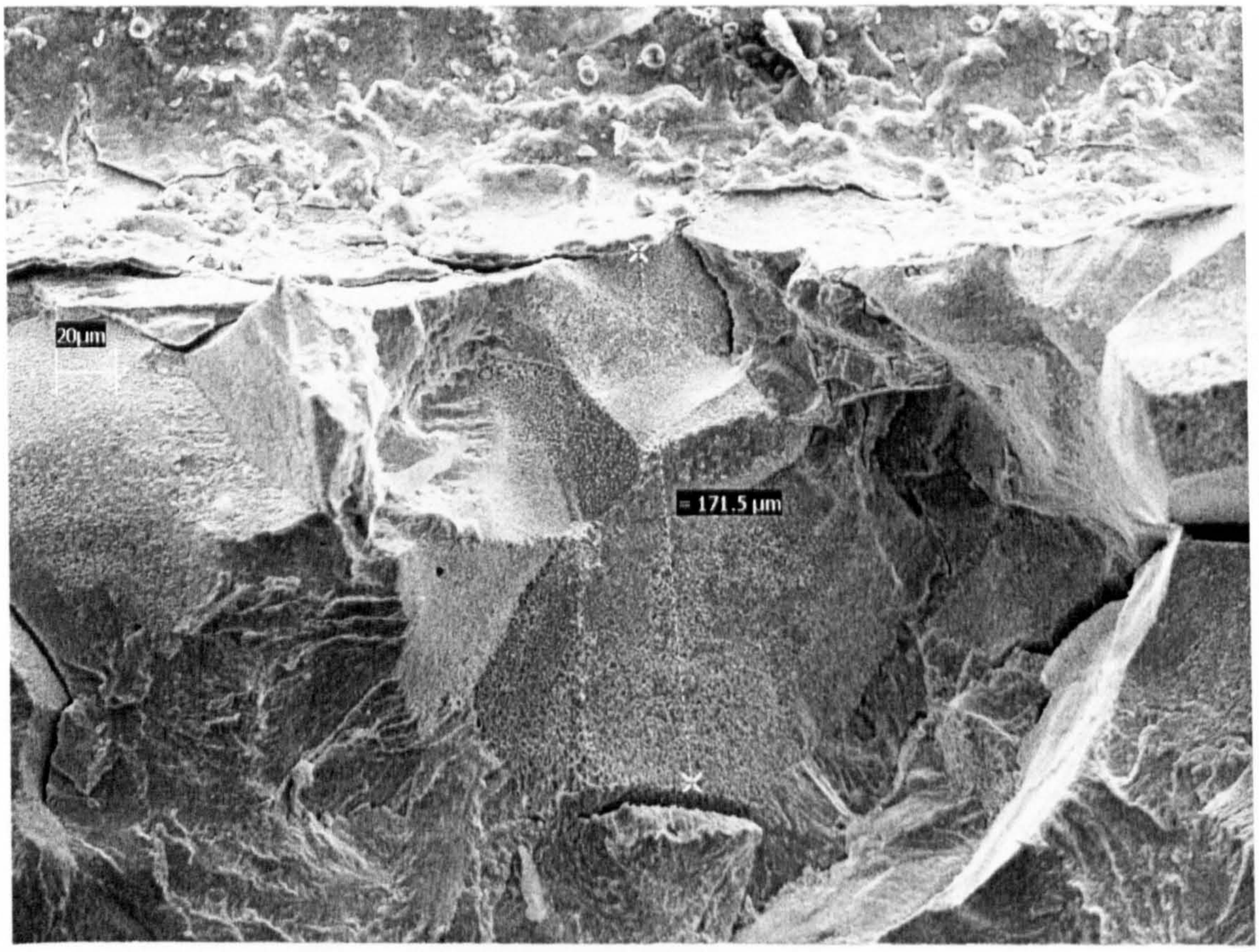

(b) Z=2.6, X=0.171

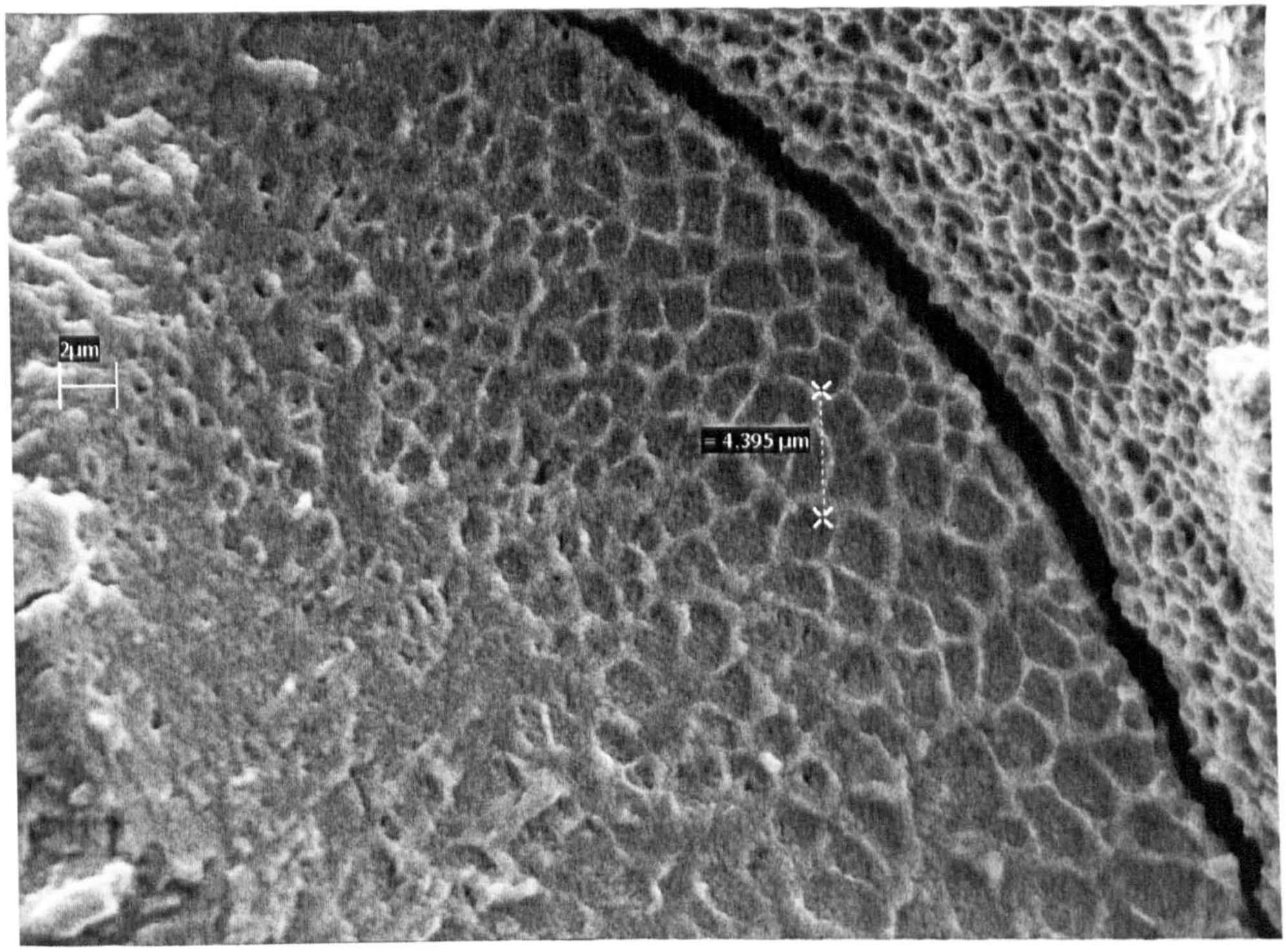

(c) Z=9.0, X=0.364

Figure 8.13 Scanning electron micrograph showing creep cavities in double punched C(T) fracture surface. See Figure 8.15 for illustration of X and Z.

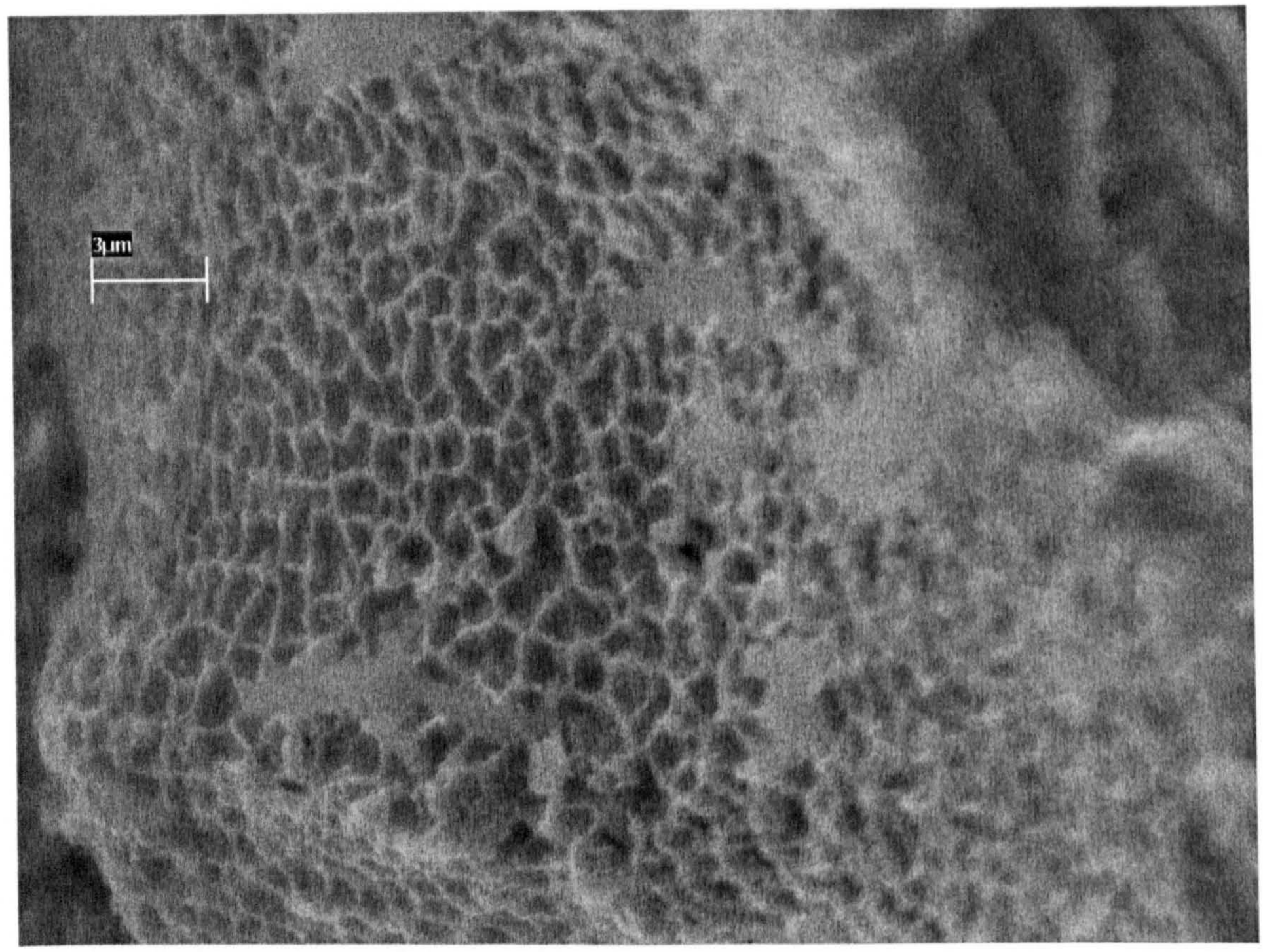

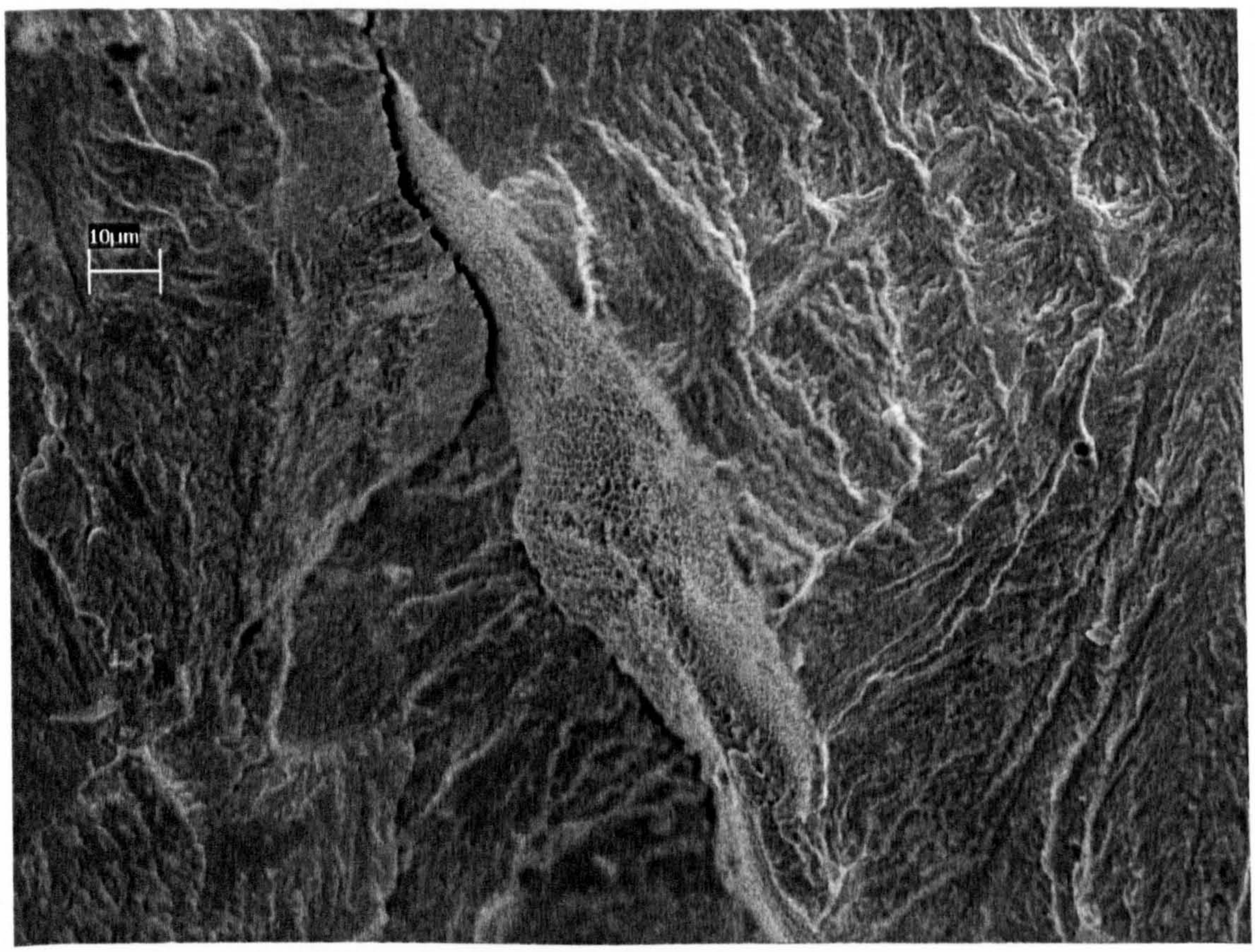

Figure 8.14 Scanning electron micrograph showing formation of creep cavities in single punched C(T) specimen fracture surface.

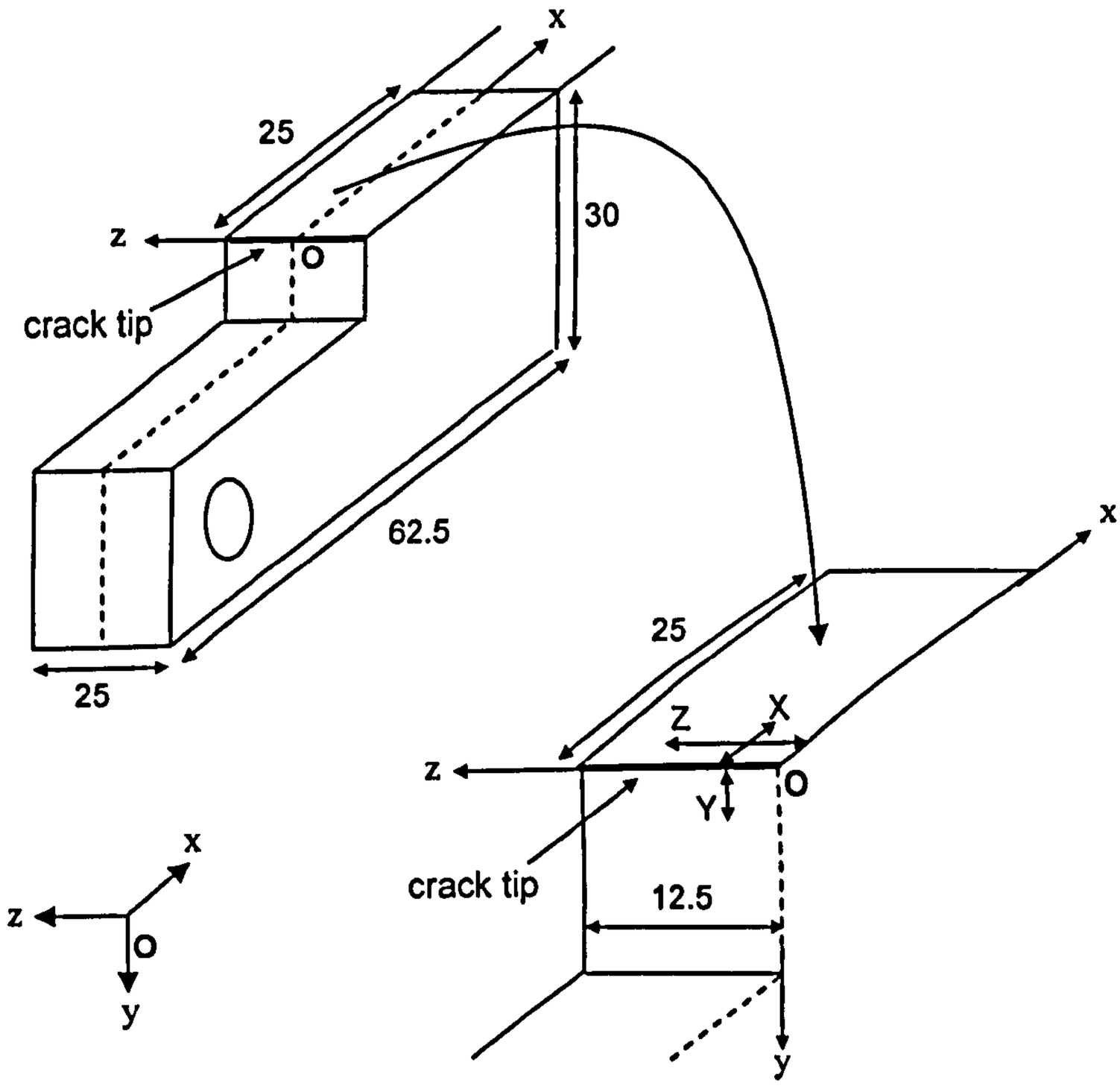

Figure 8.15 Section through the fracture surface of C(T) specimen illustrating the positions X and Z used in Figures 8.12 to 8.14 to measure the extent and location of creep cavitation.

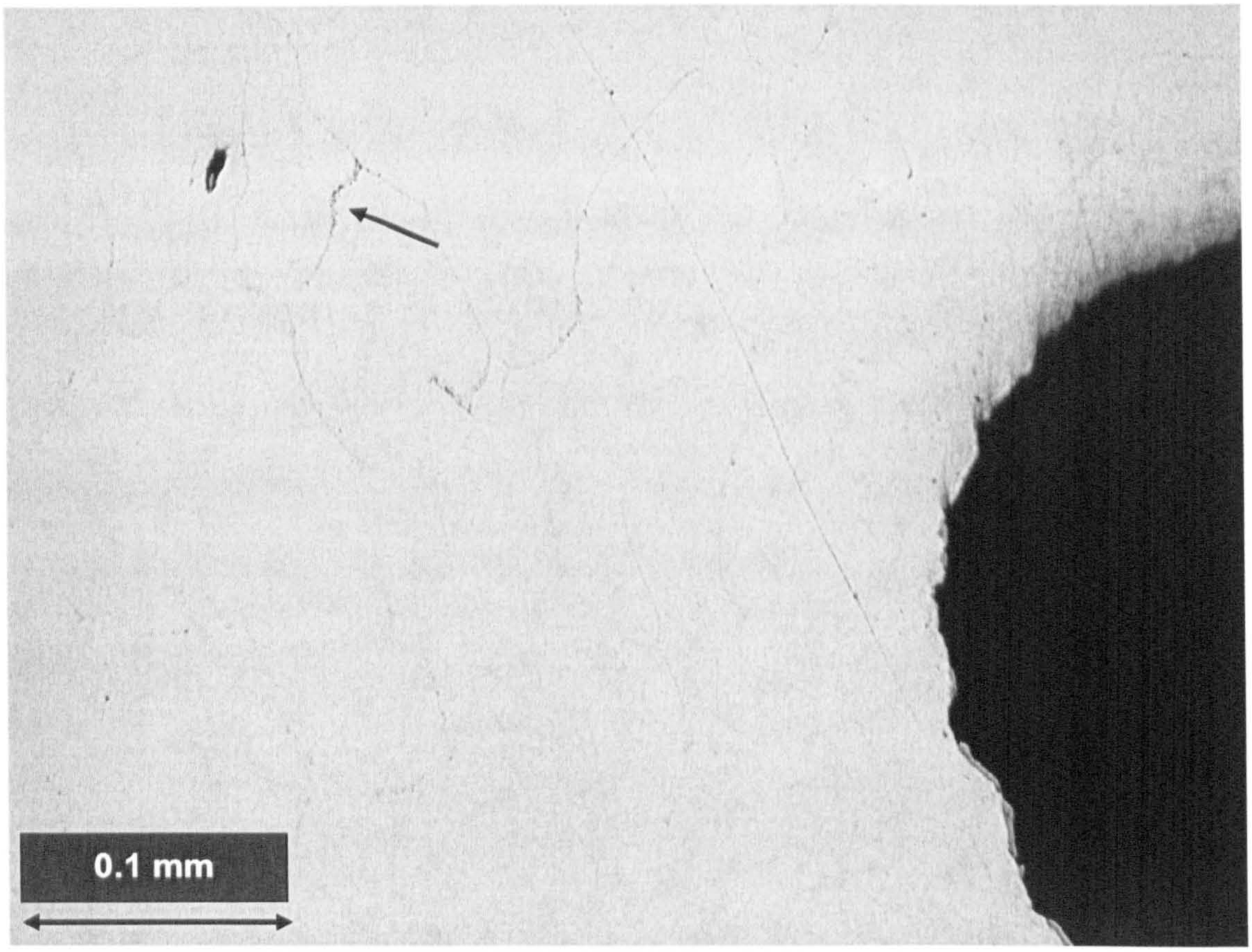

Figure 8.16 Optical micrograph taken from the mid-thickness plane of figure-of-eight side punched and thermally aged (at 550°C for 3900 hours) showing creep cavities along grain boundaries.

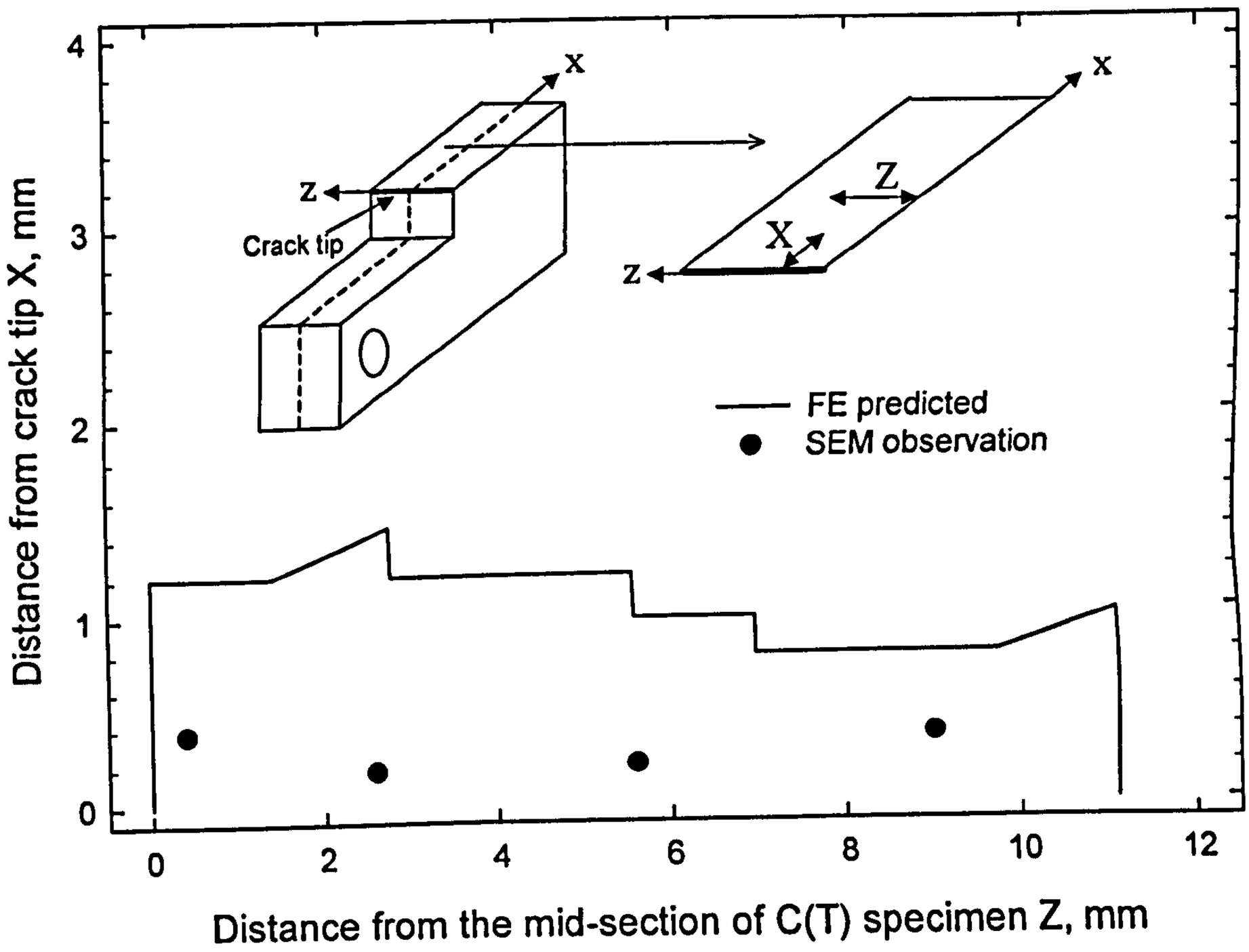

(a) double punch

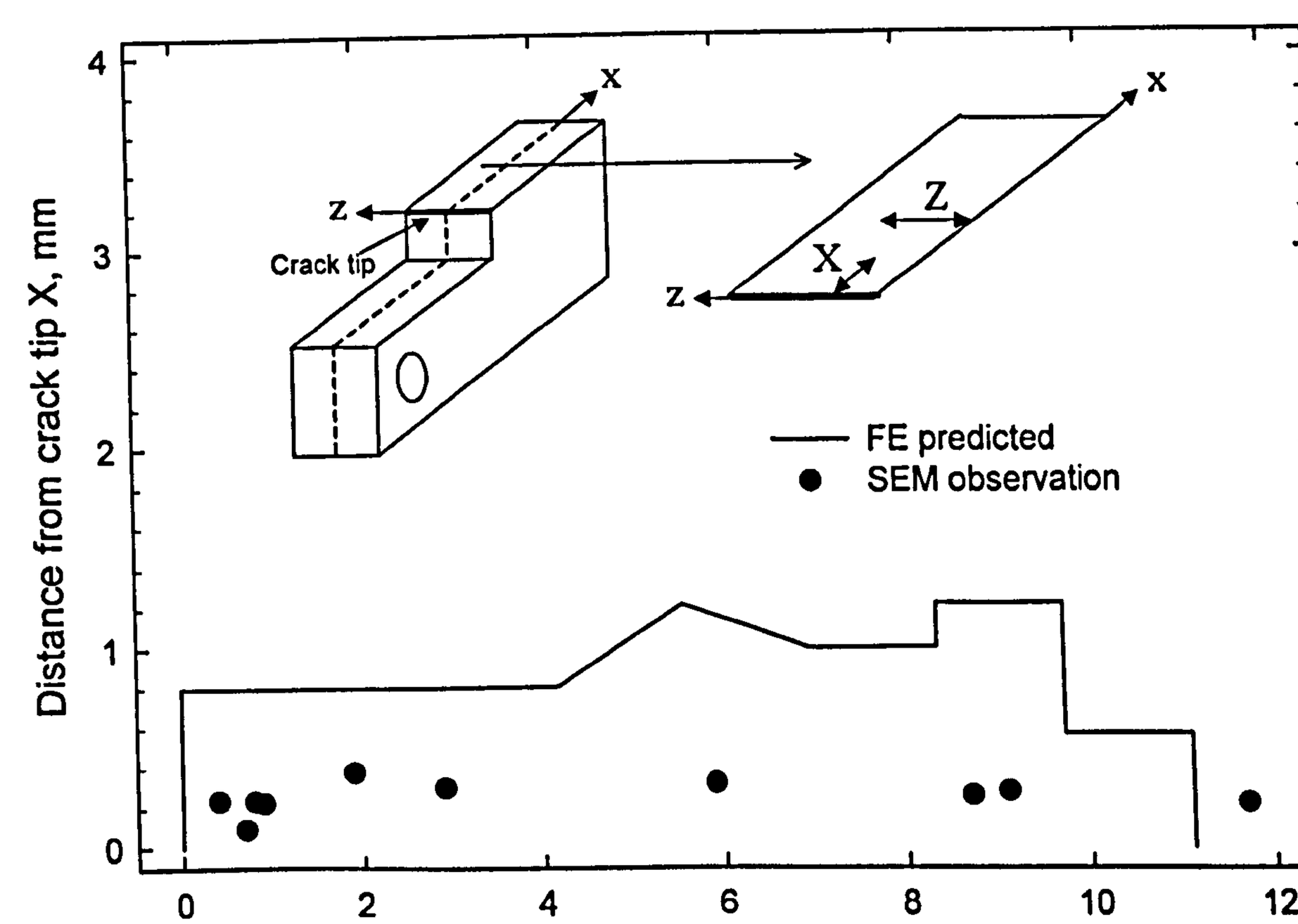

(b) Figure-of-eight punch

Figure 8.17 FE predicted and SEM observed damage regions on the fracture surface of punched C(T) specimens.

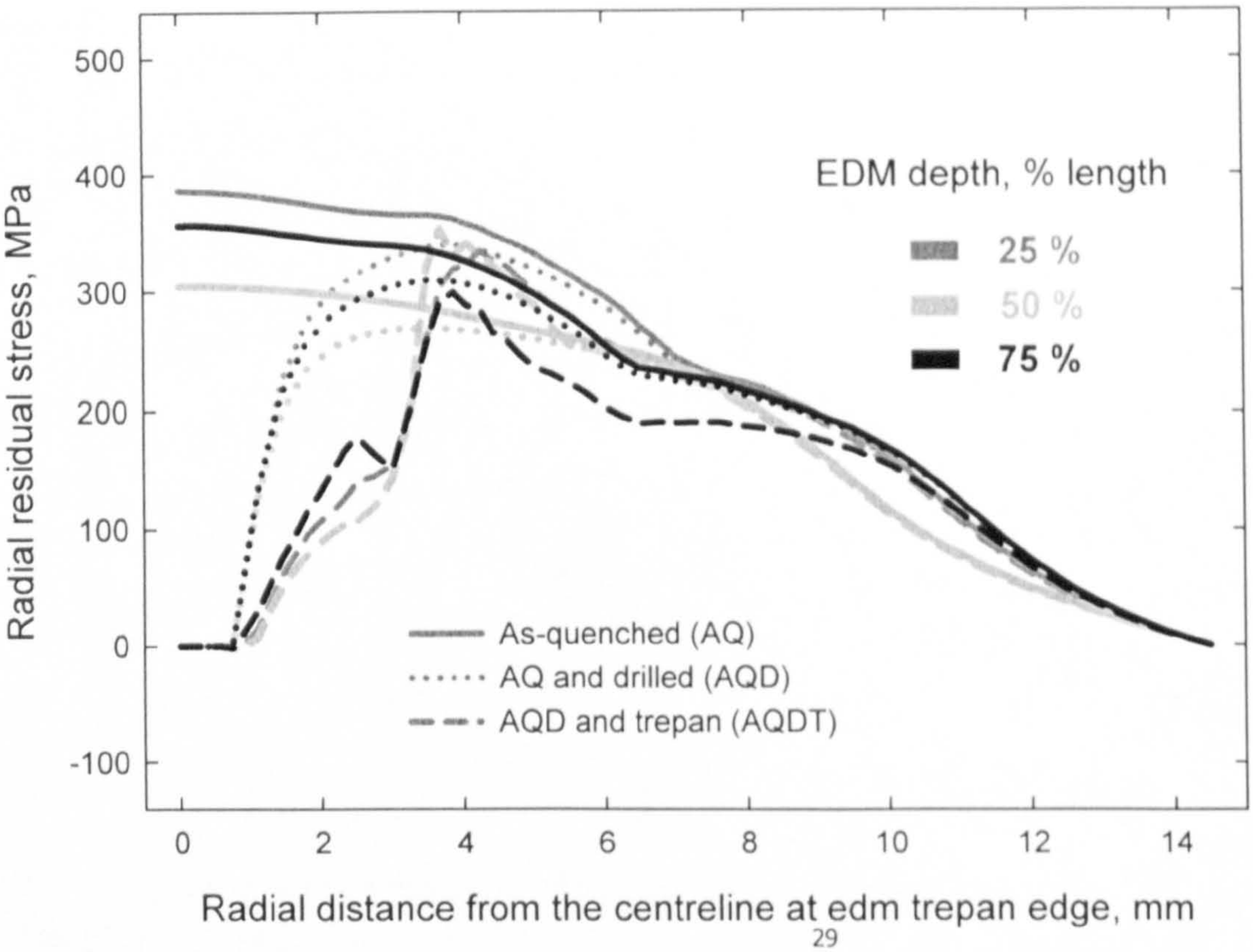

(a) Radial component

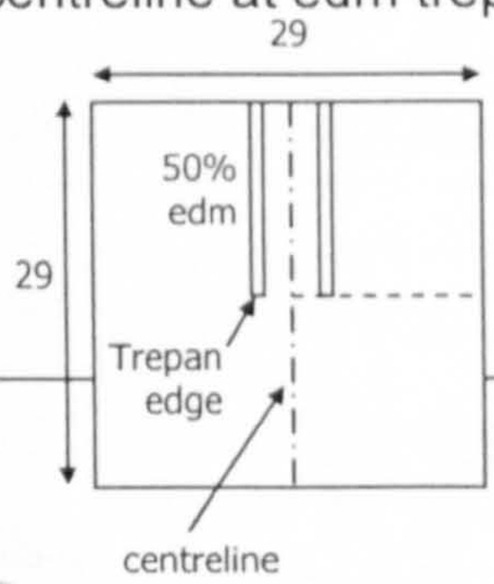

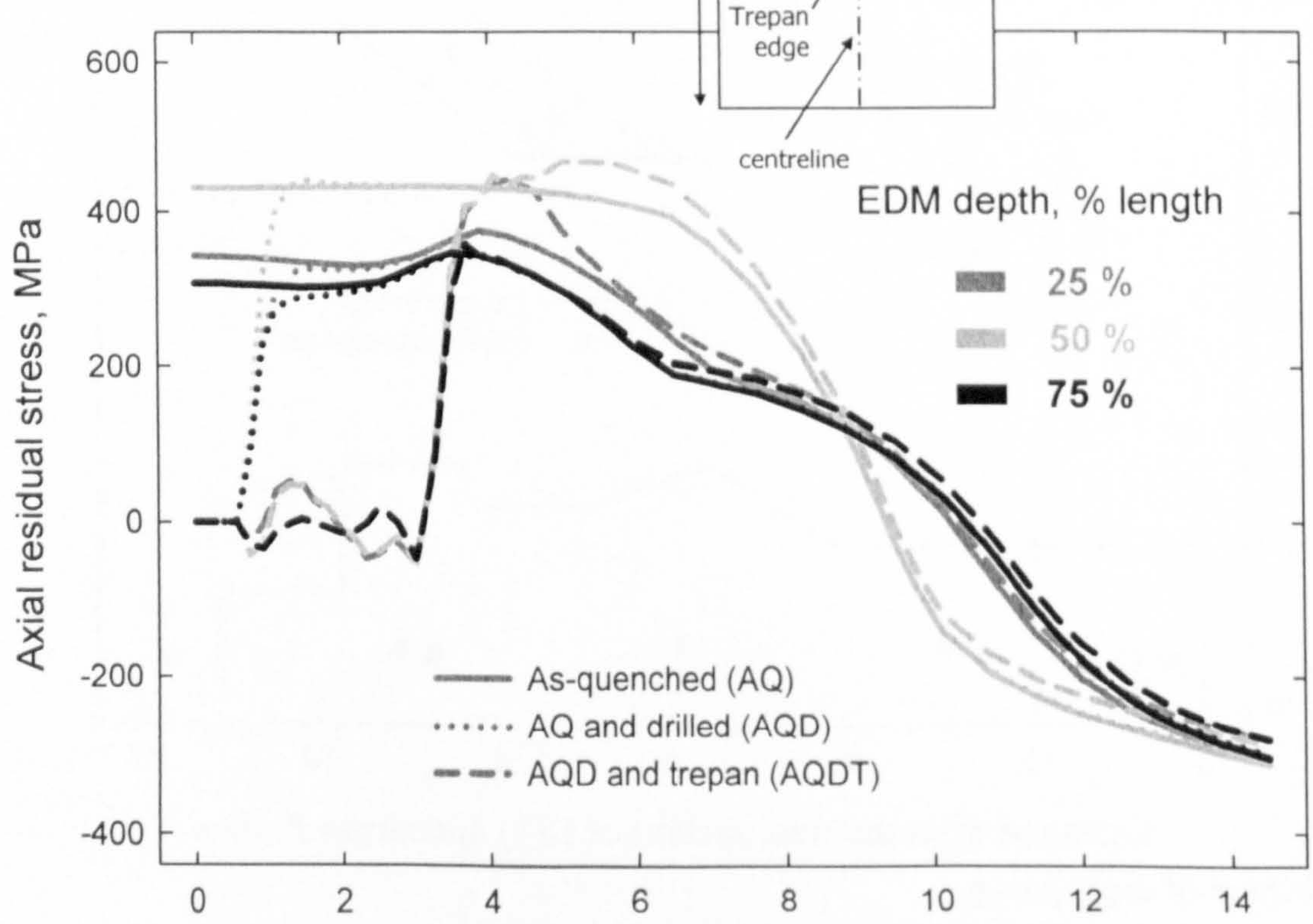

(b) Axial component

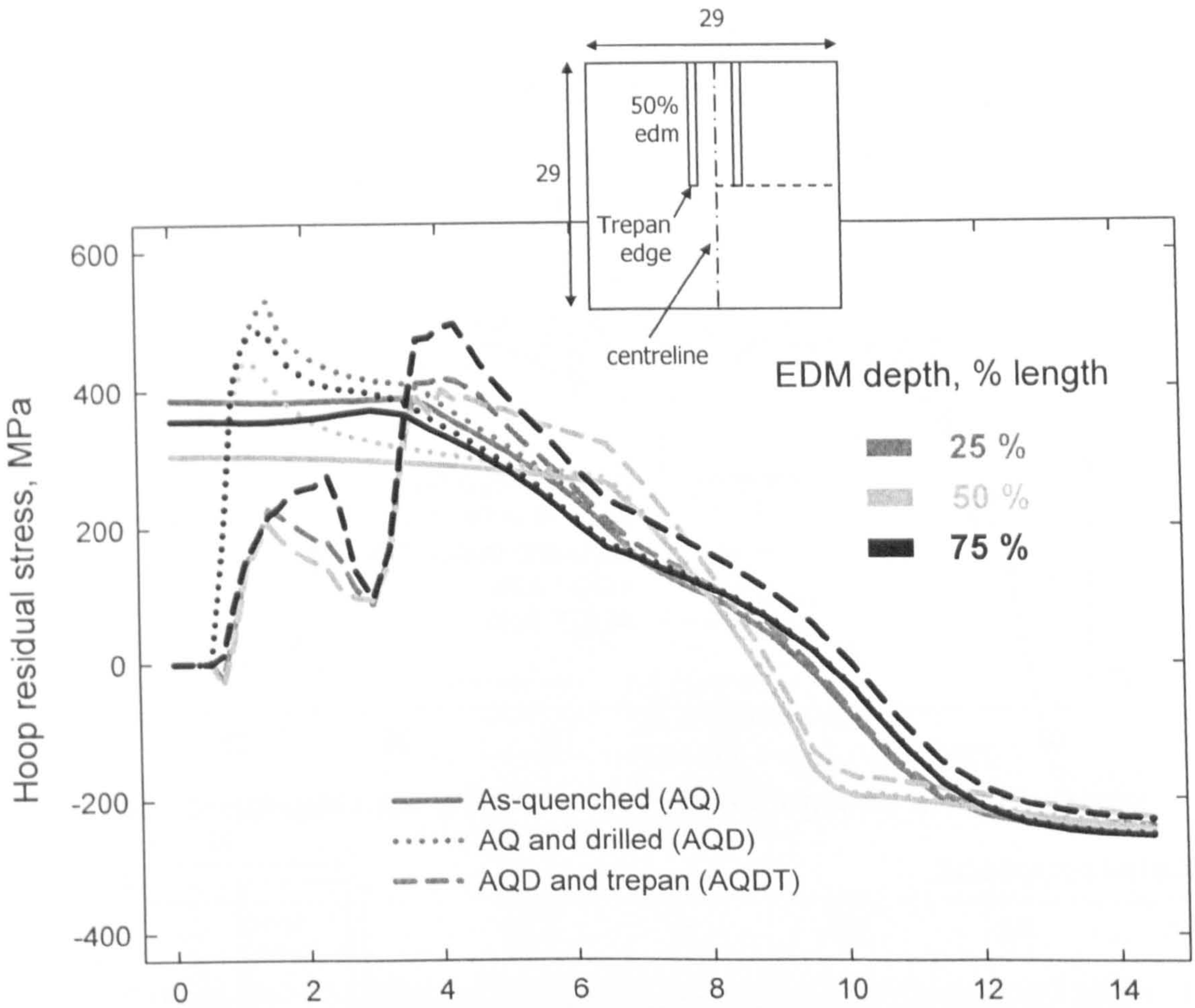

(c) Hoop component

Figure 9.1 FE predicted (a) radial, (b) axial and (c) hoop residual stress distribution across a radial plane from the centreline towards the outer surface in a pre-trepanned quenched cylinder with variable edm depths along the trepan edge.

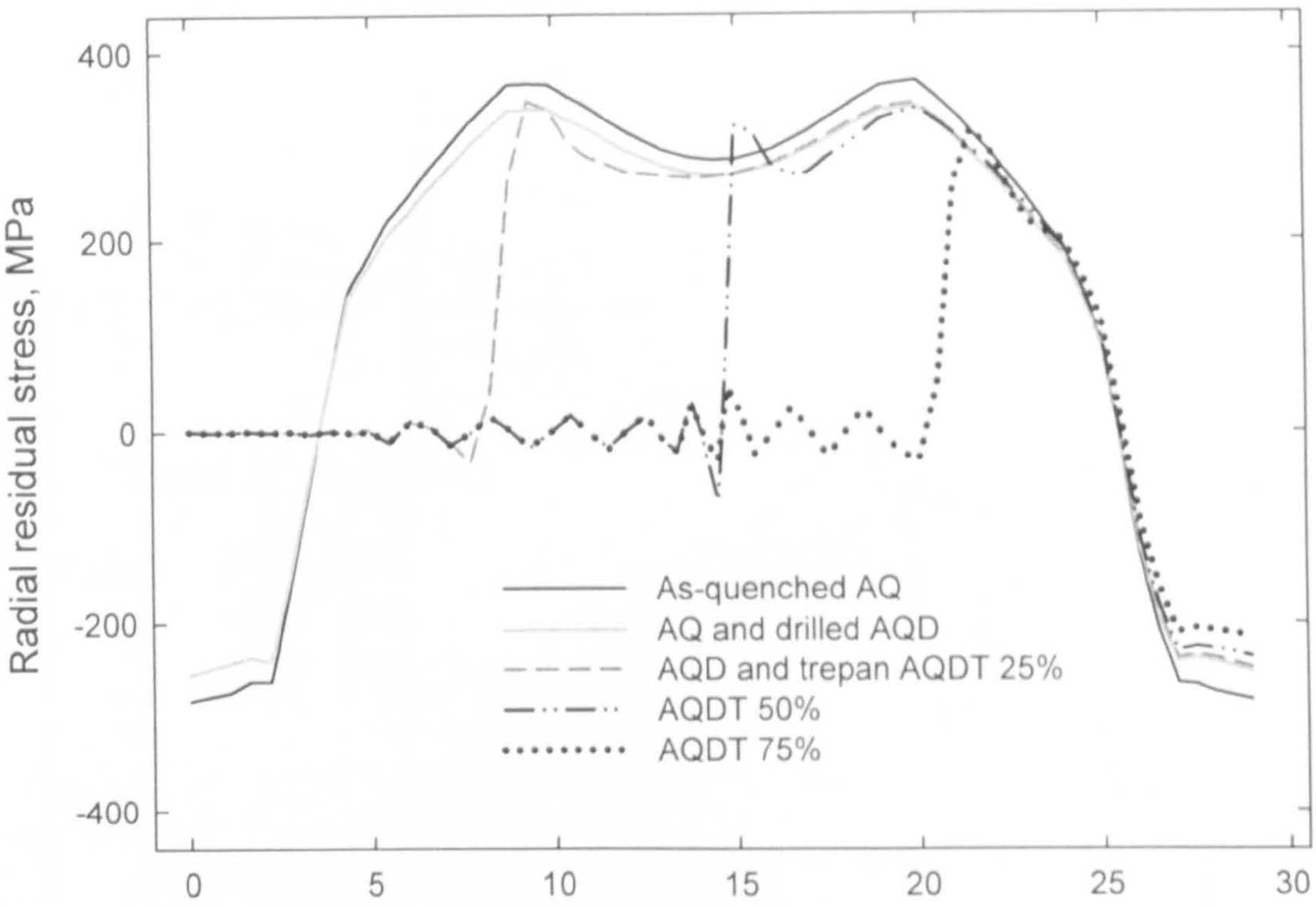

(a) Radial component

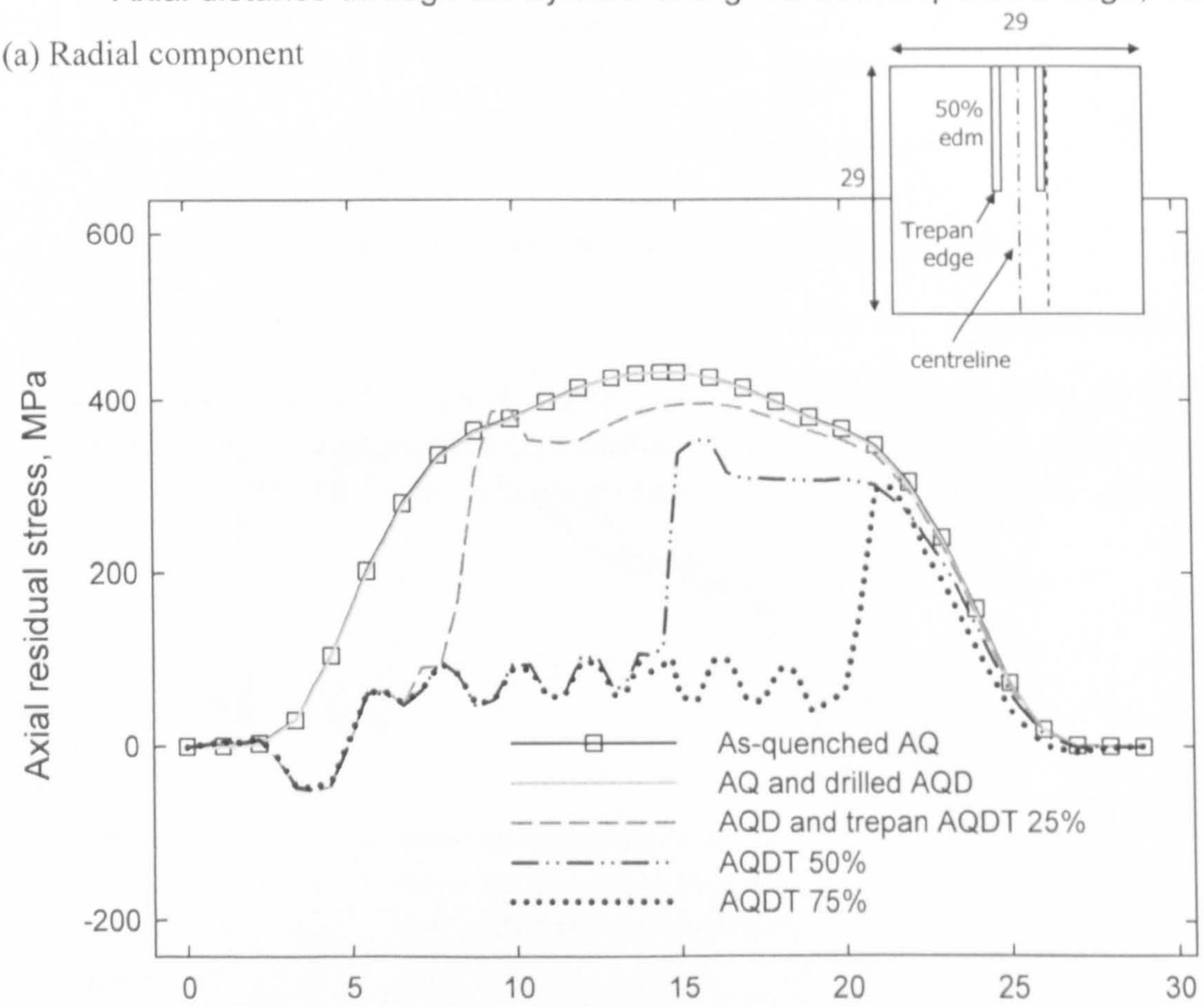

(b) Axial component

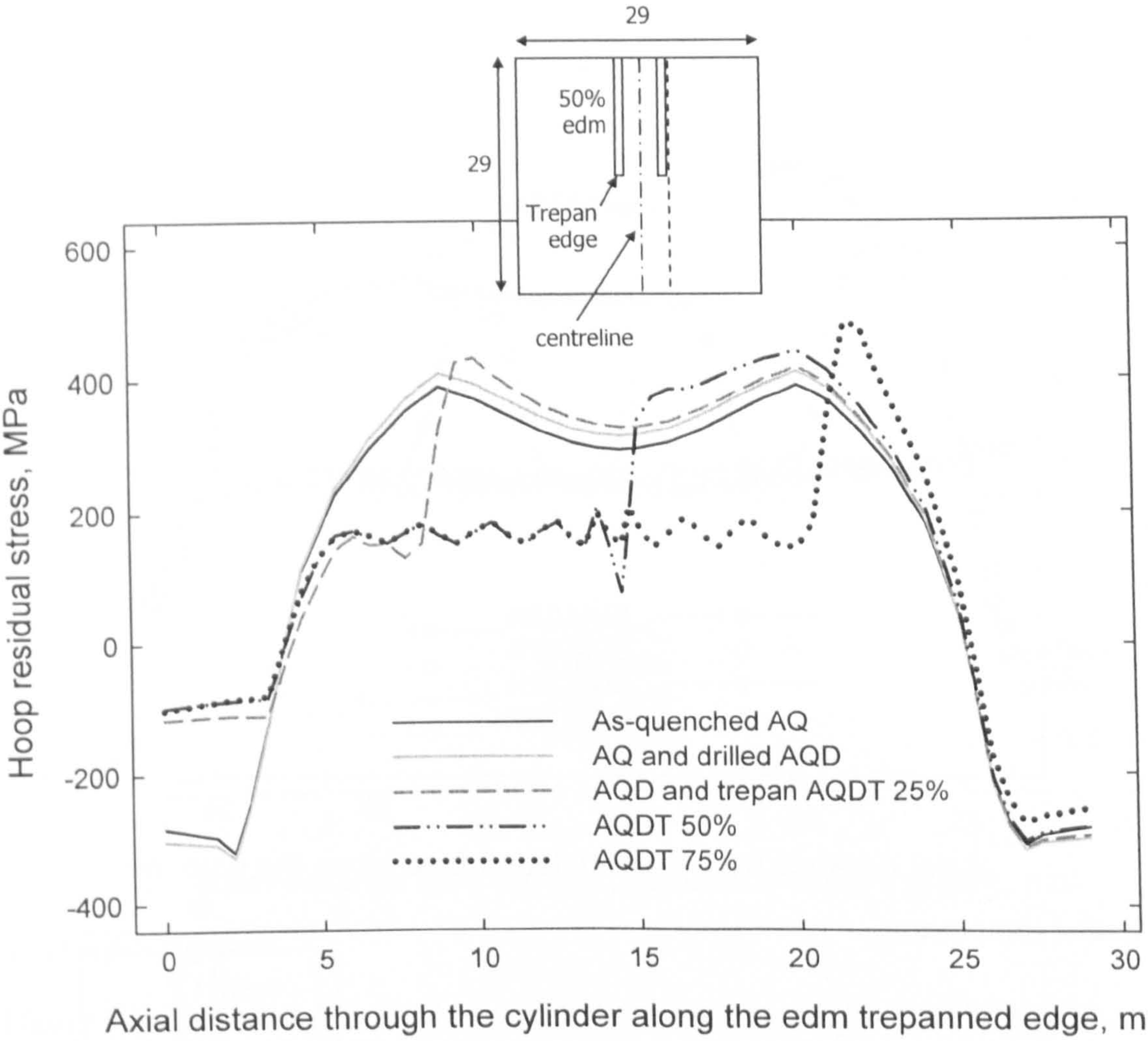

(c) Hoop component

Figure 9.2 FE predicted (a) radial, (b) axial and (c) hoop residual stress distribution along an axial line in a pre-trepanned quenched cylinder with variable edm depths along the trepan edge.

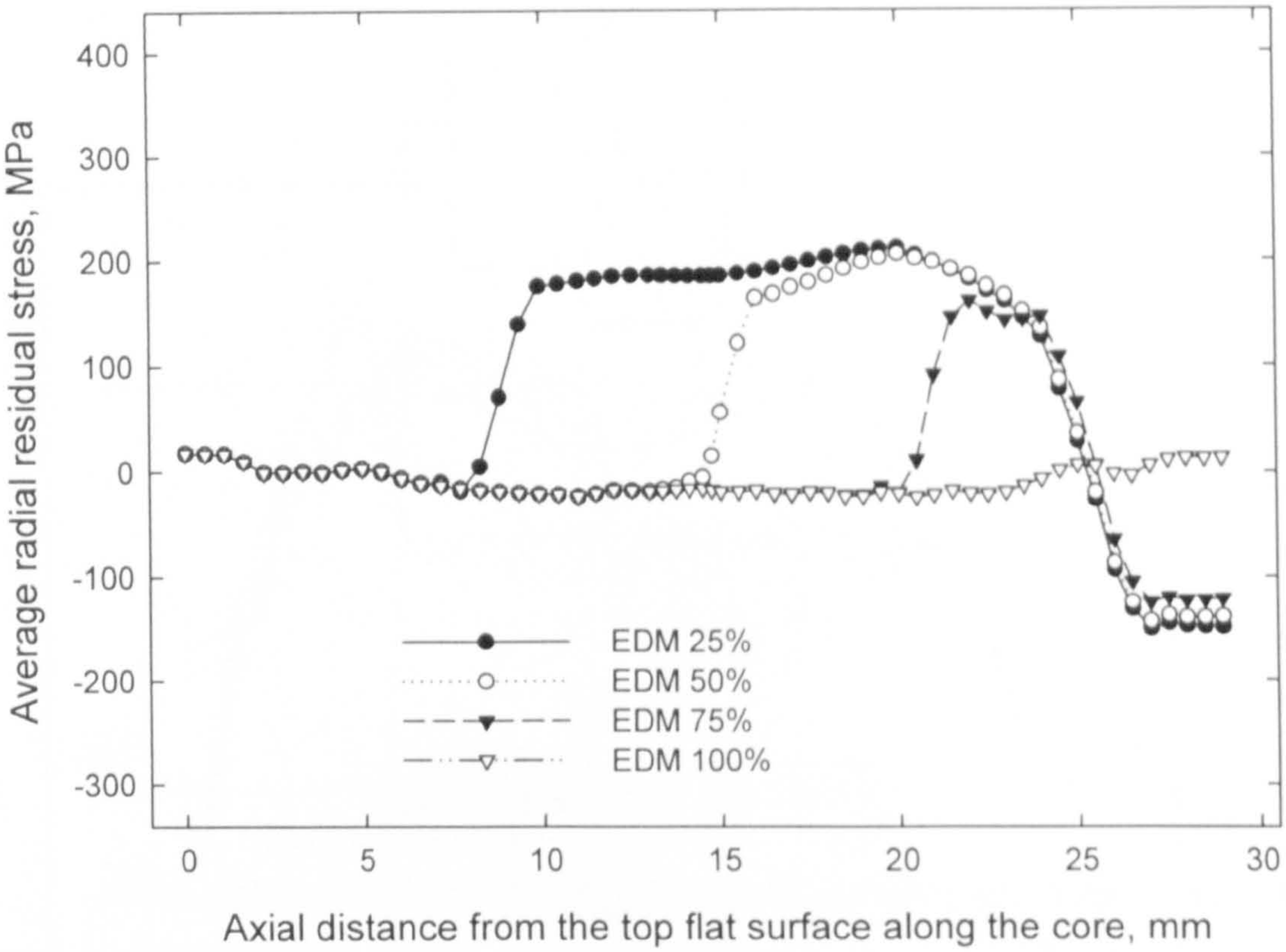

(a) Radial component

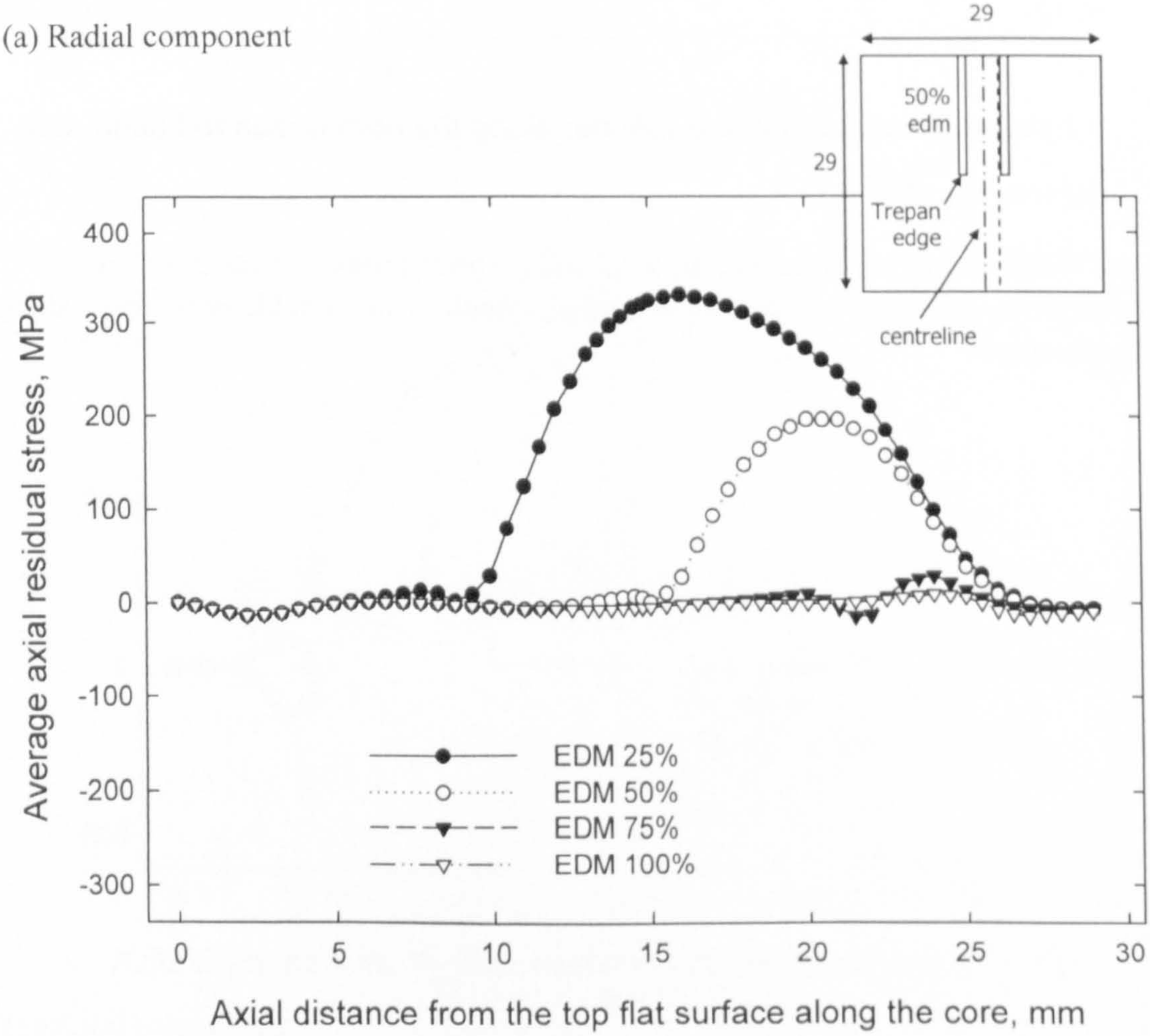

(b) Axial component

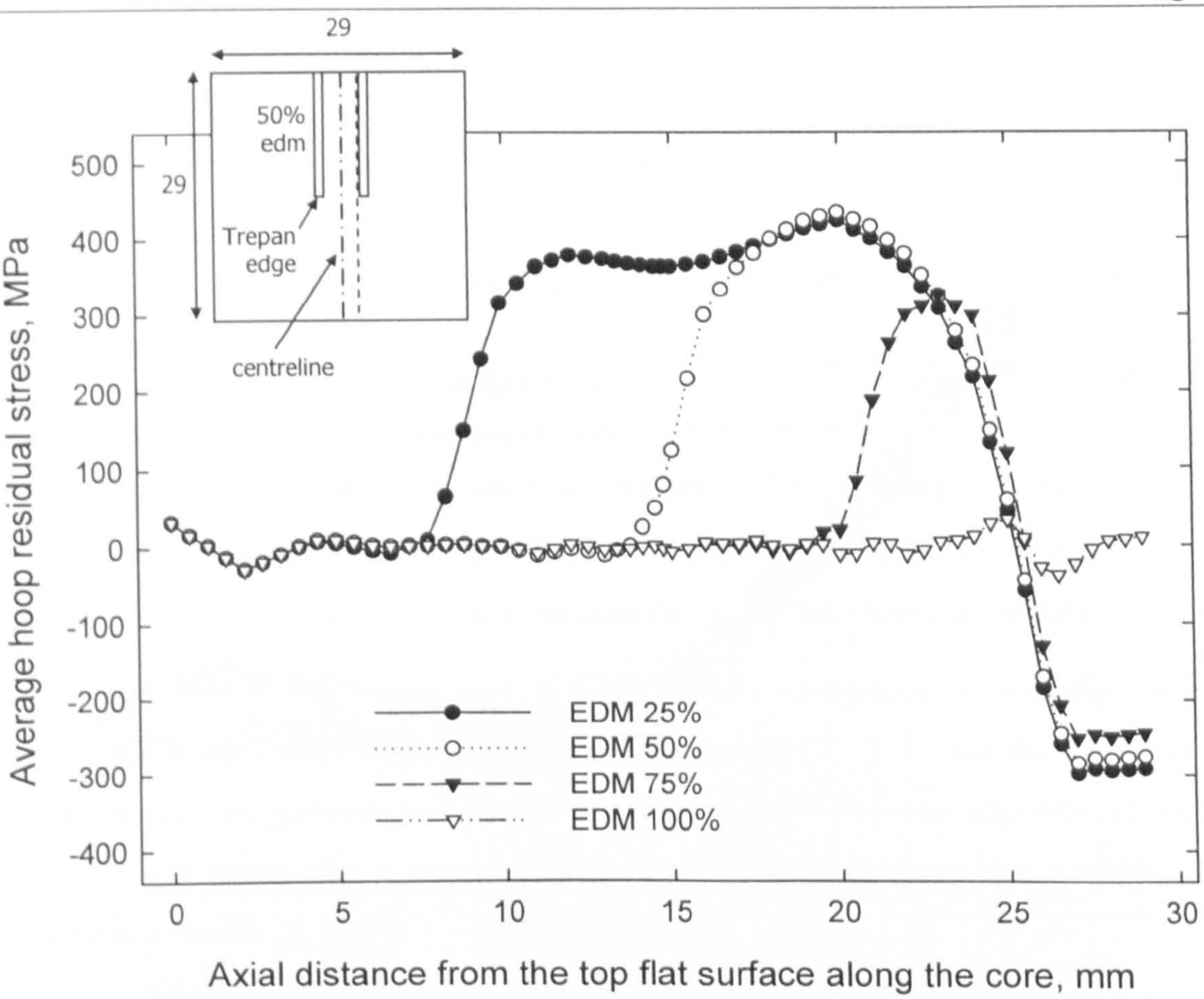

(c) Hoop component

Figure 9.3 FE predicted residual stress distribution (a) radial, (b) axial and (c) hoop components in the deep hole core for different edm trepan depths.

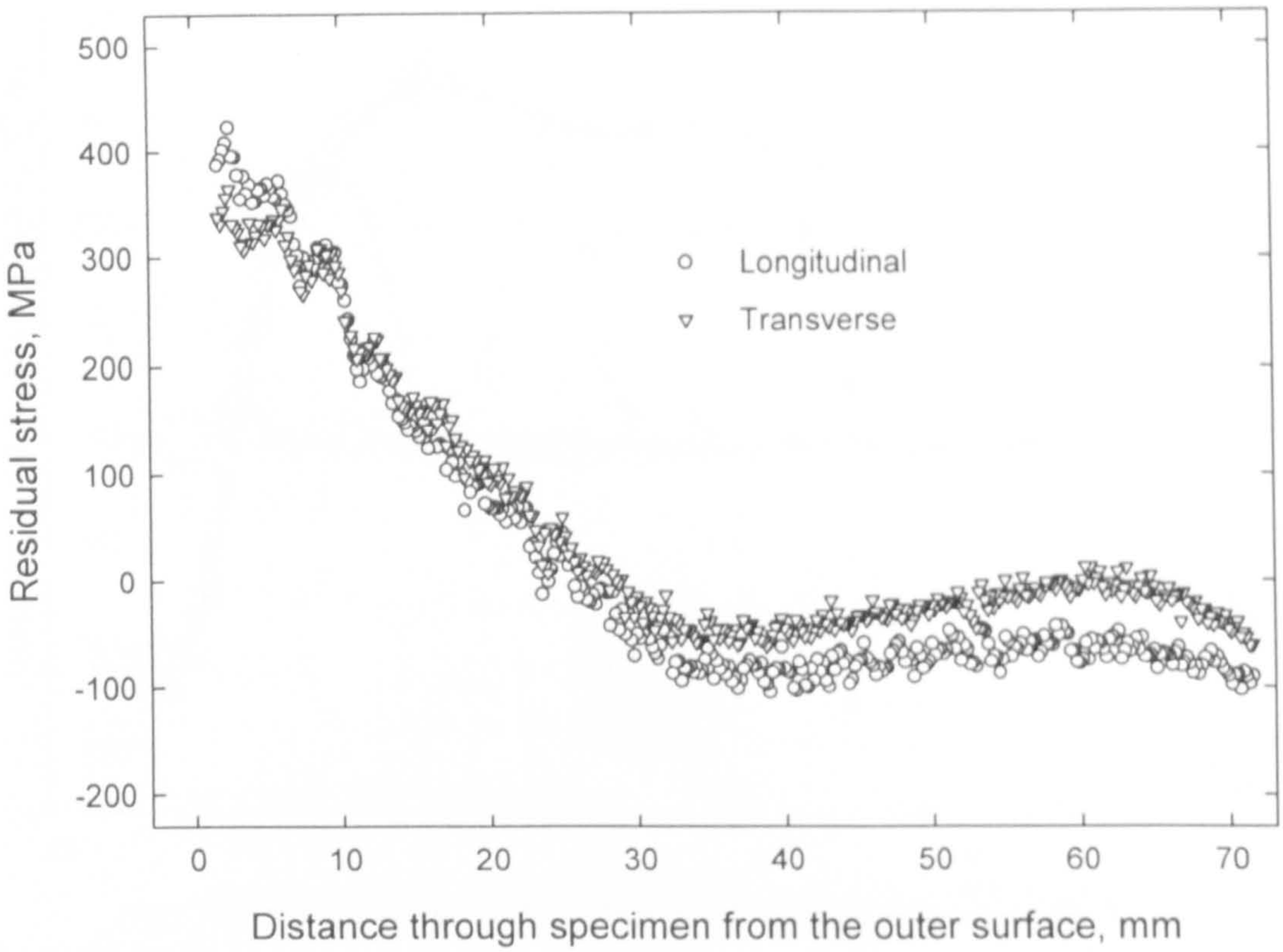

Figure 9.4 Measured residual stresses at the nozzle as-welded state at the flank position (Hole 1).

Appendix A

Mapping Methodology

The finite element interpolation process outlined in this section is for a two-dimensional element but also applies to three-dimensional elements [Tipping 2004]. The following assumes access to the shape functions that relate the GEOMETRY of the nodal topology to any local element coordinate (ξ, η). The shape function should also have the first differentials of the local coordinates w.r.t. the global coordinates.

For a finite element mesh the GEOMETRY is a continuous variable field defining the real space occupied by the mesh. Each global point (X, Y) in this field maps onto a single location in only one element (or on the boundary of several adjoining elements). As this point maps onto a single location in an element it also has a unique local element coordinate (ξ, η).

To find the local element coordinate for a given global point can be done using the simple iterative processes.

In global space:

$$(x, y)_{n+1} = (x, y)_n + (dx, dy)_n \tag{A-1}$$

which maps into the element local space:

$$(\xi, \eta)_{n+1} = (\xi, \eta)_n + (d\xi, d\eta)_n \tag{A-2}$$

From the initial guess for the initial guess for $(\xi, \eta)_n$ using the shape function and the GEOMETRY of the element topology gives an initial $(x, y)_n$. From which the global errors $(dx, dy)_n$ are:

$$dx_n = X - x_n \tag{A-3}$$

$$dy_n = Y - y_n \tag{A-4}$$

These global errors can be transformed into the element local coordinate system errors using:

$$dx = \frac{\partial x}{\partial \xi} d\xi + \frac{\partial x}{\partial \eta} d\eta \tag{A-5}$$

$$dy = \frac{\partial y}{\partial \xi} d\xi + \frac{\partial y}{\partial \eta} d\eta \tag{A-6}$$

Rewriting in matrix form:

$$\begin{bmatrix} dx \\ dy \end{bmatrix} = \begin{bmatrix} \frac{\partial x}{\partial \xi}, \frac{\partial x}{\partial \eta} \\ \frac{\partial y}{\partial \xi}, \frac{\partial y}{\partial \eta} \end{bmatrix} \begin{bmatrix} d\xi \\ d\eta \end{bmatrix} \tag{A-7}$$

Since the Jacobian matrix is:

$$[J] = \begin{bmatrix} \frac{\partial x}{\partial \xi}, \frac{\partial y}{\partial \xi} \\ \frac{\partial x}{\partial \eta}, \frac{\partial y}{\partial \eta} \end{bmatrix} \tag{A-8}$$

Therefore:

$$\begin{bmatrix} dx \\ dy \end{bmatrix} = [J]^T \begin{bmatrix} d\xi \\ d\eta \end{bmatrix} \tag{A-9}$$

and:

$$\begin{bmatrix} d\xi \\ d\eta \end{bmatrix} = [J]^{T-1} \begin{bmatrix} dx \\ dy \end{bmatrix} \tag{A-10}$$

The flow diagram for the interpolation process is shown below.

Note: If the global error is still large once the local error becomes small then the point lies outside of the current element and another element must be tried. It is also necessary to check that the local coordinate remains within the valid range (usually -1 to +1) unless extrapolation is to be allowed. Extrapolation should only be allowed for elements on the surface of the mesh. Once the correct (element, Local coordinate) has been found it can be used to interpolate any variable in that element.

Flow chart for interpolation process

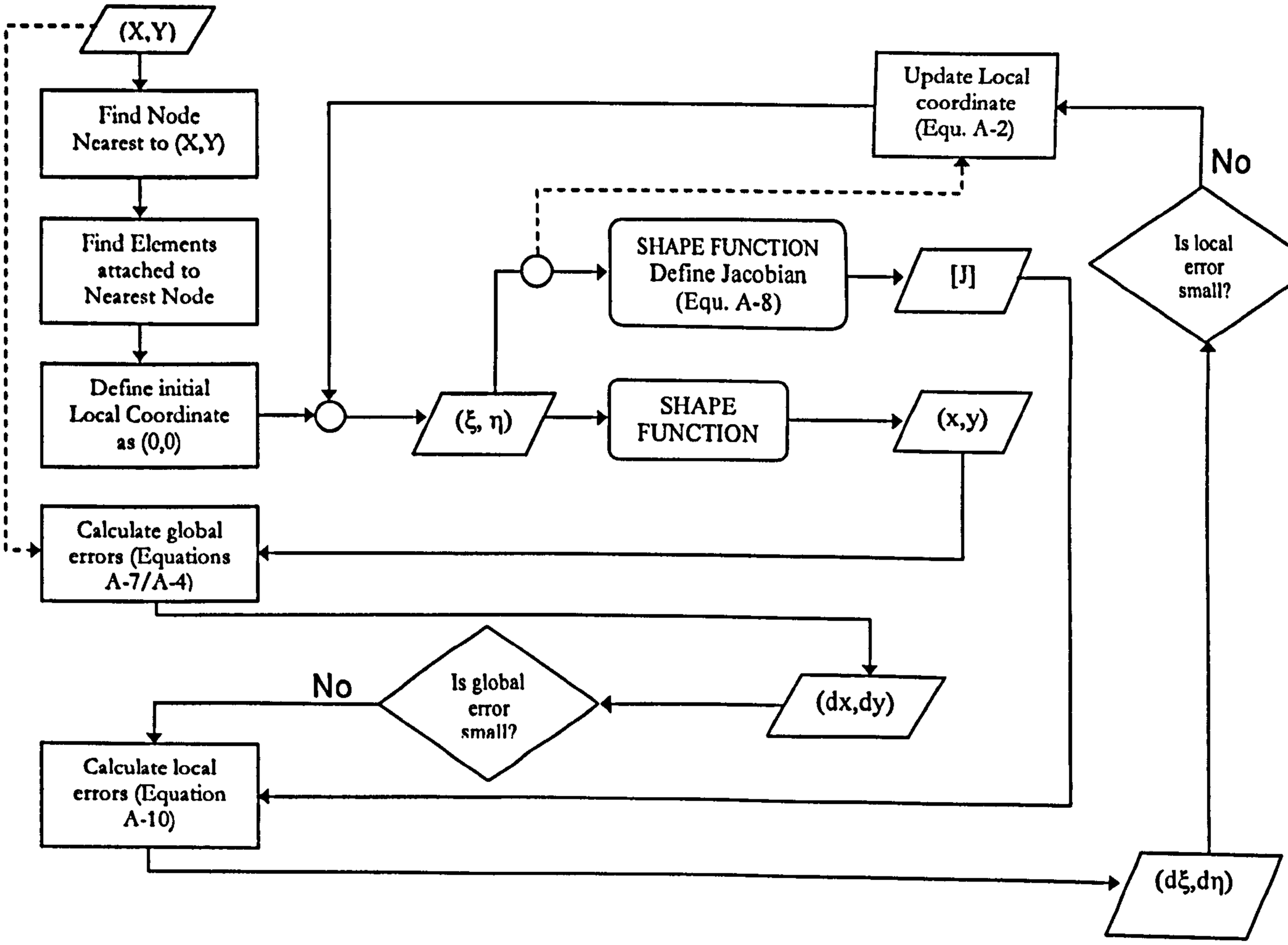

Appendix B

Tensile test of 35mm mock up

Tensile properties for type 316H stainless steel base material have been measured at room temperature and at a slow strain rate of 7.0×10^{-6} s^{-1}. The test specimens were machined from the base material extracted from a girth-welded pipe containing a repair weld. The general arrangement of the pipe is shown in Figure B-1 with the excavated material illustrated by the shaded region. Four tensile specimens were manufactured from the excavated material. The specimens of gauge length 65mm and gauge diameter 12.5mm were machined in the axial direction of the base pipe in accordance with the ASTM handbook.

Three student-type strain gauges were attached to each tensile test specimen. A quasi-static load was applied to the tensile specimen using the load instrument Instron in the workshop of the Department of Mechanical Engineering at the University of Bristol. A static load was applied at the rate of 0.003 mm/s with an upper limit of displacement-loading set at 30 mm. Figure B-2 shows the general arrangement of the test specimen held in position in the Instron rig. Also shown are the strain gauges attached to the specimen. The load versus time data was recorded in a data logger with a frequency of 10 scans per second. The strains from the strain gauges were simultaneously recorded as a function of time using the Measurement Smart System 6000. For this recording, a frequency of 10 scans per second was sufficient.

The strain history is shown in Figure B-3. Initially, the strain rises linearly with time before reaching a non-linear region about 150 seconds later, when the strain rate further increases and the strain continues to rise linearly. The strain gauges became insensitive after reaching a strain of about 16000με about 450 seconds later, at which point the strain readings were stopped.

The applied load history is shown in Figure B-4. The load increased linearly for the first 150 seconds. Therefore the load reached a non-linear region and the rate of loading decreased. This corresponded to the non-linear region in the strain history which is better illustrated in Figure B-5 where both load and strain are plotted with time. The stress was obtained by dividing the load by the original cross-section area of the test specimen. Figure B-6 shows these stresses plotted against the measured strains.

Young's modulus was then calculated to about 189 GPa and 0.2% proof stress (yield stress) to about 225 MPa. These material properties have been used in the finite element studies to generate residual stresses in a 35mm offset repair weld pipe using the block-dump welding analysis and the subsequent deep-hole simulation presented in Section 5.2.3.

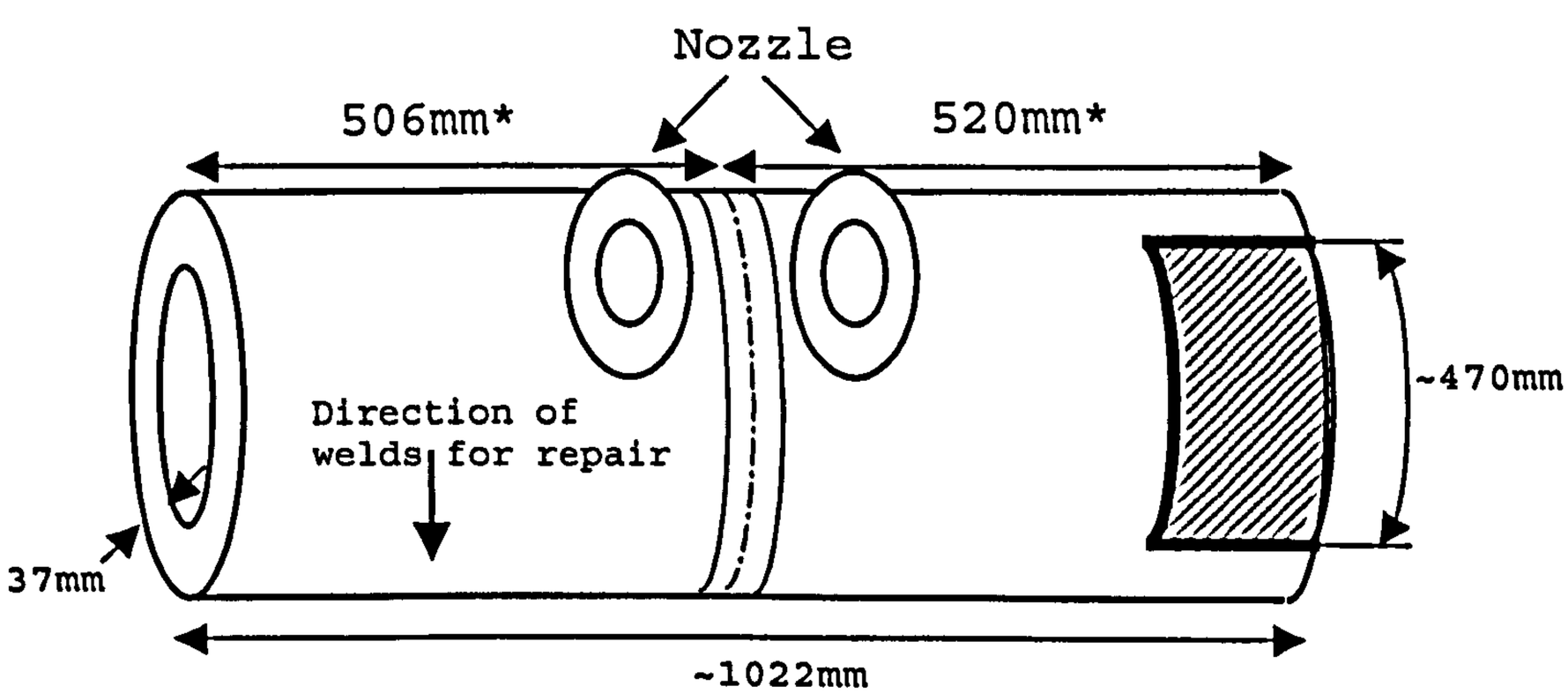

*Girth weld centreline measured from either ends at the centre of girth weld. Note - total length of pipe varies around the circumference, 1022mm is an approximate value.

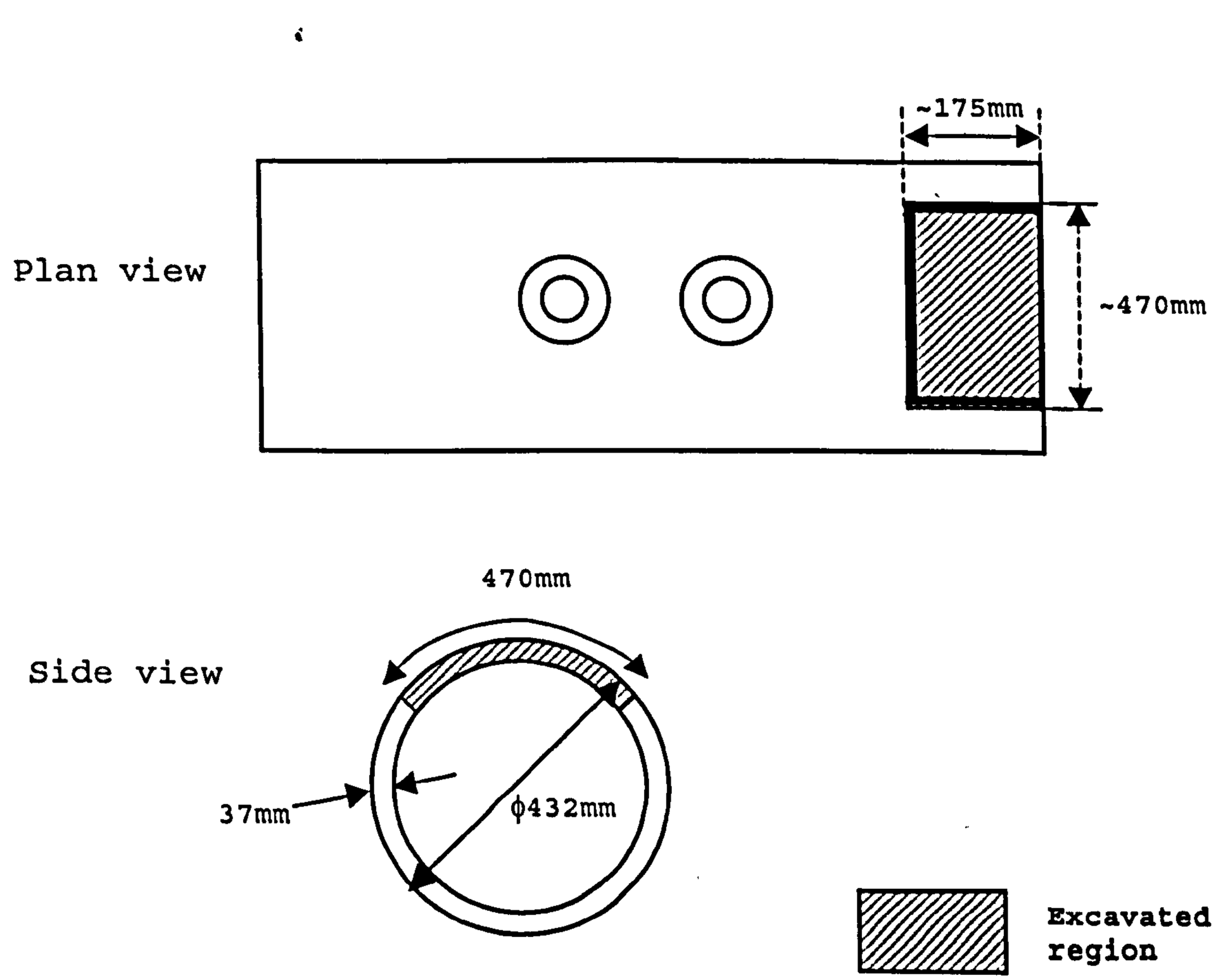

Figure B-1 General arrangement of girth welded pipe with a repair weld.

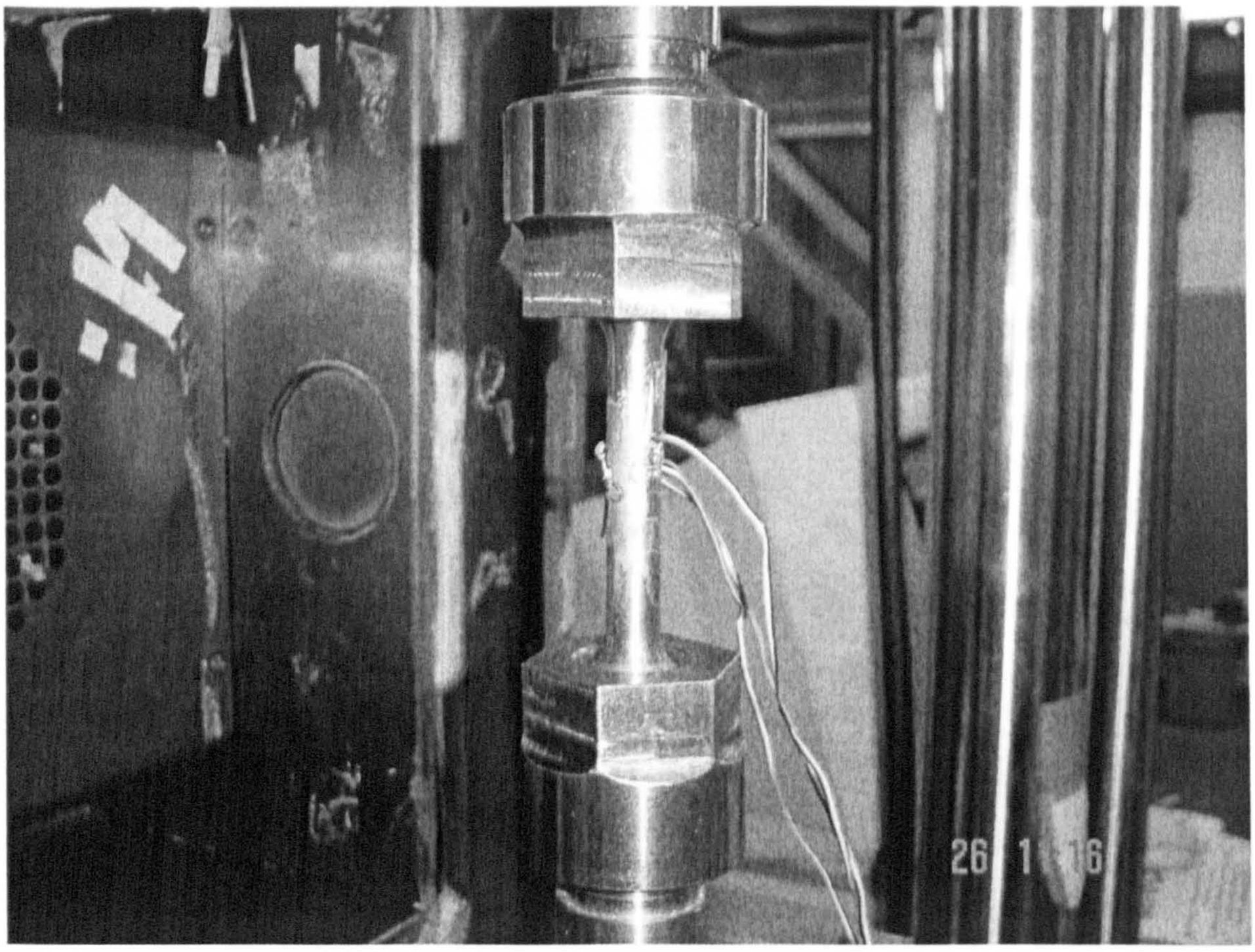

Figure B-2 Tensile specimen under loading using Instron. Three student type strain gages recorded the corresponding strains during loading.

Figure B-3 Measured strain history.

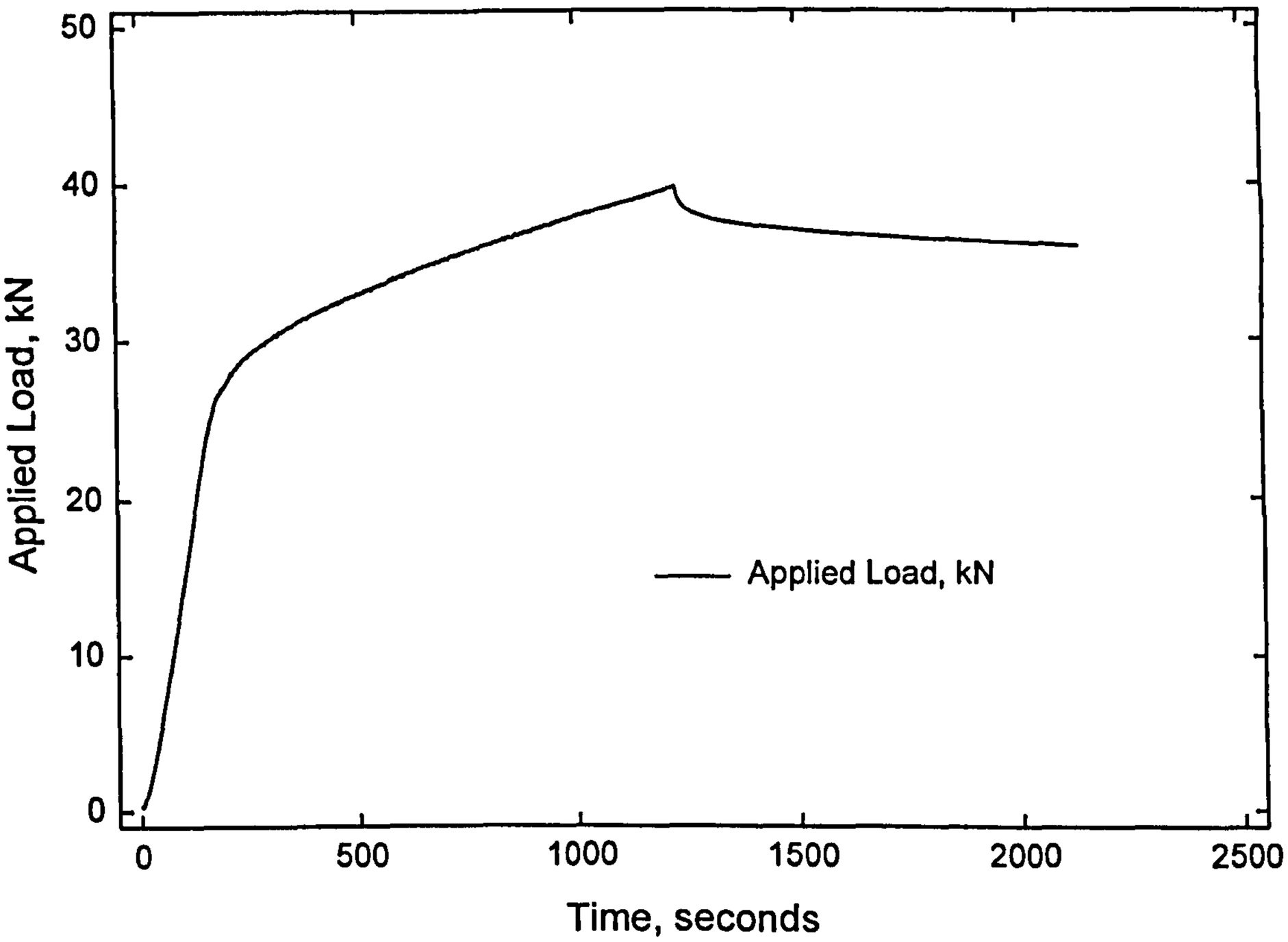

Figure B-4 Applied load history.

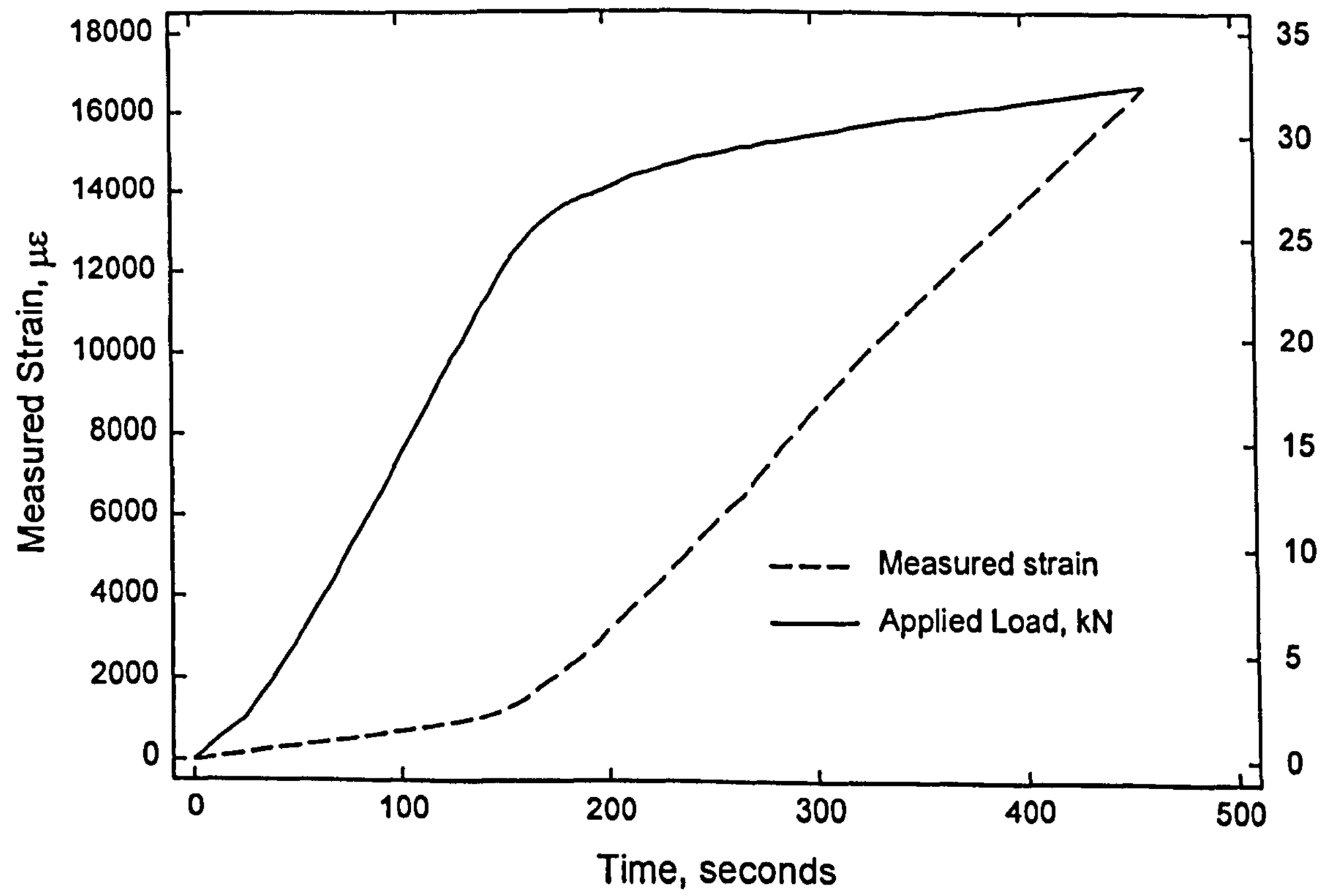

Figure B-5 Load-strain history.

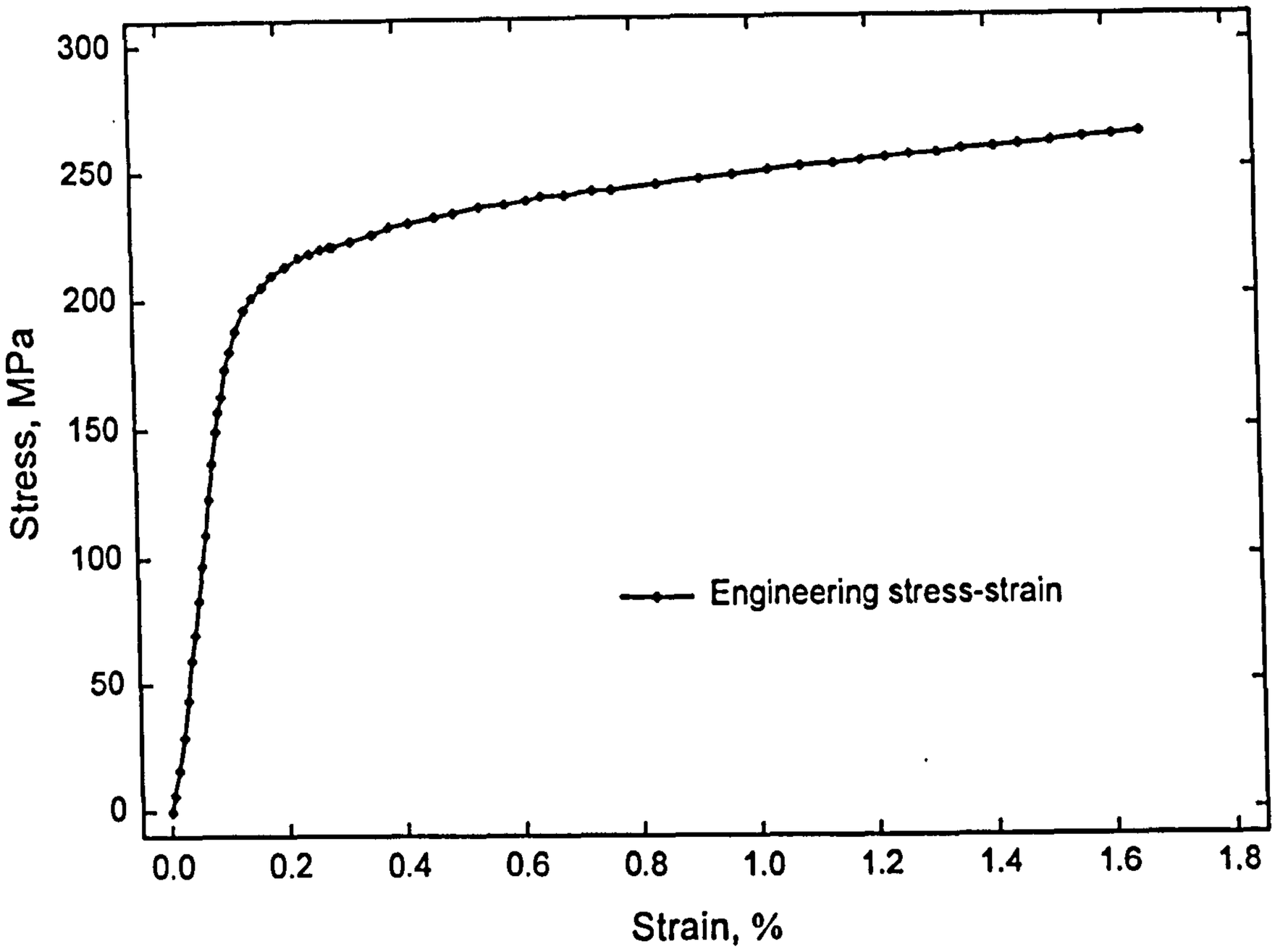

Figure B-6 Engineering stress-strain curve.